COMPUTATIONAL FLUID DYNAMICS EVALUATION OF PIPELINE GAS STRATIFICATION AT LOW FLUID FLOW DUE TO TEMPERATURE EFFECTS

A Thesis

by

PARDEEP SINGH BRAR

Submitted to the Office of Graduate Studies of
Texas A&M University
in partial fulfillment of the requirements for the degree of

MASTER OF SCIENCE

December 2004

Major Subject: Mechanical Engineering

COMPUTATIONAL FLUID DYNAMICS EVALUATION OF PIPELINE GAS STRATIFICATION AT LOW FLUID FLOW DUE TO TEMPERATURE EFFECTS

A Thesis

by

PARDEEP SINGH BRAR

Submitted to Texas A&M University
in partial fulfillment of the requirements
for the degree of

MASTER OF SCIENCE

Approved as to style and content by:

Gerald Morrison (Chair of Committee)	Dennis O'Neal (Member)
Stuart Scott (Member)	Dennis O'Neal (Head of Department)

December 2004

Major Subject: Mechanical Engineering

ABSTRACT

Computational Fluid Dynamics Evaluation of Pipeline Gas Stratification at Low Fluid Flow due to Temperature Effects. (December 2004)

Pardeep Singh Brar, B.E., Birla Institute of Technology

Chair of Advisory Committee: Dr. Gerald Morrison

It has been found through experiments at Southwest Research Institute that temperature differences between the gas and wall of the pipe through which the gas is flowing can greatly influence the gas flow in the pipe line and give different velocity magnitudes at the top and bottom half of the pipe. The effect on the flow is observed to worsen at low fluid flow and high temperature differences. This effect has been observed by ultrasonic flow meters which measure the chord average gas velocity at four heights across the pipe. A significant variance in chord averaged velocities is apparent at these conditions. CFD analysis was performed. Low flow velocities of 0.1524 m/sec, 0.3048 m/sec and 0.6096 m/sec and temperature differences of 5.5°K, 13.8°K and 27.7°K were considered. When these conditions were imposed onto the three different geometries, it was seen that the heating caused increased errors in the ultrasonic meter response. For the single elbow and double elbow pipe configurations, the errors were below 0.5% for constant wall temperature conditions but rose to 1% for sinusoid varying wall temperature conditions. The error was seen to increase as the axial velocity became more stratified due to momentum or temperature effects. The case of maximum error was noted for the double

elbow geometry with sinusoid wall temperature condition where a swirl type of flow was noted to create localized velocity maxima at the center of the pipe. This part of the pipe was barely touched by the ultrasonic meter acoustic path giving maximum error of 1.4%. A thermal well was placed in the path of the gas flow in the pipe to observe the temperature response on the surface of the thermal well. It was noted that the thermal well surface temperature differed by 1.4% for most cases with gas velocity below 0.6096 m/sec.

DEDICATION

To my family for their love and support.

ACKNOWLEDGMENTS

I would like to express my gratitude to Dr. Gerald Morrison for his valuable guidance and support. I sincerely appreciate his time, effort and patience throughout the duration of my thesis project.

I wish to thank Dr. Dennis O'Neal and Dr. Stuart Scott for their counsel and support during the project.

A big thank you to GTI for their support without which this project would not have been initiated, let alone completed.

I would also like to thank my friends Ammar, Anil, Budz, Greg, Mabbu, Manny, Hari, Rimz, Soyuz and VJ for their company and support during my thesis research.

.

TABLE OF CONTENTS

CHAPTER Page

LIST OF FIGURES

FIGURE Page

FIGURE Page

LIST OF TABLES

CHAPTER I

INTRODUCTION

1.1 Background

Gas stratification in pipe flow has received much attention due to its potential to lead to incorrect measurements of temperature, velocity, density and flow rate. This is highly undesirable for the oil and gas industries that transport gases from the well to the consumers. Usually metering runs in pipelines carrying gases are exposed to ambient air. Buried pipelines have metering runs above ground. Air temperatures might be hotter or colder than the gas temperature. On a hot day, it is possible that the top half of the pipeline that is exposed to the solar radiation tends to get hotter compared to the bottom half of the pipeline which is unexposed. This causes a difference in temperature on the top and bottom half of the pipeline which in turn can cause a density change in the layers of the gas flowing in the pipe. The gas in the top half of the pipeline will get hotter and hence lighter compared to the bottom half. This can lead to varying measurements of velocity at different heights along a cross section of the pipeline. The case is similar for a very cold night where the top half of the pipeline can get colder due to radiant cooling to the sky than the half not exposed to the sky. The gas flow will tend to vary along the

---

This thesis follows the style of ASME *Journal of Fluids Engineering*.

pipeline and might behave in a different manner than expected. It was found through experiments at Southwest Research Institute that temperature differences between the wall of the pipeline and the gas can greatly influence the gas flow in the pipeline producing different velocities in the top and bottom half of the pipe. The flow was observed to worsen at low fluid flow (which increases the probability of gas stratification) and high temperature differences (which increases the probability of a density gradient across the pipe cross section). This effect was measured by Ultrasonic flow meters which measure the chord average gas velocity at various heights across the pipe. A significant variance in chord averaged velocities was apparent at these conditions. In further experiments at SwRI conducted by Dr. Thomas Morrow, it was noted that static gas pressure can also cause incorrect measurements of velocity profile through density and viscosity changes. This has led to the investigation of the exact behavior of gas flow through the metering run by using computational fluid dynamics (CFD). The main purpose of this research is to note the response of the ultrasonic meter to different boundary conditions and gas flow patterns. The ultrasonic flow meter measures the average velocity on four chords which cross the pipe and are at different heights. This produces an averaging effect. However, temperatures are measured at a single point in a thermal well. The accuracy of this point measurement will be investigated.

1.2 CFD Approach

CFD analysis is widely used in aerospace, automotive and biomedical engineering. CFD has been used to study heat transfer and fluid flow problems. Initially it was used to confirm experimental results, but now it is used to determine solutions to problems which are otherwise difficult to solve through experiments. The boundary conditions used in the computations must include field like conditions so there can be proper correspondence between the experimental results and numerical results.

1.3 Objectives

The objectives of this research are to simulate three different pipe flows at flow rates below 0.6096 m/sec (2 ft/sec) with varying pipe wall temperatures to determine to what extent the fluid flow is varied by the heat transfer. The affects of temperature, velocity and density gradients generated by the heat transfer upon the flow field, ultrasonic flow meter response and thermal well response were observed.

CHAPTER II

PROBLEM MODEL AND DESCRIPTION

2.1 Setting GAMBIT and FLUENT Conditions

The geometries were built and meshed using GAMBIT 2.0 and boundary conditions were applied using the commercial code Fluent 6.1.22 [1].

The simulations were for gas flow through a pipe of a constant diameter 0.3048 m (12 inch) with the inlet gas temperature, operating pressure and wall temperature conditions specified. Simulations for three different inlet flow rates and different temperature conditions were performed. The following assumptions were made to solve the problem:

1) Turbulence Model: The parameters ρ , D and μ were constant at the inlet. For the lowest flow rate, the Reynolds Number (Re_D) was 220,000; hence the flow was fully turbulent. It was of great importance to choose the turbulence model that encapsulates the physics of the flow and produces the most realistic results. The turbulence model used for this study was the RNG $K-\varepsilon$ model. (Yakhot and Orszag 1986). The RNG $K-\varepsilon$ model in Fluent 6.1.22 claims to produce more realistic results for a wide range of fluid flows including heat transfer. The standard $K-\varepsilon$ method yields large turbulent diffusivity and leads to unrealistic results for gas flow. The difference between the standard $K-\varepsilon$ model and RNG $K-\varepsilon$ method appears in the ε (epsilon) equation.

2) Buoyancy: The Richardson Number (Ri) is an excellent basis for deciding whether to include buoyant forces (free convection) in the equations to be solved. Buoyancy is considered very important in case $Ri = Gr / Re^2 > 1$. The density gradient is very important because of the presence of temperature differences on the top and bottom of the pipe. Ri was found to be greater than one for this study and hence the effects of buoyancy are included in the simulations.

2.2 Equations

The RNG $\kappa - \varepsilon$ model is derived from the instantaneous Navier Stokes Equations. The differential transport equations for κ and ε are:

$$\frac{\partial \rho \kappa}{\partial t} + \frac{\partial \rho u_i \kappa}{\partial x_i} = \frac{\partial}{\partial x_i}\left[\frac{\mu}{\sigma_k}\frac{\partial \kappa}{\partial x_i}\right] + G_k - \rho\varepsilon \tag{1}$$

$$\frac{\partial \rho \varepsilon}{\partial t} + \frac{\partial \rho u_i \varepsilon}{\partial x} = \frac{\partial}{\partial x}\left[\frac{\mu}{\sigma_\varepsilon}\frac{\partial \varepsilon}{\partial x_i}\right] + C_1\frac{\varepsilon}{\kappa}G_\kappa - C_2\rho\frac{\varepsilon^2}{\kappa} \tag{2}$$

where G_k is the generation term for κ and is given by:

$$G_{k=}\mu_t\left[\frac{\partial u_j}{\partial x_l}+\frac{\partial u_l}{\partial x_j}\right]\frac{\partial u_j}{\partial x_l} \tag{3}$$

and the effective viscosity is given by:

$$\mu_t = \rho C_\mu \frac{\kappa^2}{\varepsilon} \tag{4}$$

The coefficients used were:

C_1=1.44, C_2=1.92, C_μ=0.09, σ_k=1.0 and σ_ε=1.3.

2.3 Dimensions, Grid and Boundary Conditions

The grid was made of primarily hexahedral cells. Three pipe geometries are considered. The first is a straight pipe of 100 diameters (100 D) length. The second geometry is a 5 D straight pipe followed by a 90° elbow and another straight pipe. The third arrangement is the straight pipe preceded by two 90° elbows out of plane separated by 5 D of straight pipe. All geometries include a one hundred diameter length of horizontal straight pipe before the exit. The inlet of this straight length of the pipe is located at the center of the coordinate axes. Only the straight pipe case includes a thermal well which is used to measure the temperature of the flowing gas in the meter run. The thermal well was meshed separately using tetrahedral cells. The difficulty encountered in building the grid was the mapping together all other areas of interest consistently. GAMBIT's Cooper

Algorithm was used for meshing all curved (non-rectangular) surfaces. The dimensions of the model are as shown in Table 1.

Table 1 – Dimensions of the model.

NAME	MEASURE (Meters)
Nominal Diameter	0.3048
Z – Direction (Direction of Flow)	100 x D = 30.48 (from Inlet)
Elbow Radius	0.3048
Short Straight Pipe Length	5 x D = 1.524
Elbow Angle	90 Degrees

Figures 1 - 6 show the three types of geometries considered for this research.

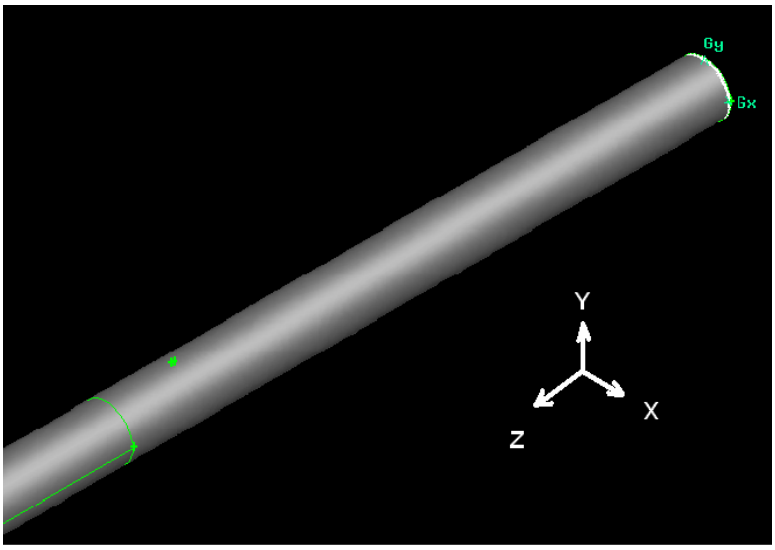

Figure 1 - Shaded view of straight pipe.

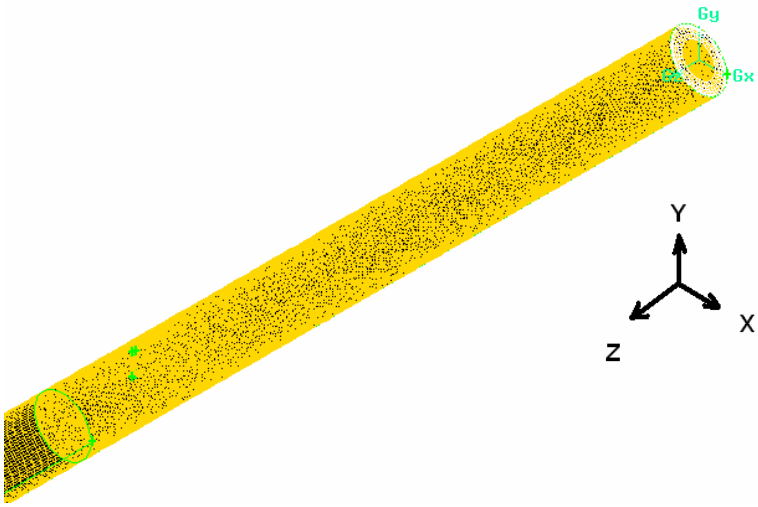

Figure 2 - Grid view of straight pipe.

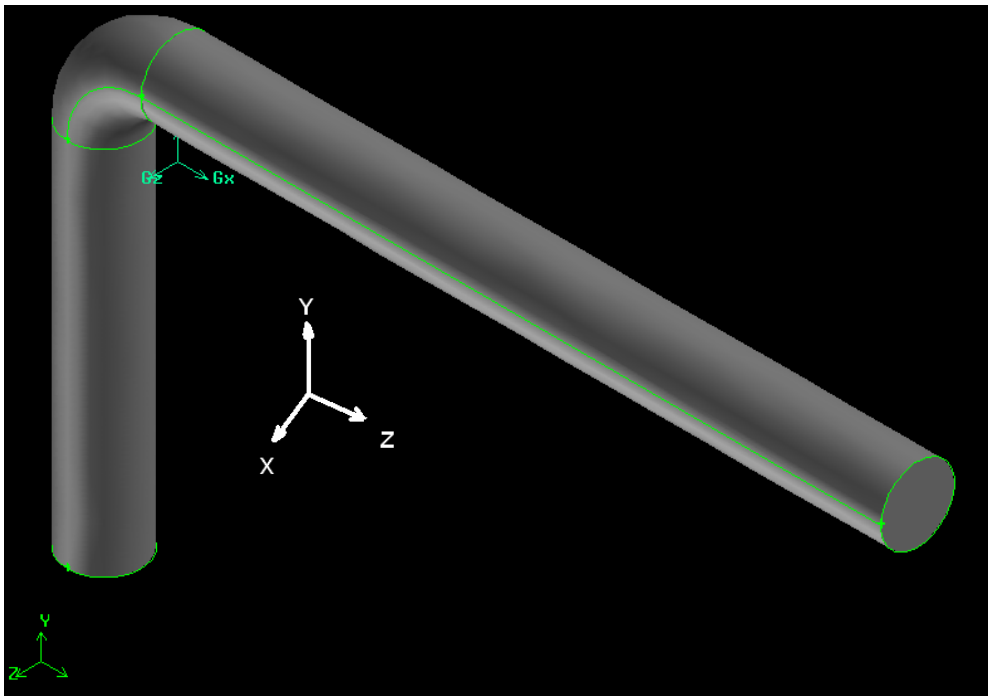

Figure 3 - Shaded view of pipe with single elbow.

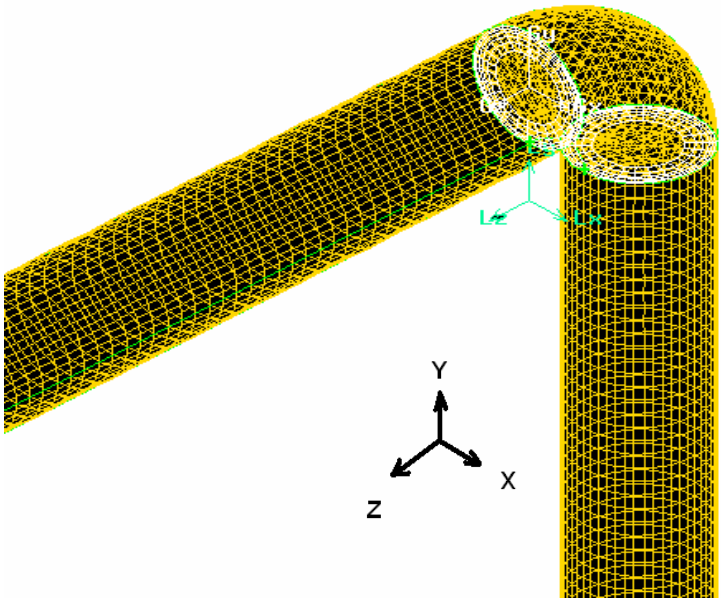

Figure 4 - Grid view of pipe with single elbow.

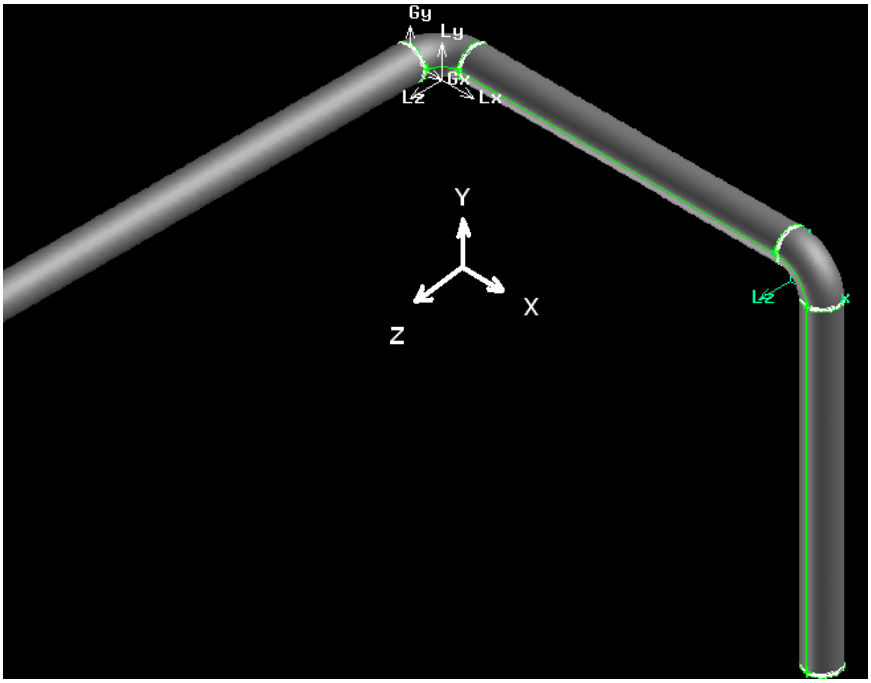

Figure 5 - Shaded view of double elbow pipe.

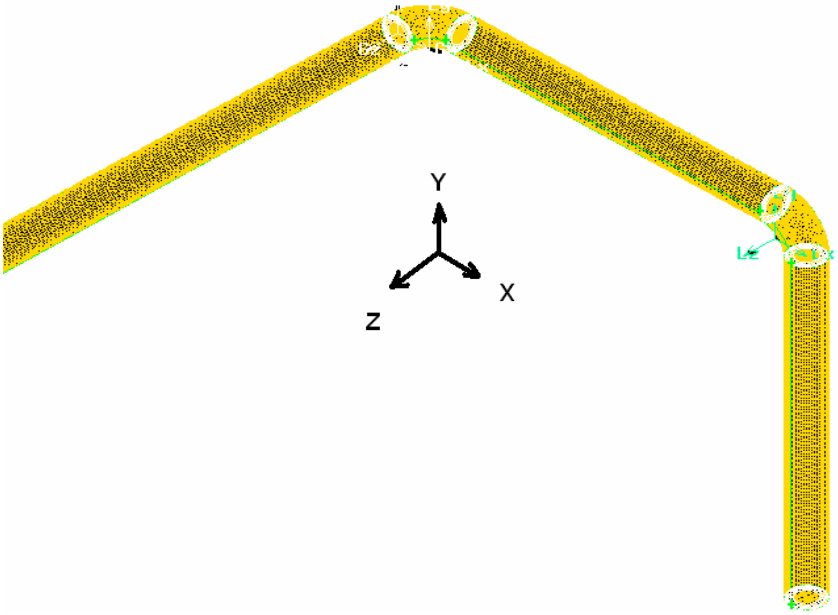

Figure 6 - Grid view of double elbow pipe.

The mesh size is approximately 240,000 nodes. The grid spacing is kept at 0.5 units for hexahedral cells and 0.3 units for tetrahedral cells. The inlet, exit and elbows of the pipe line were gridded using boundary layer meshes of size 0.05 units. It was estimated that the overall Y^+ value of less than 500 in all cases for all associated boundary conditions would produce realistic results. Grid size returning Y^+ values higher than 500 were refined using Grid Adaptation and were run again for more realistic results. The geometry was checked for acceptable accuracy using GAMBIT's mesh examination tool. The following are the boundary conditions (Table 2).

Table 2 – Boundary conditions applied to the geometry.

DESCRIPTION	BOUNDARY CONDITIONS
Inlet	Velocity Inlet
Exit	Pressure Outlet
Walls	No-slip Condition
Walls – Temperature Variation	No-slip Condition
T - Well	No-slip Condition

2.4 Heat Transfer on Thermal Well

T-Well condition is the boundary condition used in cases where the geometry includes a thermal well. Walls-Temperature Variation is present as a boundary condition when a non-uniform temperature variation is used on the walls to simulate radiant heating or cooling. The heat flow condition on the T-well wall is set up as a Convective boundary condition and a constant heat transfer coefficient is given as an input for accurate heat transfer analysis across the cylinder. The heat transfer coefficient (h) was determined using the expression give by Churchill and Bernstein mentioned in Incropera and DeWitt [2].

$$\mathrm{Nu_D} = 0.3 + \frac{0.62\,\mathrm{Re}_D^{\frac{1}{2}}\,\mathrm{Pr}^{\frac{1}{3}}}{\left[1+\left(0.4/\mathrm{Pr}\right)^{\frac{2}{3}}\right]^{\frac{1}{4}}}\left[1+\left(\frac{\mathrm{Re}_D}{282000}\right)^{\frac{5}{8}}\right]^{\frac{4}{5}} \tag{5}$$

Also, a varying heat transfer coefficient value is used on the cylinder, when the pipeline temperature is constant, to enhance the accuracy of the heat transfer analysis. The varying heat transfer coefficient (h) was determined over the cylinder from experimentally obtained graphs and correlations mentioned in NACA TM 1050 [3] and Fage & Falkner [4]. Using this graph, the values of Nu with changing circumferential angle were found for the three different Reynolds number cases which were investigated. It is noted that the heat transfer coefficient (h) depends, on the Re of the flow and on the

location on the cylindrical surface. Here, the cylindrical surface is the surface of thermal well. Hence, we can write the relation:

$$\mathbf{Nu = f\,(Re, \phi)}$$

It was observed through experiments [3, 4] that the heat transfer coefficient drops to a minimum just before $\phi = \mathbf{90^o}$. It rises again till the back of the thermal well. The results are assumed to be symmetrical and same behavior is expected on the other side of the thermal well.

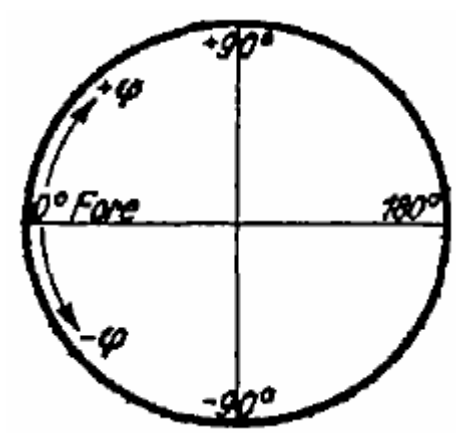

Figure 7 - Angle measured from forward stagnation point in the direction of fluid flow [3].

Figure 7 shows the angle being measured from the forward stagnation point for the flow flowing from left to right in the above case. Figure 8 shows the Nusselt number distribution along ϕ for different Reynolds number flows.

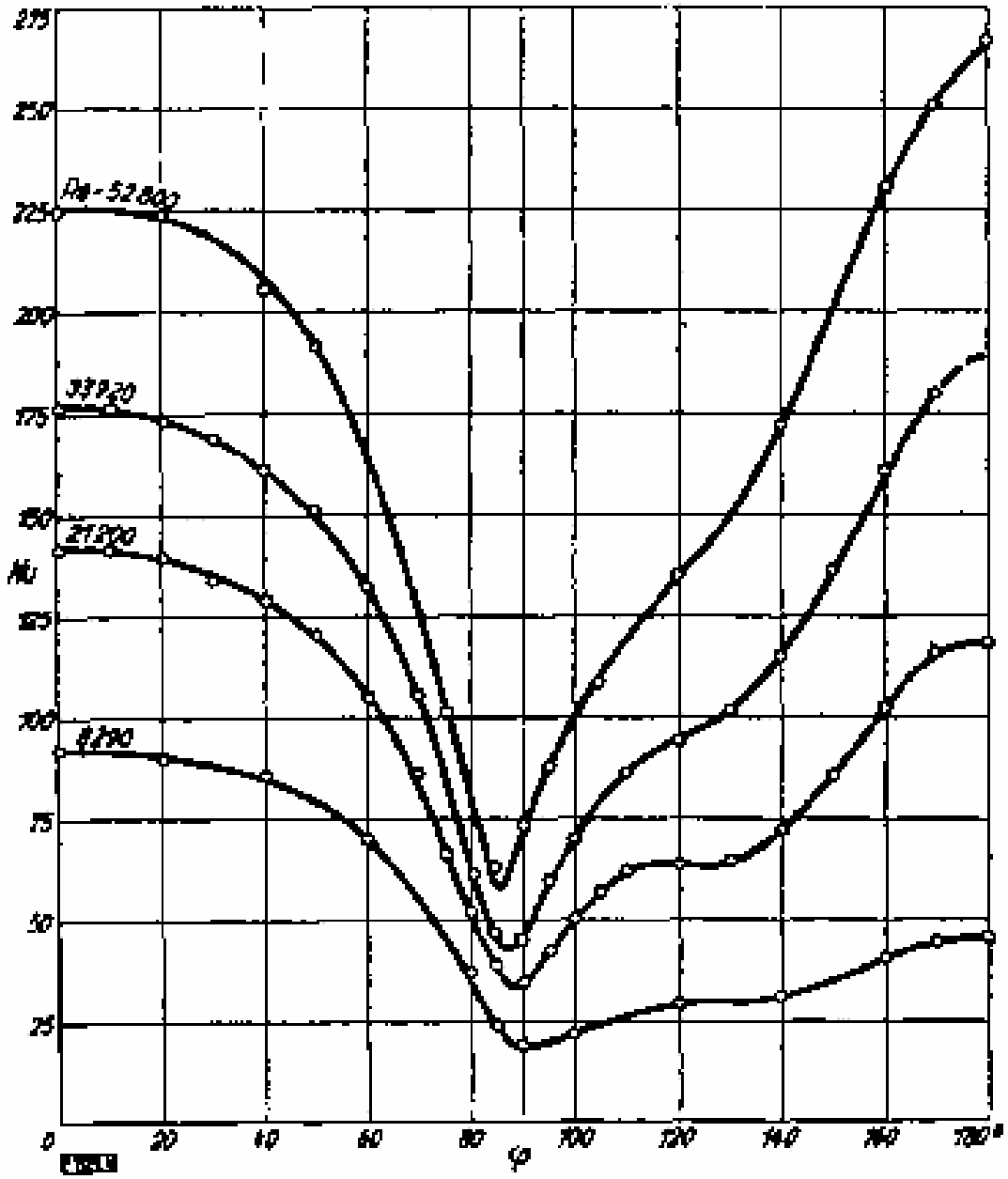

Figure 8 - Nu vs. circumferential angle for different Reynolds number [3].

In addition to the computational analysis of temperature distribution on the surface of the thermal well, we performed theoretical analysis on the thermal well. This helps determine whether a simple analytical solution will produce adequate results.

A one dimensional finite difference method was used to solve the energy equation for the thermal well. The thermal well is a hollow cylinder that is 0.1143 m long and 0.01905 m in diameter which is inserted into the flow radially from the pipe wall. It is made of plain carbon steel having thermal conductivity of 16.27 W/m-K.

The inside of the cylinder (hollow) is taken as an insulated wall whereas conduction takes place through the material and convection on the outside surface due to gas flow having different temperatures. We know the wall temperature of the pipe and so know the temperature at the closed end of the thermal well. It is important for our analysis to consider the temperature distribution at the surface, especially at the free end of the thermal well. The following figure shows us the energy balance performed on a thermal well element about the nodal region (center point of element). Conduction acts within the material as is shown and the inside of the hollow cylinder is taken as hollow. Convection acts on the surface of the cylinder.

As our case is that of steady state, we have the following energy equation.

$E_{in} + E_g = 0$

As in our case there is no heat generation, $E_g = 0$ and are left with $E_{in} = 0$. We have made certain assumptions in writing the equations for the thermal well. It can be seen that the

length/diameter (L/D) ratio is very large for this case – so we can assume the system to be a 1-D problem and hence solve the problem as a one dimensional case. We can take our new system to be as in Figure 9. Figure 10 shows one control volume of the thermal well along its length.

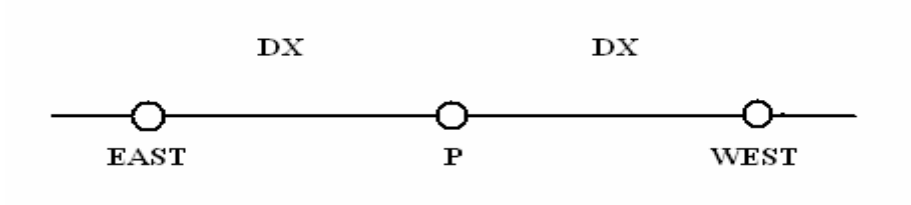

Figure 9 – The nodal form of the system.

The control volume can be broken into a number of such control volumes and a conservation equation will be written for each of the nodes of unknown temperature. Each control volume has an east end (E) and a west end (W) and all equations of that node is made with reference to node P. DX is the distance between the nodes which is taken to be uniform here, that is we have considered a uniform grid. Let us assume we know the east end to be the left most node of the system-next to the pipe wall, which is TE (known). Both conduction and convection effects are seen at the end of the nodal system.

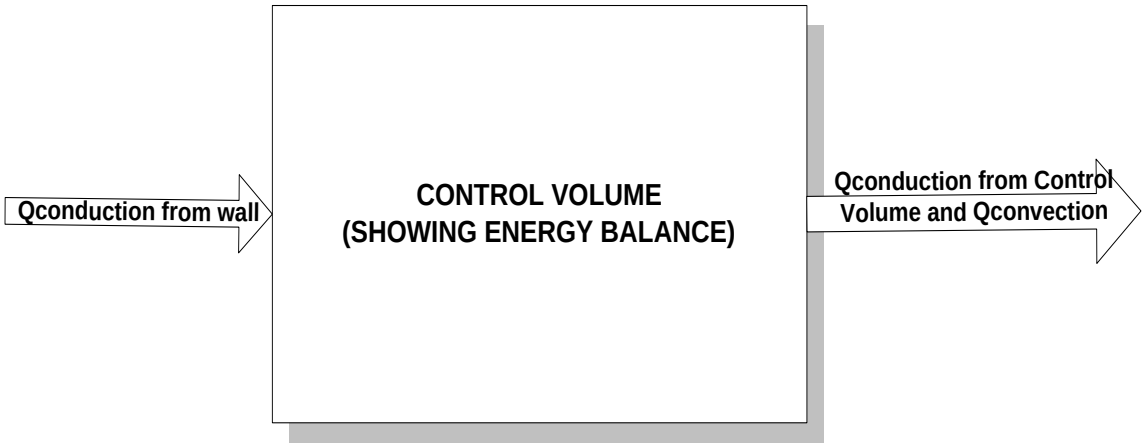

Figure 10 –Energy flow through the system.

The energy balance of the above system can be written as:

$$Q_{conduction} = Q_{conduction} + \frac{\partial \text{Qconduction}}{\partial x} dx + Q_{convection}$$

where

$$Q_{conduction} = -k*A*\frac{dT}{dx}$$

$$Q_{convection} = h*A*\Delta T$$

On simplifying the above equation, applying forward difference and integrating both sides from west (W) to east (E), we get the following form of equation:

$$\frac{k_E A_E (T_E - T_P)}{\delta x_E} - \frac{k_W A_W (T_P - T_W)}{\delta x_W} = 2\pi r h * (T_P - T_\infty) * \Delta x$$

This is the general equation for this system and can be applied to any control volume. These equations are calculated for each node and a matrix is formed such that [A] [T] =[C] where A is the coefficient matrix (square matrix), T is the matrix of unknown temperatures and C is the matrix of constants made available from the system of equations.

[T]= [A^{-1}] [C] will give us the required column matrix of temperatures at different nodes. Figure 11 is the code written in FORTRAN 90 so as to carry out the above mentioned procedure.

```
!! PROGRAM TO FIND TEMPERATURE DISTRIBUTION ON THERMAL WELL
IMPLICIT NONE
INTEGER I,N
PARAMETER (N = 40)
DOUBLE PRECISION KE,KW,DXW,DXE,AW,AP,AE,A,B,T
DOUBLE PRECISION PI,R,AREA,PER,H,TAMB,Ta,L
OPEN (UNIT=50,FILE="INPUT.TXT")
OPEN (UNIT=1, FILE="A.TXT")
OPEN (UNIT=2, FILE="B.TXT")
OPEN (UNIT=3, FILE="T.TXT")
DIMENSION
```

Figure 11 – Program to solve for temperature distribution on surface of thermal well.

```
KE(N),KW(N),DXW(N),DXE(N),AW(N),AP(N),AE(N),A(N,3),B(N),T(N+2)
!! CONSTANTS AND GIVEN BOUNDARY CONDITIONS
READ (50,*)R
READ (50,*)L
READ (50,*)H
READ (50,*)Ta
READ (50,*)TAMB
PI = 4.0d0*(ATAN(1.0d0))
AREA = PI*R*R   !Cross sectional area
PER = 2.0d0*PI*R !Perimeter
DO 10 I = 1,N
KE(I) = 16.27d0
KW(I) = 16.27d0
DXE(I) = L/N
DXW(I) = L/N
10 CONTINUE
!! MATRIX INITIALIZATION FOR TDMA ALGORITHM

DO 20 I = 1,N
AW(I) = KW(I)*AREA/DXW(I)
AE(I) = KE(I)*AREA/DXE(I)
```

Figure 11 – Continued.

```
AP(I) = (AW(I) + AE(I)) + H*PER*(DXW(I)+DXE(I))/2.0d0
B(I) = H*PER*(DXW(I)+DXE(I))*TAMB/2.0d0
20 CONTINUE
!! BOUNDARY CONDITIONS
AP(1) = (AE(1) + 2.0d0*AW(1)) + H*PER*(DXW(1)+DXE(1))/2.0do
B(1) = B(1) + 2.0d0*AW(1)*Ta
!IMPLEMENTING THE NEUMANN BOUNDARY CONDITION
AP(N) = AW(N) +  H*PER*(DXW(N)+DXE(N))/2.0d0
B(N) = H*PER*(DXW(N)+DXE(N))*TAMB/2.0d0
!REMOVING THE EFFECT OF THE BOUNDARY POINTS
AW(1) = 0.0d0
AE(N) = 0.0d0
DO I = 1, N
A(I,1) = -AW(I)
A(I,2) = AP(I)
A(I,3) = -AE(I)
END DO
WRITE (1,100) (A(I,1),A(I,2),A(I,3),I=1,N)
WRITE (2,101) (B(I),I=1,N)
CALL THOMAS(N,A,B)
! WRITING THE TEMPERATURE SOLUTION MATRIX
```

Figure 11 – Continued.

```
T(1) = Ta
T(N+2) = B(N)
DO I = 1,N
T(I+1) = B(I)
END DO
WRITE (3,101) (T(I),I=1,N+2)
100 FORMAT (F16.10,F16.10,F16.10)
101 FORMAT (F16.10)
150 FORMAT (6F6.3)
STOP
END
!!      TDMA SUBROUTINE ALGORITHM
SUBROUTINE THOMAS(N,A,B)
!       Algorithm to solve a tri-diagonal system
!       N: Number of Equations
!       B: Solution Vector
INTEGER I,N
DOUBLE PRECISION A,B
DIMENSION A(N,3),B(N)
A(1,3) = -A(1,3)/A(1,2)
B(1) = B(1) / A(1,2)
DO I=2,N
```

Figure 11 – Continued.

```
A(I,3) = -A(I,3) / (A(I,2)+A(I,1)*A(I-1,3))

B(I) = (B(I)-A(I,1)*B(I-1)) / (A(I,2)+A(I,1)*A(I-1,3))

END DO
DO I = N-1, 1, -1

B(I) = A(I,3)*B(I+1)+B(I)

END DO

RETURN

END
```

Figure 11 – Continued.

CHAPTER III

SIMULATIONS

3.1 Geometry Shapes

All simulations were run using the FLUENT [1] computer code, version 6.1.22. In order to analyze gas flow through pipelines, three different geometries were selected and agreed upon by SwRI, TAMU and Gas Research Institute (GRI). All pipes are of 0.3048 m (12 inch) nominal diameter, 7.8740 x 10^{-4} m (0.031 inch) wall thickness and made of plain carbon steel. The three geometries are as follows:

1) 100 diameters length straight horizontal pipe with thermal well located at 5 diameters length from the inlet of the pipe on the top of the pipe.

2) 5 diameters length straight vertical pipe with a 90 degree bend followed by 100 diameters length straight horizontal pipe.

3) Two 5 diameters length straight pipes with 90 degree out of plane bends followed by 100 diameters length straight pipe. The elbows are all out of plane such that all three straight pipes are orthogonal to each other.

The thermal well is of 0.01905 m (0.75 inch) nominal diameter, 0.1143 m (4.5 inch) length and 6.35 x 10^{-3} m (0.25 inches) wall thickness.

3.2 Inlet Conditions

The bulk average velocities are 0.1524 m/s (½ ft/s), 0.3048 m/s (1 ft/s) and 0.6096 m/s (2 ft/s). As mentioned above, the first geometry will include a thermal well in its flow path having dimensions commonly used by gas industries. The flow at the pipe inlet will be fully developed pipe flow depicting flow across any cross section in a long pipeline. These values were obtained by running a simulation on a pipe with similar boundary conditions and patching the fully developed velocity profile at its exit as an inlet to the pipe under consideration. The values of Turbulent Kinetic Energy (κ) and Turbulence Dissipation (ε) were also patched at the inlet to the pipe. The gas temperature (60 ^{o} F ~ 288 ^{o} K) and operating pressure (4.136 MPa) were specified at the pipe inlet. The temperature distribution on the surface of the thermal well is also of interest to us.

The wall temperature conditions were constant values and temperatures that varied azimuthally by 5.5^{o}K (10°F), 13.8^{o}K (25°F) and 27.7^{o}K (50°F) above and below the specified gas temperature. For some of the cases the wall temperature conditions were varied azimuthally by making use of User Defined Functions (UDF's) in Fluent 6.1.22. UDF's are functions that can be called in Fluent while the simulation is being set up and helps in enhancing the standard features of the code. The following is the UDF used for sinusoidal temperature variation depicting the temperature difference between top and bottom half of the pipe.

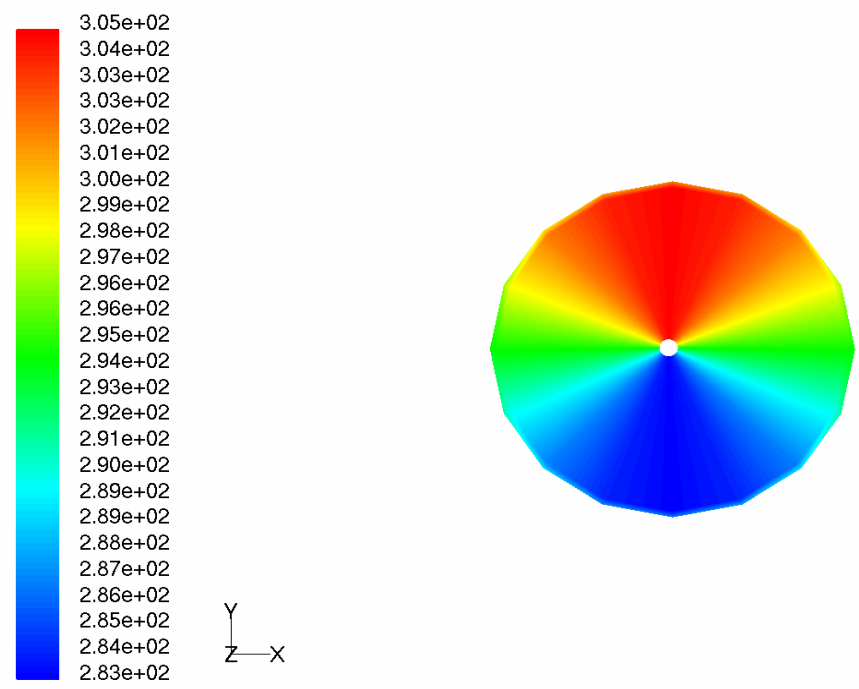

Figure 12 - Azimuthal temperature distributions on geometry walls.

Figure 12 gives an example of the sinusoidal variation of temperature on the pipe walls. Figure 13 shows the program written as a user defined function in FLUENT to vary temperature on pipe walls.

```
/* UDF- Sinusoidal Variation of Temperature (ΔT=25 ° F) on the Wall */
#include "udf.h"
#define PI 3.141592456
DEFINE_PROFILE (temp_profile, thread, position)
/* This is a macro that helps in defining a profile function */
{
```

Figure 13 – Program to compute sinusoidal temperature variation on pipe wall.

```
Real d [ND_ND];
Double x, y, Val, Theta;
Face_t f;
begin_f_loop (f, thread)
        {
F_CENTROID (d, f, thread);
/* Helps locating origin of the profile function. */
        x=d [0];
        y=d [1];
        Theta=atan2(y, x);
        VAL= ((PI*Theta)/ (2*PI));
        F_PROFILE (f, thread, position) = 294.2+13.888*(sin (2* (VAL)));
 /* All temperature values are in Kelvin */
        }
end_f_loop (f, thread)
}
/* End of Program */
```

Figure 13 – continued.

3.3 Methodology of Simulating USM Response

The ultrasonic flow meter measurements were compared to the measurements given by the CFD analysis. The CFD analysis is assumed to be the true value as it was noted that the mass was conserved in all cases and that no mass was lost though the volumetric flow rate was varying in the pipe. The simulated ultrasonic meter measurements based upon the CFD analysis depict results that would be produced in the field by the Daniel ultrasonic four path flow meter.

The simulated results were produced by performing a line integral over the acoustic chords of the ultrasonic flow meter. Each acoustic chord measures the average velocity on its path. The four acoustic paths are located at 0.0470916 m (0.309*R) and 0.1232916 m (0.809*R) above and below the pipe centerline. The indexes used to point at the four different acoustic paths are P047, M047, P123 and M123 where P stands for positive values (for paths above X axis) and M for negative values (for paths below X axis). The USM bulk average velocity is then calculated by the following equation:

USM Vb = (P047_V+M047_V)*0.3618 + (P123_V+M123_V)*0.1382

Since the meter can be located anywhere along the length of the pipe, the meter's response was simulated along the entire pipe length. To accomplish this task, a rectangular grid was made at four heights of the pipe cross section depicting the four planes that the ultrasonic meter would sweep going down the length of the pipe towards the exit.

The average gas velocity across each plane at various axial locations were calculated and multiplied with the constant factors provided by the Daniel ultrasonic flow meter manual to produce the average gas velocity in the pipe which were compared with the CFD results.

CHAPTER IV

RESULTS AND CONCLUSIONS

There are four aspects which vary the flow in the pipe systems.

1) Pipe geometry

2) Wall temperature conditions

3) Flow velocity

4) Magnitude of temperature difference

We shall describe the effects of the above four facets as a whole as below with detailed examination in a subsequent section.

4.1 Single Elbow Pipe

In this geometry, the flow makes a 90° bend before it enters the 100 diameter length of horizontal pipe. Due to this, the flow direction at the inlet of the straight end of the pipe is not purely axial. The cross axis gas flow pattern consisting of two counter rotating vortices with up flow across the pipe centerline and down flow along the pipe wall. This is observed in all cases of the single elbow geometry (see Figure–B-21 and Figure B-24). The axes shown on Figure 14 apply to all figures that follow. Gravity acts in the negative Y direction.

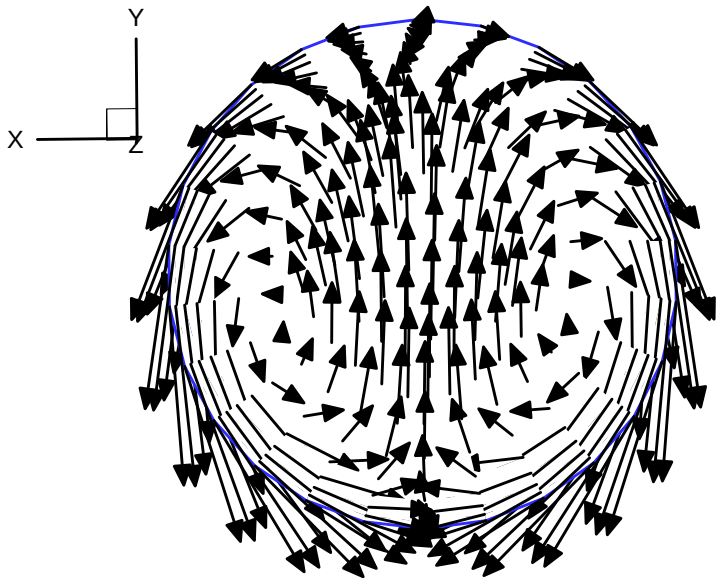

Figure 14 – The flow pattern for single elbow pipe flow.

For the case of no heat transfer, this double vortex structure decays as the flow progresses downstream. As the temperature on the wall is changed and the gas is heated or cooled by the pipe wall, buoyancy effects will start acting upon the flow as the density of the gas changes. The more dense gas starts to flow downward and the heated gas tries to rise. We shall describe these phenomena in detail.

a) Cold wall temperature condition

In general, for this case, the gas near the walls becomes colder compared to the gas in the middle and flows down along the walls pushing the hot gas to the top. The cold gas on the bottom loses its velocity due to wall friction whereas the hot gas gains velocity.

As a consequence, the flow velocity at the top side of the pipe increases and the lower side of the pipe shows low velocity. The double vortex structure decays more rapidly than for the no heat transfer case since the cold dense fluid resists being pumped to the top of the pipe and the hot fluid resists pumping to the bottom. It is seen that at low gas velocity, the temperature difference dominates the flow pattern while at high velocities, the temperature difference is less influential (see Figures B-111 and B-114). This can be explained as the gas having low velocity or more residence time is heated more compared to gas at high velocity. There is more time for the heat to travel through the gas layers from the walls towards the middle of the pipe (see Figures B-11 and B-179). We can see that the highest temperature reached by the gas at low gas velocity is about 0.3 % more than the high gas velocity case. It is also noted that at high velocities, there is more mixing of the gas which results in the temperature and velocity variation across a cross-section of the pipe being less (see Figure B-227 and Figure B-228). Mixing of the gas leads to a more uniform distribution of temperature and velocity in the pipe or in that part of the pipe cross-section.

The flow pattern, as shown in Figure 5, aids in the direction of motion of the gas and is a dominant feature at high velocities. It was observed at low velocities, the circulation is much less compared to higher gas velocities. The gas velocity on the walls is noted to be higher at high gas velocities as the flow along the walls in the top half of the pipe and the flow pattern both move in the same downward direction.

b) Hot wall temperature conditions

For this case, the gas near the walls becomes hotter compared to the gas in the middle and the buoyancy force attempts to move the fluid up along the walls opposing the vortex structure. This hot gas motion also attempts to push the cold gas down across the pipe centerline. The cold gas on the bottom gains velocity as it is pushed down due to gravity effects whereas the hot gas loses its velocity owing to wall friction. As a consequence, the flow velocity on the bottom side of the pipe increases and the upper side of the pipe shows low velocity. The balance between momentum and heat transfer induced secondary flow changes for the conditions studied.

At low flow velocity and high temperature difference, it is found that the gas velocity at the top half of the pipe is low (Figure 15). This is due to the gas on the pipe centerline which has large velocity being cold and not rising as only gas near the walls is heated. This is not the case at high velocities as high velocity increases mixing making the cold gas rise (Figure 16).

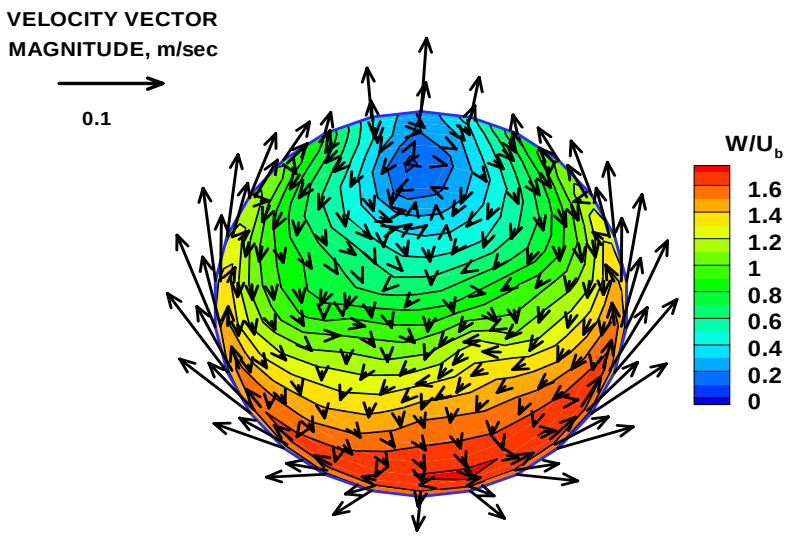

Figure 15 – Gas velocity on top of the pipe at low V and high ΔT.

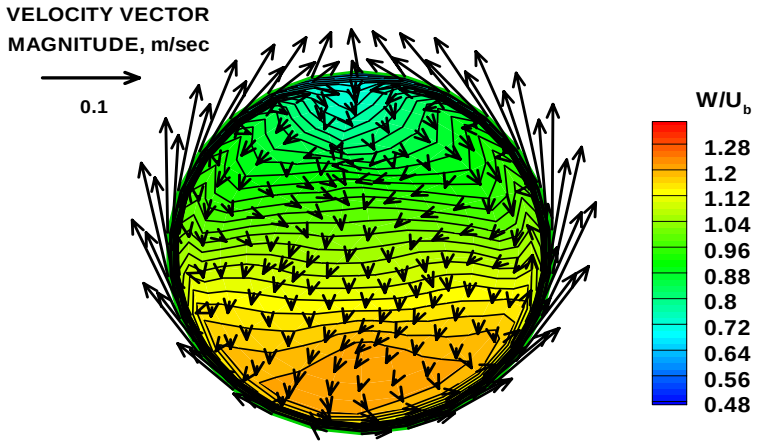

Figure 16 – Less stratified gas due to more mixing of gas at high V and low ΔT.

c) Cold top and hot bottom temperature conditions

The gas near the upper wall becomes cooler and the gas next to the lower wall becomes hotter. Due to buoyancy effects, the hot gas on the bottom tends to move up and the cooler gas on top tends to move down. As a consequence, there is a lot of mixing at the center line and the temperature and velocity variation across a cross-section of the pipe is lessened. It is found that the maximum velocity is at the lower sides of the pipe instead of at the center (see Figure 17). This is due to the effects of flow pattern. The cold gas on top is aided by the motion of the flow in addition to buoyancy. In the lower half of the pipe, the gas tends to move up but is not helped by the fluid momentum, leading to less upward flow and the cold and hot gas mix at the lower sides of the pipe. This is the reason why the lower sides of the pipe have maximum velocity (Figure 17). At high velocities, the gas velocity at the upper half of the pipe is higher compared at lower velocities due to the fact that gas is heated at the lower half of the pipe and momentum of the gas is dominant (Figure 18).

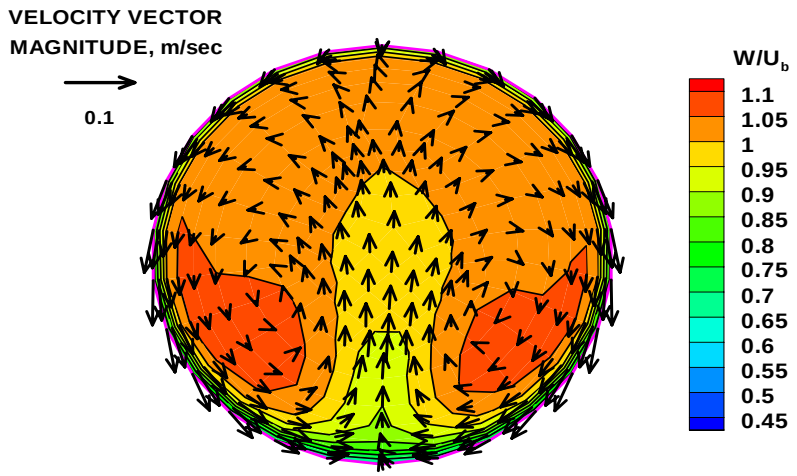

Figure 17 – Influence on gas flow for one elbow pipe at low V.

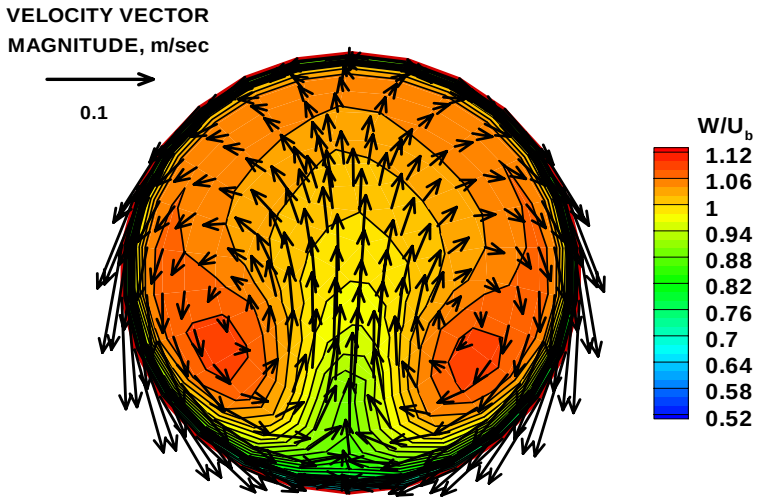

Figure 18 – Influence on gas flow for one elbow pipe at high V.

d) Hot top cold bottom temperature conditions

In general, for this case, the gas near the upper wall becomes hotter and the gas next to the lower wall becomes cooler. Due to buoyancy effects, the hot gas tends to move up and the cooler gas tends to move down. The motion is not aided in the upper half of the pipe by the momentum induced double vortex structure, but in the lower half of the pipe, the cold gas and the flow pattern are in the same direction. The gas on the top side pushes the gas towards the center and so does the gas on the lower side. This makes the gas in the middle of the pipe gain velocity due to momentum. At low flow velocity, the temperature effects are more dominant than the gas momentum whereas at higher velocities, the momentum of the gas and its pattern is more dominant owing to gas residence time. The maximum velocity is found on a horizontal plane at the center of the pipe due to mixing in the upper and lower sides of the pipe (Figure 19).

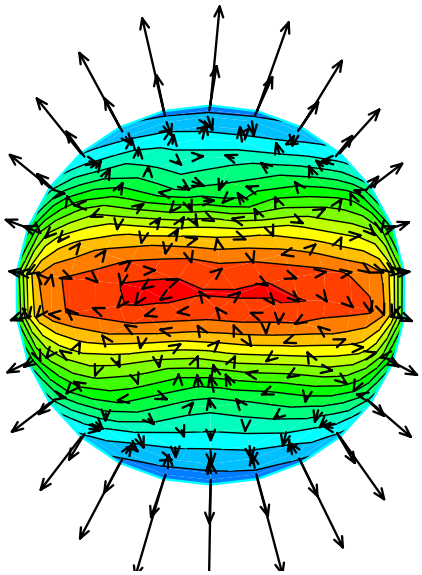

Figure 19 –Worst case of gas stratification for single elbow geometry.

4.2 Discussion of Appendix B

In this section, we shall discuss the density, temperature and axial velocity contours for the case of the Single Elbow geometry, and the bulk average velocity values compared to the simulated ultrasonic meter measurements. The simulated ultrasonic measurements were calculated using Tecplot 10 software [5], by constructing uniform grids at the chord heights of the pipe cross-section corresponding to the acoustic chords of the ultrasonic meter. Calculating the average cross pipe chord values at different axial locations on these planes and multiplying these values by constants simulated the response of a Daniel Ultrasonic flow meter mounted at different locations along the pipe length.

For the purpose of better reading and understanding, we have used a proper format and order of display in all appendices. Appendices A, B and C are broken into four sections corresponding to the wall temperature conditions. The first part of each section consists of density, temperature and velocity contours at pipe cross-sections which are animated to sweep down the length of the pipe. The second part consists of density, temperature and velocity contours at the chord heights corresponding to the acoustic chords of the ultrasonic meter. The third part consists of the graph plots of simulated bulk average velocity of the ultrasonic meter, bulk average velocity form CFD analysis and individual chord velocities calculated at the chord heights. In Appendices A, B and C Figures 1 to 36, 85 to 120 and 169 to 204 are the animated sweeps, Figures 37 to 72, 121 to 156 and 205 to 240 are the chord contours and Figures 73 to 84, 157 to 168 and 241 to 252 are

the graph plots comparing the simulated and computationally calculated chord average velocities.

As we know, variation in temperature of a gas goes hand in hand with density of the gas. At high temperature conditions, we find the gas to decrease in density and vice versa. We can hence group these two aspects of the flow contours shown and can analyze one aspect with the understanding that the other behaves in the opposite manner.

For the case of hot top and cold bottom, the gas next to the wall on top will decrease in density due to increasing temperature and the gas at the bottom will increase in density due to decreasing temperature. The density is seen to uniformly decrease from top to bottom of the pipe cross section (see Figures B-179 and B-182). Due to buoyancy effects, the hot gas tends to move up and the cooler gas tends to move down. This leads to gas stratification in the pipe (see Figures B-171 and B-174). The gas on the top side pushes the gas towards the center and so does the gas on the lower side. This makes the gas in the middle of the pipe gain velocity due to momentum (see Figures B-177). This can also be seen from the graph comparing the bulk average velocities. The CFD V_b and USM V_b are in good agreement. The bulk average velocity is observed to stay constant through out the length of the pipe (see Figures B-241 through B-243). It is observed that amongst all the cases, maximum variation in axial velocity across the pipe cross-section is found in this case, especially in the low velocity condition (see Figure B-171). This is not desired for ultrasonic meter measurements as it can lead to incorrect measurements of flow parameters such as axial velocity.

In the case of cold top and hot bottom, the gas next to the wall at the bottom will decrease in density due to increasing temperature and the gas on the top will increase in density due to decrease in temperature. It is seen that high density gas is present next to the wall for most of the pipe's inner surface besides the lower side (see Figure B-193). It is also seen that the density well within the interiors of the pipe hardly varies as the gas flows down the pipe (see Figure B-193). Due to buoyancy effects, the hot gas on the bottom tends to move up and the cooler gas on top tends to move down. As a consequence, there is a lot of mixing at the center line and the temperature and velocity variation across a cross-section of the pipe is lessened (see Figures B79 though B-81). This can also be seen from the graph comparing the bulk average velocities (see Figures B-247 through B-249). The CFD V_b and USM V_b are in good agreement.

The case of uniform wall temperature conditions is slightly different regarding the bulk average velocities. For uniform hot wall temperature conditions, the density on the top side of the pipe is less than at the bottom. Due to gravity effects, the denser gas moves down (see Figures B-46 and B-49). The maximum velocity is found in the bottom half of the pipe (see Figures B-48 and B-51). It is seen that the bulk average velocity increases with increase in temperature difference. At higher temperature differences, the bulk average velocity increases along the length of the pipe (see Figures B-76 through B-78). This may be due to the heating of the gas making it less dense and increasing in velocity as it progresses towards the end of the pipe.

CFD V_b and USM V_b were found to differ by almost 6% in the worst case.

In case of cold wall conditions, the density on the bottom side of the pipe is found to be the highest (see Figures B-28 and B-31). Maximum velocity is found in the upper half of the pipe (see Figures B117 and B-120). In this case, the CFD bulk average velocity decreases with increase in temperature difference (see Figures B-250 through B-252). This may be due to the gas being less heated or denser compared to the heated wall case and so velocity decreases as the gas progresses to the end of the pipe. USM V_b and CFD V_b are not found in agreement.

Figures 20 through 23 present how the simulated ultrasonic meter responds to different boundary conditions and how much it differs from the CFD Analysis results.

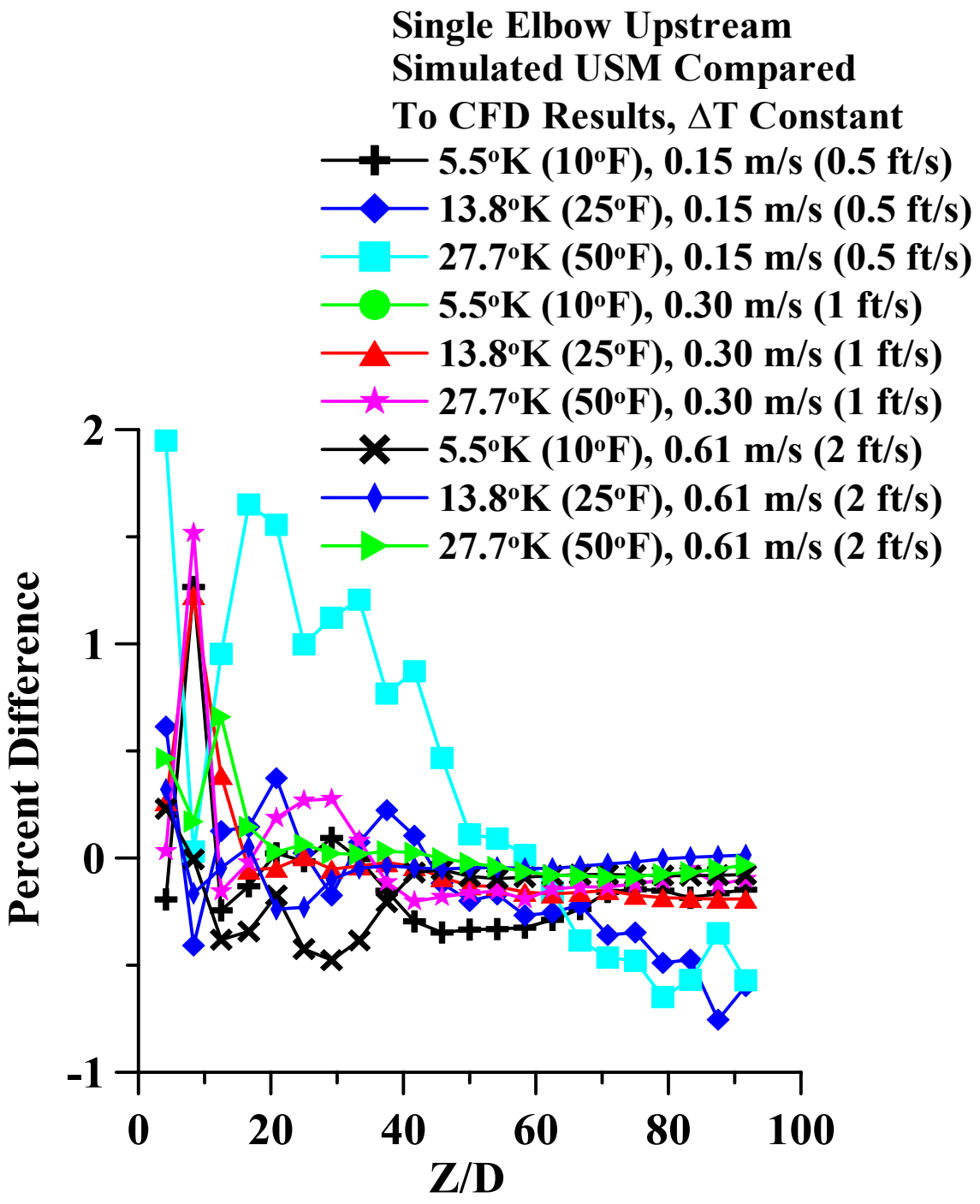

Figure 20 - Ultrasonic flow meter response for single elbow pipe having all cases of gas velocity for all constant positive wall temperatures.

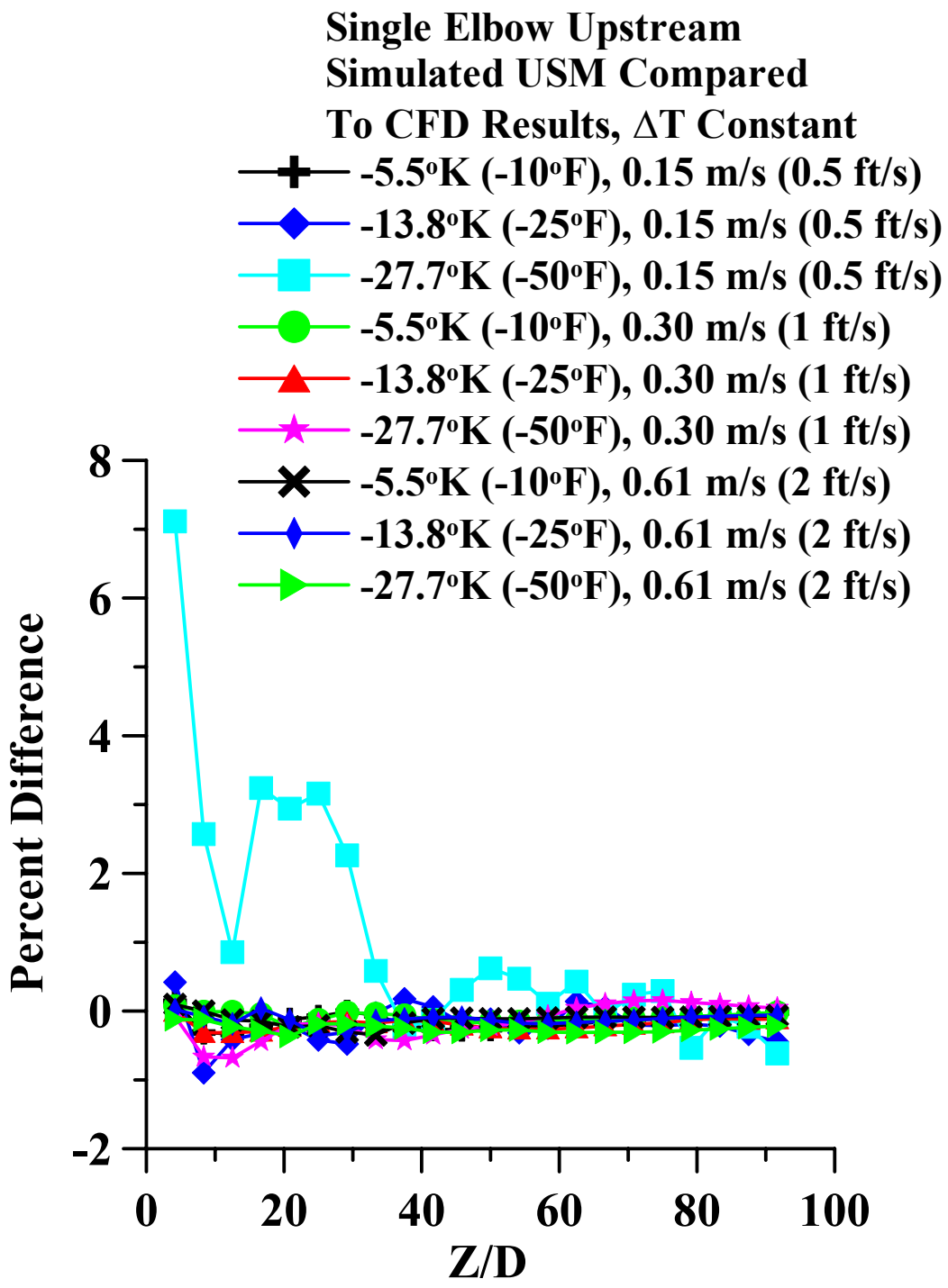

Figure 21 - Ultrasonic flow meter response for single elbow pipe having all cases of gas velocity for all constant negative wall temperatures.

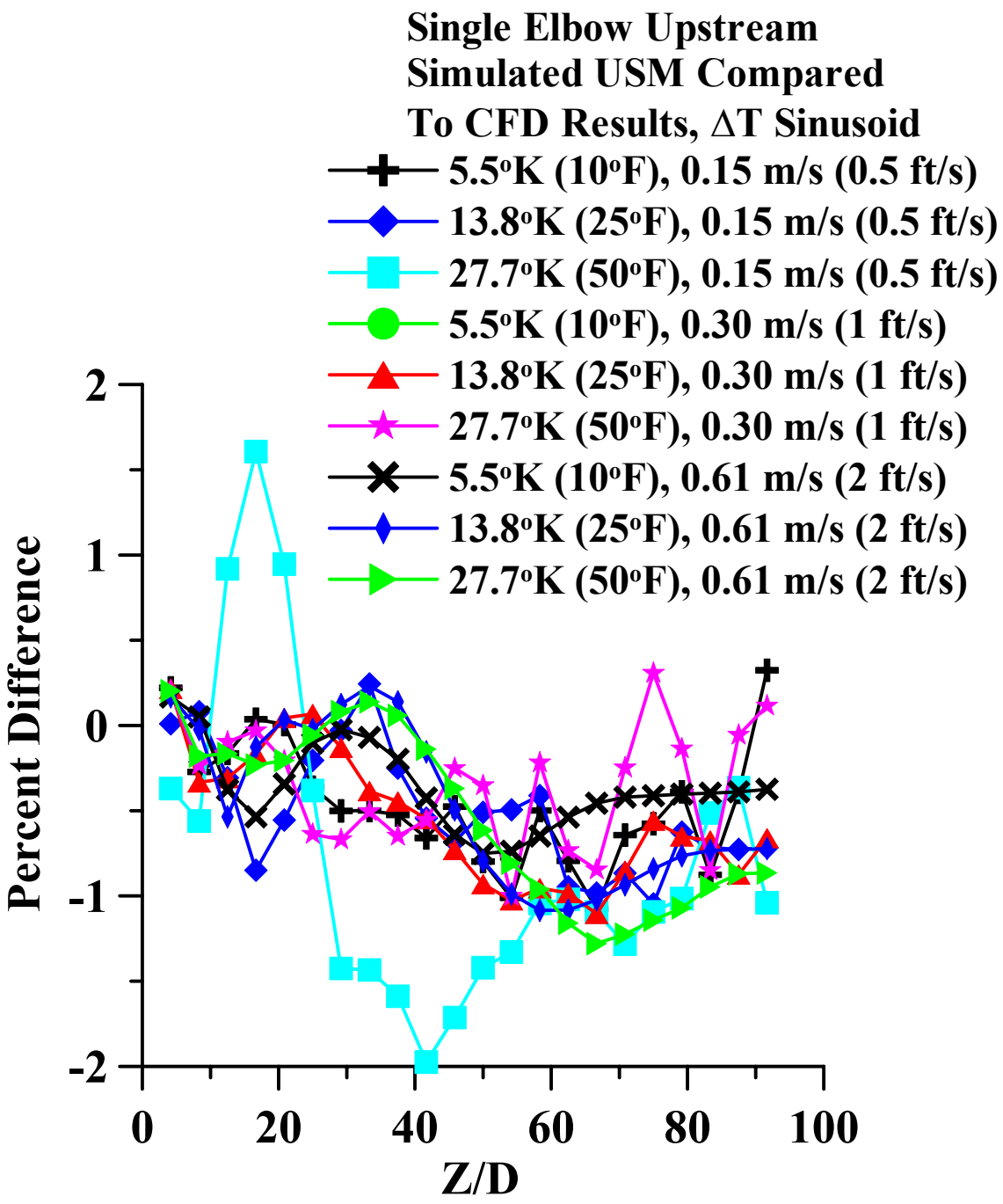

Figure 22 - Ultrasonic flow meter response for single elbow pipe having all cases of gas velocity for all sinusoid positive wall temperatures.

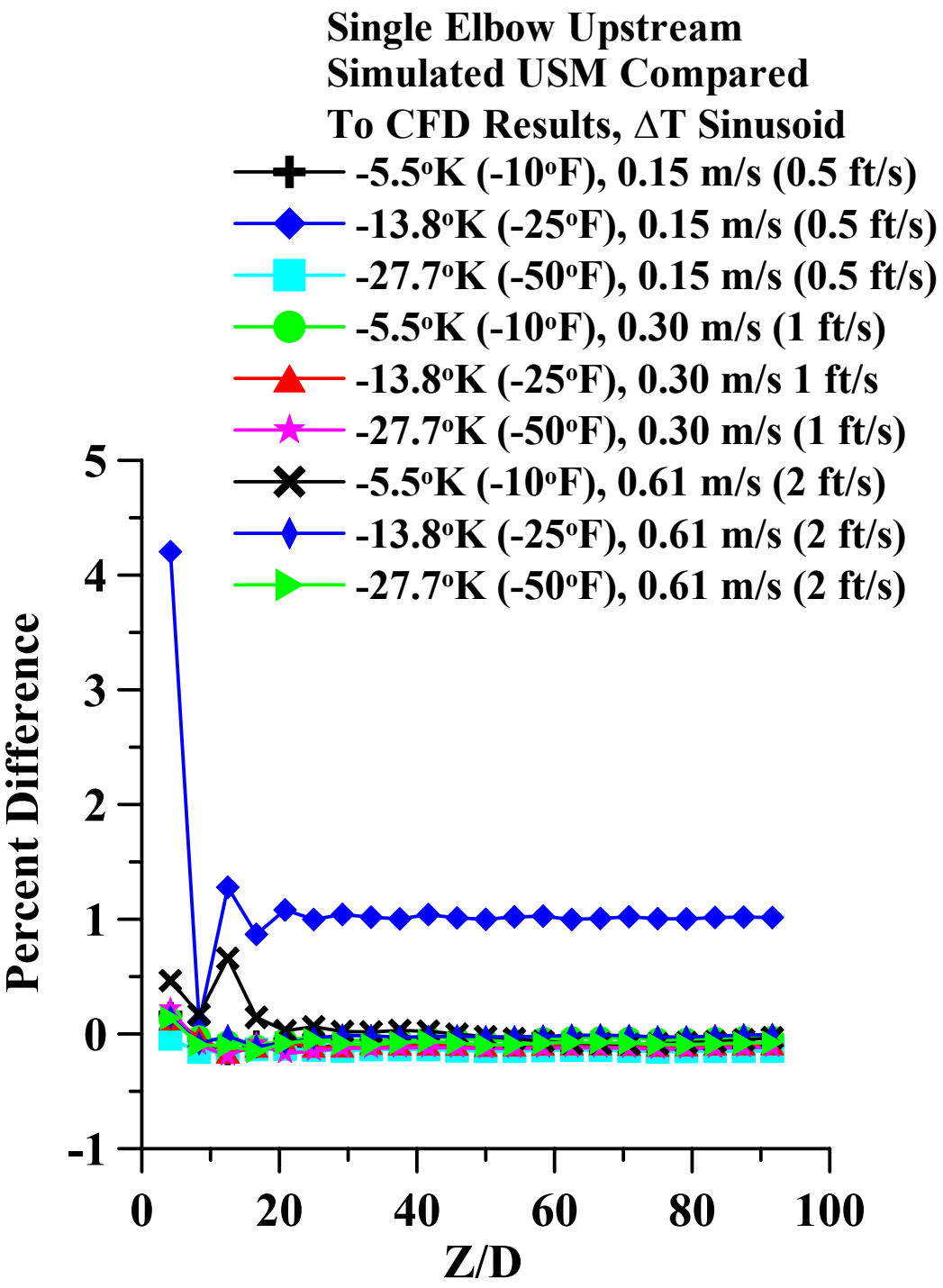

Figure 23 - Ultrasonic flow meter response for single elbow pipe having all cases of gas velocity for all sinusoid negative wall temperatures.

Figures 20 through 23 show the percentage error in the response of the Daniel ultrasonic four path flow meter for single elbow pipe configuration compared to the CFD analysis results. The single elbow constant temperature hot pipe (Figure 20) shows an error of less than 0.3% for most of the pipe length after Z/D=20. The initial high errors in the graph can be due to the presence of large temperature and velocity gradients near the elbow to which the flow accommodates as it progresses downstream. It can be seen that the highest temperature difference and lowest velocity case posses the maximum error. The single elbow constant temperature cold pipe (Figure 21) shows an error of less than 0.4% for most of the pipe length after Z/D=20. It can be seen that the error decreases as the flow progresses downstream. The highest temperature difference and lowest velocity case showed maximum error. The single elbow hot top and cold bottom pipe (Figure 22) has an error of about 1% for most of the pipe length. The flow does not seem to accommodate well with the high velocity and temperature gradients and the error is seen to fluctuate appreciably. This is the case where the axial velocity is maximum on a horizontal plane passing through the pipe centerline.

The highest temperature difference and lowest velocity case showed maximum error again. The single elbow cold top and hot bottom pipe (Figure 23) shows an error of less than 0.2% for most of the pipe length after Z/D=20. This does not hold true for one case- V=0.1524m/sec and $\Delta T=13.8^{o}K$ which shows an error of 1%. No explanation can be provided for this aspect at the present time. The axial velocities and flow field appear to be converged.

4.3 Double Elbow Pipe

In this geometry, the flow passes through two 90° bends that are mutually perpendicular to each other before it enters the 100 diameter length of horizontal straight pipe. Due to this, the flow direction at the inlet of the straight end of the pipe is not purely axial. The gas flow pattern observed in all cases of single elbow geometry is as below:

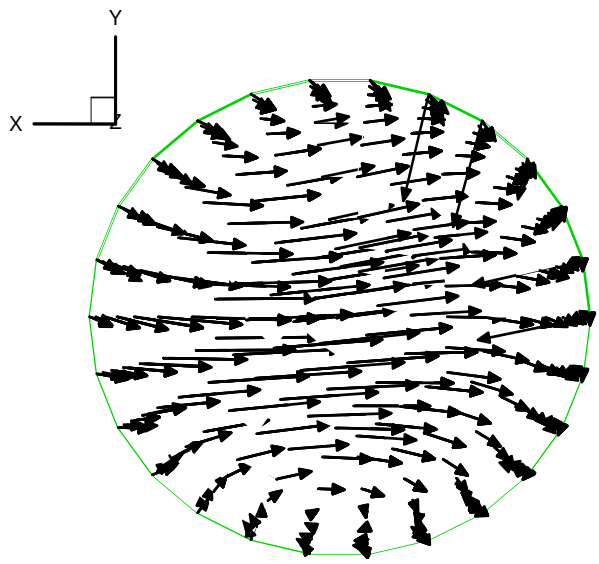

Figure 24 - Flow pattern of double elbow geometry.

As we can see in Figure 24, the change in geometry causes a swirl in the flow at the inlet to the straight end of the pipe. The swirl is found to be clock-wise in motion. As the temperature on the wall is changed, the buoyancy effects will start acting upon the density of the gas changes and the heavier gas starts to flow downward. We shall

describe these phenomena in an overall manner here followed by details in variation with velocity and temperature differences.

a) Cold wall temperature condition

In general, for this case, the gas near the walls becomes colder compared to the gas in the middle and flows down along the walls pushing the hot gas to the top. The hot gas gains velocity being less dense and the cold gas loses its velocity being next to the wall and denser. As a consequence, the flow velocity at the top side of the pipe increases and the lower side of the pipe shows low velocity due to mixing of gas. The gas enters and moves clock-wise and then the gas moves upwards from the sides due to cold temperature on the walls pushing this fluid down (Figure 25). The gas moves upwards at the middle of the pipe as the gas on the side walls moves downward and is aided by the flow pattern on the right half of the pipe (Figure 26). The following figure shows the above phenomena:

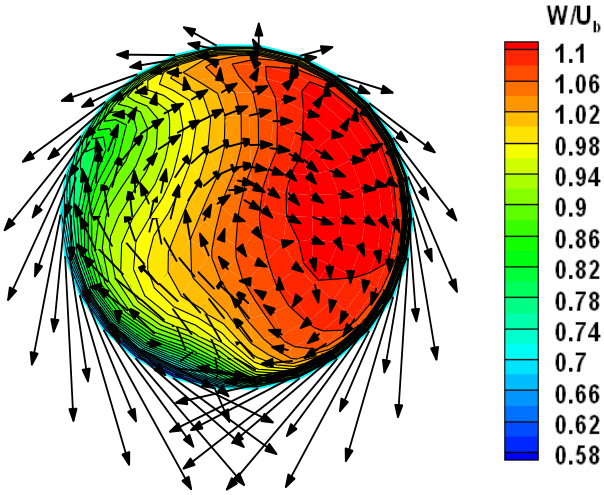

Figure 25–Gas changing direction of swirl.

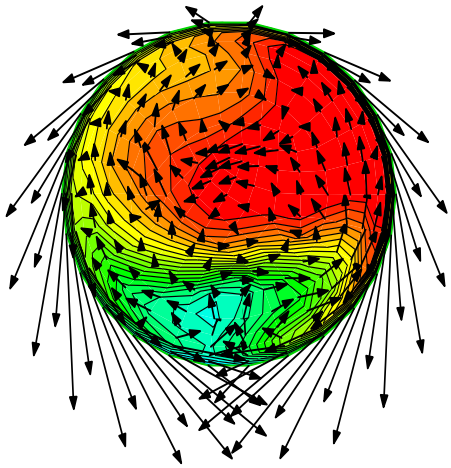

Figure 26-Swirl shift.

It was observed that maximum gas stratification was found at low gas velocities and high temperature difference. This can be explained by maximum gas residence time and high temperature gradient. High gas velocity means more mixing of the gas and dissipation of heat and velocity through out the pipe leading to less gas stratification.

b) Hot wall temperature condition

In general, for this case, the gas near the walls become hotter compared to the gas in the middle and moves upwards along the walls pushing the cold gas down. As a consequence, the flow velocity at the top of the pipe decreases due to mixing of gases and the lower side of the pipe shows high velocity. At low velocities, the flow is temperature dominated. The maximum gas velocity is found to be at the lower side of the pipe cross-section. At high velocities, the maximum gas velocity is found to be at the lower right side of the pipe and then moves to the lower side of the pipe (as shown below). Figure 27 shows the gas flow at two different times, the left figure occurring about 20 diameters length before the figure on the right.

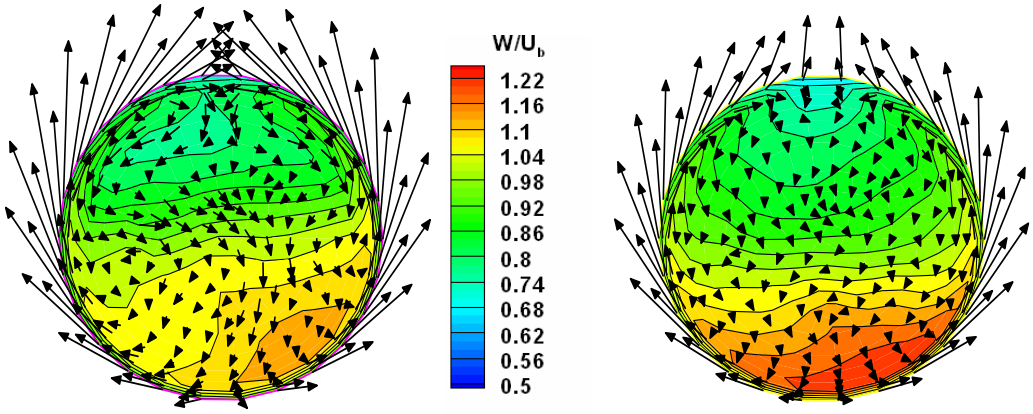

Figure 27 – Gas velocity shifting to the sides as flow progresses.

c) Cold top and hot bottom temperature conditions

The gas near the upper wall becomes cooler and the gas next to the lower wall becomes hotter. Due to buoyancy effects, the hot gas tends to move up and the cooler gas tends to move down.

In this case, the swirl motion of the gas shows to have a profound impact on the flow characteristics all the way to the end of the pipe. If the temperature difference on the wall is high, the gas flow is aided by the swirl and the velocity of the swirl is found to be high. In case the temperature difference on the wall is low, the swirl velocity is found to be low, though the swirl still exists. This can be explained by the flow pattern of the gas in the pipe. The gas rotates clock wise-the temperature on the top-right side of the pipe is cold, the gas will be pushed down due to buoyancy effects and the temperature on the left-bottom side of the pipe is hot, the gas is pushed up. This adds to the momentum gained by the gas due to its velocity. The higher the temperature difference, more the momentum the gas gains in addition to the velocity momentum-helping it rotate at a higher rate. Also, it is seen that in cases of high gas velocity, the maximum velocity is noted at the center of the pipe and there is less velocity gradient compared to the cases of low gas velocity where the velocity gradient is high. Figure 28 shows how the flow forms a swirl. The figure on the left in 12 diameters down the pipe and the figure on the right are 40 diameters down the pipe.

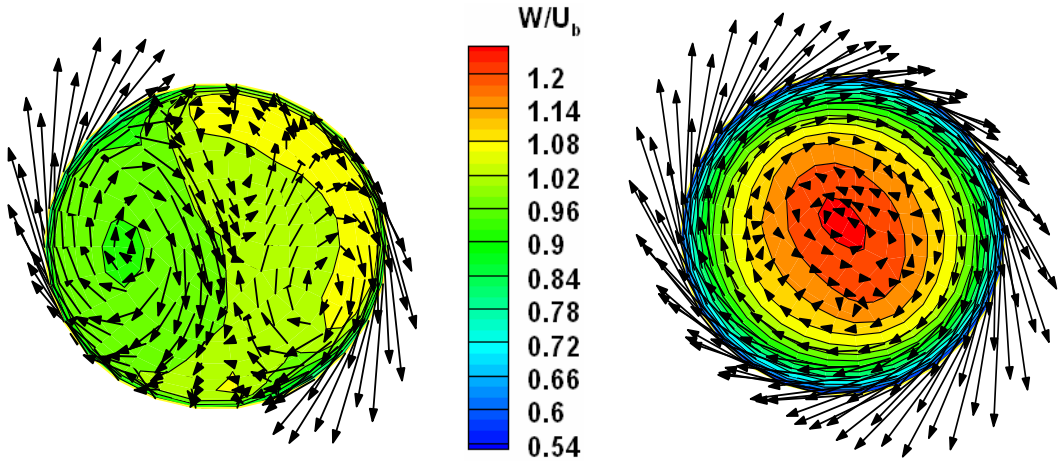

Figure 28 – Swirl development for double elbow.

d) Hot top cold bottom temperature conditions

In general, for this case, the gas near the upper wall becomes hotter and the gas next to the lower wall becomes cooler. Due to buoyancy effects, the hot gas tends to move up and the cooler gas tends to move down. This is very similar to the previous flow, when we observe it from the flow pattern point of view. In this too the flow is being supported by the temperature effects and the flow direction of the swirl at two places, but this case does not produce a swirl flow in the pipe. This can be due to the gravity acting downwards and the temperature difference can not gather that much of momentum. This leads to gas stratification with the more dense gas on the bottom walls of the pipe. The gas on the top side pushes the gas towards the center and so does the gas on the lower side. This makes the gas in the middle of the pipe gain velocity due to momentum. At low flow velocity, the temperature effects are more dominant than the gas momentum whereas at higher velocities, the momentum of the gas and its pattern is more dominant

owing to gas residence time. The maximum velocity is found on a horizontal plane at the center of the pipe due to mixing in the upper and lower ends of the pipe. Figure 29 shows how the gas velocity attains maximum momentum at the center starting from the sides. The figure on the left is 10 diameters downstream and the figure on the right is 30 diameters downstream.

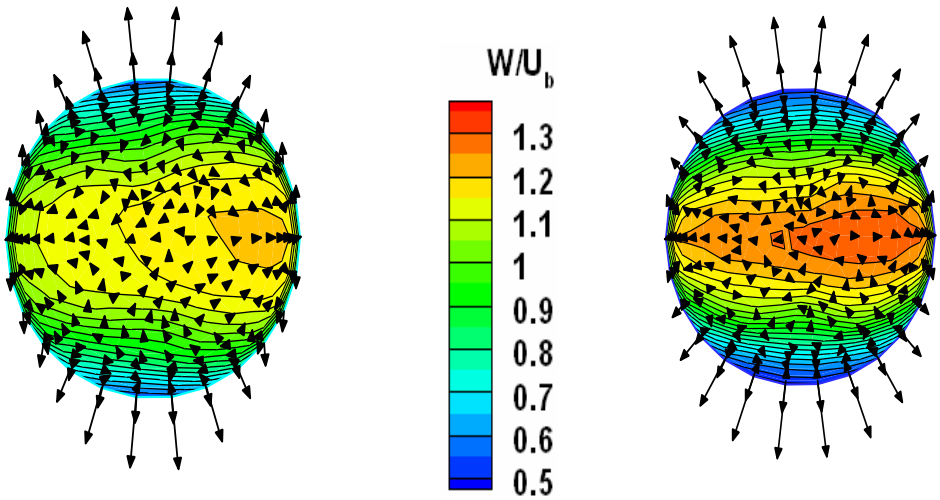

Figure 29 – Gas attains maximum velocity at center.

4.4 Discussion of Appendix C

In this section, we shall discuss the density, temperature and axial velocity contours for the case of the double elbow geometry, and the bulk average velocity plots compared to the simulated ultrasonic meter measurements.

For the case of hot top and cold bottom temperature condition, the top side of the pipe shows low density and the bottom side shows high density. The interior portion of the

pipe shows nearly constant density through out the pipe length (see Figure C-1 and Figure C-4). The gas near the upper wall becomes hotter and the gas next to the lower wall becomes cooler. Due to buoyancy effects, the hot gas tends to move up and the cooler gas tends to move down. This makes the gas near the center of the pipe gain velocity due to momentum; hence showing maximum velocity at the center of the pipe and progressively decreasing towards the walls of the pipe (see Figure C-3 and Figure C-6). This can also be seen from the graph showing the comparison between CFD V_b and USM V_b, which show good agreement. The difference in bulk average velocity increases with increase in temperature difference (see Figure C-73 through Figure C-75). This leads to more gas stratification, more layers of different gas velocities giving different chord values for various parameters - this is undesirable for ultrasonic flow meter measurements and temperature measurements that lead to incorrect data collection. It is also noted that the bulk average velocity across a cross-section of the pipe is the maximum for this case of flow (see Figure C-241 through Figure C-243).

In the case of cold top and hot bottom temperature conditions, the density varies negligibly across the cross section of the pipe and so the gas has a uniform density distribution (see Figure C-223 and Figure C-226). As we had seen in the previous section, due to the flow pattern and wall temperature conditions, a swirl is created in the pipe which in turn leads to churning of the gas. This leads to less gas stratification due to temperature effects making correct temperature measurements possible. A small portion on the top side of the wall shows higher density compared to the lower side of the pipe. The gas near the upper wall becomes cooler and the gas next to the lower wall becomes

hotter. Due to buoyancy effects, the hot gas tends to move up and the cooler gas tends to move down. We notice a swirl in the flow through the pipe with maximum velocity at the center of the pipe and progressively decreasing towards the walls. The change in bulk average velocity is much less and stays constant through out the length of the pipe (see Figure C-247 through Figure C-249). The axial velocities across the cross section of the pipe vary by a large margin. The CFD V_b and USM V_b are not in agreement. This is due to the fact that there are two factors affecting the flow here. One is the temperature factor which causes the accumulation of momentum at the horizontal centerline plane making the chord average velocity values give incorrect results. Also, in this case, a swirl is found in the gas flow as discussed before. This makes the velocity conditions even more inaccurate.

The case of uniform wall temperature conditions is slightly different regarding the bulk average velocities. For hot wall conditions, the gas is of low density on the top and progressively increases on the way down to the bottom of the pipe (see Figure C-13 and Figure C-16). The gas near the walls becomes hotter compared to the gas in the middle and moves upwards along the walls pushing the cold gas down. As a consequence, the flow velocity at the top side of the pipe decreases due to mixing of gases and the lower side of the pipe shows high velocity (see Figure C-15 and Figure C-18). The difference in bulk average velocity across the pipe cross-section is very large and increases with increase in temperature difference (see Figure C-244 to Figure C-246). The CFD bulk average velocity increases with increase in temperature difference along the length of the pipe, almost by about 6% in the worst case. This may be due to the heating of the gas

making it less dense and increasing in velocity as it progresses towards the end of the pipe. This negatively affects the USM V_b as this leads to narrowing down of high velocity at a location in the pipe, which makes the chord average velocity values produce incorrect results.

When the pipe is uniformly cold, the gas is of high density at the bottom of the pipe and progressively decreases towards the upper side of the pipe (see Figure C-193 and Figure C-196). The hot gases gain velocity being less dense and the cold gas loses its velocity being next to the wall and denser. As a consequence, the flow velocity at the top side of the pipe increases and the lower side of the pipe shows low velocity due to mixing of gas (see Figure C-195 and Figure C-198). The CFD bulk average velocity decreases with increase in temperature difference by about 4% in the worst case where as the difference in axial velocity across the cross section of the pipe increases with increase in temperature difference (see Figure C-250 through Figure C-252). This may be due to the gas being cold or denser compared to the heated wall case and so velocity decreases as the gas progresses to the end of the pipe.

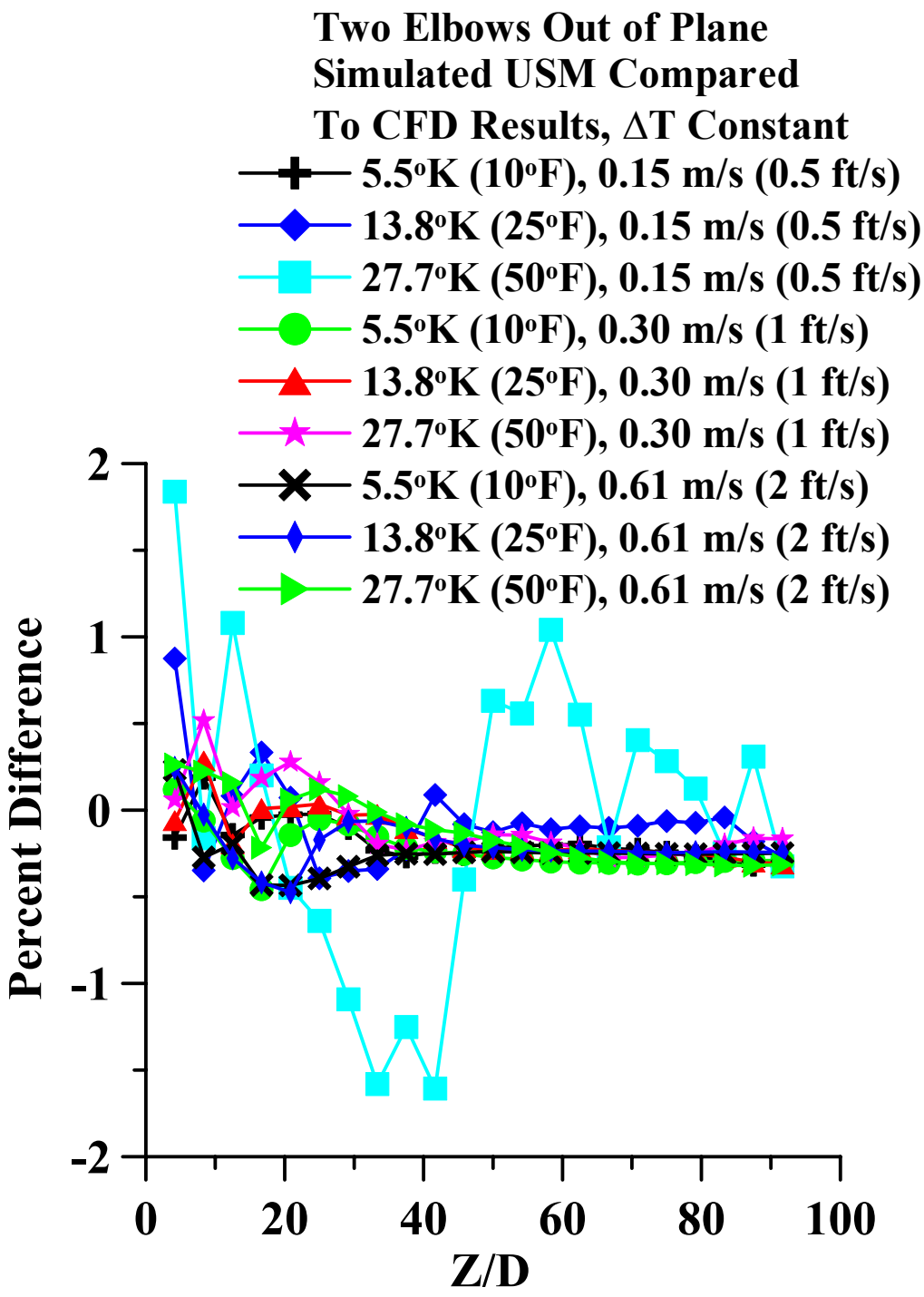

Figure 30 - Ultrasonic flow meter response for double elbow pipe having all cases of gas velocity for all constant positive wall temperatures.

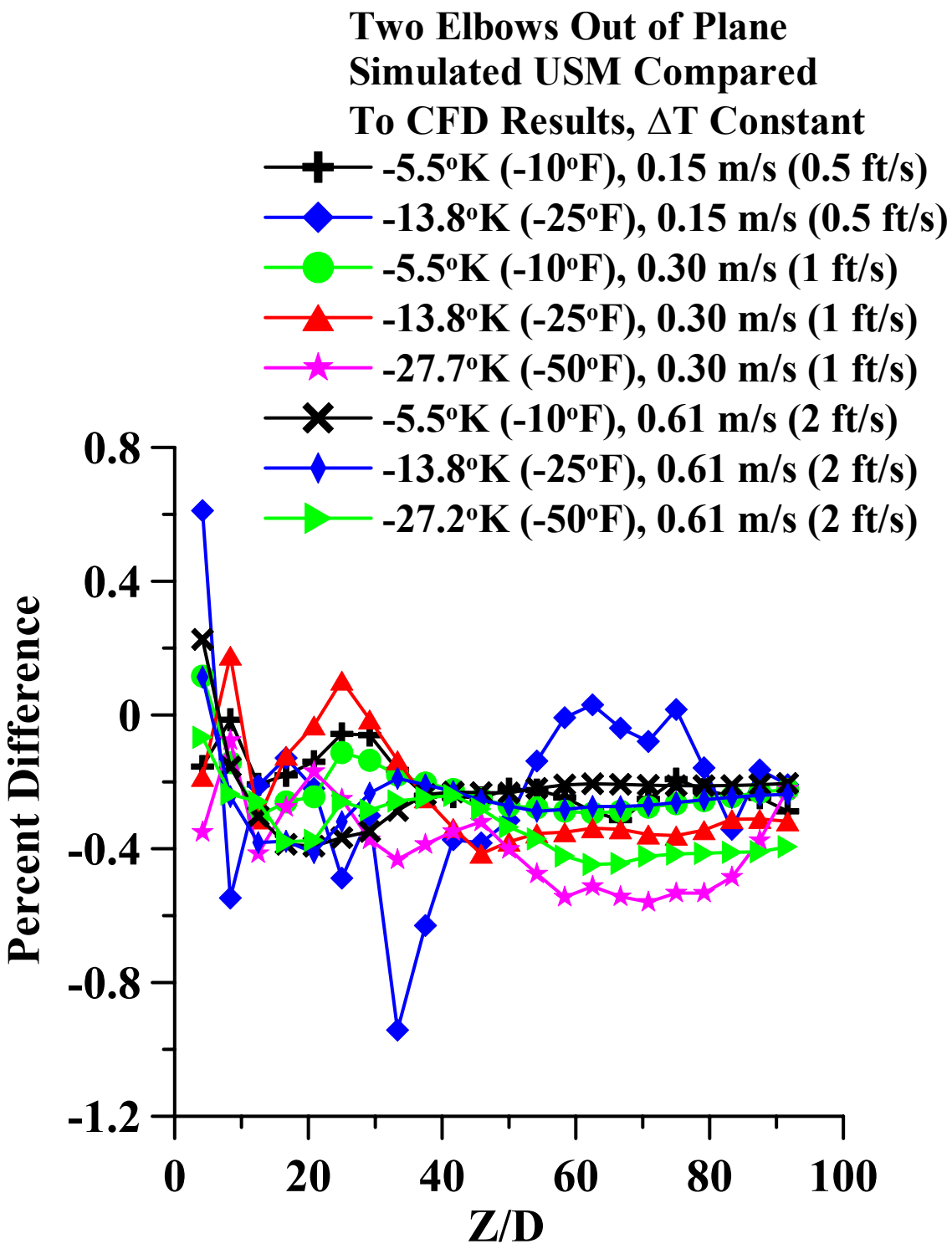

Figure 31- Ultrasonic flow meter response for double elbow pipe having all cases of gas velocity for all constant negative wall temperatures.

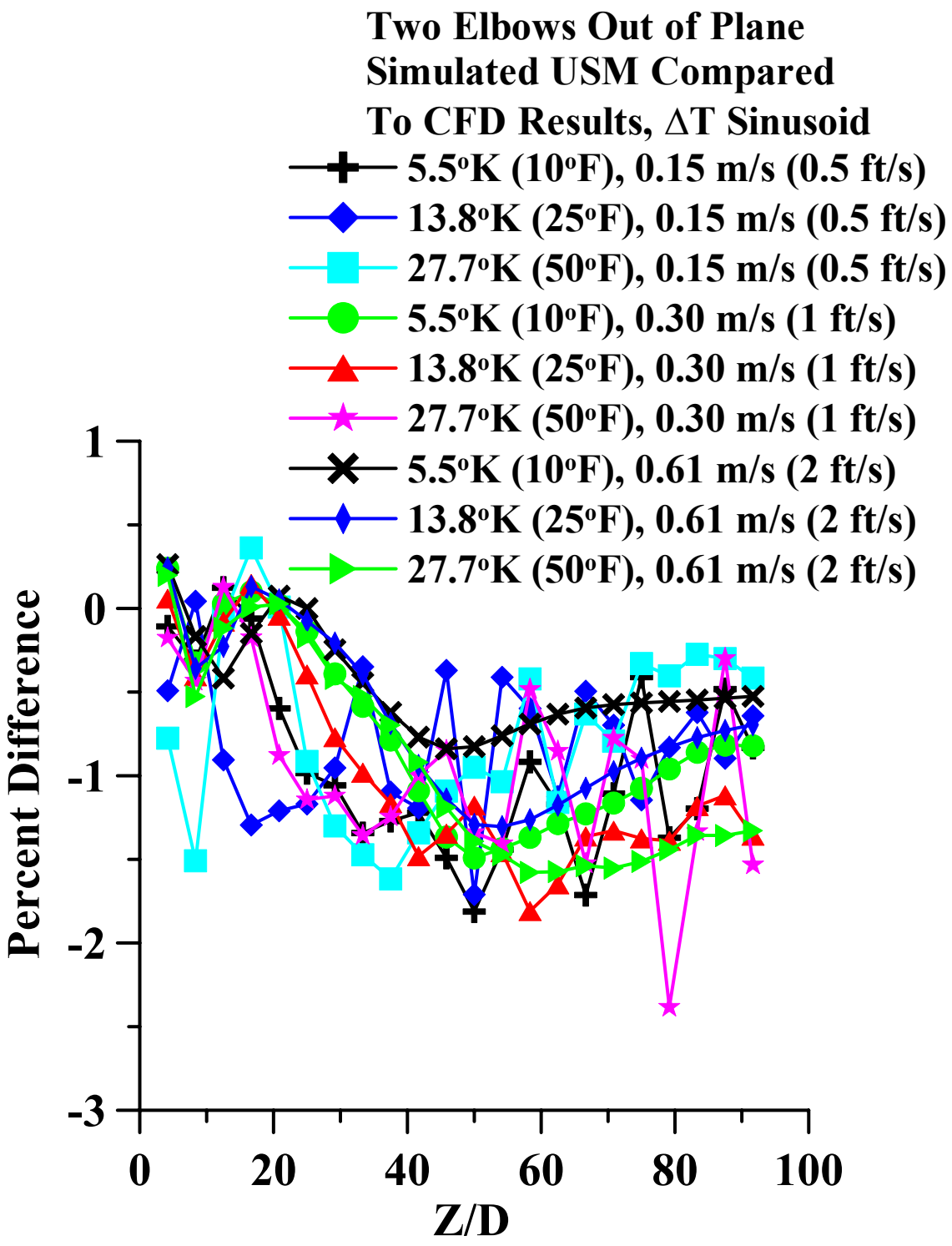

Figure 32 - Ultrasonic flow meter response for double elbow pipe having all cases of gas velocity for all sinusoid positive wall temperatures.

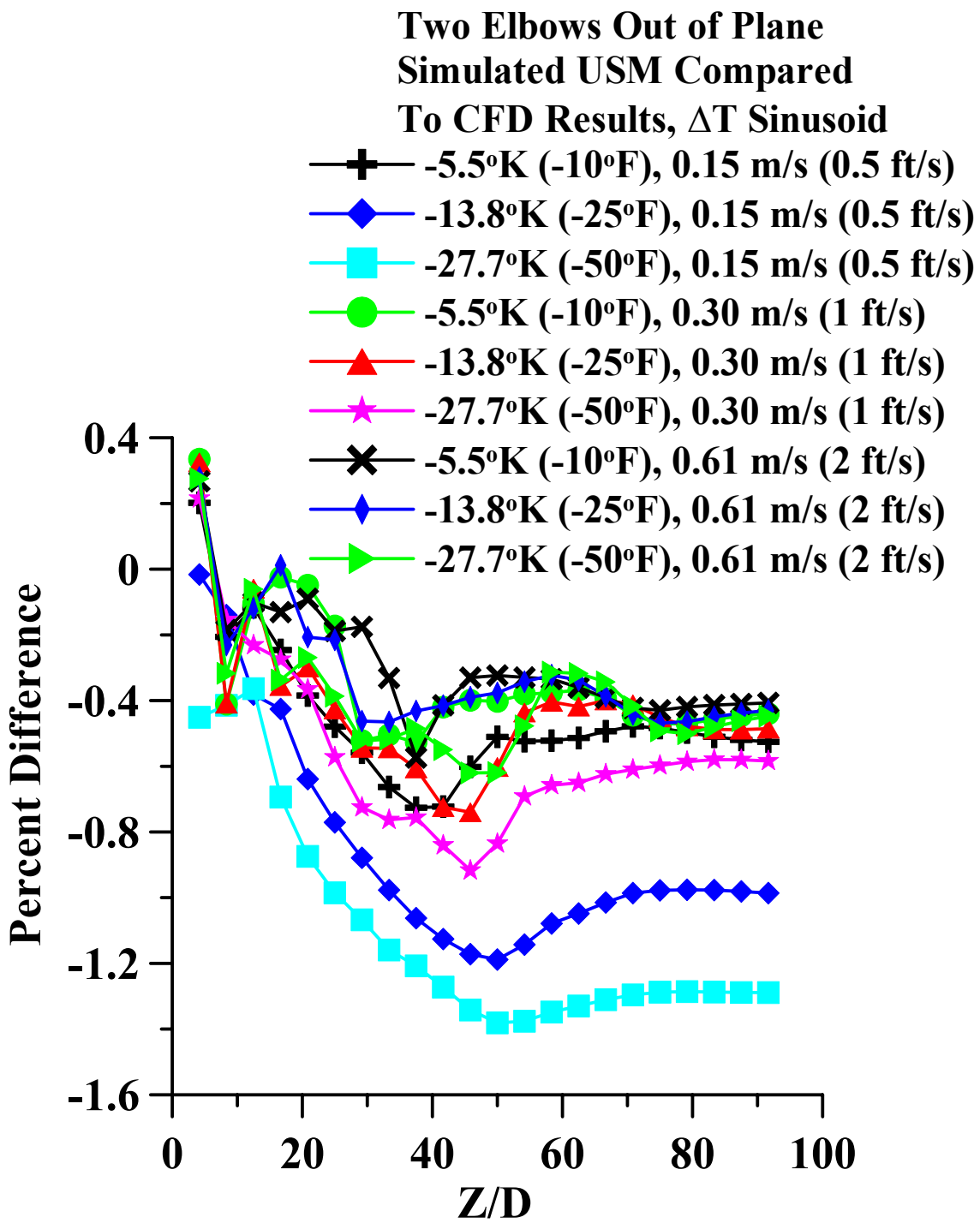

Figure 33 - Ultrasonic flow meter response for double elbow pipe having all cases of gas velocity for all sinusoid negative wall temperatures.

Figures 30 through 33 show the percentage error in the response of the Daniel ultrasonic four path flow meter for the double elbow pipe configuration on compared to the CFD analysis results. The double elbow constant temperature hot pipe (Figure 30) shows an error of less than 0.5% for most of the pipe length after Z/D=20. The initial high errors in the graph can be due to the presence of large temperature and velocity gradients near the elbow to which the flow accommodates as it progresses downstream. The highest temperature difference and lowest velocity case showed maximum error. The double elbow constant temperature cold pipe (Figure 31) shows an error of less than 0.5% for most of the pipe length after Z/D=20. It can be seen that the error decreases as the flow progresses downstream. The highest temperature difference and lowest velocity case showed maximum error. The double elbow hot top and cold bottom pipe (Figure 32) shows an error of less than 0.3% for most of the pipe length, but showed a negative bias of up to 2%. The flow does not seem to accommodate well with the high velocity and temperature gradients and the error is seen to fluctuate appreciably. This may be due to the strong buoyant forces present in the flow field due to localized maximum velocity at the center of the pipe. The highest temperature difference and lowest velocity case showed maximum error again. The double elbow cold top and hot bottom pipe (Figure 33) shows an error of less than 0.4% for most of the pipe length after Z/D=20 except for the two largest temperature differences at the lowest velocity. Here the error is a maximum of 1.5%. It can be seen that the error decreases as the flow progresses downstream and shows a negative bias in almost all cases. This flow field was different

from all other cases and maximum error was noted due to the reason that a single swirl was found in the flow field and axial velocity was maximum at the pipe center line.

4.5 Straight Pipe

The straight pipe has a thermal well placed 10 diameter lengths downstream of the pipe inlet. This thermal well causes a wake behind the thermal well and it is important to note how far it has its effects. This will help in knowing where to place flow meters for measuring parameters more accurately. The temperature distribution on the surface of the thermal well will be compared the analytical results. This will indicate whether a simple analytical solution produces an adequate result.

a) Cold wall temperature condition

In general, for this case, the gas near the walls become colder compared to the gas in the middle and flows down along the walls pushing the hot gas to the top. Maximum velocity is found to be at the top of the pipe. In this case however, the effect of flow of gas is rare as the flow is mostly axial and temperature effects are more dominant.

b) Hot wall temperature condition

In general, for this case, the gas near the walls becomes hotter compared to the gas in the middle and moves upwards along the walls pushing the cold gas down. Maximum velocity is found to be at the bottom of the pipe. Some pockets of low velocity were observed at low temperature differences after the thermal well (Figure 34). This was due

to the fact that the temperature difference was not enough to move the hot gas up (against gravity) at the sides of the pipe.

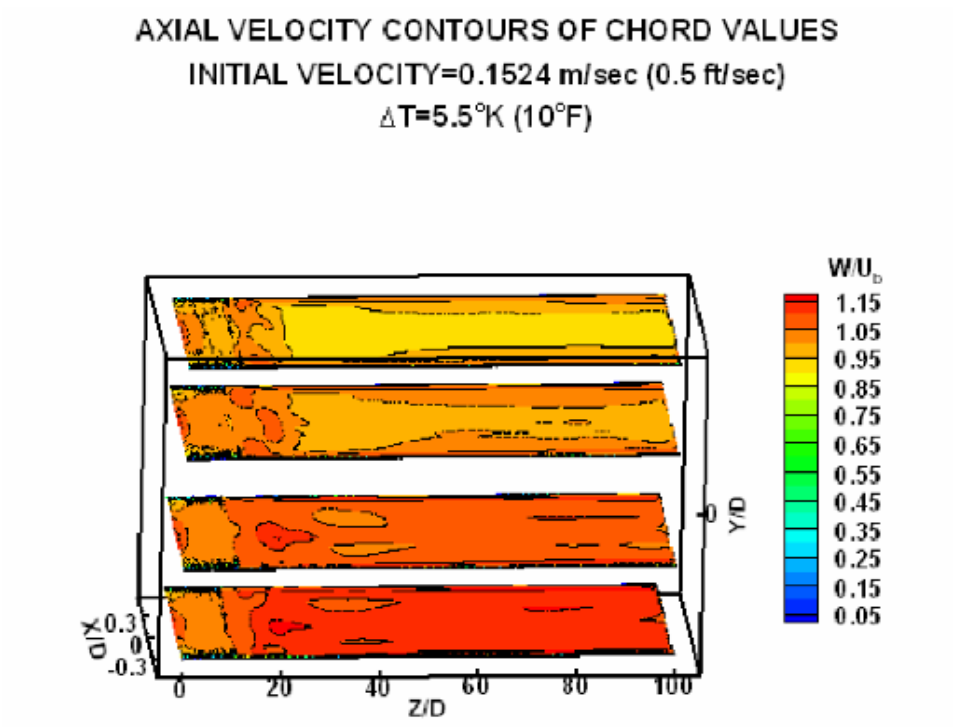

Figure 34 - Pockets of low velocity observed at low ΔT

c) Cold top and hot bottom temperature conditions

The gas near the upper wall becomes cooler and the gas next to the lower wall becomes hotter. Due to buoyancy effects, the hot gas tends to move up and the cooler gas tends to move down. It was also observed that the fluid moved in a wave like pattern in some cases as shown in Figure 35 and Figure 36. This waviness can be due to the instabilities

caused by thermal stratification as this wave like pattern was only found at high temperature differences.

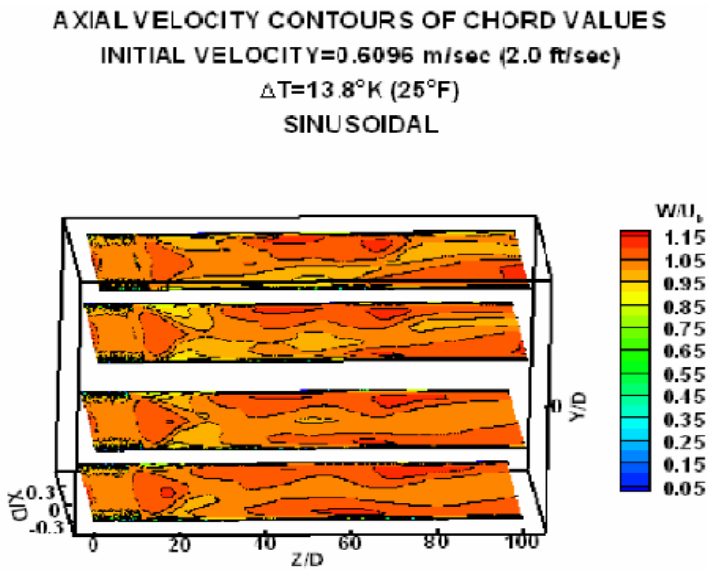

Figure 35 – Swirl flow pattern.

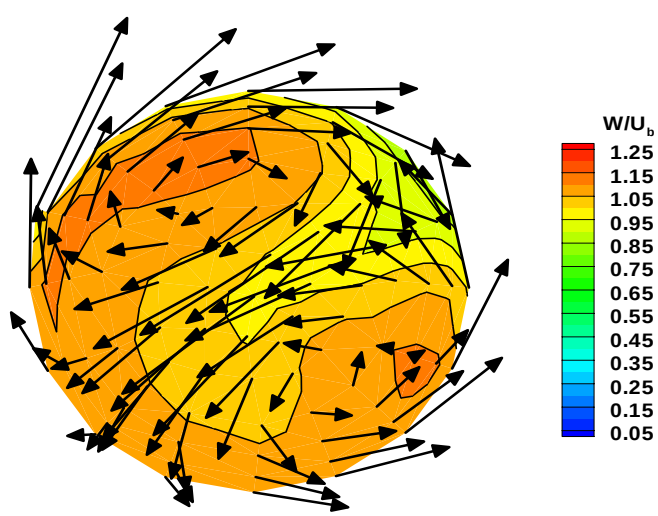

Figure 36 – Showing swirl flow pattern at a later stage in pipe flow.

d) Hot top cold bottom temperature conditions

For this case, the gas near the upper wall becomes hotter and the gas next to the lower wall becomes cooler. Due to buoyancy effects, the hot gas tends to move up and the cooler gas tends to move down. Maximum velocity is found to be at the center of the pipe as the gas at upper end and lower end of the pipe push the gas to the center of the pipe. Figure 37 shows the above clearly.

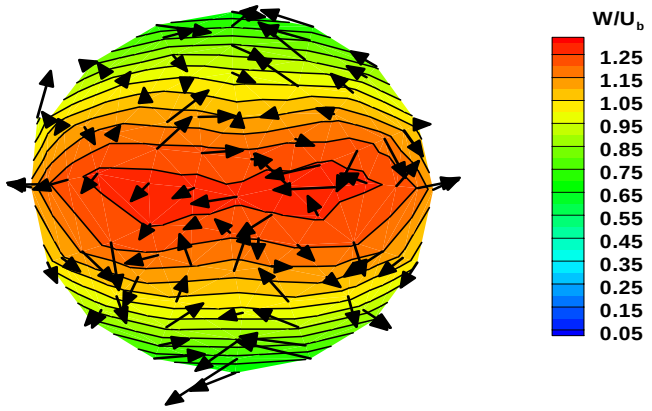

Figure 37 – Maximum velocity at the center of the pipe.

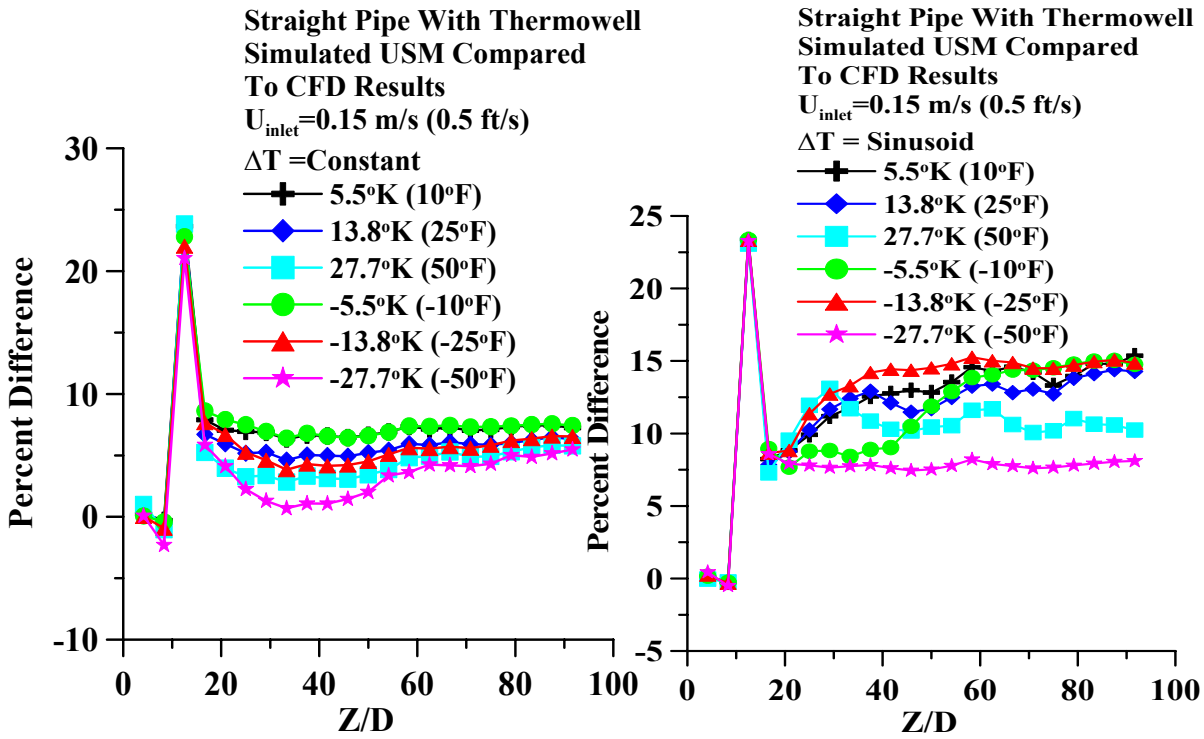

Figure 38 - Ultrasonic flow meter response for straight pipe configuration having 0.5 ft/sec bulk velocity.

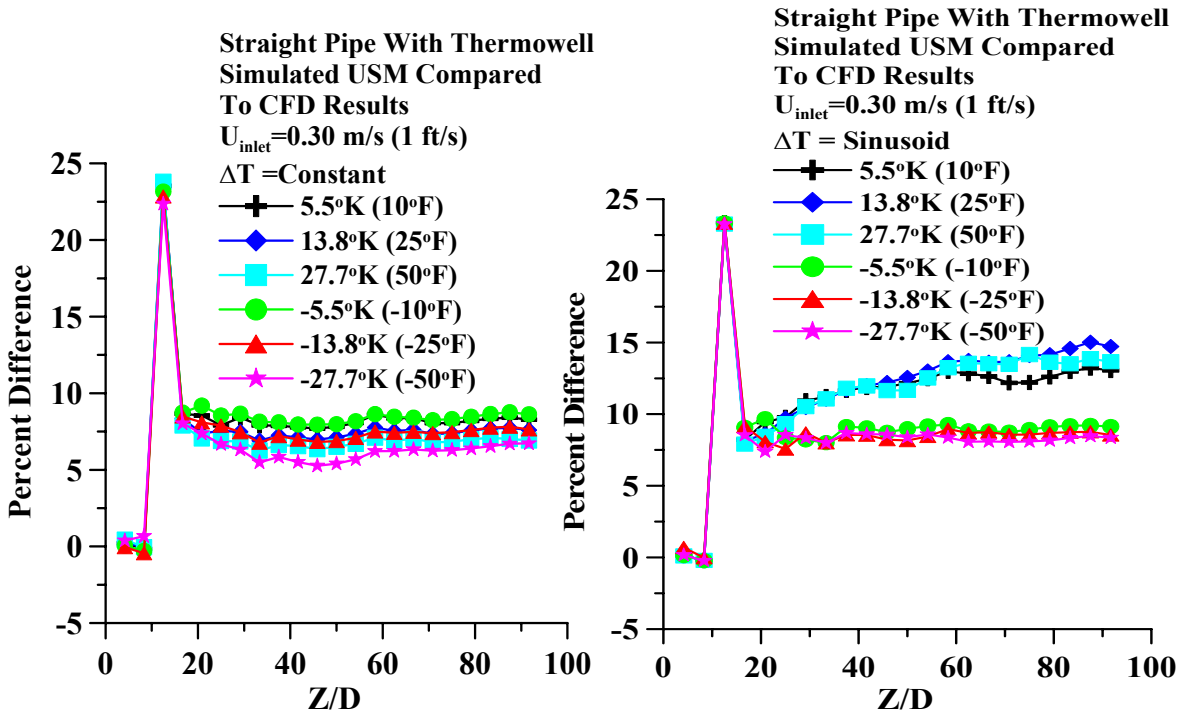

Figure 39 - Ultrasonic flow meter response for straight pipe configuration having 1.0 ft/sec bulk velocity.

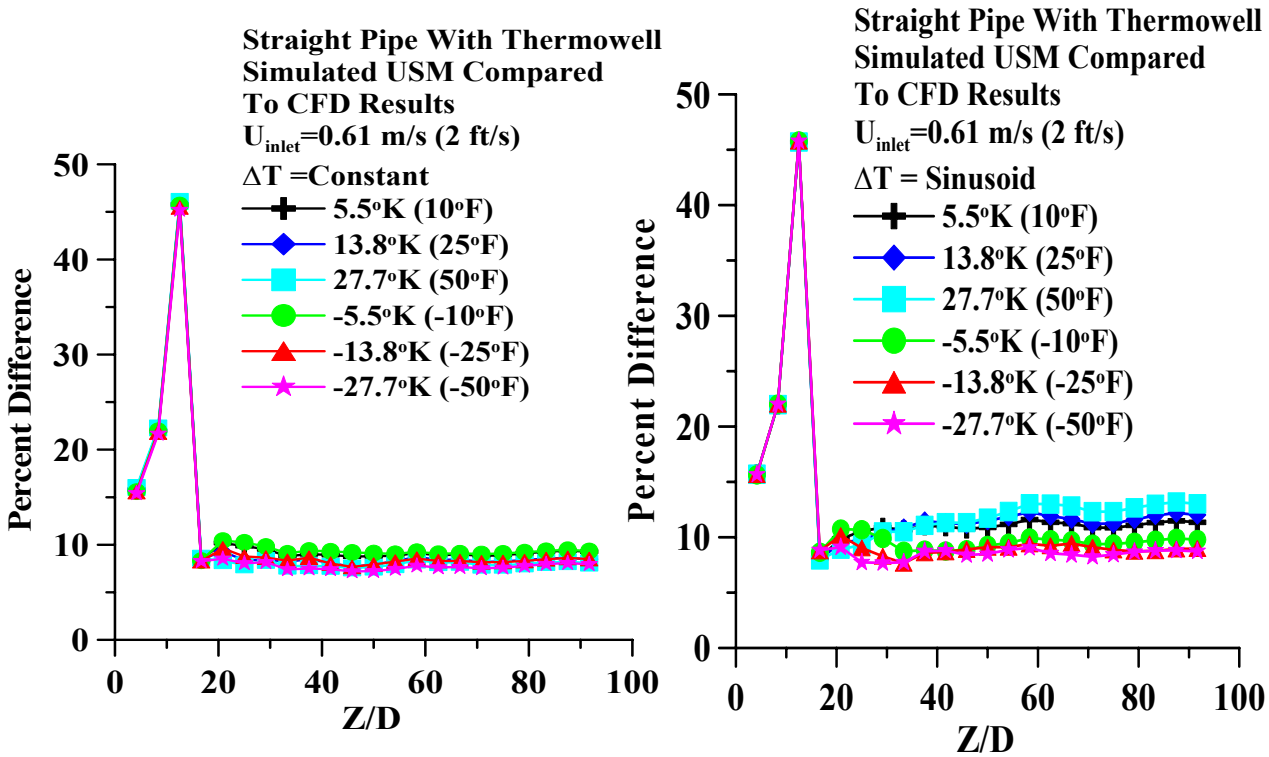

Figure 40 - Ultrasonic flow meter response for straight pipe configuration having 2.0 ft/sec bulk velocity.

Figures 38 through 40 show the percentage error in the response of the Daniel ultrasonic four path flow meter for the straight pipe configuration compared to the CFD analysis results. The USM response is found to vary appreciably from the true CFD results because it was not possible to integrate the acoustic chord lines properly and errors crept in during re-gridding. Re-gridding was required as the FLUENT files could not be loaded into Tecplot directly unlike the cases of single and double elbow pipes. Figure 38 shows that all temperature cases for lowest flow rate have an error of less than 8% for constant temperature pipe and 16% for sinusoid varied wall temperature pipe. A very small error in the flow rate at the pipe inlet shows that the analysis is correct besides the later portion. The initial high error in the graph is due to the presence of the thermal well at Z/D=10. It can be seen that the error increases appreciably in the case of sinusoidal varied wall temperature. The straight pipe (Figure 39) which shows all temperature cases for 0.3048 m/sec flow rate shows an error of less than 8% for constant temperature pipe and 15% for sinusoid varied wall temperature pipe. The initial high error in the graph is due to the presence of the thermal well at Z/D=10. The highest temperature difference and lowest velocity case showed maximum error. The straight pipe (Figure 40) which shows all temperature cases for highest flow rate shows an error of less than 11% for constant temperature pipe and 15% for sinusoid varied wall temperature pipe. An error of 15% in the flow rate at the pipe inlet shows that the line integral of the acoustic paths can be dubious. The initial high error in the graph is due to the presence of the thermal well at Z/D=10.

4.6 Discussion of Appendix A, Appendix D and Appendix E

In this section, the density, temperature and axial velocity contours for the case of Straight pipe geometry will be discussed, and the bulk average velocity plots compared to the simulated ultrasonic meter measurements. The temperature effects of the wall and gas on the thermal well that is placed ten diameters length downstream of the pipe inlet shall also be discussed.

For the case of hot top and cold bottom temperature condition, the top side of the pipe shows low density and the bottom side shows high density. The interior portion of the pipe shows gas stratification due to heating with the density progressively increasing towards the bottom side of the pipe as shown by Figure A-172 and Figure A-208. Due to buoyancy effects, the hot gas tends to move up and the cooler gas tends to move down. Maximum velocity is found to be at the center of the pipe as the gas at the upper and lower sides of the pipe push the gas to the center of the pipe (see Figure A-174). The gas velocity is seen to progressively decrease towards the walls of the pipe. The CFD V_b does not change along the pipe but the change in axial velocity increases with increase in temperature difference (see Figure A-243 through Figure A-245). USM V_b is off from CFD V_b by about 10% in the worst case and increases from the inlet value as the flow progresses downstream.

The results, concerning the measurement of chord bulk average velocity values, show that the deviation of the CFD V_b from the USM V_b can be very high. It is found to be of the order of 8% to 10% which is very large compared to the percentage difference of

0.5% to 2% for the single elbow and double elbow. The reason for this is the inability of Tecplot software to load the fluent files directly on to its platform. We had to re-grid the fluent case and data files so as to gather results form those files. Tecplot could not load the cases of straight pipe directly unlike the cases of single and double elbow. Due to this, velocity information next to the walls in the case of straight tube which were used in the calculation of the chord average velocities could not be gathered. This lead to higher values of USM V_b in all cases of straight tube. This can be seen in Figures A-241 through A-252.

When the top is cold and bottom hot, the density is essentially uniform as the swirling motion of the gas leads to proper mixing of the gas in the pipe (see Figure A-190 and Figure A-226). Due to the motion of the gas, maximum velocity is found to be in the middle of the pipe and progressively reduces towards the walls. It is seen that the change in bulk average velocity across the cross section of the pipe is much less than the previous case and the CFD V_b stays constant (see Figure A-247 through Figure A-249). This is due to the swirling motion of the gas that leads to more mixing of the gas which in turn makes the distribution of temperature more uniform avoiding stratification. USM V_b is off from CFD V_b by about 9% in the worst case and increases from the inlet value as the flow progresses downstream.

In case of uniformly heated wall, the gas density is found to be low at the top end of the pipe and progressively increases towards the bottom end of the pipe (see Figure A-186). Maximum velocity is found to be at the bottom end of the pipe. It is found that the bulk

average velocity of the gas does not vary across the pipe cross section and CFD V_b increases with increase in temperature difference (see Figures A-244 through A-246). USM V_b is off from CFD V_b by about 8% in the worst case and increases from the inlet value as the flow progresses downstream.

In case of uniformly cold wall, the gas density is found to be the highest at the lower side of the pipe cross section due to buoyancy effects. Maximum velocity is found to be at the top side of the pipe (see Figures A-222 and A-119). It is found that bulk average velocity of the gas does not vary across the cross section but and CFD V_b decreases with increase in temperature difference.

In Appendix D, we have included the temperature contours around the thermal well with a diameter of pipe length on each side. This illustrates which case results in the thermal well temperature being the same temperature as the surrounding gas.

It was seen that all cases of V3 (=0.6096 m/sec) produced good measurements of thermal well temperature (see Figures D25 through D36). It can be observed as the temperature contours next to the thermal well are of the same contour level as the neighboring gas temperature contour level – showing their would be no discrepancy in temperature measurement. This may be due to the fact that at high velocities there is more mixing of gases leading to less stratification and more uniform distribution of temperature. At high velocities, the heat transfer rate to the thermal well also increases. The following cases did not result in accurate temperature measurements, as we can see

in the contours that the temperature on the walls of the thermal well is different from that of the gas around it.

V = 0.1524 m/sec and ΔT = +13.8 K.

V = 0.1524 m/sec and ΔT = -5.5 K (Sinusoidal).

V = 0.1524 m/sec and ΔT = -13.8 K (Sinusoidal).

V = 0.1524 m/sec and ΔT = -27.7 K (Sinusoidal).

V = 0.1524 m/sec and ΔT = -27.7 K.

V = 0.3048 m/sec and ΔT = +5.5 K.

V = 0.3048 m/sec and ΔT = -13.8 K.

V = 0.3048 m/sec and ΔT = -27.7 K.

As can be seen, most of the cases showing inaccurate temperature measurements are that of the lowest velocity. Due to low velocity, gas residence time increases with which the gas has more time to be heated and hence stratified. Also, at high temperature differences, discrepancies creep in. For positive ΔT, the temperature is over estimated and for negative ΔT, the temperature is under estimated. Figure 41 shows an example of in-accuracy in temperature measurement that can be easily noted by observing the contours.

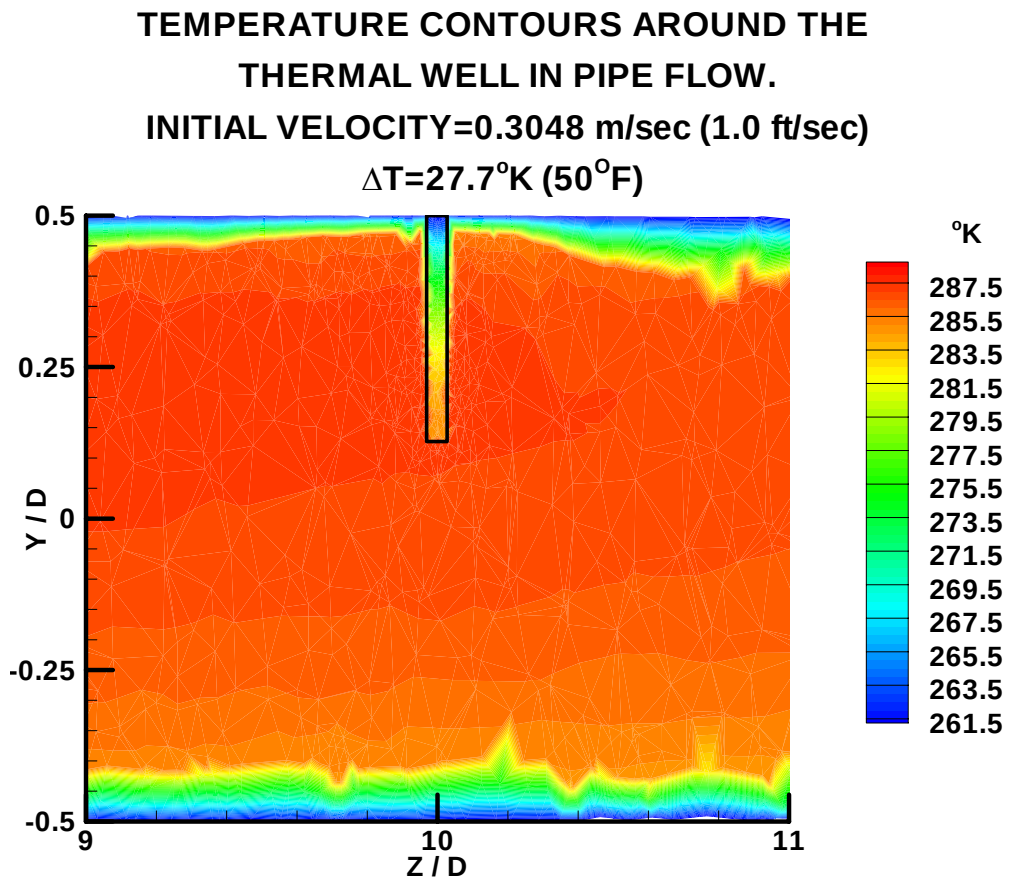

Figure 41 – Thermal well giving incorrect temperature measurements.

4.7 Comparison of Analytical and CFD Analysis on Thermal Well

CFD analysis has been performed for the flow over the cylindrical thermal well that resulted in illustrating how the temperature response of the thermal well would be in different flow conditions. What is required in addition to this CFD analysis is a bench mark that will show how different the temperature response of the thermal well is from a simple one dimensional analytical analysis. This would also help in knowing of any

discrepancies in temperature measurement, which is the case if the analytical and CFD analysis results differ appreciably.

Appendix E contains figures comparing the CFD analysis results and analytic results – graphs showing variation of temperature along the length of the thermal well.

A finite difference method was employed in solving this problem analytically. A hollow cylinder with its base temperature (end of the thermal well next to the pipe wall) known and mixed boundary condition along the length of the thermal well to the end of the cylinder (free end of the thermal well) was modeled. Equations were formulated using conservation of energy and rewritten in discretized form.

It can be seen from Figures E-11 through E-14 that the CFD results compared to the simple analytical analysis under-estimate high wall temperatures and over-estimate low wall temperatures. It is seen that for negative sinusoidal temperature variations (-SinT), the CFD analysis shows under-estimation of the cylinder free end temperature by about 0.7% for gas velocity V1 (=0.1524 m/sec), 1.1% for gas velocity V2 (=0.3048 m/sec) and 1.2% for gas velocity V3 (=0.6096 m/sec). For constant high wall temperature conditions (+T), it can be seen from Figure E-7 through Figure E-12 that the free end temperature of the cylinder is under-estimated by the CFD analysis by almost 1.5% for gas velocity V1 (=0.1524 m/sec), 1.2% for gas velocity V2 (=0.3048 m/sec) and 0.3% for gas velocity V3 (=0.6096 m/sec). It is seen that for positive sinusoidal temperature variations (+SinT), the CFD analysis shows over estimation of the free end of the cylinder by about 0.7% for gas velocity V1 (=0.1524 m/sec), 0.3% for gas velocity V2

(=0.3048 m/sec) and 0.25% for gas velocity V3 (=0.6096 m/sec) - refer to Figure E-3 and Figure E-4. For constant cold wall temperature conditions (-T), it can be seen from Figure E-19 through Figure E-24 that the temperature is not measured correctly at both ends of the cylindrical thermal well and the under-estimation of temperature at the free end is about 0.7% for gas velocity V1 (=0.1524 m/sec), 0.3% for gas velocity V2 (=0.3048 m/sec) and 0.4% for gas velocity V3 (=0.6096 m/sec).

4.8 Conclusions and Recommendations

It can be seen from the contours and discussions that both flow pattern and temperature difference play a major role in stratifying the flow through the pipe. In a case where both flow pattern and temperature difference are working together, the flow has been observed to change drastically and the ultrasonic meter measurements have given highly inaccurate results.

In the case of single and double elbow pipe configuration, heating caused increased errors in the response of the ultrasonic flow meter. For the cases of single and double elbow geometries, it was noted that the errors were below 0.5% for all cases except when the wall temperature conditions changed to sinusoid variation. The sinusoid variation in the wall temperature resulted in localized velocity maxima at the center of the pipe. The ultrasonic meter acoustic paths barely touched the centerline of the pipe giving a maximum error of 1% below the true value. The error was noted to increase due to heavy stratification at the center of the pipe due to momentum and thermal effects.

The fact that the ultrasonic meter acoustic paths miss the high and low velocity regions due to stratification is the root cause of all the errors noted in the USM response.

It is also noted that in case of uniform wall temperature conditions, both uniformly hot and cold cases give an error in the ultrasonic meter measurements. The variation of gas velocity across the pipe cross section is noted maximum in these cases, even more than the temperature varying cases. This makes the ultrasonic meter register different gas velocity reading at different heights of the pipe cross section. The bulk average velocity is noted to increase or decrease on varying the temperature difference on the walls.

The largest error was produced in the case of double elbow geometry having sinusoid wall temperature variation. These conditions lead to a swirl type flow in the pipe causing localized velocity maxima at the center of the pipe. Unlike the previous cases of vertical stratification of gas, the flow in this case was essentially axisymmetric. This produced an error of 1.4% in the USM response for the highest degree of swirl.

The thermal well response indicates that below 2 ft/sec a thermal well would give inaccurate measurements of temperature. The analytical results were found to suffice for determining the temperature response of the thermal well. On comparing the two cases it was found that the maximum difference in temperature measurement was less than 1.5%.

It is recommended for further scope of this research that the cases should be run for larger gas velocity ranges and larger temperature differences. Also, it would be

interesting to note how the flow varies on the vertical acoustic paths in addition to the horizontal acoustic paths.

REFERENCES

[1] FLUENT, Inc, 2004, *FLUENT Tutorial Version 6.1.22*, Lebanon, NH.

[2] Incropera, F. and DeWitt, D., 1996, *Fundamentals of Heat and Mass Transfer*, Fourth Edition, John Wiley & Sons Inc., Indianapolis, IN.

[3] Schmidt, E. and Wenner, K., 1941, "Heat Transfer over the Circumference of a Heated Cylinder in Transverse Flow," National Advisory Committee for Aeronautics Technical Memorandum No. 1050.

[4] Fage, A., and Falkner, V.M., 1931, "Further Experiments on the Flow around a Circular Cylinder," Research & Memorandum No. 1369, British Academic Research Collaboration.

[5] Tecplot, Inc, 2003, *Tecplot Tutorial Version* 10, Bellevue, WA.

APPENDICES

These appendices are meant to be viewed on the monitor, not printed. If the reader desires further information, please contact the author.

For the purpose of better reading and understanding, we have used a proper format and order of display in all appendices. Appendices A, B and C are broken into four sections corresponding to the wall temperature conditions. The first part of each section consists of density, temperature and velocity contours at pipe cross-sections which are animated to sweep down the length of the pipe.

The second part consists of density, temperature and velocity contours at the chord heights corresponding to the acoustic chords of the ultrasonic meter. The third part consists of the graph plots of simulated bulk average velocity of the ultrasonic meter, bulk average velocity form CFD analysis and individual chord velocities calculated at the chord heights.

In Appendices A, B and C Figures 1 to 36, 85 to 120 and 169 to 204 are the animated sweeps (to view animation, click an individual figure), Figures 37 to 72, 121 to 156 and 205 to 240 are the chord contours and Figures 73 to 84, 157 to 168 and 241 to 252 are the graph plots comparing the simulated and computationally calculated chord average velocities.

In Appendix D, we have included the temperature contours around the thermal well with a diameter of pipe length on each side. This illustrates which case results in the thermal well temperature being the same temperature as the surrounding gas.

Appendix E contains figures comparing the CFD analysis results and analytic results – graphs showing variation of temperature along the length of the thermal well.

APPENDIX A

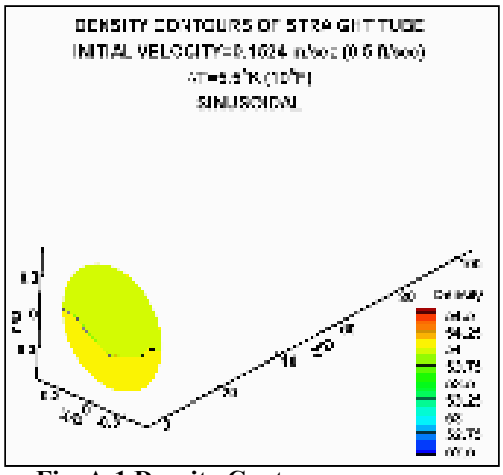

Fig. A-1 Density Contours
V_0=0.1524 m/sec, ΔT_{wall}=5.5°K Sinusoidal

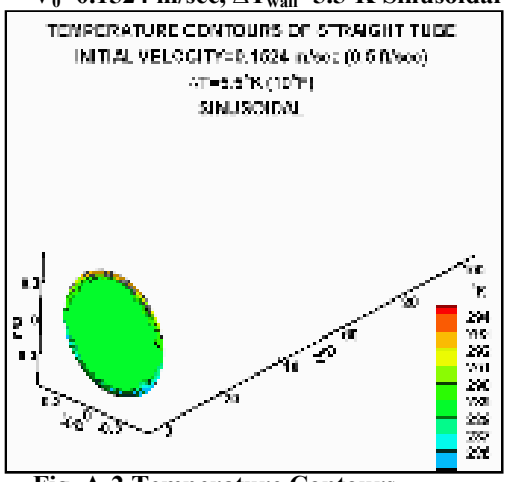

Fig. A-2 Temperature Contours
V_0=0.1524 m/sec, ΔT_{wall}=5.5°K Sinusoidal

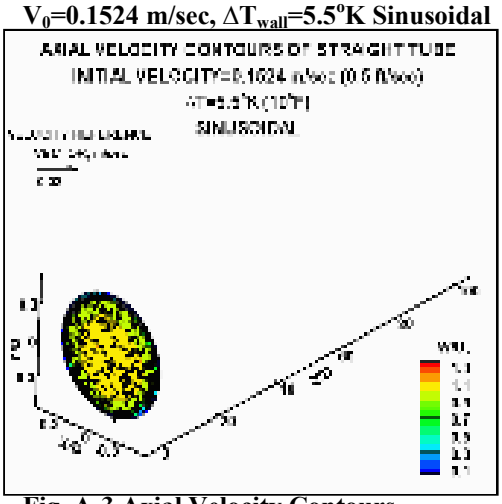

Fig. A-3 Axial Velocity Contours
V_0=0.1524 m/sec, ΔT_{wall}=5.5°K Sinusoidal

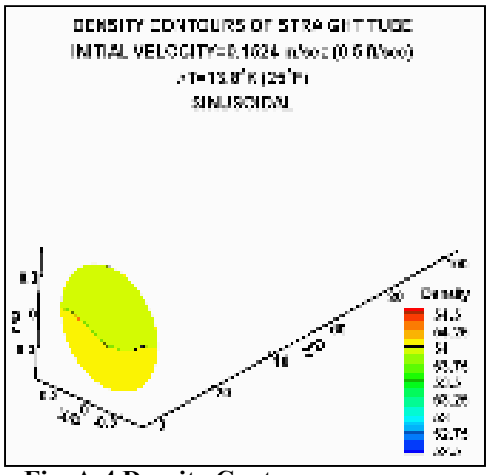

Fig. A-4 Density Contours
V_0=0.1524 m/sec, ΔT_{wall}=13.8°K Sinusoidal

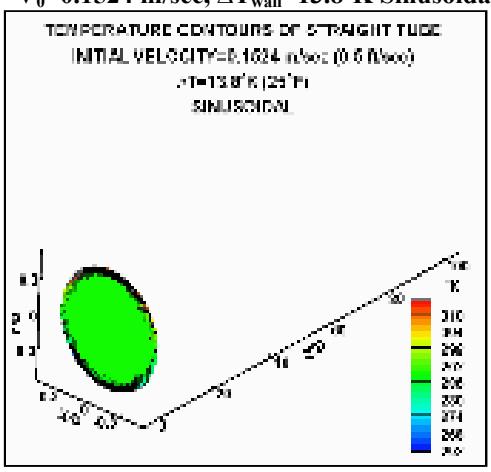

Fig. A-5 Temperature Contours
V_0=0.1524 m/sec, ΔT_{wall}=13.8°K Sinusoidal

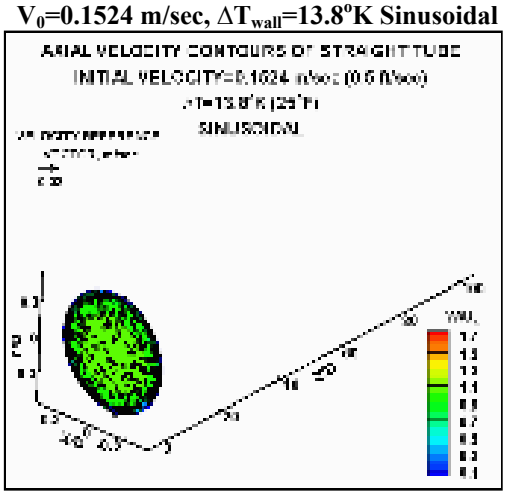

Fig. A-6 Axial Velocity Contours
V_0=0.1524 m/sec, ΔT_{wall}=13.8°K Sinusoidal

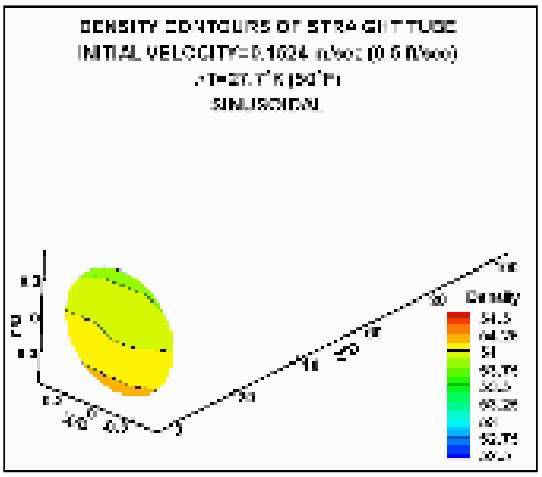

Fig. A-7 Density Contours
V_0=0.1524 m/sec, ΔT_{wall}=27.7°K Sinusoidal

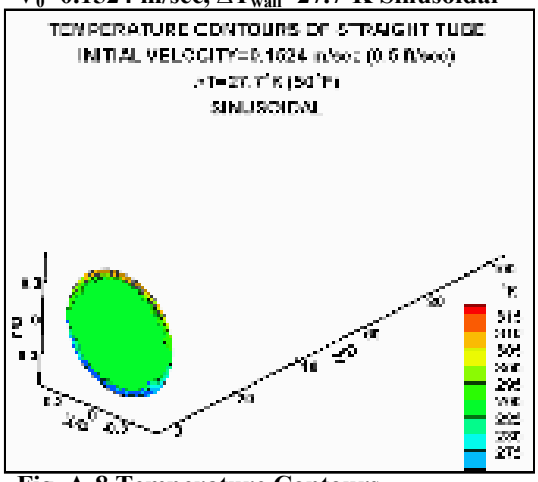

Fig. A-8 Temperature Contours
V_0=0.1524 m/sec, ΔT_{wall}=27.7°K Sinusoidal

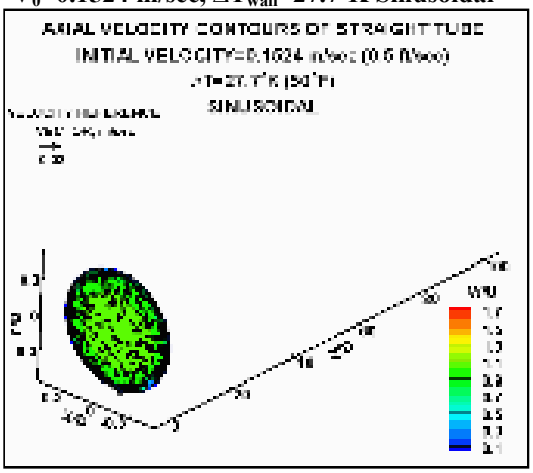

Fig. A-9 Axial Velocity Contours
V_0=0.1524 m/sec, ΔT_{wall}=27.7°K Sinusoidal

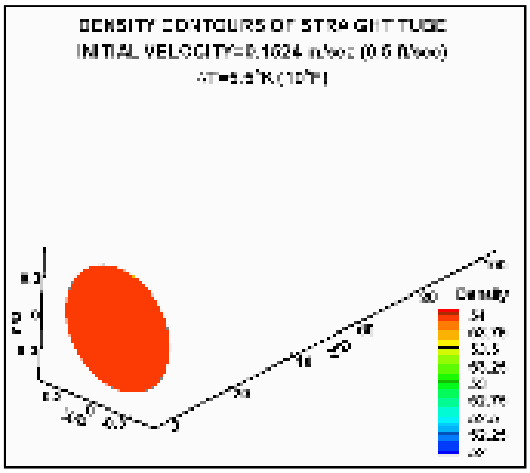

Fig. A-10 Density Contours
V_0=0.1524 m/sec, ΔT_{wall}=5.5°K

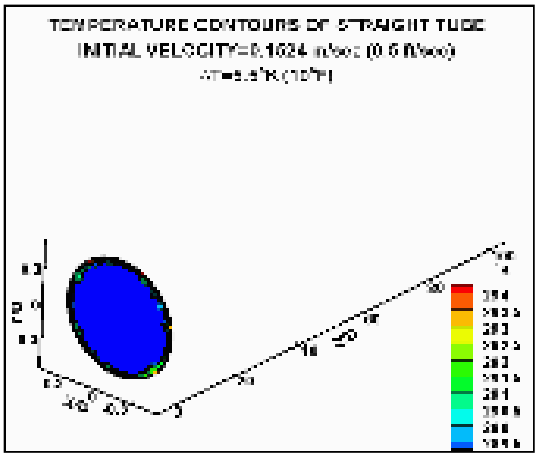

Fig. A-11 Temperature Contours
V_0=0.1524 m/sec, ΔT_{wall}=5.5°K

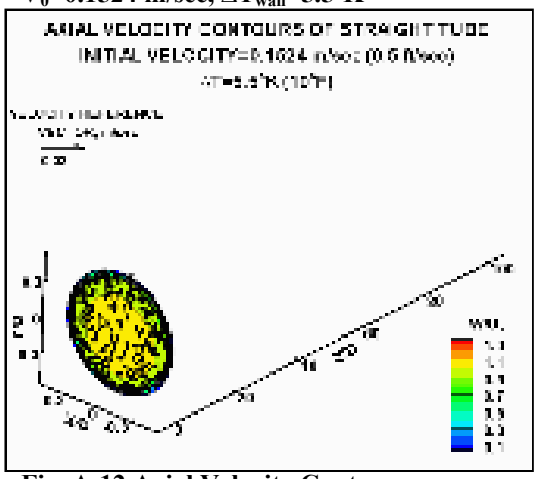

Fig. A-12 Axial Velocity Contours
V_0=0.1524 m/sec, ΔT_{wall}=5.5°K

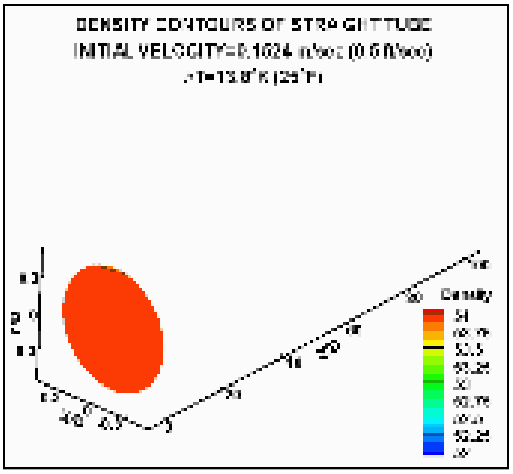

Fig. A-13 Density Contours
V_0=0.1524 m/sec, ΔT_{wall}=13.8°K

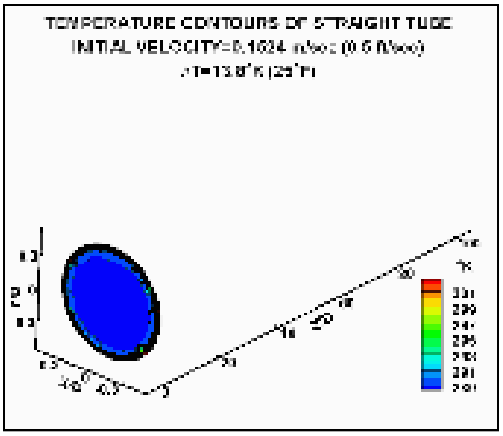

Fig. A-14 Temperature Contours
V_0=0.1524 m/sec, ΔT_{wall}=13.8°K

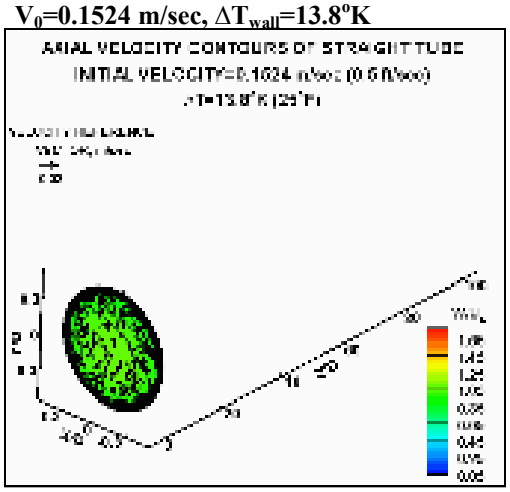

Fig. A-15 Axial Velocity Contours
V_0=0.1524 m/sec, ΔT_{wall}=13.8°K

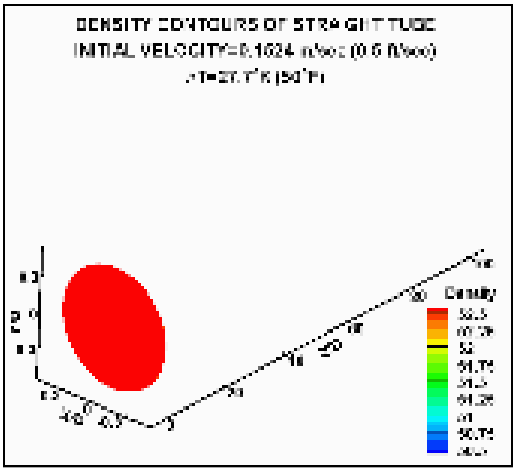

Fig. A-16 Density Contours
V_0=0.1524 m/sec, ΔT_{wall}=27.7°K

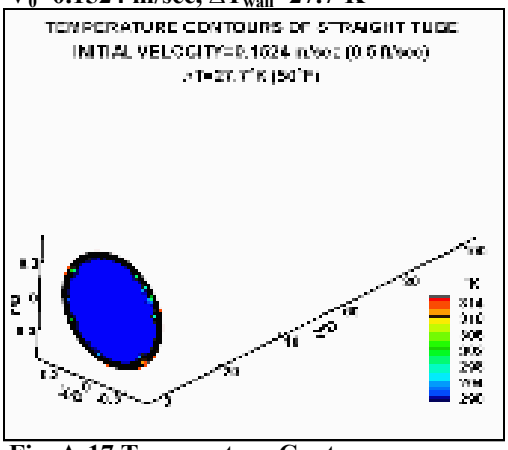

Fig. A-17 Temperature Contours
V_0=0.1524 m/sec, ΔT_{wall}=27.7°K

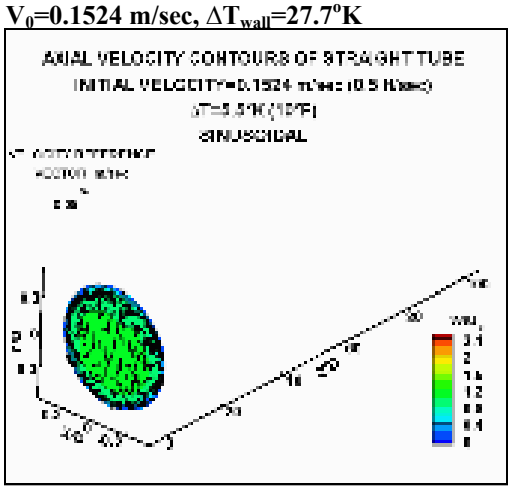

Fig. A-18 Axial Velocity Contours
V_0=0.1524 m/sec, ΔT_{wall}=27.7°K

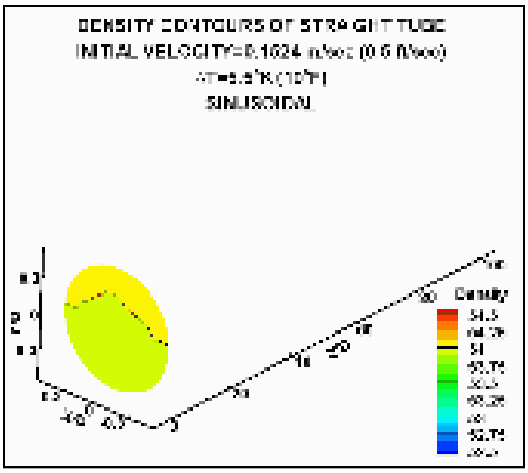

Fig. A-19 Density Contours
V_0=0.1524 m/sec, ΔT_{wall}=-5.5°K Sinusoidal

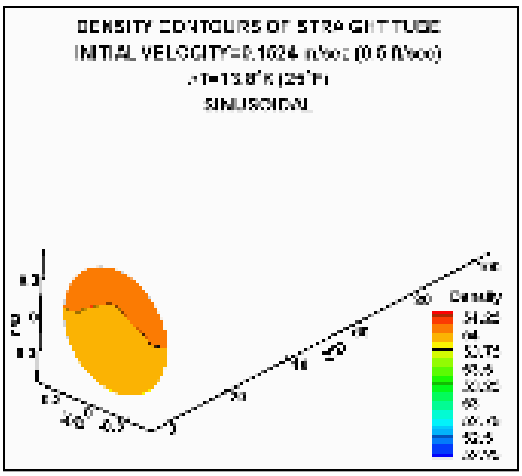

Fig. A-22 Density Contours
V_0=0.1524 m/sec, ΔT_{wall}=-13.8°K Sinusoidal

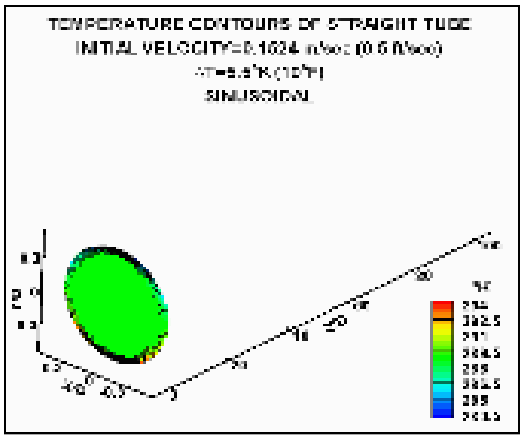

Fig. A-20 Temperature Contours
V_0=0.1524 m/sec, ΔT_{wall}=-5.5°K Sinusoidal

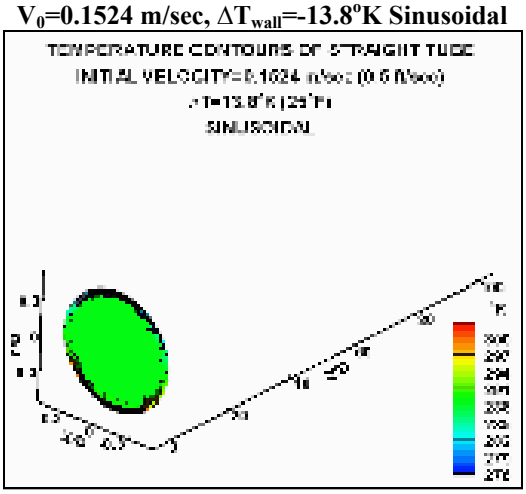

Fig. A-23 Temperature Contours
V_0=0.1524 m/sec, ΔT_{wall}=-13.8°K Sinusoidal

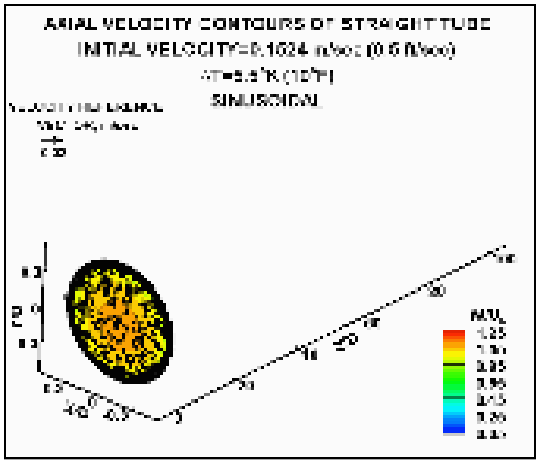

Fig. A-21Axial Velocity Contours
V_0=0.1524 m/sec, ΔT_{wall}=-5.5°K Sinusoidal

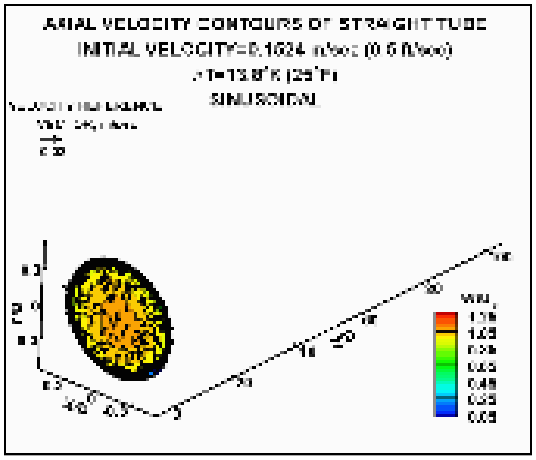

Fig. A-24 Axial Velocity Contours
V_0=0.1524 m/sec, ΔT_{wall}=-13.8°K Sinusoidal

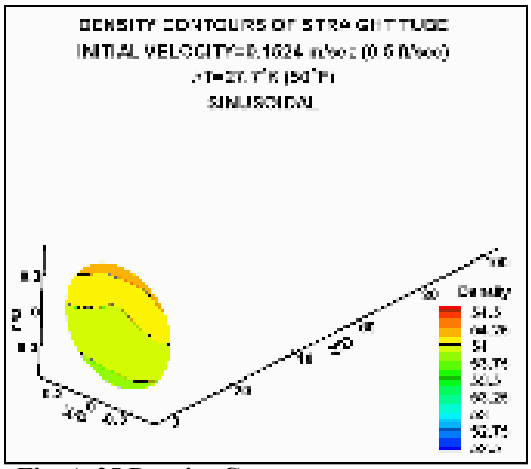

Fig. A-25 Density Contours
V_0=0.1524 m/sec, ΔT_{wall}=-27.7°K Sinusoidal

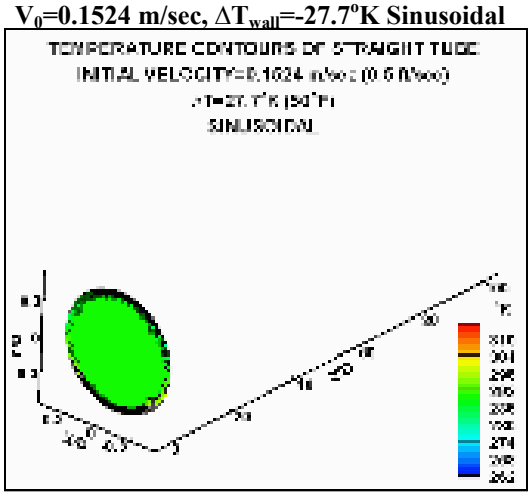

Fig. A-26 Temperature Contours
V_0=0.1524 m/sec, ΔT_{wall}=-27.7°K Sinusoidal

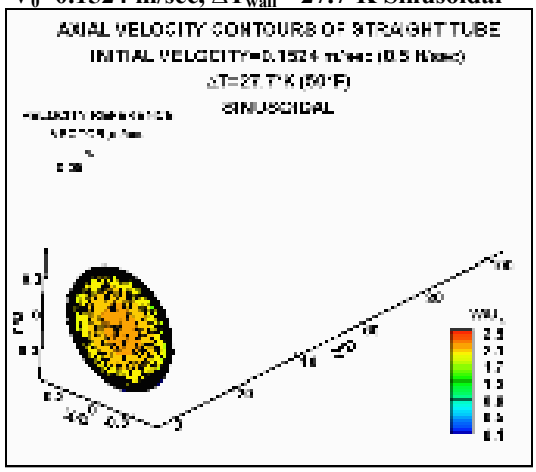

Fig. A-27 Axial Velocity Contours
V_0=0.1524 m/sec, ΔT_{wall}=-27.7°K Sinusoidal

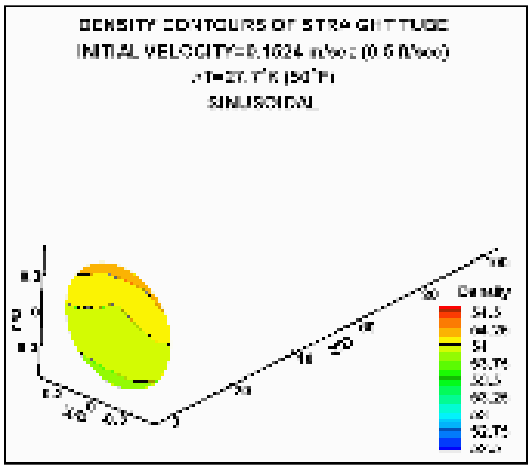

Fig. A-28 Density Contours
V_0=0.1524 m/sec, ΔT_{wall}=-5.5°K

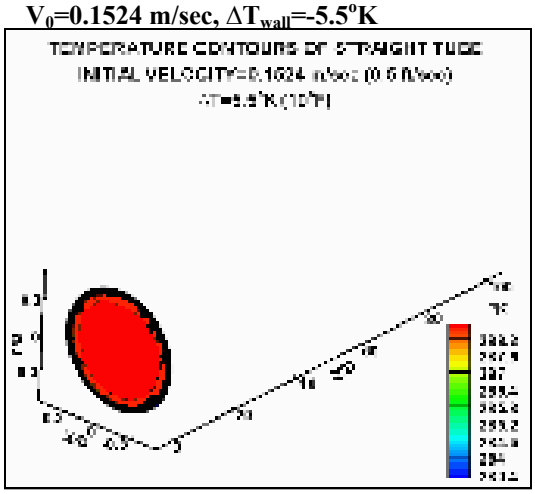

Fig. A-29 Temperature Contours
V_0=0.1524 m/sec, ΔT_{wall}=-5.5°K

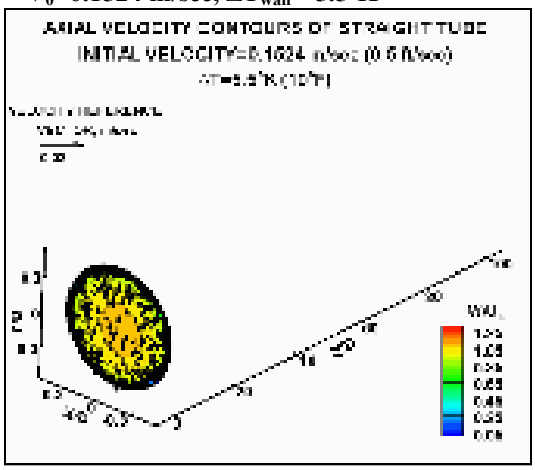

Fig. A-30 Axial Velocity Contours
V_0=0.1524 m/sec, ΔT_{wall}=-5.5°K

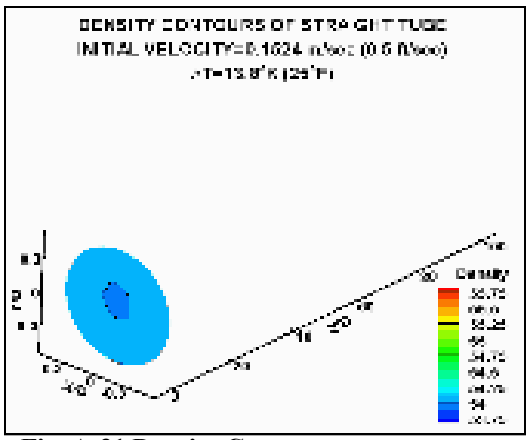

Fig. A-31 Density Contours
V_0=0.1524 m/sec, ΔT_{wall}=-13.8°K

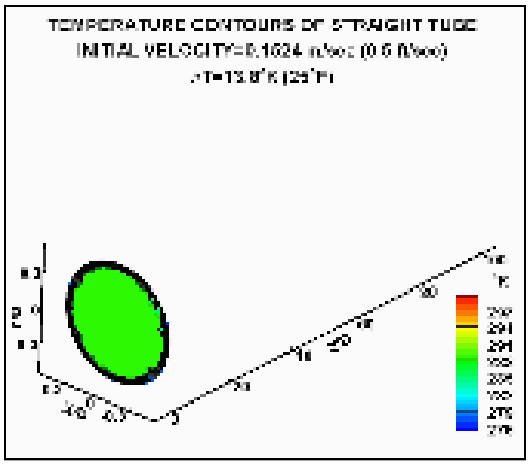

Fig. A-32 Temperature Contours
V_0=0.1524 m/sec, ΔT_{wall}=-13.8°K

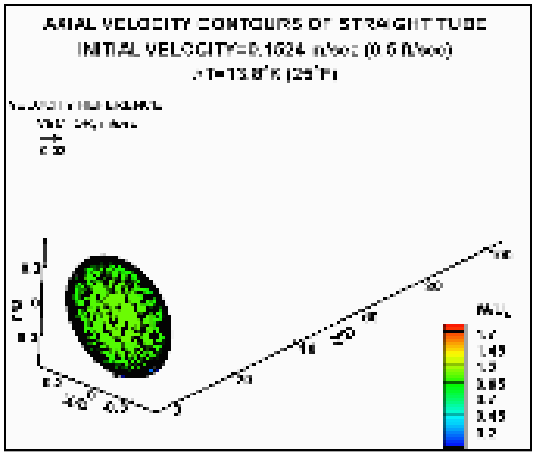

Fig. A-33 Axial Velocity Contours
V_0=0.1524 m/sec, ΔT_{wall}=-13.8°K

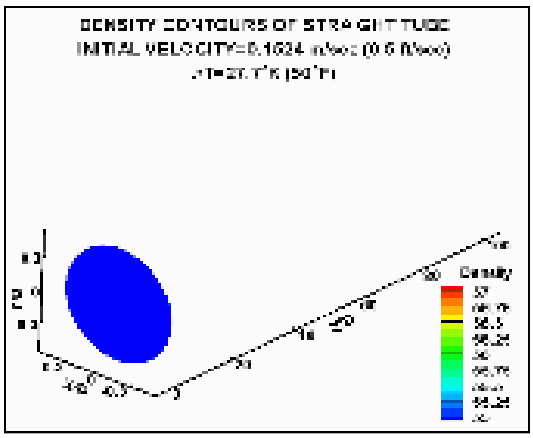

Fig. A-34 Density Contours
V_0=0.1524 m/sec, ΔT_{wall}=-27.7°K

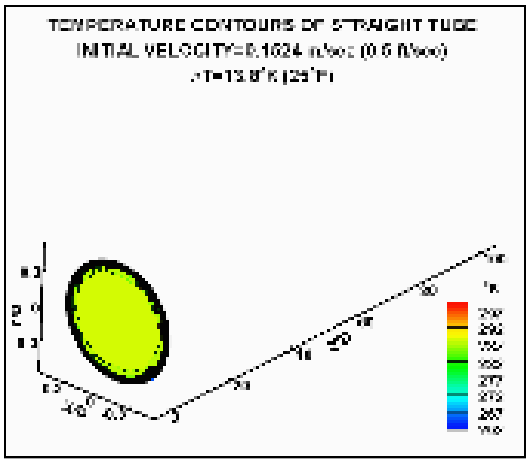

Fig. A-35 Temperature Contours
V_0=0.1524 m/sec, ΔT_{wall}=-27.7°K

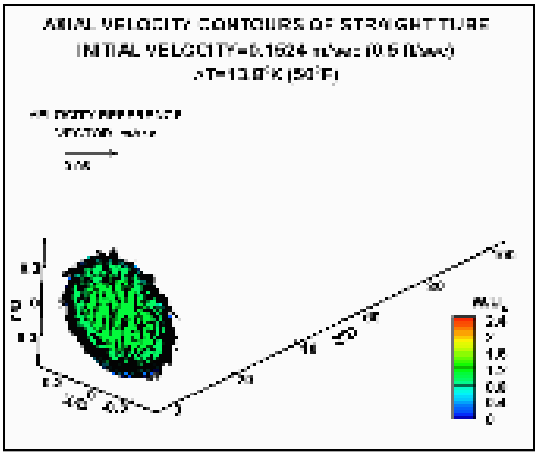

Fig. A-36 Axial Velocity Contours
V_0=0.1524 m/sec, ΔT_{wall}=-27.7°K

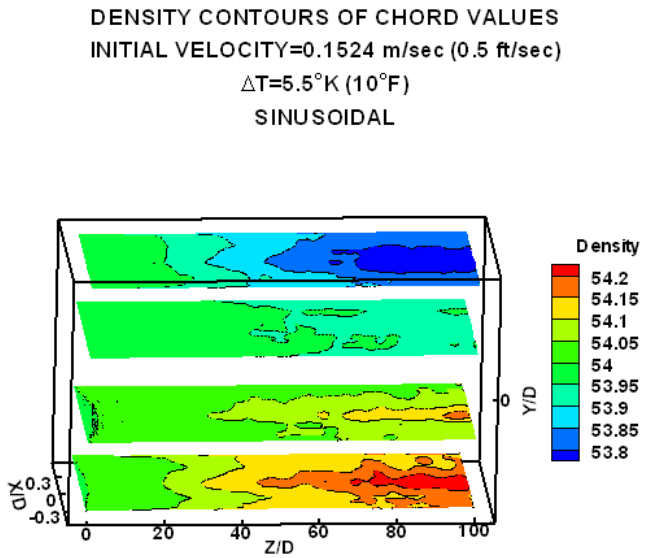

Fig. A-37 Density Slice Contours
V_0=0.1524 m/sec, ΔT_{wall}=5.5°K Sinusoidal

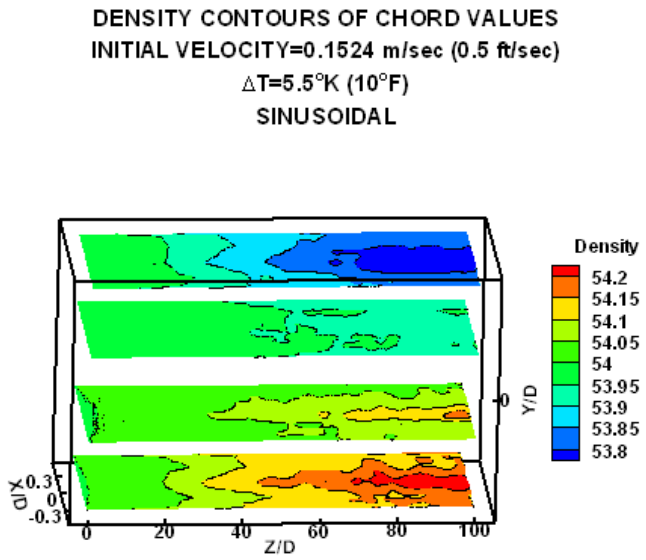

Fig. A-38 Temperature Slice Contours
V_0=0.1524 m/sec, ΔT_{wall}=5.5°K Sinusoidal

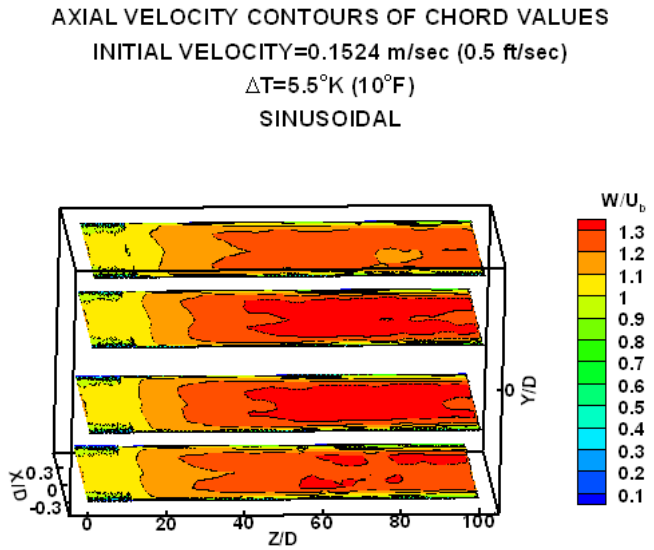

Fig. A-39 Axial Velocity Slice Contours
V_0=0.1524 m/sec, ΔT_{wall}=5.5°K Sinusoidal

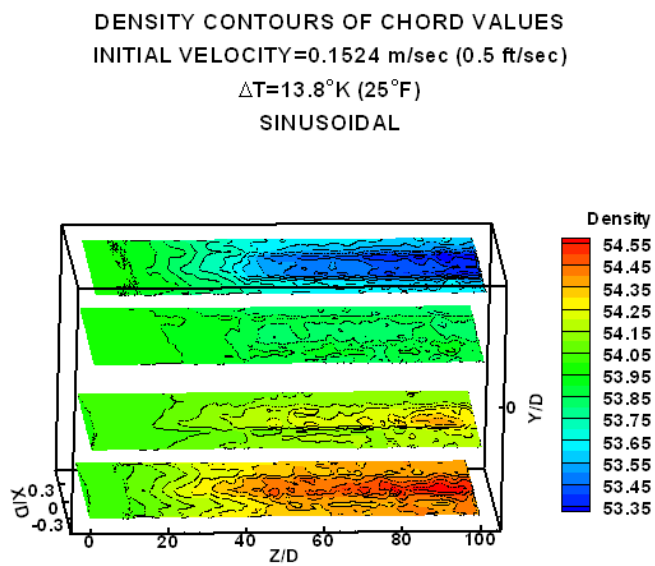

Fig. A-40 Density Slice Contours
V_0=0.1524 m/sec, ΔT_{wall}=13.8°K Sinusoidal

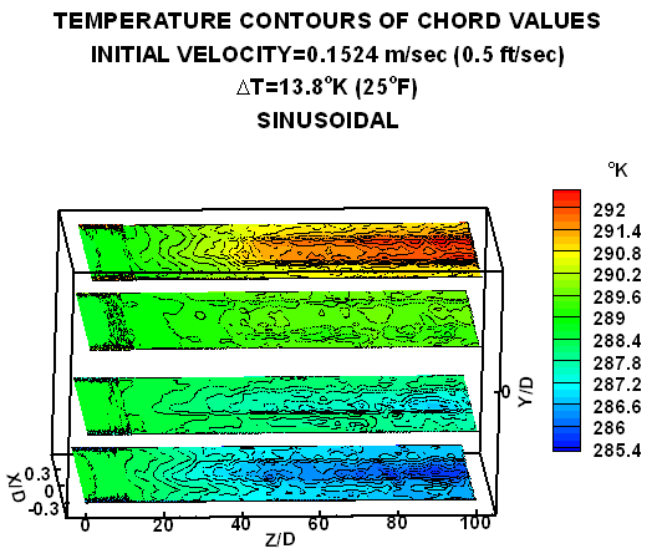

V_0=0.1524 m/sec, ΔT_{wall}=13.8°K Sinusoidal

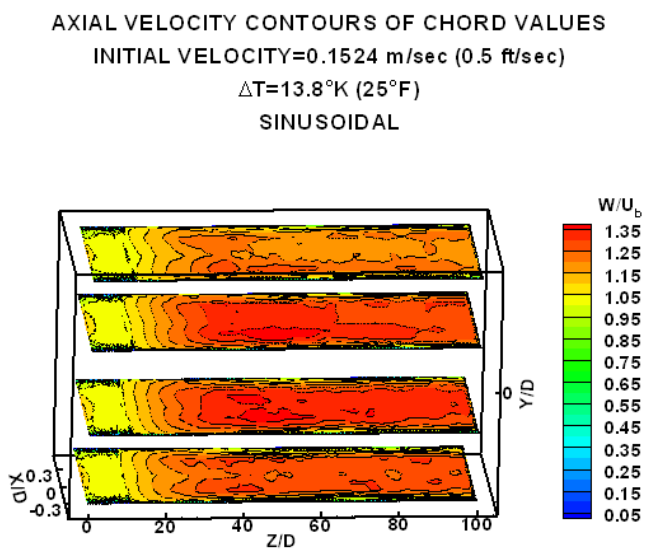

V_0=0.1524 m/sec, ΔT_{wall}=13.8°K Sinusoidal

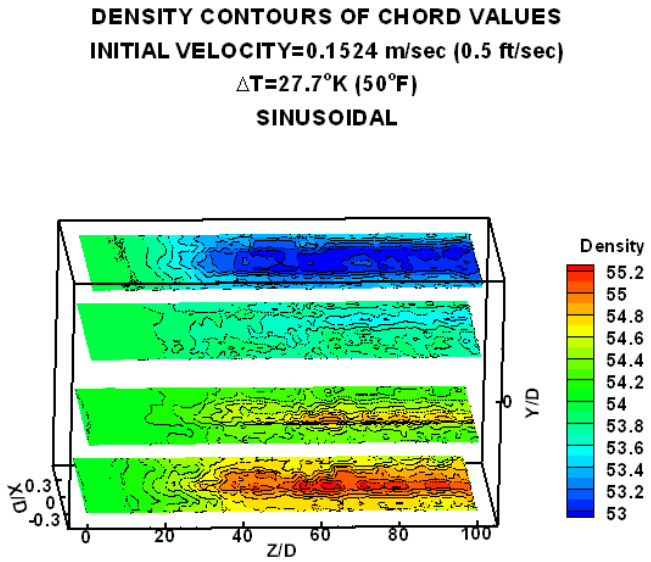

Fig. A-43 Density Slice Contours
V_0=0.1524 m/sec, ΔT_{wall}=27.7°K Sinusoidal

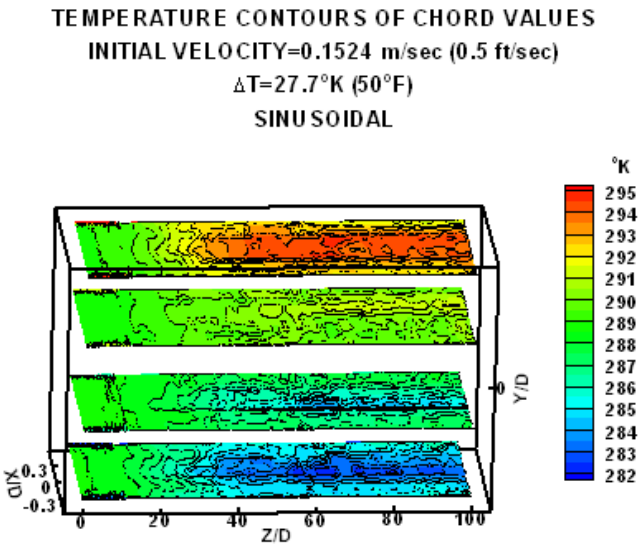

Fig. A-44 Temperature Slice Contours
V_0=0.1524 m/sec, ΔT_{wall}=27.7°K Sinusoidal

AXIAL VELOCITY CONTOURS OF CHORD VALUES
INITIAL VELOCITY=0.1524 m/sec (0.5 ft/sec)
ΔT=27.7°K (50°F)
SINUSOIDAL

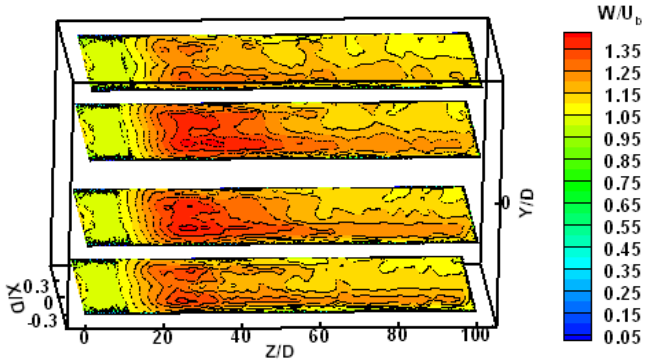

Fig. A-45 Axial Velocity Slice Contours
V_0=0.1524 m/sec, ΔT_{wall}=27.7°K Sinusoidal

DENSITY CONTOURS OF CHORD VALUES
INITIAL VELOCITY=0.1524 m/sec (0.5 ft/sec)
ΔT=5.5°K (10°F)

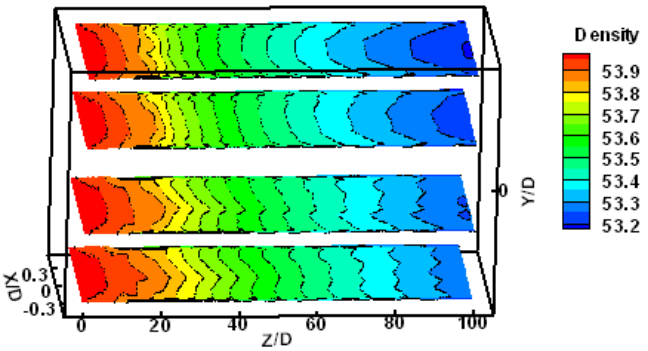

Fig. A-46 Density Slice Contours
V_0=0.1524 m/sec, ΔT_{wall}=5.5°K

TEMPERATURE CONTOURS OF CHORD VALUES
INITIAL VELOCITY=0.1524 m/sec (0.5 ft/sec)
ΔT=5.5°K (10°F)

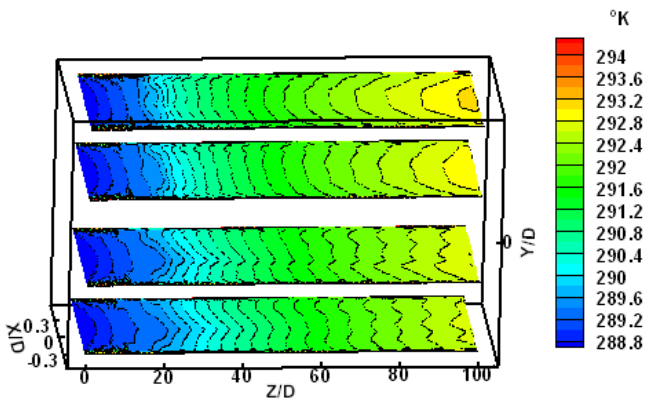

Fig. A-47 Temperature Slice Contours
V_0=0.1524 m/sec, ΔT_{wall}=5.5°K

AXIAL VELOCITY CONTOURS OF CHORD VALUES
INITIAL VELOCITY=0.1524 m/sec (0.5 ft/sec)
ΔT=5.5°K (10°F)

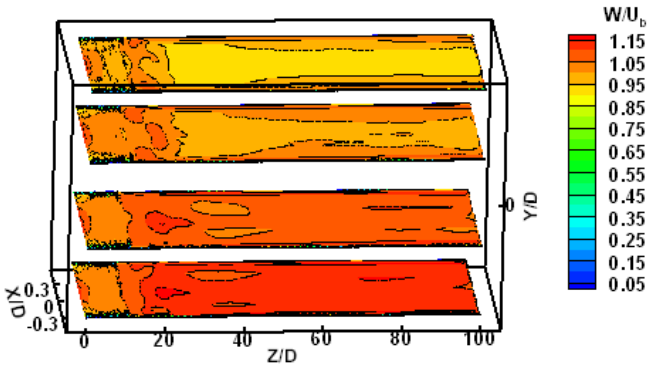

Fig. A-48 Axial Velocity Slice Contours
V_0=0.1524 m/sec, ΔT_{wall}=5.5°K

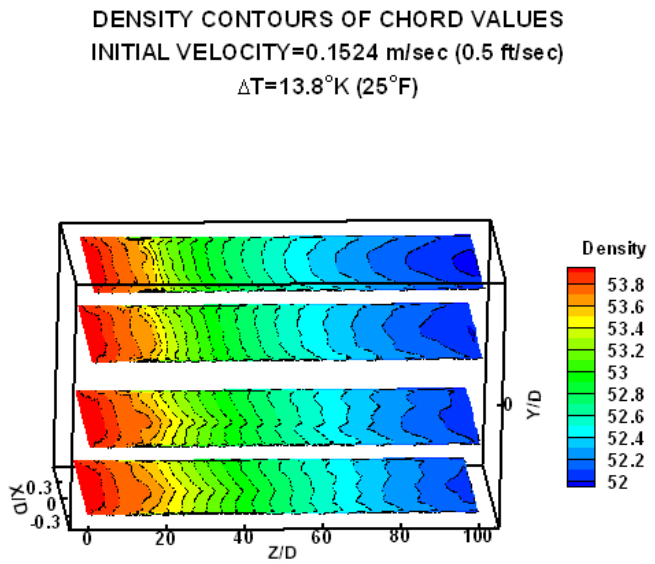

Fig. A-49 Density Slice Contours
V_0=0.1524 m/sec, ΔT_{wall}=13.8°K

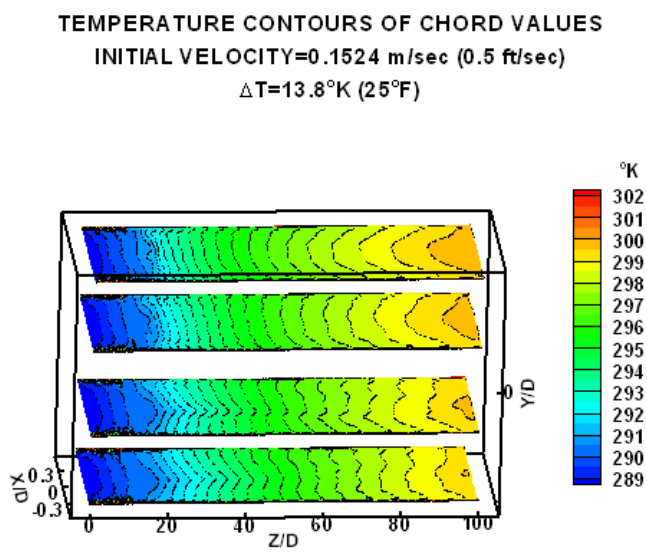

Fig. A-50 Temperature Slice Contours
V_0=0.1524 m/sec, ΔT_{wall}=13.8°K

AXIAL VELOCITY CONTOURS OF CHORD VALUES
INITIAL VELOCITY=0.1524 m/sec (0.5 ft/sec)
ΔT=13.8°K (25°F)

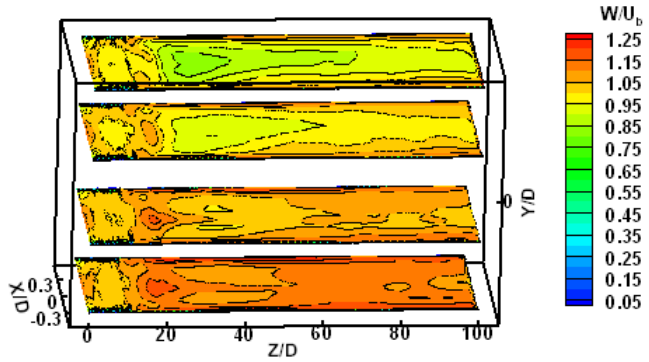

Fig. A-51 Axial Velocity Slice Contours
V_0=0.1524 m/sec, ΔT_{wall}=13.8°K

DENSITY CONTOURS OF CHORD VALUES
INITIAL VELOCITY=0.1524 m/sec (0.5 ft/sec)
ΔT=27.7°K (50°F)

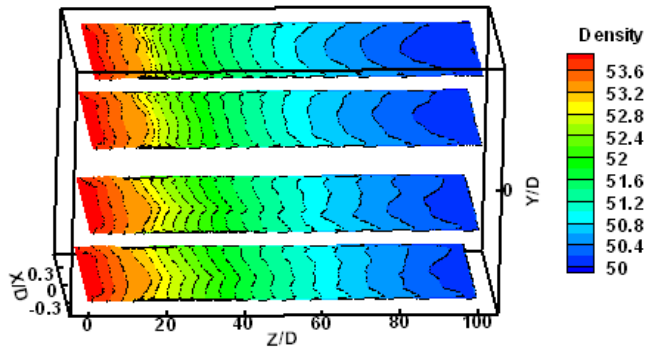

Fig. A-52 Density Slice Contours
V_0=0.1524 m/sec, ΔT_{wall}=27.7°K

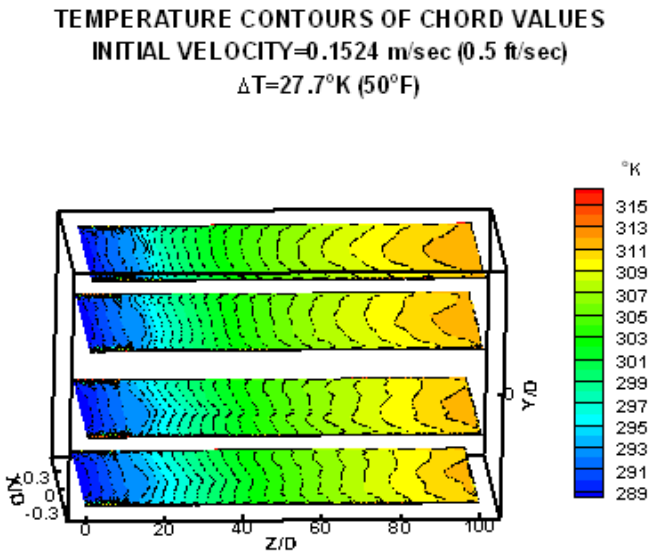

Fig. A-53 Temperature Slice Contours
V_0=0.1524 m/sec, ΔT_{wall}=27.7°K

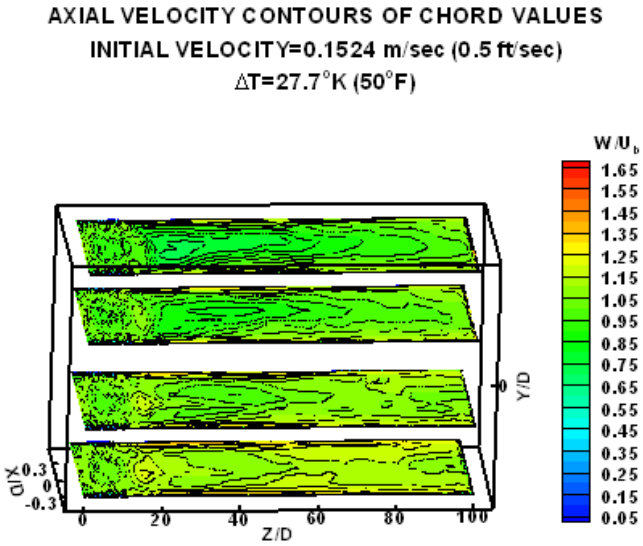

Fig. A-54 Axial Velocity Slice Contours
V_0=0.1524 m/sec, ΔT_{wall}=27.7°K

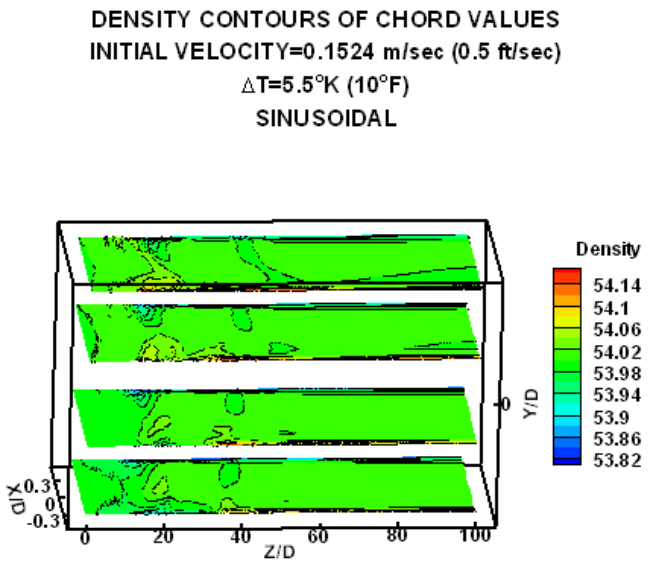

Fig. A-55 Density Slice Contours
V_0=0.1524 m/sec, ΔT_{wall}=-5.5°K Sinusoidal

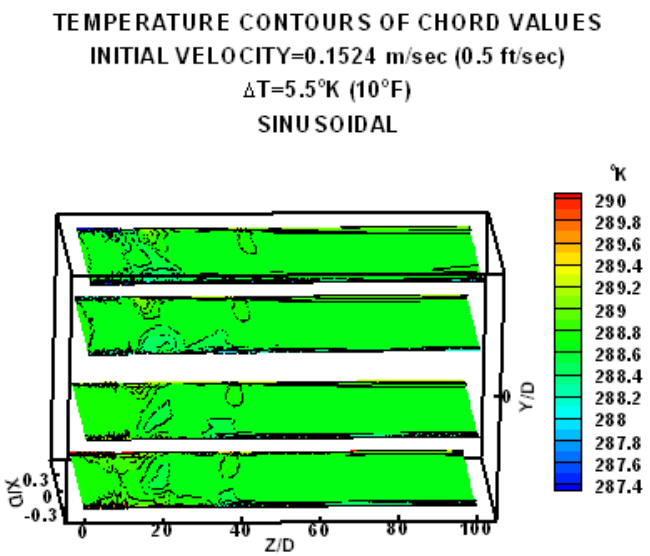

Fig. A-56 Temperature Slice Contours
V_0=0.1524 m/sec, ΔT_{wall}=-5.5°K Sinusoidal

AXIAL VELOCITY CONTOURS OF CHORD VALUES
INITIAL VELOCITY=0.1524 m/sec (0.5 ft/sec)
ΔT=5.5°K (10°F)
SINUSOIDAL

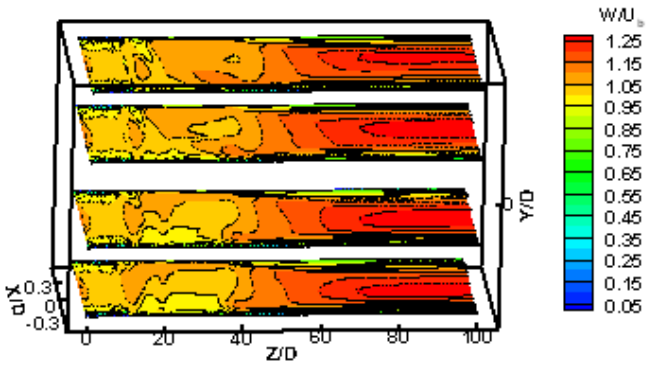

Fig. A-57 Axial Velocity Slice Contours
V_0=0.1524 m/sec, ΔT_{wall}=-5.5°K Sinusoidal

DENSITY CONTOURS OF CHORD VALUES
INITIAL VELOCITY=0.1524 m/sec (0.5 ft/sec)
ΔT=13.8°K (25°F)
SINUSOIDAL

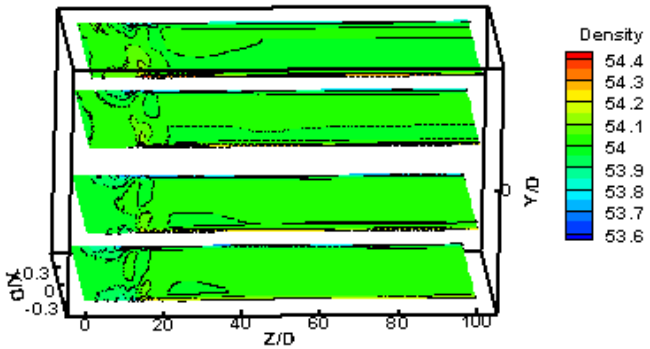

Fig. A-58 Density Slice Contours
V_0=0.1524 m/sec, ΔT_{wall}=-13.8°K Sinusoidal

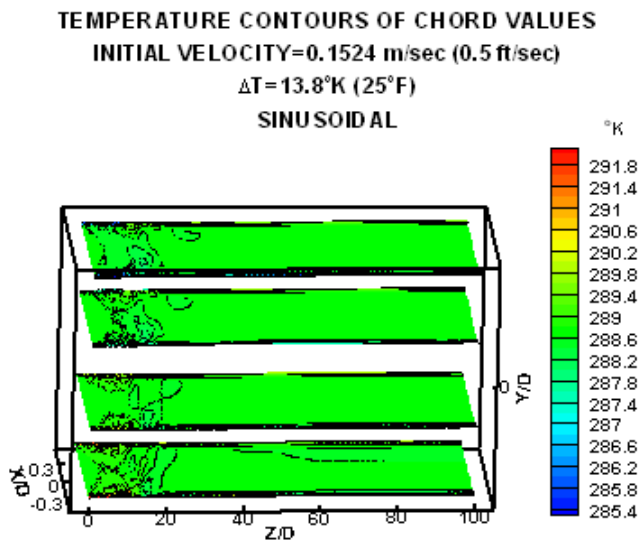

Fig. A-59 Temperature Slice Contours
V_0=0.1524 m/sec, ΔT_{wall}=-13.8°K Sinusoidal

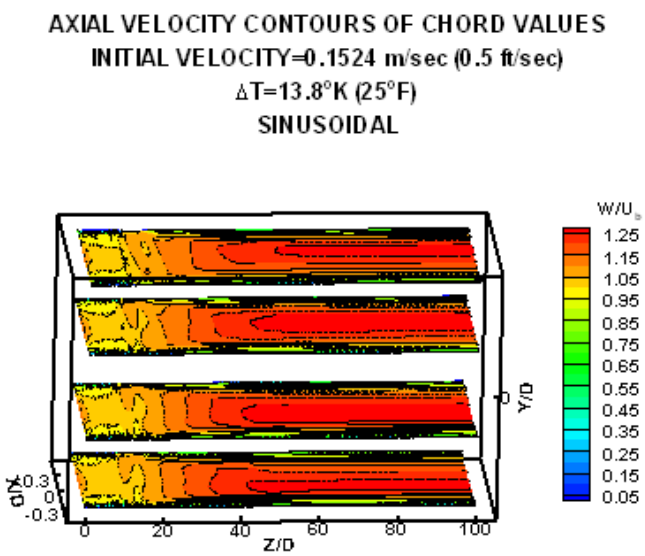

Fig. A-60 Axial Velocity Slice Contours
V_0=0.1524 m/sec, ΔT_{wall}=-13.8°K Sinusoidal

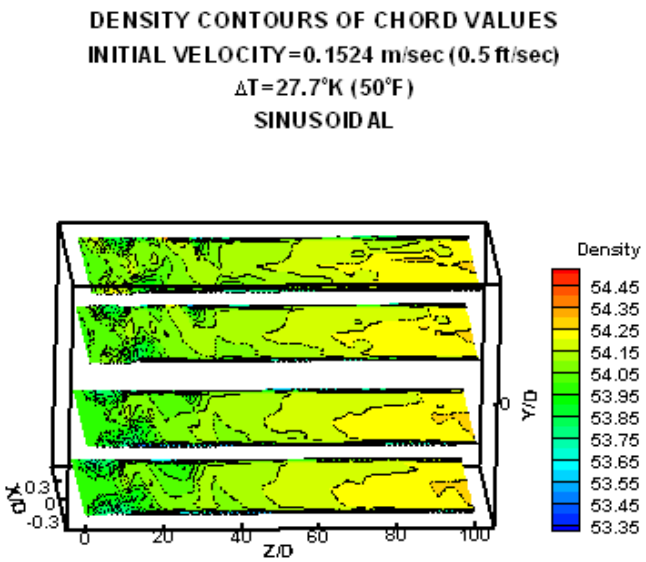

Fig. A-61 Density Slice Contours
V_0=0.1524 m/sec, ΔT_{wall}=-27.7°K Sinusoidal

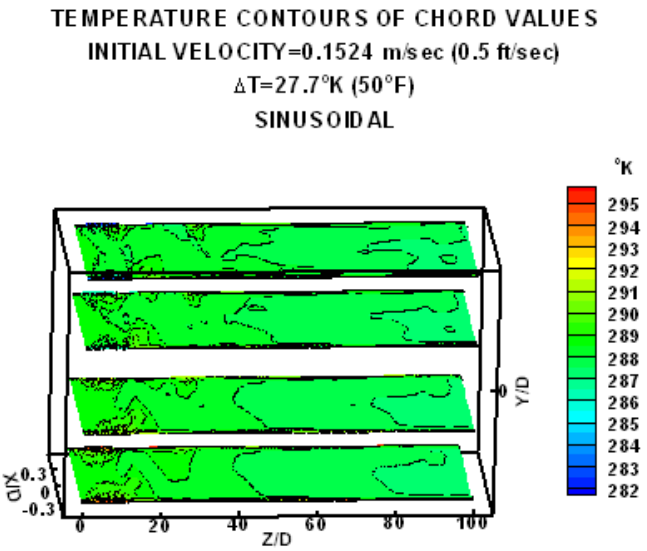

Fig. A-62 Temperature Slice Contours
V_0=0.1524 m/sec, ΔT_{wall}=-27.7°K Sinusoidal

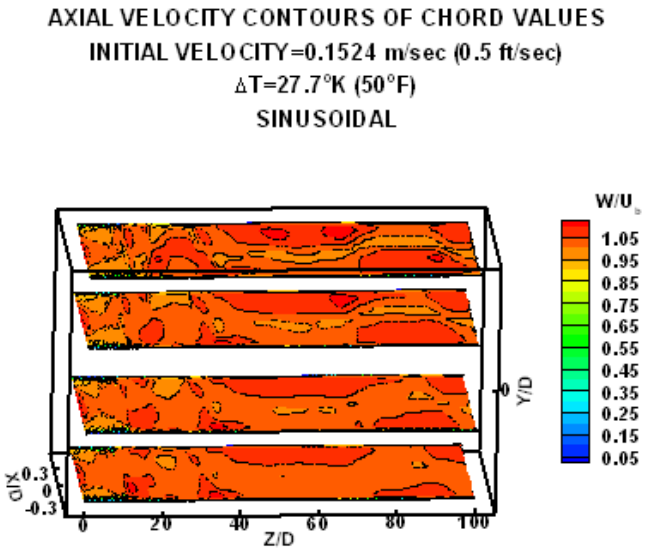

Fig. A-63 Axial Velocity Slice Contours
V_0=0.1524 m/sec, ΔT_{wall}=-27.7°K Sinusoidal

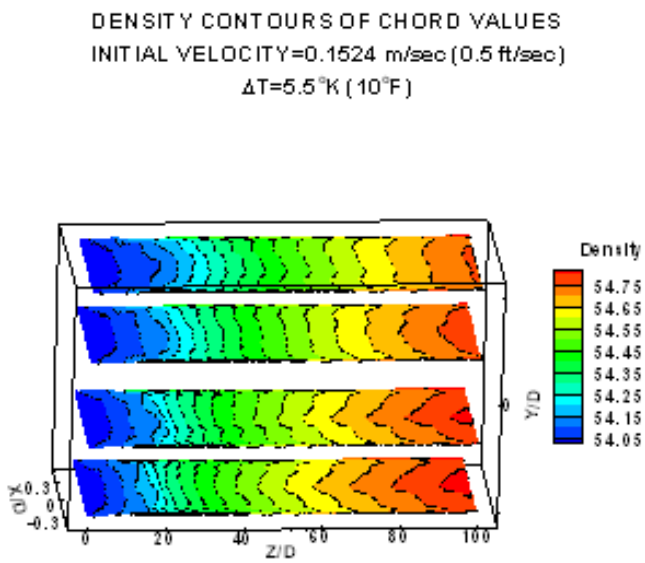

Fig. A-64 Density Slice Contours
V_0=0.1524 m/sec, ΔT_{wall}=-5.5°K

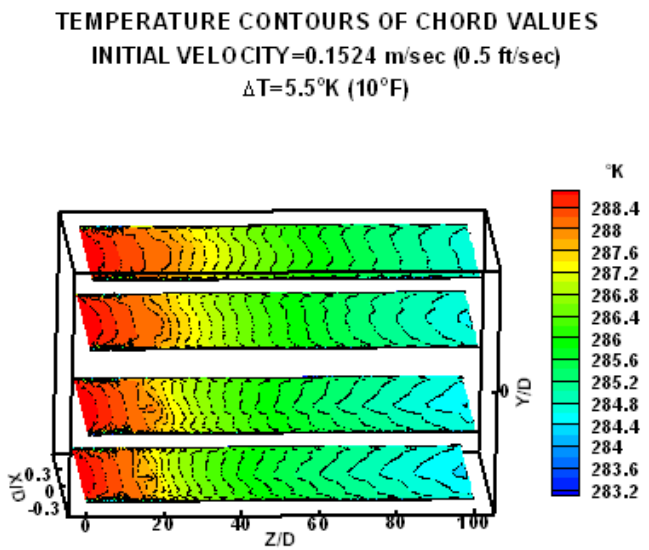

Fig. A-65 Temperature Slice Contours
V_0=0.1524 m/sec, ΔT_{wall}=-5.5°K

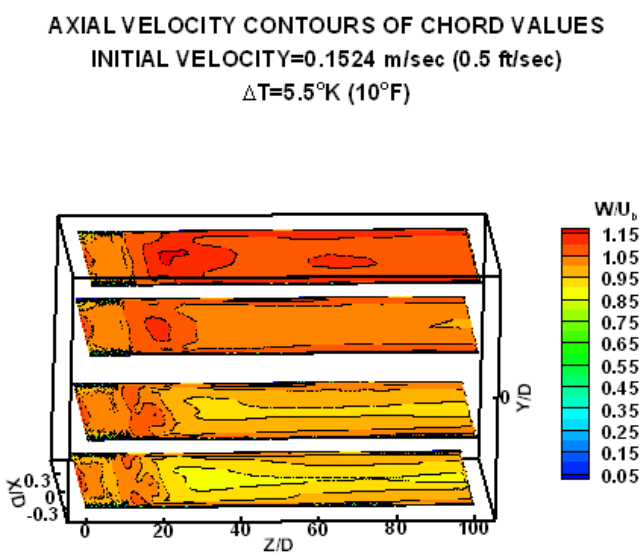

Fig. A-66 Axial Velocity Slice Contours
V_0=0.1524 m/sec, ΔT_{wall}=-5.5°K

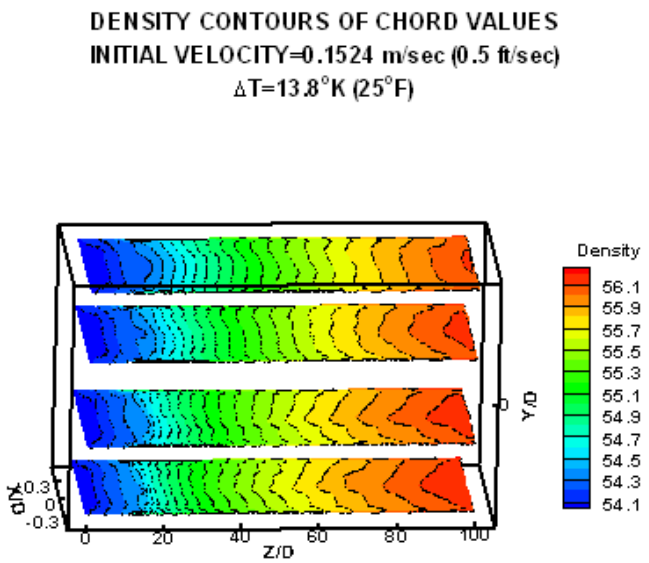

Fig. A-67 Density Slice Contours
V_0=0.1524 m/sec, ΔT_{wall}=-13.8°K

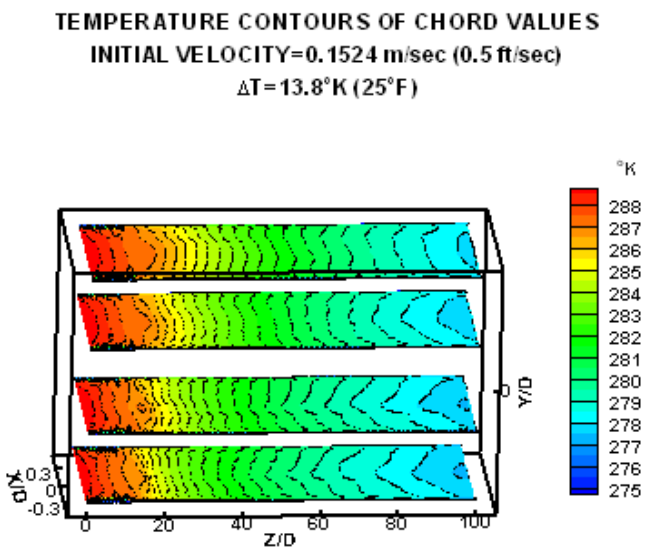

Fig. A-68 Temperature Slice Contours
V_0=0.1524 m/sec, ΔT_{wall}=-13.8°K

AXIAL VELOCITY CONTOURS OF CHORD VALUES
INITIAL VELOCITY=0.1524 m/sec (0.5 ft/sec)
ΔT=13.8°K (25°F)

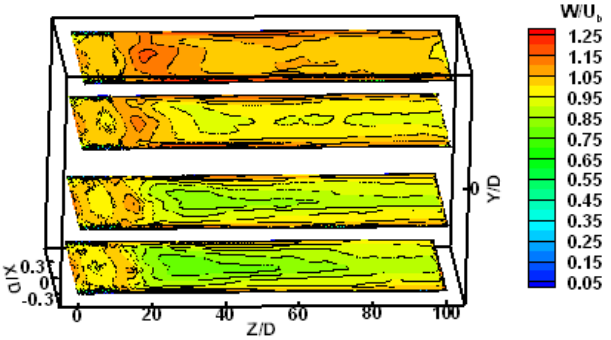

Fig. A-69 Axial Velocity Slice Contours
V_0=0.1524 m/sec, ΔT_{wall}=-13.8°K

DENSITY CONTOURS OF CHORD VALUES
INITIAL VELOCITY=0.1524 m/sec (0.5 ft/sec)
ΔT=27.7°K (50°F)

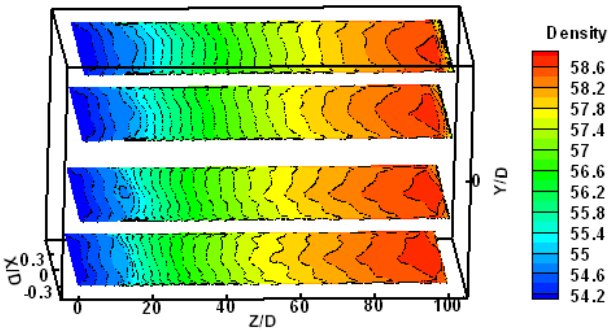

Fig. A-70 Density Slice Contours
V_0=0.1524 m/sec, ΔT_{wall}=-27.7°K

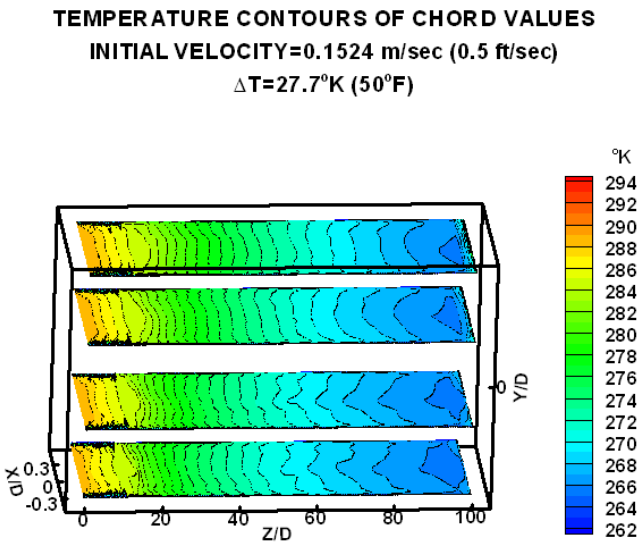

Fig. A-71 Temperature Slice Contours
V_0=0.1524 m/sec, ΔT_{wall}=-27.7°K

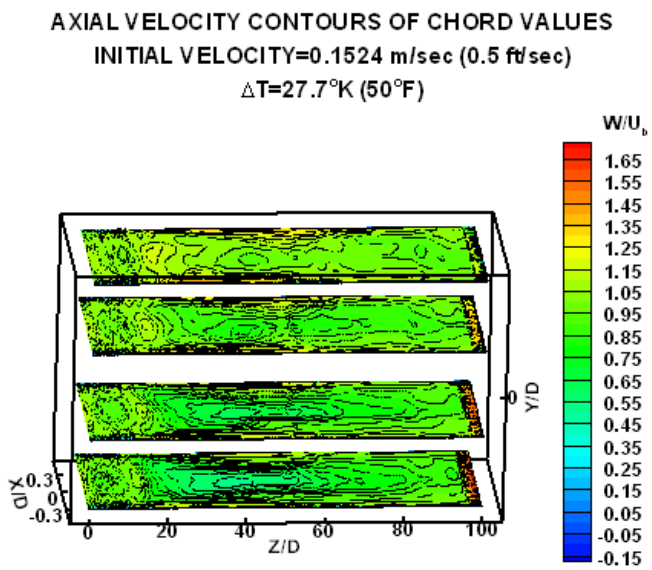

Fig. A-72 Axial Velocity Slice Contours
V_0=0.1524 m/sec, ΔT_{wall}=-27.7°K

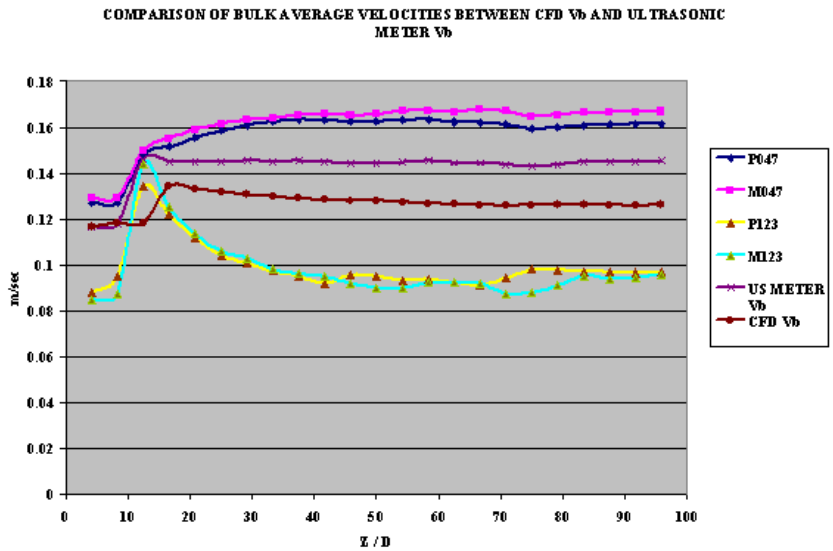

Fig. A-73 Comparison between CFD Vb and Ultrasonic Vb.
V_0=0.1524 m/sec, ΔT_{wall}=5.5°K Sinusoidal

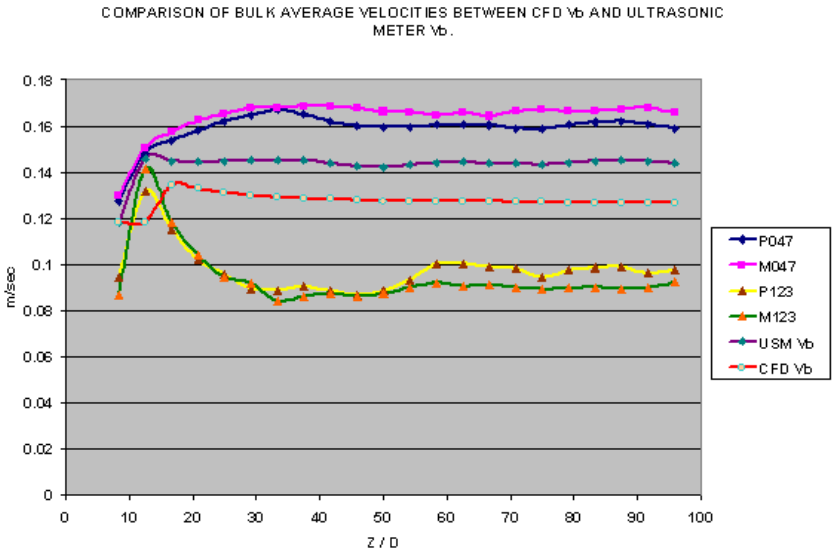

Fig. A-74 Comparison between CFD Vb and Ultrasonic Vb.
V_0=0.1524 m/sec, ΔT_{wall}=13.8°K Sinusoidal

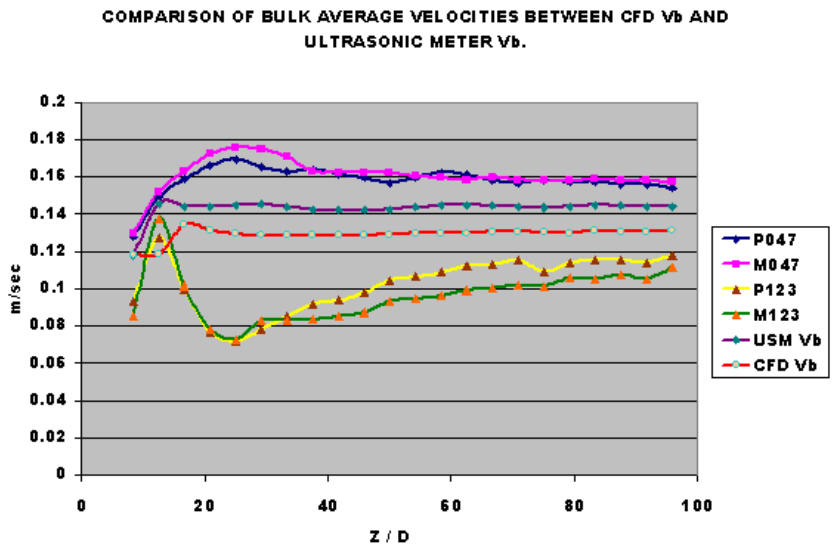

Fig. A-75 Comparison between CFD Vb and Ultrasonic Vb.
V_0=0.1524 m/sec, ΔT_{wall}=27.7°K Sinusoidal

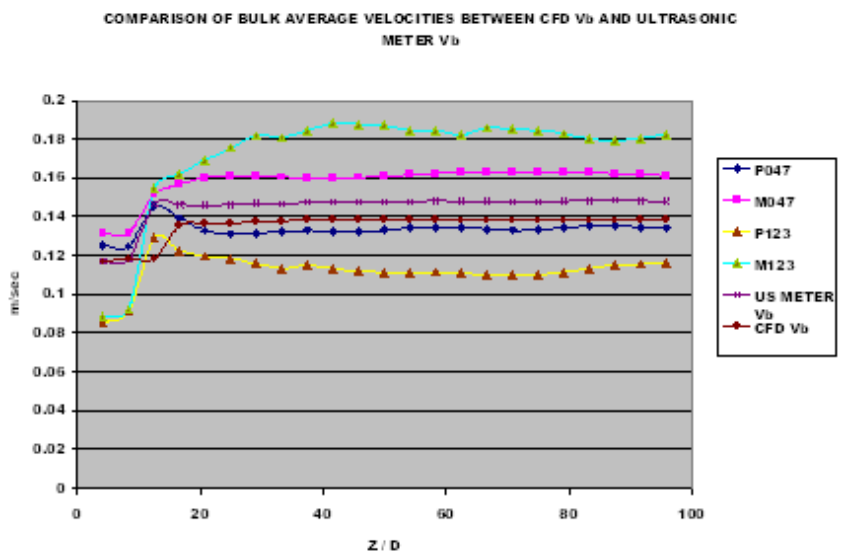

Fig. A-76 Comparison between CFD Vb and Ultrasonic Vb.
V_0=0.1524 m/sec, ΔT_{wall}=5.5°K

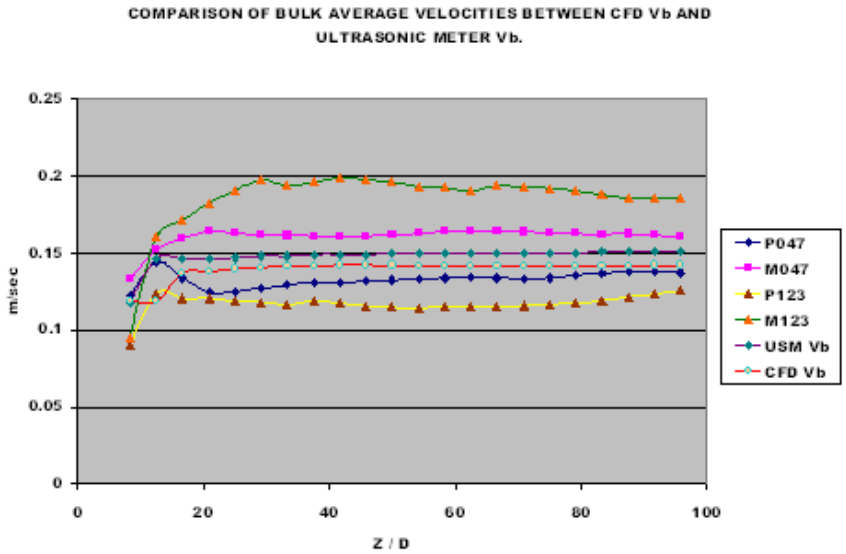

Fig. A-77 Comparison between CFD Vb and Ultrasonic Vb.
V_0=0.1524 m/sec, ΔT_{wall}=13.8^{o}K

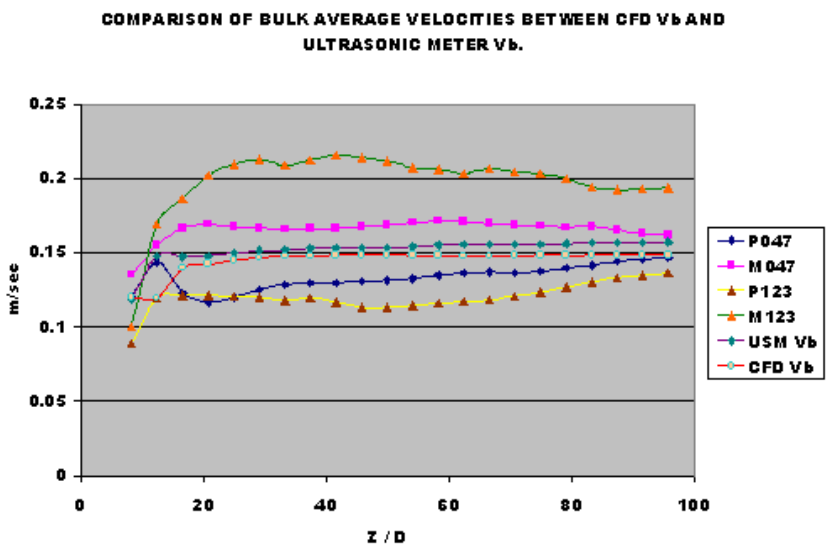

Fig. A-78 Comparison between CFD Vb and Ultrasonic Vb.
V_0=0.1524 m/sec, ΔT_{wall}=27.7^{o}K

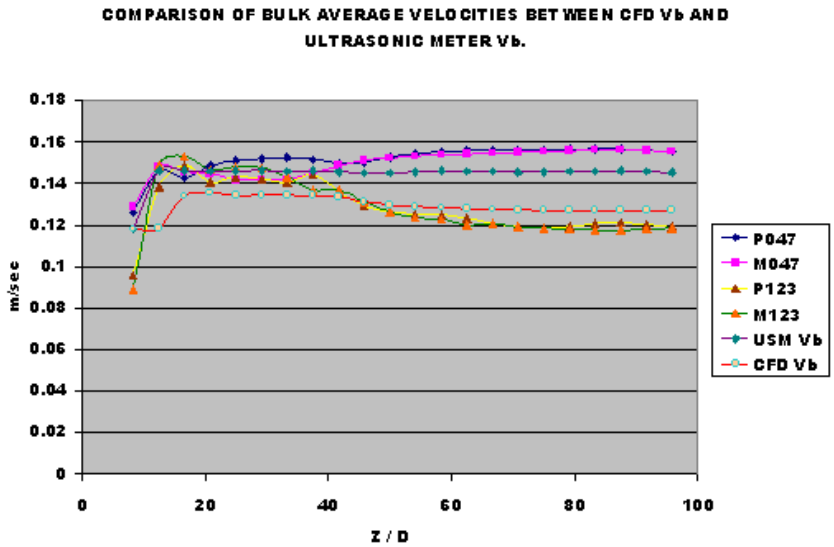

Fig. A-79 Comparison between CFD Vb and Ultrasonic Vb.
V_0=0.1524 m/sec, ΔT_{wall}=-5.5°K Sinusoidal

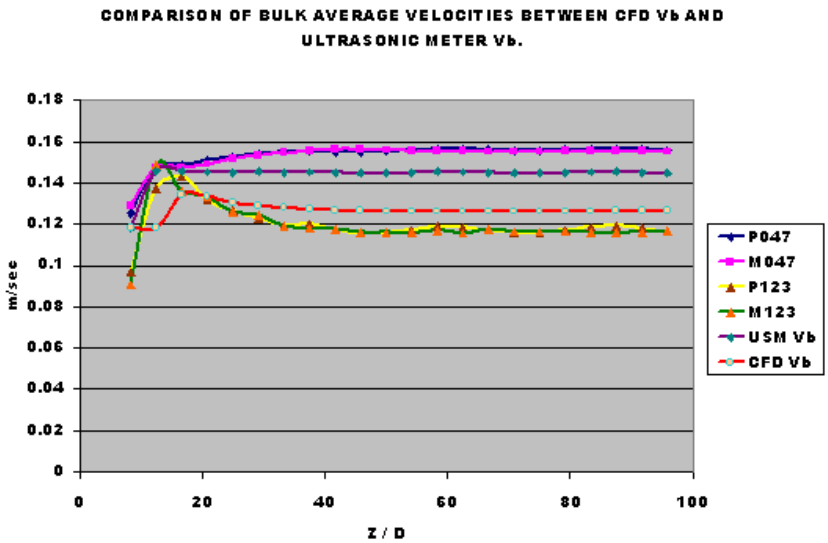

Fig. A-80 Comparison between CFD Vb and Ultrasonic Vb.
V_0=0.1524 m/sec, ΔT_{wall}=-13.8°K Sinusoidal

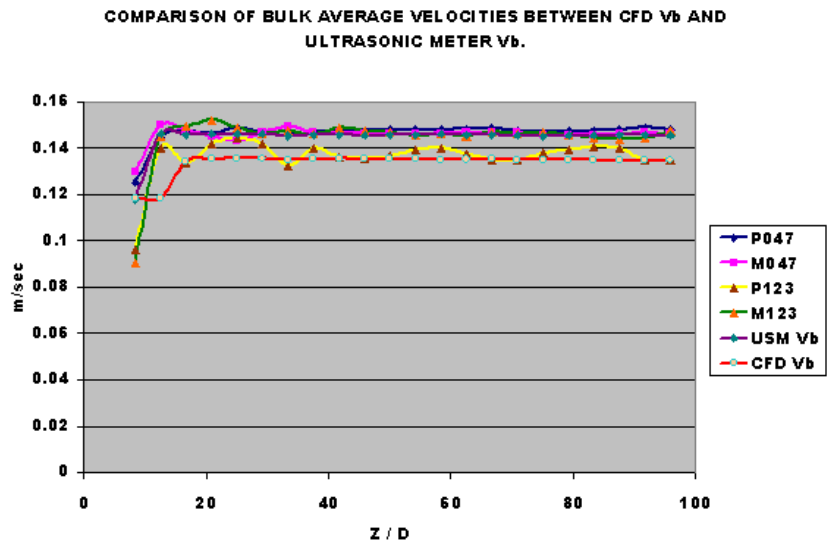

Fig. A-81 Comparison between CFD Vb and Ultrasonic Vb.
V_0=0.1524 m/sec, ΔT_{wall}=-27.7°K Sinusoidal

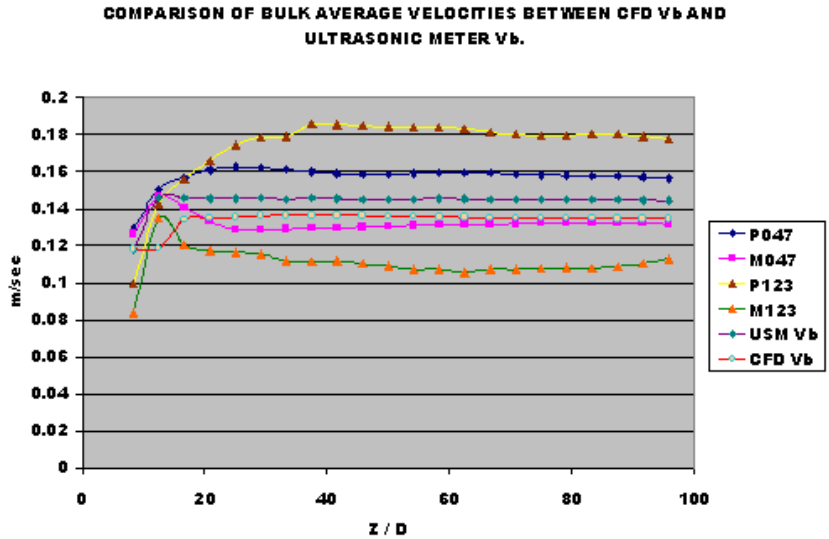

Fig. A-82 Comparison between CFD Vb and Ultrasonic Vb.
V_0=0.1524 m/sec, ΔT_{wall}=-5.5°K

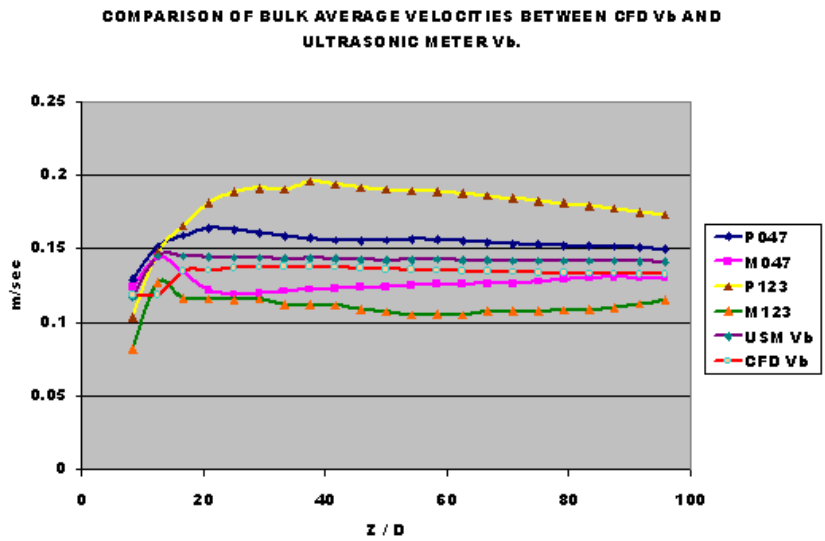

Fig. A-83 Comparison between CFD Vb and Ultrasonic Vb.
V_0=0.1524 m/sec, ΔT_{wall}=-13.8°K

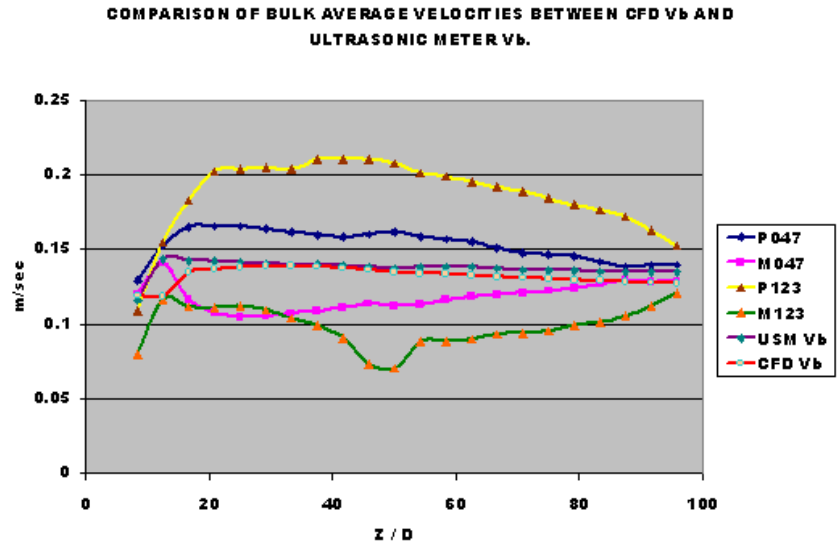

Fig. A-84 Comparison between CFD Vb and Ultrasonic Vb.
V_0=0.1524 m/sec, ΔT_{wall}=-27.7°K

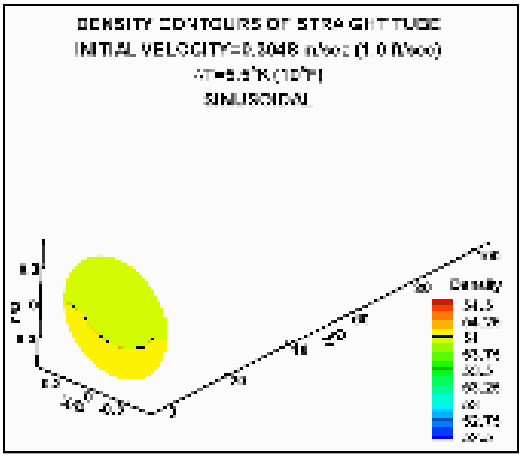

Fig. A-85 Density Contours
V_0=0.3048 m/sec, ΔT_{wall}=5.5°K Sinusoidal

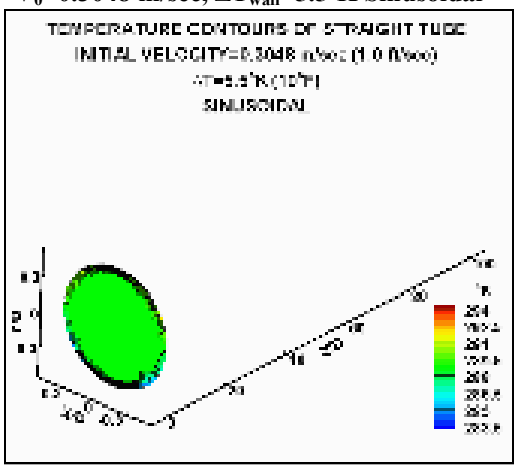

Fig. A-86 Temperature Contours
V_0=0.3048 m/sec, ΔT_{wall}=5.5°K Sinusoidal

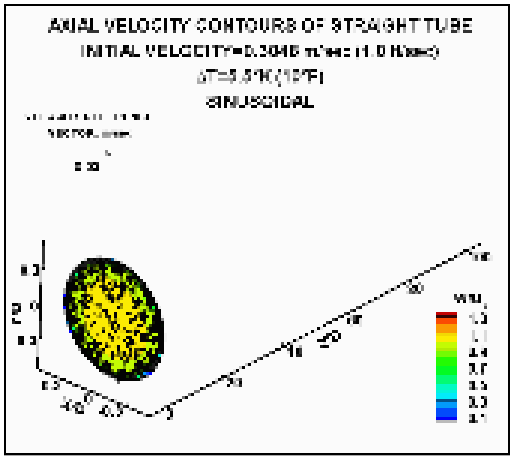

Fig. A-87 Axial Velocity Contours
V_0=0.3048 m/sec, ΔT_{wall}=5.5°K Sinusoidal

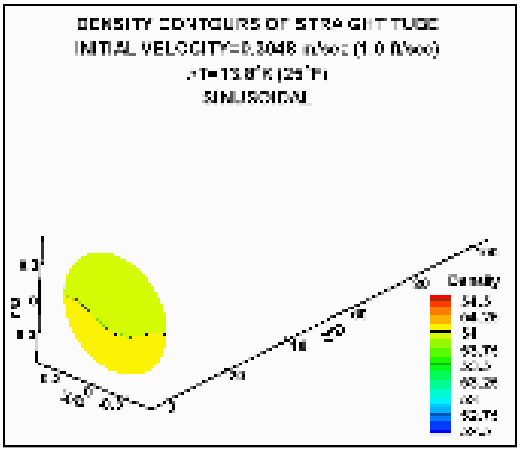

Fig. A-88 Density Contours
V_0=0.3048 m/sec, ΔT_{wall}=13.8°K Sinusoidal

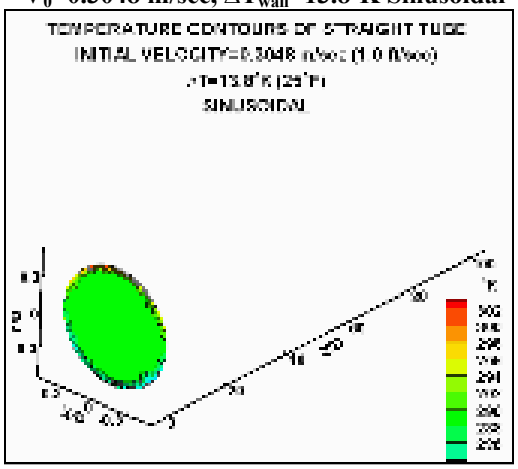

Fig. A-89 Temperature Contours
V_0=0.3048 m/sec, ΔT_{wall}=13.8°K Sinusoidal

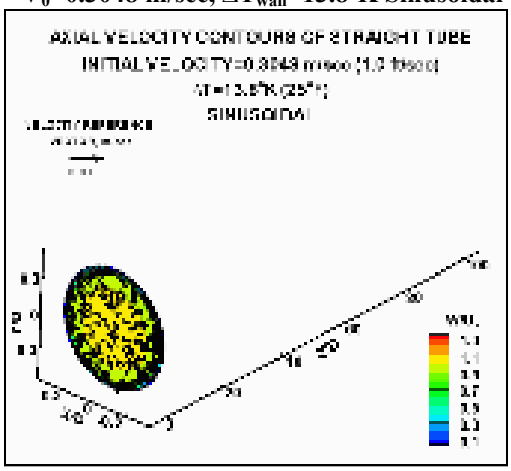

Fig. A-90 Axial Velocity Contours
V_0=0.3048 m/sec, ΔT_{wall}=13.8°K Sinusoidal

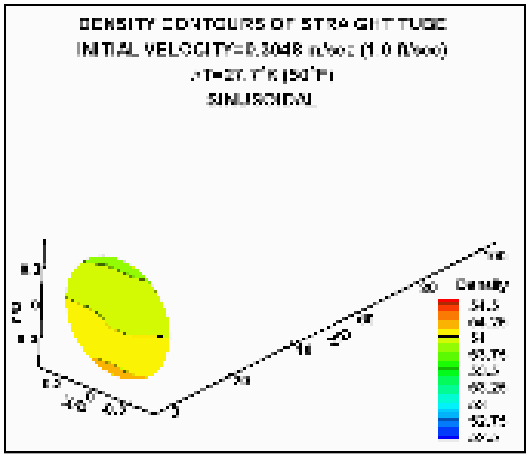

Fig. A-91 Density Contours
V_0=0.3048 m/sec, ΔT_{wall}=27.7°K Sinusoidal

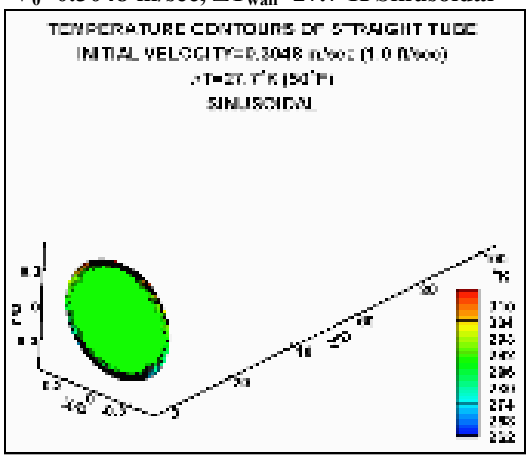

Fig. A-92 Temperature Contours
V_0=0.3048 m/sec, ΔT_{wall}=27.7°K Sinusoidal

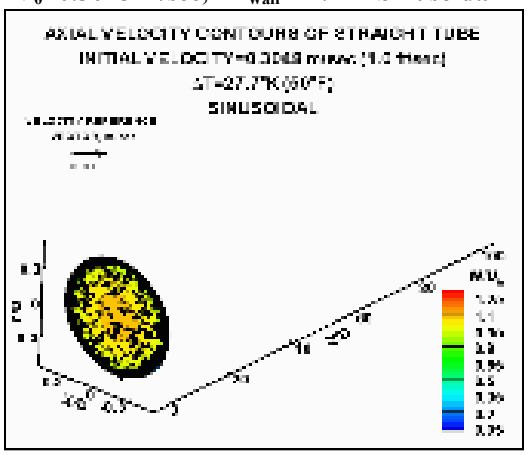

Fig. A-93 Axial Velocity Contours
V_0=0.3048 m/sec, ΔT_{wall}=27.7°K Sinusoidal

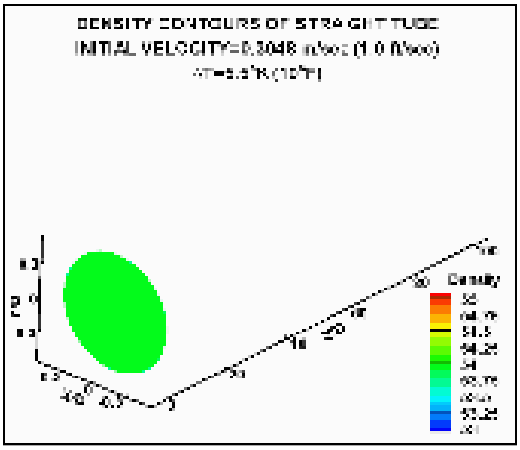

Fig. A-94 Density Contours
V_0=0.3048 m/sec, ΔT_{wall}=5.5°K

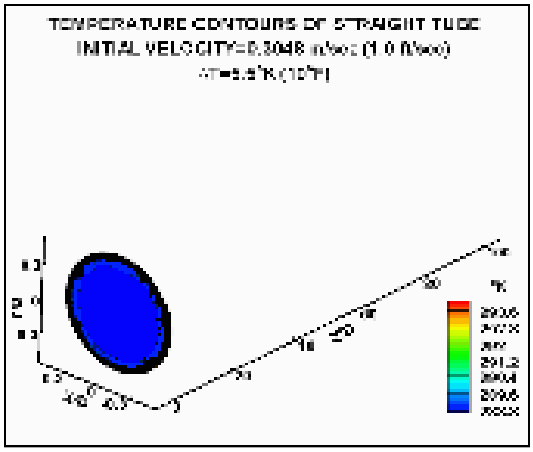

Fig. A-95 Temperature Contours
V_0=0.3048 m/sec, ΔT_{wall}=5.5°K

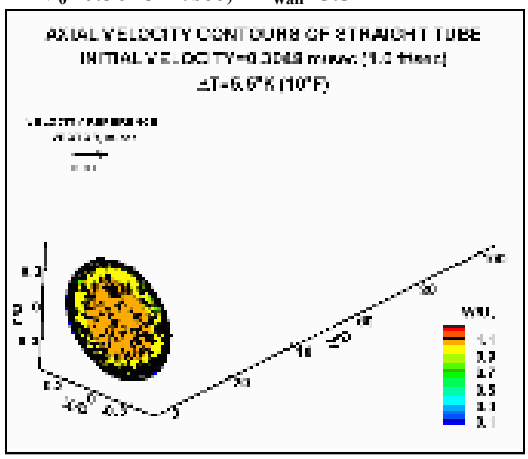

Fig. A-96 Axial Velocity Contours
V_0=0.3048 m/sec, ΔT_{wall}=5.5°K

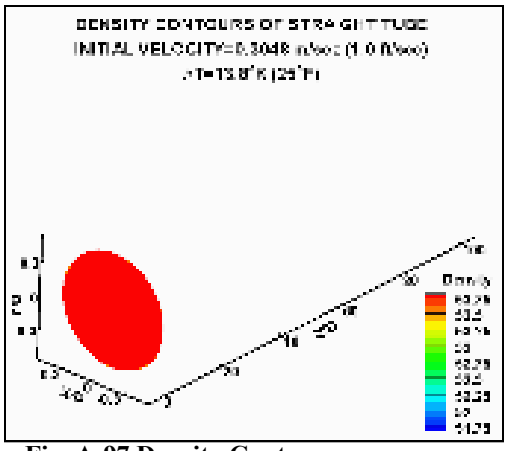

Fig. A-97 Density Contours
V_0=0.3048 m/sec, ΔT_{wall}=13.8°K

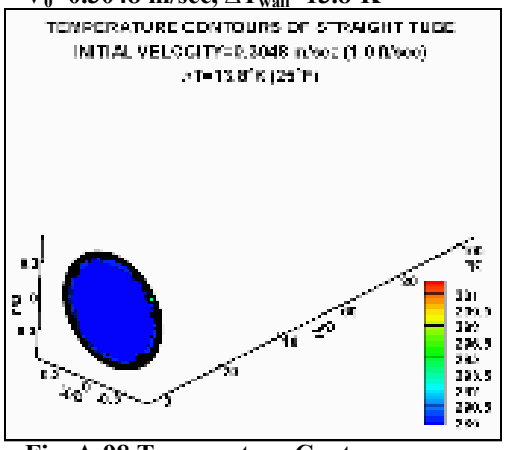

Fig. A-98 Temperature Contours
V_0=0.3048 m/sec, ΔT_{wall}=13.8°K

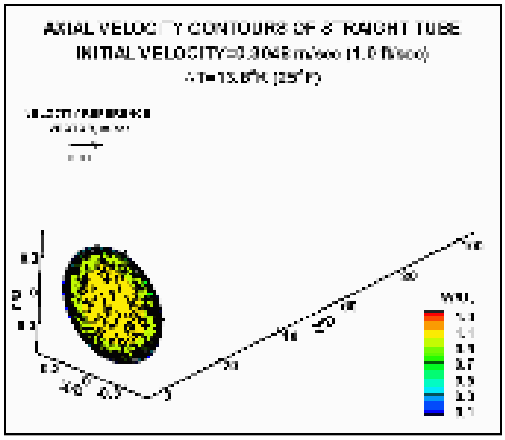

Fig. A-99 Axial Velocity Contours
V_0=0.3048 m/sec, ΔT_{wall}=13.8°K

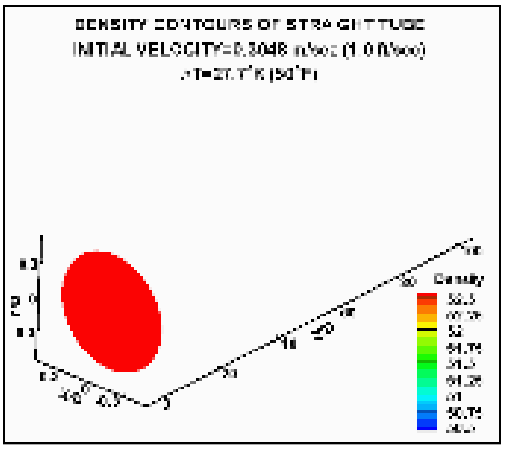

Fig. A-100 Density Contours
V_0=0.3048 m/sec, ΔT_{wall}=27.7°K

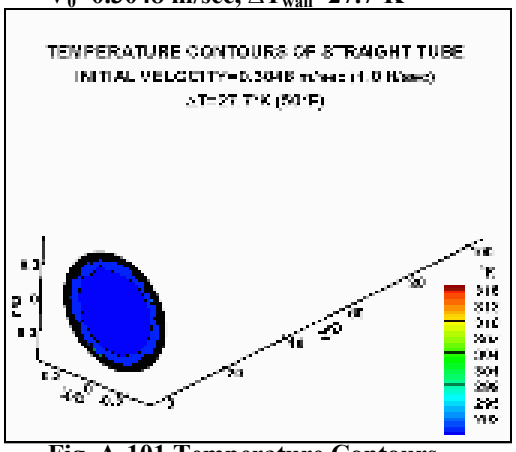

Fig. A-101 Temperature Contours
V_0=0.3048 m/sec, ΔT_{wall}=27.7°K

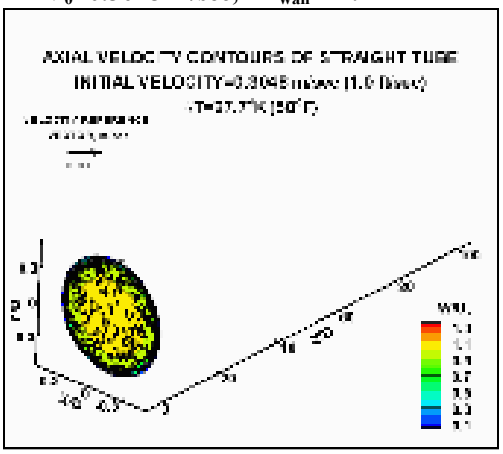

Fig. A-102 Axial Velocity Contours
V_0=0.3048 m/sec, ΔT_{wall}=27.7°K

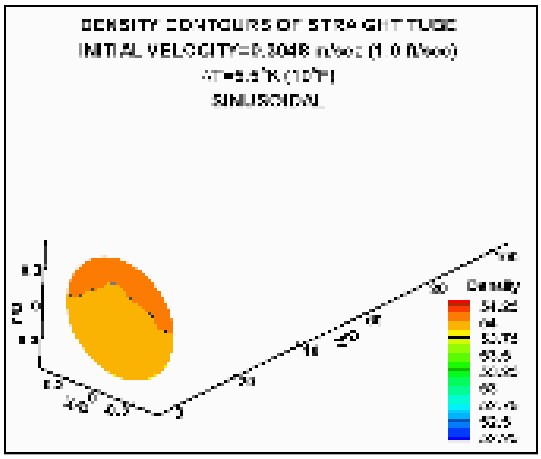

Fig. A-103 Density Contours
V_0=0.3048 m/sec, ΔT_{wall}=-5.5°K Sinusoidal

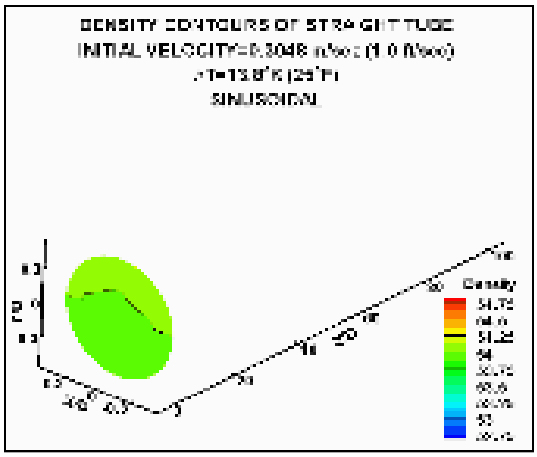

Fig. A-106 Density Contours
V_0=0.3048 m/sec, ΔT_{wall}=-13.8°K Sinusoidal

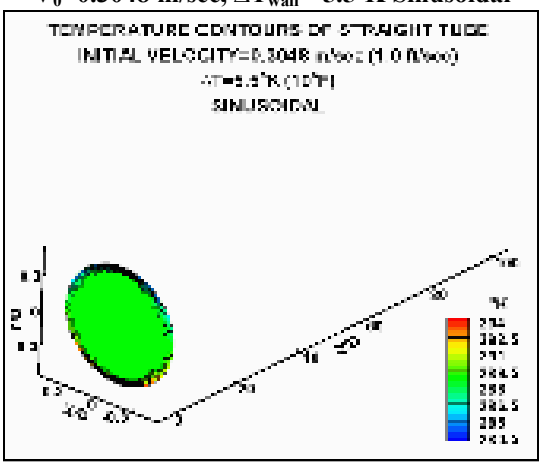

Fig. A-104 Temperature Contours
V_0=0.3048 m/sec, ΔT_{wall}=-5.5°K Sinusoidal

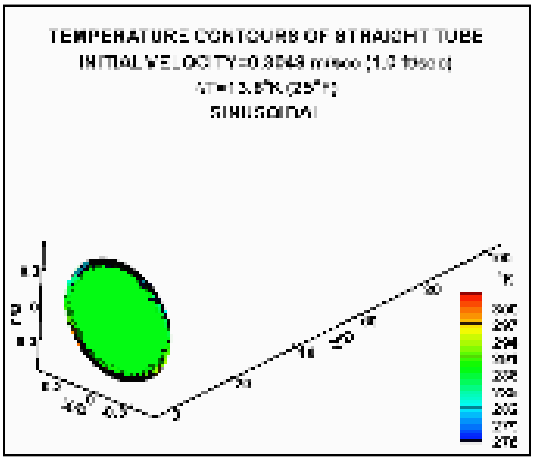

Fig. A-107 Temperature Contours
V_0=0.3048 m/sec, ΔT_{wall}=-13.8°K Sinusoidal

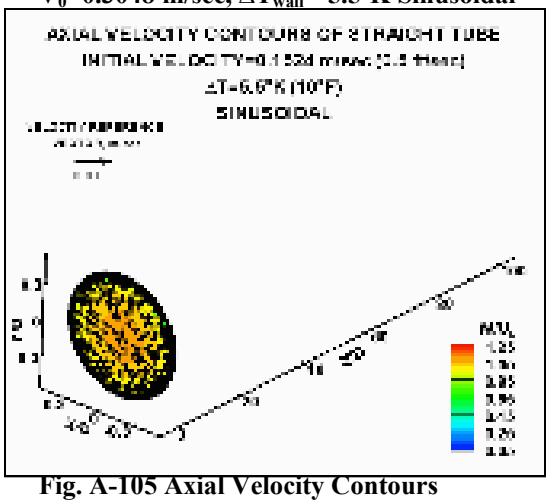

Fig. A-105 Axial Velocity Contours
V_0=0.3048 m/sec, ΔT_{wall}=-5.5°K Sinusoidal

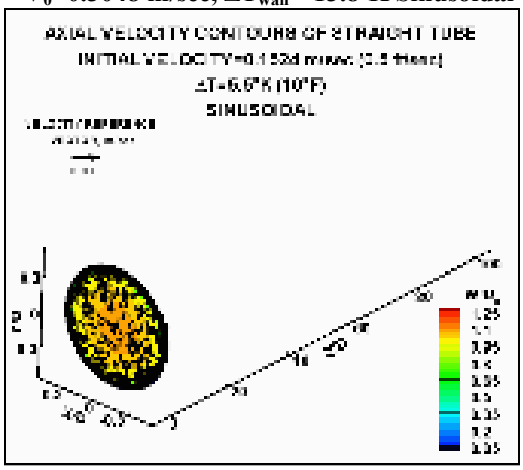

Fig. A-108 Axial Velocity Contours
V_0=0.3048 m/sec, ΔT_{wall}=-13.8°K Sinusoidal

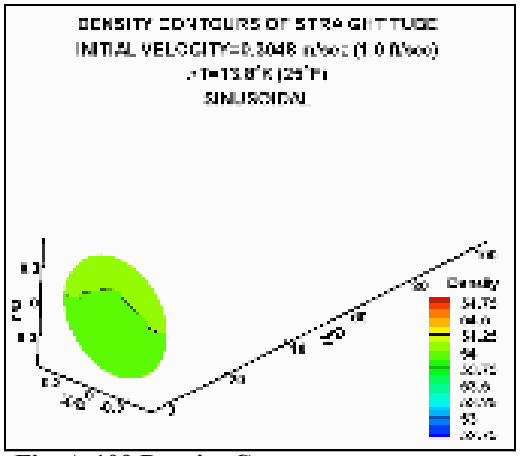

Fig. A-109 Density Contours
V_0=0.3048 m/sec, ΔT_{wall}=-27.7°K Sinusoidal

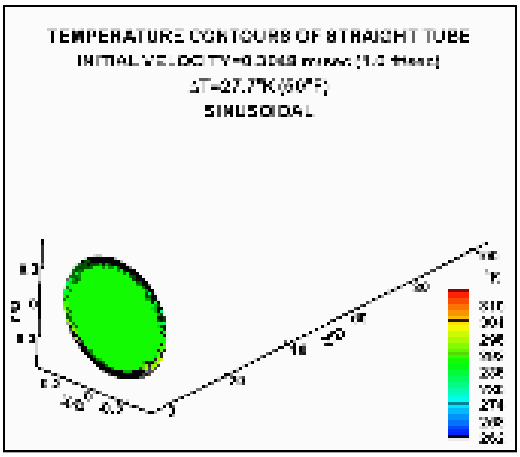

Fig. A-110 Temperature Contours
V_0=0.3048 m/sec, ΔT_{wall}=-27.7°K Sinusoidal

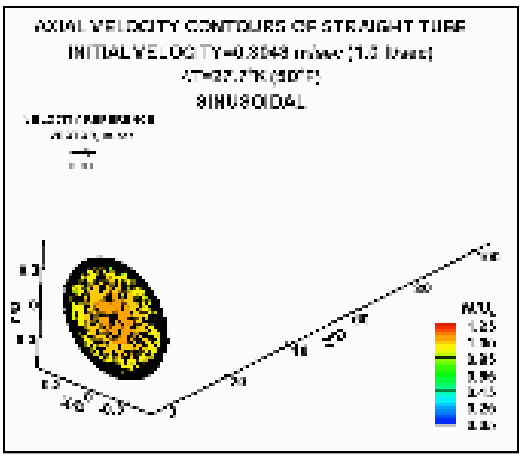

Fig. A-11 Axial Velocity Contours
V_0=0.3048 m/sec, ΔT_{wall}=-27.7°K Sinusoidal

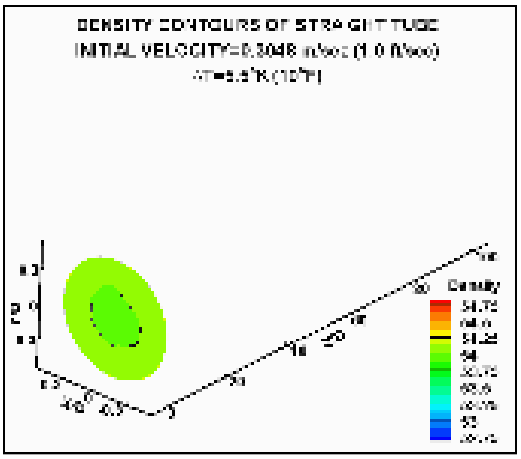

Fig. A-112 Density Contours
V_0=0.3048 m/sec, ΔT_{wall}=-5.5°K

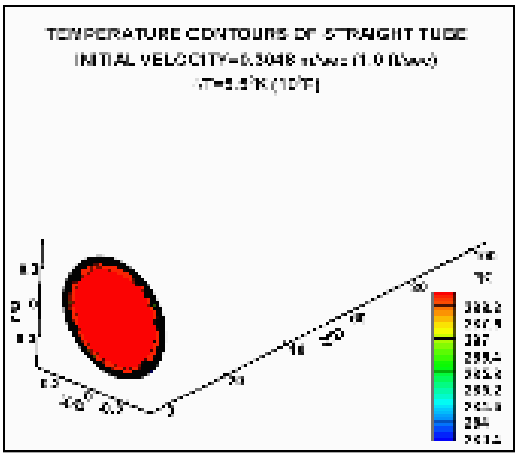

Fig. A-113 Temperature Contours
V_0=0.3048 m/sec, ΔT_{wall}=-5.5°K

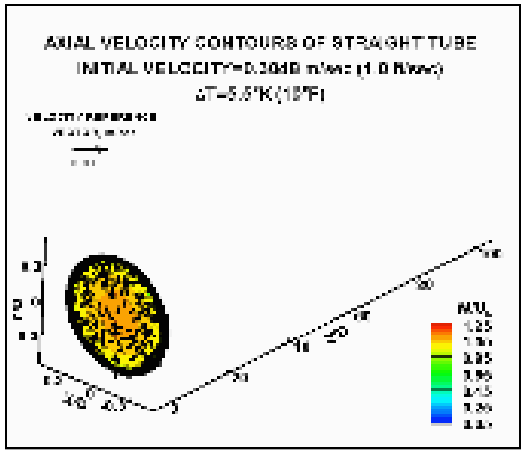

Fig. A-114 Axial Velocity Contours
V_0=0.3048 m/sec, ΔT_{wall}=-5.5°K

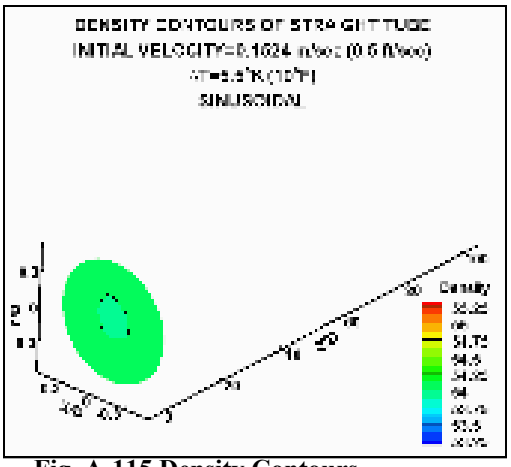

Fig. A-115 Density Contours
V_0=0.3048 m/sec, ΔT_{wall}=-13.8°K

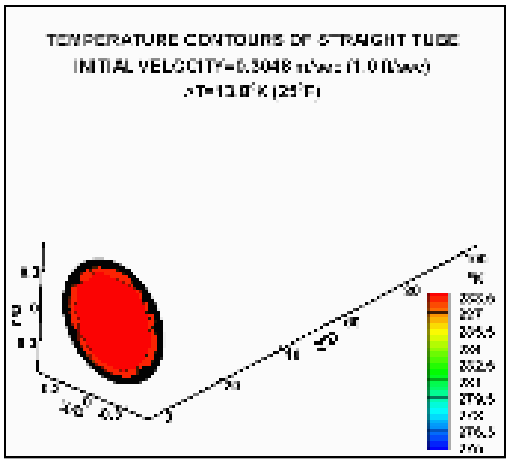

Fig. A-116 Temperature Contours
V_0=0.3048 m/sec, ΔT_{wall}=-13.8°K

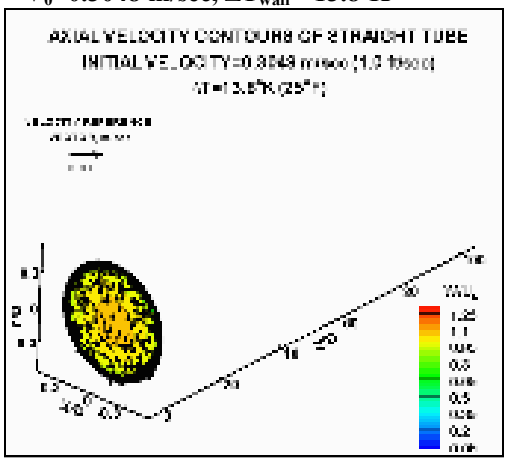

Fig. A-117 Axial Velocity Contours
V_0=0.3048 m/sec, ΔT_{wall}=-13.8°K

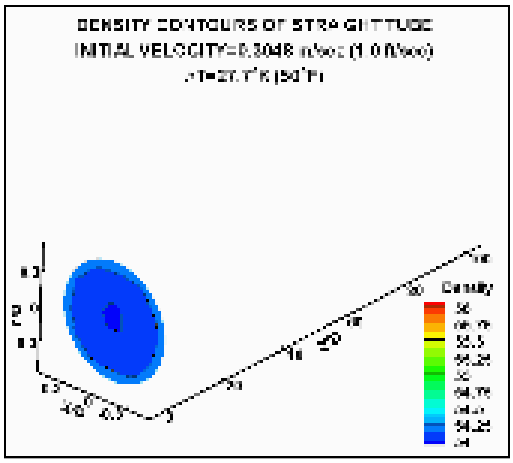

Fig. A-118 Density Contours
V_0=0.3048 m/sec, ΔT_{wall}=-27.7°K

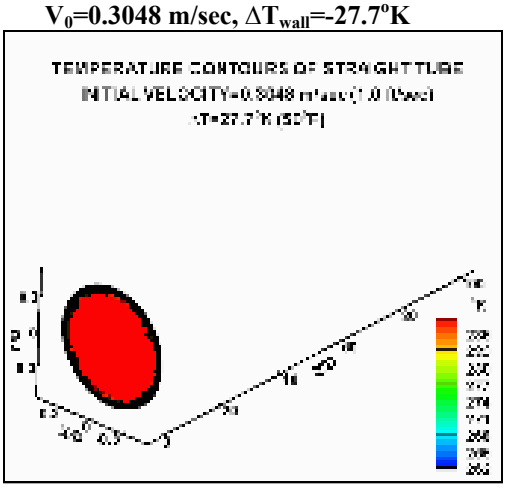

Fig. A-119 Temperature Contours
V_0=0.3048 m/sec, ΔT_{wall}=-27.7°K

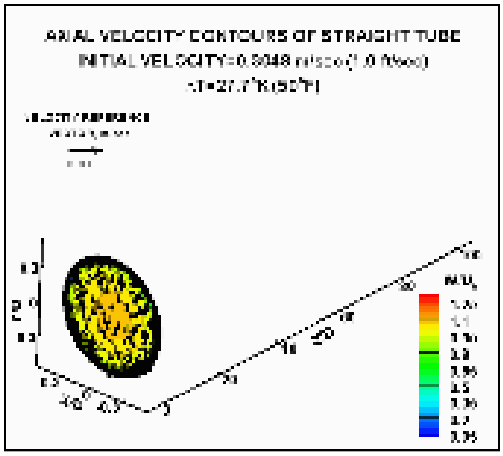

Fig. A-120 Axial Velocity Contours
V_0=0.3048 m/sec, ΔT_{wall}=-27.7°K

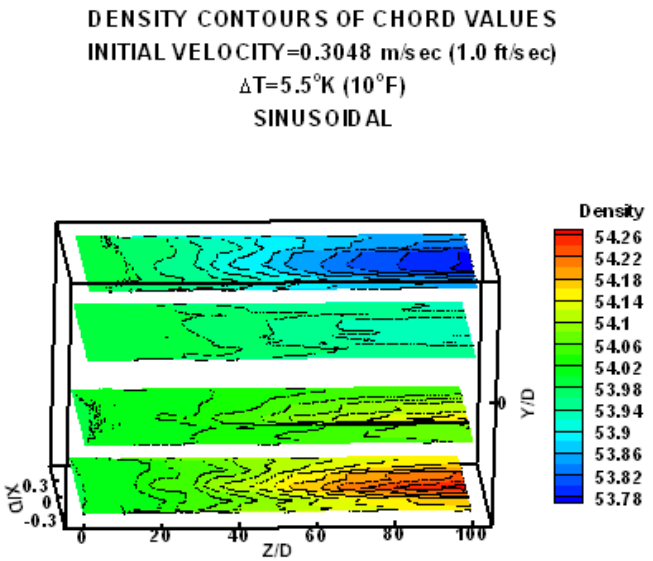

Fig. A-121 Density Slice Contours
V_0=0.3048 m/sec, ΔT_{wall}=5.5°K Sinusoidal

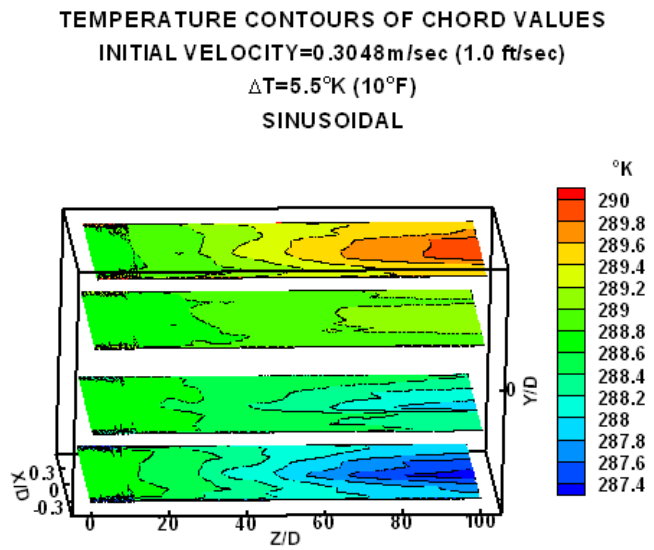

Fig. A-122 Temperature Slice Contours
V_0=0.3048 m/sec, ΔT_{wall}=5.5°K Sinusoidal

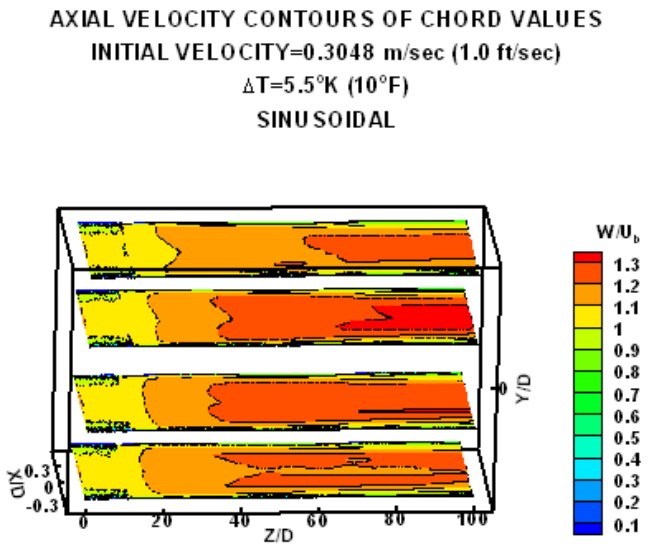

Fig. A-123 Axial Velocity Slice Contours
V_0=0.3048 m/sec, ΔT_{wall}=5.5°K Sinusoidal

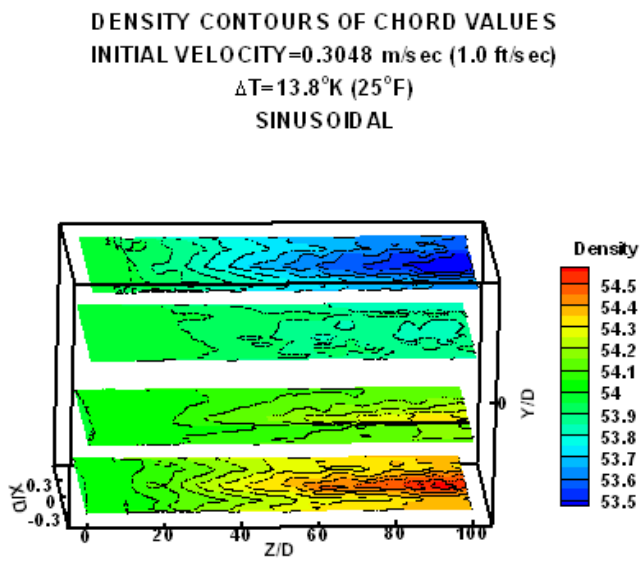

Fig. A-124 Density Slice Contours
V_0=0.3048 m/sec, ΔT_{wall}=13.8°K Sinusoidal

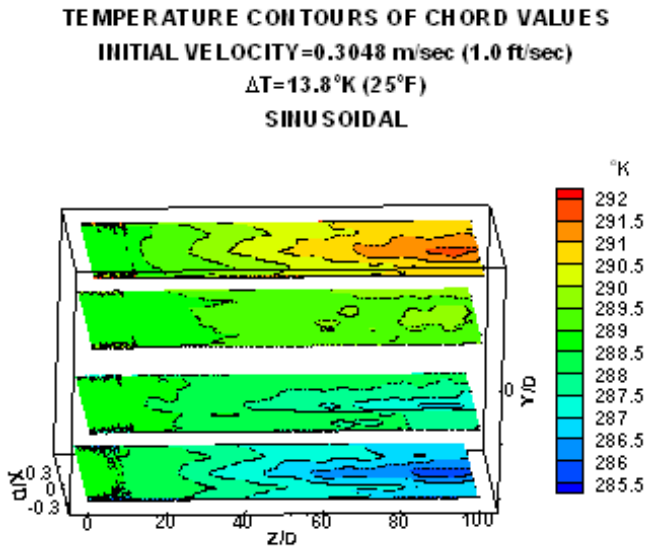

Fig. A-125 Temperature Slice Contours
V_0=0.3048 m/sec, ΔT_{wall}=13.8°K Sinusoidal

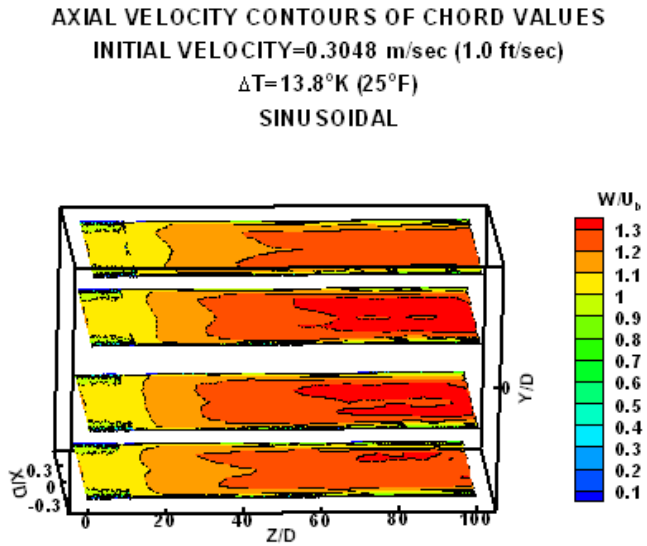

Fig. A-126 Axial Velocity Slice Contours
V_0=0.3048 m/sec, ΔT_{wall}=13.8°K Sinusoidal

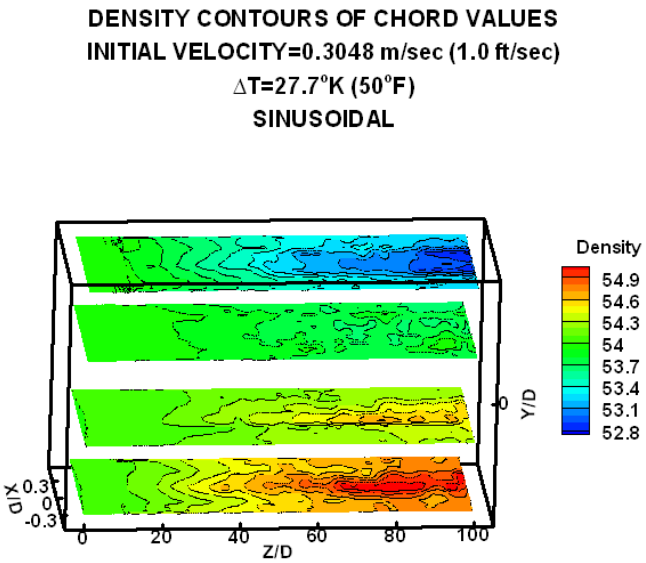

Fig. A-127 Density Slice Contours
V_0=0.3048 m/sec, ΔT_{wall}=27.7°K Sinusoidal

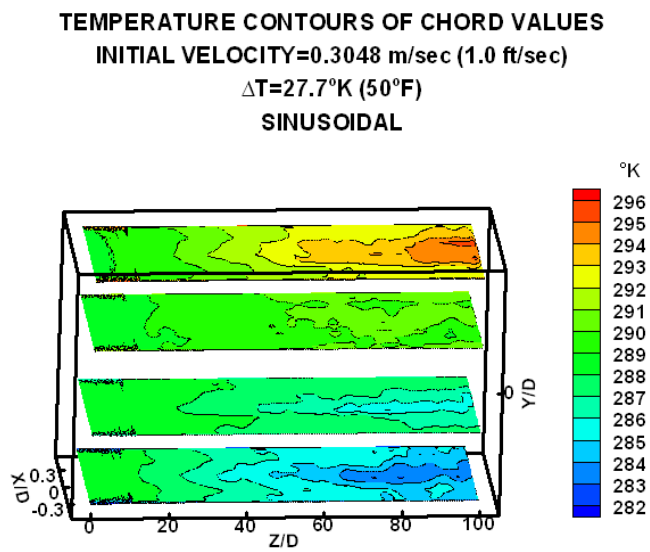

Fig. A-128 Temperature Slice Contours
V_0=0.3048 m/sec, ΔT_{wall}=27.7°K Sinusoidal

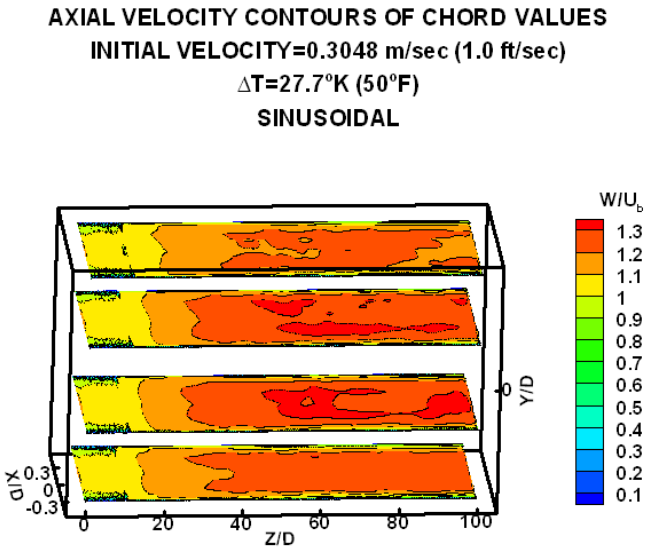

Fig. A-129 Axial Velocity Slice Contours
V_0=0.3048 m/sec, ΔT_{wall}=27.7°K Sinusoidal

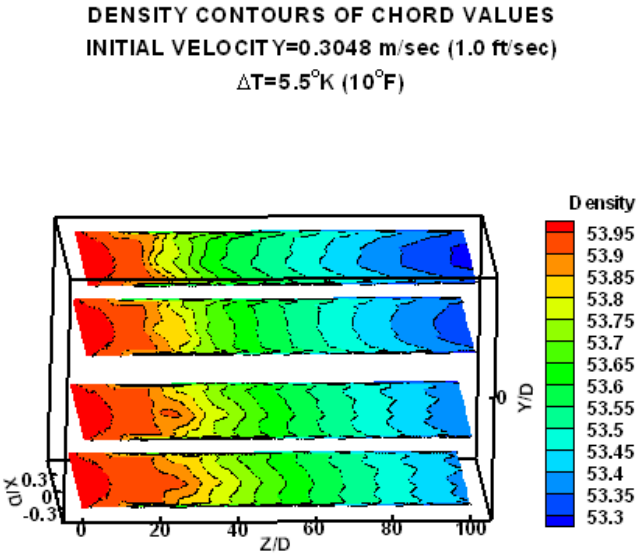

Fig. A-130 Density Slice Contours
V_0=0.3048 m/sec, ΔT_{wall}=5.5°K

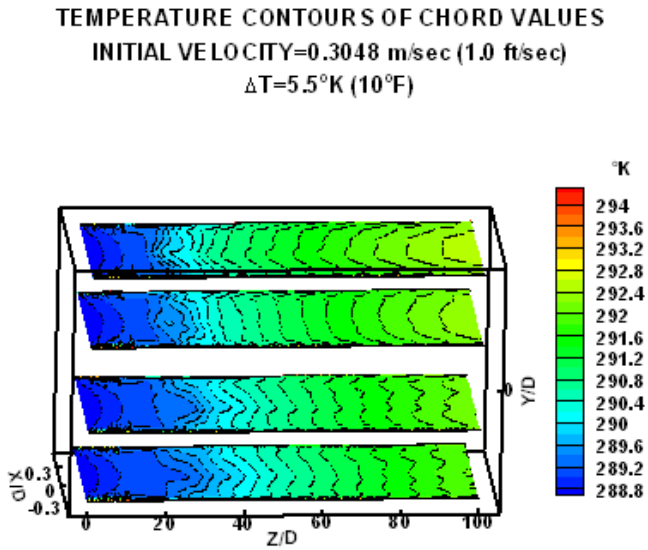

Fig. A-131 Temperature Slice Contours
V_0=0.3048 m/sec, ΔT_{wall}=5.5°K

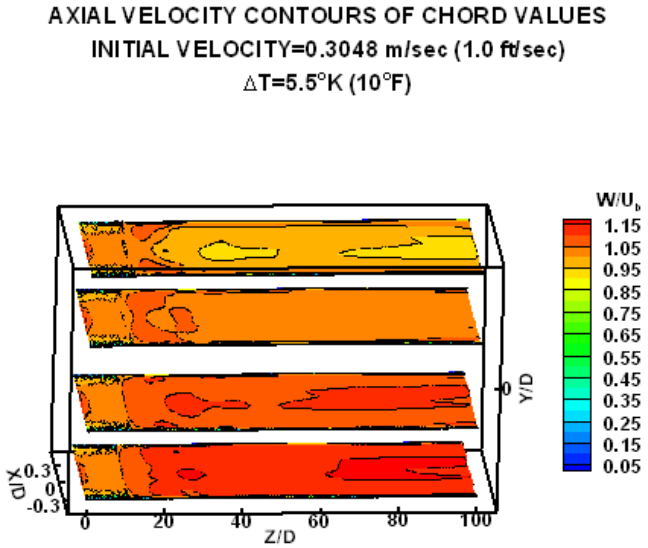

Fig. A-132 Axial Velocity Slice Contours
V_0=0.3048 m/sec, ΔT_{wall}=5.5°K

DENSITY CONTOURS OF CHORD VALUES
INITIAL VELOCITY=0.3048 m/sec (1.0 ft/sec)
ΔT=13.8°K (25°F)

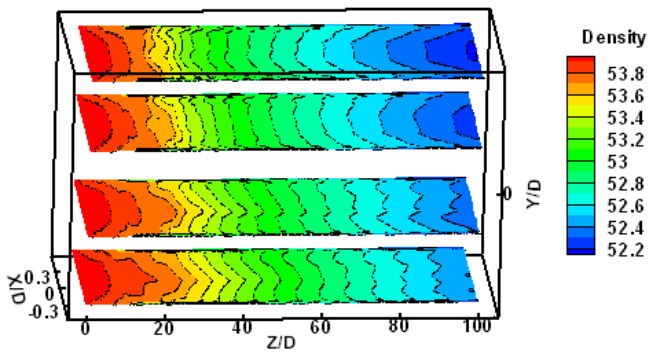

Fig. A-133 Density Slice Contours
V_0=0.3048 m/sec, ΔT_{wall}=13.8°K

TEMPERATURE CONTOURS OF CHORD VALUES
INITIAL VELOCITY=0.3048 m/sec (1.0 ft/sec)
ΔT=13.8°K (25°F)

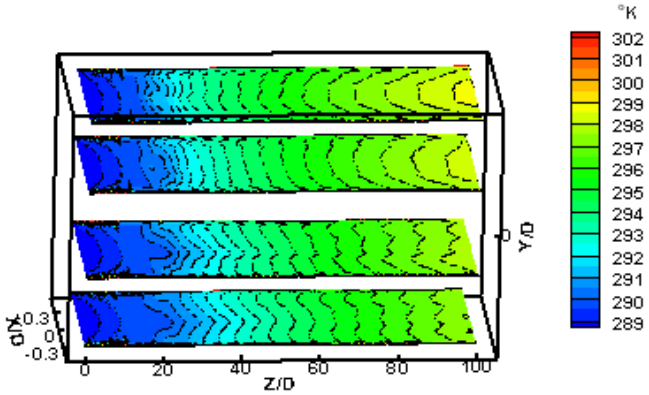

Fig. A-134 Temperature Slice Contours
V_0=0.3048 m/sec, ΔT_{wall}=13.8°K

AXIAL VELOCITY CONTOURS OF CHORD VALUES
INITIAL VELOCITY=0.3048 m/sec (1.0 ft/sec)
ΔT=13.8°K (25°F)

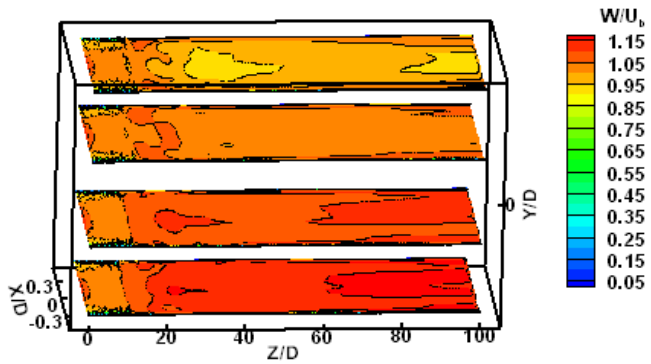

Fig. A-135 Axial Velocity Slice Contours
V_0=0.3048 m/sec, ΔT_{wall}=13.8°K

DENSITY CONTOURS OF CHORD VALUES
INITIAL VELOCITY=0.3048 m/sec (1.0 ft/sec)
ΔT=27.7°K (50°F)

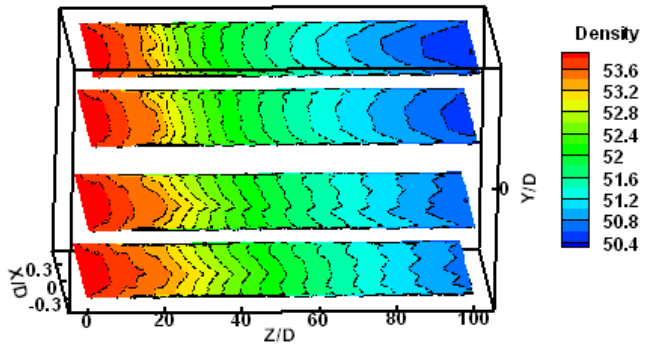

Fig. A-136 Density Slice Contours
V_0=0.3048 m/sec, ΔT_{wall}=27.7°K

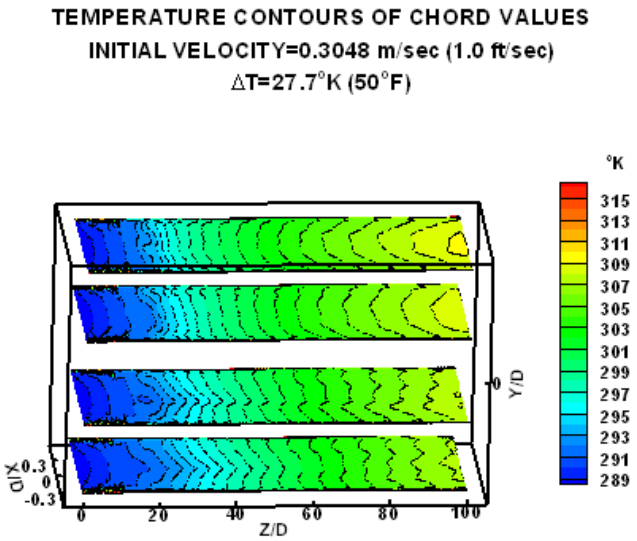

Fig. A-137 Temperature Slice Contours
V_0=0.3048 m/sec, ΔT_{wall}=27.7°K

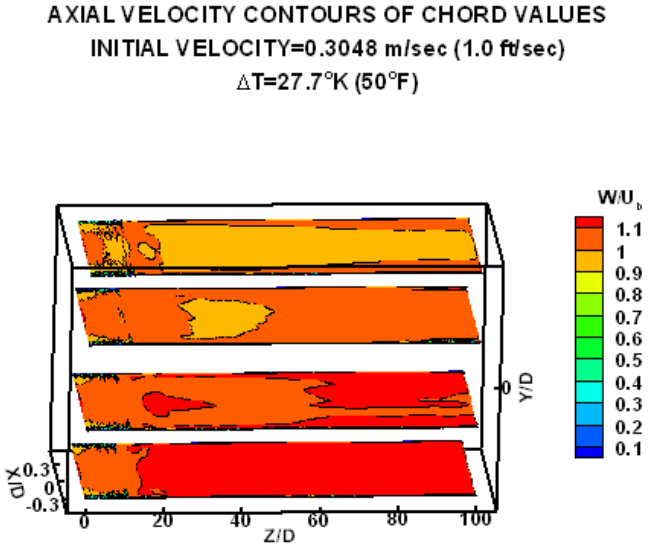

Fig. A-138 Axial Velocity Slice Contours
V_0=0.3048 m/sec, ΔT_{wall}=27.7°K

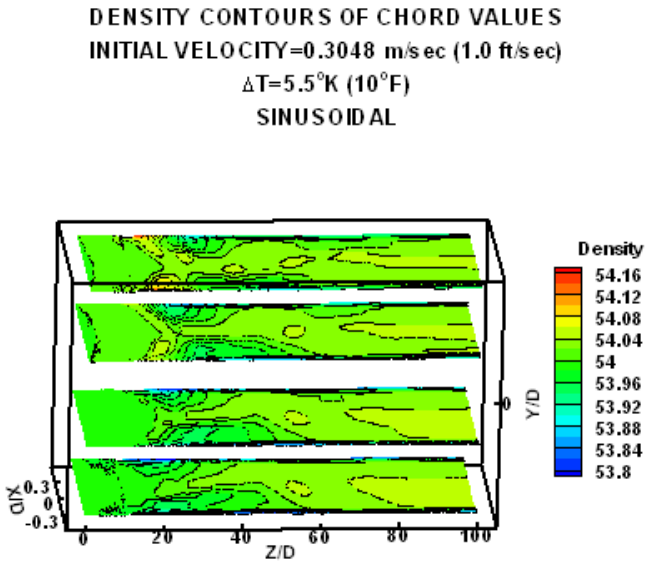

Fig. A-139 Density Slice Contours
V_0=0.3048 m/sec, ΔT_{wall}=-5.5°K Sinusoidal

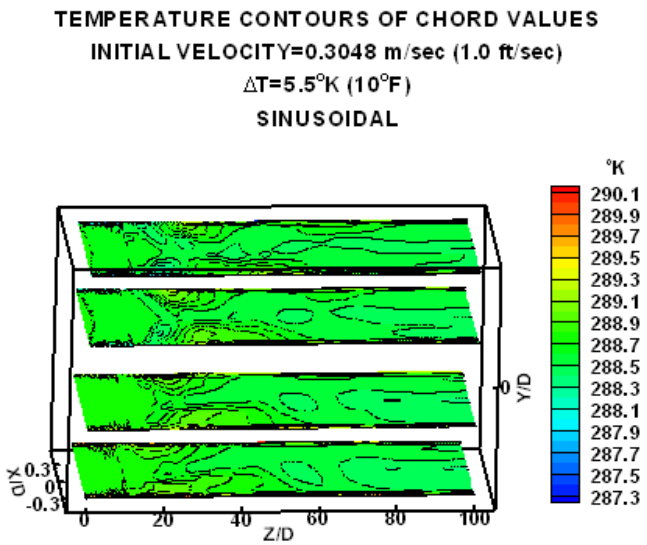

Fig. A-140 Temperature Slice Contours
V_0=0.3048 m/sec, ΔT_{wall}=-5.5°K Sinusoidal

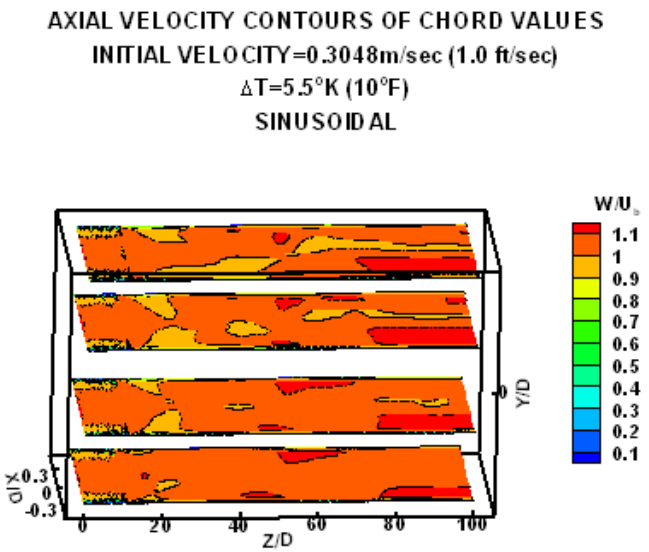

Fig. A-141 Axial Velocity Slice Contours
V_0=0.3048 m/sec, ΔT_{wall}=-5.5°K Sinusoidal

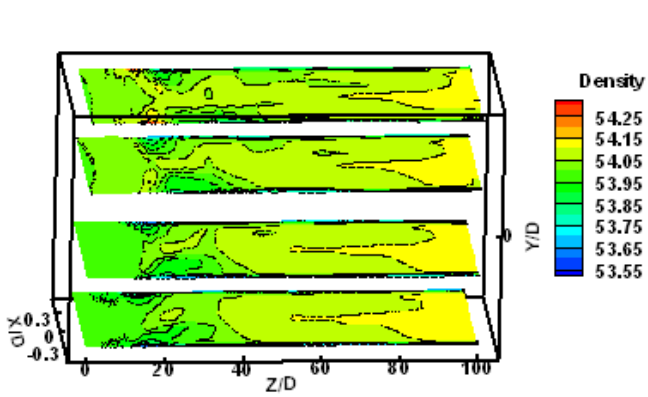

Fig. A-142 Density Slice Contours
V_0=0.3048 m/sec, ΔT_{wall}=-13.8°K Sinusoidal

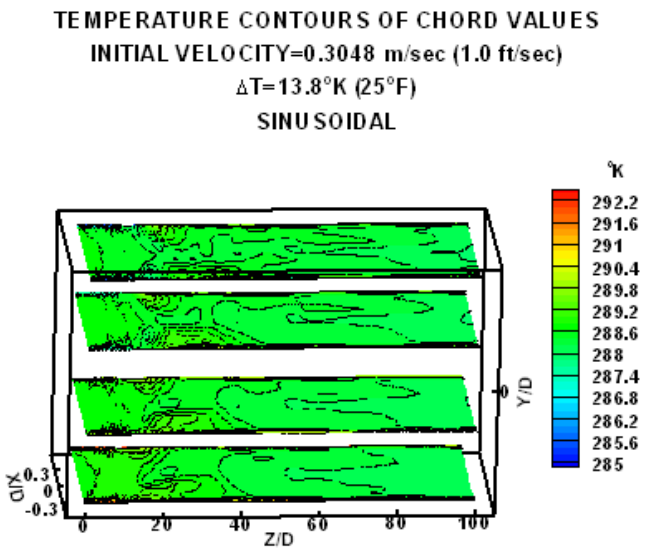

Fig. A-143 Temperature Slice Contours
V_0=0.3048 m/sec, ΔT_{wall}=-13.8°K Sinusoidal

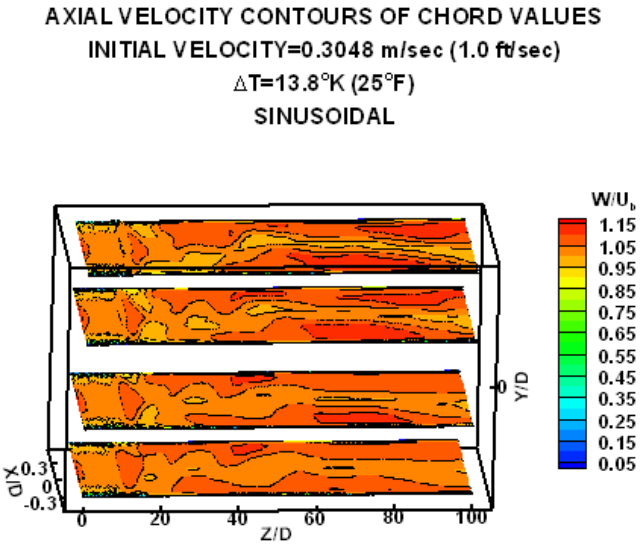

Fig. A-144 Axial Velocity Slice Contours
V_0=0.3048 m/sec, ΔT_{wall}=-13.8°K Sinusoidal

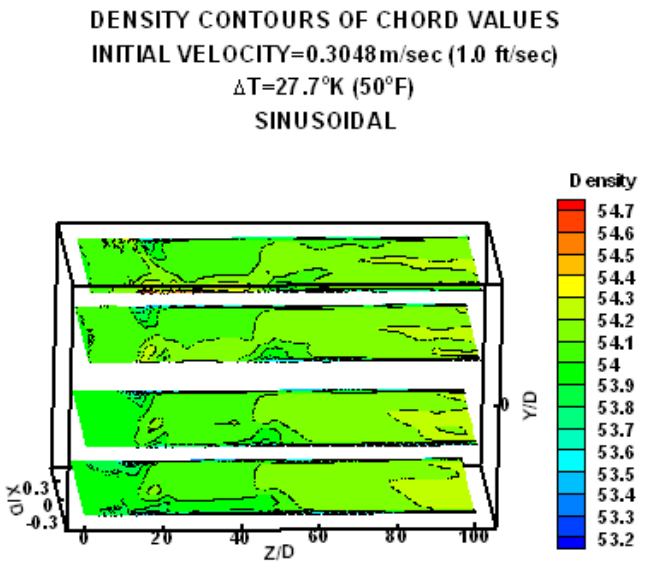

Fig. A-145 Density Slice Contours
V_0=0.3048 m/sec, ΔT_{wall}=-27.7°K Sinusoidal

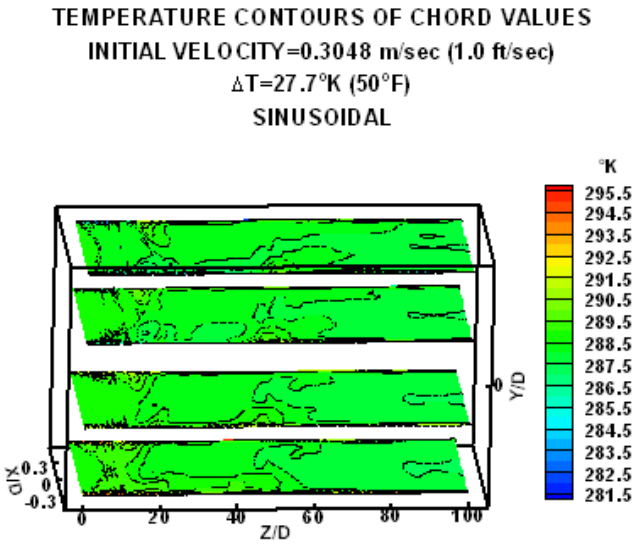

Fig. A-146 Temperature Slice Contours
V_0=0.3048 m/sec, ΔT_{wall}=-27.7°K Sinusoidal

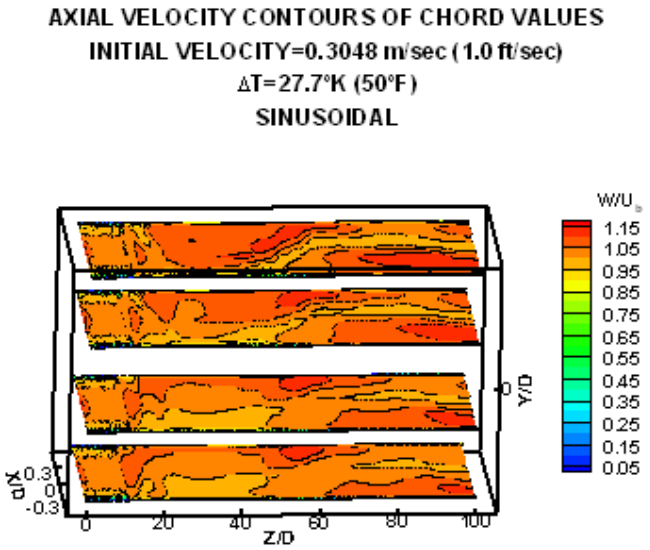

Fig. A-147 Axial Velocity Slice Contours
V_0=0.3048 m/sec, ΔT_{wall}=-27.7°K Sinusoidal

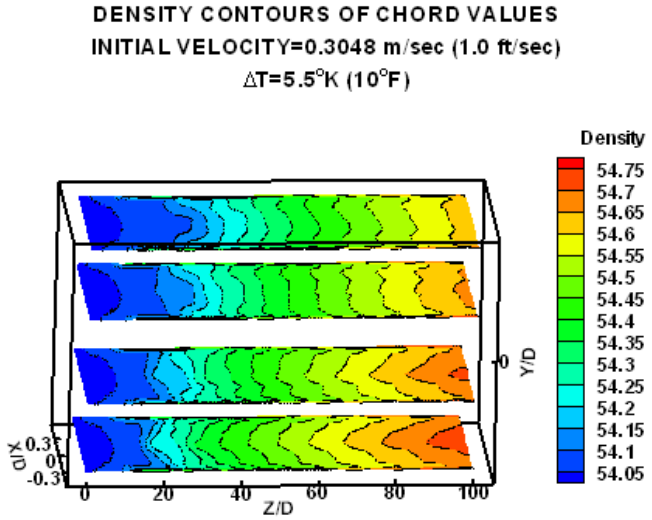

Fig. A-148 Density Slice Contours
V_0=0.3048 m/sec, ΔT_{wall}=-5.5°K

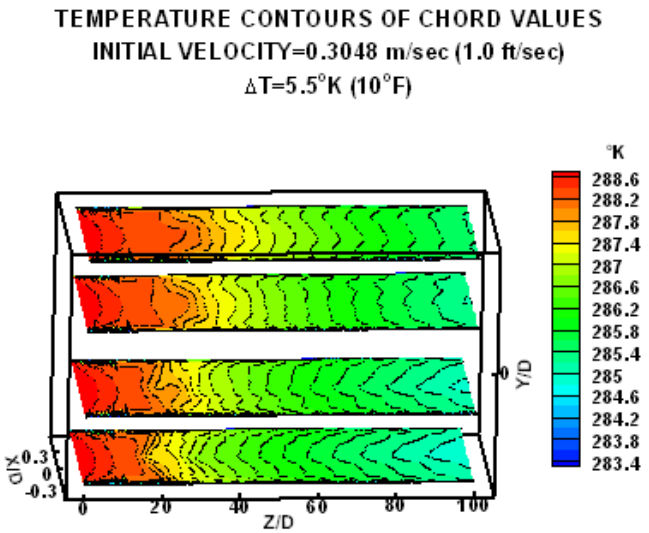

Fig. A-149 Temperature Slice Contours
V_0=0.3048 m/sec, ΔT_{wall}=-5.5°K

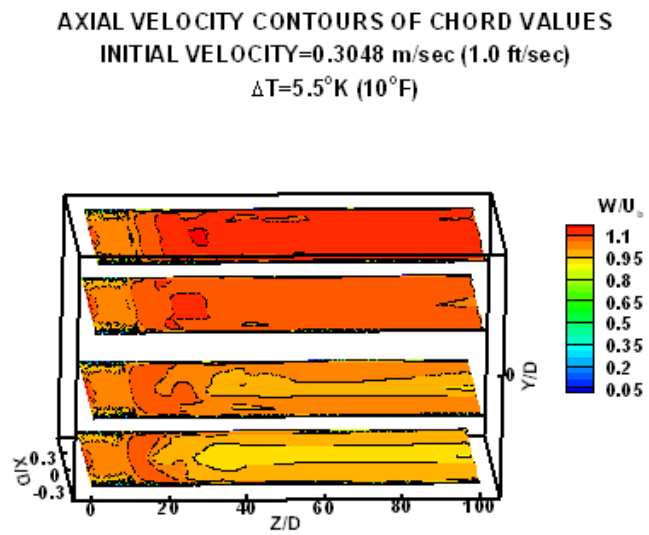

Fig. A-150 Axial Velocity Slice Contours
V_0=0.3048 m/sec, ΔT_{wall}=-5.5°K

DENSITY CONTOURS OF CHORD VALUES
INITIAL VELOCITY=0.3048 m/sec (1.0 ft/sec)
ΔT=13.8°K (25°F)

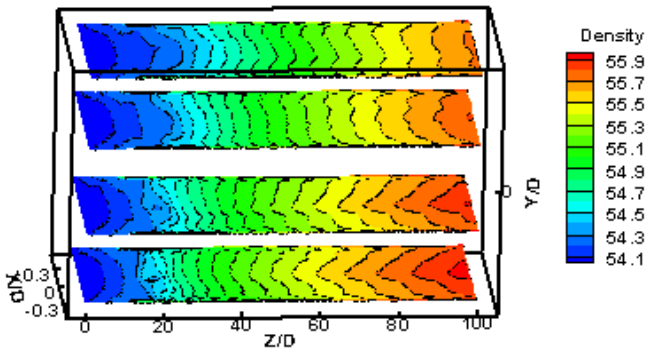

Fig. A-151 Density Slice Contours
V_0=0.3048 m/sec, ΔT_{wall}=-13.8°K

TEMPERATURE CONTOURS OF CHORD VALUES
INITIAL VELOCITY=0.3048 m/sec (1.0 ft/sec)
ΔT=13.8°K (25°F)

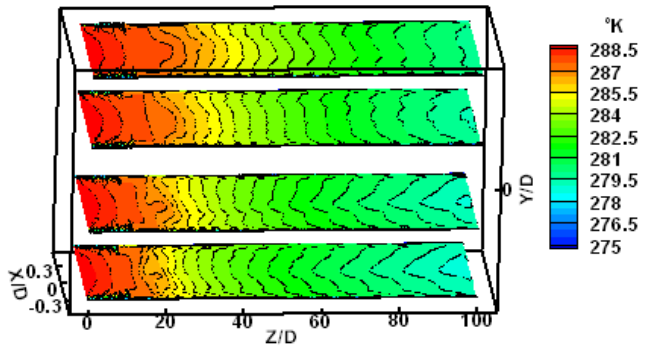

Fig. A-152 Temperature Slice Contours
V_0=0.3048 m/sec, ΔT_{wall}=-13.8°K

AXIAL VELOCITY CONTOURS OF CHORD VALUES
INITIAL VELOCITY=0.3048 m/sec (1.0 ft/sec)
ΔT=13.8°K (25°F)

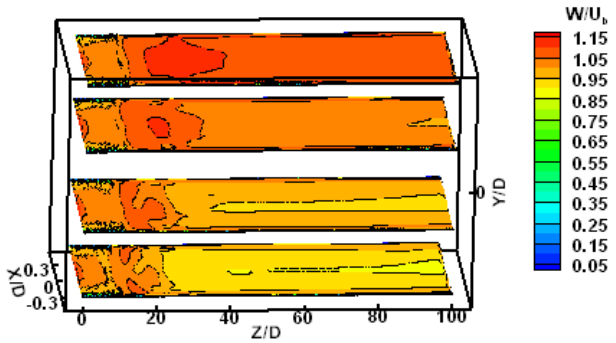

Fig. A-153 Axial Velocity Slice Contours
V_0=0.3048 m/sec, ΔT_{wall}=-13.8°K

DENSITY CONTOURS OF CHORD VALUES
INITIAL VELOCITY=0.3048 m/sec (1.0 ft/sec)
ΔT=27.7°K (50°F)

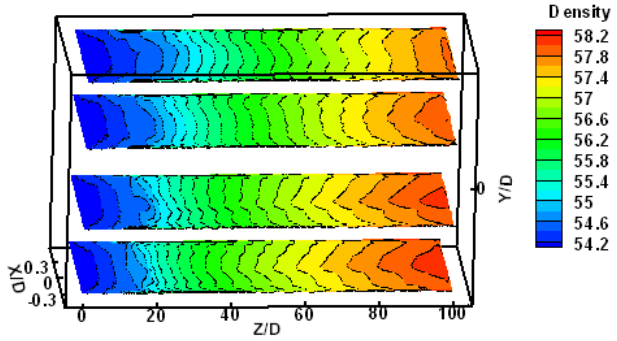

Fig. A-154 Density Slice Contours
V_0=0.3048 m/sec, ΔT_{wall}=-27.7°K

TEMPERATURE CONTOURS OF CHORD VALUES
INITIAL VELOCITY=0.3048 m/sec (1.0 ft/sec)
ΔT=27.7°K (50°F)

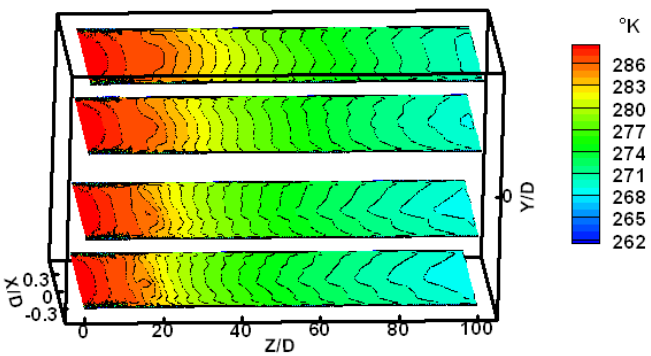

Fig. A-155 Temperature Slice Contours
V_0=0.3048 m/sec, ΔT_{wall}=-27.7°K

AXIAL VELOCITY CONTOURS OF CHORD VALUES
INITIAL VELOCITY=0.3048 m/sec (1.0 ft/sec)
ΔT=27.7°K (50°F)

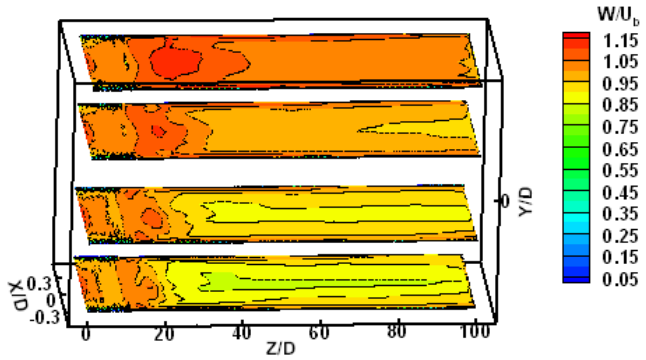

Fig. A-156 Axial Velocity Slice Contours
V_0=0.3048 m/sec, ΔT_{wall}=-27.7°K

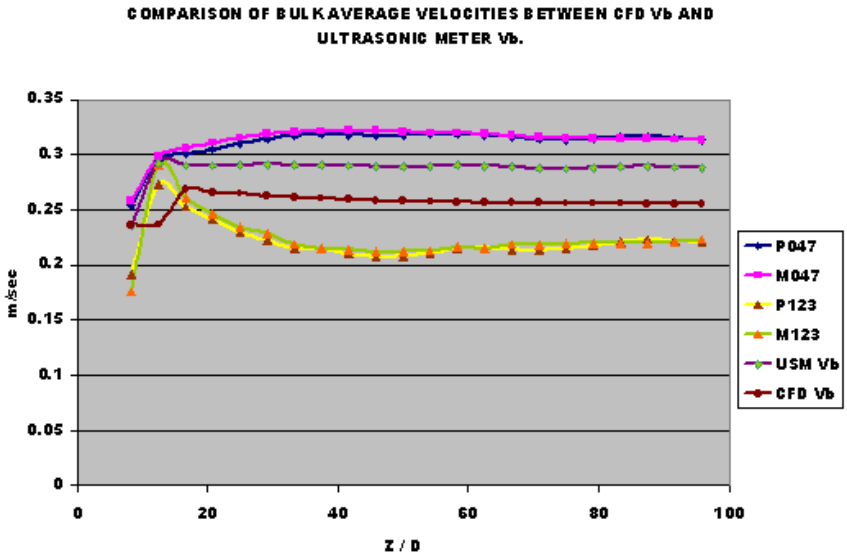

Fig. A-157 Comparison between CFD Vb and Ultrasonic Vb.
V_0=0.3048 m/sec, ΔT_{wall}=5.5°K Sinusoidal

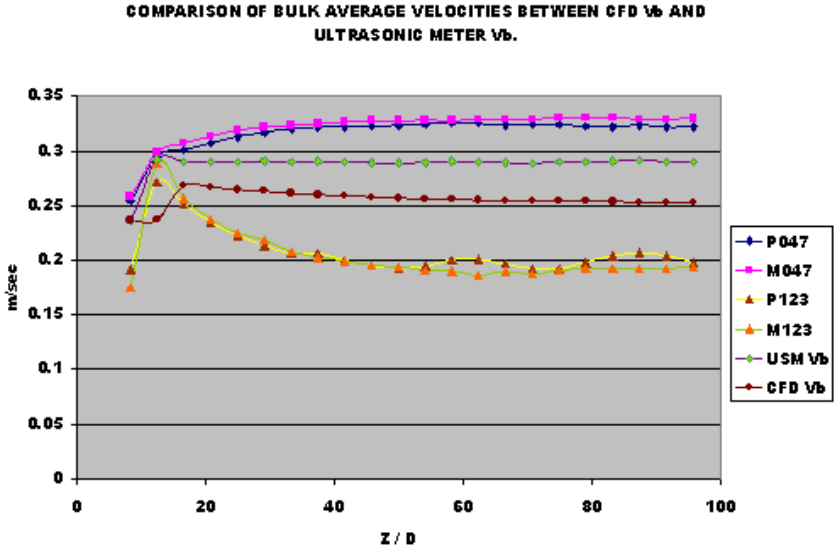

Fig. A-158 Comparison between CFD Vb and Ultrasonic Vb.
V_0=0.3048 m/sec, ΔT_{wall}=13.8°K Sinusoidal

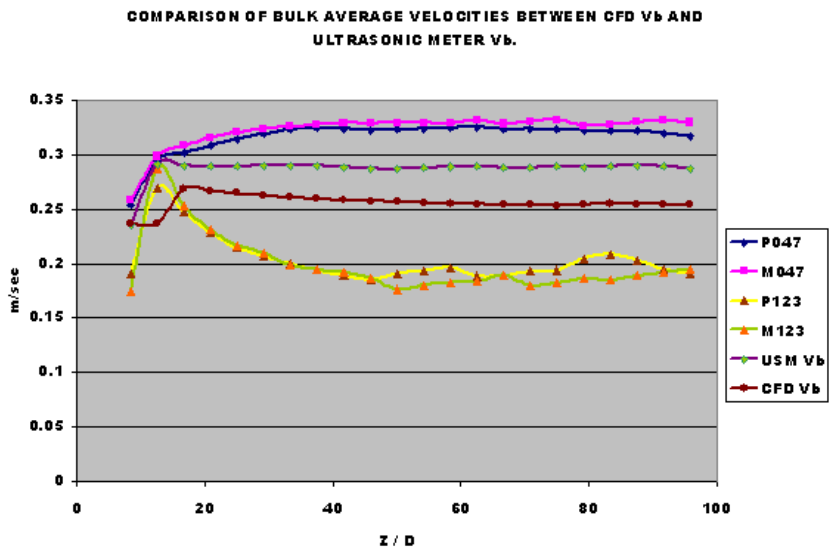

Fig. A-159 Comparison between CFD Vb and Ultrasonic Vb.
V_0=0.3048 m/sec, ΔT_{wall}=27.7°K Sinusoidal

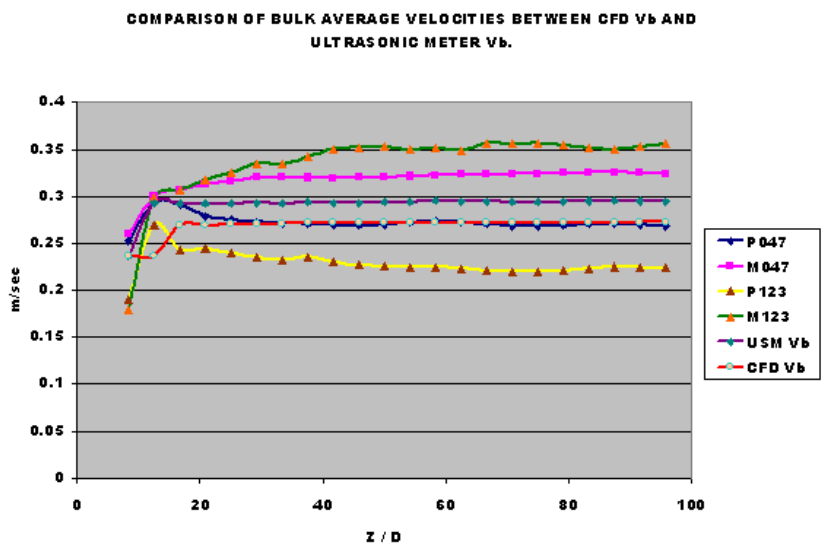

Fig. A-160 Comparison between CFD Vb and Ultrasonic Vb.
V_0=0.3048 m/sec, ΔT_{wall}=5.5°K

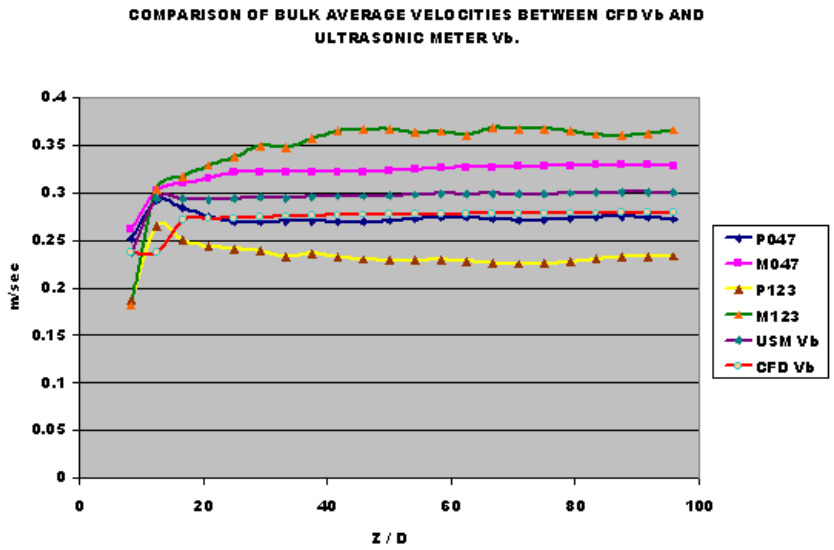

Fig. A-161 Comparison between CFD Vb and Ultrasonic Vb.
V_0=0.3048 m/sec, ΔT_{wall}=13.8^{o}K

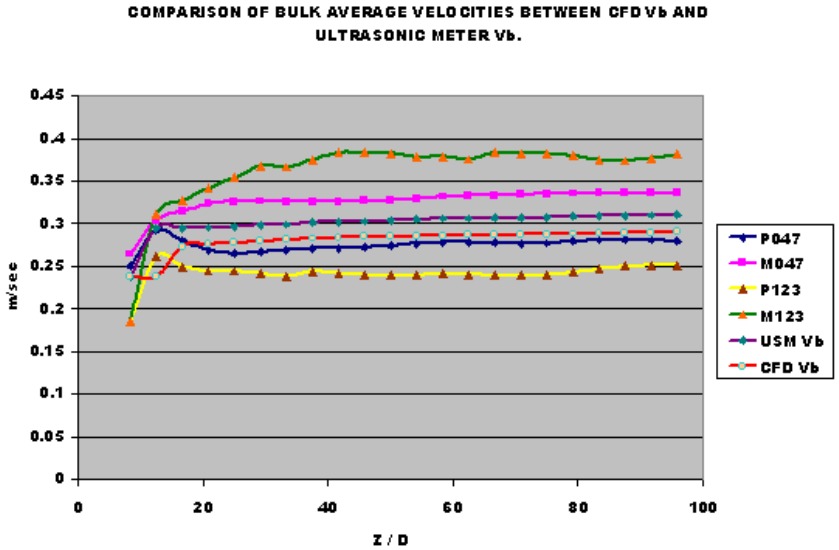

Fig. A-162 Comparison between CFD Vb and Ultrasonic Vb.
V_0=0.3048 m/sec, ΔT_{wall}=27.7^{o}K

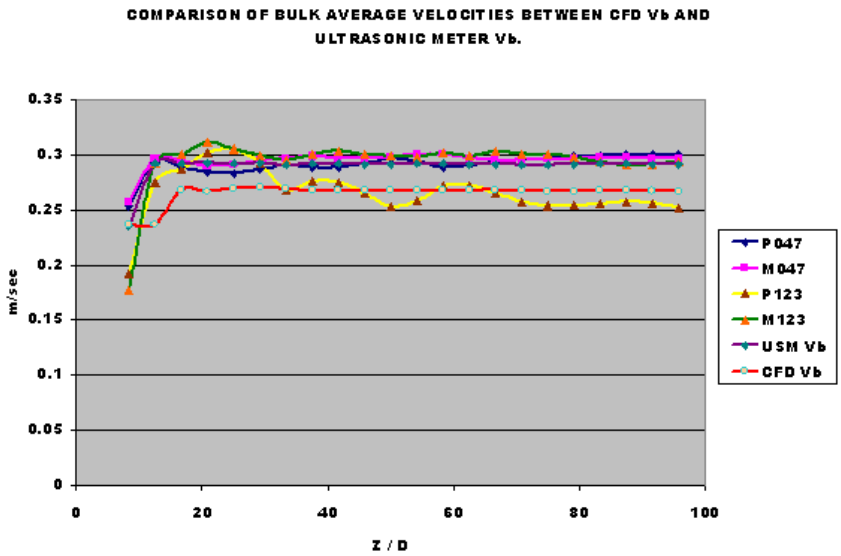

Fig. A-163 Comparison between CFD Vb and Ultrasonic Vb.
V_0=0.3048 m/sec, ΔT_{wall}=-5.5°K Sinusoidal

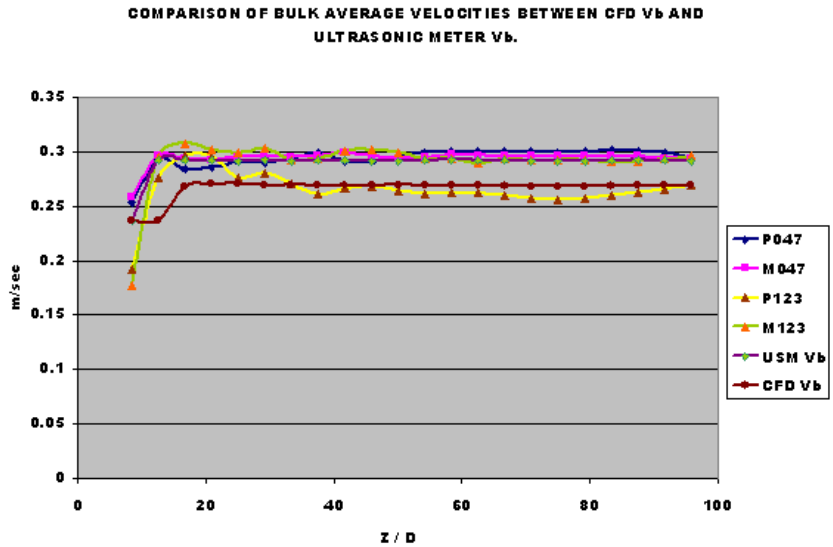

Fig. A-164 Comparison between CFD Vb and Ultrasonic Vb.
V_0=0.3048 m/sec, ΔT_{wall}=-13.8°K Sinusoidal

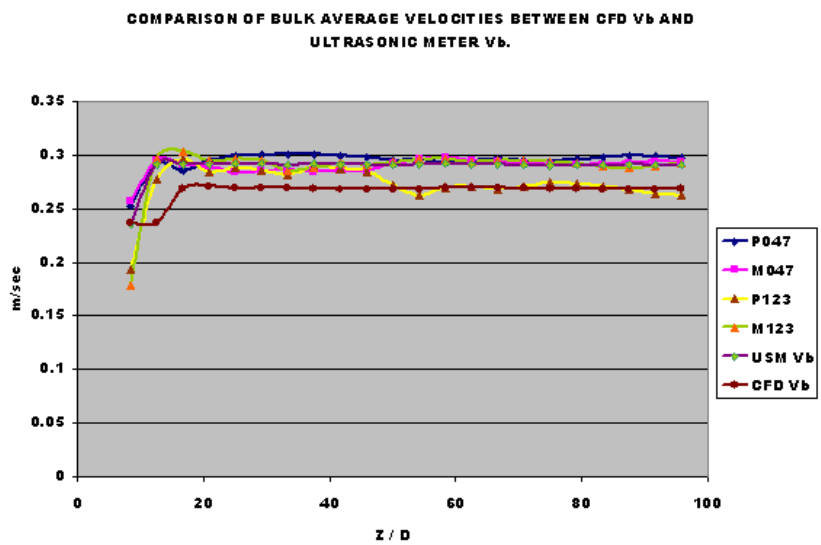

Fig. A-165 Comparison between CFD Vb and Ultrasonic Vb.
V_0=0.3048 m/sec, ΔT_{wall}=-27.7°K Sinusoidal

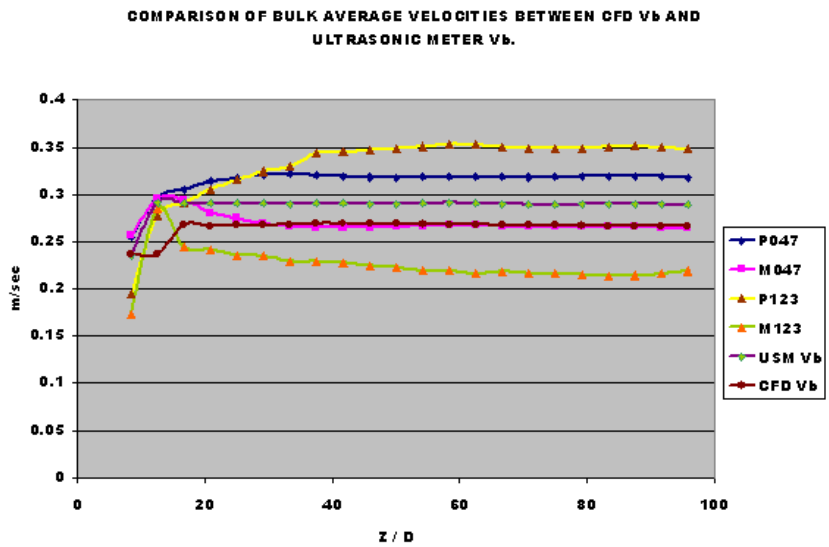

Fig. A-166 Comparison between CFD Vb and Ultrasonic Vb.
V_0=0.3048 m/sec, ΔT_{wall}=-5.5°K

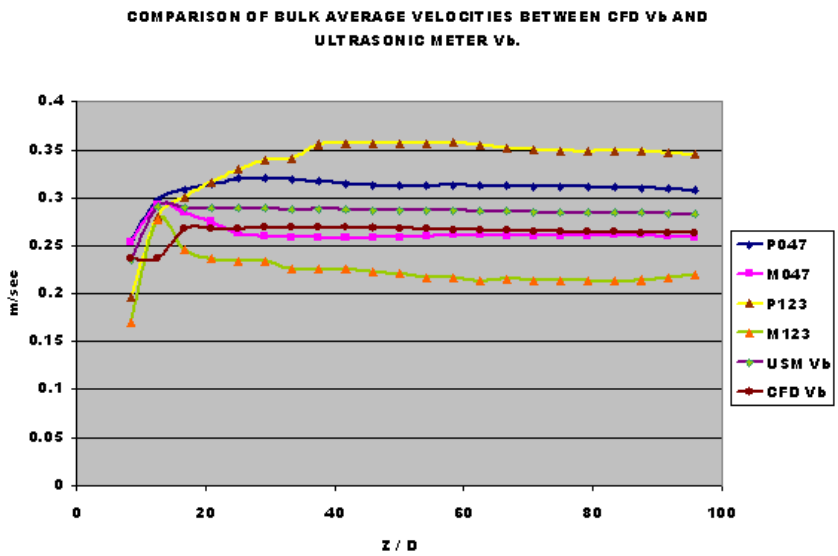

Fig. A-167 Comparison between CFD Vb and Ultrasonic Vb.
V_0=0.3048 m/sec, ΔT_{wall}=-13.8°K

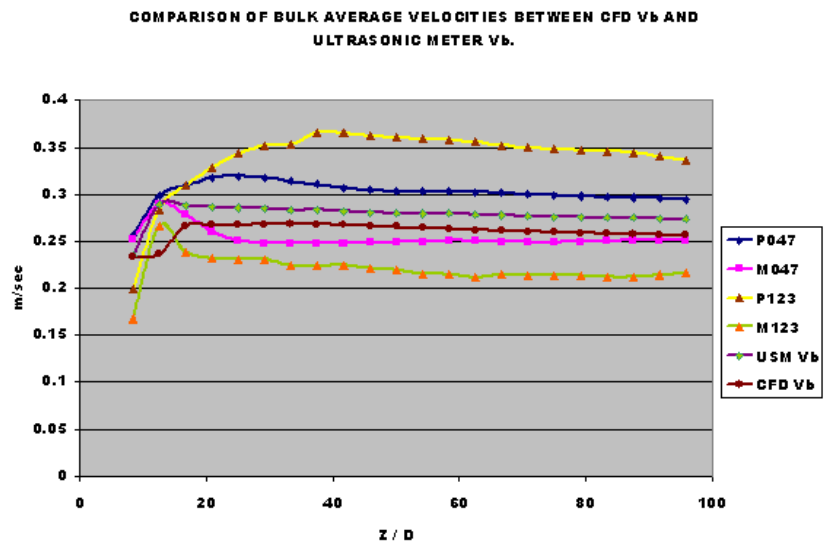

Fig. A-168 Comparison between CFD Vb and Ultrasonic Vb.
V_0=0.3048 m/sec, ΔT_{wall}=-27.7°K

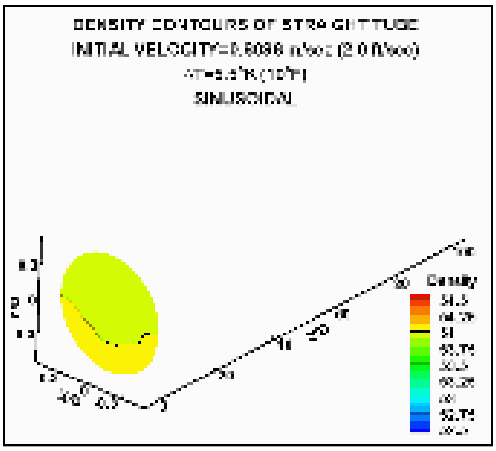

Fig. A-169 Density Contours
V_0=0.6096 m/sec, ΔT_{wall}=5.5°K Sinusoidal

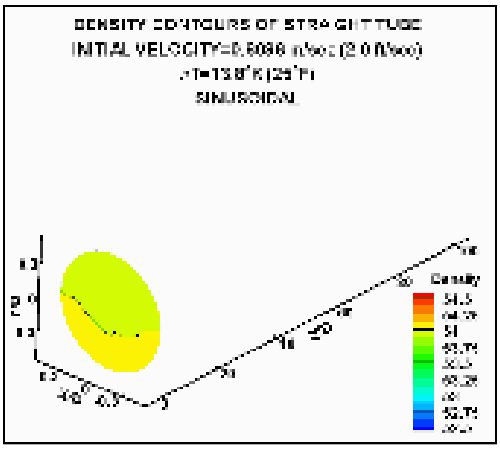

Fig. A-172 Density Contours
V_0=0.6096 m/sec, ΔT_{wall}=13.8°K Sinusoidal

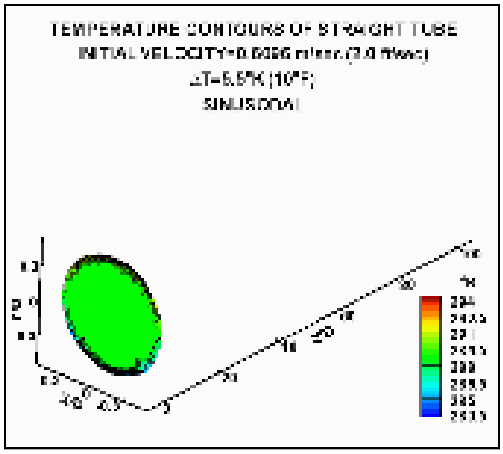

Fig. A-170 Temperature Contours
V_0=0.6096 m/sec, ΔT_{wall}=5.5°K Sinusoidal

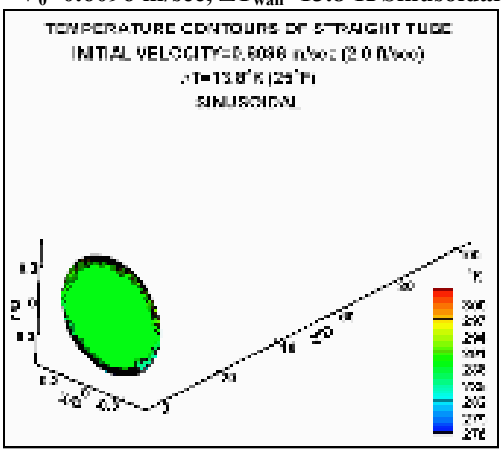

Fig. A-173 Temperature Contours
V_0=0.6096 m/sec, ΔT_{wall}=13.8°K Sinusoidal

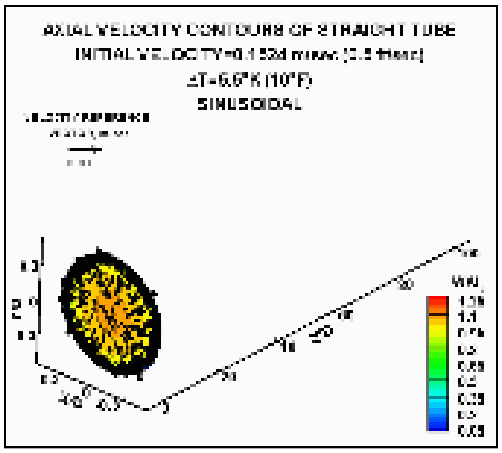

Fig. A-171 Axial Velocity Contours
V_0=0.6096 m/sec, ΔT_{wall}=5.5°K Sinusoidal

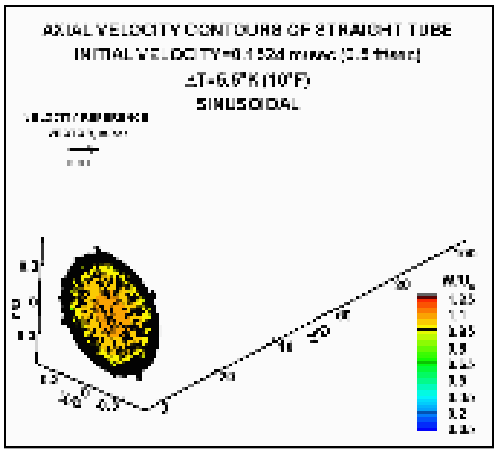

Fig. A-174 Axial Velocity Contours
V_0=0.6096 m/sec, ΔT_{wall}=13.8°K Sinusoidal

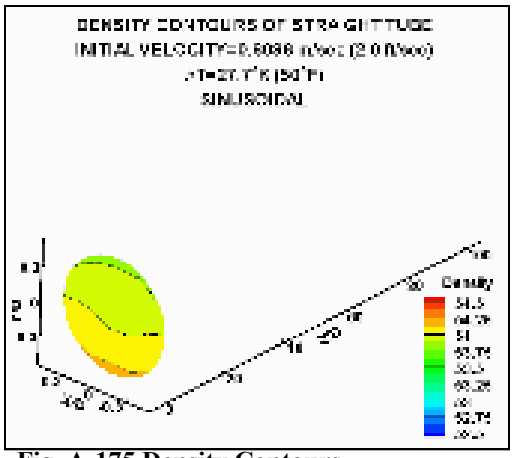

Fig. A-175 Density Contours
V_0=0.6096 m/sec, ΔT_{wall}=27.7°K Sinusoidal

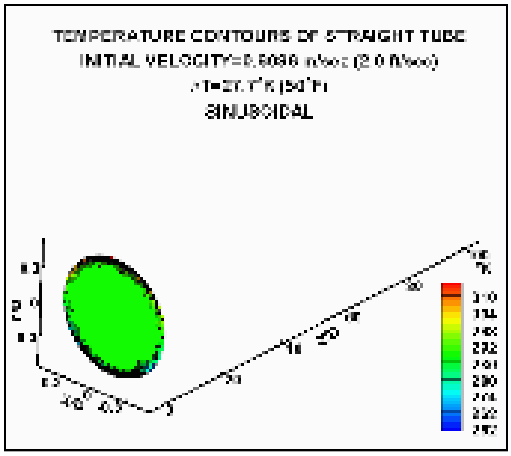

Fig. A-176 Temperature Contours
V_0=0.6096 m/sec, ΔT_{wall}=27.7°K Sinusoidal

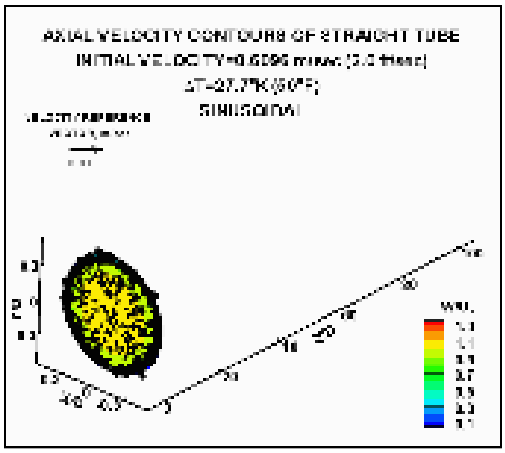

Fig. A-177 Axial Velocity Contours
V_0=0.6096 m/sec, ΔT_{wall}=27.7°K Sinusoidal

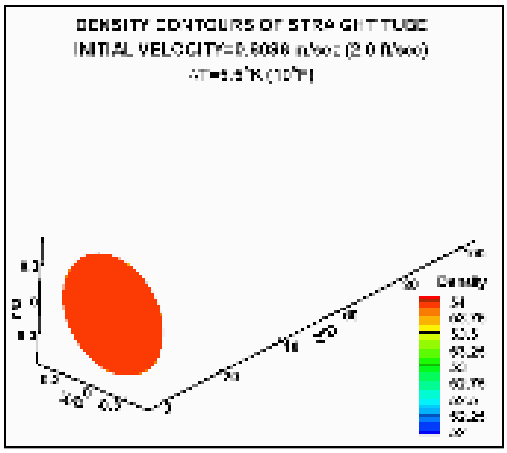

Fig. A-178 Density Contours
V_0=0.6096 m/sec, ΔT_{wall}=5.5°K

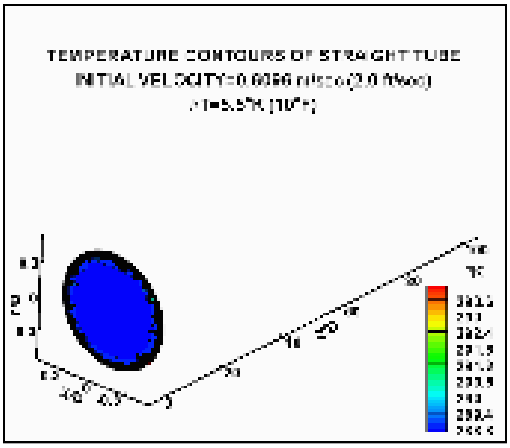

Fig. A-179 Temperature Contours
V_0=0.6096 m/sec, ΔT_{wall}=5.5°K

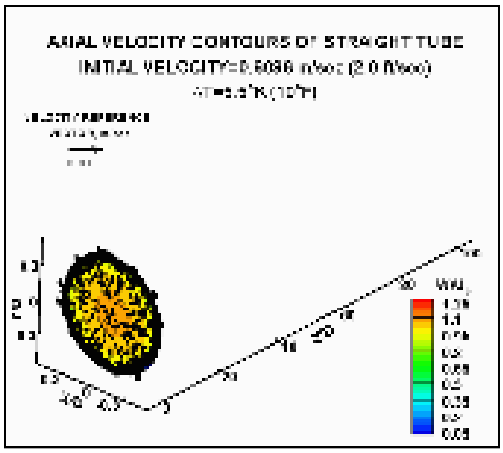

Fig. A-180 Axial Velocity Contours
V_0=0.6096 m/sec, ΔT_{wall}=5.5°K

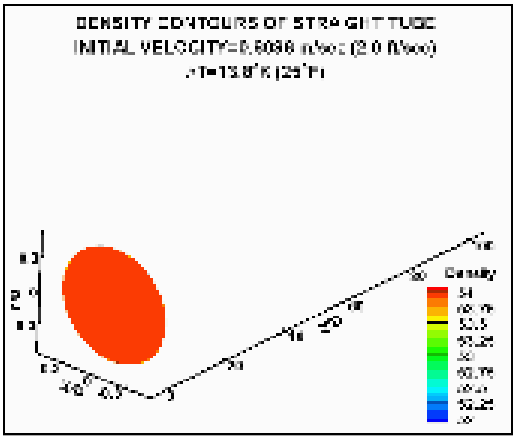

Fig. A-181 Density Contours
V_0=0.6096 m/sec, ΔT_{wall}=13.8°K

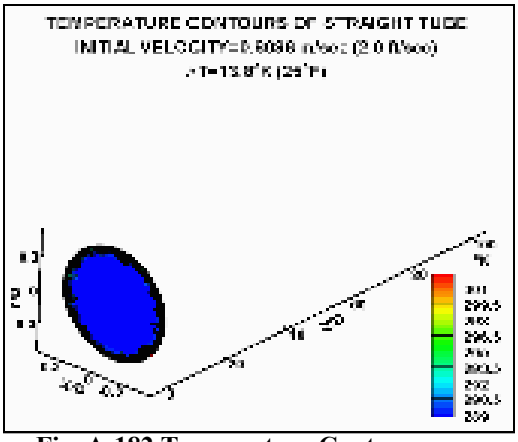

Fig. A-182 Temperature Contours
V_0=0.6096 m/sec, ΔT_{wall}=13.8°K

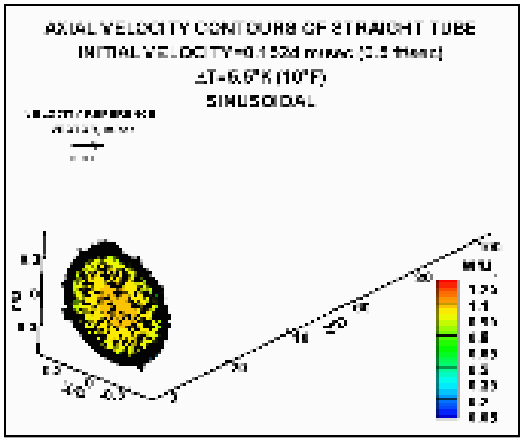

Fig. A-183 Axial Velocity Contours
V_0=0.6096 m/sec, ΔT_{wall}=13.8°K

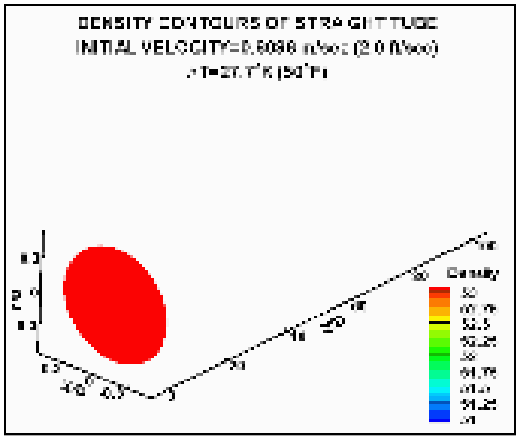

Fig. A-184 Density Contours
V_0=0.6096 m/sec, ΔT_{wall}=27.7°K

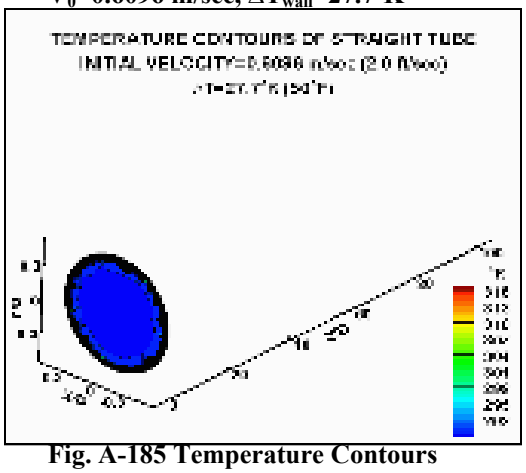

Fig. A-185 Temperature Contours
V_0=0.6096 m/sec, ΔT_{wall}=27.7°K

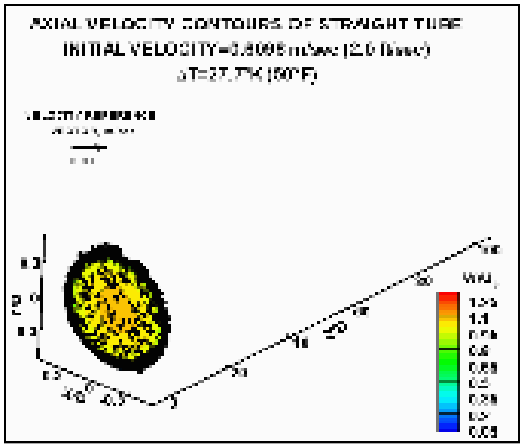

Fig. A-186 Axial Velocity Contours
V_0=0.6096 m/sec, ΔT_{wall}=27.7°K

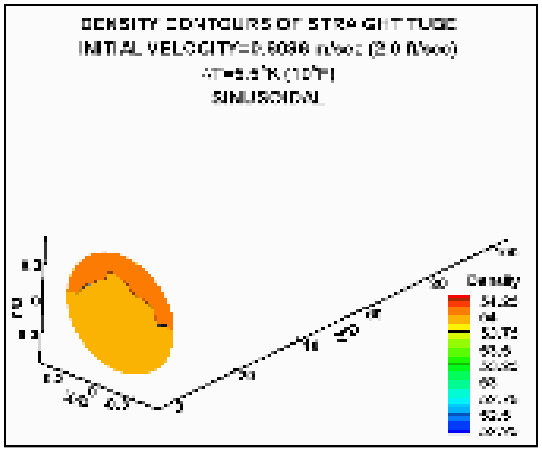

Fig. A-187 Density Contours
V_0=0.6096 m/sec, ΔT_{wall}=-5.5°K Sinusoidal

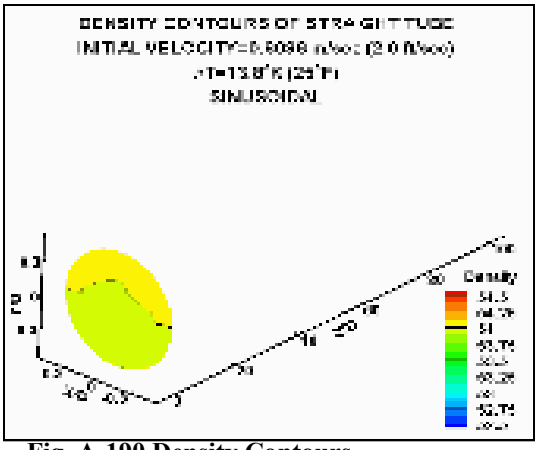

Fig. A-190 Density Contours
V_0=0.6096 m/sec, ΔT_{wall}=-13.8°K Sinusoidal

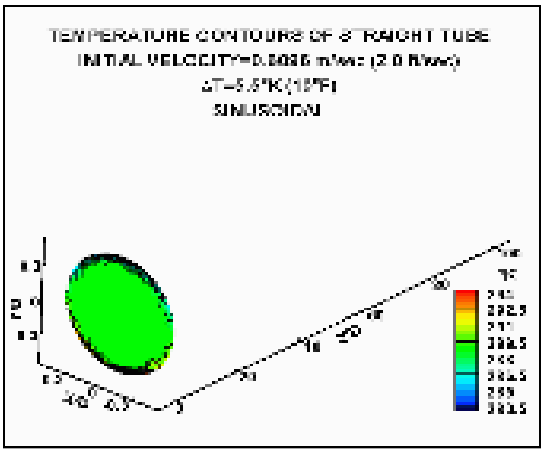

Fig. A-188 Temperature Contours
V_0=0.6096 m/sec, ΔT_{wall}=-5.5°K Sinusoidal

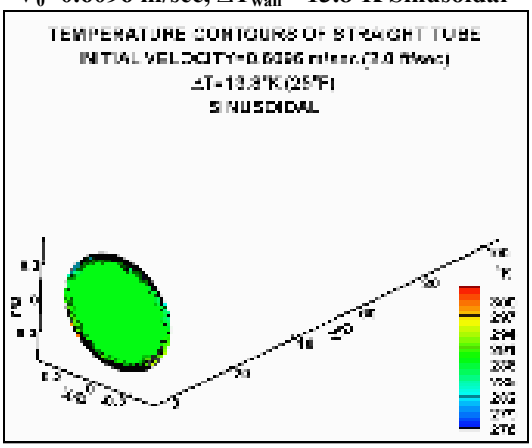

Fig. A-191 Temperature Contours
V_0=0.6096 m/sec, ΔT_{wall}=-13.8°K Sinusoidal

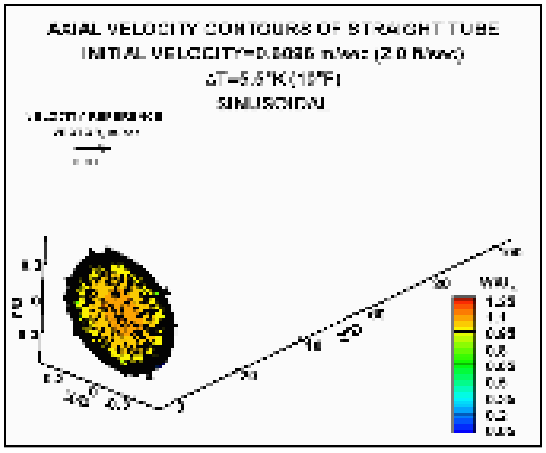

Fig. A-189 Axial Velocity Contours
V_0=0.6096 m/sec, ΔT_{wall}=-5.5°K Sinusoidal

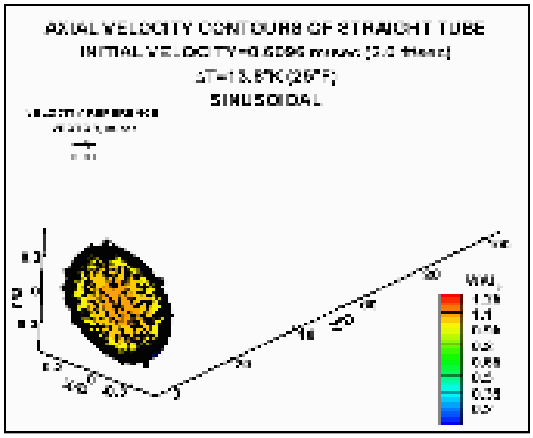

Fig. A-192 Axial Velocity Contours
V_0=0.6096 m/sec, ΔT_{wall}=-13.8°K Sinusoidal

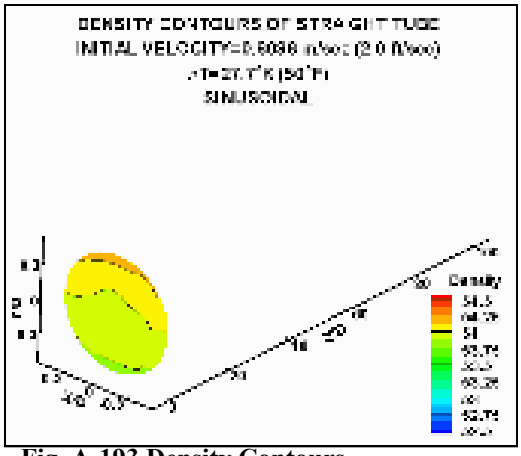

Fig. A-193 Density Contours
V_0=0.6096 m/sec, ΔT_{wall}=-27.7°K Sinusoidal

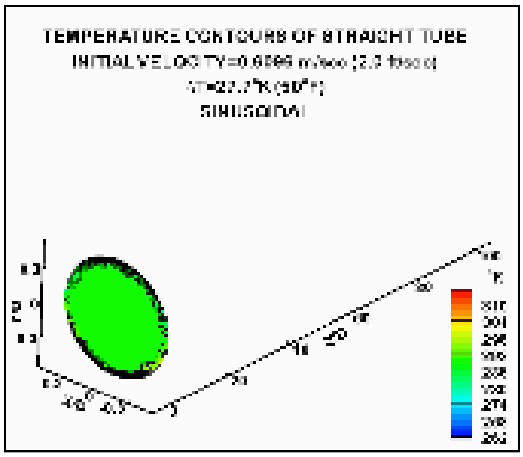

Fig. A-194 Temperature Contours
V_0=0.6096 m/sec, ΔT_{wall}=-27.7°K Sinusoidal

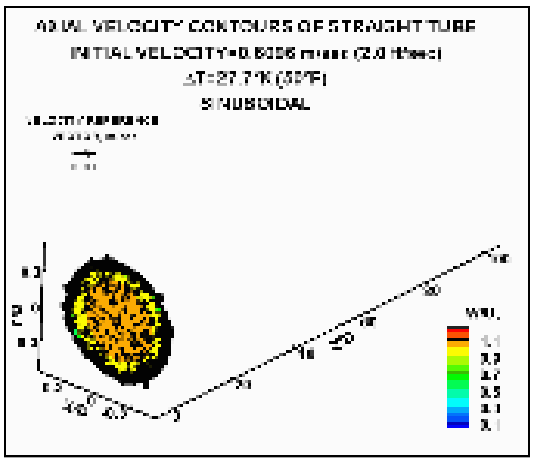

Fig. A-195 Axial Velocity Contours
V_0=0.6096 m/sec, ΔT_{wall}=-27.7°K Sinusoidal

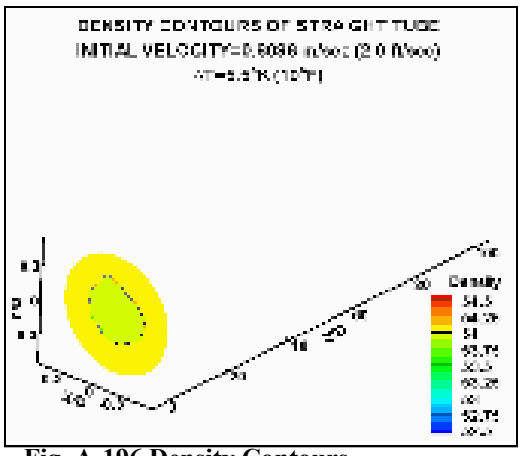

Fig. A-196 Density Contours
V_0=0.6096 m/sec, ΔT_{wall}=-5.5°K

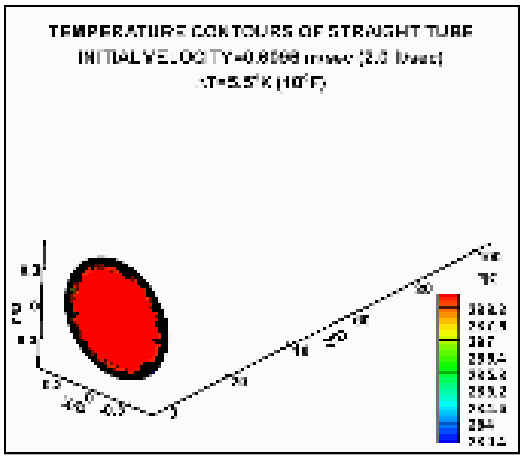

Fig. A-197 Temperature Contours
V_0=0.6096 m/sec, ΔT_{wall}=-5.5°K

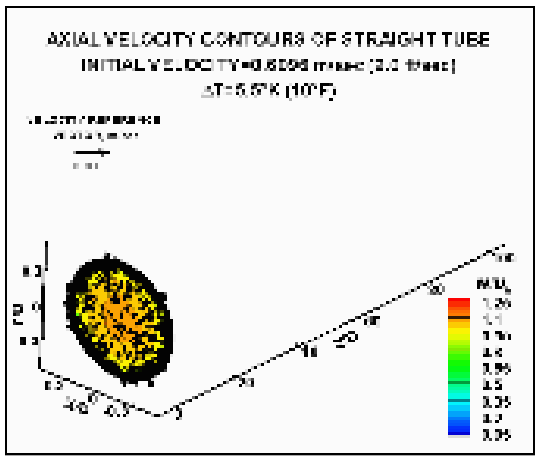

Fig. A-198 Axial Velocity Contours
V_0=0.6096 m/sec, ΔT_{wall}=-5.5°K

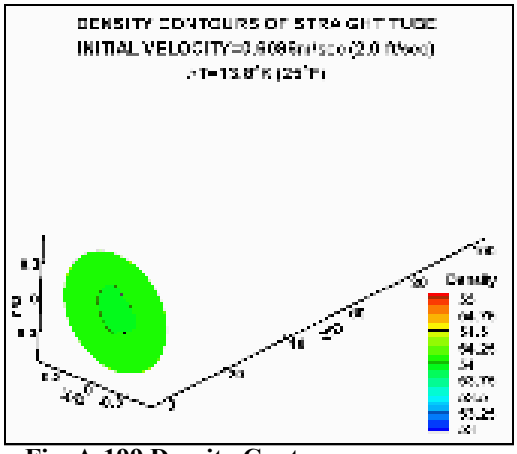

Fig. A-199 Density Contours
V_0=0.6096 m/sec, ΔT_{wall}=-13.8°K

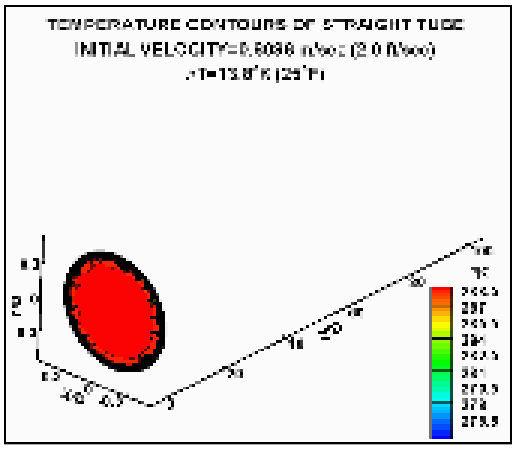

Fig. A-200 Temperature Contours
V_0=0.6096 m/sec, ΔT_{wall}=-13.8°K

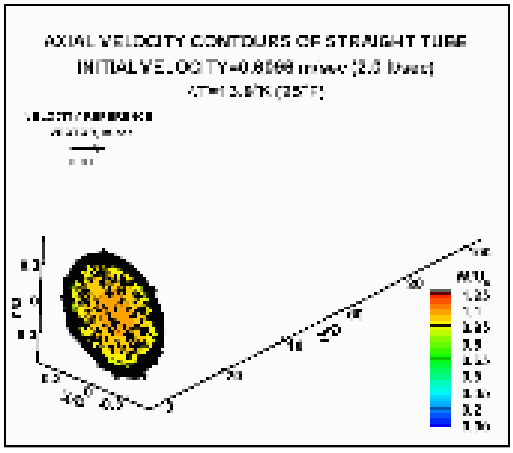

Fig. A-201 Axial Velocity Contours
V_0=0.6096 m/sec, ΔT_{wall}=-13.8°K

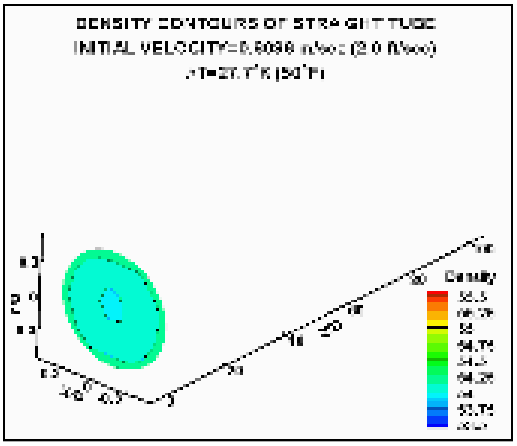

Fig. A-202 Density Contours
V_0=0.6096 m/sec, ΔT_{wall}=-27.7°K

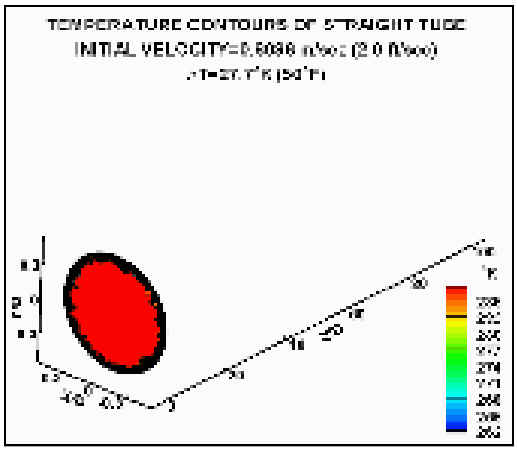

Fig. A-203 Temperature Contours
V_0=0.6096 m/sec, ΔT_{wall}=-27.7°K

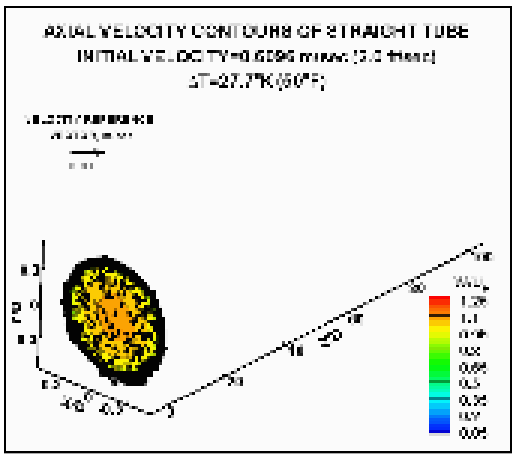

Fig. A-204 Axial Velocity Contours
V_0=0.6096 m/sec, ΔT_{wall}=-27.7°K

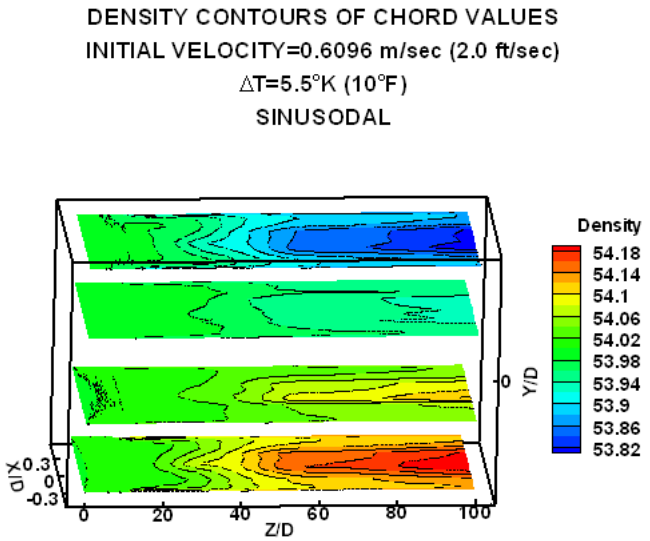

Fig. A-205 Density Slice Contours
V_0=0.6096 m/sec, ΔT_{wall}=5.5°K Sinusoidal

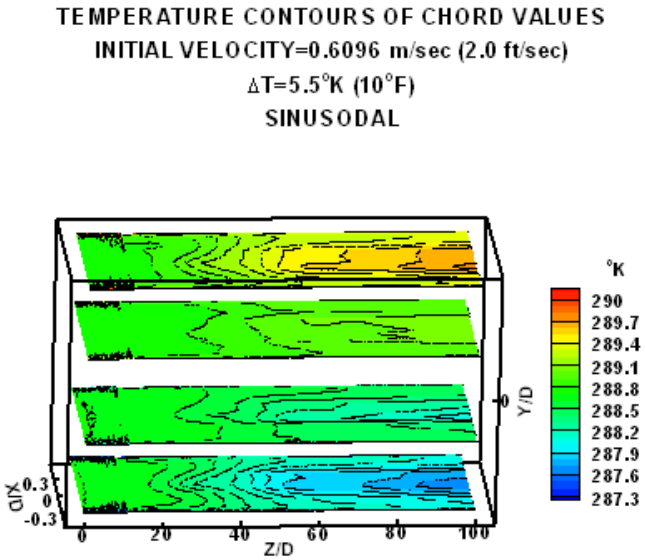

Fig. A-206 Temperature Slice Contours
V_0=0.6096 m/sec, ΔT_{wall}=5.5°K Sinusoidal

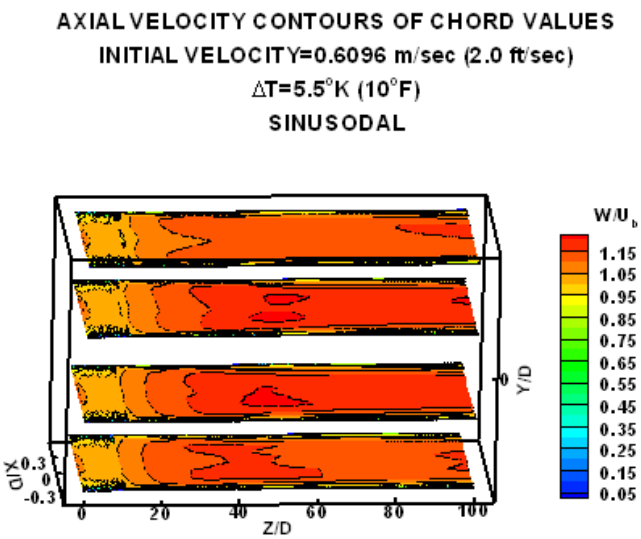

Fig. A-207 Axial Velocity Slice Contours
V_0=0.6096 m/sec, ΔT_{wall}=5.5°K Sinusoidal

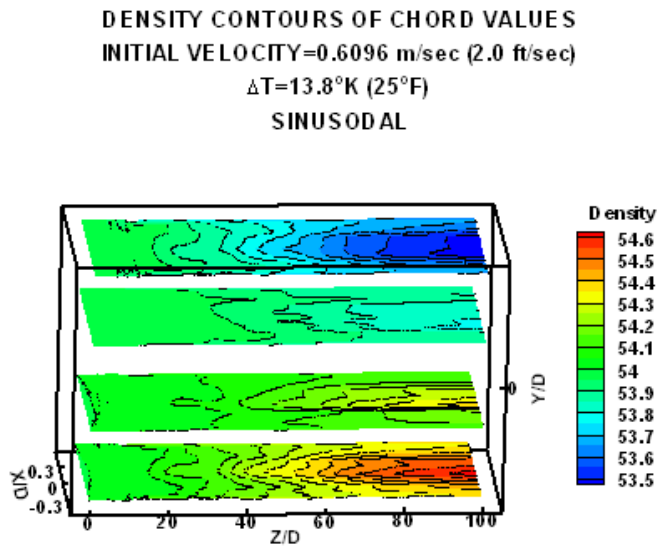

Fig. A-208 Density Slice Contours
V_0=0.6096 m/sec, ΔT_{wall}=13.8°K Sinusoidal

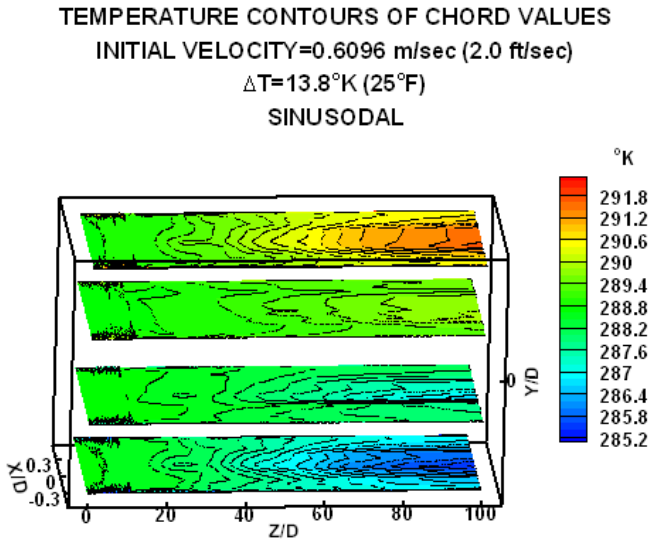

Fig. A-209 Temperature Slice Contours
V_0=0.6096 m/sec, ΔT_{wall}=13.8°K Sinusoidal

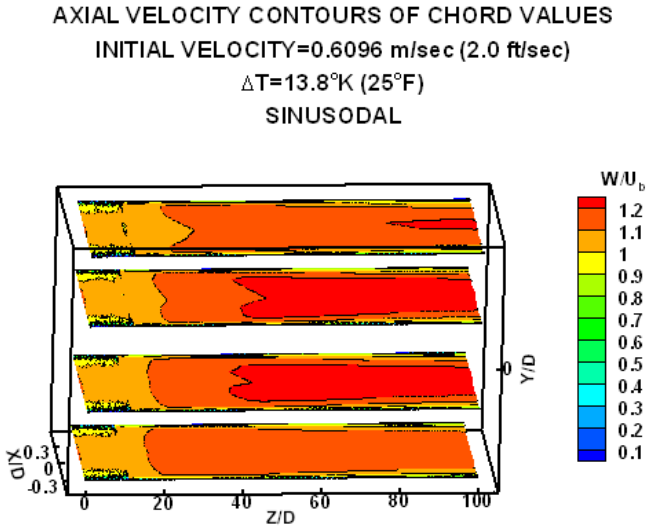

Fig. A-210 Axial Velocity Slice Contours
V_0=0.6096 m/sec, ΔT_{wall}=13.8°K Sinusoidal

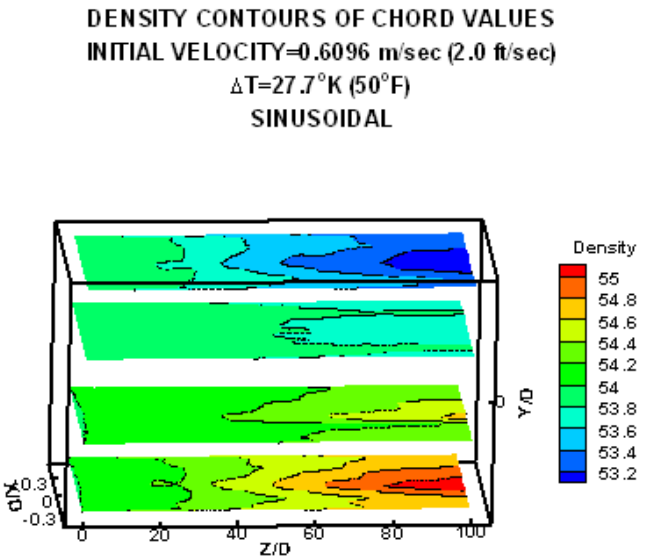

Fig. A-211 Density Slice Contours
V_0=0.6096 m/sec, ΔT_{wall}=27.7°K Sinusoidal

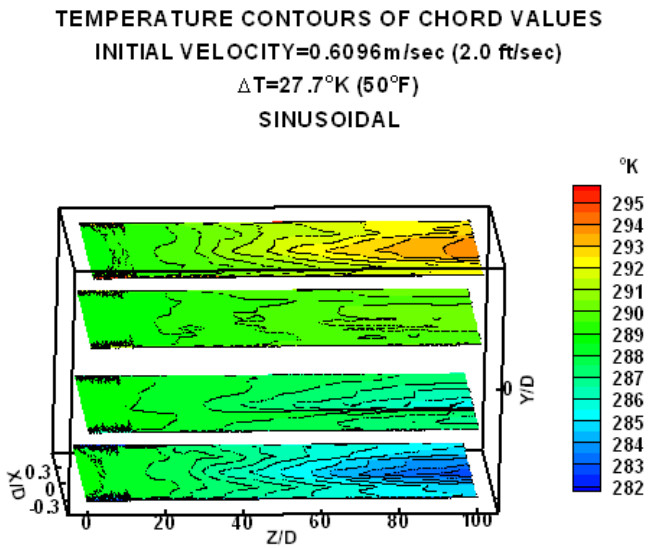

Fig. A-212 Temperature Slice Contours
V_0=0.6096 m/sec, ΔT_{wall}=27.7°K Sinusoidal

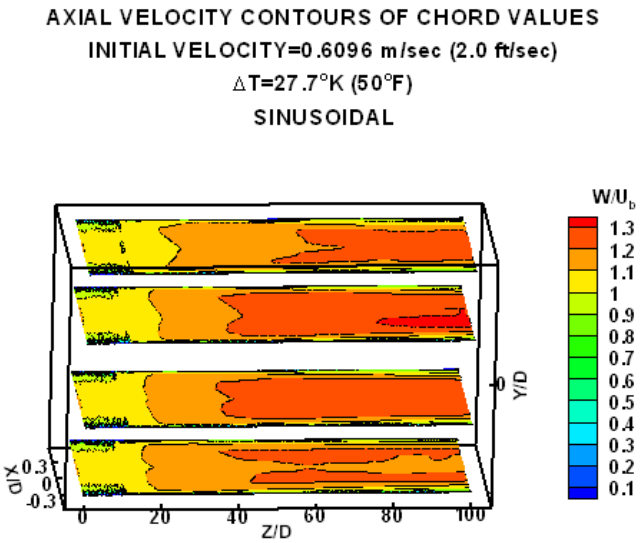

Fig. A-213 Axial Velocity Slice Contours
V_0=0.6096 m/sec, ΔT_{wall}=27.7°K Sinusoidal

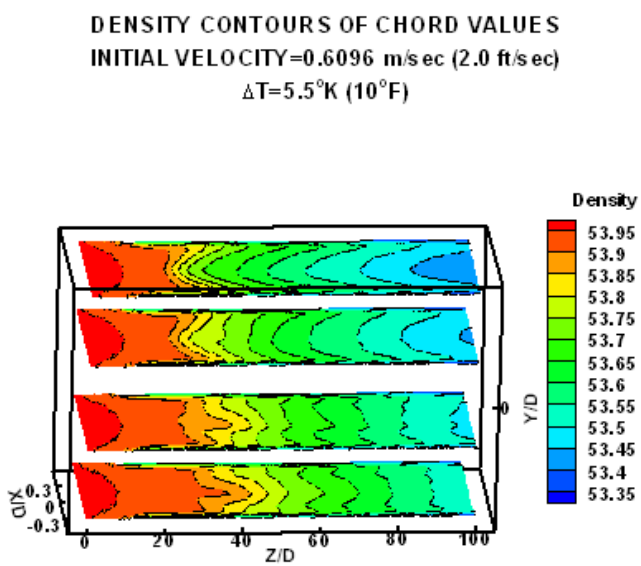

Fig. A-214 Density Slice Contours
V_0=0.6096 m/sec, ΔT_{wall}=5.5°K

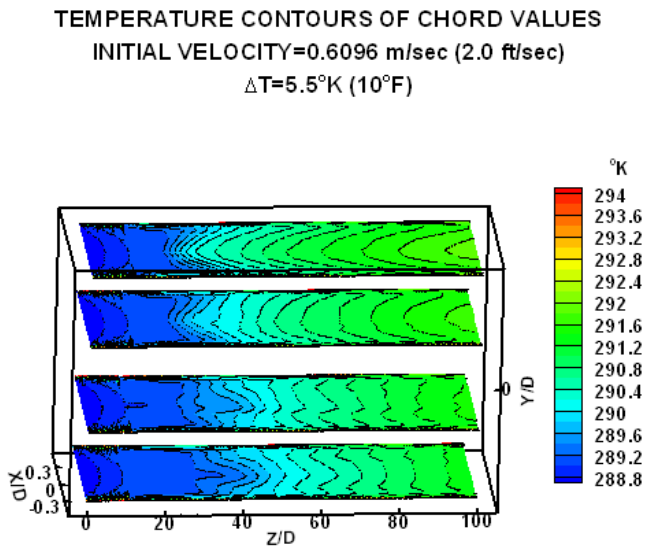

Fig. A-215 Temperature Slice Contours
V_0=0.6096 m/sec, ΔT_{wall}=5.5°K

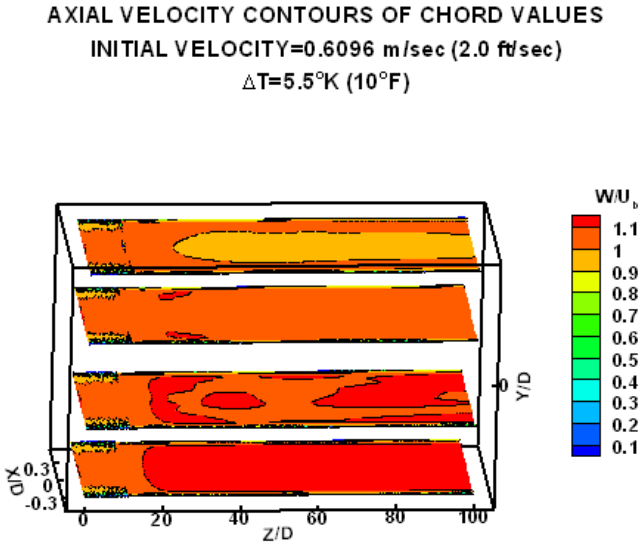

Fig. A-216 Axial Velocity Slice Contours
V_0=0.6096 m/sec, ΔT_{wall}=5.5°K

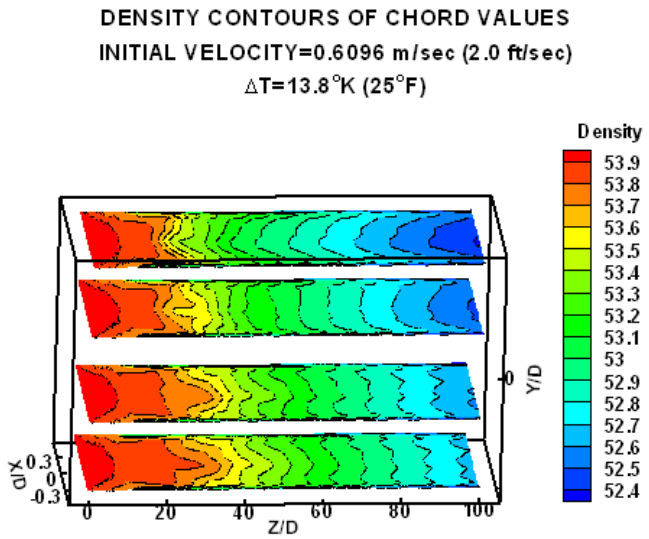

Fig. A-217 Density Slice Contours
V_0=0.6096 m/sec, ΔT_{wall}=13.8°K

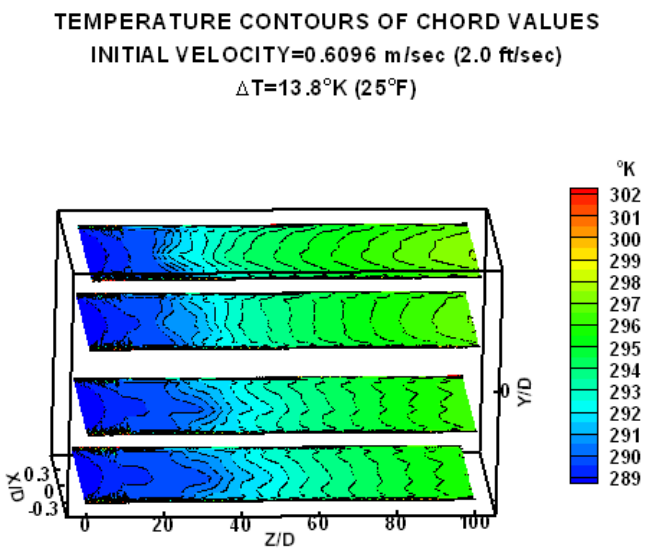

Fig. A-218 Temperature Slice Contours
V_0=0.6096 m/sec, ΔT_{wall}=13.8°K

AXIAL VELOCITY CONTOURS OF CHORD VALUES
INITIAL VELOCITY=0.6096 m/sec (2.0 ft/sec)
ΔT=13.8°K (25°F)

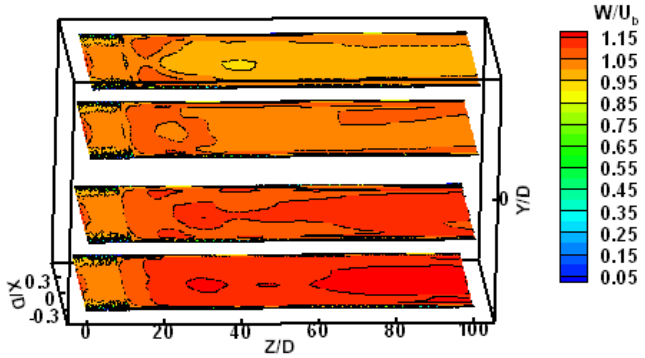

Fig. A-219 Axial Velocity Slice Contours
V_0=0.6096 m/sec, ΔT_{wall}=13.8°K

DENSITY CONTOURS OF CHORD VALUES
INITIAL VELOCITY=0.6096 m/sec (2.0 ft/sec)
ΔT=27.7°K (50°F)

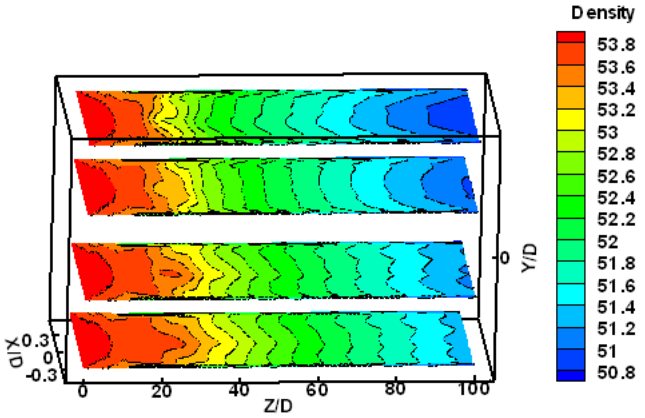

Fig. A-220 Density Slice Contours
V_0=0.6096 m/sec, ΔT_{wall}=27.7°K

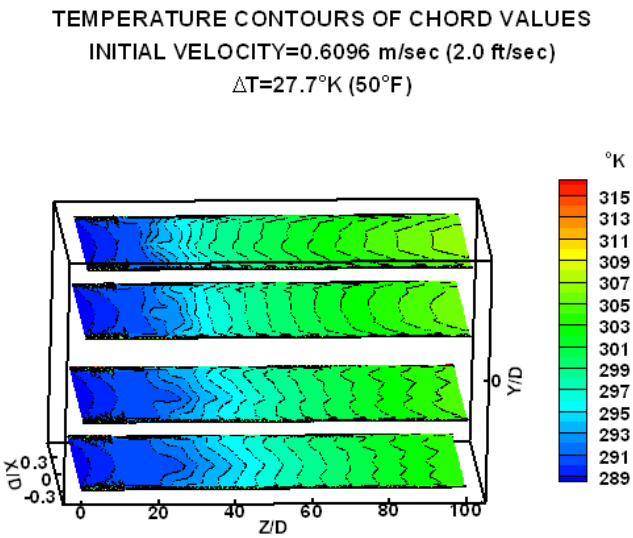

Fig. A-221 Temperature Slice Contours
V_0=0.6096 m/sec, ΔT_{wall}=27.7°K

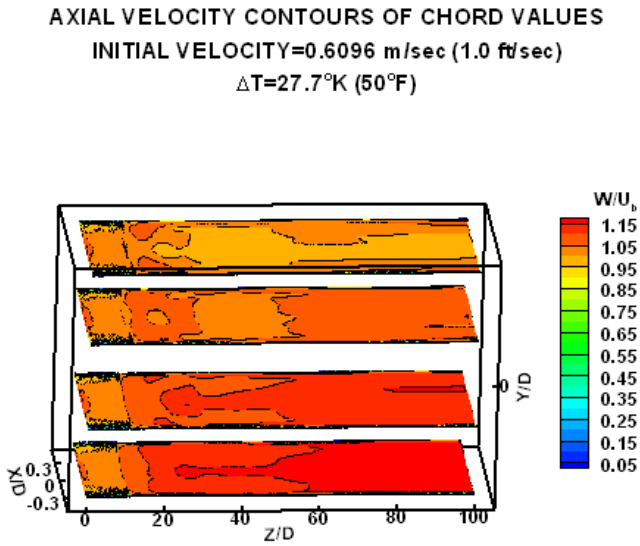

Fig. A-222 Axial Velocity Slice Contours
V_0=0.6096 m/sec, ΔT_{wall}=27.7°K

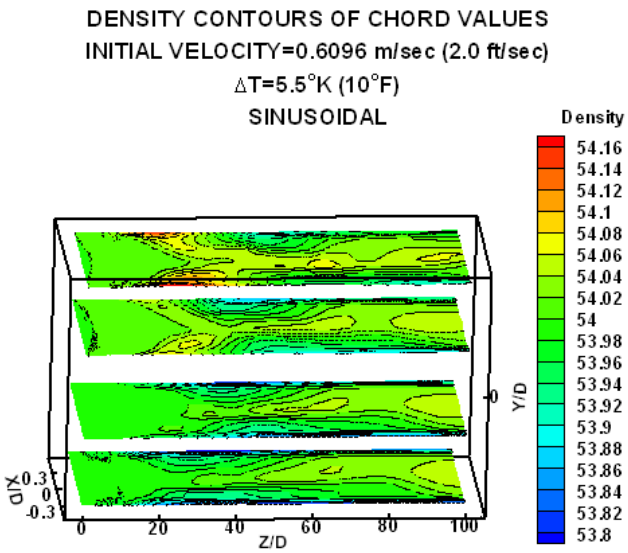

Fig. A-223 Density Slice Contours
V_0=0.6096 m/sec, ΔT_{wall}=-5.5°K Sinusoidal

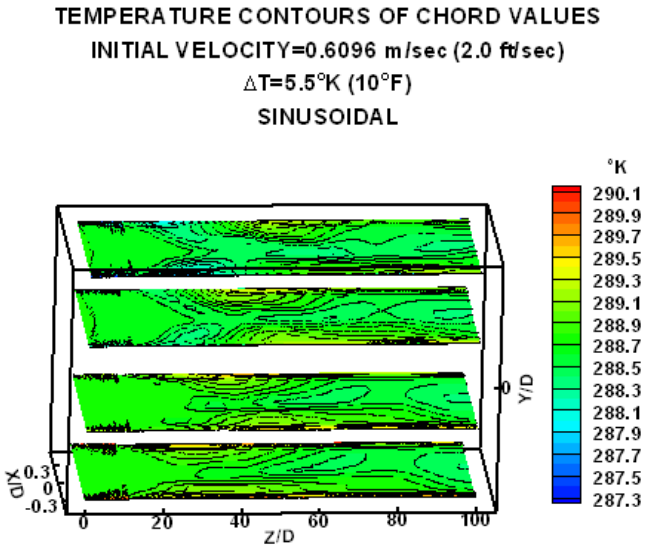

Fig. A-224 Temperature Slice Contours
V_0=0.6096 m/sec, ΔT_{wall}=-5.5°K Sinusoidal

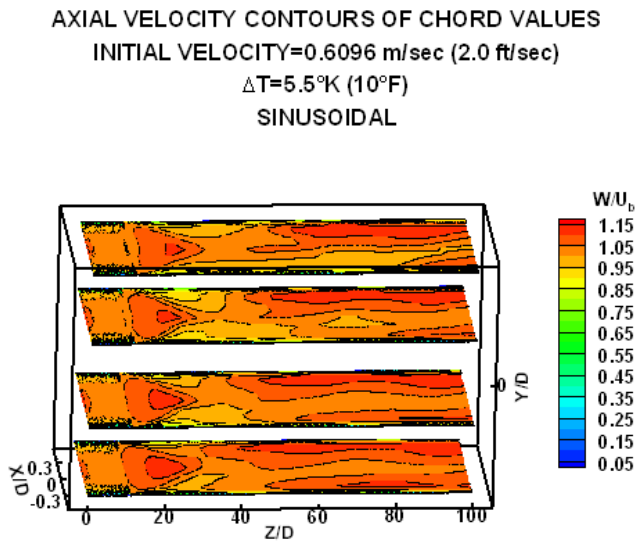

Fig. A-225 Axial Velocity Slice Contours
V_0=0.6096 m/sec, ΔT_{wall}=-5.5°K Sinusoidal

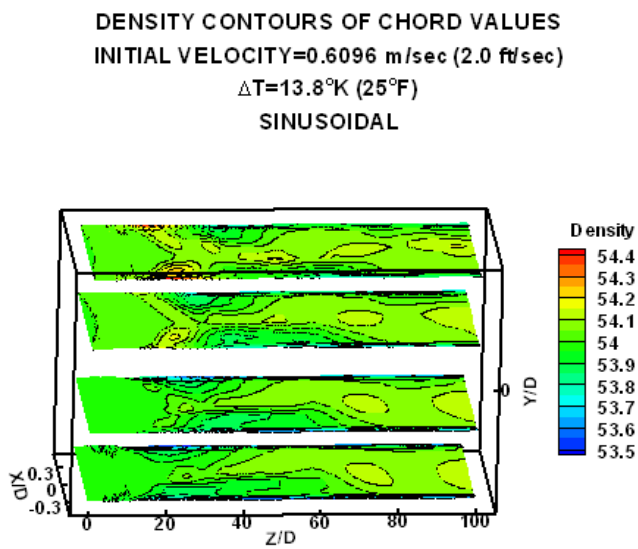

Fig. A-226 Density Slice Contours
V_0=0.6096 m/sec, ΔT_{wall}=-13.8°K Sinusoidal

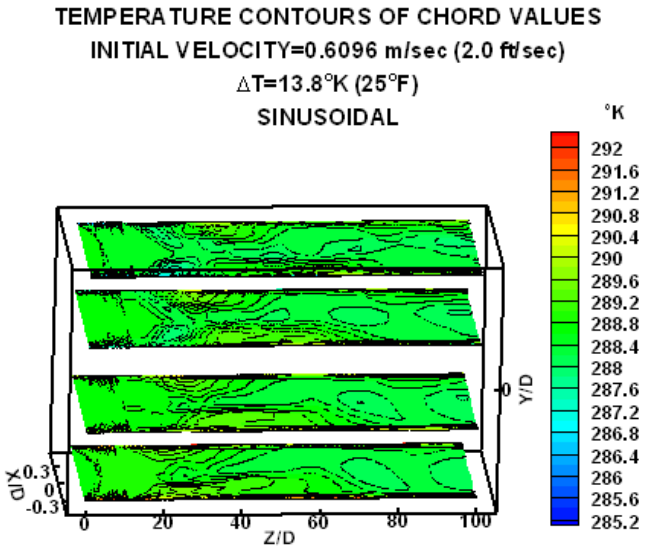

Fig. A-227 Temperature Slice Contours
V_0=0.6096 m/sec, ΔT_{wall}=-13.8°K Sinusoidal

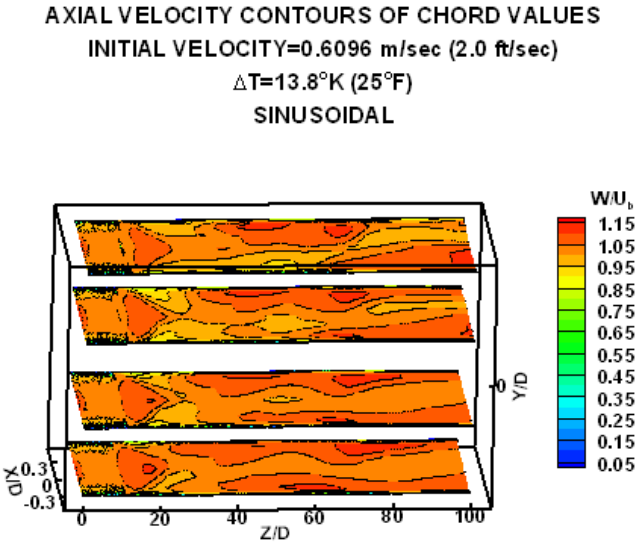

Fig. A-228 Axial Velocity Slice Contours
V_0=0.6096 m/sec, ΔT_{wall}=-13.8°K Sinusoidal

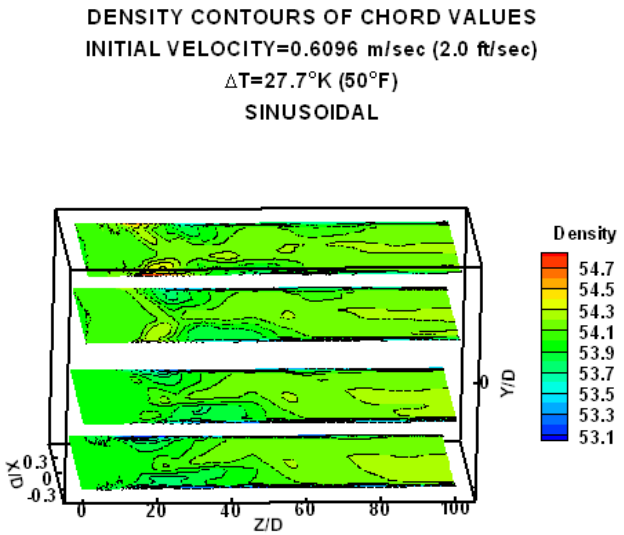

Fig. A-229 Density Slice Contours
V_0=0.6096 m/sec, ΔT_{wall}=-27.7°K Sinusoidal

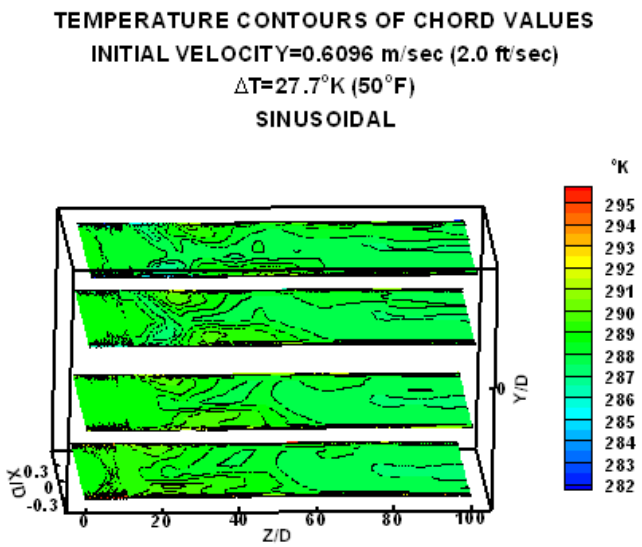

Fig. A-230 Temperature Slice Contours
V_0=0.6096 m/sec, ΔT_{wall}=-27.7°K Sinusoidal

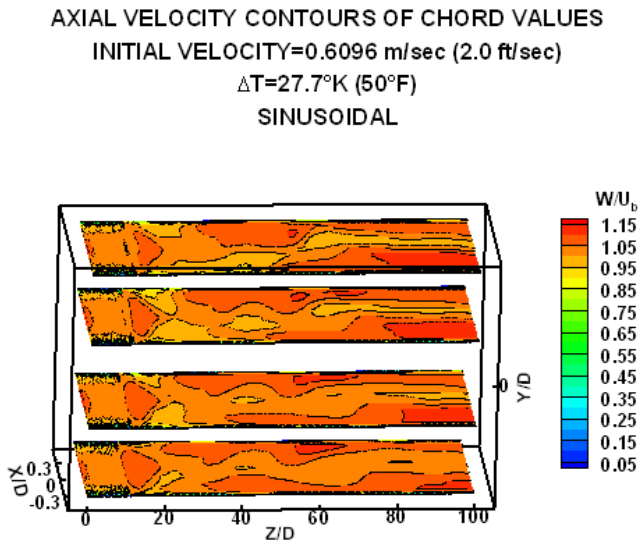

Fig. A-231 Axial Velocity Slice Contours
V_0=0.6096 m/sec, ΔT_{wall}=-27.7°K Sinusoidal

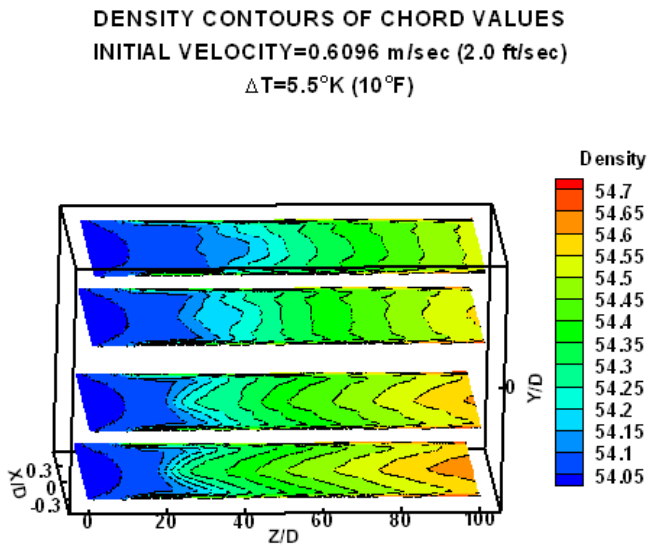

Fig. A-232 Density Slice Contours
V_0=0.6096 m/sec, ΔT_{wall}=-5.5°K

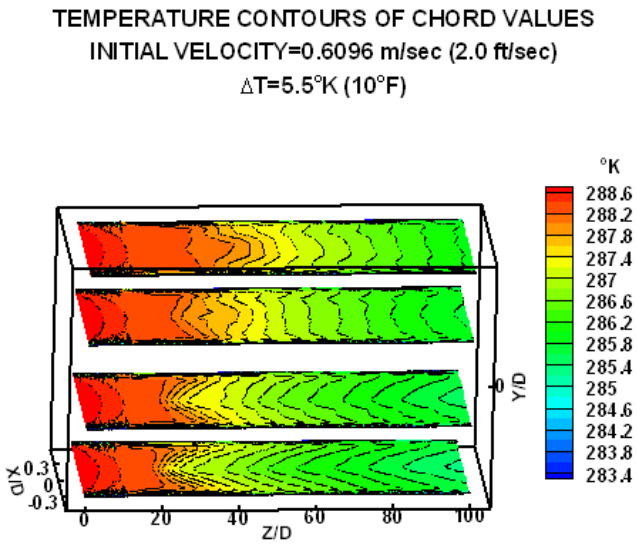

Fig. A-233 Temperature Slice Contours
V_0=0.6096 m/sec, ΔT_{wall}=-5.5°K

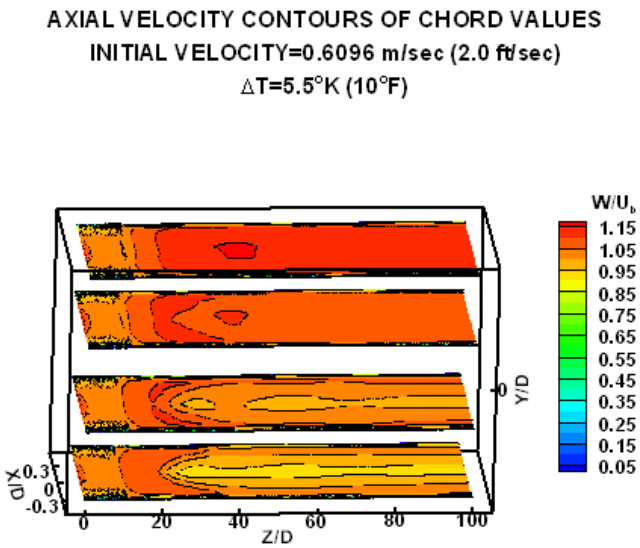

Fig. A-234 Axial Velocity Slice Contours
V_0=0.6096 m/sec, ΔT_{wall}=-5.5°K

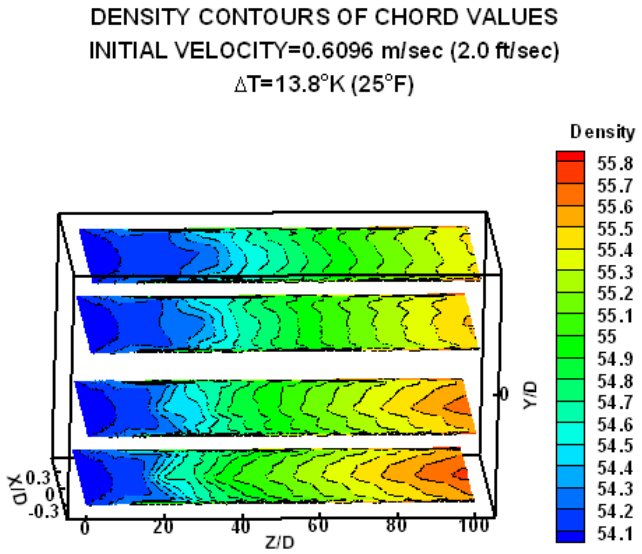

Fig. A-235 Density Slice Contours
V_0=0.6096 m/sec, ΔT_{wall}=-13.8°K

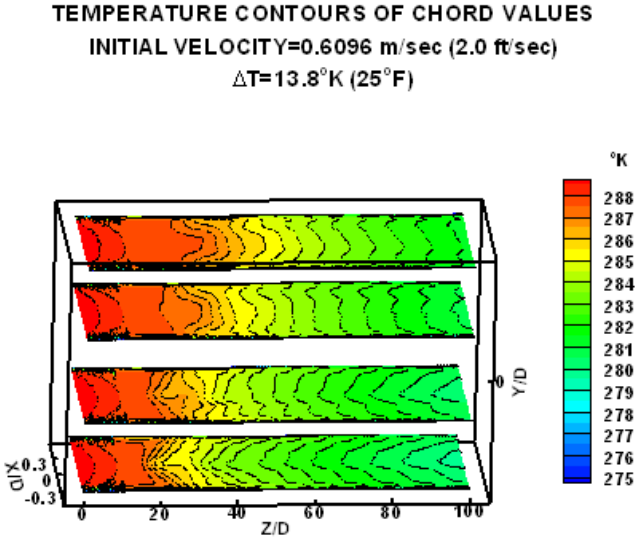

Fig. A-236 Temperature Slice Contours
V_0=0.6096 m/sec, ΔT_{wall}=-13.8°K

AXIAL VELOCITY CONTOURS OF CHORD VALUES
INITIAL VELOCITY=0.6096 m/sec (2.0 ft/sec)
ΔT=13.8°K (25°F)

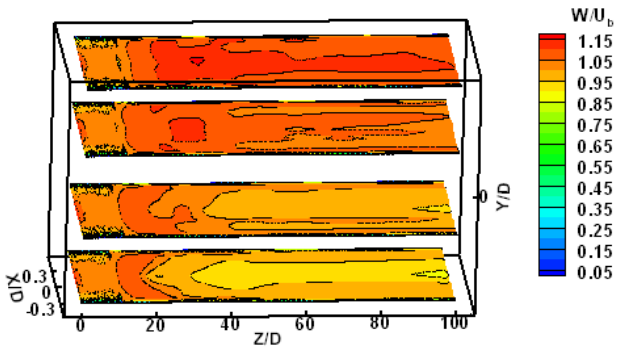

Fig. A-237 Axial Velocity Slice Contours
V_0=0.6096 m/sec, ΔT_{wall}=-13.8°K

DENSITY CONTOURS OF CHORD VALUES
INITIAL VELOCITY=0.6096 m/sec (2.0 ft/sec)
ΔT=27.7°K (50°F)

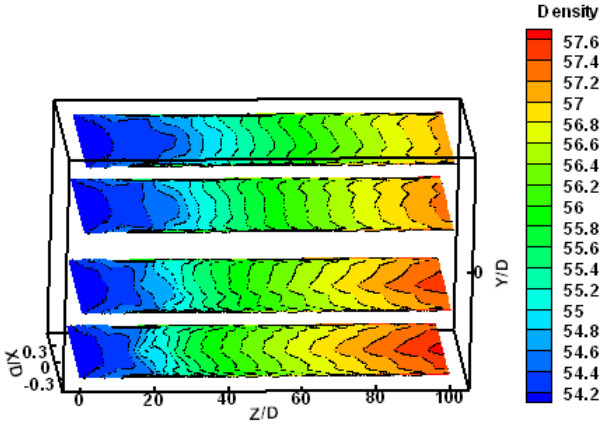

Fig. A-238 Density Slice Contours
V_0=0.6096 m/sec, ΔT_{wall}=-27.7°K

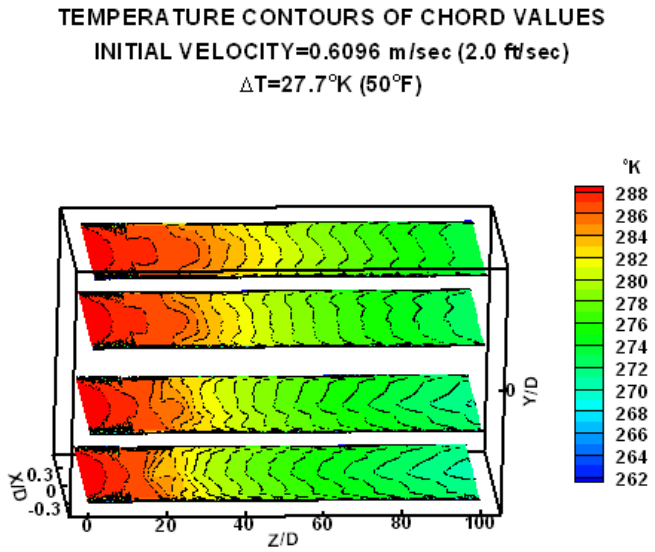

Fig. A-239 Temperature Slice Contours
V_0=0.6096 m/sec, ΔT_{wall}=-27.7°K

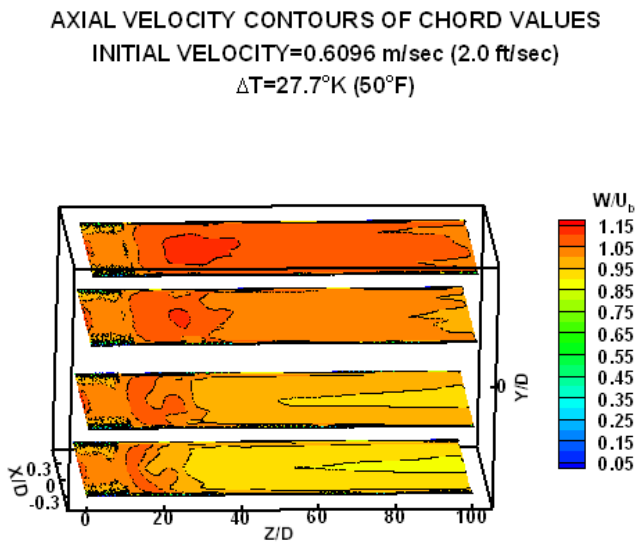

Fig. A-240 Axial Velocity Slice Contours
V_0=0.6096 m/sec, ΔT_{wall}=-27.7°K

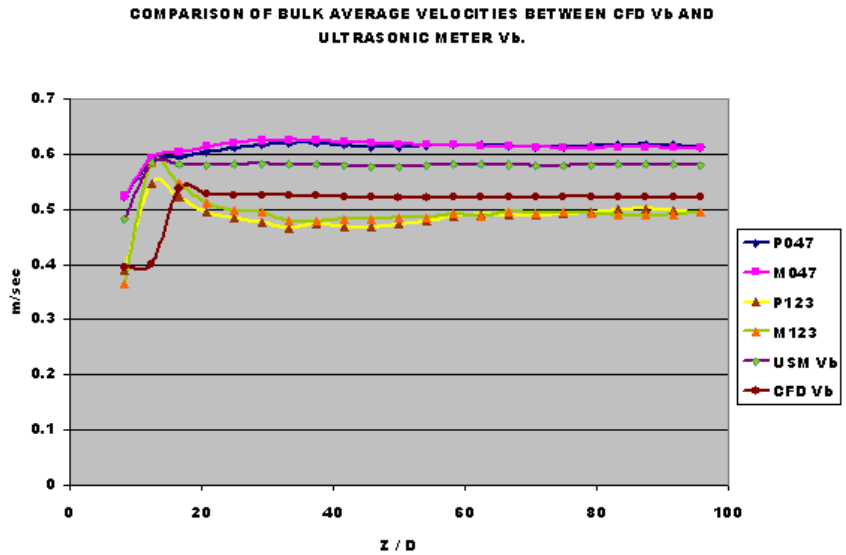

Fig. A-241 Comparison between CFD Vb and Ultrasonic Vb. V_0=0.6096 m/sec, ΔT_{wall}=5.5°K Sinusoidal

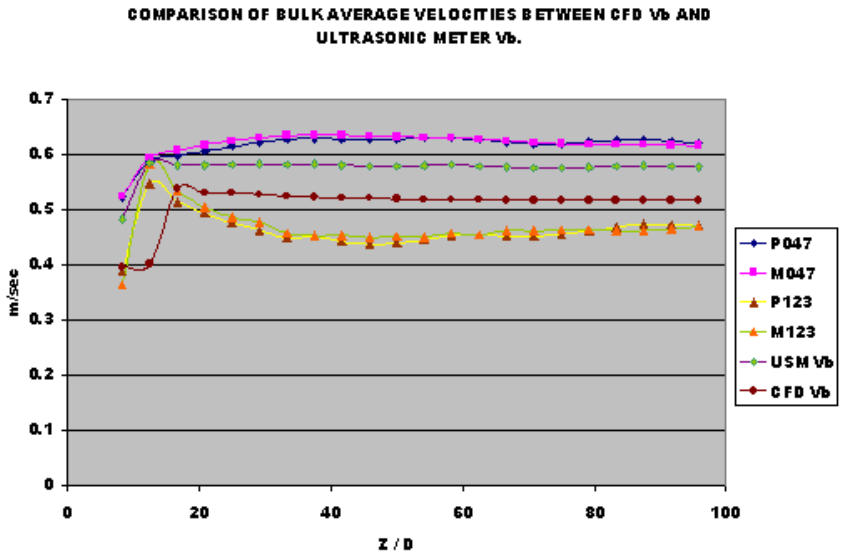

Fig. A-242 Comparison between CFD Vb and Ultrasonic Vb. V_0=0.6096 m/sec, ΔT_{wall}=13.8°K Sinusoidal

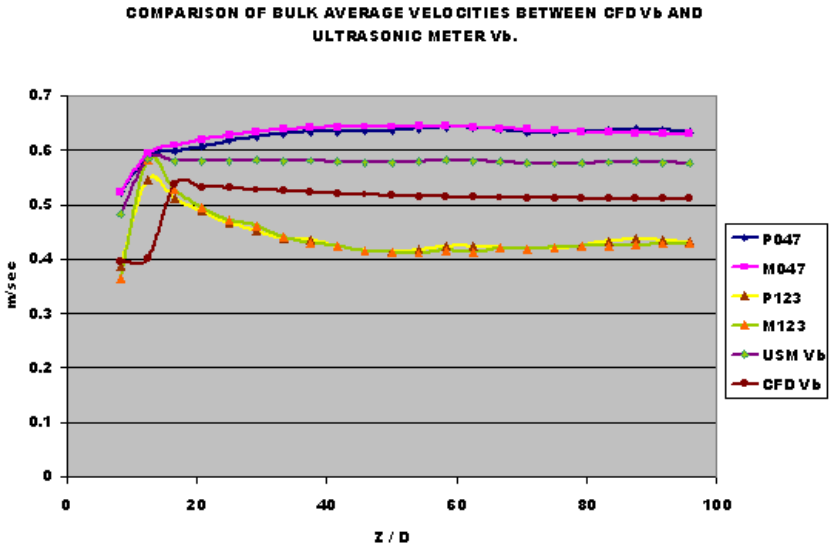

Fig. A-243 Comparison between CFD Vb and Ultrasonic Vb.
V_0=0.6096 m/sec, ΔT_{wall}=27.7°K Sinusoidal

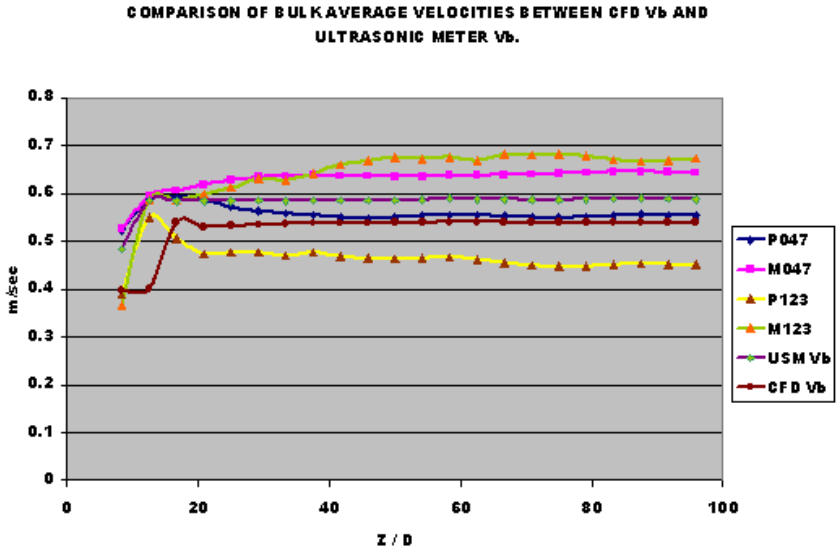

Fig. A-244 Comparison between CFD Vb and Ultrasonic Vb.
V_0=0.6096 m/sec, ΔT_{wall}=5.5°K

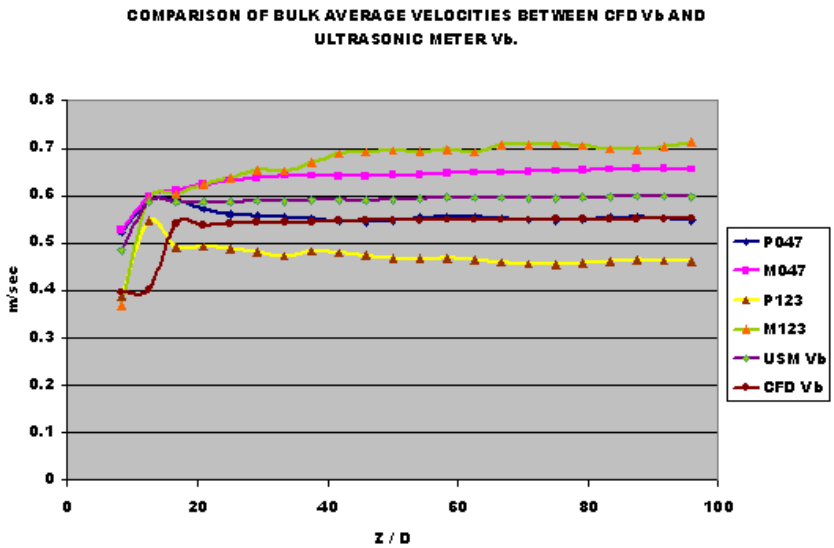

Fig. A-245 Comparison between CFD Vb and Ultrasonic Vb.
V_0=0.6096 m/sec, ΔT_{wall}=13.8^{o}K

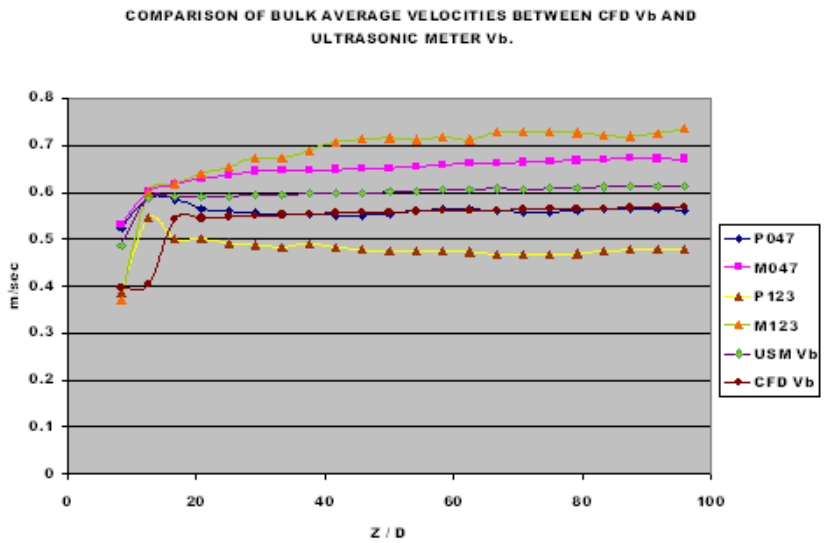

Fig. A-246 Comparison between CFD Vb and Ultrasonic Vb.
V_0=0.6096 m/sec, ΔT_{wall}=27.7^{o}K

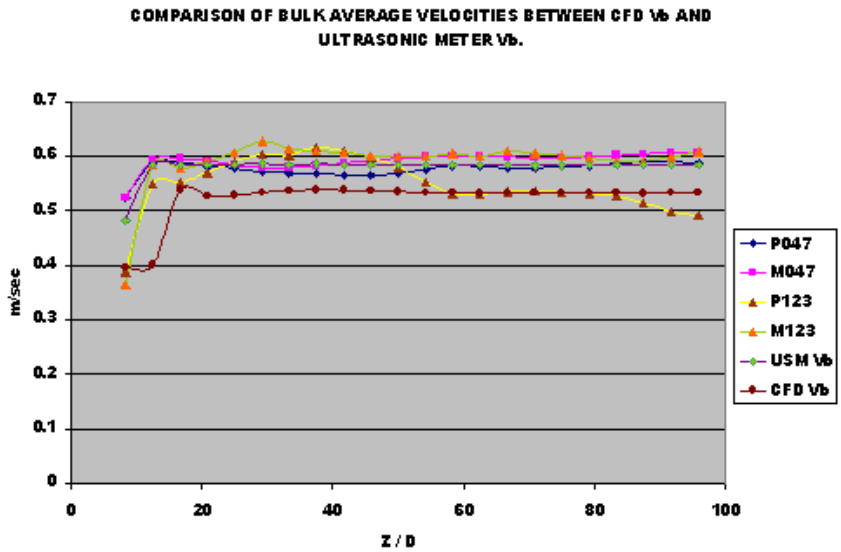

Fig. A-247 Comparison between CFD Vb and Ultrasonic Vb.
V_0=0.6096 m/sec, ΔT_{wall}=-5.5°K Sinusoidal

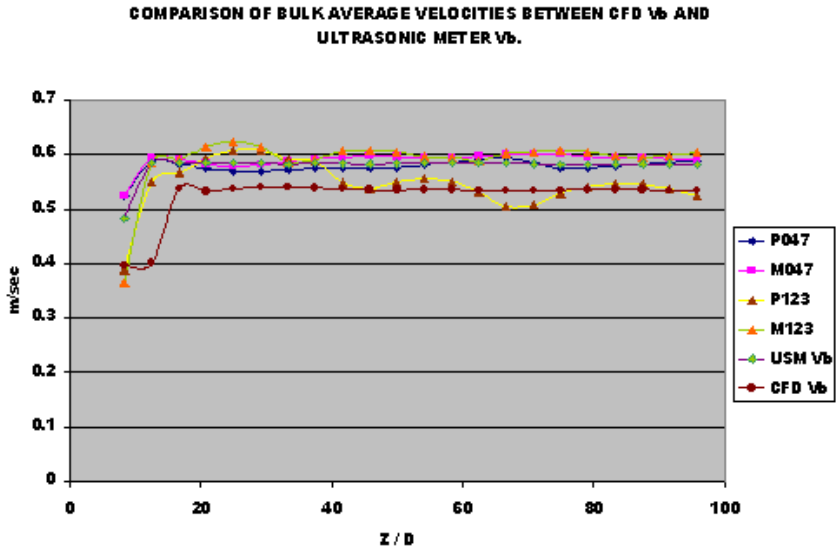

Fig. A-248 Comparison between CFD Vb and Ultrasonic Vb.
V_0=0.6096 m/sec, ΔT_{wall}=-13.8°K Sinusoidal

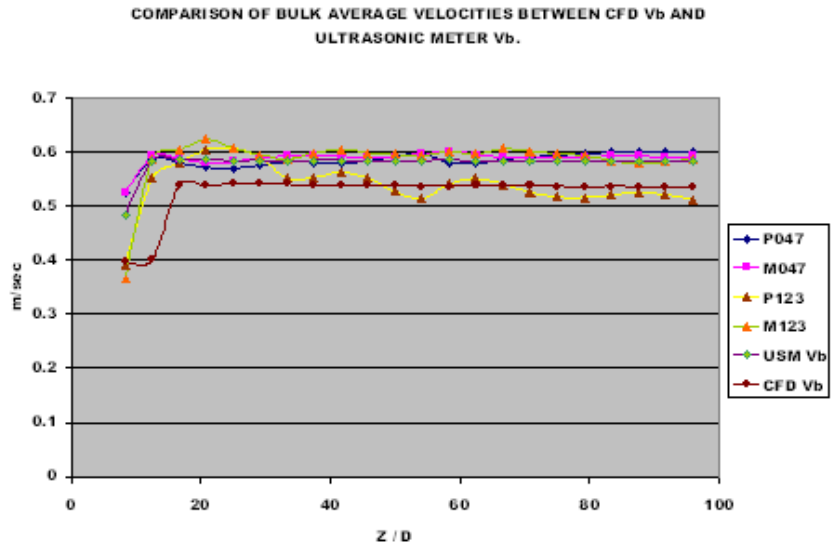

Fig. A-249 Comparison between CFD Vb and Ultrasonic Vb.
V_0=0.6096 m/sec, ΔT_{wall}=-27.7°K Sinusoidal

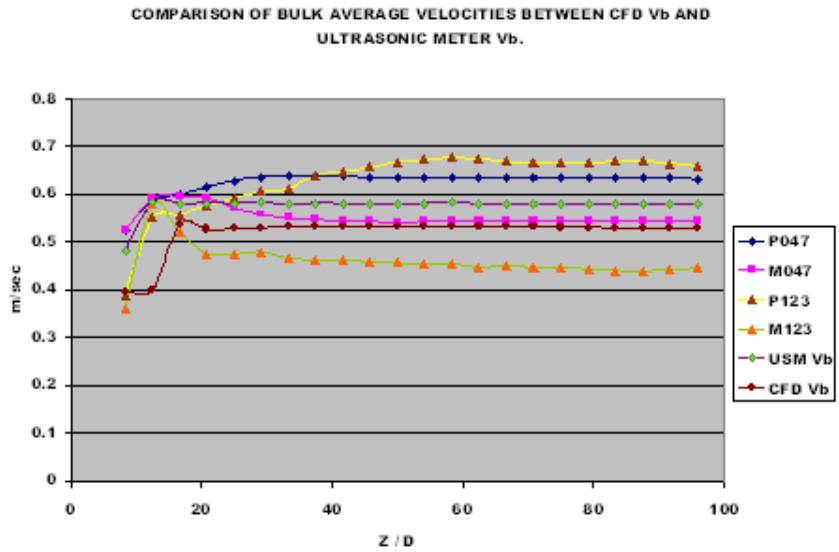

Fig. A-250 Comparison between CFD Vb and Ultrasonic Vb.
V_0=0.6096 m/sec, ΔT_{wall}=-5.5°K

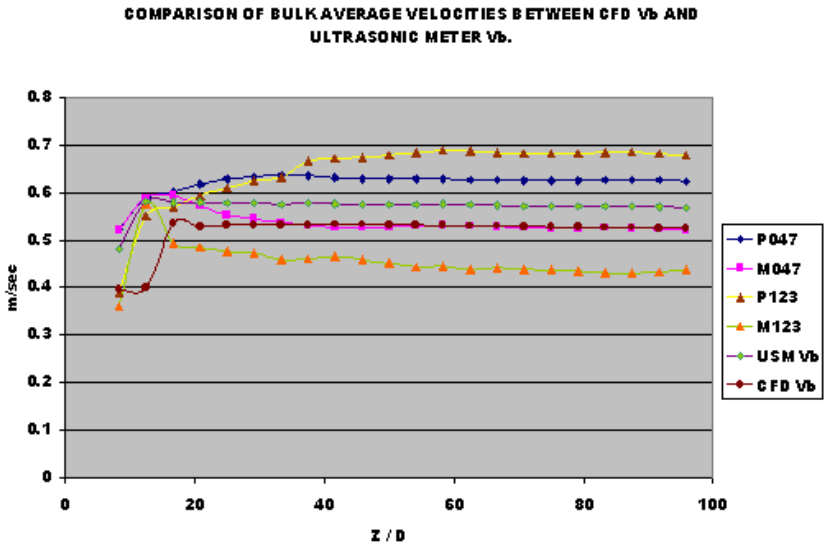

Fig. A-251 Comparison between CFD Vb and Ultrasonic Vb.
V_0=0.6096 m/sec, ΔT_{wall}=-13.8°K

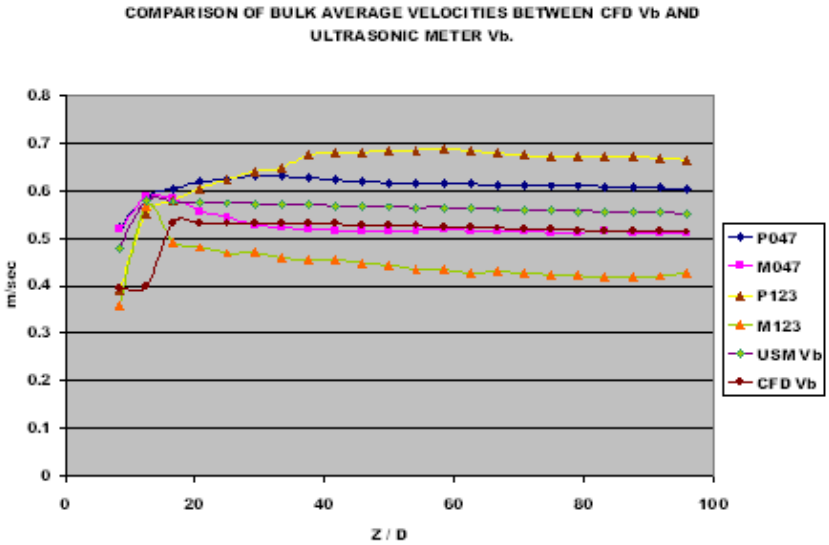

Fig. A-252 Comparison between CFD Vb and Ultrasonic Vb.
V_0=0.6096 m/sec, ΔT_{wall}=-27.7°K

APPENDIX B

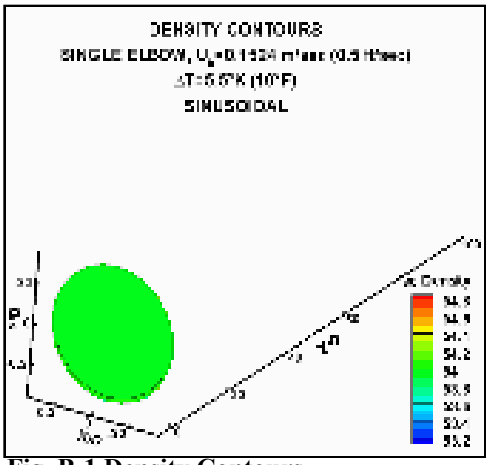

Fig. B-1 Density Contours
V_0=0.1524 m/sec, ΔT_{wall}=5.5°K Sinusoidal

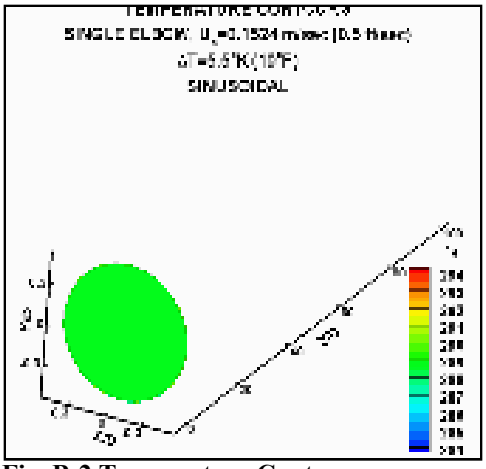

Fig. B-2 Temperature Contours
V_0=0.1524 m/sec, ΔT_{wall}=5.5°K Sinusoidal

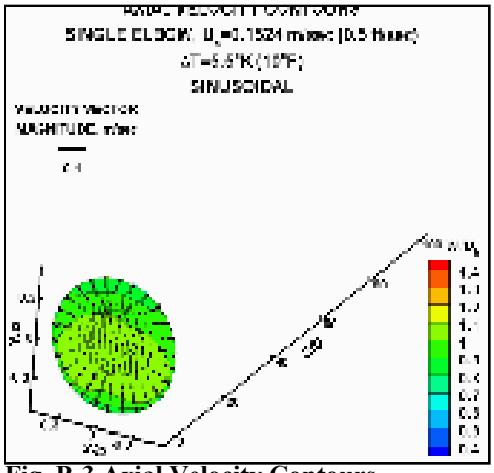

Fig. B-3 Axial Velocity Contours
V_0=0.1524 m/sec, ΔT_{wall}=5.5°K Sinusoidal

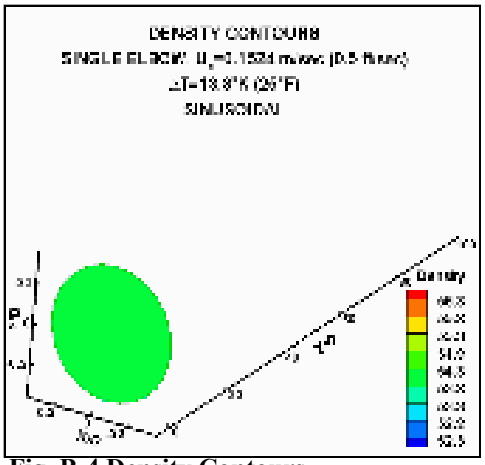

Fig. B-4 Density Contours
V_0=0.1524 m/sec, ΔT_{wall}=13.8°K Sinusoidal

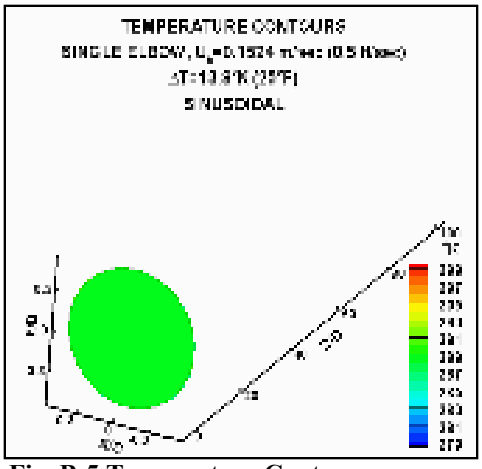

Fig. B-5 Temperature Contours
V_0=0.1524 m/sec, ΔT_{wall}=13.8°K Sinusoidal

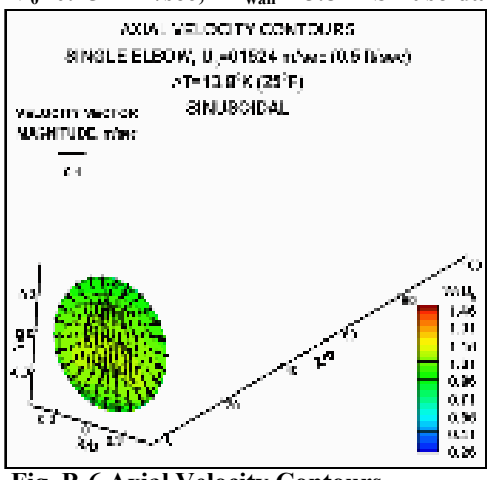

Fig. B-6 Axial Velocity Contours
V_0=0.1524 m/sec, ΔT_{wall}=13.8°K Sinusoidal

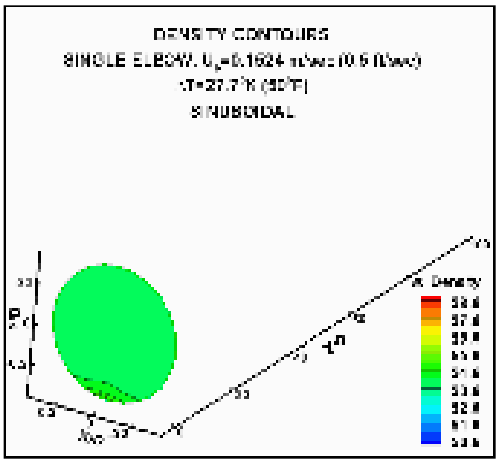

Fig. B-7 Density Contours
V_0=0.1524 m/sec, ΔT_{wall}=27.7°K Sinusoidal

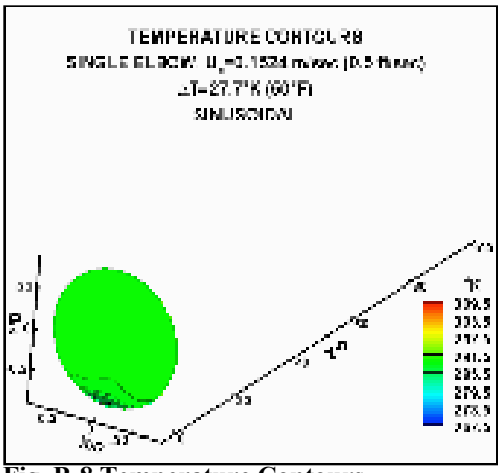

Fig. B-8 Temperature Contours
V_0=0.1524 m/sec, ΔT_{wall}=27.7°K Sinusoidal

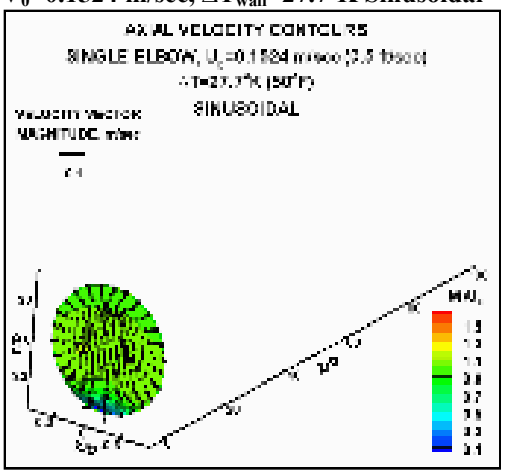

Fig. B-9 Axial Velocity Contours
V_0=0.1524 m/sec, ΔT_{wall}=27.7°K Sinusoidal

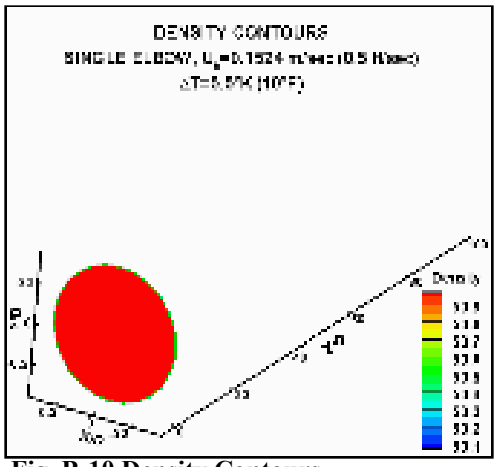

Fig. B-10 Density Contours
V_0=0.1524 m/sec, ΔT_{wall}=5.5°K

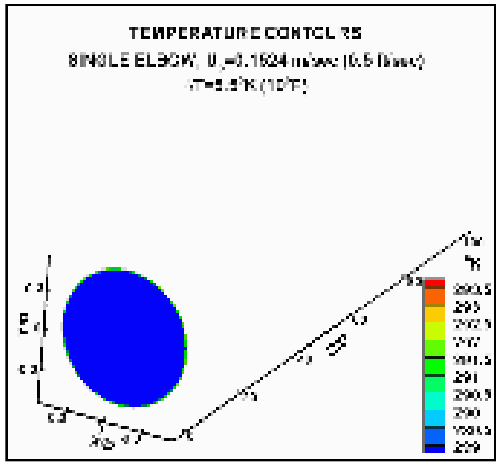

Fig. B-11 Temperature Contours
V_0=0.1524 m/sec, ΔT_{wall}=5.5°K

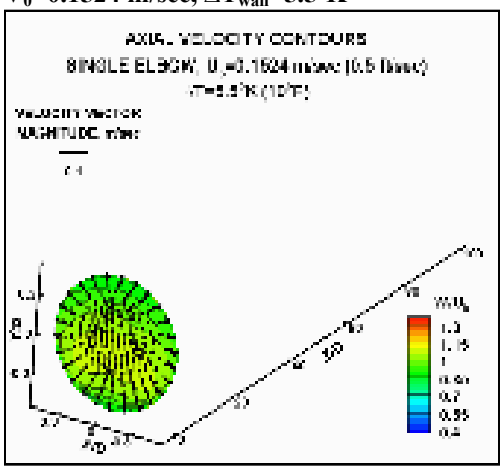

Fig. B-12 Axial Velocity Contours
V_0=0.1524 m/sec, ΔT_{wall}=5.5°K

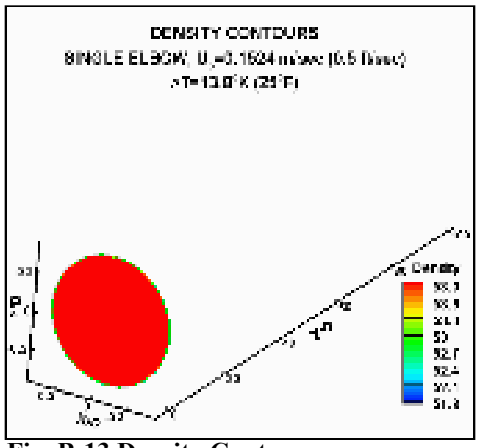

Fig. B-13 Density Contours
V_0=0.1524 m/sec, ΔT_{wall}=13.8°K

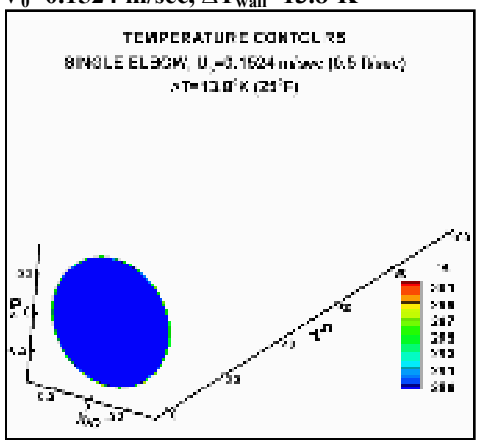

Fig. B-14 Temperature Contours
V_0=0.1524 m/sec, ΔT_{wall}=13.8°K

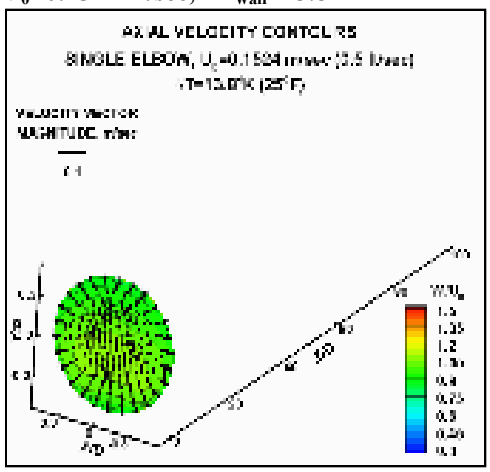

Fig. B-15 Axial Velocity Contours
V_0=0.1524 m/sec, ΔT_{wall}=13.8°K

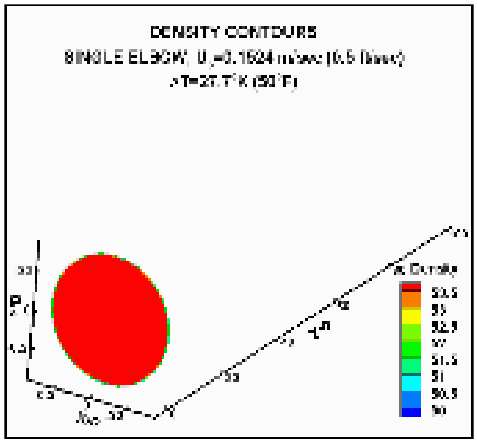

Fig. B-16 Density Contours
V_0=0.1524 m/sec, ΔT_{wall}=27.7°K

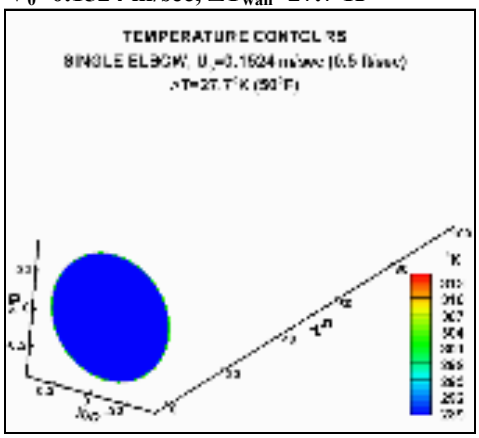

Fig. B-17 Temperature Contours
V_0=0.1524 m/sec, ΔT_{wall}=27.7°K

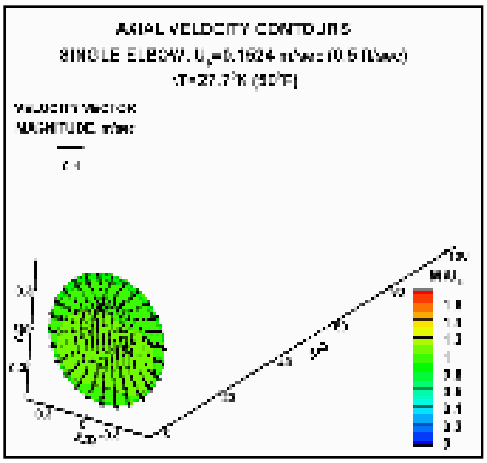

Fig. B-18 Axial Velocity Contours
V_0=0.1524 m/sec, ΔT_{wall}=27.7°K

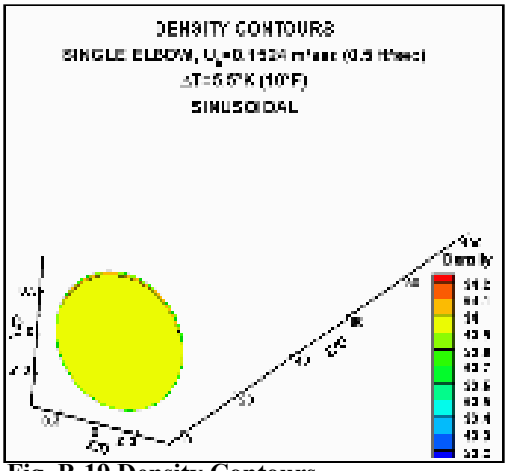

Fig. B-19 Density Contours
V_0=0.1524 m/sec, ΔT_{wall}=-5.5°K Sinusoidal

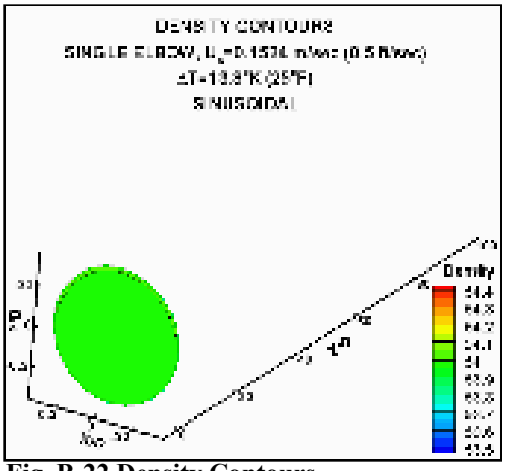

Fig. B-22 Density Contours
V_0=0.1524 m/sec, ΔT_{wall}=-13.8°K Sinusoidal

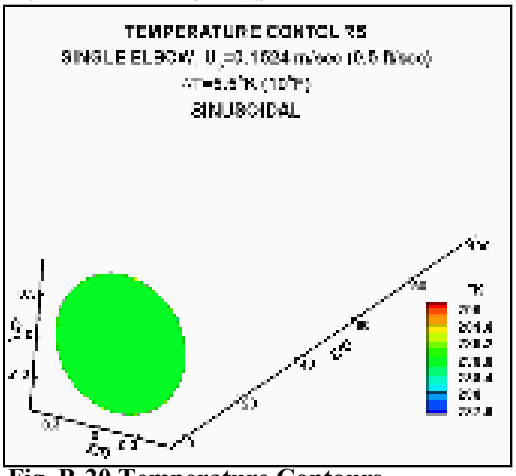

Fig. B-20 Temperature Contours
V_0=0.1524 m/sec, ΔT_{wall}=-5.5°K Sinusoidal

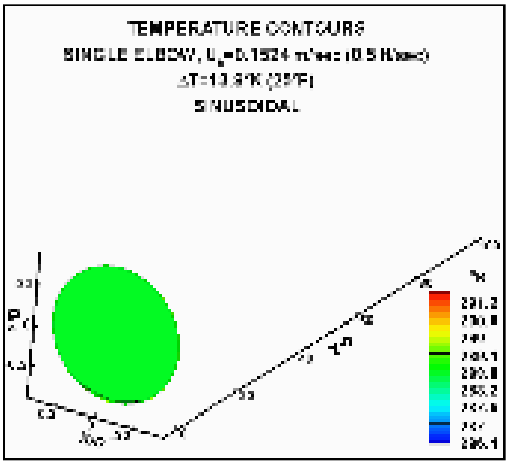

Fig. B-23 Temperature Contours
V_0=0.1524 m/sec, ΔT_{wall}=-13.8°K Sinusoidal

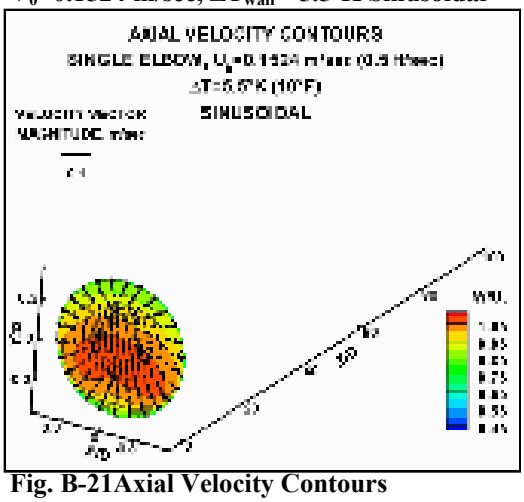

Fig. B-21Axial Velocity Contours
V_0=0.1524 m/sec, ΔT_{wall}=-5.5°K Sinusoidal

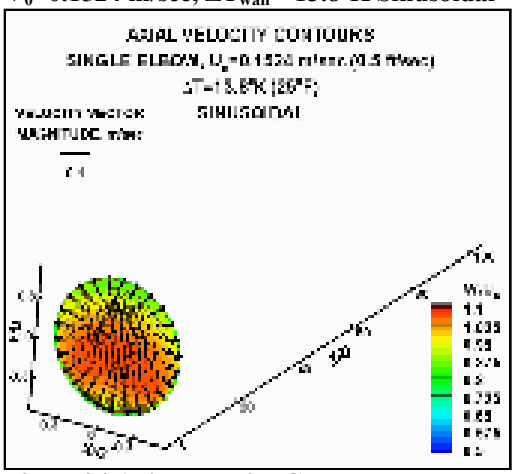

Fig. B-24 Axial Velocity Contours
V_0=0.1524 m/sec, ΔT_{wall}=-13.8°K Sinusoidal

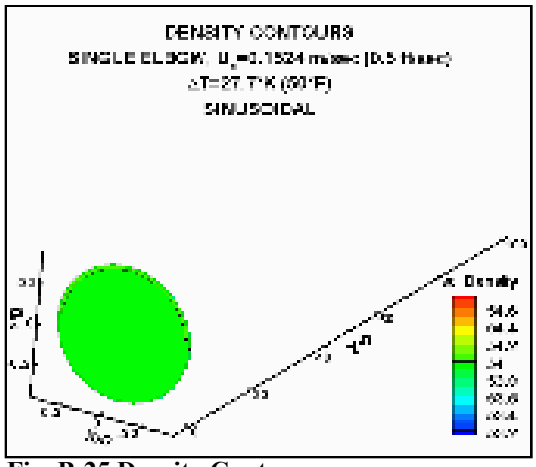

Fig. B-25 Density Contours
V_0=0.1524 m/sec, ΔT_{wall}=-27.7°K Sinusoidal

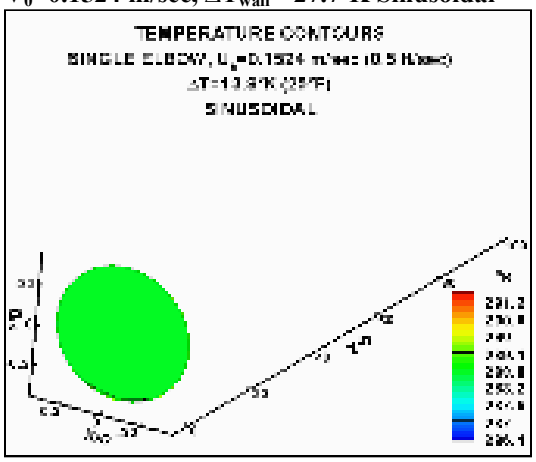

Fig. B-26 Temperature Contours
V_0=0.1524 m/sec, ΔT_{wall}=-27.7°K Sinusoidal

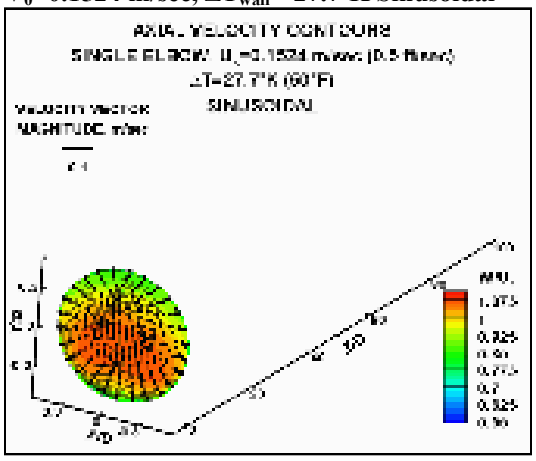

Fig. B-27 Axial Velocity Contours
V_0=0.1524 m/sec, ΔT_{wall}=-27.7°K Sinusoidal

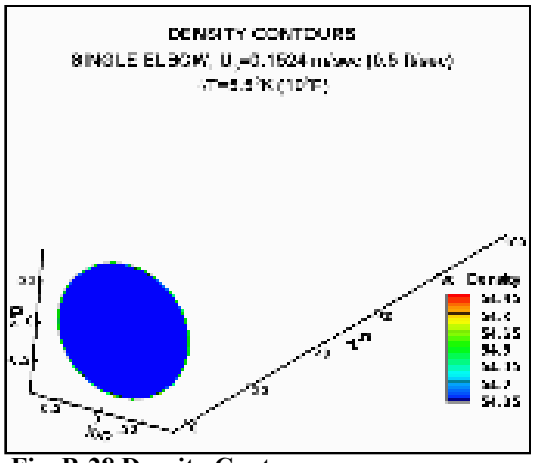

Fig. B-28 Density Contours
V_0=0.1524 m/sec, ΔT_{wall}=-5.5°K

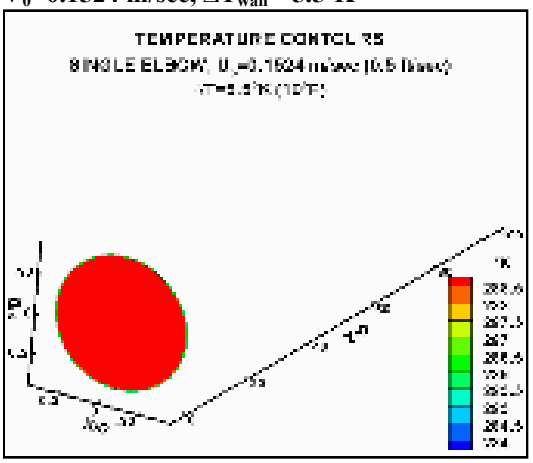

Fig. B-29 Temperature Contours
V_0=0.1524 m/sec, ΔT_{wall}=-5.5°K

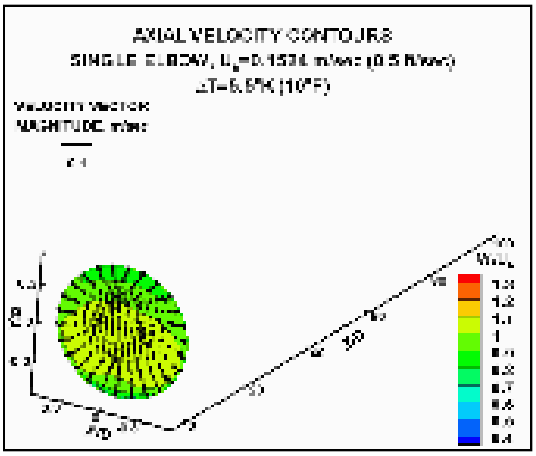

Fig. B-30 Axial Velocity Contours
V_0=0.1524 m/sec, ΔT_{wall}=-5.5°K

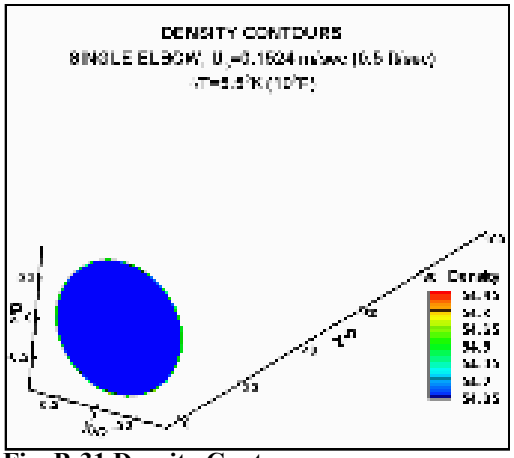

Fig. B-31 Density Contours
V_0=0.1524 m/sec, ΔT_{wall}=-13.8°K

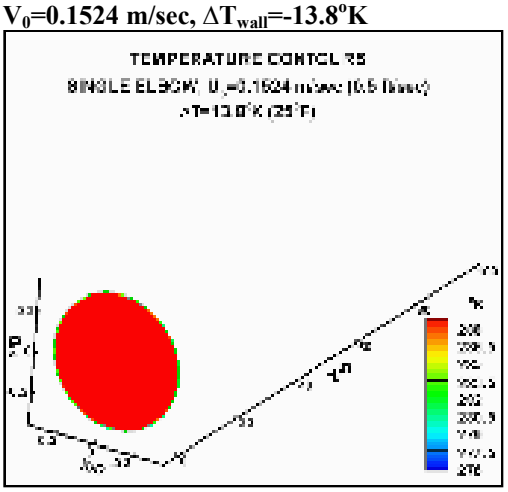

Fig. B-32 Temperature Contours
V_0=0.1524 m/sec, ΔT_{wall}=-13.8°K

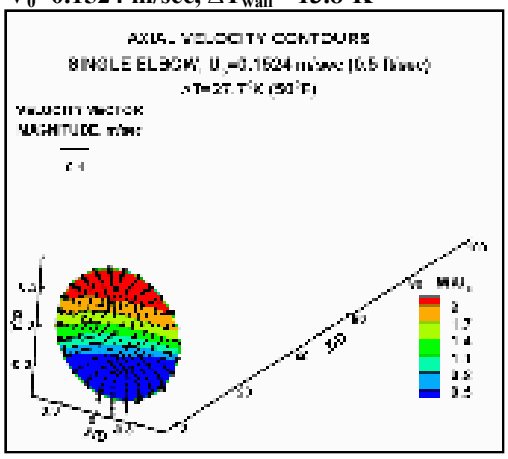

Fig. B-33 Axial Velocity Contours
V_0=0.1524 m/sec, ΔT_{wall}=-13.8°K

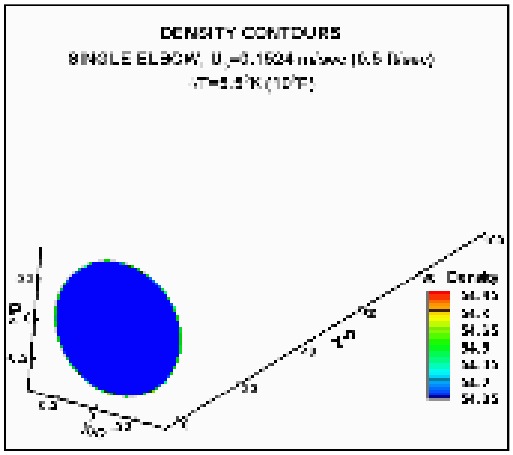

Fig. B-34 Density Contours
V_0=0.1524 m/sec, ΔT_{wall}=-27.7°K

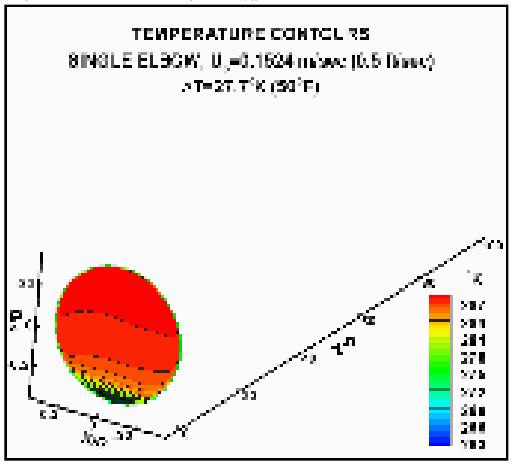

Fig. B-35 Temperature Contours
V_0=0.1524 m/sec, ΔT_{wall}=-27.7°K

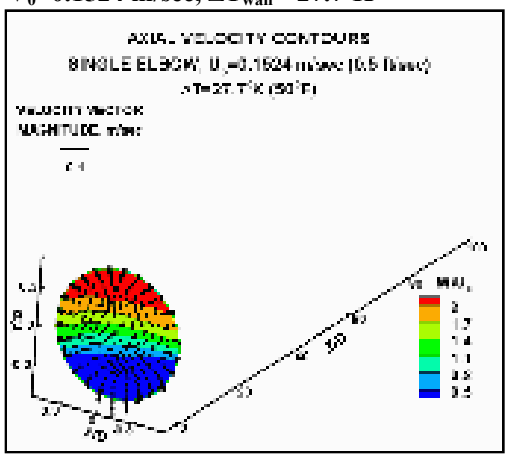

Fig. B-36 Axial Velocity Contours
V_0=0.1524 m/sec, ΔT_{wall}=-27.7°K

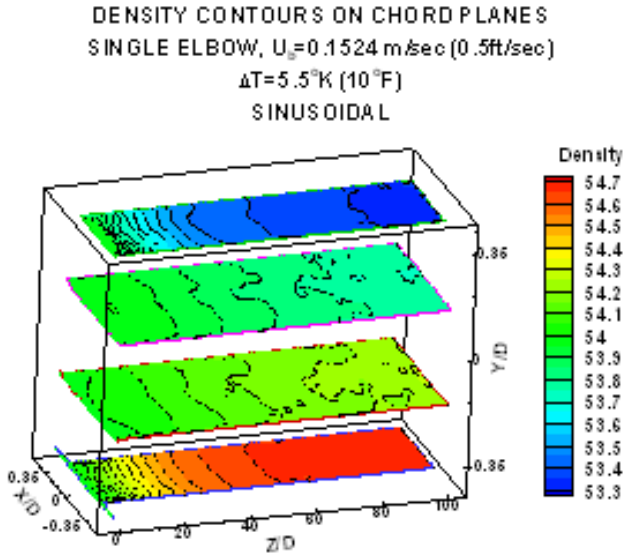

Fig. B-37 Density Slice Contours
V_0=0.1524 m/sec, ΔT_{wall}=5.5°K Sinusoidal

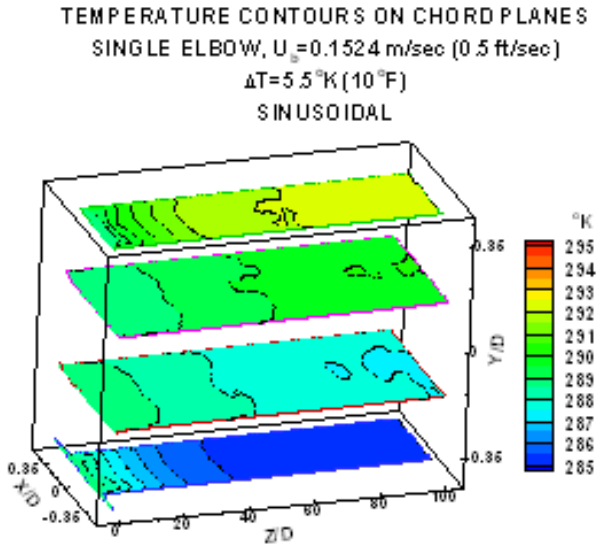

Fig. B-38 Temperature Slice Contours
V_0=0.1524 m/sec, ΔT_{wall}=5.5°K Sinusoidal

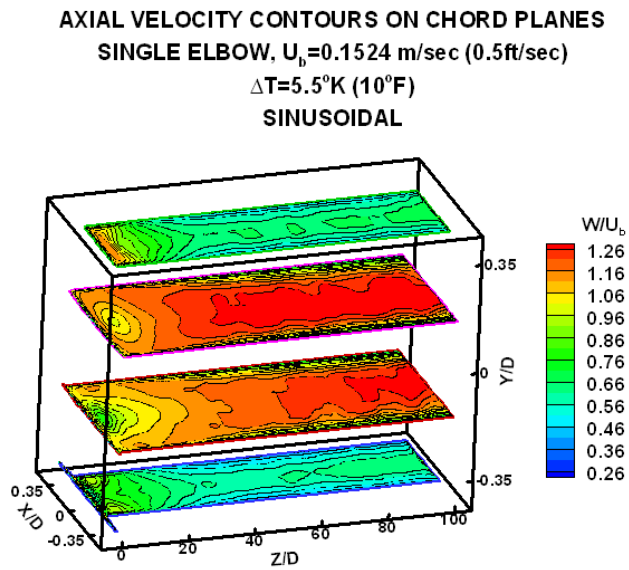

Fig. B-39 Axial Velocity Slice Contours
V_0=0.1524 m/sec, ΔT_{wall}=5.5°K Sinusoidal

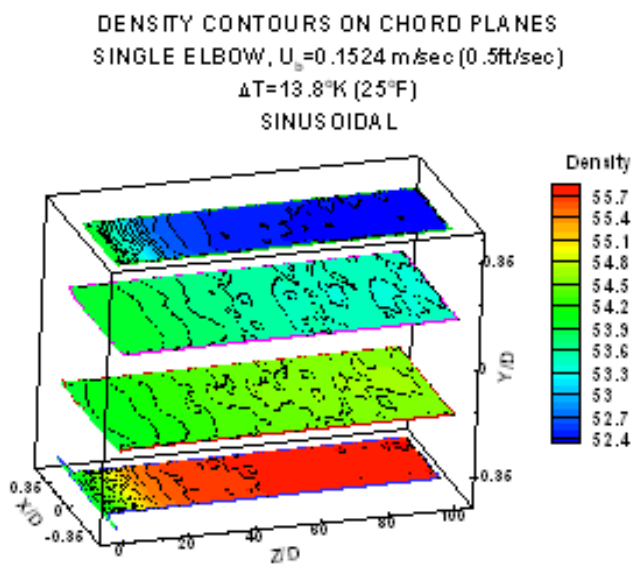

Fig. B-40 Density Slice Contours
V_0=0.1524 m/sec, ΔT_{wall}=13.8°K Sinusoidal

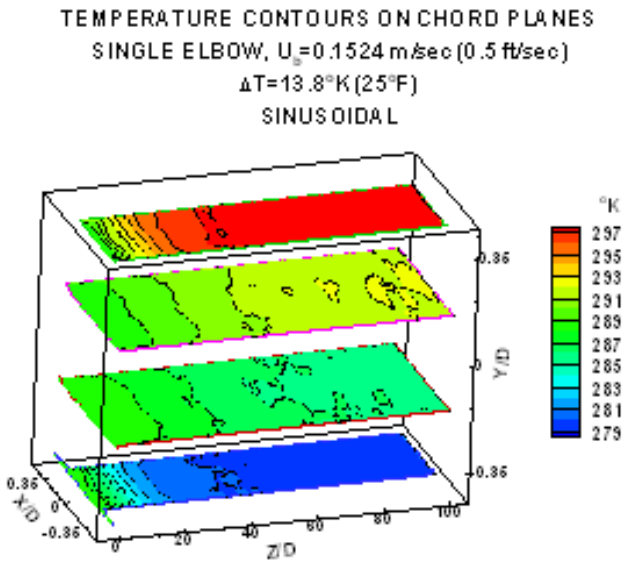

Fig. B-41 Temperature Slice Contours
V_0=0.1524 m/sec, ΔT_{wall}=13.8°K Sinusoidal

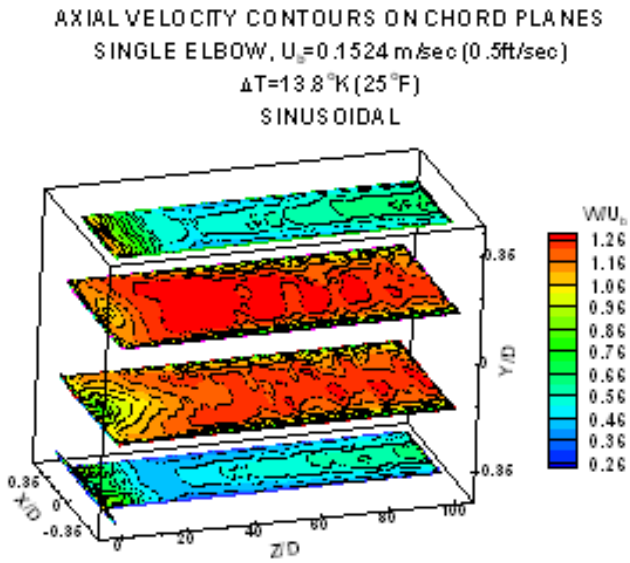

Fig. B-42 Axial Velocity Slice Contours
V_0=0.1524 m/sec, ΔT_{wall}=13.8°K Sinusoidal

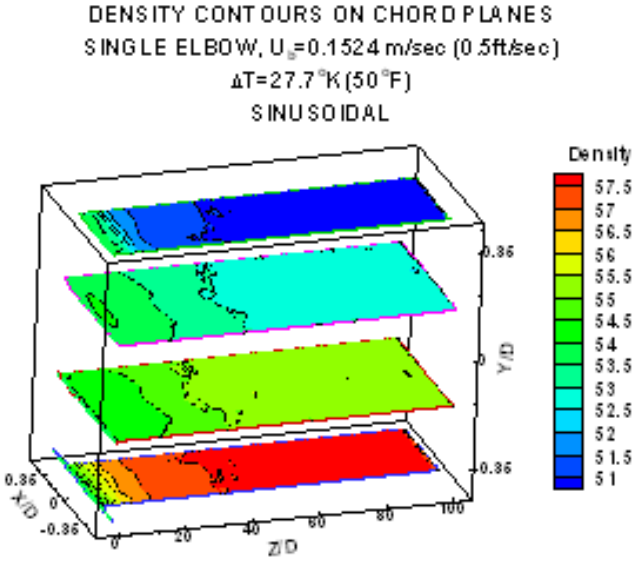

Fig. B-43 Density Slice Contours
V_0=0.1524 m/sec, ΔT_{wall}=27.7°K Sinusoidal

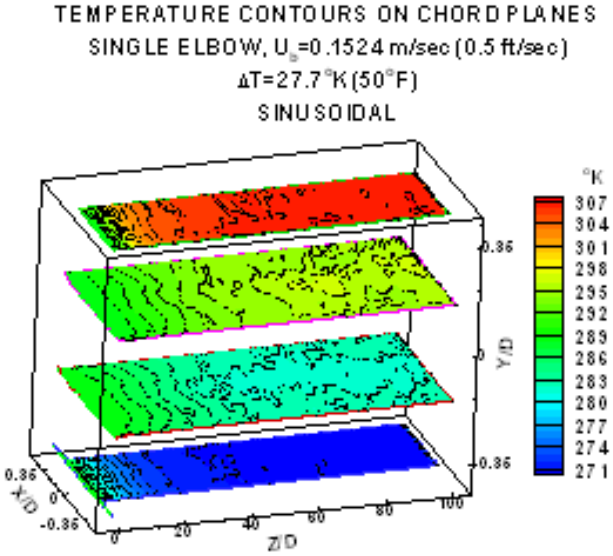

Fig. B-44 Temperature Slice Contours
V_0=0.1524 m/sec, ΔT_{wall}=27.7°K Sinusoidal

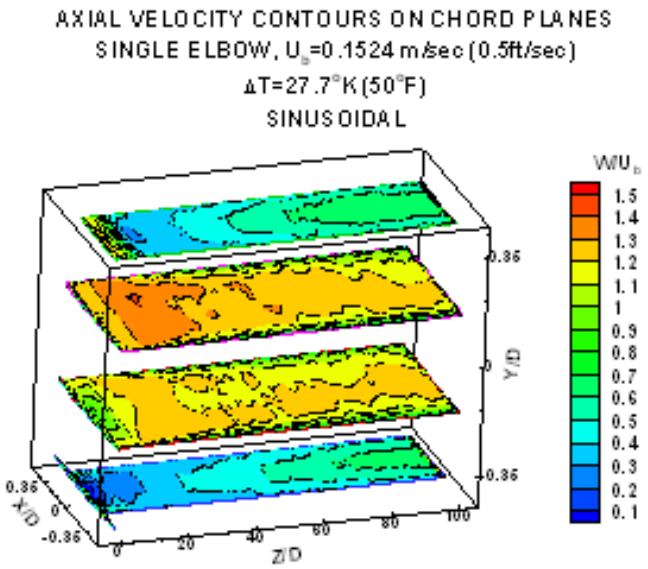

Fig. B-45 Axial Velocity Slice Contours
V_0=0.1524 m/sec, ΔT_{wall}=27.7°K Sinusoidal

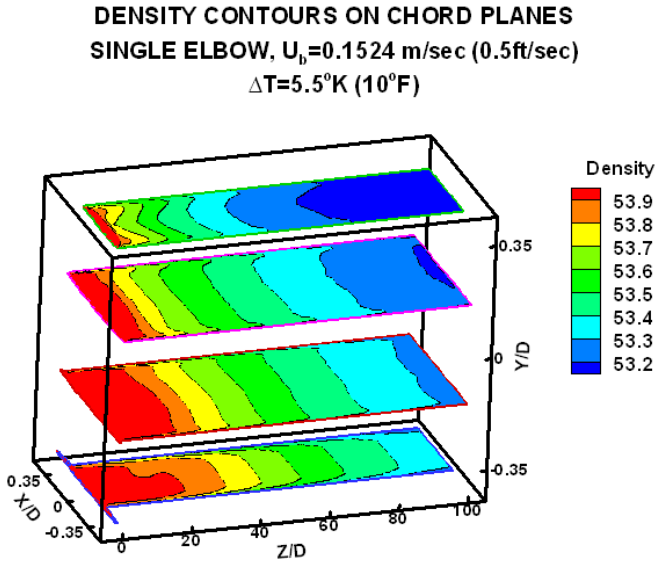

Fig. B-46 Density Slice Contours
V_0=0.1524 m/sec, ΔT_{wall}=5.5°K

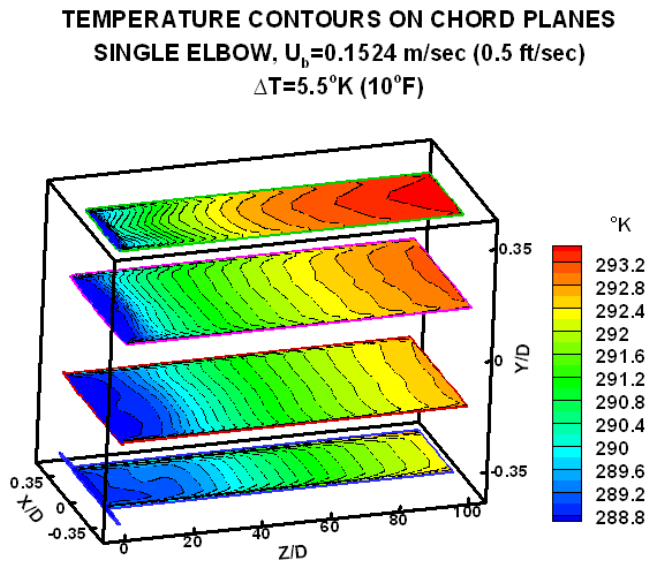

Fig. B-47 Temperature Slice Contours
V_0=0.1524 m/sec, ΔT_{wall}=5.5°K

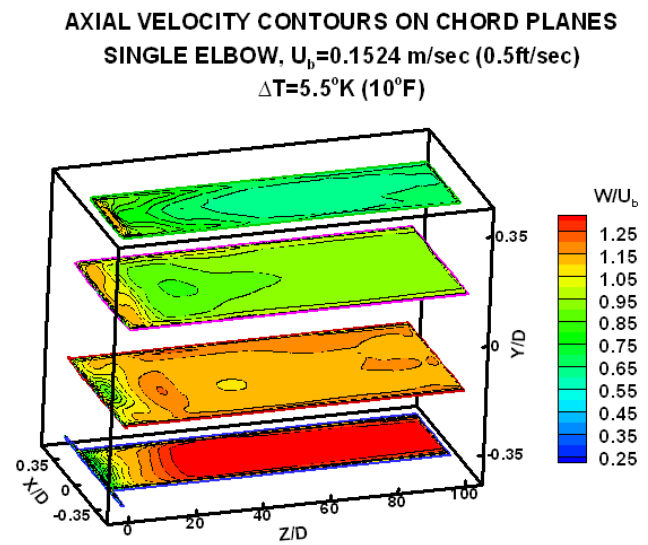

Fig. B-48 Axial Velocity Slice Contours
V_0=0.1524 m/sec, ΔT_{wall}=5.5°K

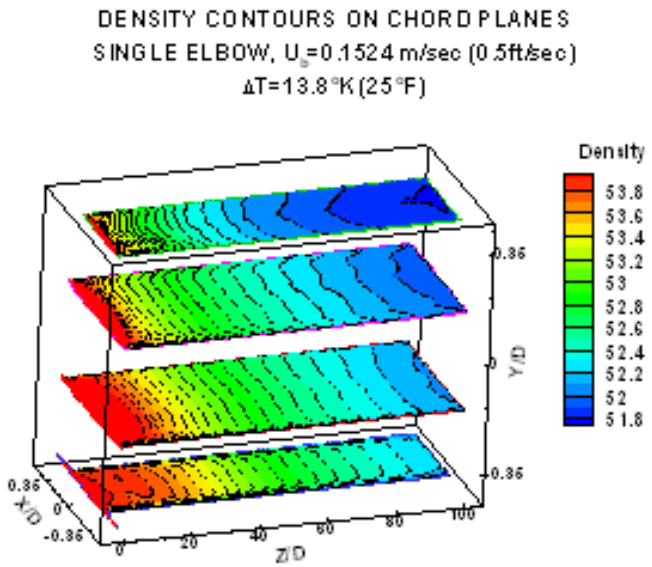

Fig. B-49 Density Slice Contours
V_0=0.1524 m/sec, ΔT_{wall}=13.8°K

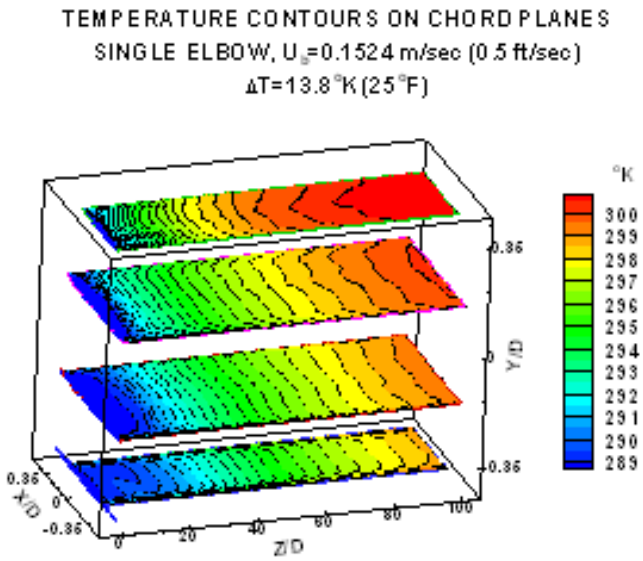

Fig. B-50 Temperature Slice Contours
V_0=0.1524 m/sec, ΔT_{wall}=13.8°K

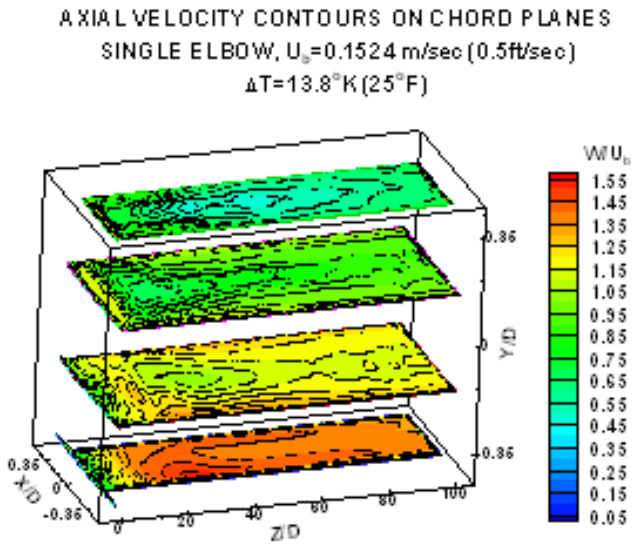

Fig. B-51 Axial Velocity Slice Contours
V_0=0.1524 m/sec, ΔT_{wall}=13.8°K

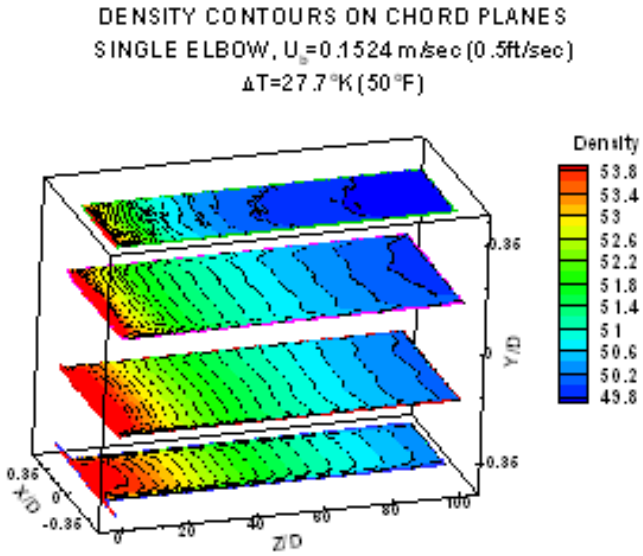

Fig. B-52 Density Slice Contours
V_0=0.1524 m/sec, ΔT_{wall}=27.7°K

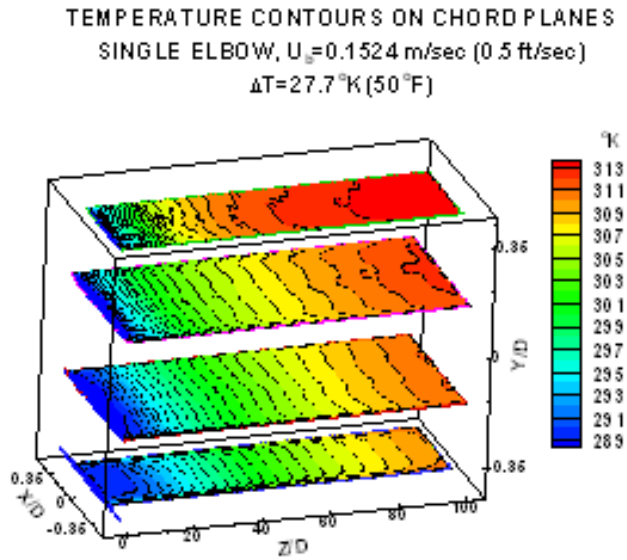

Fig. B-53 Temperature Slice Contours
V_0=0.1524 m/sec, ΔT_{wall}=27.7°K

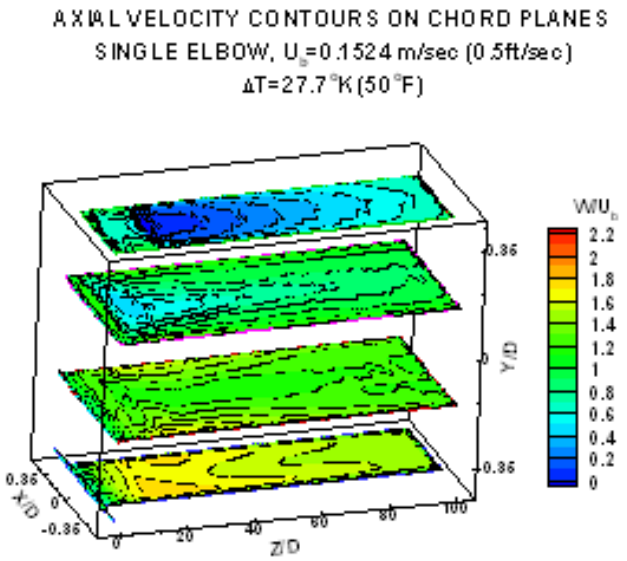

Fig. B-54 Axial Velocity Slice Contours
V_0=0.1524 m/sec, ΔT_{wall}=27.7°K

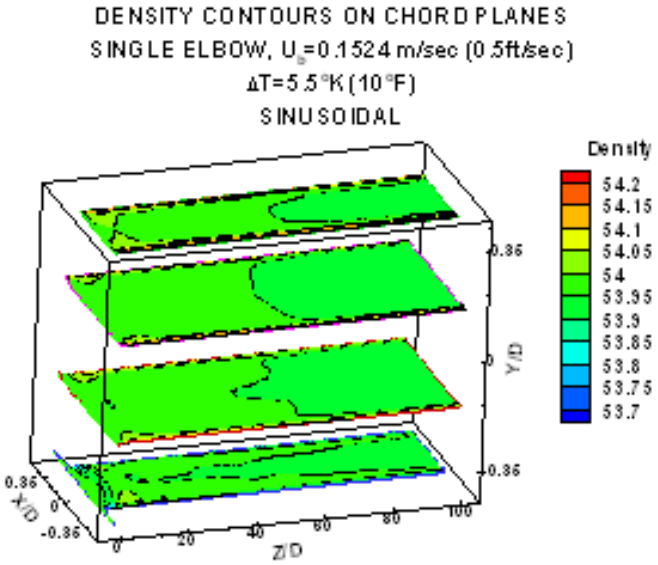

Fig. B-55 Density Slice Contours
V_0=0.1524 m/sec, ΔT_{wall}=-5.5°K Sinusoidal

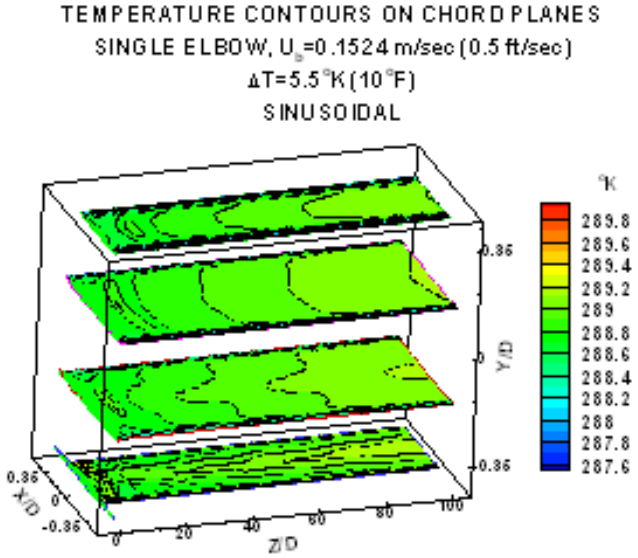

Fig. B-56 Temperature Slice Contours
V_0=0.1524 m/sec, ΔT_{wall}=-5.5°K Sinusoidal

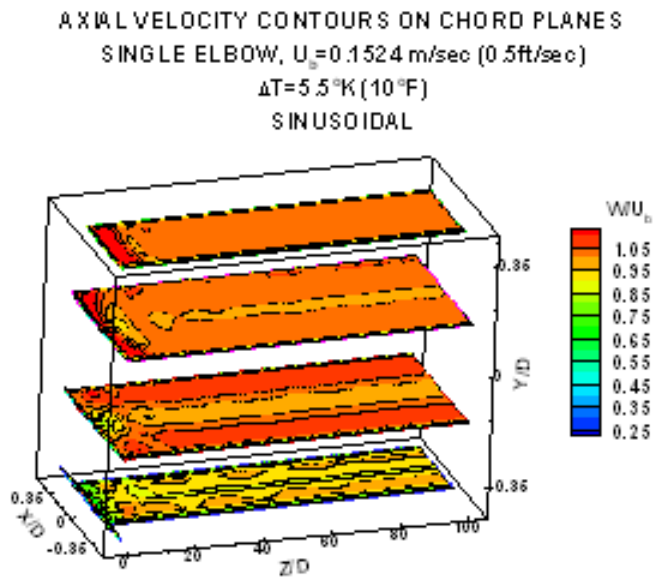

Fig. B-57 Axial Velocity Slice Contours
V_0=0.1524 m/sec, ΔT_{wall}=-5.5°K Sinusoidal

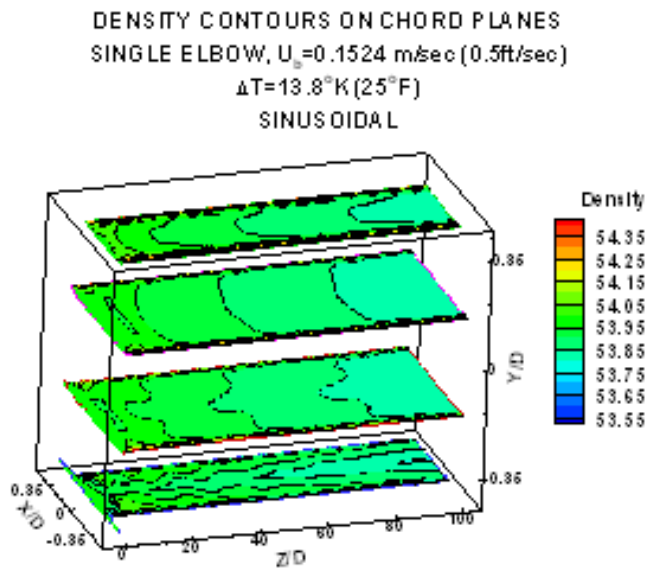

Fig. B-58 Density Slice Contours
V_0=0.1524 m/sec, ΔT_{wall}=-13.8°K Sinusoidal

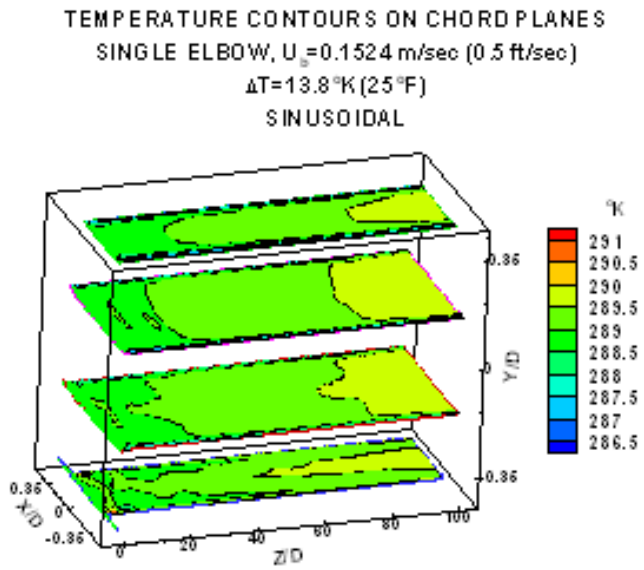

Fig. B-59 Temperature Slice Contours
V_0=0.1524 m/sec, ΔT_{wall}=-13.8°K Sinusoidal

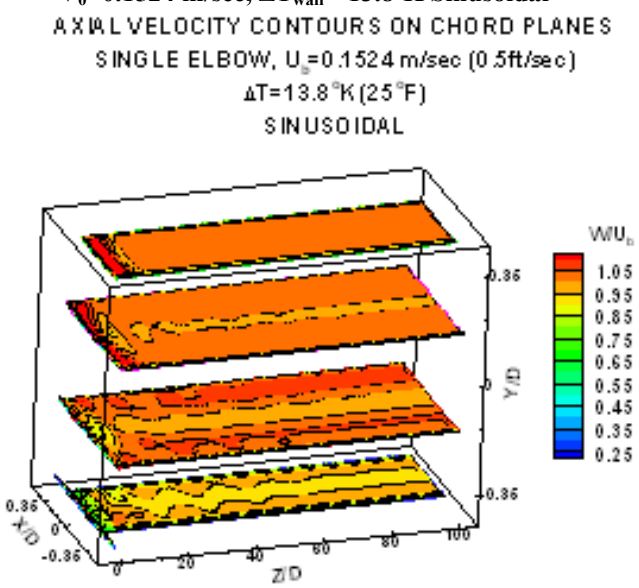

Fig. B-60 Axial Velocity Slice Contours
V_0=0.1524 m/sec, ΔT_{wall}=-13.8°K Sinusoidal

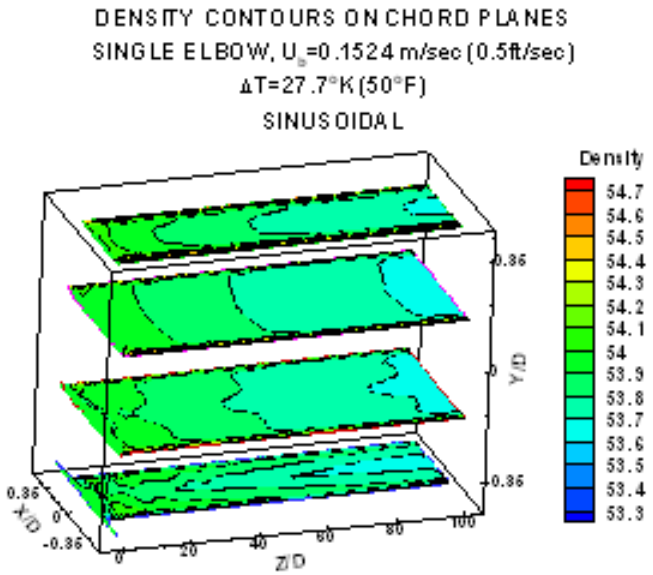

Fig. B-61 Density Slice Contours
V_0=0.1524 m/sec, ΔT_{wall}=-27.7°K Sinusoidal

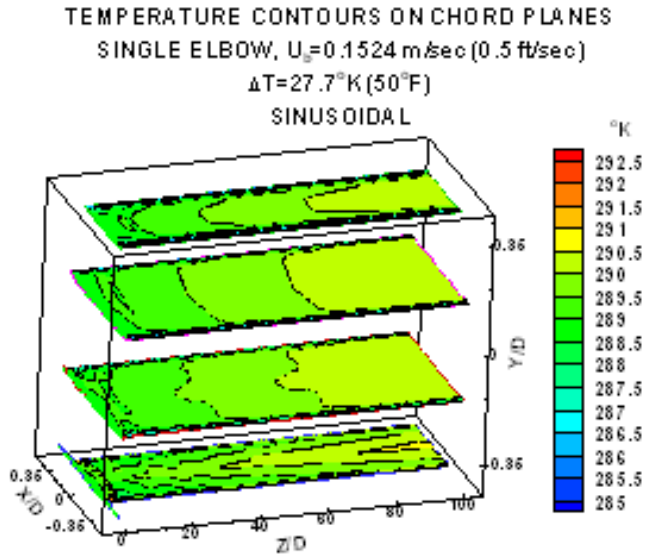

Fig. B-62 Temperature Slice Contours
V_0=0.1524 m/sec, ΔT_{wall}=-27.7°K Sinusoidal

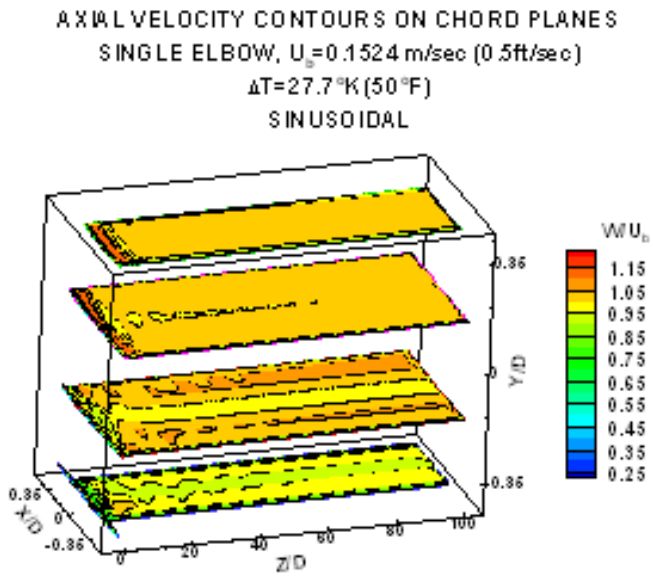

Fig. B-63 Axial Velocity Slice Contours
V_0=0.1524 m/sec, ΔT_{wall}=-27.7°K Sinusoidal

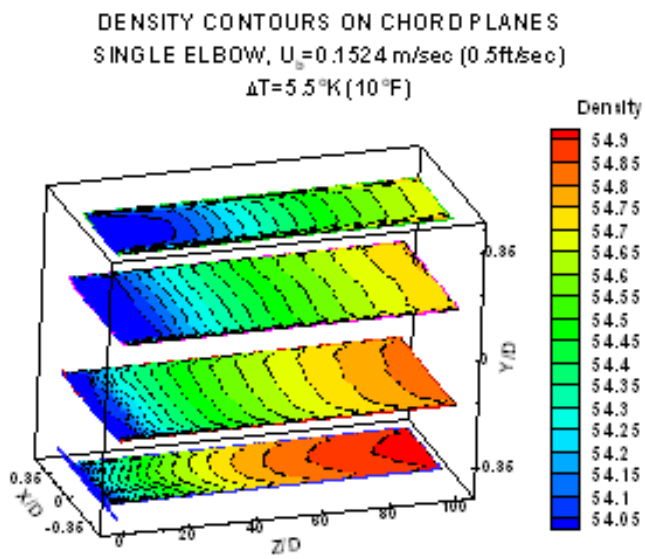

Fig. B-64 Density Slice Contours
V_0=0.1524 m/sec, ΔT_{wall}=-5.5°K

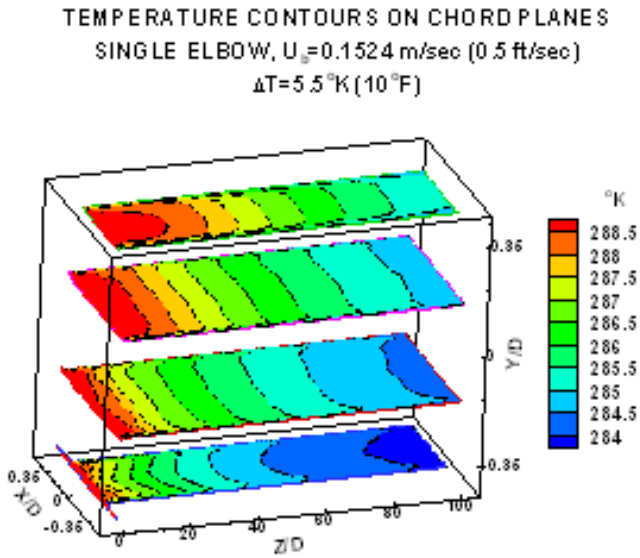

Fig. B-65 Temperature Slice Contours
V_0=0.1524 m/sec, ΔT_{wall}=-5.5°K

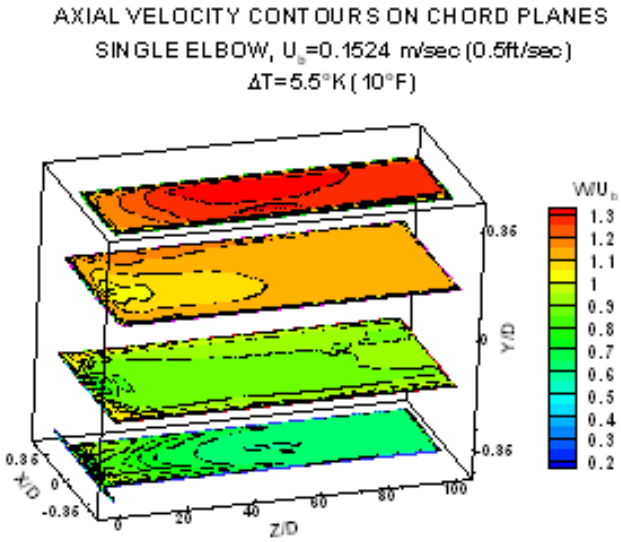

Fig. B-66 Axial Velocity Slice Contours
V_0=0.1524 m/sec, ΔT_{wall}=-5.5°K

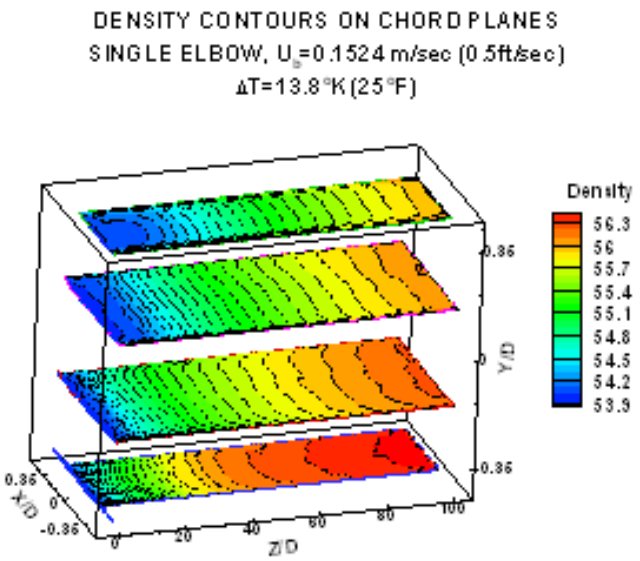

Fig. B-67 Density Slice Contours
V_0=0.1524 m/sec, ΔT_{wall}=-13.8°K

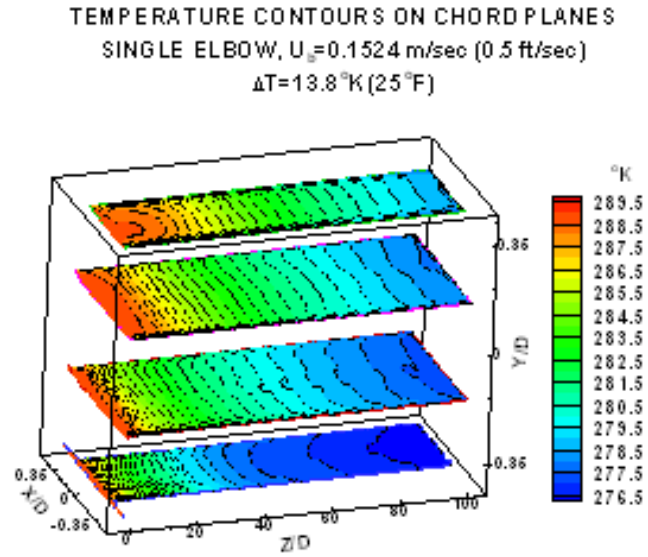

Fig. B-68 Temperature Slice Contours
V_0=0.1524 m/sec, ΔT_{wall}=-13.8°K

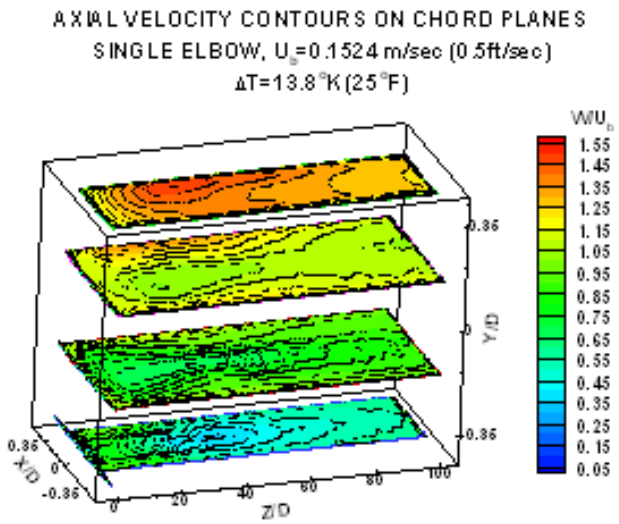

Fig. B-69 Axial Velocity Slice Contours
V_0=0.1524 m/sec, ΔT_{wall}=-13.8°K

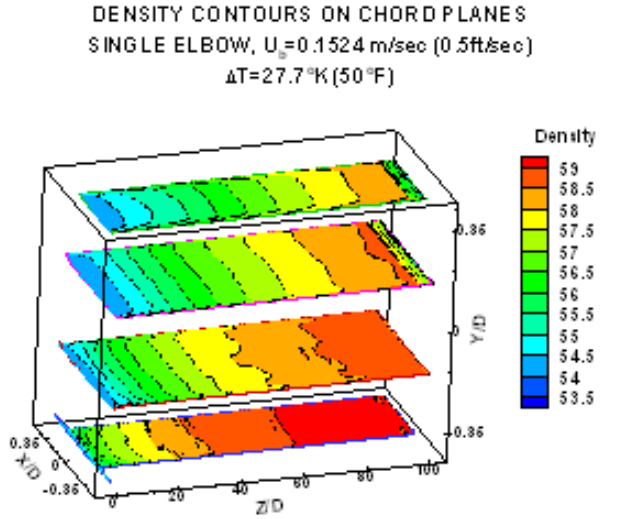

Fig. B-70 Density Slice Contours
V_0=0.1524 m/sec, ΔT_{wall}=-27.7°K

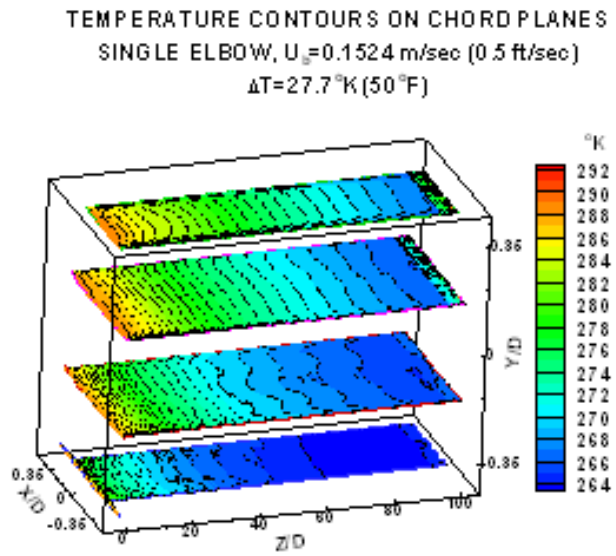

Fig. B-71 Temperature Slice Contours
V_0=0.1524 m/sec, ΔT_{wall}=-27.7°K

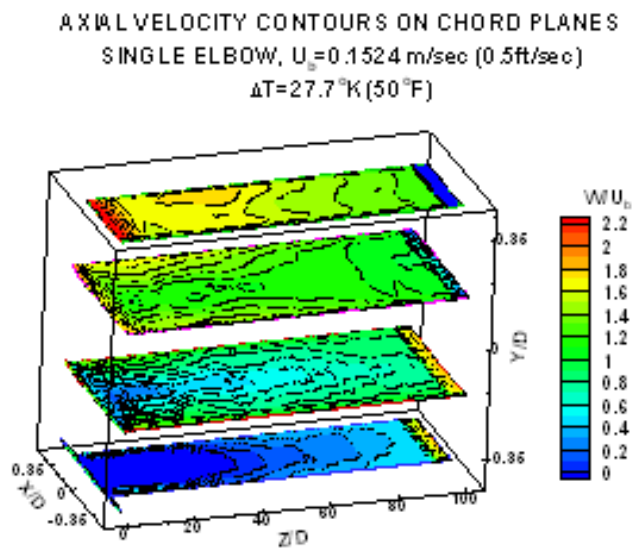

Fig. B-72 Axial Velocity Slice Contours
V_0=0.1524 m/sec, ΔT_{wall}=-27.7°K

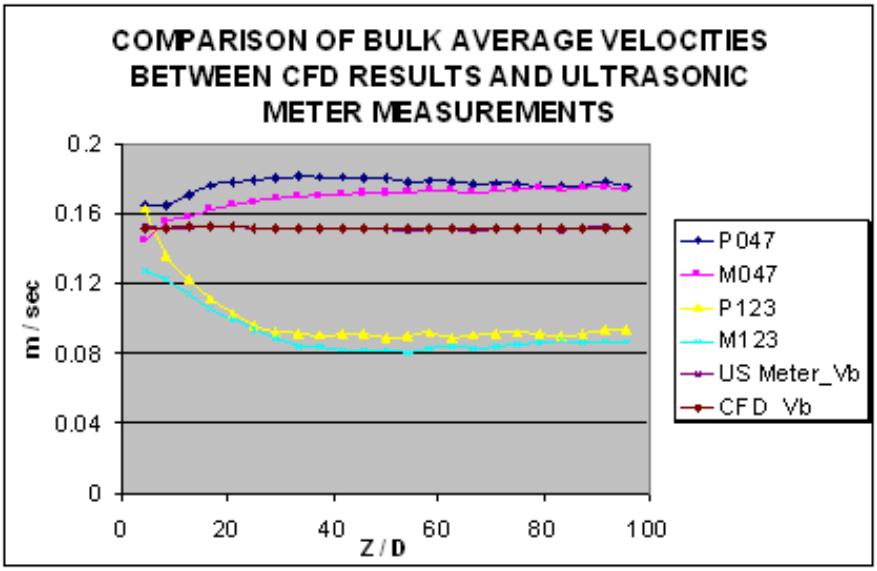

Fig. B-73 Comparison between CFD Vb and Ultrasonic Vb.
V_0=0.1524 m/sec, ΔT_{wall}=5.5°K Sinusoidal

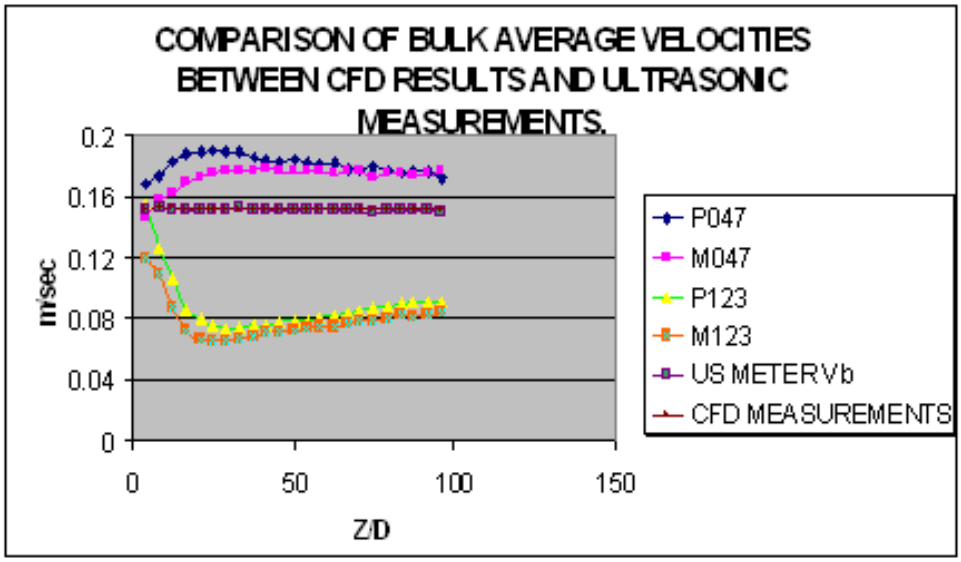

Fig. B-74 Comparison between CFD Vb and Ultrasonic Vb.
V_0=0.1524 m/sec, ΔT_{wall}=13.8°K Sinusoidal

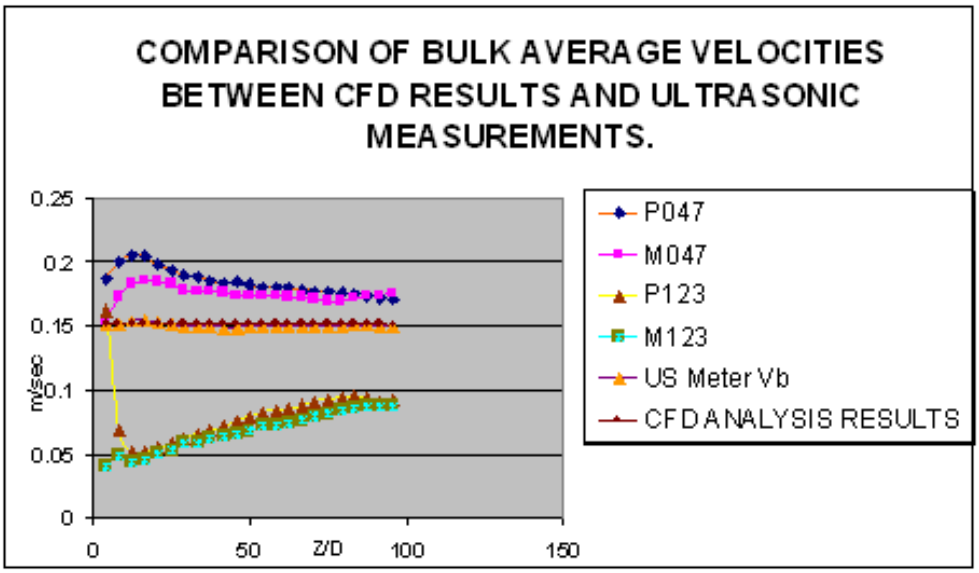

Fig. B-75 Comparison between CFD Vb and Ultrasonic Vb.
V_0=0.1524 m/sec, ΔT_{wall}=27.7°K Sinusoidal

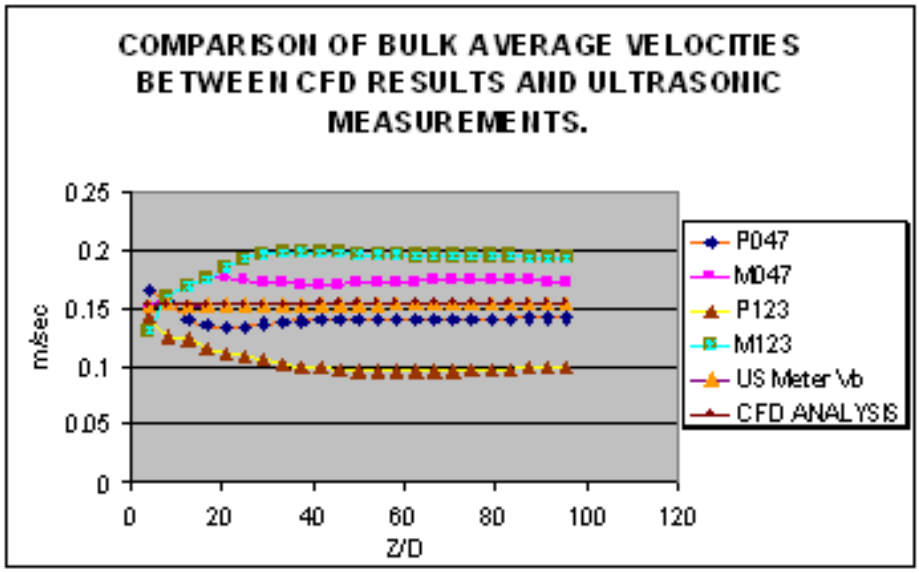

Fig. B-76 Comparison between CFD Vb and Ultrasonic Vb.
V_0=0.1524 m/sec, ΔT_{wall}=5.5°K

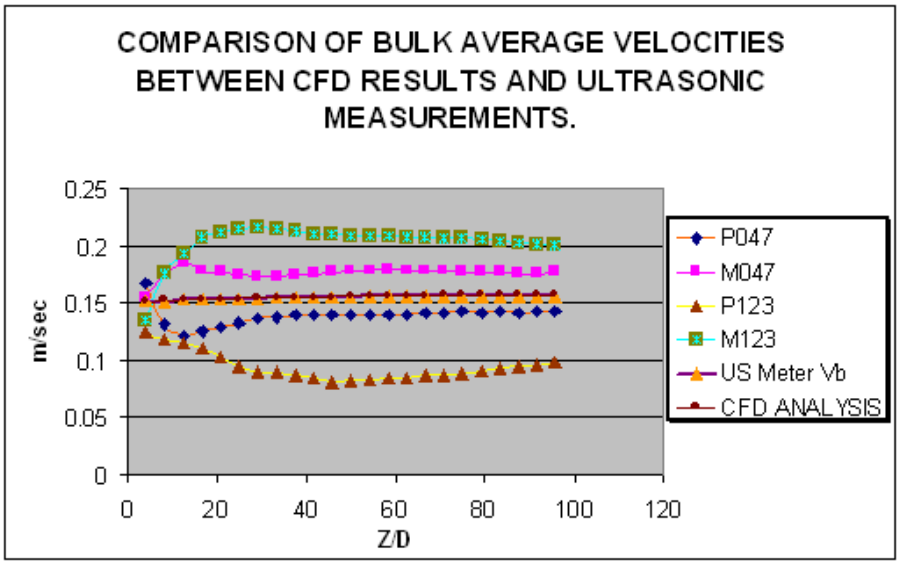

Fig. B-77 Comparison between CFD Vb and Ultrasonic Vb.
V_0=0.1524 m/sec, ΔT_{wall}=13.8°K

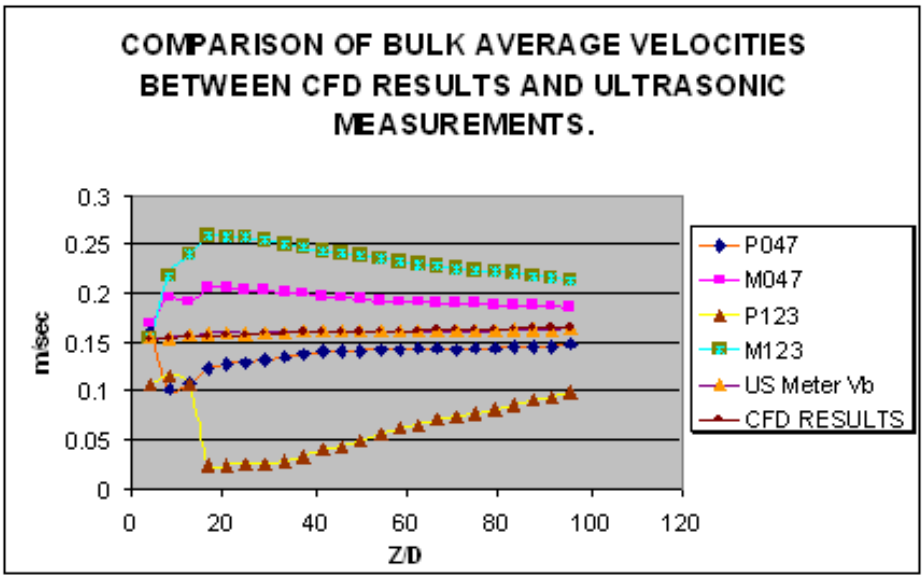

Fig. B-78 Comparison between CFD Vb and Ultrasonic Vb.
V_0=0.1524 m/sec, ΔT_{wall}=27.7°K

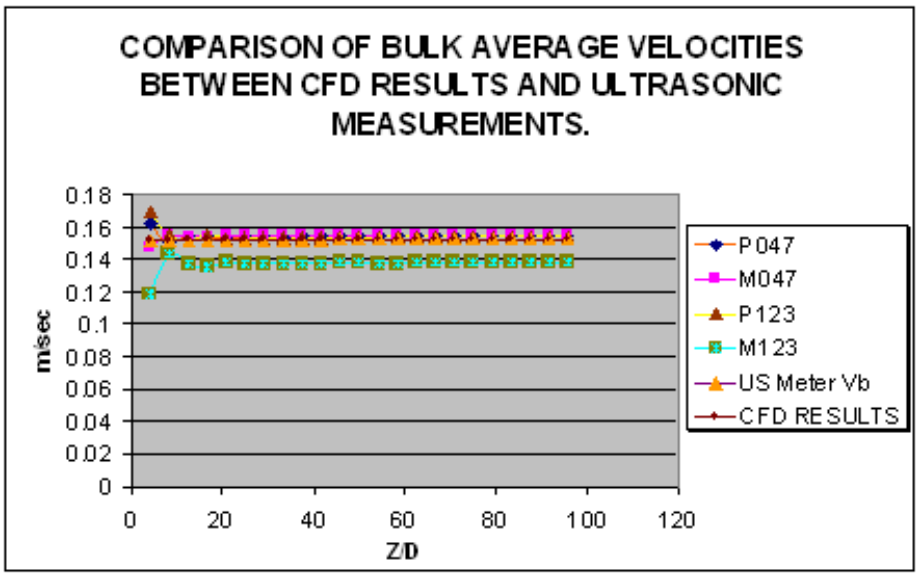

Fig. B-79 Comparison between CFD Vb and Ultrasonic Vb.
V_0=0.1524 m/sec, ΔT_{wall}=-5.5°K Sinusoidal

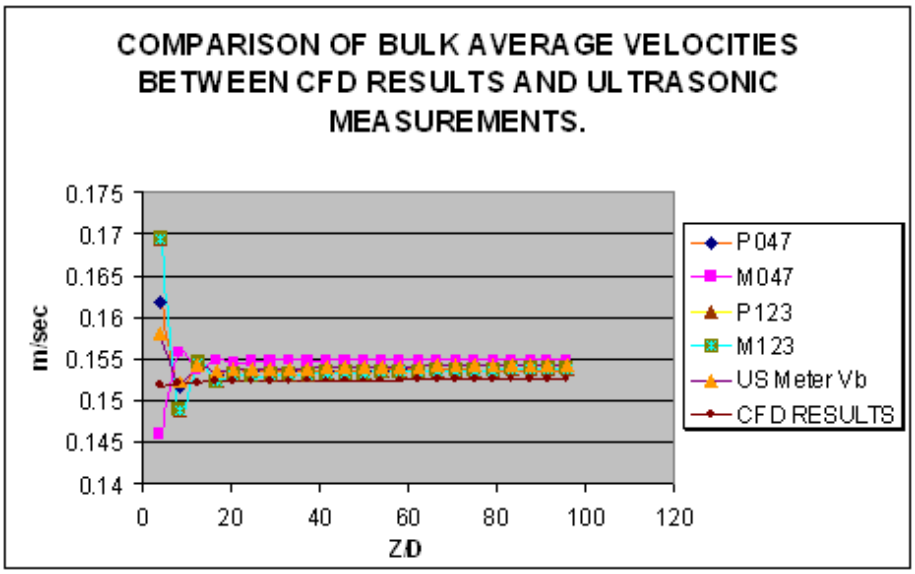

Fig. B-80 Comparison between CFD Vb and Ultrasonic Vb.
V_0=0.1524 m/sec, ΔT_{wall}=-13.8°K Sinusoidal

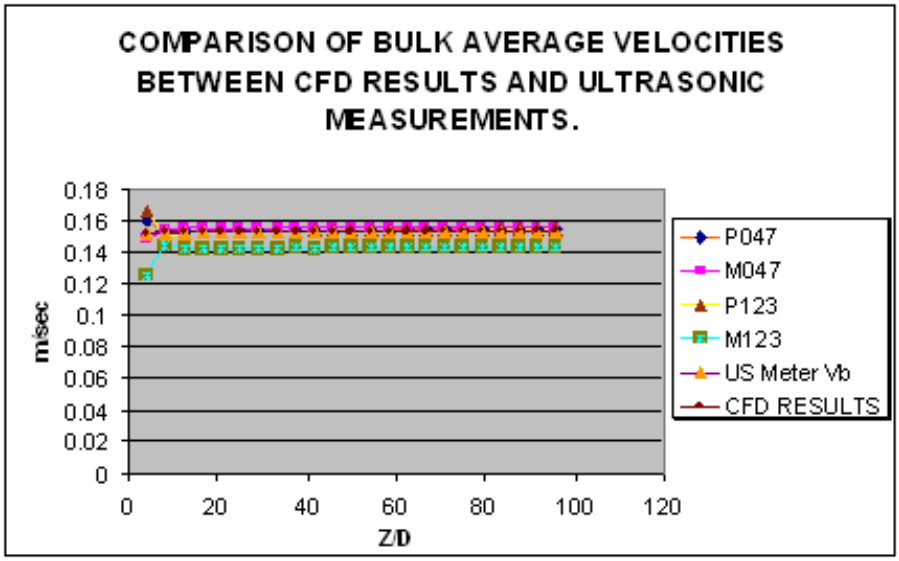

Fig. B-81 Comparison between CFD Vb and Ultrasonic Vb.
V_0=0.1524 m/sec, ΔT_{wall}=-27.7°K Sinusoidal

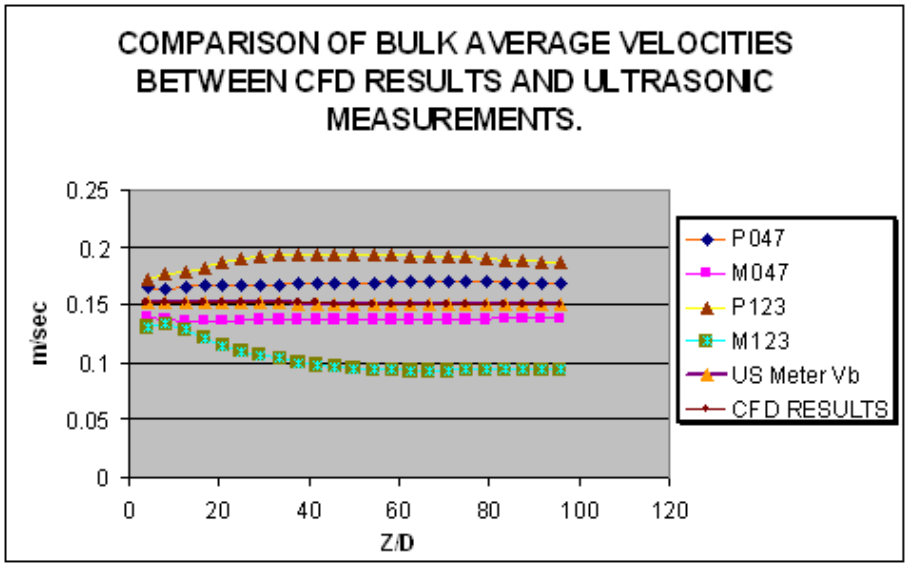

Fig. B-82 Comparison between CFD Vb and Ultrasonic Vb.
V_0=0.1524 m/sec, ΔT_{wall}=-5.5°K

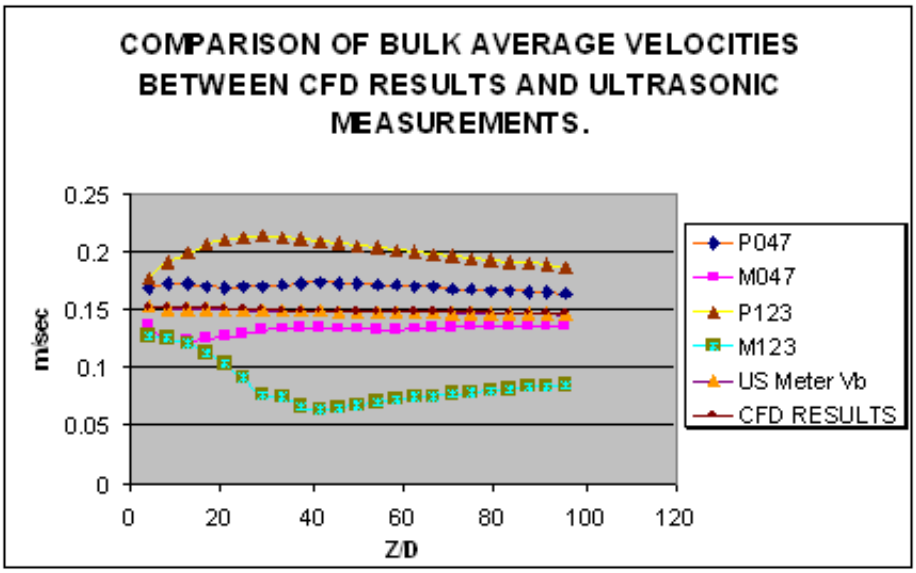

Fig. B-83 Comparison between CFD Vb and Ultrasonic Vb.
V_0=0.1524 m/sec, ΔT_{wall}=-13.8°K

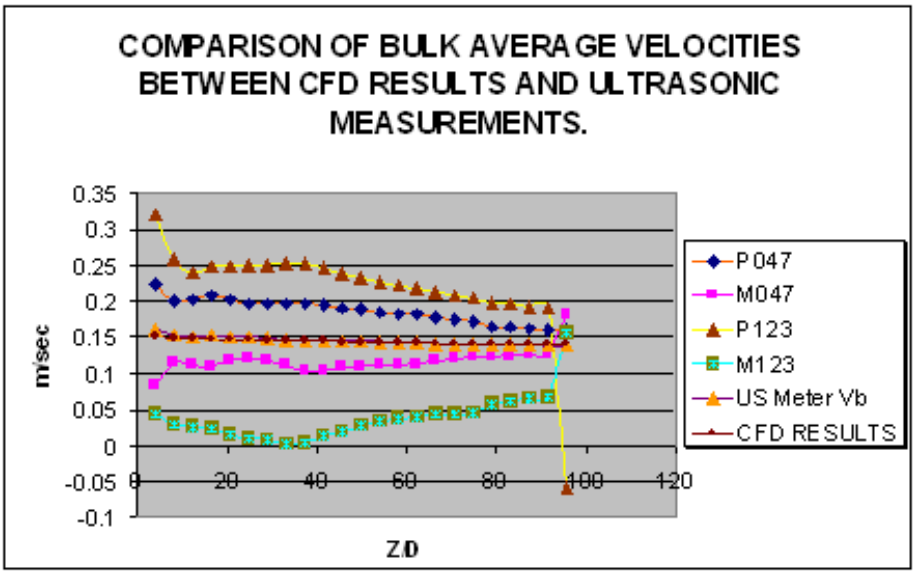

Fig. B-84 Comparison between CFD Vb and Ultrasonic Vb.
V_0=0.1524 m/sec, ΔT_{wall}=-27.7°K

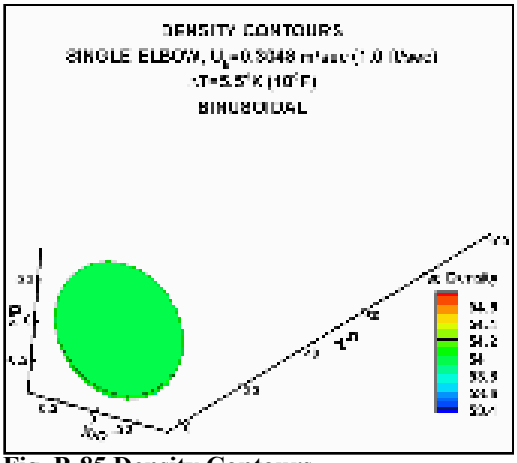

Fig. B-85 Density Contours
V_0=0.3048 m/sec, ΔT_{wall}=5.5°K Sinusoidal

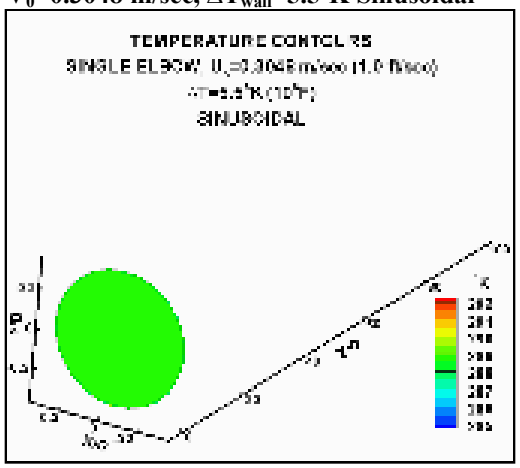

Fig. B-86 Temperature Contours
V_0=0.3048 m/sec, ΔT_{wall}=5.5°K Sinusoidal

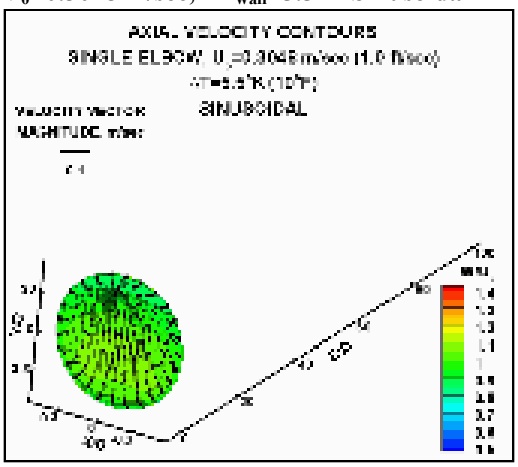

Fig. B-87 Axial Velocity Contours
V_0=0.3048 m/sec, ΔT_{wall}=5.5°K Sinusoidal

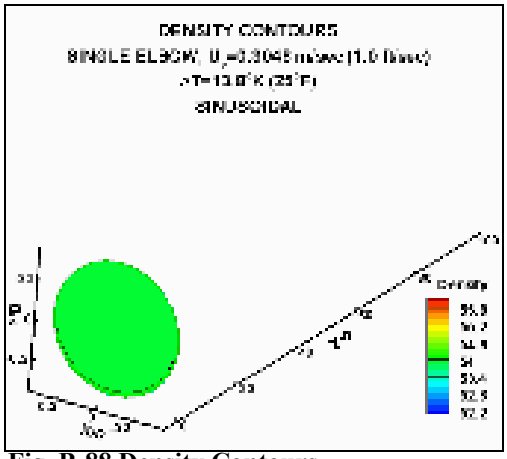

Fig. B-88 Density Contours
V_0=0.3048 m/sec, ΔT_{wall}=13.8°K Sinusoidal

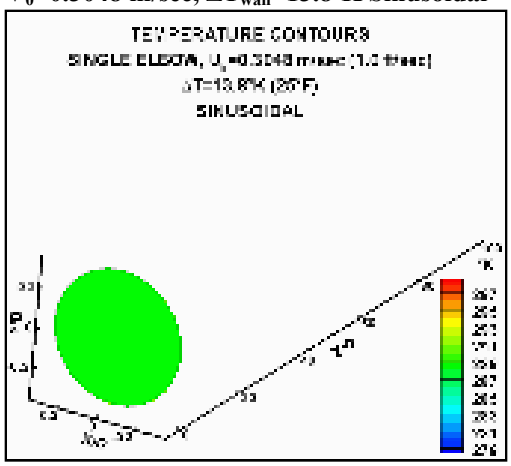

Fig. B-89 Temperature Contours
V_0=0.3048 m/sec, ΔT_{wall}=13.8°K Sinusoidal

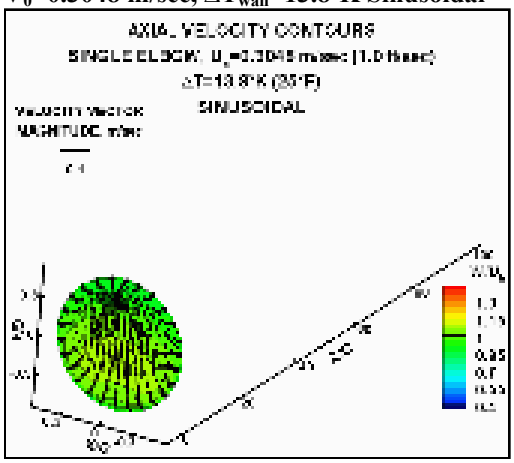

Fig. B-90 Axial Velocity Contours
V_0=0.3048 m/sec, ΔT_{wall}=13.8°K Sinusoidal

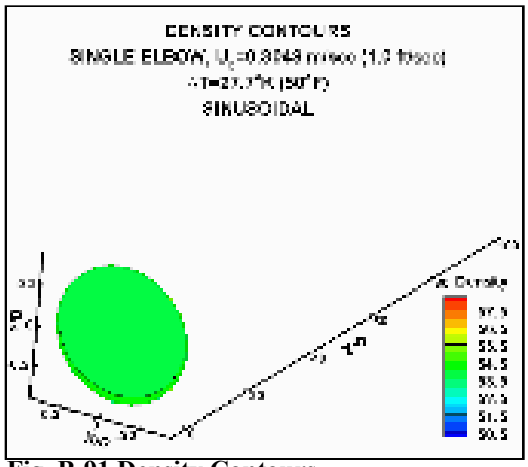

Fig. B-91 Density Contours
V_0=0.3048 m/sec, ΔT_{wall}=27.7°K Sinusoidal

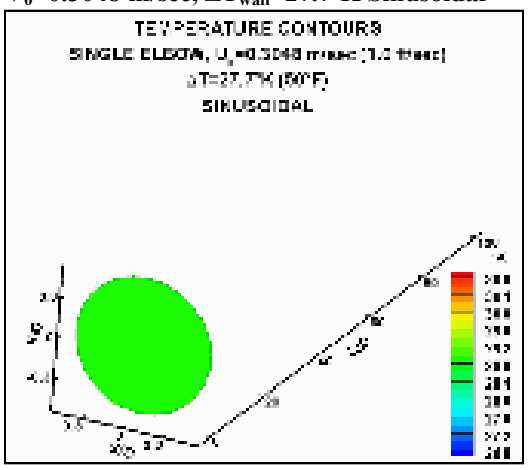

Fig. B-92 Temperature Contours
V_0=0.3048 m/sec, ΔT_{wall}=27.7°K Sinusoidal

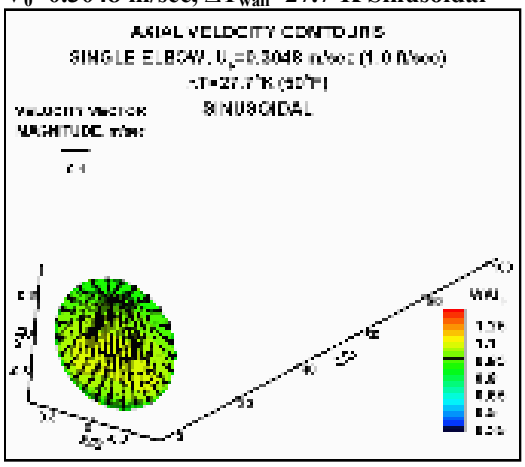

Fig. B-93 Axial Velocity Contours
V_0=0.3048 m/sec, ΔT_{wall}=27.7°K Sinusoidal

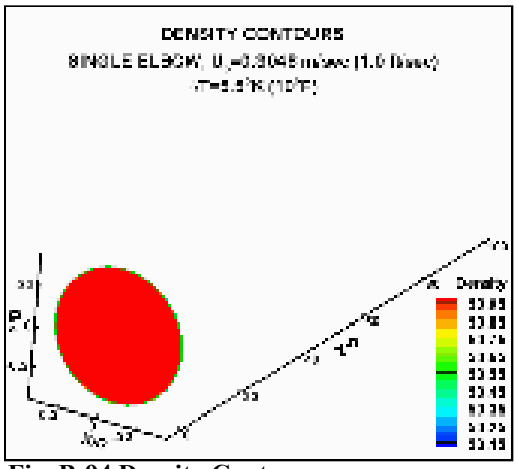

Fig. B-94 Density Contours
V_0=0.3048 m/sec, ΔT_{wall}=5.5°K

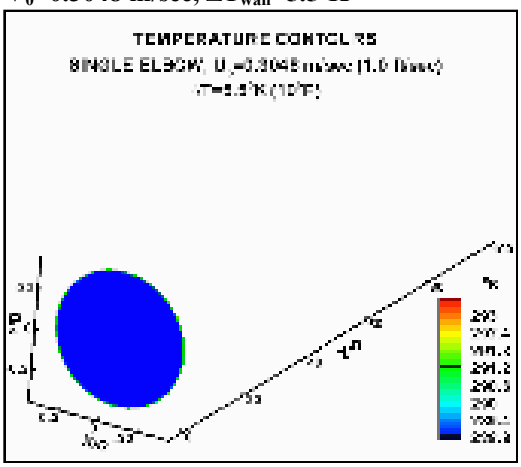

Fig. B-95 Temperature Contours
V_0=0.3048 m/sec, ΔT_{wall}=5.5°K

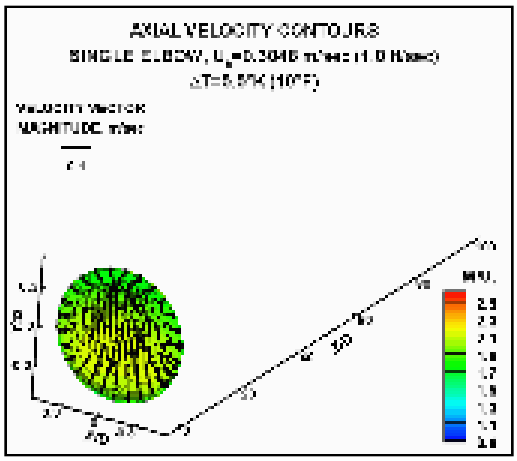

Fig. B-96 Axial Velocity Contours
V_0=0.3048 m/sec, ΔT_{wall}=5.5°K

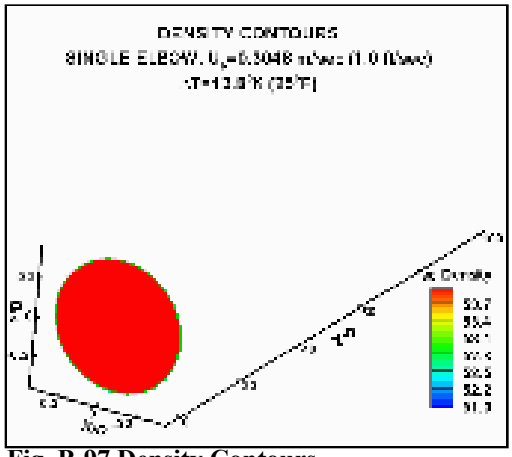

Fig. B-97 Density Contours
V_0=0.3048 m/sec, ΔT_{wall}=13.8°K

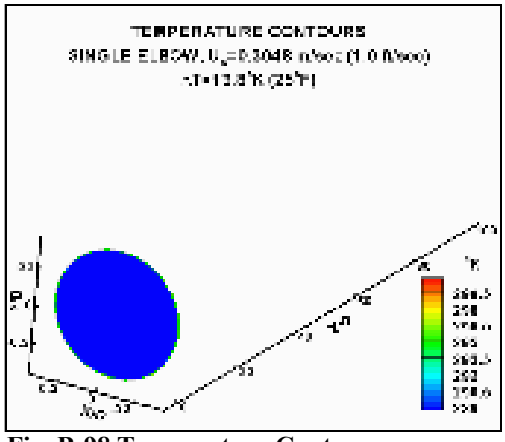

Fig. B-98 Temperature Contours
V_0=0.3048 m/sec, ΔT_{wall}=13.8°K

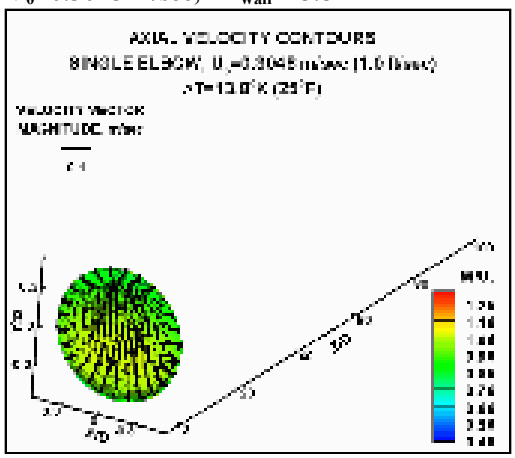

Fig. B-99 Axial Velocity Contours
V_0=0.3048 m/sec, ΔT_{wall}=13.8°K

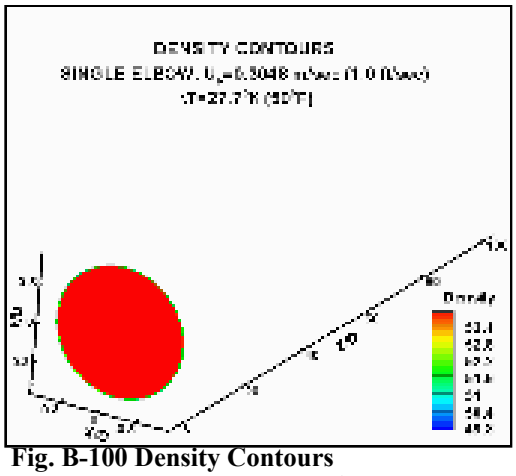

Fig. B-100 Density Contours
V_0=0.3048 m/sec, ΔT_{wall}=27.7°K

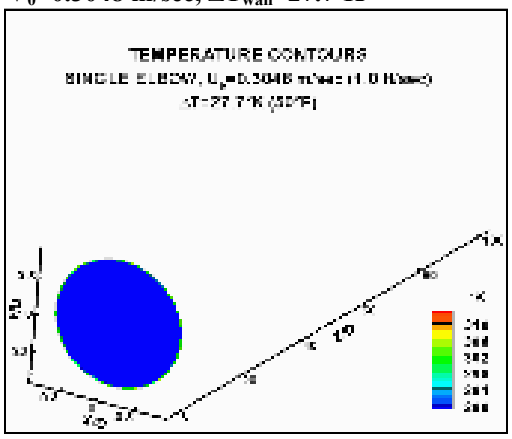

Fig. B-101 Temperature Contours
V_0=0.3048 m/sec, ΔT_{wall}=27.7°K

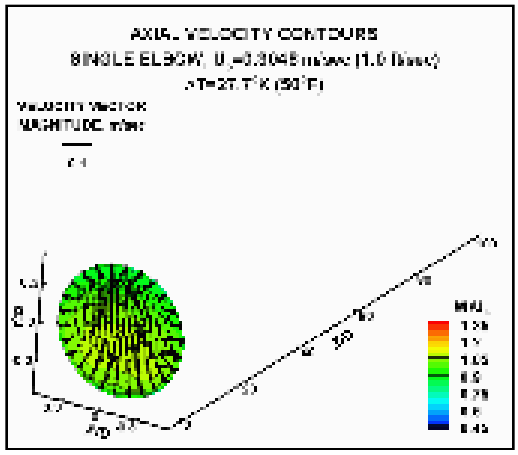

Fig. B-102 Axial Velocity Contours
V_0=0.3048 m/sec, ΔT_{wall}=27.7°K

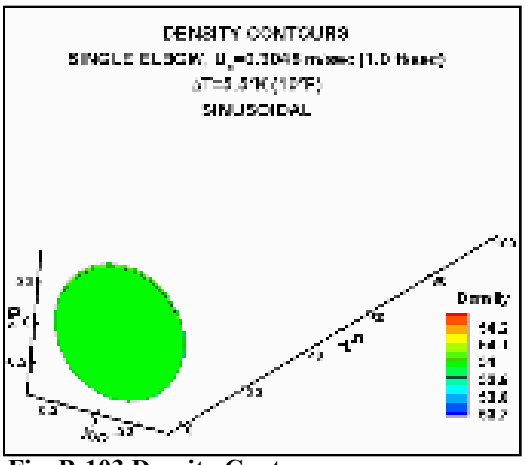

Fig. B-103 Density Contours
V_0=0.3048 m/sec, ΔT_{wall}=-5.5°K Sinusoidal

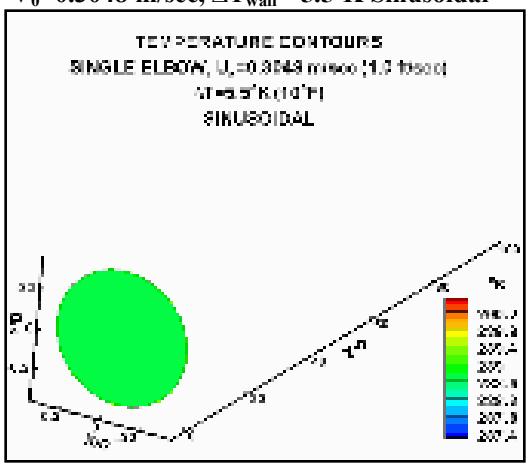

Fig. B-104 Temperature Contours
V_0=0.3048 m/sec, ΔT_{wall}=-5.5°K Sinusoidal

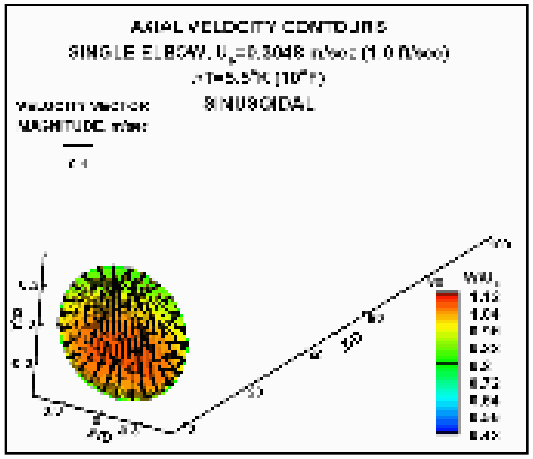

Fig. B-105 Axial Velocity Contours
V_0=0.3048 m/sec, ΔT_{wall}=-5.5°K Sinusoidal

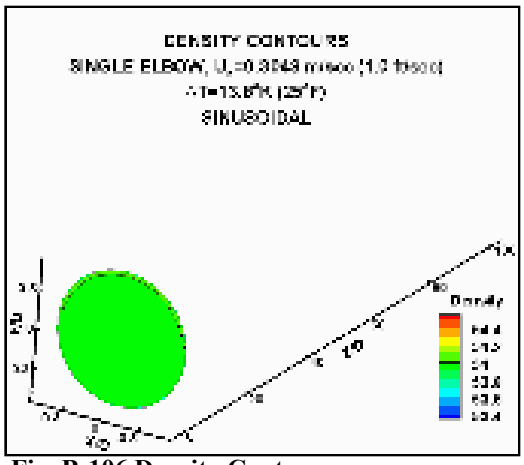

Fig. B-106 Density Contours
V_0=0.3048 m/sec, ΔT_{wall}=-13.8°K Sinusoidal

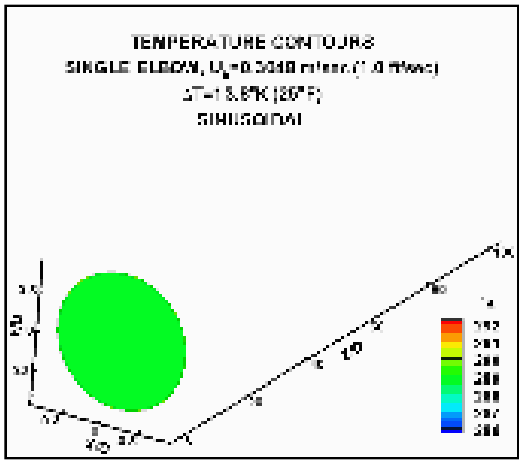

Fig. B-107 Temperature Contours
V_0=0.3048 m/sec, ΔT_{wall}=-13.8°K Sinusoidal

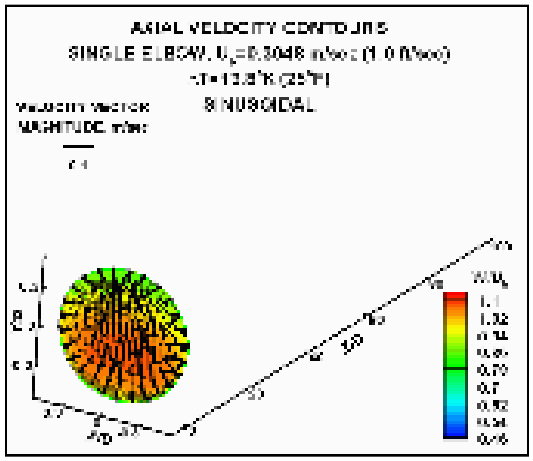

Fig. B-108 Axial Velocity Contours
V_0=0.3048 m/sec, ΔT_{wall}=-13.8°K Sinusoidal

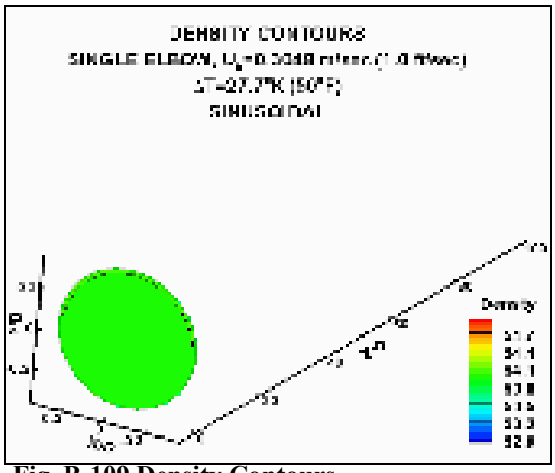

Fig. B-109 Density Contours
V_0=0.3048 m/sec, ΔT_{wall}=-27.7°K Sinusoidal

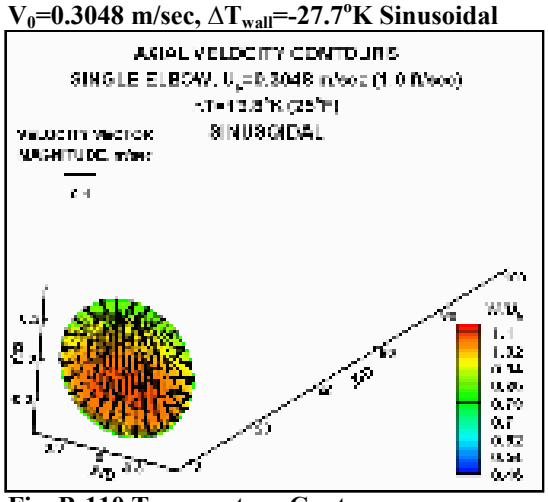

Fig. B-110 Temperature Contours
V_0=0.3048 m/sec, ΔT_{wall}=-27.7°K Sinusoidal

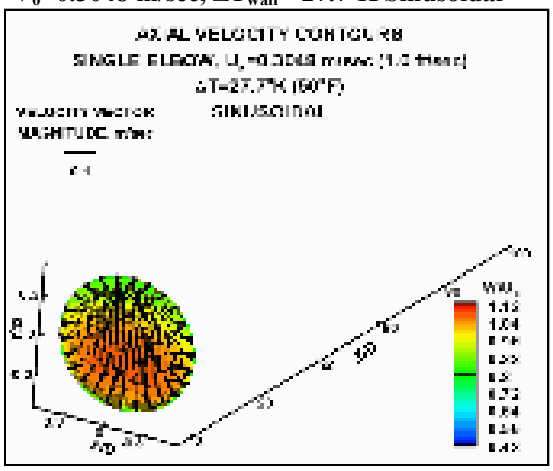

Fig. B-11 Axial Velocity Contours
V_0=0.3048 m/sec, ΔT_{wall}=-27.7°K Sinusoidal

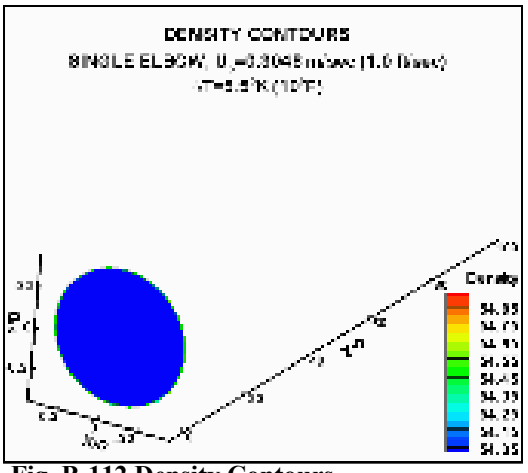

Fig. B-112 Density Contours
V_0=0.3048 m/sec, ΔT_{wall}=-5.5°K

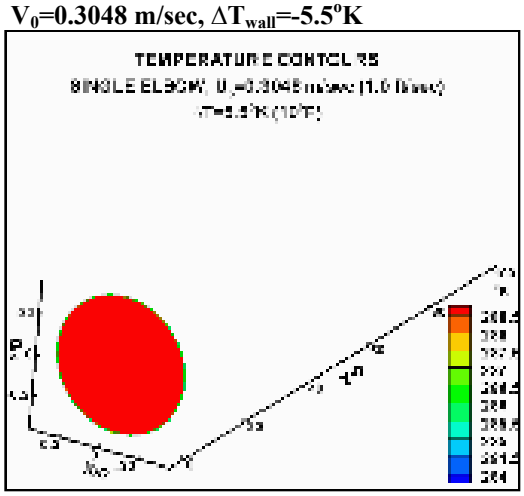

Fig. B-113 Temperature Contours
V_0=0.3048 m/sec, ΔT_{wall}=-5.5°K

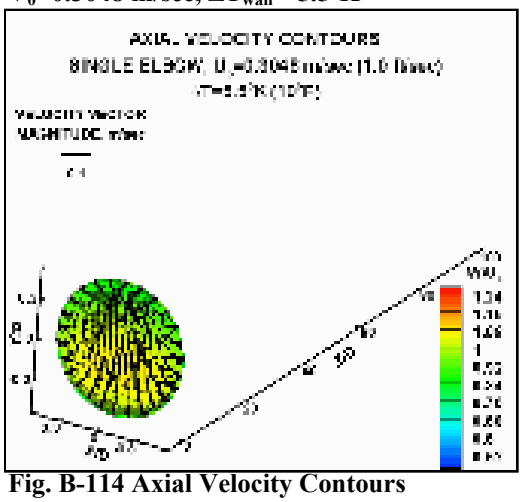

Fig. B-114 Axial Velocity Contours
V_0=0.3048 m/sec, ΔT_{wall}=-5.5°K

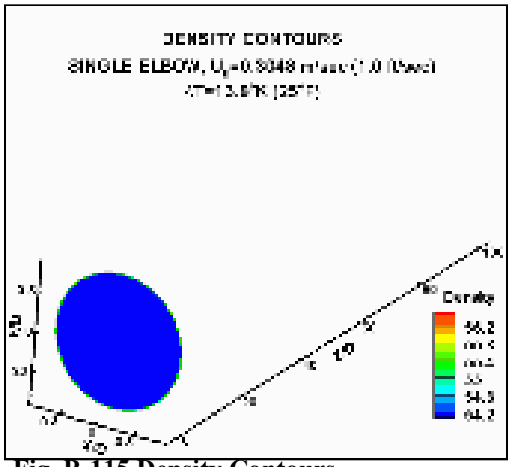

Fig. B-115 Density Contours
V_0=0.3048 m/sec, ΔT_{wall}=-13.8°K

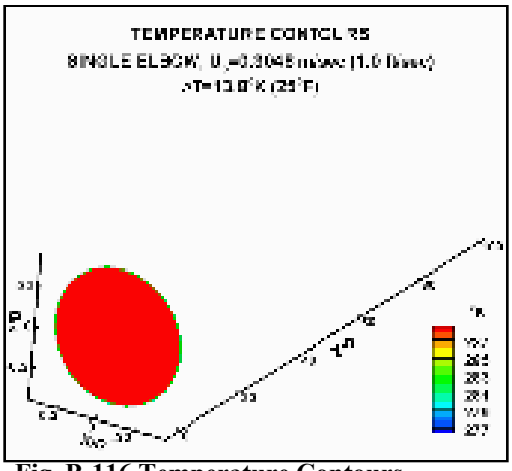

Fig. B-116 Temperature Contours
V_0=0.3048 m/sec, ΔT_{wall}=-13.8°K

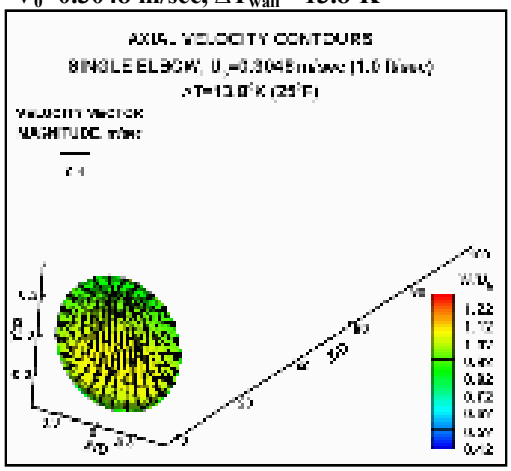

Fig. B-117 Axial Velocity Contours
V_0=0.3048 m/sec, ΔT_{wall}=-13.8°K

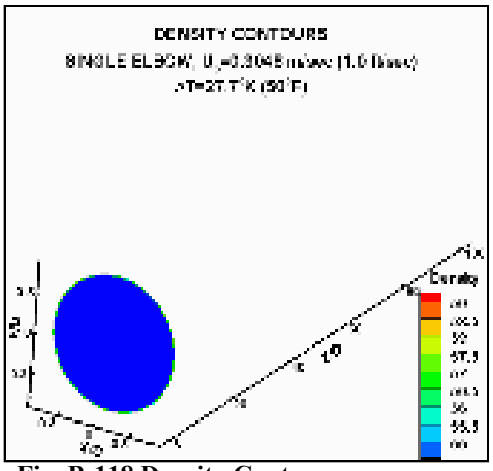

Fig. B-118 Density Contours
V_0=0.3048 m/sec, ΔT_{wall}=-27.7°K

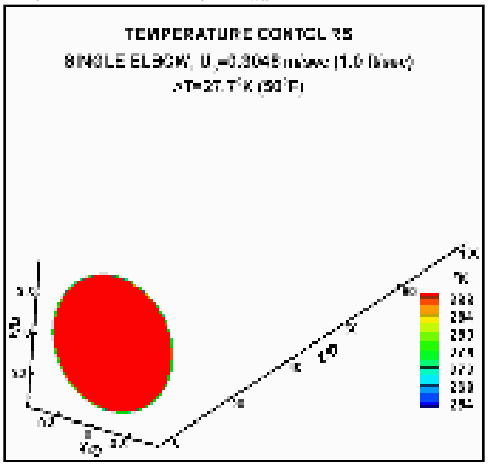

Fig. B-119 Temperature Contours
V_0=0.3048 m/sec, ΔT_{wall}=-27.7°K

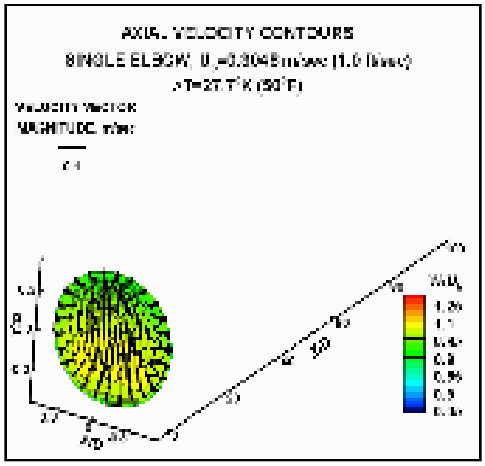

Fig. B-120 Axial Velocity Contours
V_0=0.3048 m/sec, ΔT_{wall}=-27.7°K

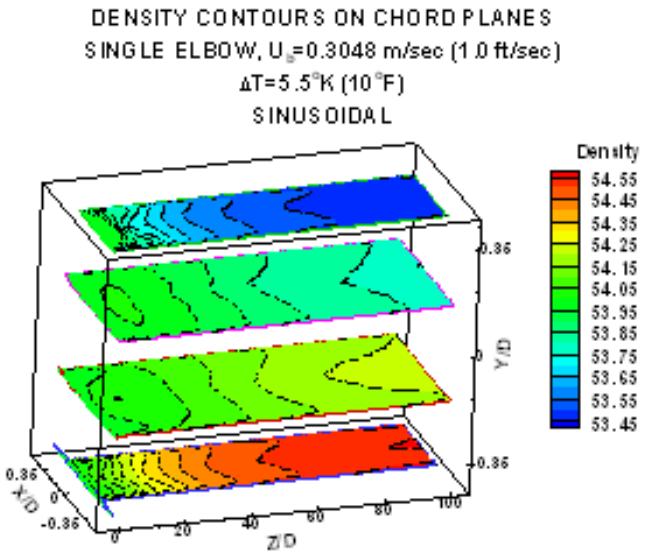

Fig. B-121 Density Slice Contours
V_0=0.3048 m/sec, ΔT_{wall}=5.5°K Sinusoidal

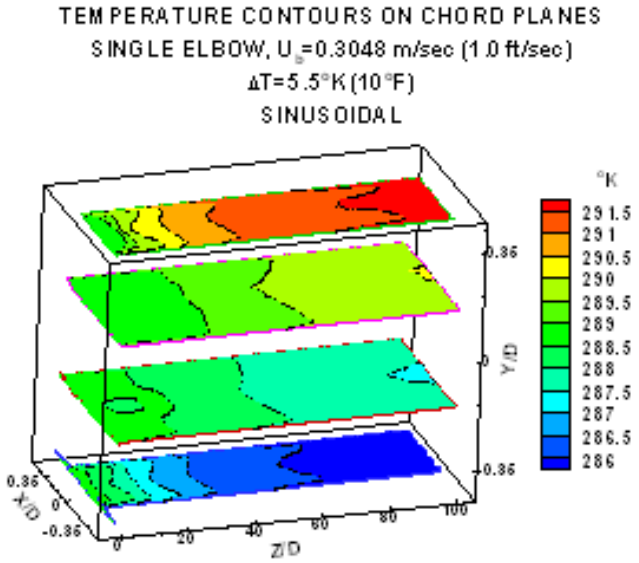

Fig. B-122 Temperature Slice Contours
V_0=0.3048 m/sec, ΔT_{wall}=5.5°K Sinusoidal

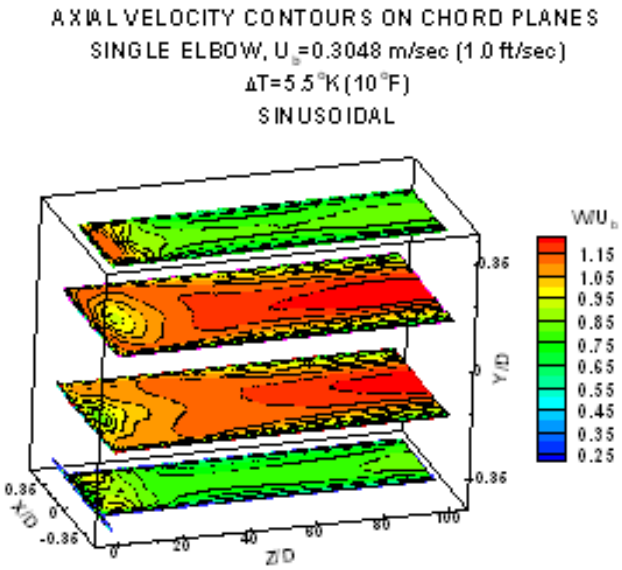

Fig. B-123 Axial Velocity Slice Contours
V_0=0.3048 m/sec, ΔT_{wall}=5.5°K Sinusoidal

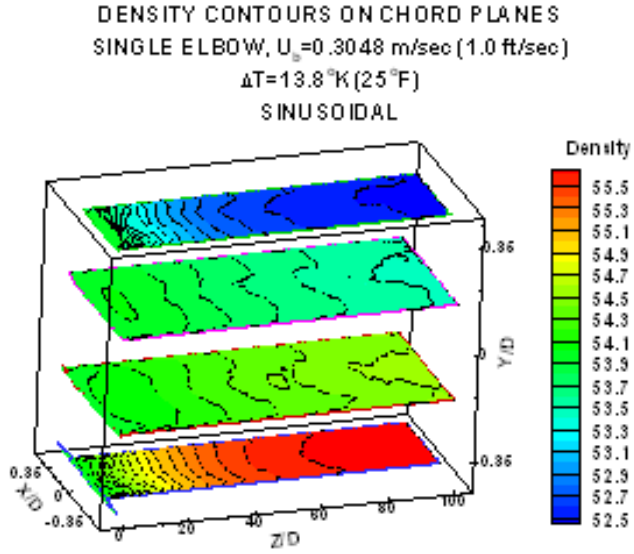

Fig. B-124 Density Slice Contours
V_0=0.3048 m/sec, ΔT_{wall}=13.8°K Sinusoidal

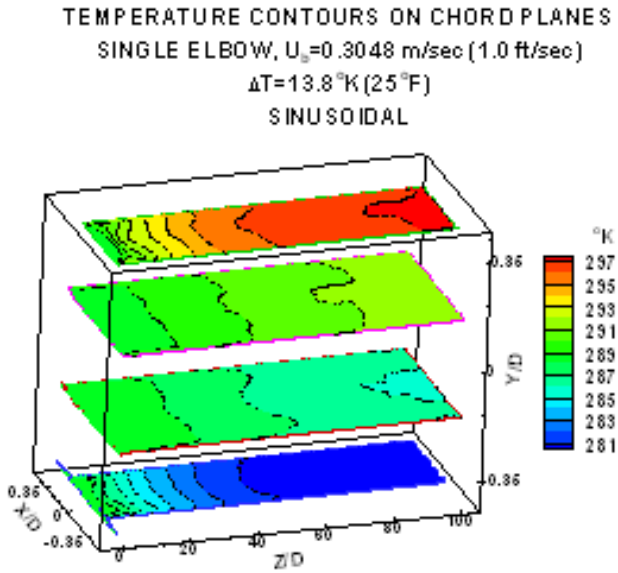

V_0=0.3048 m/sec, ΔT_{wall}=13.8°K Sinusoidal

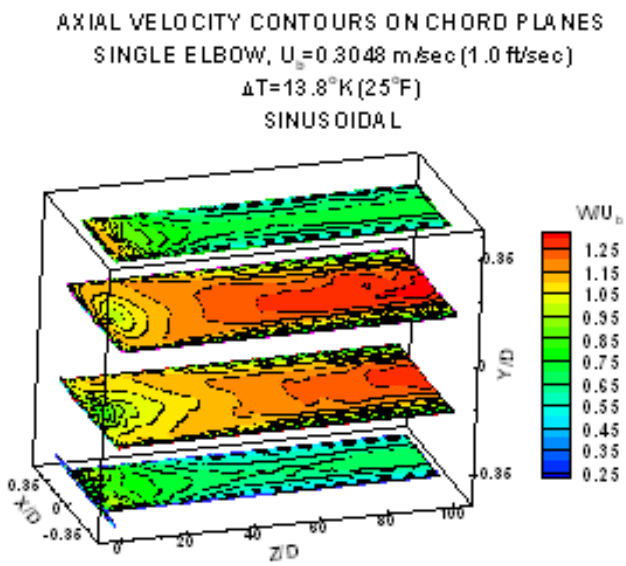

V_0=0.3048 m/sec, ΔT_{wall}=13.8°K Sinusoidal

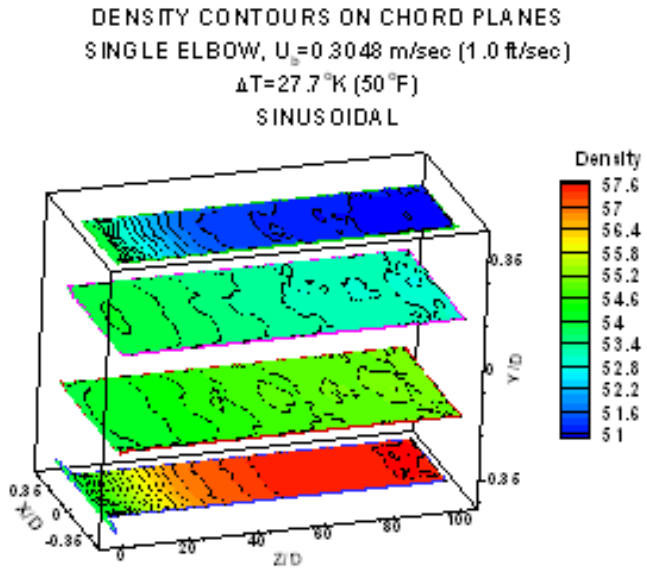

Fig. B-127 Density Slice Contours
V_0=0.3048 m/sec, ΔT_{wall}=27.7°K Sinusoidal

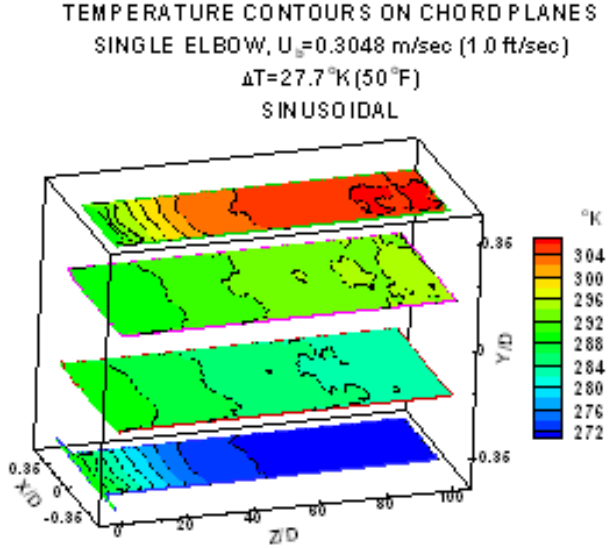

Fig. B-128 Temperature Slice Contours
V_0=0.3048 m/sec, ΔT_{wall}=27.7°K Sinusoidal

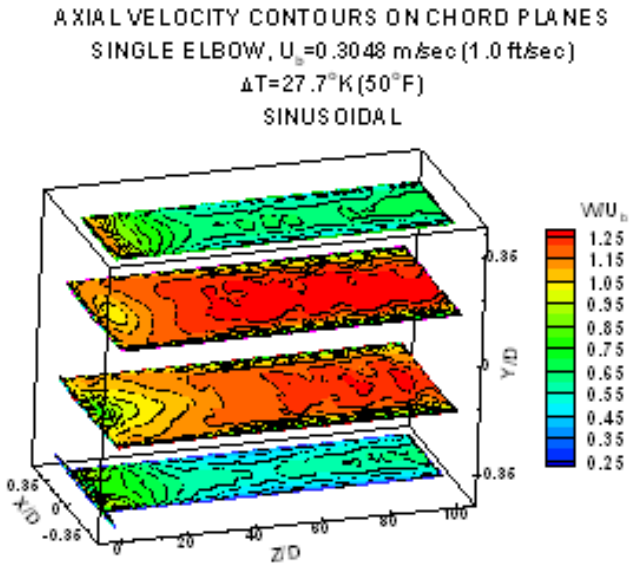

Fig. B-129 Axial Velocity Slice Contours
V_0=0.3048 m/sec, ΔT_{wall}=27.7°K Sinusoidal

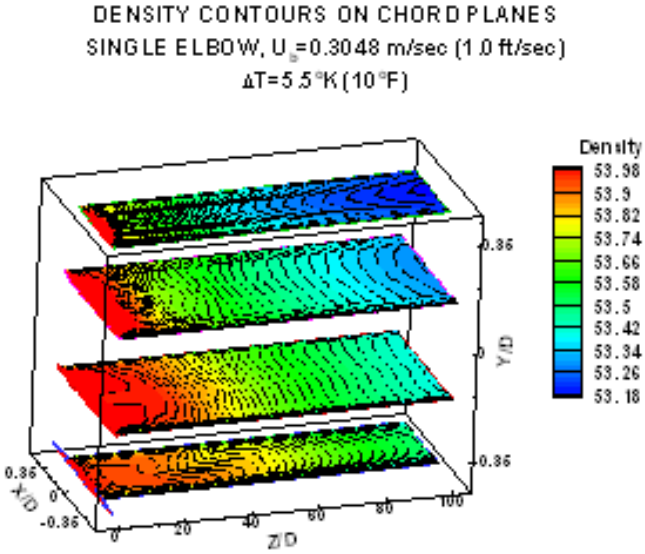

Fig. B-130 Density Slice Contours
V_0=0.3048 m/sec, ΔT_{wall}=5.5°K

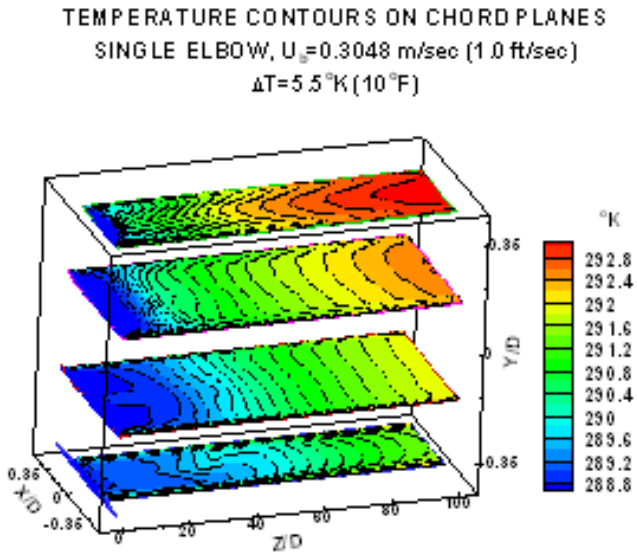

Fig. B-131 Temperature Slice Contours
V_0=0.3048 m/sec, ΔT_{wall}=5.5°K

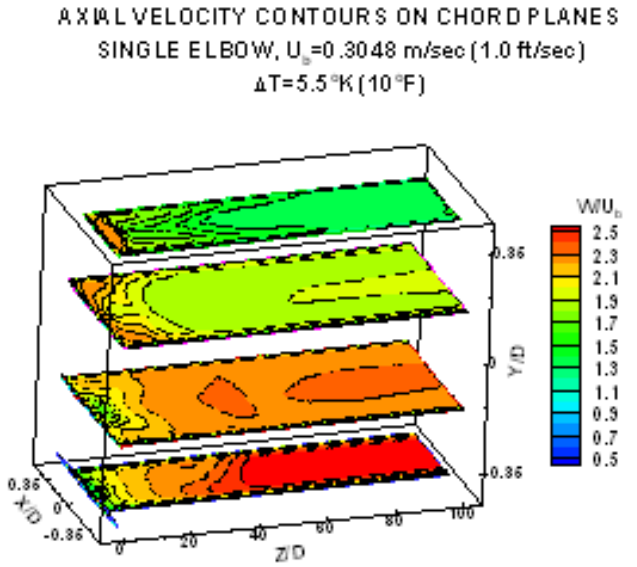

Fig. B-132 Axial Velocity Slice Contours
V_0=0.3048 m/sec, ΔT_{wall}=5.5°K

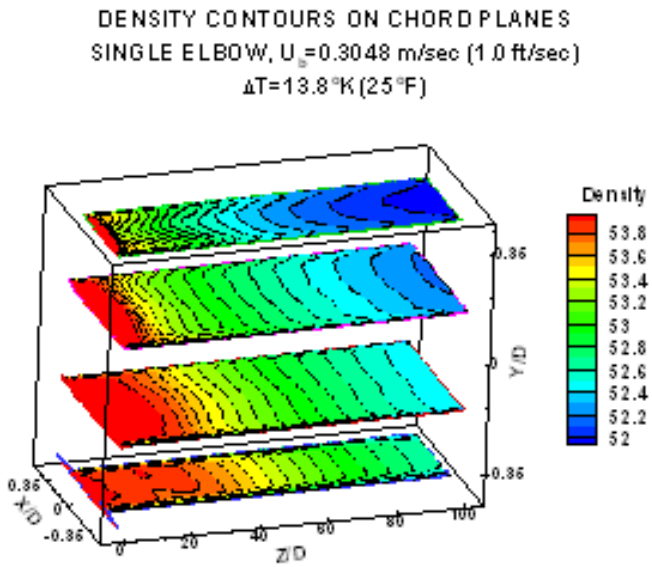

Fig. B-133 Density Slice Contours
V_0=0.3048 m/sec, ΔT_{wall}=13.8°K

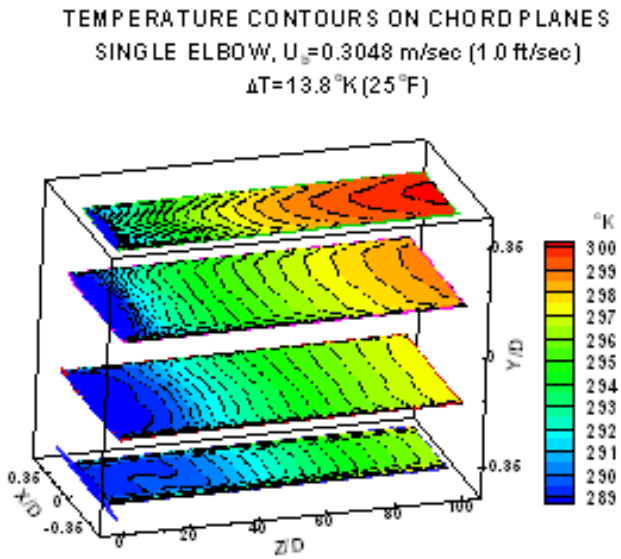

Fig. B-134 Temperature Slice Contours
V_0=0.3048 m/sec, ΔT_{wall}=13.8°K

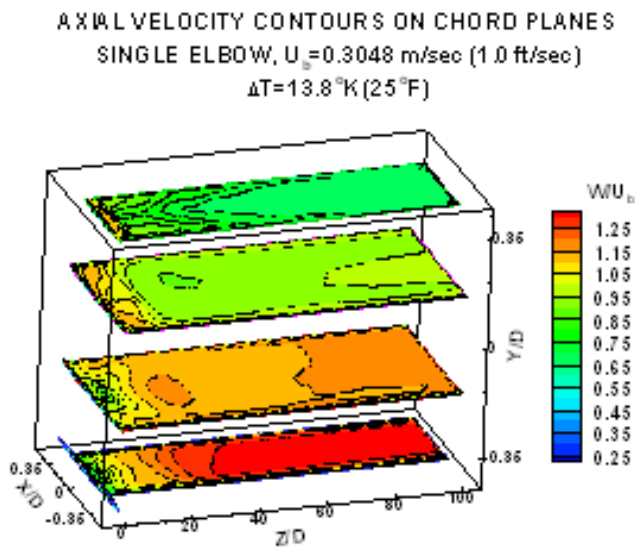

Fig. B-135 Axial Velocity Slice Contours
V_0=0.3048 m/sec, ΔT_{wall}=13.8°K

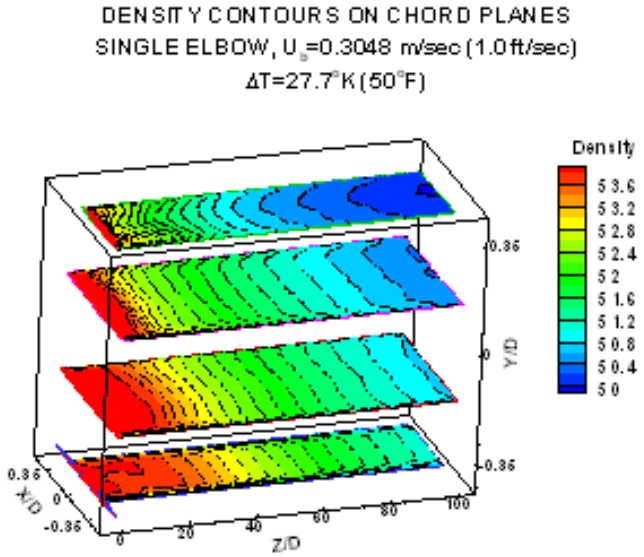

Fig. B-136 Density Slice Contours
V_0=0.3048 m/sec, ΔT_{wall}=27.7°K

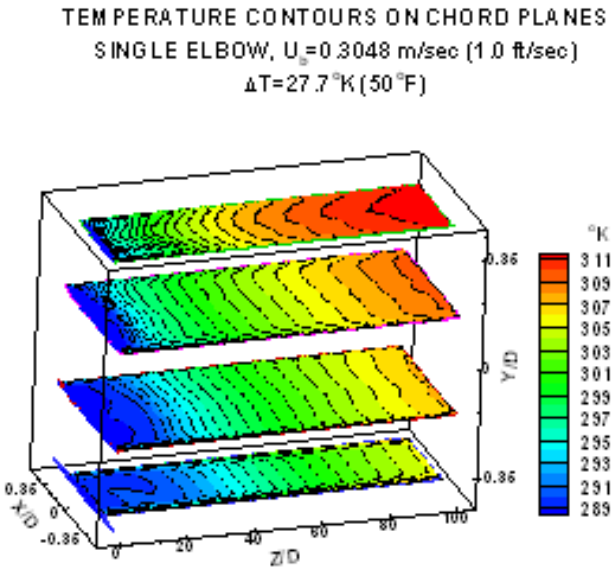

Fig. B-137 Temperature Slice Contours
V_0=0.3048 m/sec, ΔT_{wall}=27.7°K

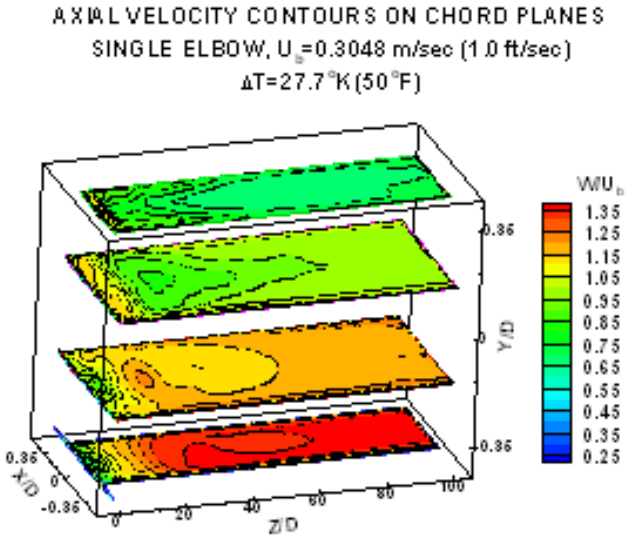

Fig. B-138 Axial Velocity Slice Contours
V_0=0.3048 m/sec, ΔT_{wall}=27.7°K

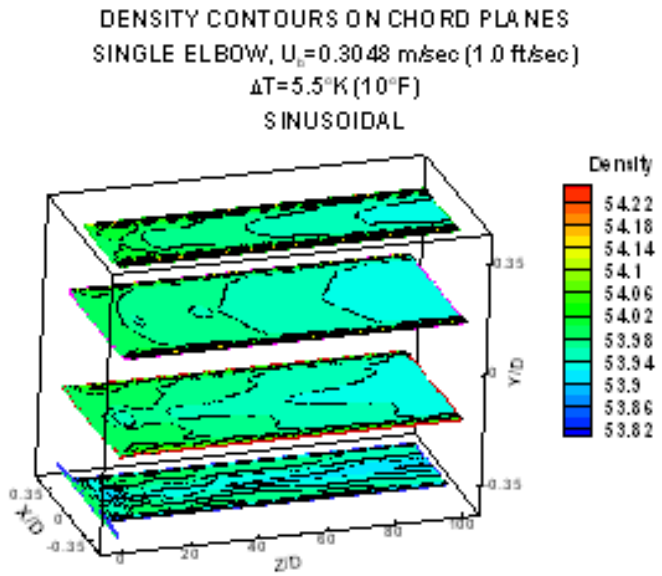

Fig. B-139 Density Slice Contours
V_0=0.3048 m/sec, ΔT_{wall}=-5.5°K Sinusoidal

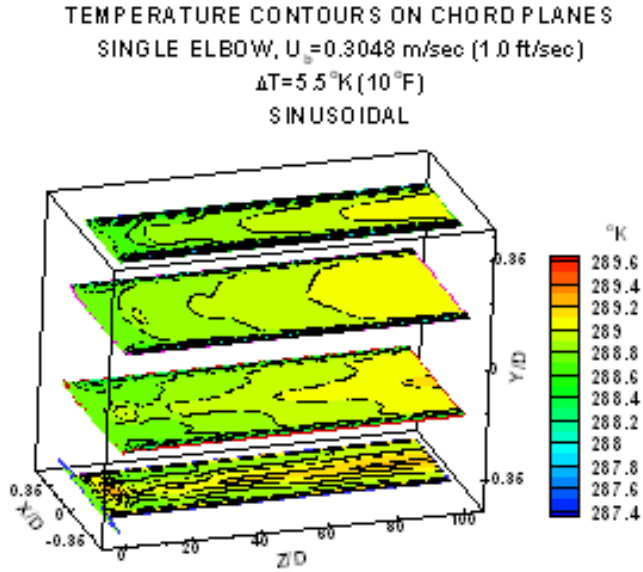

Fig. B-140 Temperature Slice Contours
V_0=0.3048 m/sec, ΔT_{wall}=-5.5°K Sinusoidal

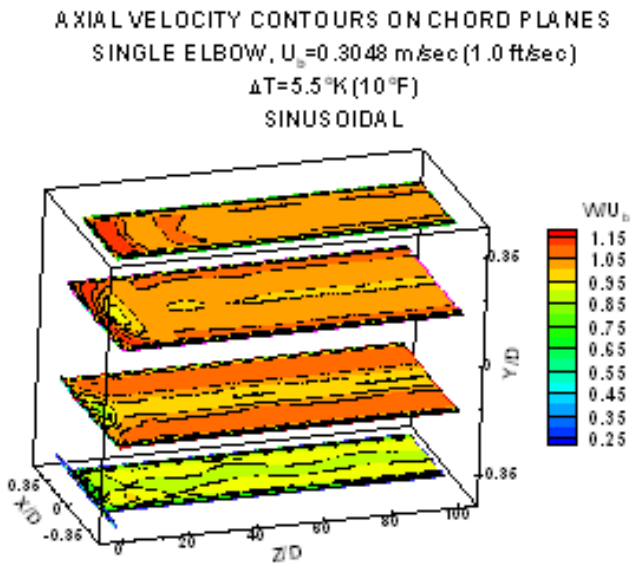

Fig. B-141 Axial Velocity Slice Contours
V_0=0.3048 m/sec, ΔT_{wall}=-5.5°K Sinusoidal

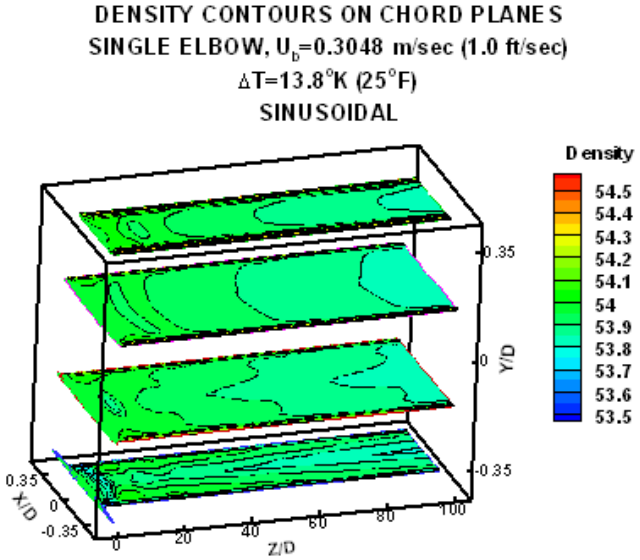

Fig. B-142 Density Slice Contours
V_0=0.3048 m/sec, ΔT_{wall}=-13.8°K Sinusoidal

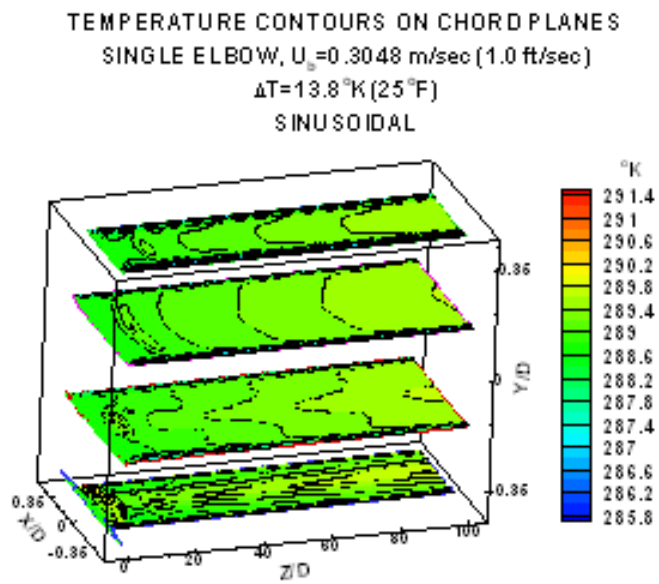

Fig. B-143 Temperature Slice Contours
V_0=0.3048 m/sec, ΔT_{wall}=-13.8°K Sinusoidal

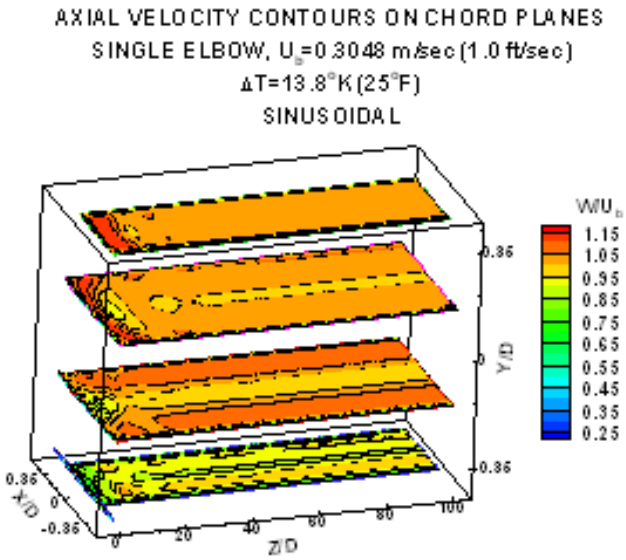

Fig. B-144 Axial Velocity Slice Contours
V_0=0.3048 m/sec, ΔT_{wall}=-13.8°K Sinusoidal

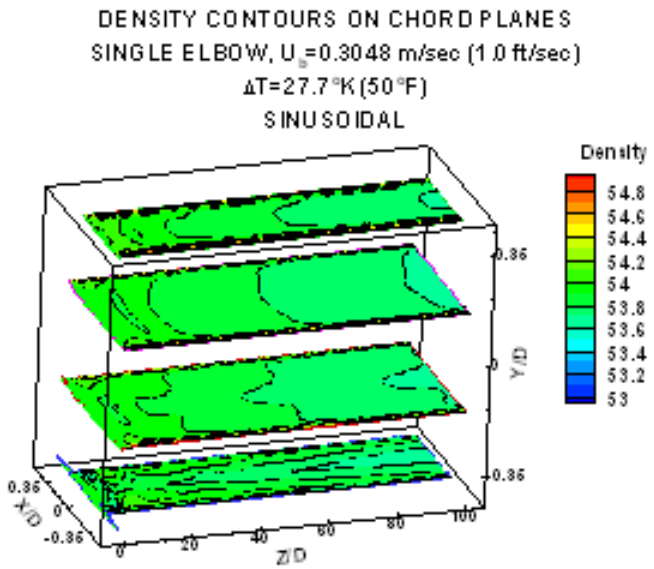

Fig. B-145 Density Slice Contours
V_0=0.3048 m/sec, ΔT_{wall}=-27.7°K Sinusoidal

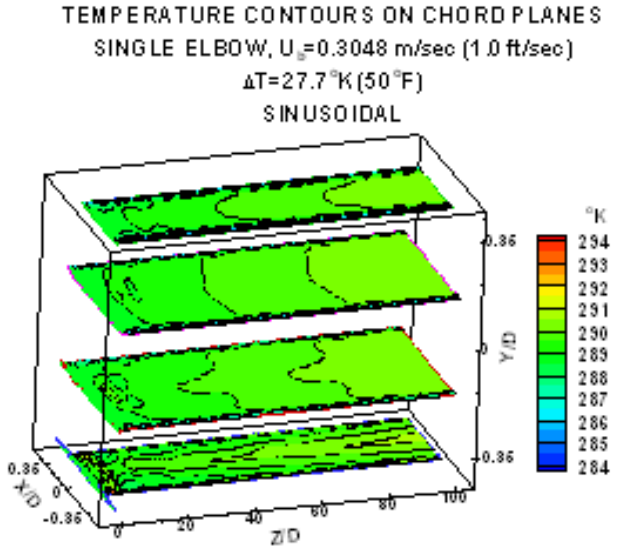

Fig. B-146 Temperature Slice Contours
V_0=0.3048 m/sec, ΔT_{wall}=-27.7°K Sinusoidal

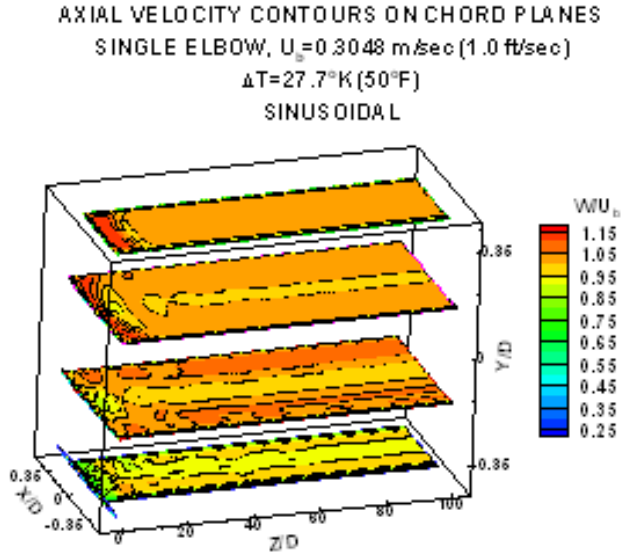

Fig. B-147 Axial Velocity Slice Contours
V_0=0.3048 m/sec, ΔT_{wall}=-27.7°K Sinusoidal

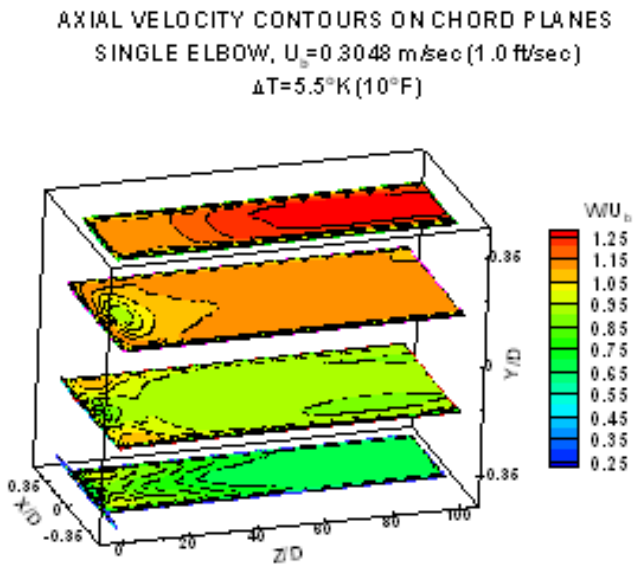

Fig. B-148 Density Slice Contours
V_0=0.3048 m/sec, ΔT_{wall}=-5.5°K

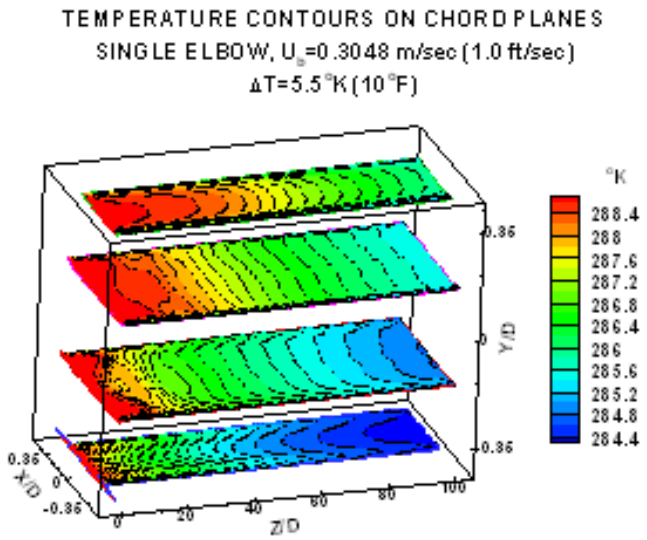

Fig. B-149 Temperature Slice Contours
V_0=0.3048 m/sec, ΔT_{wall}=-5.5°K

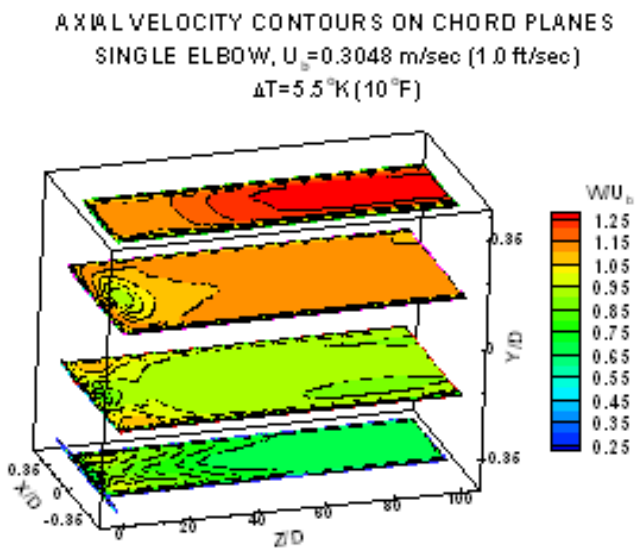

Fig. B-150 Axial Velocity Slice Contours
V_0=0.3048 m/sec, ΔT_{wall}=-5.5°K

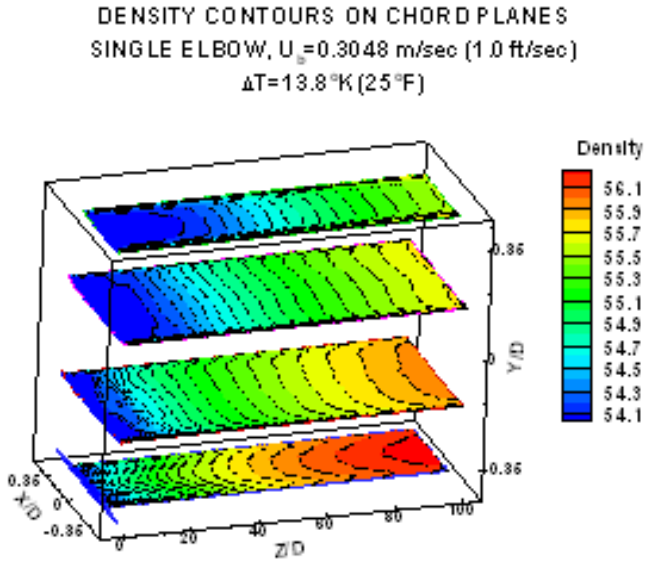

Fig. B-151 Density Slice Contours
V_0=0.3048 m/sec, ΔT_{wall}=-13.8°K

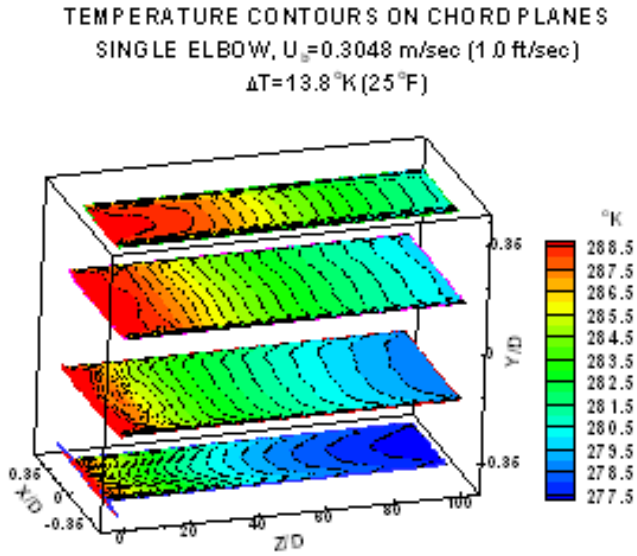

Fig. B-152 Temperature Slice Contours
V_0=0.3048 m/sec, ΔT_{wall}=-13.8°K

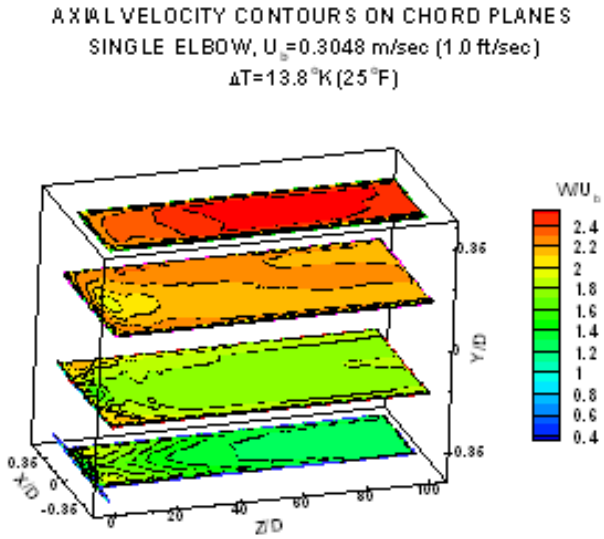

Fig. B-153 Axial Velocity Slice Contours
V_0=0.3048 m/sec, ΔT_{wall}=-13.8°K

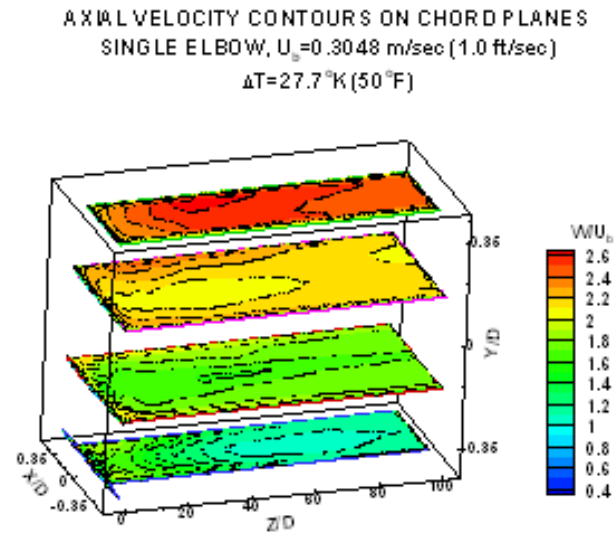

Fig. B-154 Density Slice Contours
V_0=0.3048 m/sec, ΔT_{wall}=-27.7°K

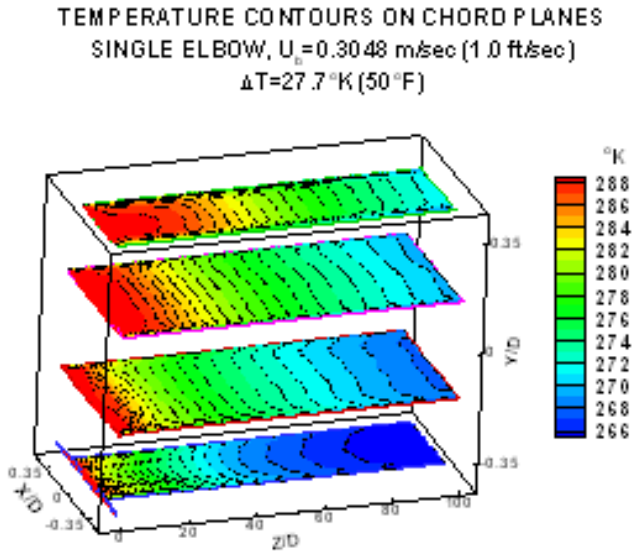

Fig. B-155 Temperature Slice Contours
V_0=0.3048 m/sec, ΔT_{wall}=-27.7°K

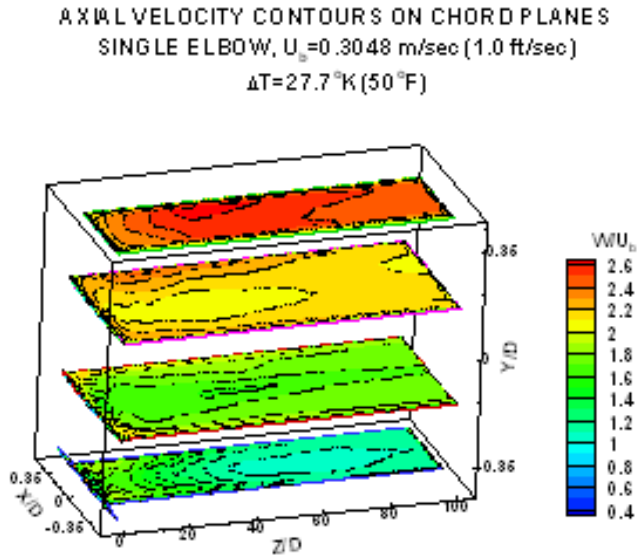

Fig. B-156 Axial Velocity Slice Contours
V_0=0.3048 m/sec, ΔT_{wall}=-27.7°K

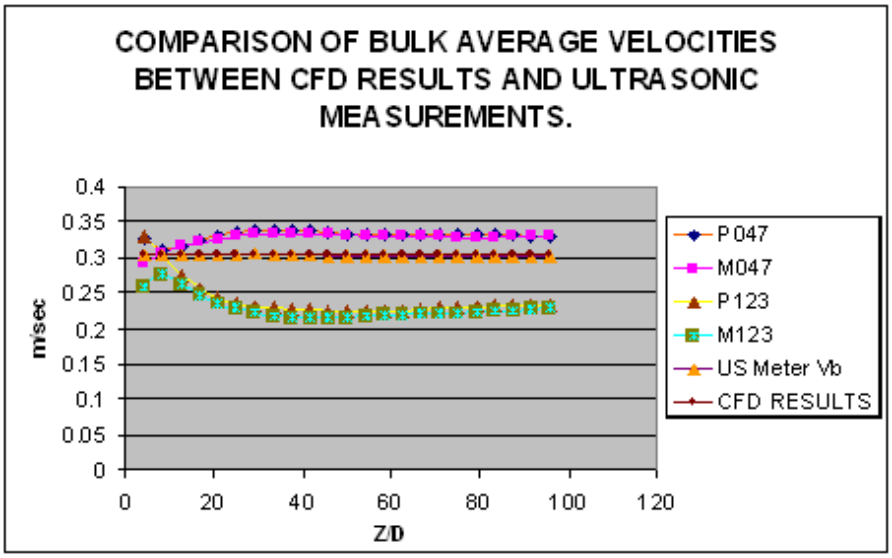

Fig. B-157 Comparison between CFD Vb and Ultrasonic Vb.
V_0=0.3048 m/sec, ΔT_{wall}=5.5°K Sinusoidal

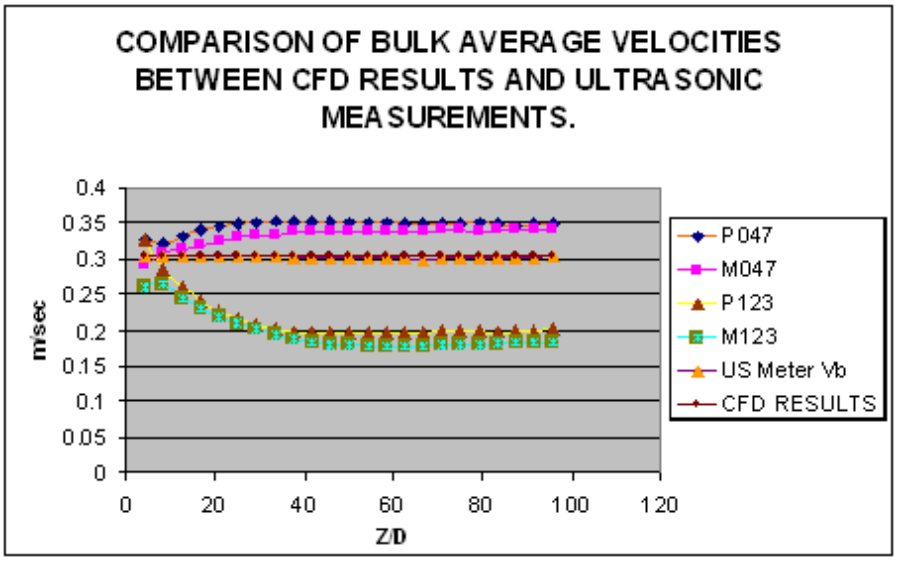

Fig. B-158 Comparison between CFD Vb and Ultrasonic Vb.
V_0=0.3048 m/sec, ΔT_{wall}=13.8°K Sinusoidal

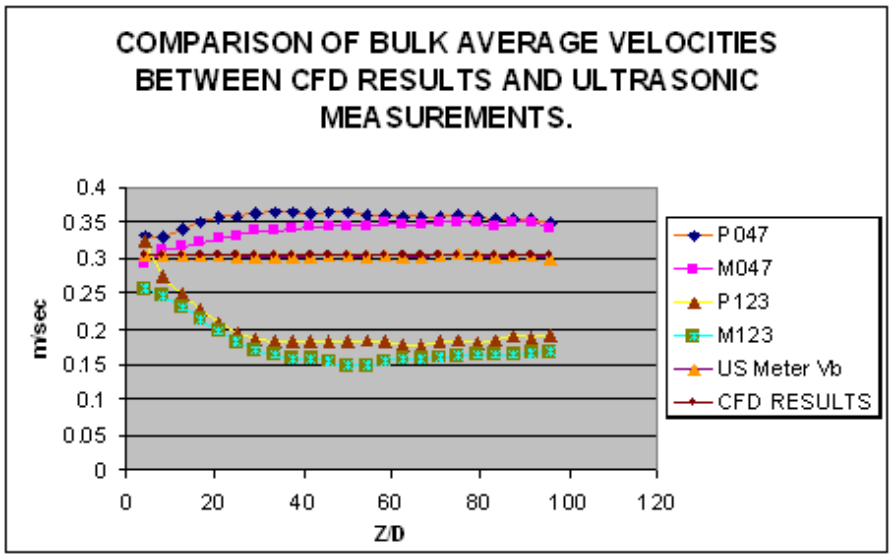

Fig. B-159 Comparison between CFD Vb and Ultrasonic Vb.
V_0=0.3048 m/sec, ΔT_{wall}=27.7°K Sinusoidal

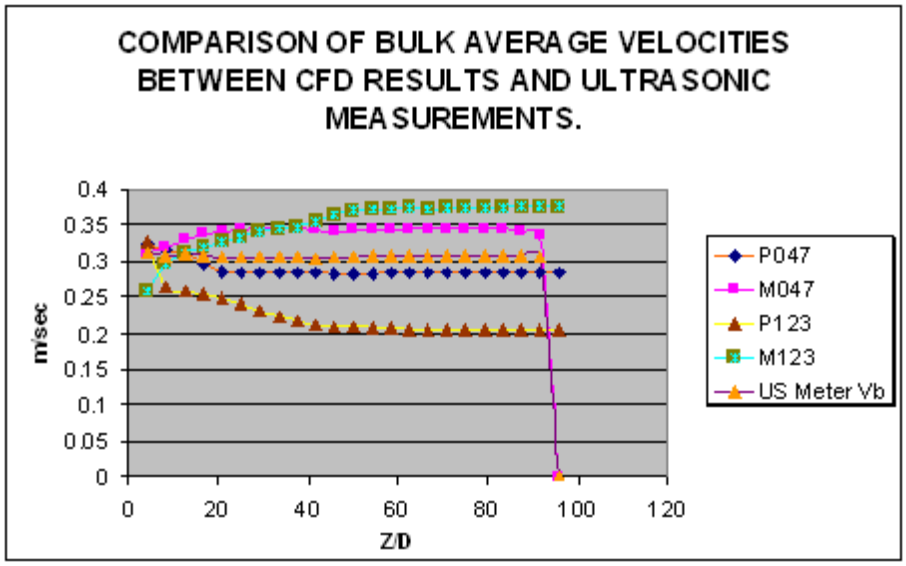

Fig. B-160 Comparison between CFD Vb and Ultrasonic Vb.
V_0=0.3048 m/sec, ΔT_{wall}=5.5°K

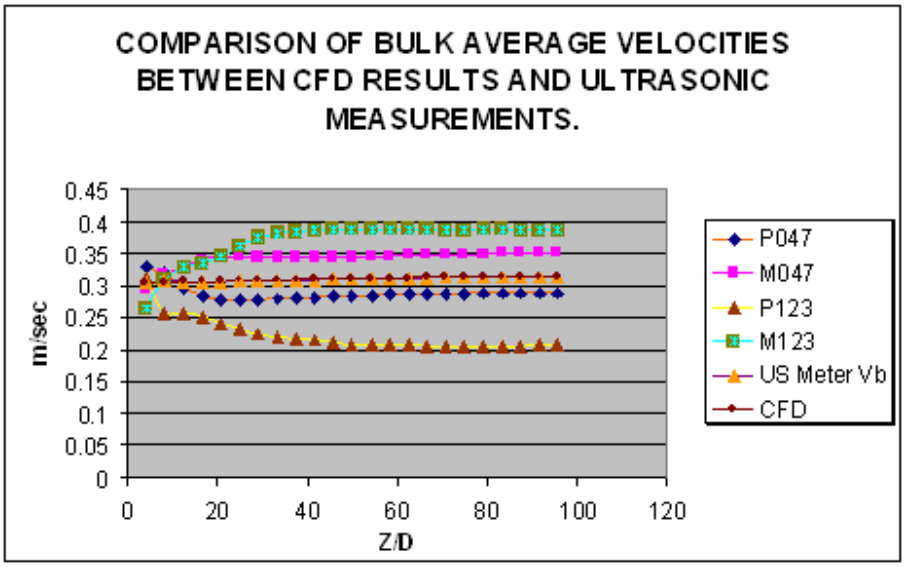

Fig. B-161 Comparison between CFD Vb and Ultrasonic Vb.
V_0=0.3048 m/sec, ΔT_{wall}=13.8°K

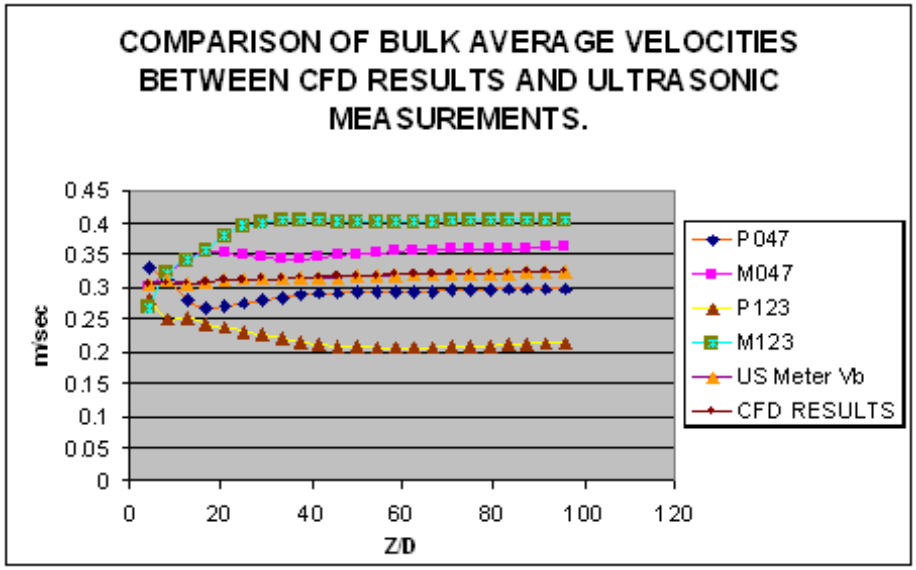

Fig. B-162 Comparison between CFD Vb and Ultrasonic Vb.
V_0=0.3048 m/sec, ΔT_{wall}=27.7°K

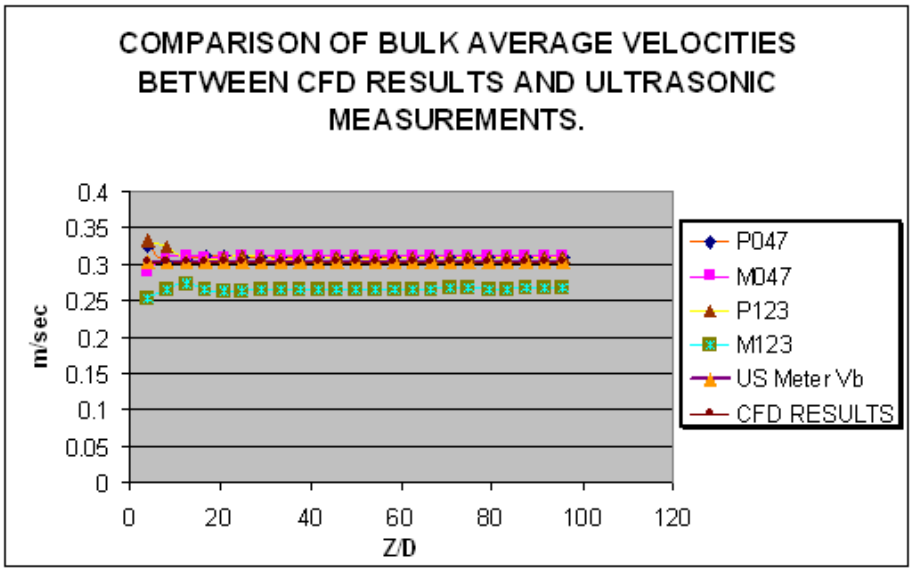

V_0=0.3048 m/sec, ΔT_{wall}=-5.5°K Sinusoidal

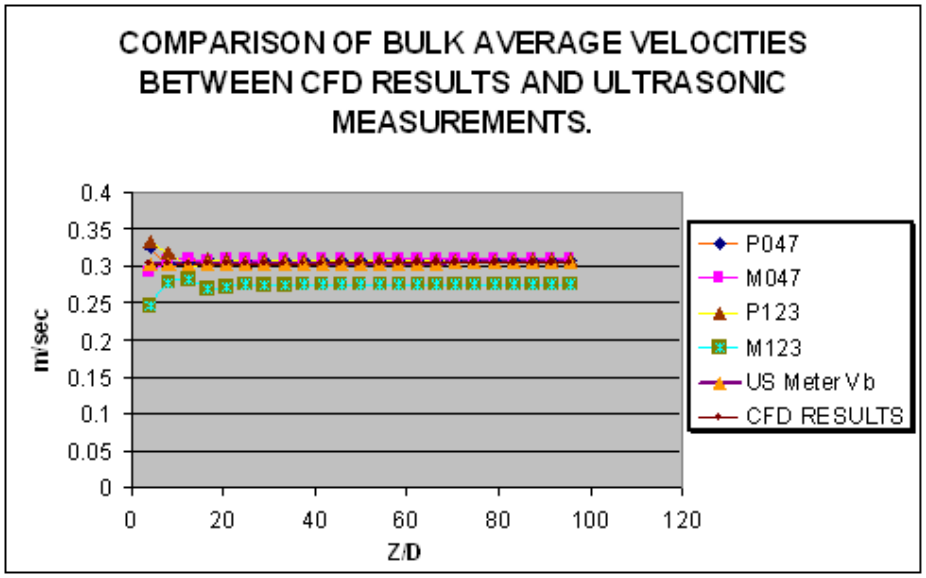

V_0=0.3048 m/sec, ΔT_{wall}=-13.8°K Sinusoidal

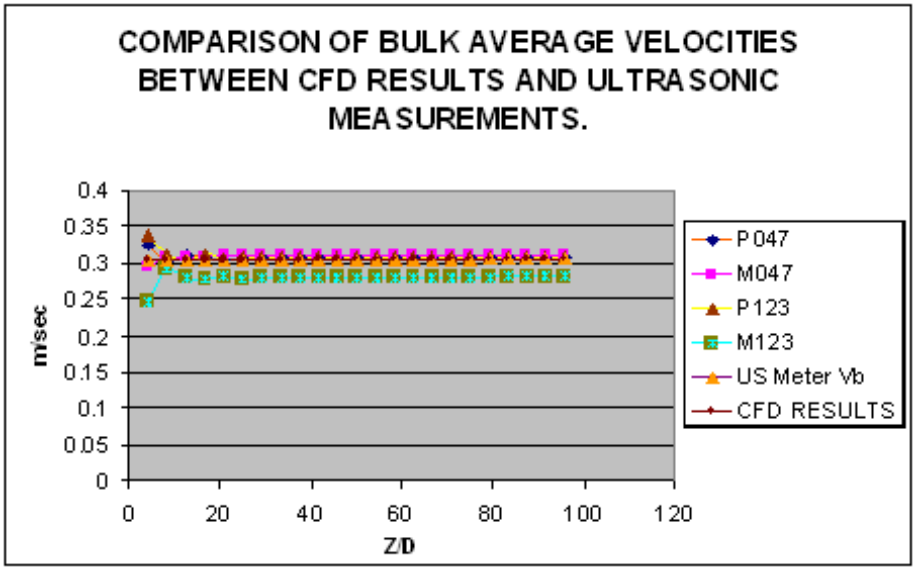

Fig. B-165 Comparison between CFD Vb and Ultrasonic Vb.
V_0=0.3048 m/sec, ΔT_{wall}=-27.7°K Sinusoidal

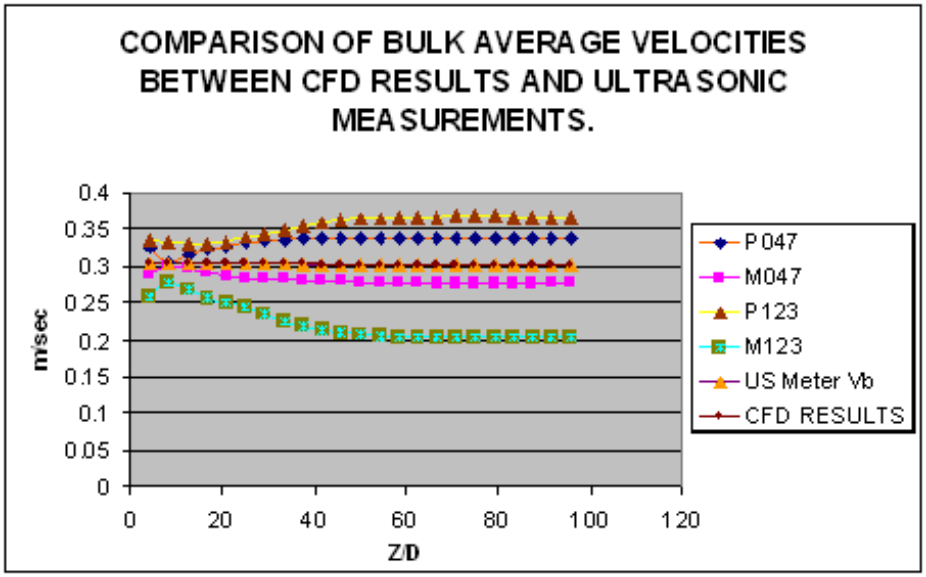

Fig. B-166 Comparison between CFD Vb and Ultrasonic Vb.
V_0=0.3048 m/sec, ΔT_{wall}=-5.5°K

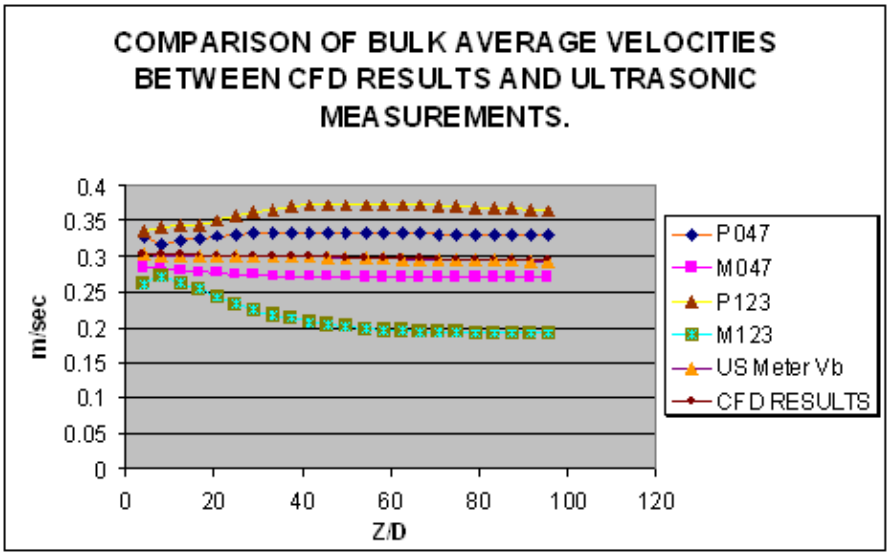

Fig. B-167 Comparison between CFD Vb and Ultrasonic Vb.
V_0=0.3048 m/sec, ΔT_{wall}=-13.8°K

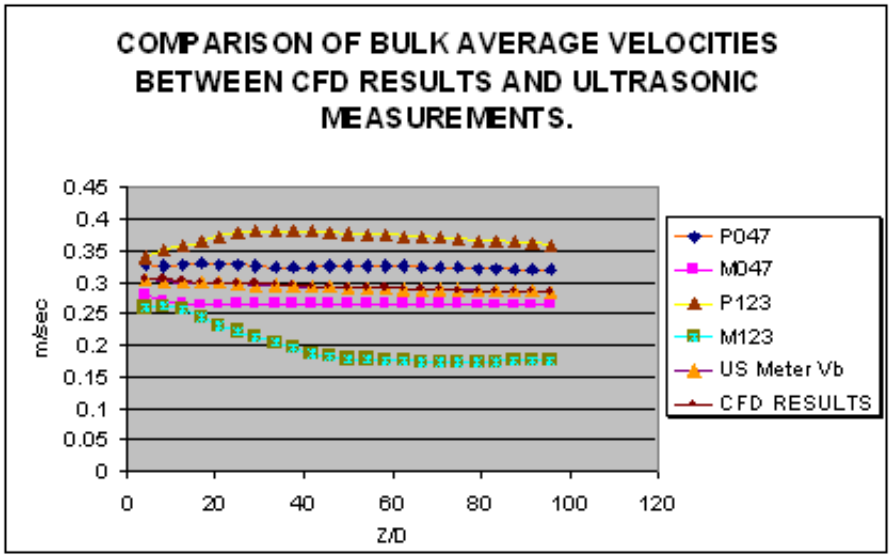

Fig. B-168 Comparison between CFD Vb and Ultrasonic Vb.
V_0=0.3048 m/sec, ΔT_{wall}=-27.7°K

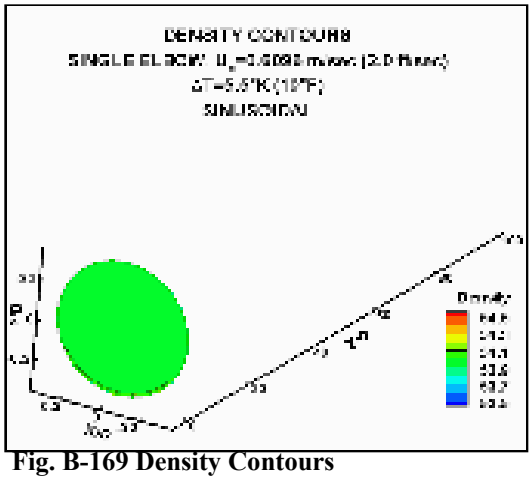

Fig. B-169 Density Contours
V_0=0.6096 m/sec, ΔT_{wall}=5.5°K Sinusoidal

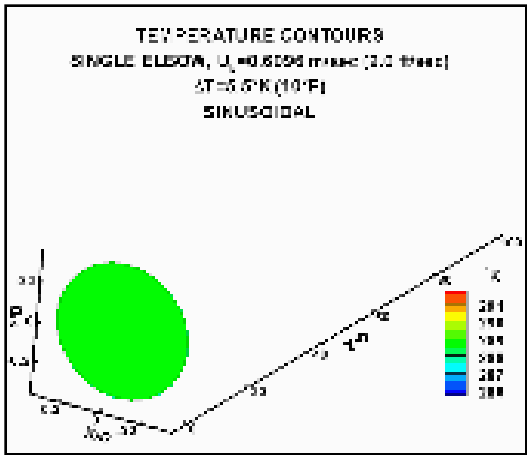

Fig. B-170 Temperature Contours
V_0=0.6096 m/sec, ΔT_{wall}=5.5°K Sinusoidal

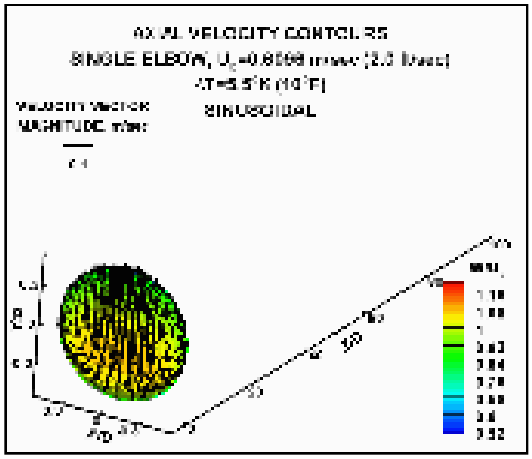

Fig. B-171 Axial Velocity Contours
V_0=0.6096 m/sec, ΔT_{wall}=5.5°K Sinusoidal

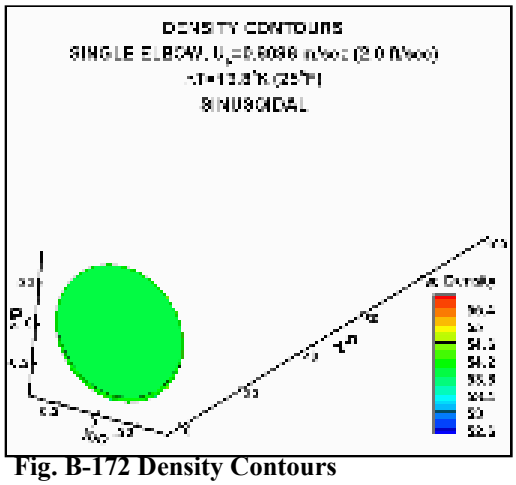

Fig. B-172 Density Contours
V_0=0.6096 m/sec, ΔT_{wall}=13.8°K Sinusoidal

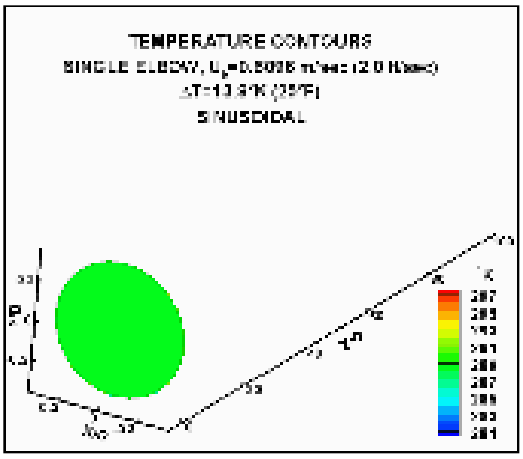

Fig. B-173 Temperature Contours
V_0=0.6096 m/sec, ΔT_{wall}=13.8°K Sinusoidal

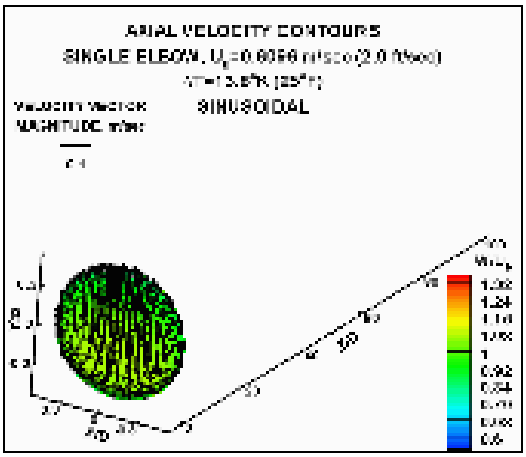

Fig. B-174 Axial Velocity Contours
V_0=0.6096 m/sec, ΔT_{wall}=13.8°K Sinusoidal

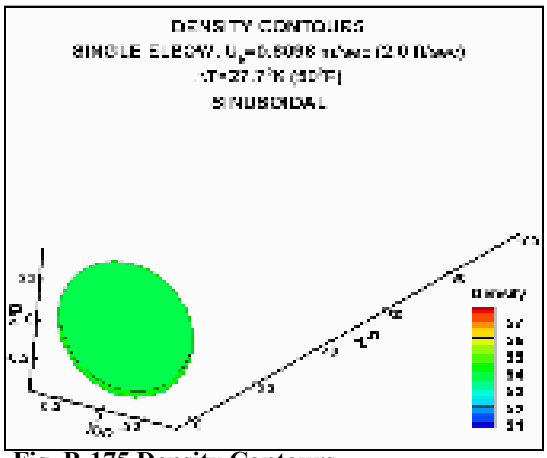

Fig. B-175 Density Contours
V_0=0.6096 m/sec, ΔT_{wall}=27.7°K Sinusoidal

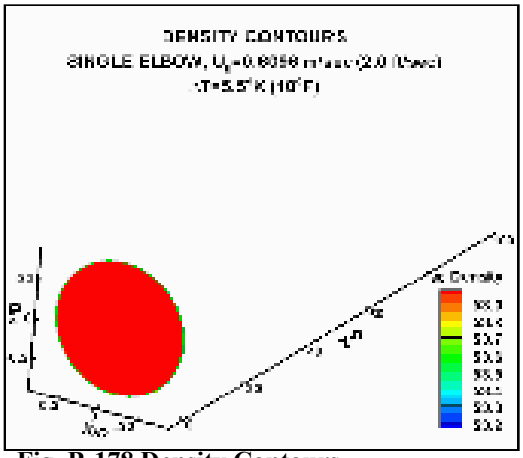

Fig. B-178 Density Contours
V_0=0.6096 m/sec, ΔT_{wall}=5.5°K

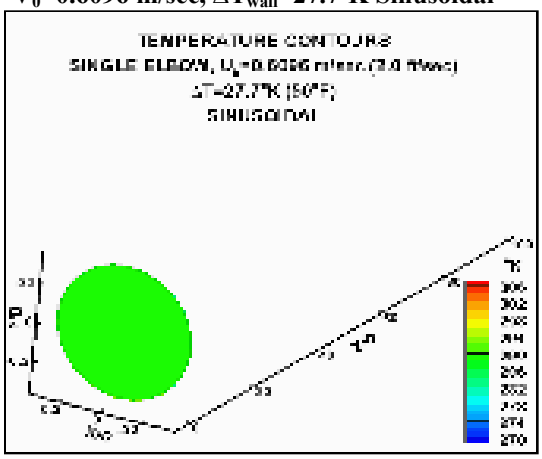

Fig. B-176 Temperature Contours
V_0=0.6096 m/sec, ΔT_{wall}=27.7°K Sinusoidal

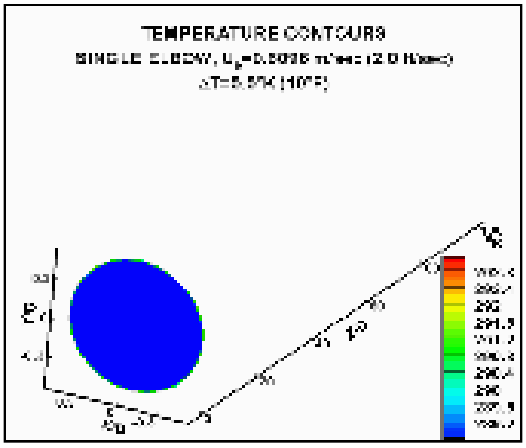

Fig. B-179 Temperature Contours
V_0=0.6096 m/sec, ΔT_{wall}=5.5°K

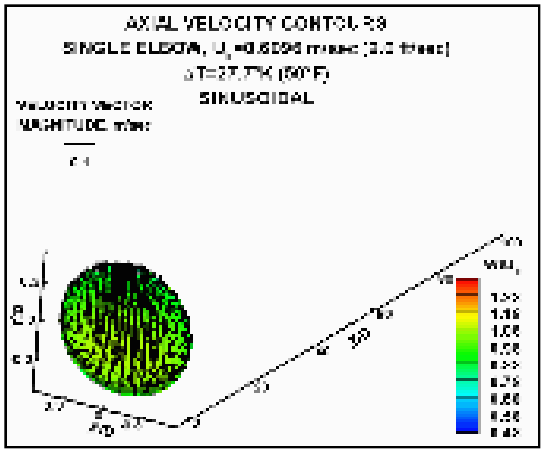

Fig. B-177 Axial Velocity Contours
V_0=0.6096 m/sec, ΔT_{wall}=27.7°K Sinusoidal

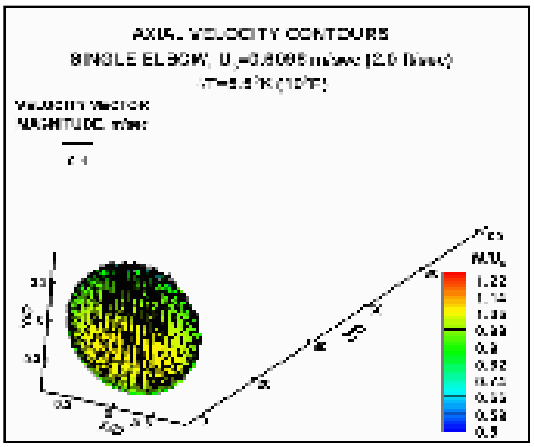

Fig. B-180 Axial Velocity Contours
V_0=0.6096 m/sec, ΔT_{wall}=5.5°K

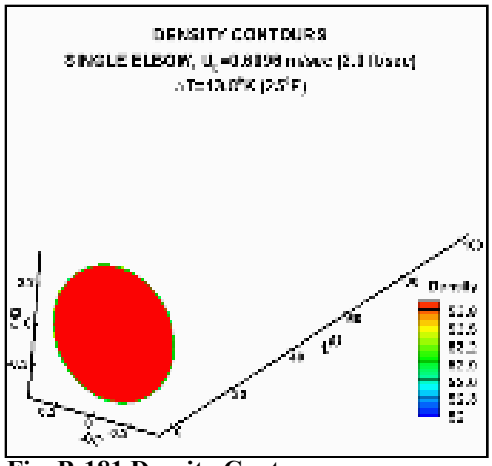

Fig. B-181 Density Contours
V_0=0.6096 m/sec, ΔT_{wall}=13.8°K

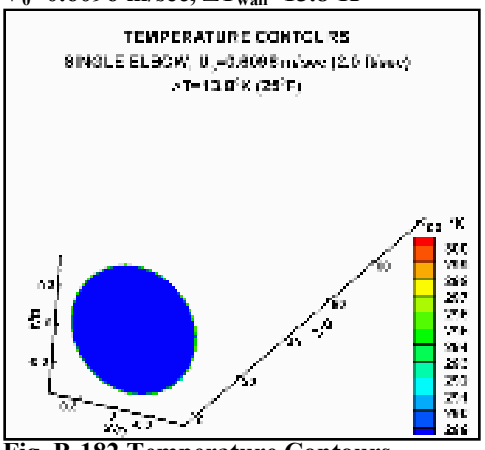

Fig. B-182 Temperature Contours
V_0=0.6096 m/sec, ΔT_{wall}=13.8°K

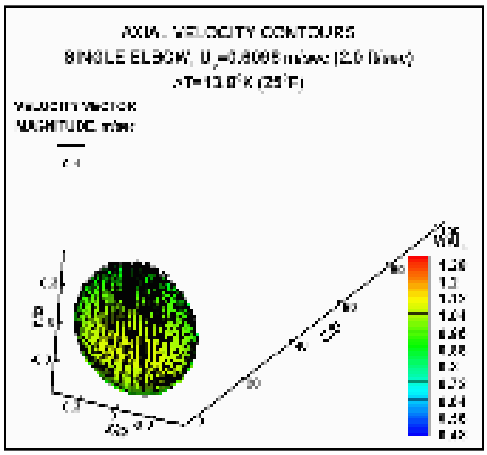

Fig. B-183 Axial Velocity Contours
V_0=0.6096 m/sec, ΔT_{wall}=13.8°K

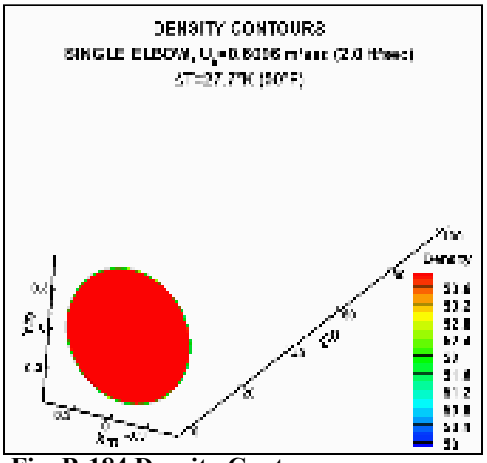

Fig. B-184 Density Contours
V_0=0.6096 m/sec, ΔT_{wall}=27.7°K

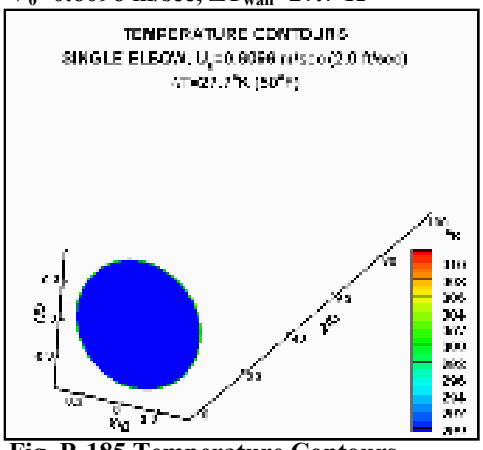

Fig. B-185 Temperature Contours
V_0=0.6096 m/sec, ΔT_{wall}=27.7°K

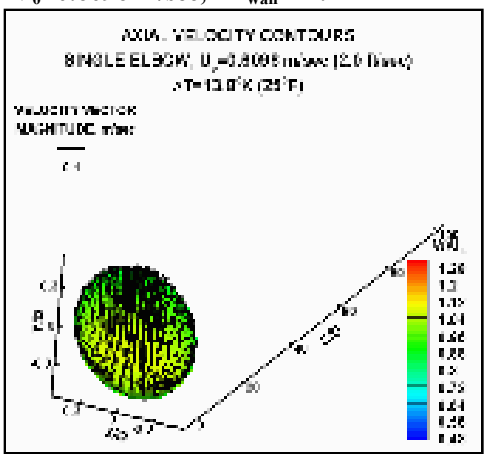

Fig. B-186 Axial Velocity Contours
V_0=0.6096 m/sec, ΔT_{wall}=27.7°K

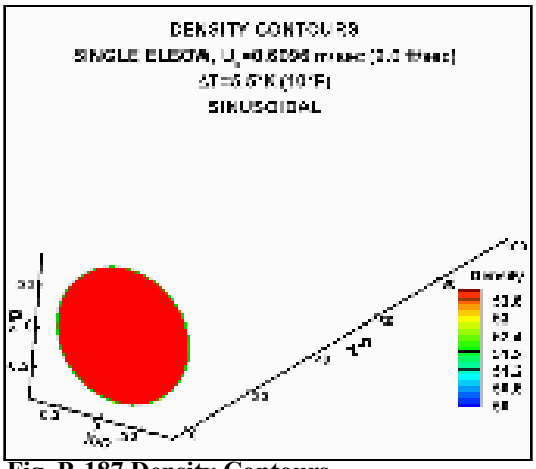

Fig. B-187 Density Contours
V_0=0.6096 m/sec, ΔT_{wall}=-5.5°K Sinusoidal

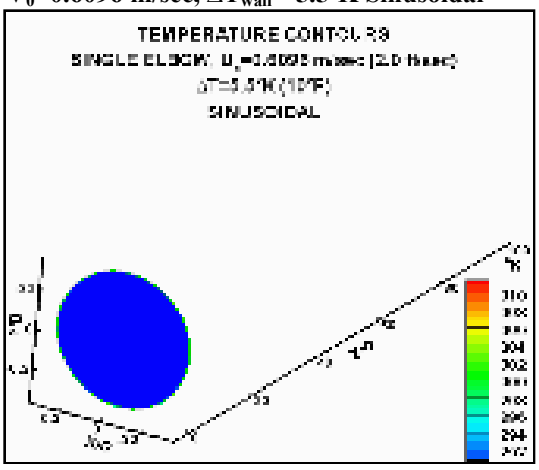

Fig. B-188 Temperature Contours
V_0=0.6096 m/sec, ΔT_{wall}=-5.5°K Sinusoidal

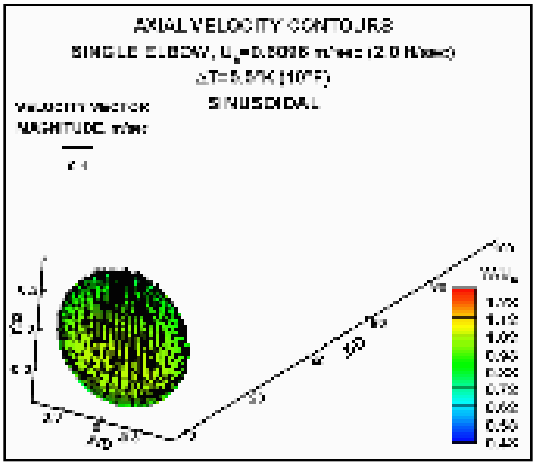

Fig. B-189 Axial Velocity Contours
V_0=0.6096 m/sec, ΔT_{wall}=-5.5°K Sinusoidal

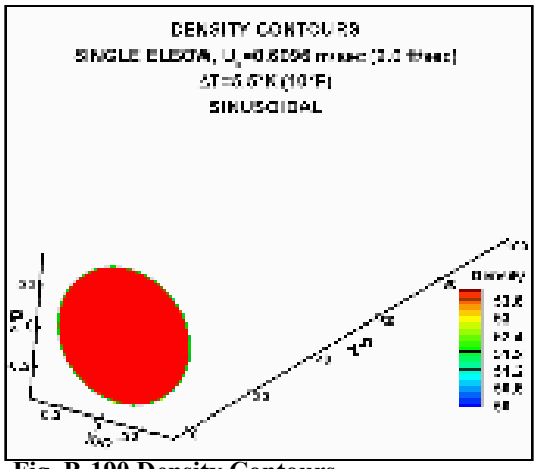

Fig. B-190 Density Contours
V_0=0.6096 m/sec, ΔT_{wall}=-13.8°K Sinusoidal

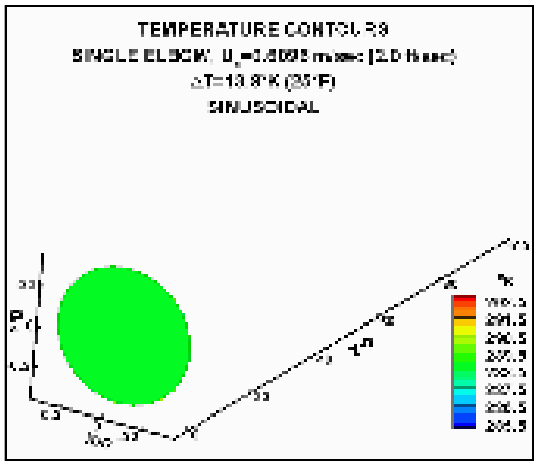

Fig. B-191 Temperature Contours
V_0=0.6096 m/sec, ΔT_{wall}=-13.8°K Sinusoidal

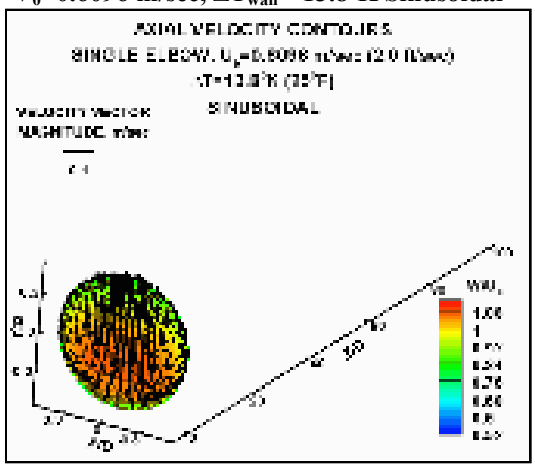

Fig. B-192 Axial Velocity Contours
V_0=0.6096 m/sec, ΔT_{wall}=-13.8°K Sinusoidal

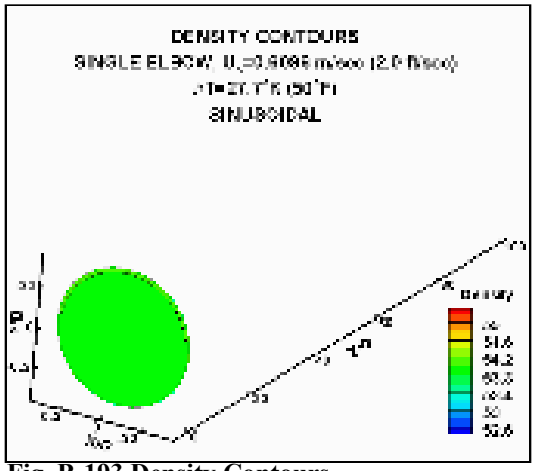

Fig. B-193 Density Contours
V_0=0.6096 m/sec, ΔT_{wall}=-27.7°K Sinusoidal

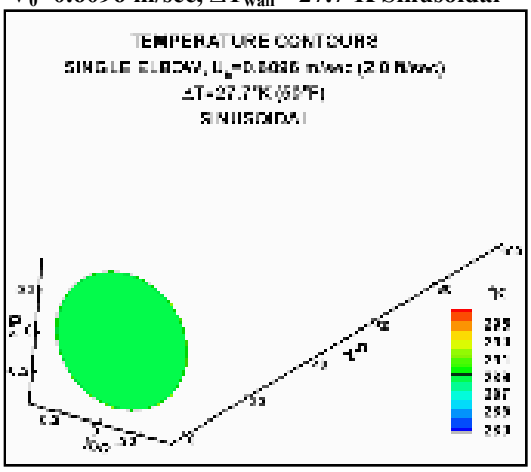

Fig. B-194 Temperature Contours
V_0=0.6096 m/sec, ΔT_{wall}=-27.7°K Sinusoidal

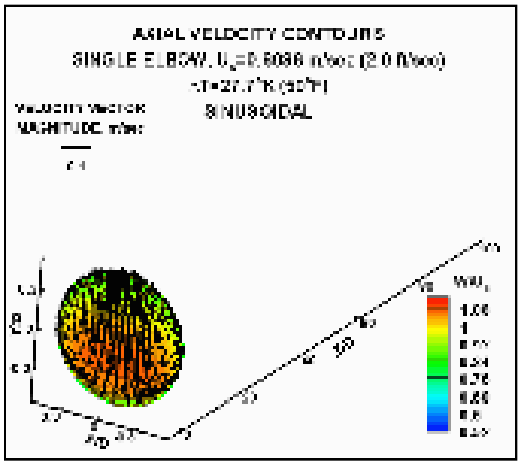

Fig. B-195 Axial Velocity Contours
V_0=0.6096 m/sec, ΔT_{wall}=-27.7°K Sinusoidal

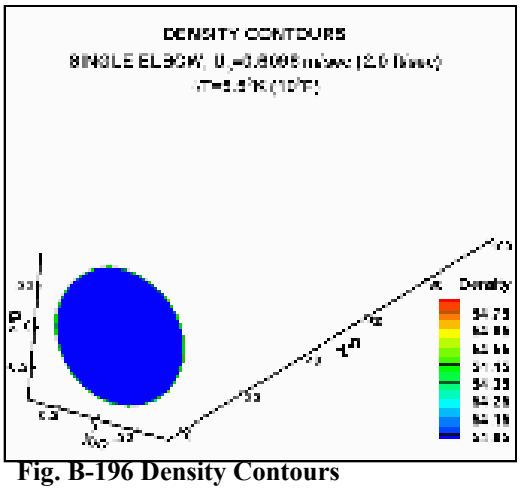

Fig. B-196 Density Contours
V_0=0.6096 m/sec, ΔT_{wall}=-5.5°K

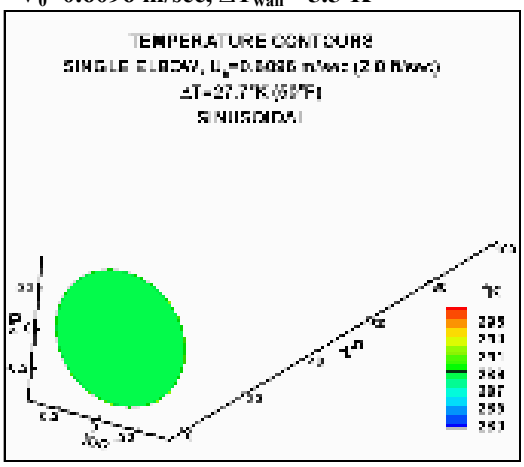

Fig. B-197 Temperature Contours
V_0=0.6096 m/sec, ΔT_{wall}=-5.5°K

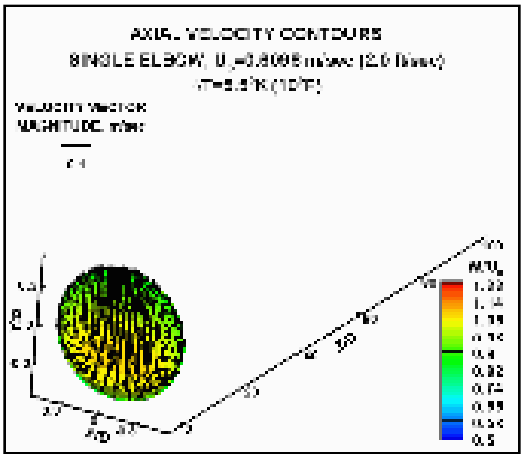

Fig. B-198 Axial Velocity Contours
V_0=0.6096 m/sec, ΔT_{wall}=-5.5°K

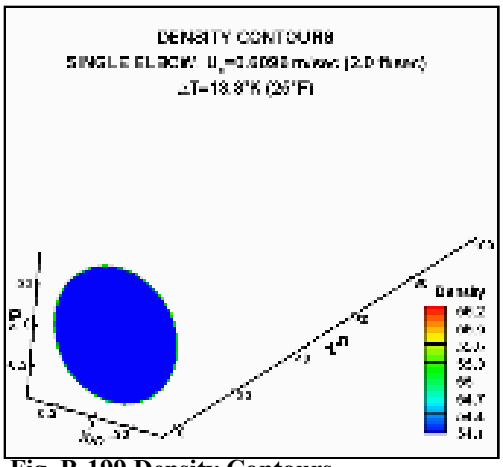

Fig. B-199 Density Contours
V_0=0.6096 m/sec, ΔT_{wall}=-13.8°K

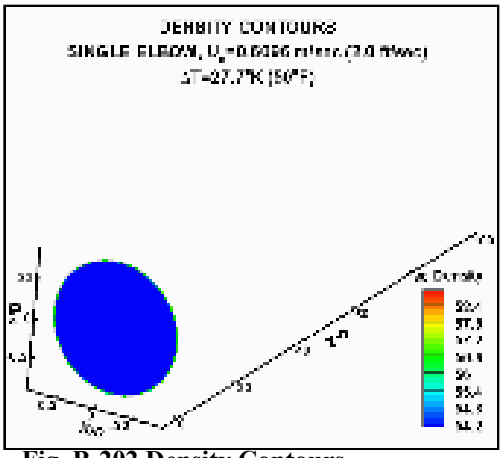

Fig. B-202 Density Contours
V_0=0.6096 m/sec, ΔT_{wall}=-27.7°K

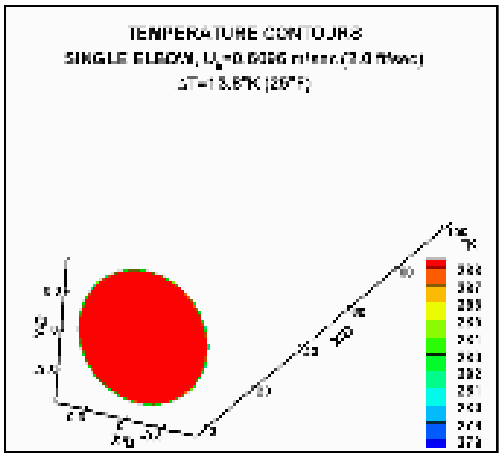

Fig. B-200 Temperature Contours
V_0=0.6096 m/sec, ΔT_{wall}=-13.8°K

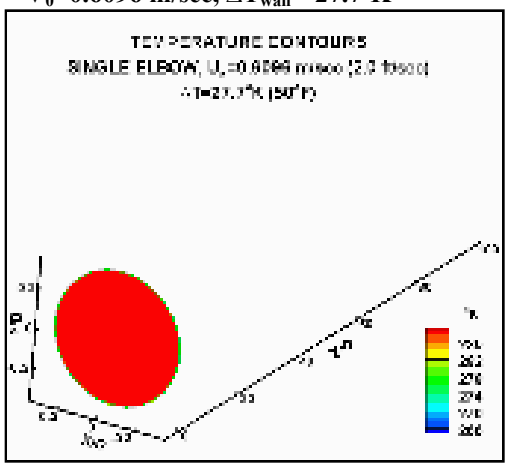

Fig. B-203 Temperature Contours
V_0=0.6096 m/sec, ΔT_{wall}=-27.7°K

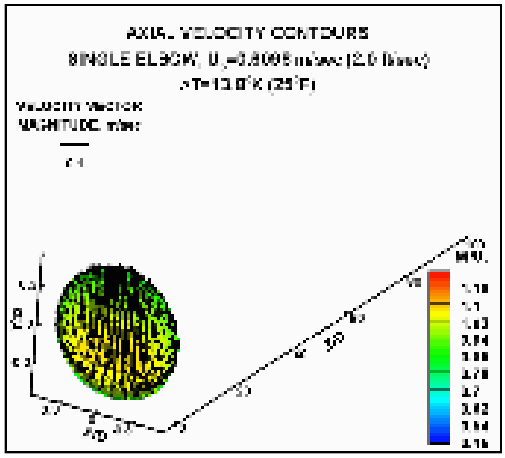

Fig. B-201 Axial Velocity Contours
V_0=0.6096 m/sec, ΔT_{wall}=-13.8°K

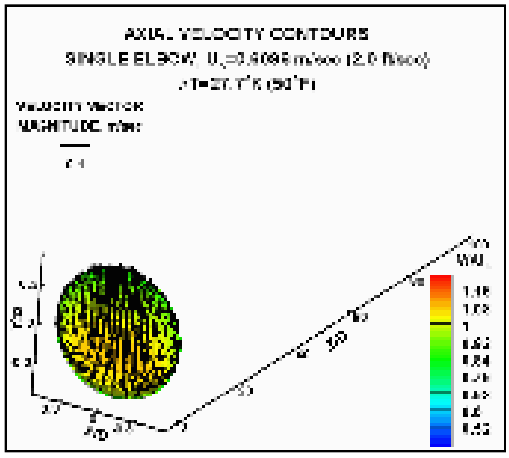

Fig. B-204 Axial Velocity Contours
V_0=0.6096 m/sec, ΔT_{wall}=-27.7°K

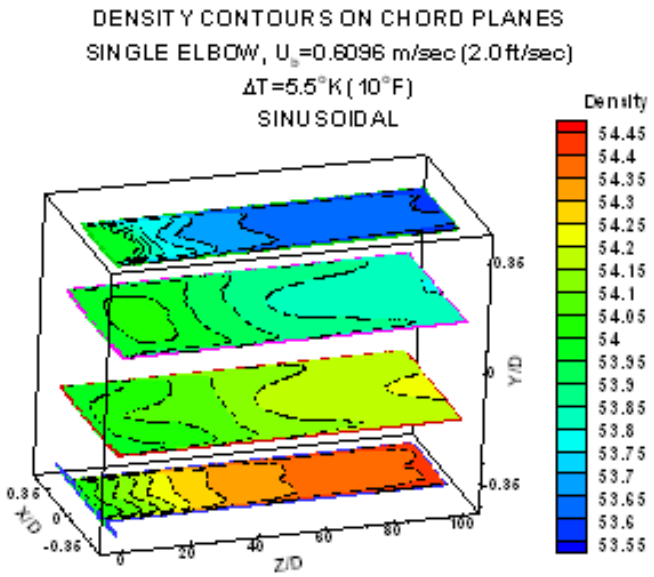

Fig. B-205 Density Slice Contours
V_0=0.6096 m/sec, ΔT_{wall}=5.5°K Sinusoidal

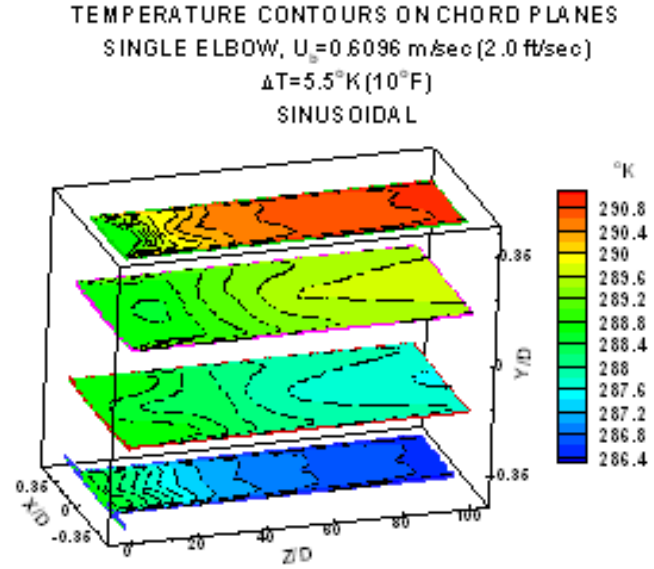

Fig. B-206 Temperature Slice Contours
V_0=0.6096 m/sec, ΔT_{wall}=5.5°K Sinusoidal

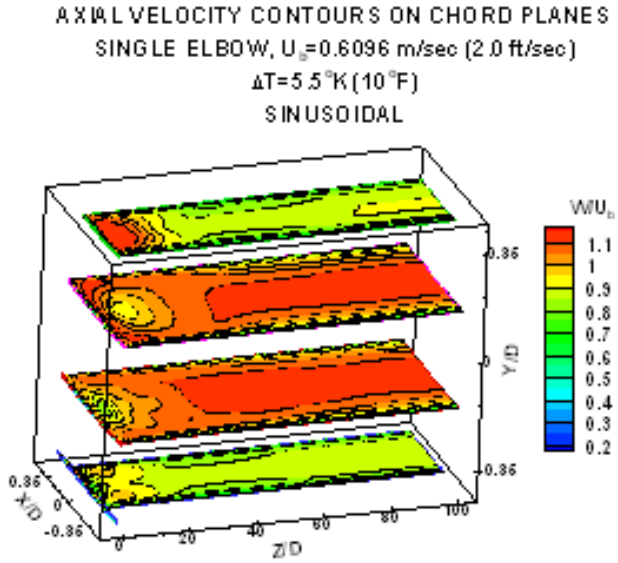

Fig. B-207 Axial Velocity Slice Contours
V_0=0.6096 m/sec, ΔT_{wall}=5.5°K Sinusoidal

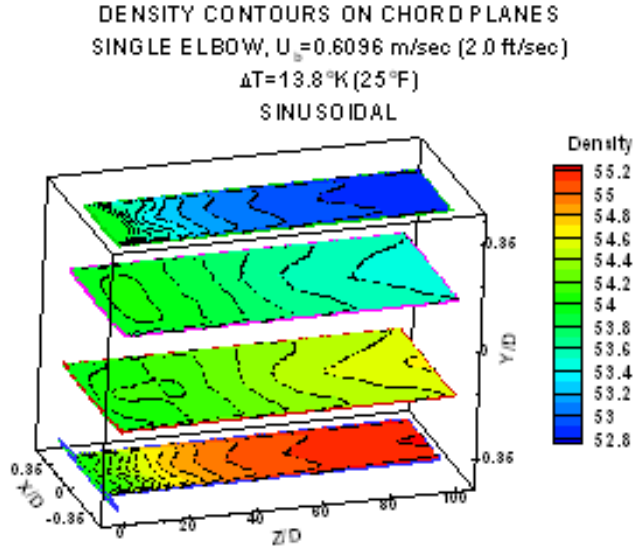

Fig. B-208 Density Slice Contours
V_0=0.6096 m/sec, ΔT_{wall}=13.8°K Sinusoidal

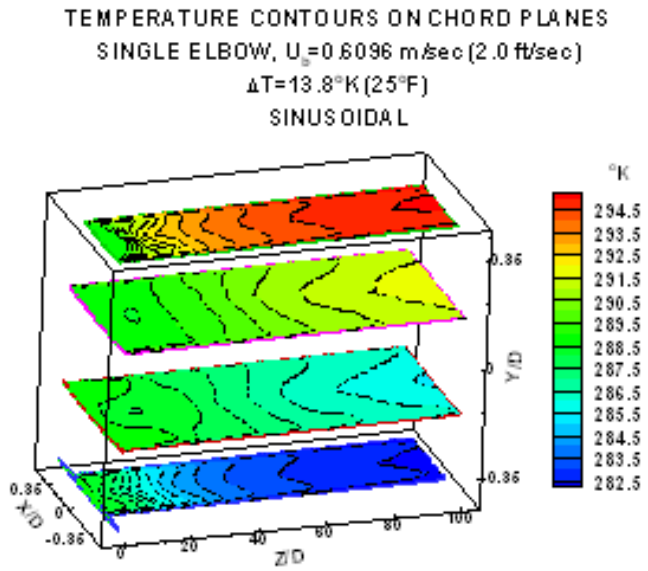

Fig. B-251 Comparison between CFD Vb and Ultrasonic Vb.
V_0=0.6096 m/sec, ΔT_{wall}=-13.8°K

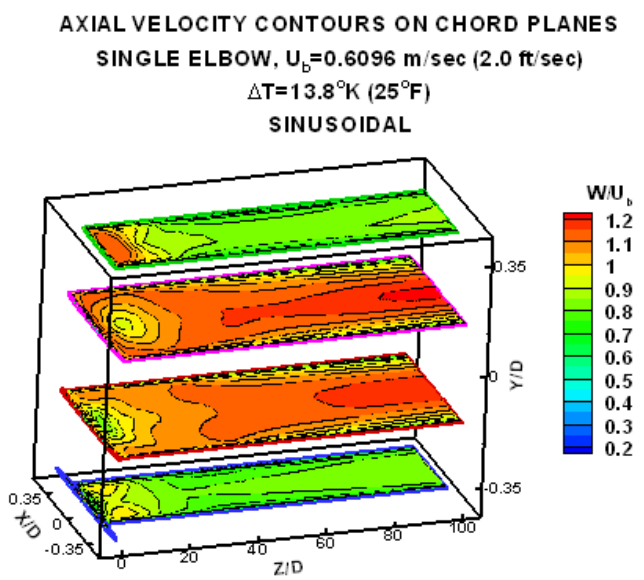

Fig. B-252 Comparison between CFD Vb and Ultrasonic Vb.
V_0=0.6096 m/sec, ΔT_{wall}=-27.7°K

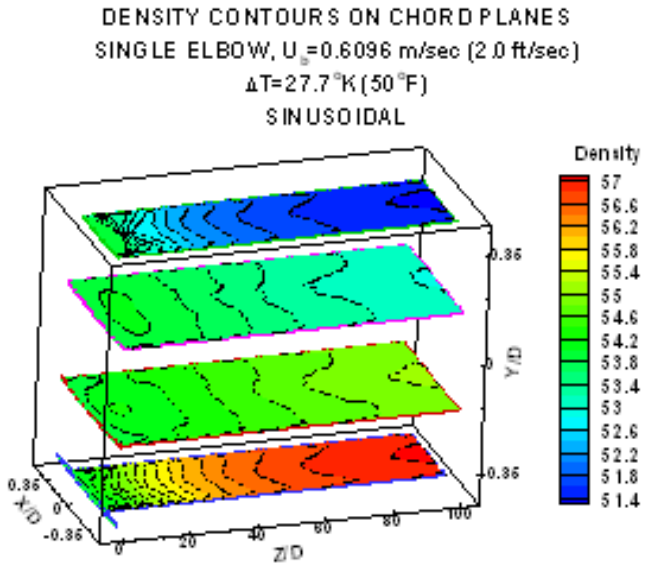

Fig. B-211 Density Slice Contours
V_0=0.6096 m/sec, ΔT_{wall}=27.7°K Sinusoidal

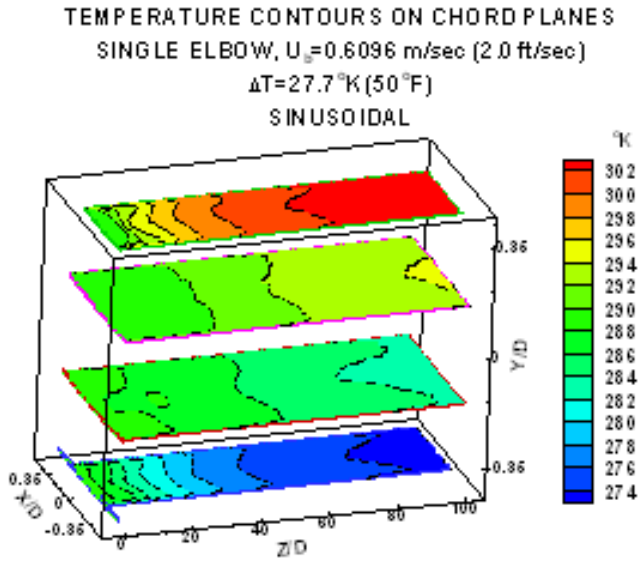

Fig. B-212 Temperature Slice Contours
V_0=0.6096 m/sec, ΔT_{wall}=27.7°K Sinusoidal

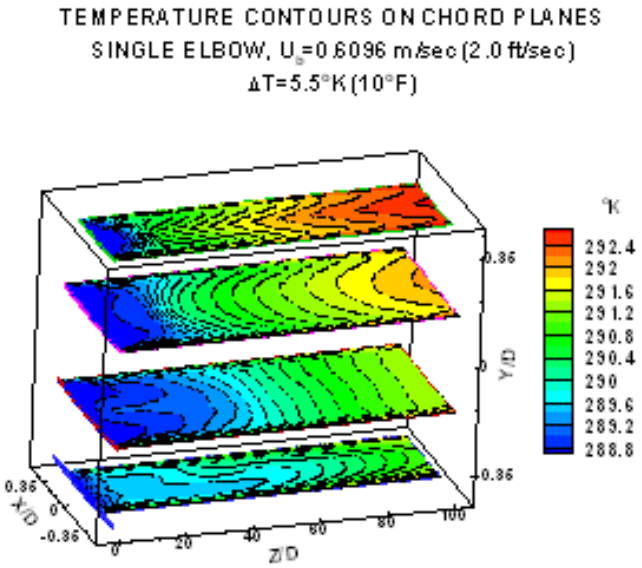

Fig. B-215 Temperature Slice Contours
V_0=0.6096 m/sec, ΔT_{wall}=5.5°K

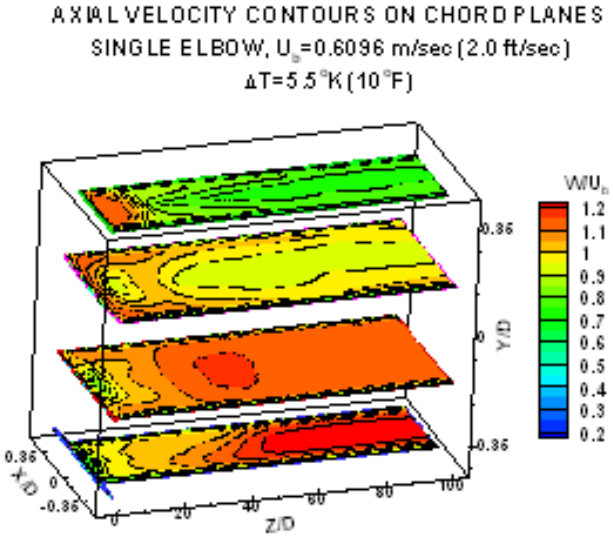

Fig. B-216 Axial Velocity Slice Contours
V_0=0.6096 m/sec, ΔT_{wall}=5.5°K

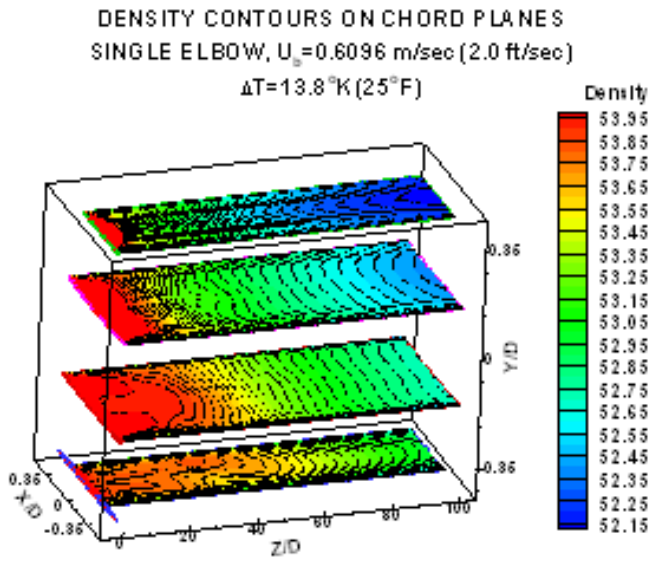

Fig. B-217 Density Slice Contours
V_0=0.6096 m/sec, ΔT_{wall}=13.8°K

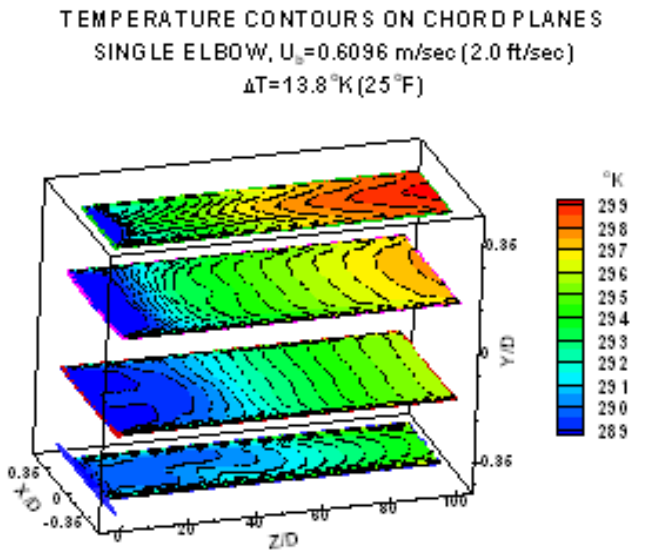

Fig. B-218 Temperature Slice Contours
V_0=0.6096 m/sec, ΔT_{wall}=13.8°K

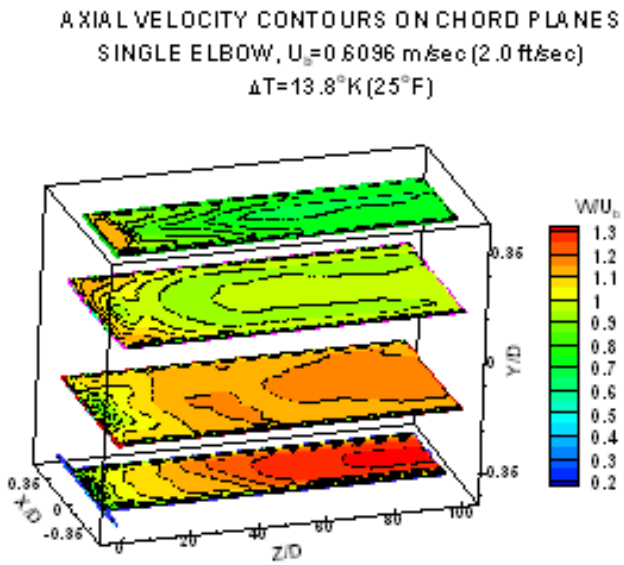

Fig. B-219 Axial Velocity Slice Contours
V_0=0.6096 m/sec, ΔT_{wall}=13.8°K

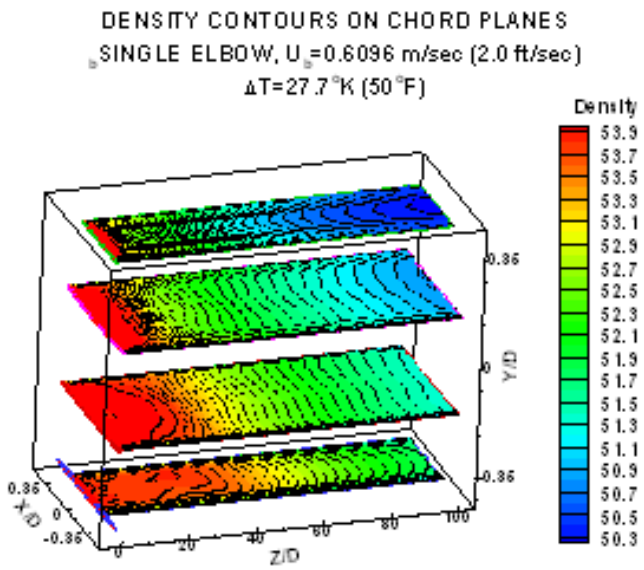

Fig. B-220 Density Slice Contours
V_0=0.6096 m/sec, ΔT_{wall}=27.7°K

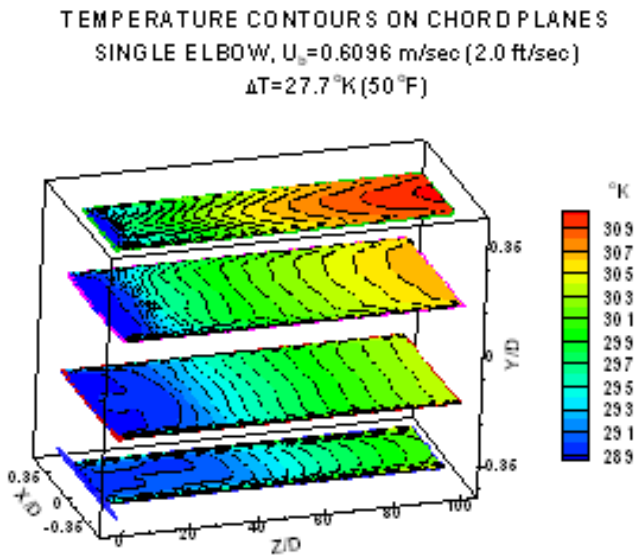

Fig. B-221 Temperature Slice Contours
V_0=0.6096 m/sec, ΔT_{wall}=27.7°K

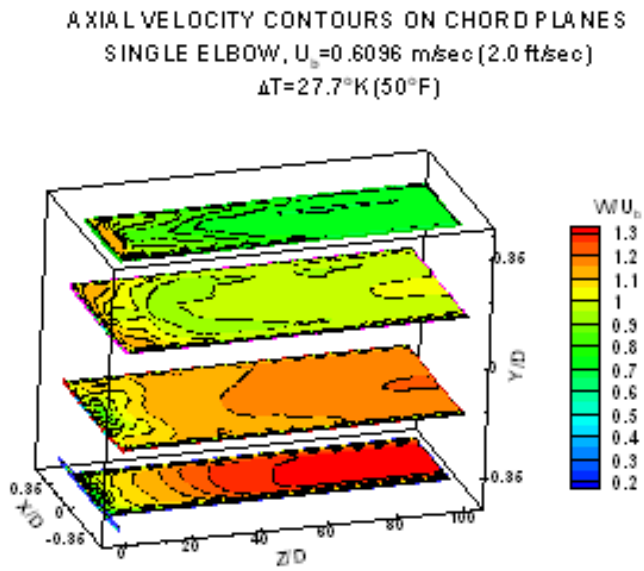

Fig. B-222 Axial Velocity Slice Contours
V_0=0.6096 m/sec, ΔT_{wall}=27.7°K

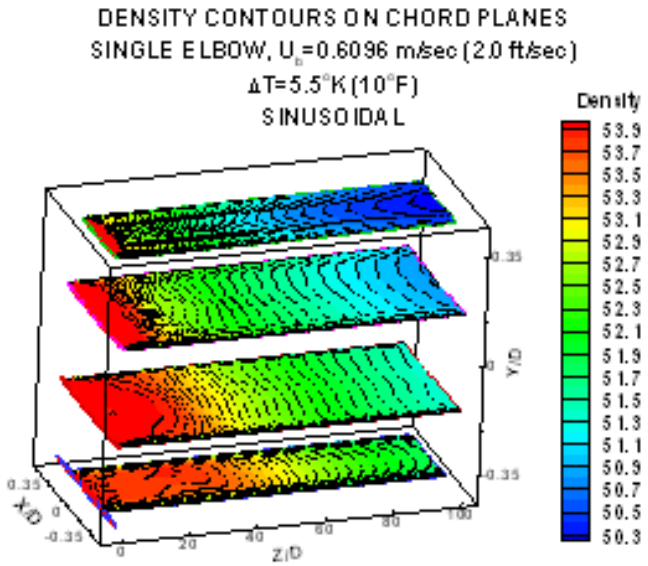

Fig. B-223 Density Slice Contours
V_0=0.6096 m/sec, ΔT_{wall}=-5.5°K Sinusoidal

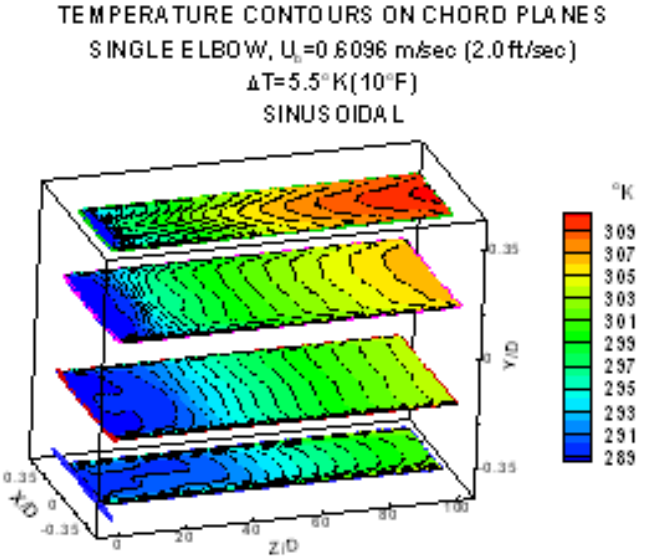

Fig. B-224 Temperature Slice Contours
V_0=0.6096 m/sec, ΔT_{wall}=-5.5°K Sinusoidal

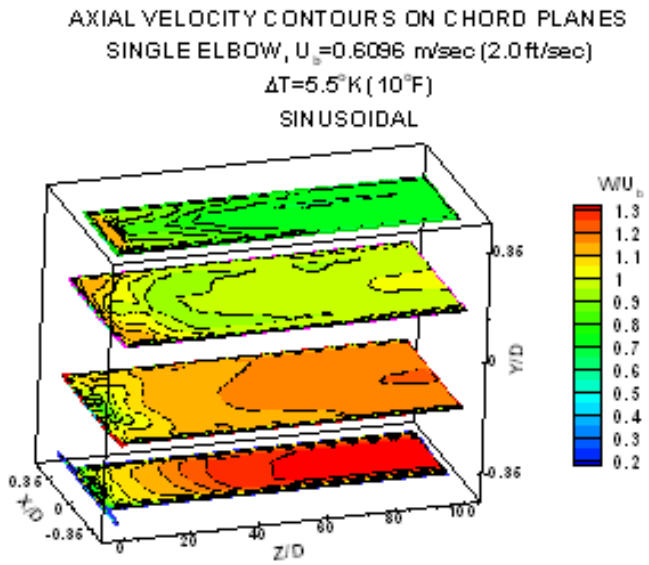

Fig. B-225 Axial Velocity Slice Contours
V_0=0.6096 m/sec, ΔT_{wall}=-5.5°K Sinusoidal

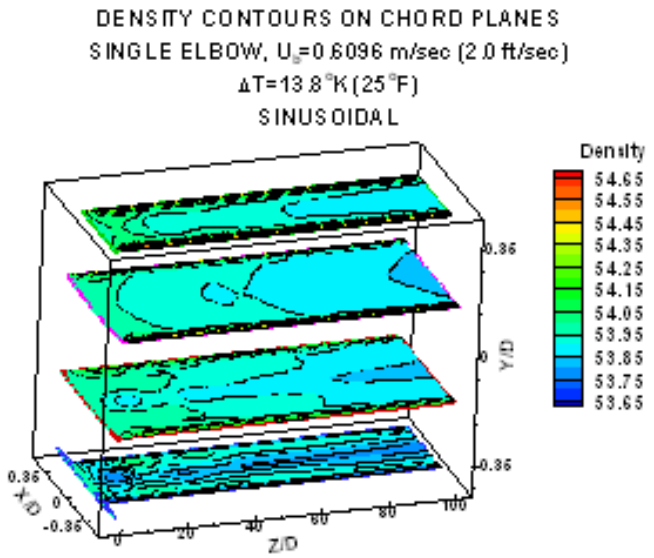

Fig. B-226 Density Slice Contours
V_0=0.6096 m/sec, ΔT_{wall}=-13.8°K Sinusoidal

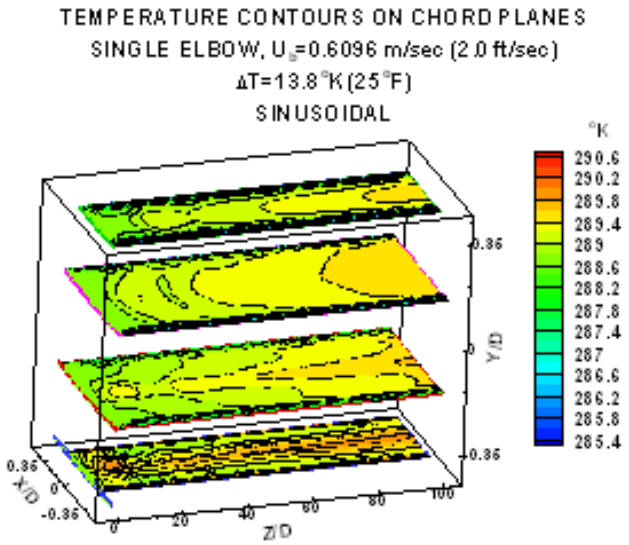

Fig. B-227 Temperature Slice Contours
V_0=0.6096 m/sec, ΔT_{wall}=-13.8°K Sinusoidal

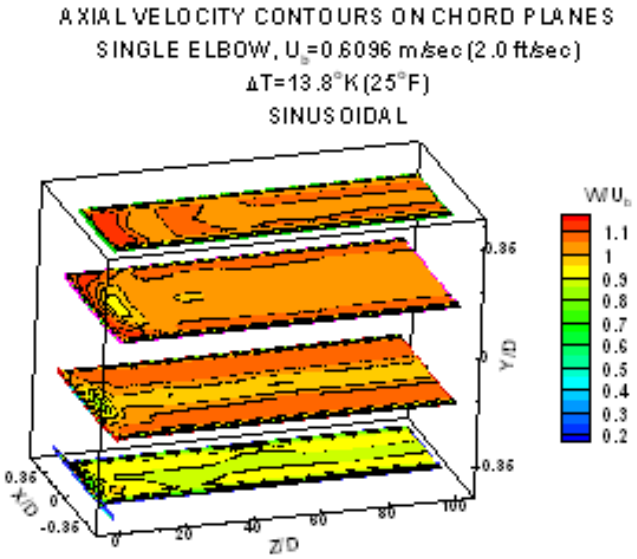

Fig. B-228 Axial Velocity Slice Contours
V_0=0.6096 m/sec, ΔT_{wall}=-13.8°K Sinusoidal

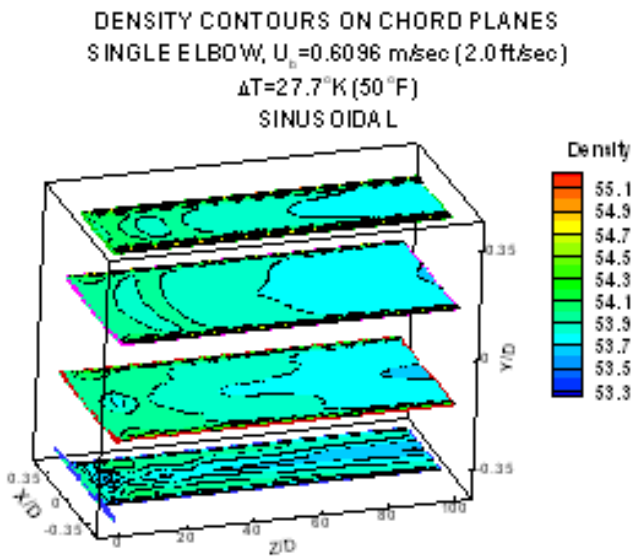

Fig. B-229 Density Slice Contours
V_0=0.6096 m/sec, ΔT_{wall}=-27.7°K Sinusoidal

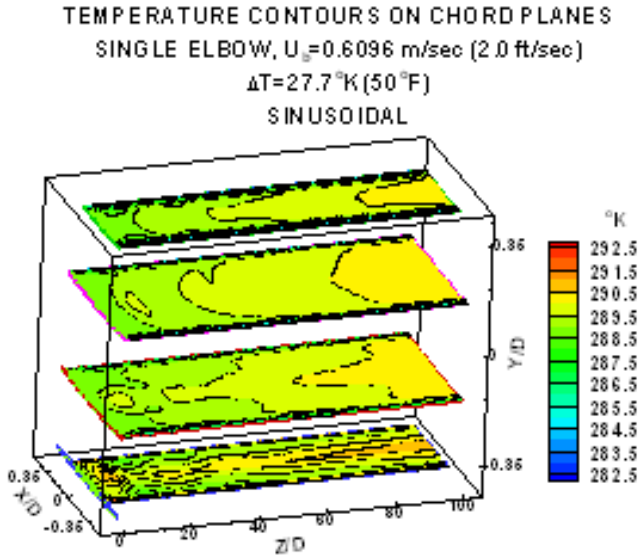

Fig. B-230 Temperature Slice Contours
V_0=0.6096 m/sec, ΔT_{wall}=-27.7°K Sinusoidal

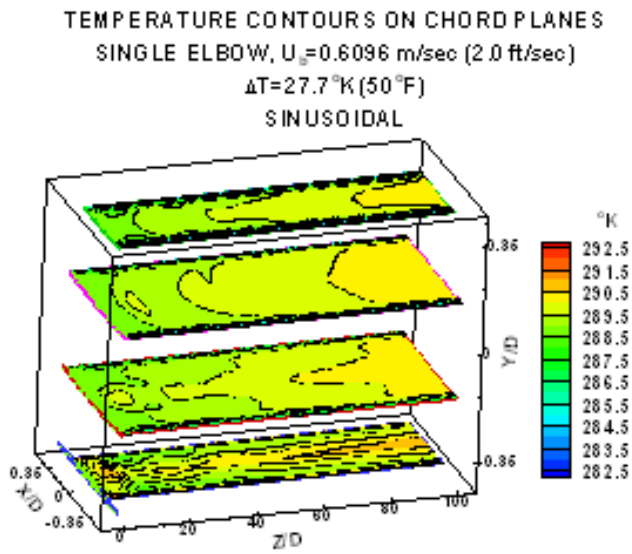

Fig. B-231 Axial Velocity Slice Contours
V_0=0.6096 m/sec, ΔT_{wall}=-27.7°K Sinusoidal

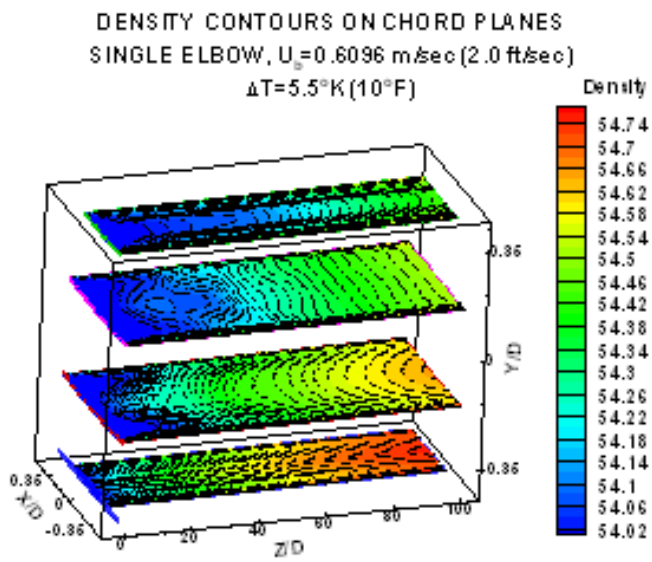

Fig. B-232 Density Slice Contours
V_0=0.6096 m/sec, ΔT_{wall}=-5.5°K

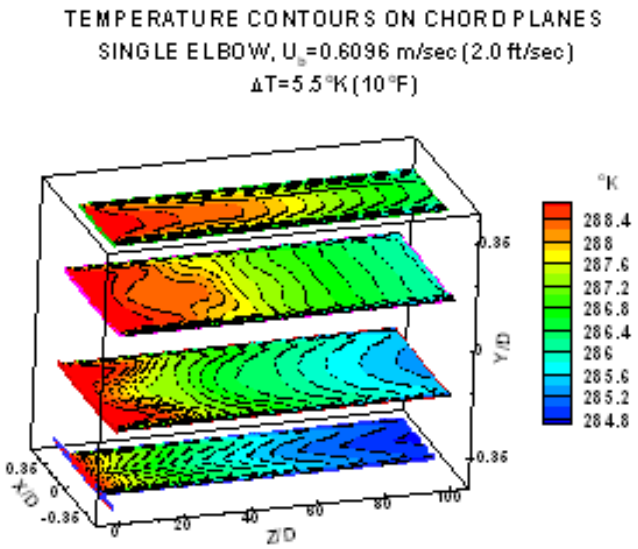

Fig. B-233 Temperature Slice Contours
V_0=0.6096 m/sec, ΔT_{wall}=-5.5°K

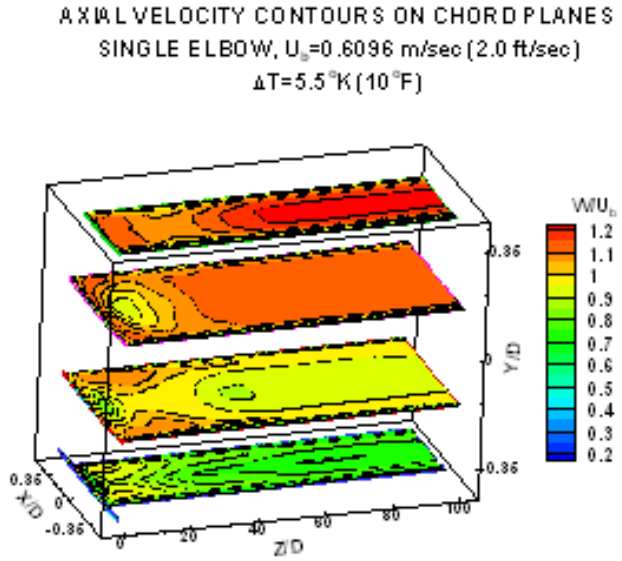

Fig. B-234 Axial Velocity Slice Contours
V_0=0.6096 m/sec, ΔT_{wall}=-5.5°K

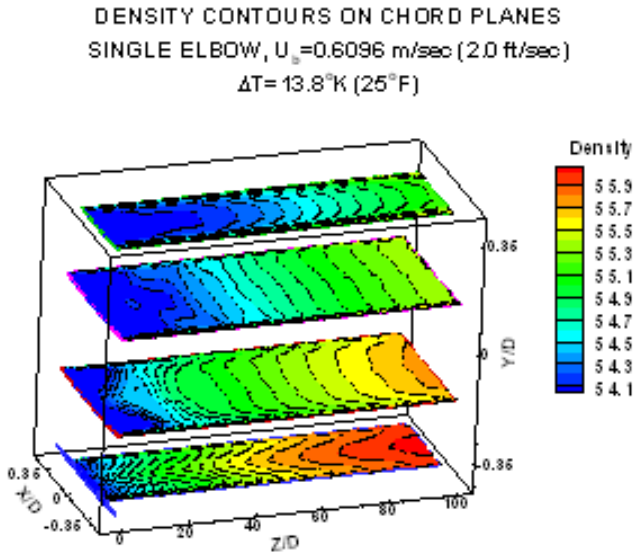

Fig. B-235 Density Slice Contours
V_0=0.6096 m/sec, ΔT_{wall}=-13.8°K

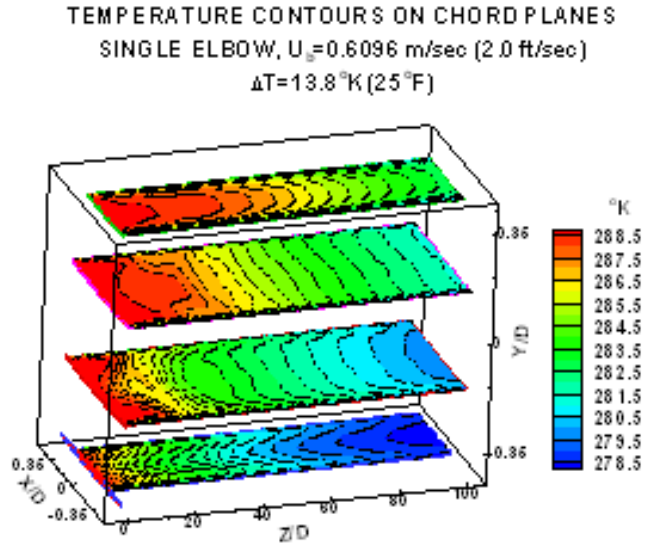

Fig. B-236 Temperature Slice Contours
V_0=0.6096 m/sec, ΔT_{wall}=-13.8°K

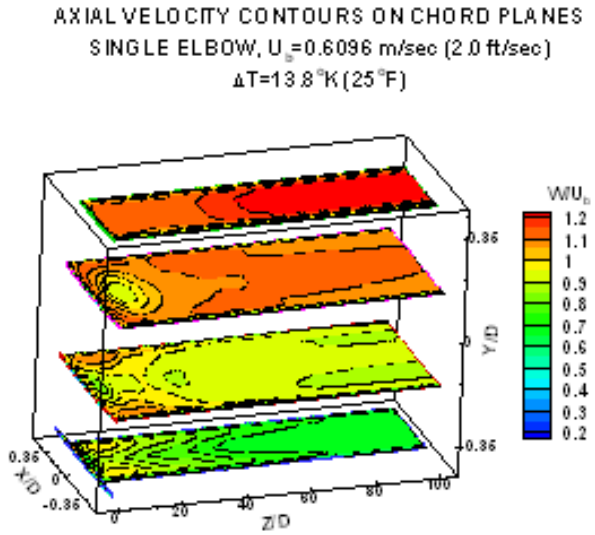

Fig. B-237 Axial Velocity Slice Contours
V_0=0.6096 m/sec, ΔT_{wall}=-13.8°K

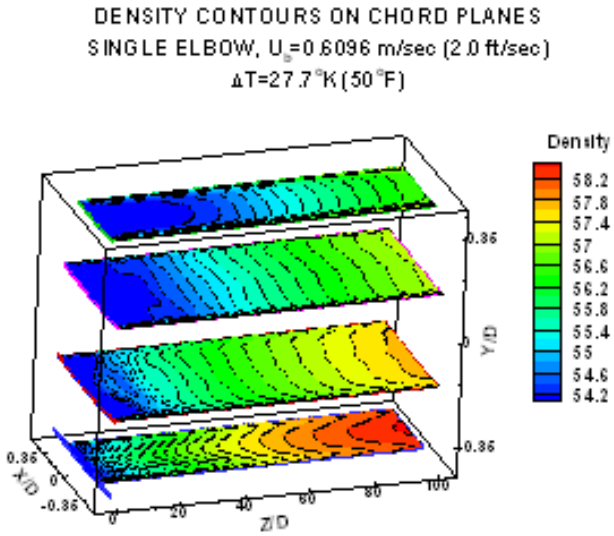

Fig. B-238 Density Slice Contours
V_0=0.6096 m/sec, ΔT_{wall}=-27.7°K

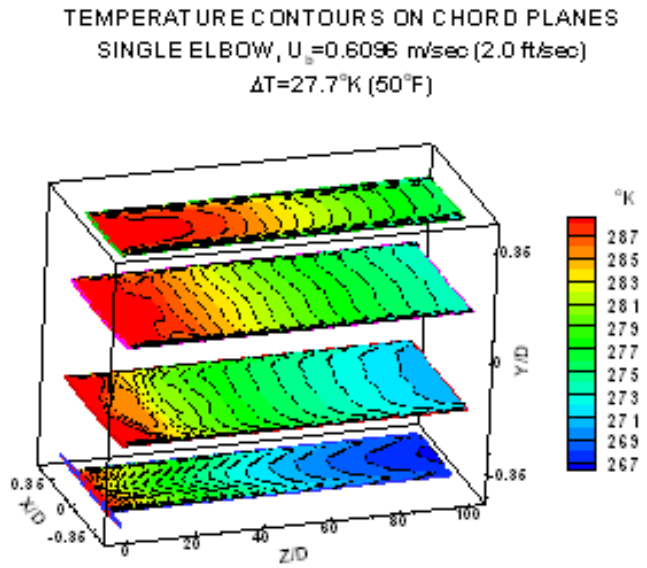

V_0=0.6096 m/sec, ΔT_{wall}=-27.7°K

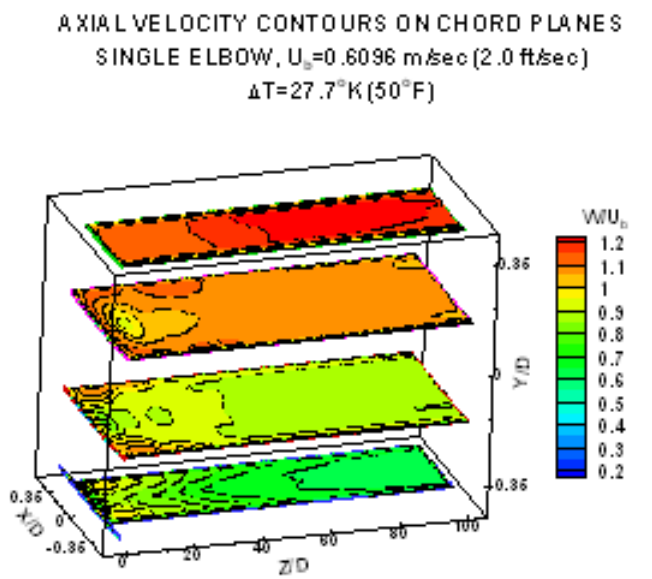

V_0=0.6096 m/sec, ΔT_{wall}=-27.7°K

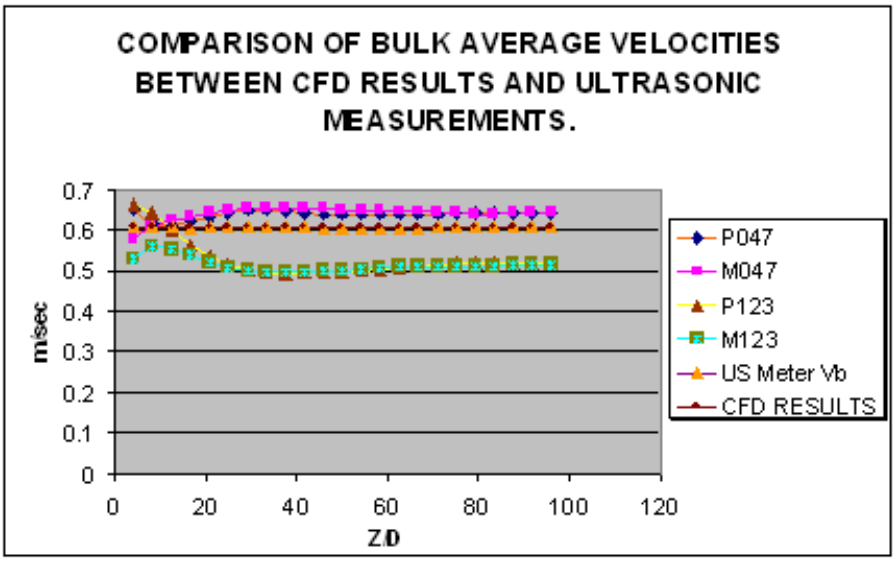

Fig. B-241 Comparison between CFD Vb and Ultrasonic Vb.
V_0=0.6096 m/sec, ΔT_{wall}=5.5°K Sinusoidal

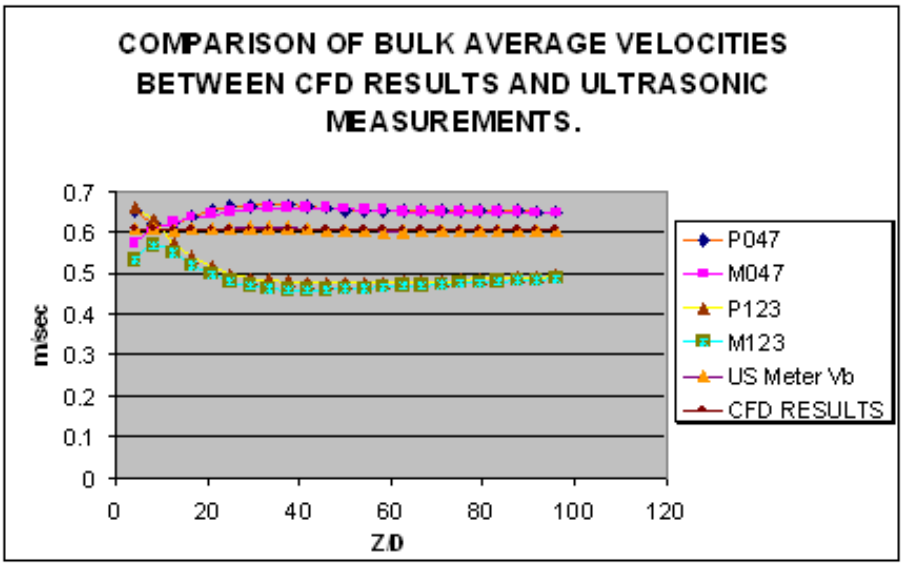

Fig. B-242 Comparison between CFD Vb and Ultrasonic Vb.
V_0=0.6096 m/sec, ΔT_{wall}=13.8°K Sinusoidal

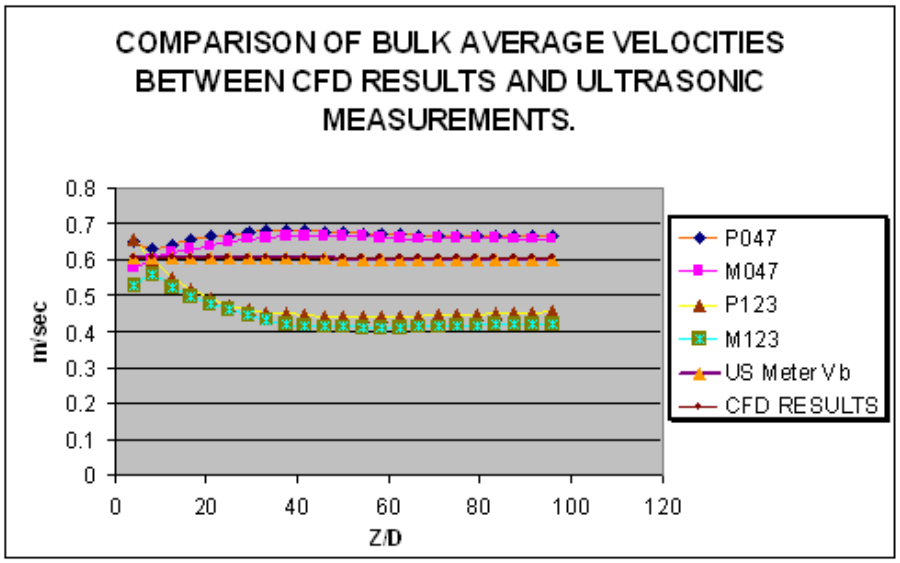

Fig. B-243 Comparison between CFD Vb and Ultrasonic Vb.
V_0=0.6096 m/sec, ΔT_{wall}=27.7°K Sinusoidal

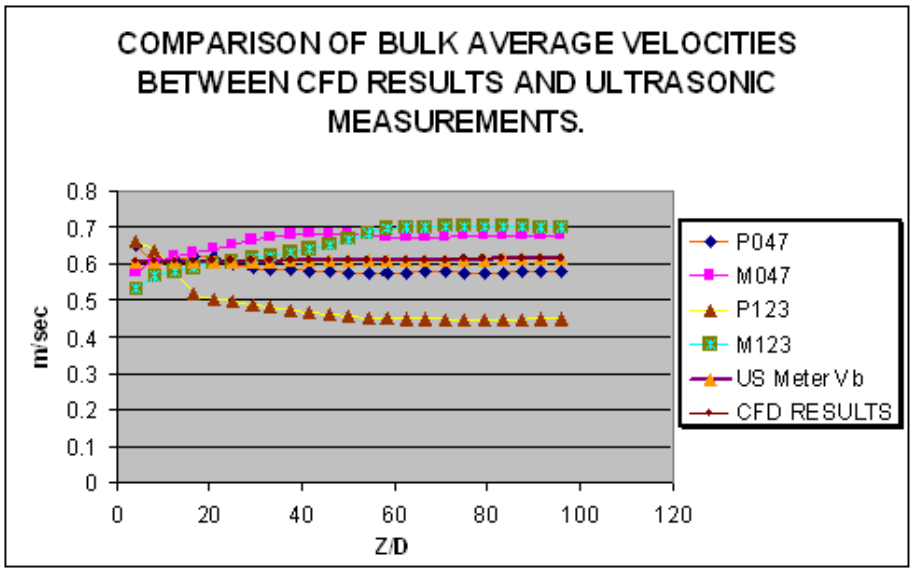

Fig. B-244 Comparison between CFD Vb and Ultrasonic Vb.
V_0=0.6096 m/sec, ΔT_{wall}=5.5°K

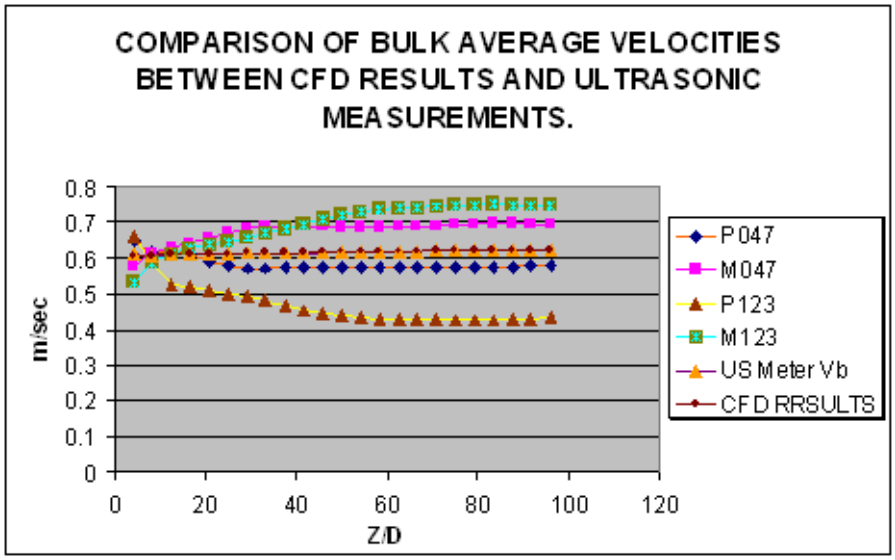

Fig. B-245 Comparison between CFD Vb and Ultrasonic Vb.
V_0=0.6096 m/sec, ΔT_{wall}=13.8°K

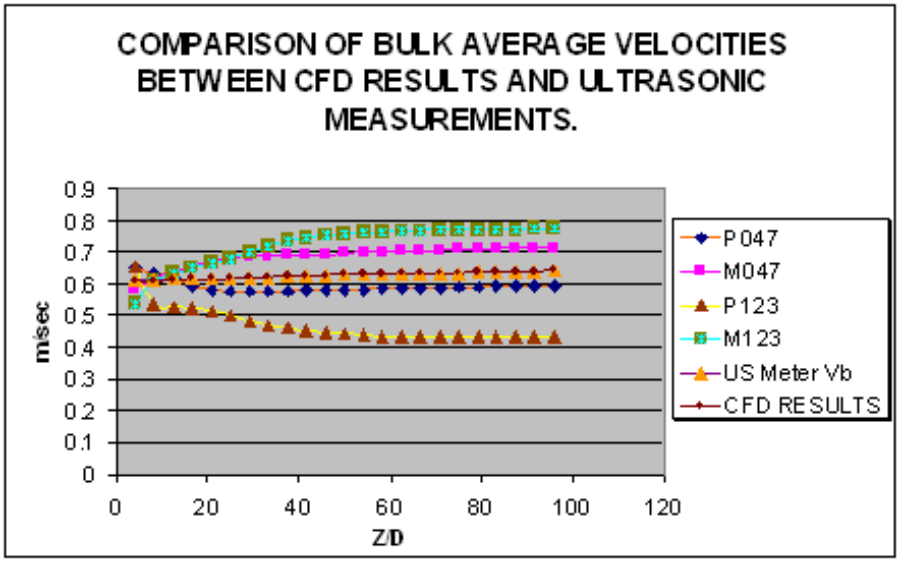

Fig. B-246 Comparison between CFD Vb and Ultrasonic Vb.
V_0=0.6096 m/sec, ΔT_{wall}=27.7°K

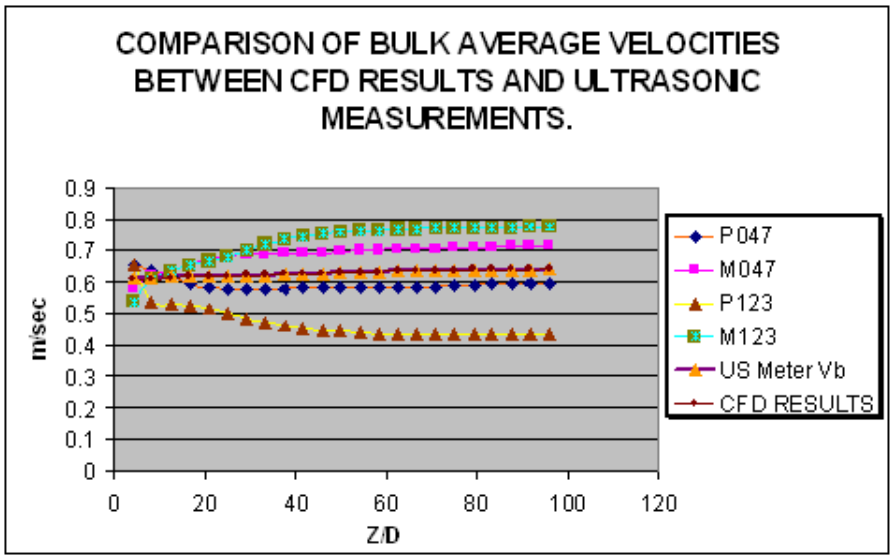

Fig. B-247 Comparison between CFD Vb and Ultrasonic Vb.
V_0=0.6096 m/sec, ΔT_{wall}=-5.5°K Sinusoidal

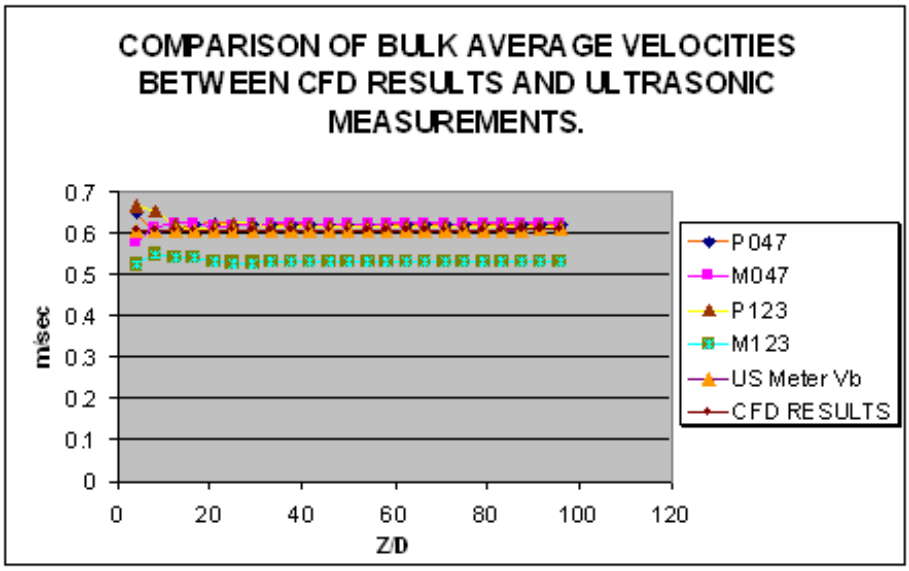

Fig. B-248 Comparison between CFD Vb and Ultrasonic Vb.
V_0=0.6096 m/sec, ΔT_{wall}=-13.8°K Sinusoidal

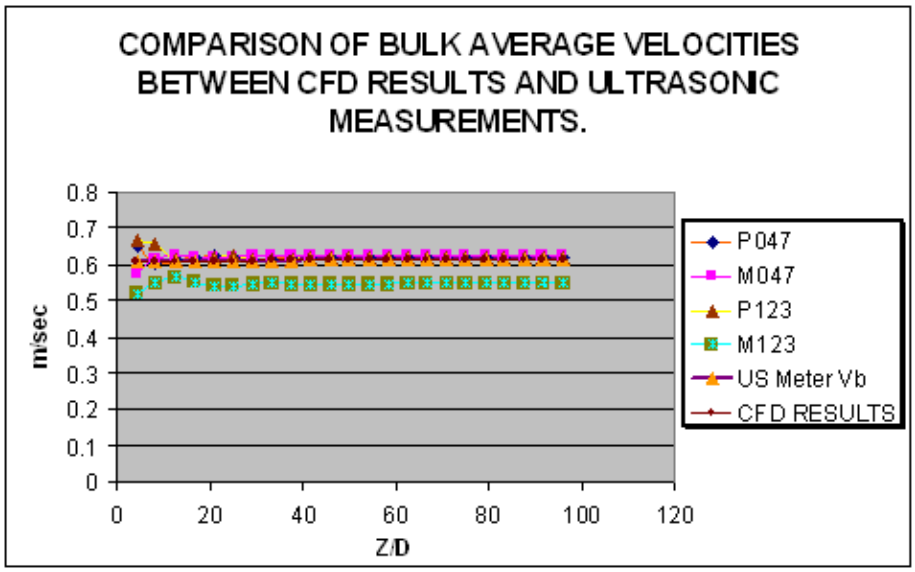

Fig. B-249 Comparison between CFD Vb and Ultrasonic Vb.
V_0=0.6096 m/sec, ΔT_{wall}=-27.7°K Sinusoidal

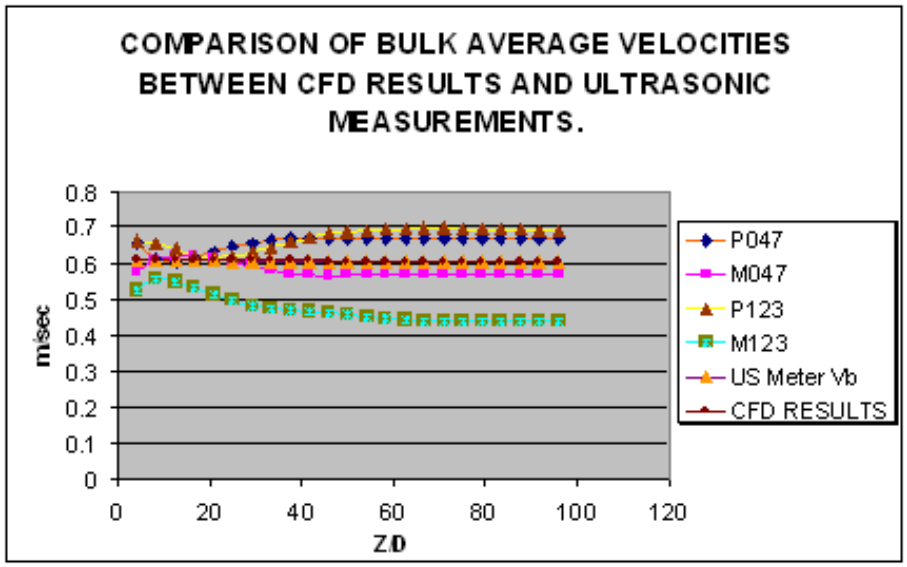

Fig. B-250 Comparison between CFD Vb and Ultrasonic Vb.
V_0=0.6096 m/sec, ΔT_{wall}=-5.5°K

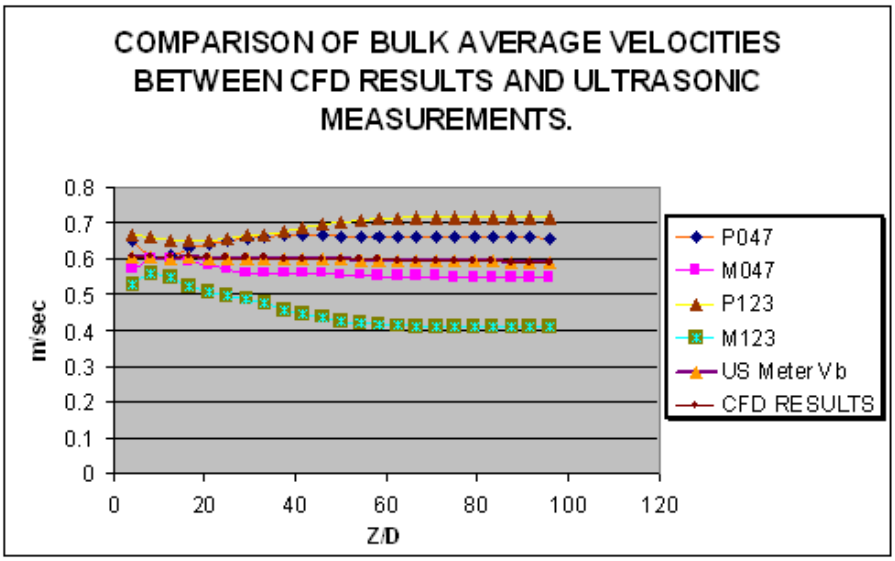

Fig. B-251 Comparison between CFD Vb and Ultrasonic Vb.
V_0=0.6096 m/sec, ΔT_{wall}=-13.8°K

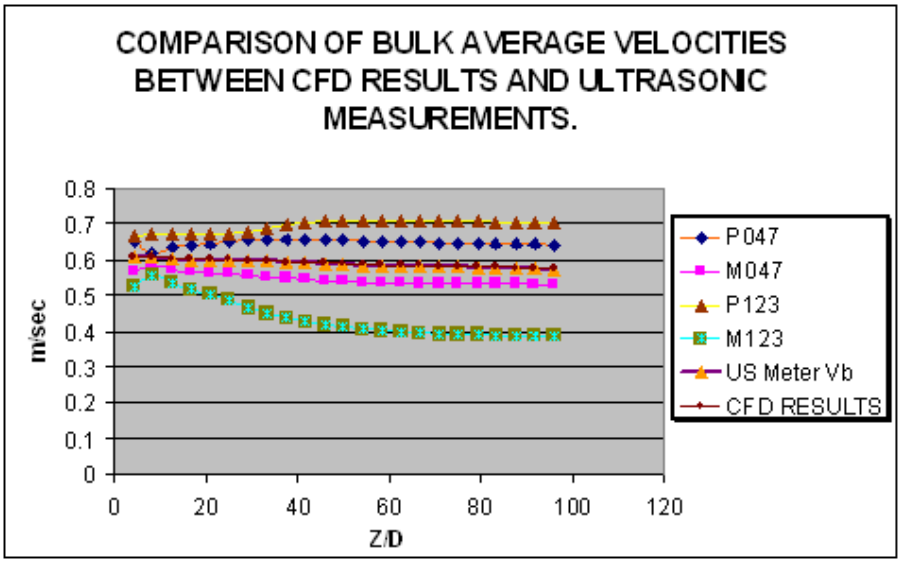

Fig. B-252 Comparison between CFD Vb and Ultrasonic Vb.
V_0=0.6096 m/sec, ΔT_{wall}=-27.7°K

APPENDIX C

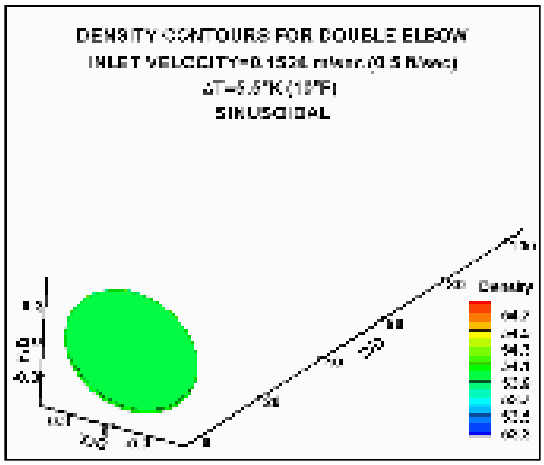

Fig. C-1 Density Contours
V_0=0.1524 m/sec, ΔT_{wall}=5.5°K Sinusoidal

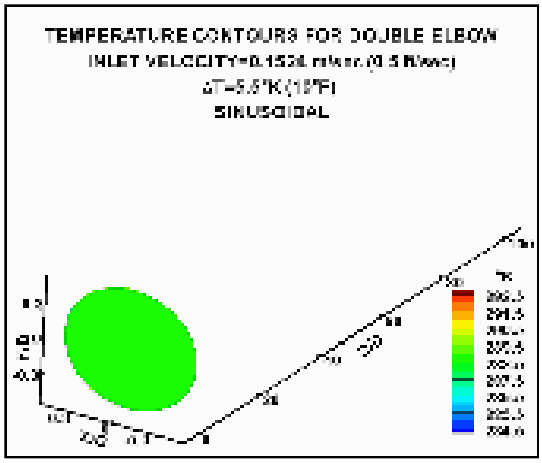

Fig. C-2 Temperature Contours
V_0=0.1524 m/sec, ΔT_{wall}=5.5°K Sinusoidal

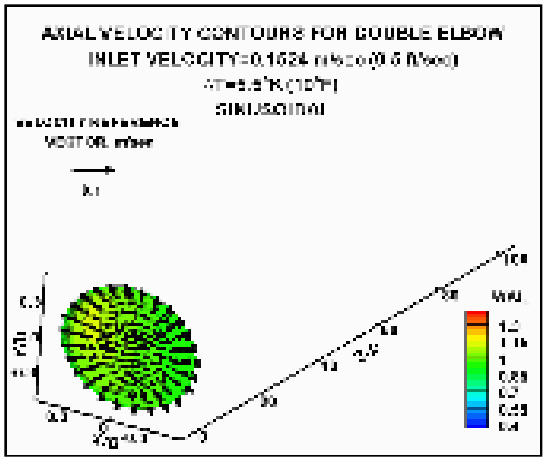

Fig. C-3 Axial Velocity Contours
V_0=0.1524 m/sec, ΔT_{wall}=5.5°K Sinusoidal

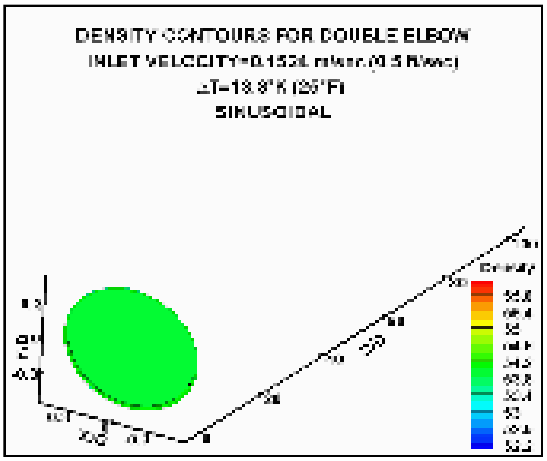

Fig. C-4 Density Contours
V_0=0.1524 m/sec, ΔT_{wall}=13.8°K Sinusoidal

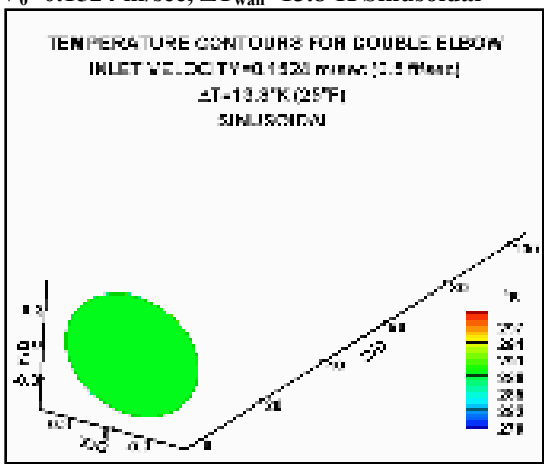

Fig. C-5 Temperature Contours
V_0=0.1524 m/sec, ΔT_{wall}=13.8°K Sinusoidal

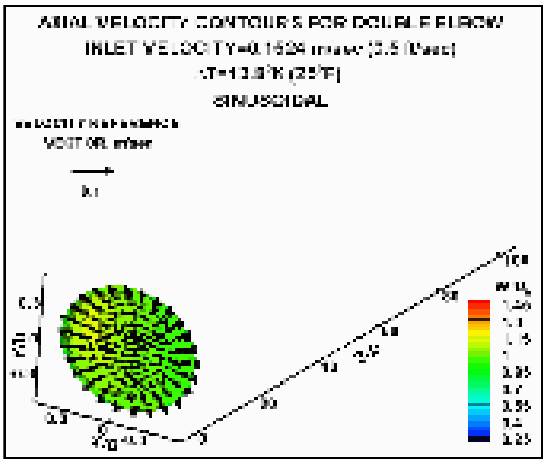

Fig. C-6 Axial Velocity Contours
V_0=0.1524 m/sec, ΔT_{wall}=13.8°K Sinusoidal

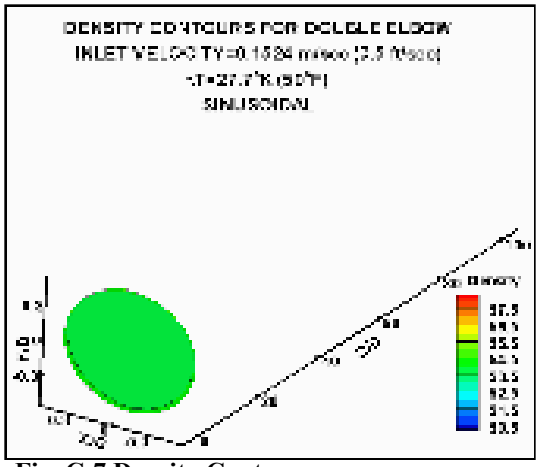

Fig. C-7 Density Contours
V_0=0.1524 m/sec, ΔT_{wall}=27.7°K Sinusoidal

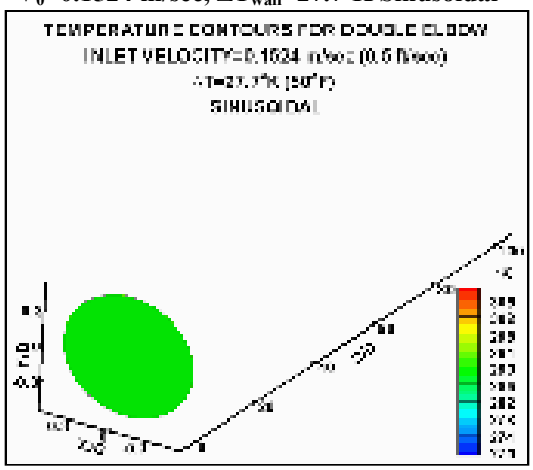

Fig. C-8 Temperature Contours
V_0=0.1524 m/sec, ΔT_{wall}=27.7°K Sinusoidal

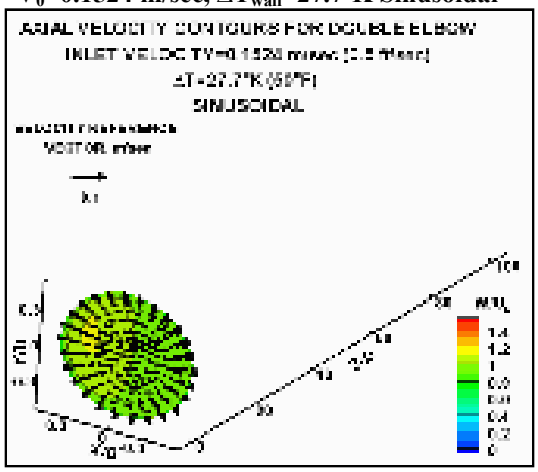

Fig. C-9 Axial Velocity Contours
V_0=0.1524 m/sec, ΔT_{wall}=27.7°K Sinusoidal

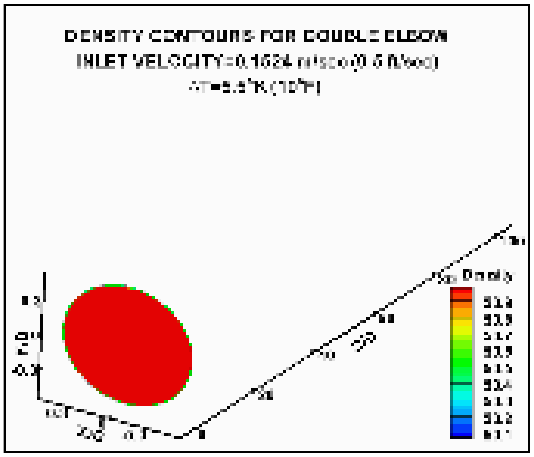

Fig. C-10 Density Contours
V_0=0.1524 m/sec, ΔT_{wall}=5.5°K

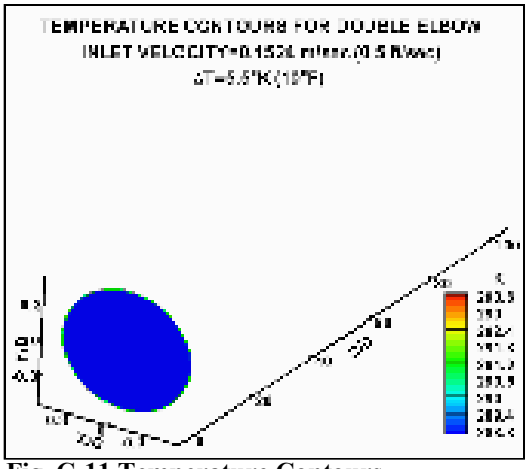

Fig. C-11 Temperature Contours
V_0=0.1524 m/sec, ΔT_{wall}=5.5°K

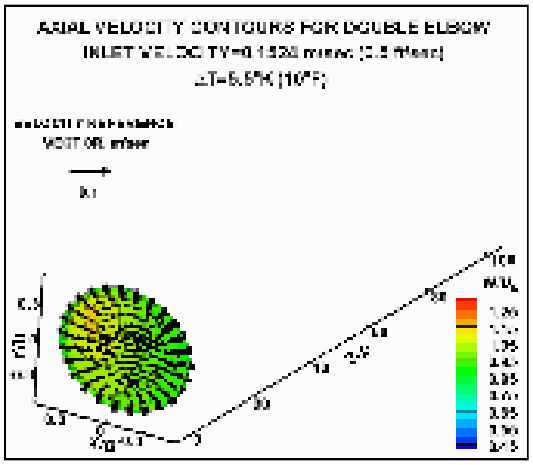

Fig. C-12 Axial Velocity Contours
V_0=0.1524 m/sec, ΔT_{wall}=5.5°K

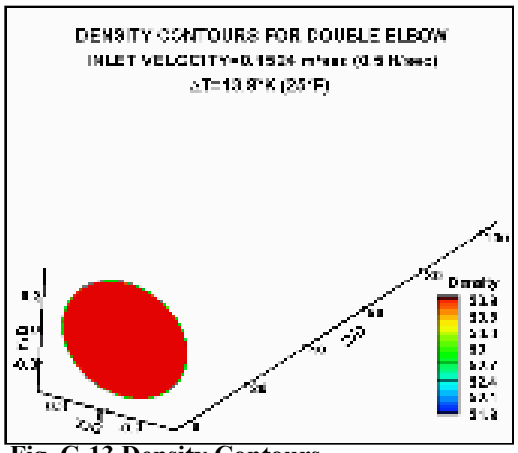

Fig. C-13 Density Contours
V_0=0.1524 m/sec, ΔT_{wall}=13.8°K

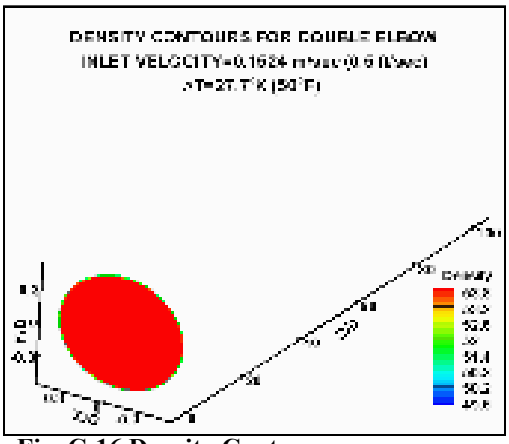

Fig. C-16 Density Contours
V_0=0.1524 m/sec, ΔT_{wall}=27.7°K

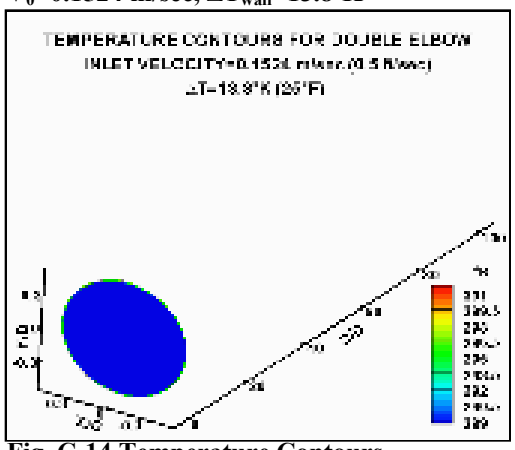

Fig. C-14 Temperature Contours
V_0=0.1524 m/sec, ΔT_{wall}=13.8°K

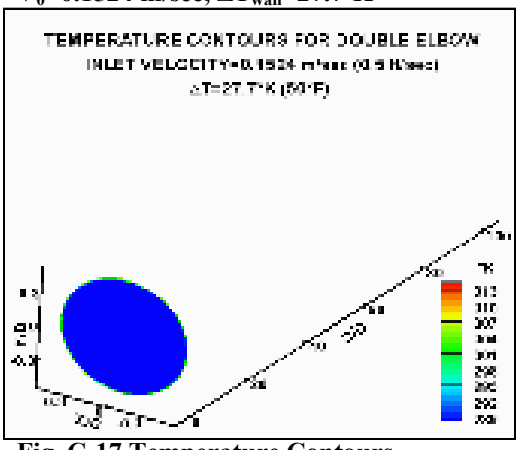

Fig. C-17 Temperature Contours
V_0=0.1524 m/sec, ΔT_{wall}=27.7°K

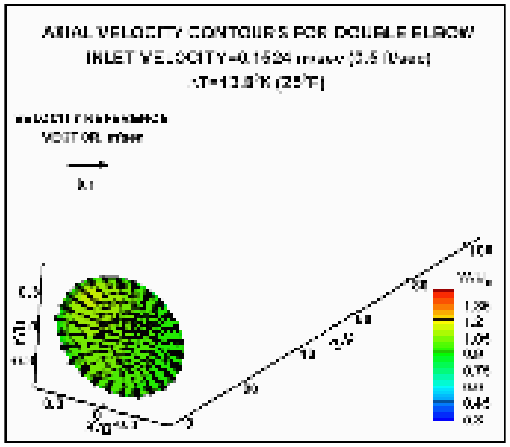

Fig. C-15 Axial Velocity Contours
V_0=0.1524 m/sec, ΔT_{wall}=13.8°K

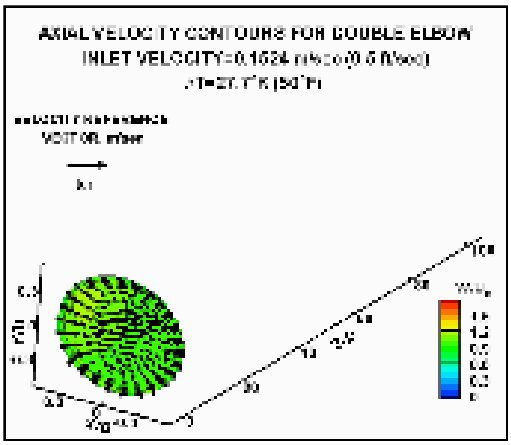

Fig. C-18 Axial Velocity Contours
V_0=0.1524 m/sec, ΔT_{wall}=27.7°K

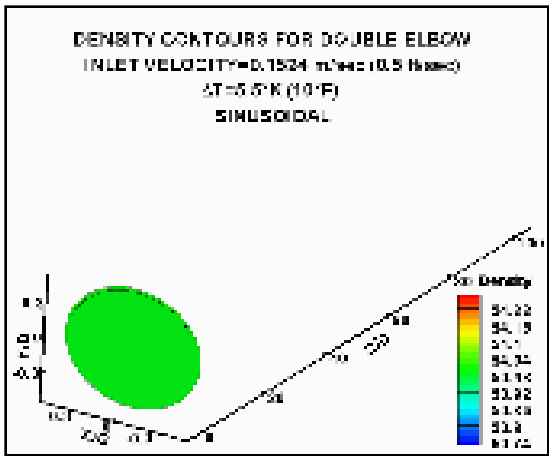

Fig. C-19 Density Contours
V_0=0.1524 m/sec, ΔT_{wall}=-5.5°K Sinusoidal

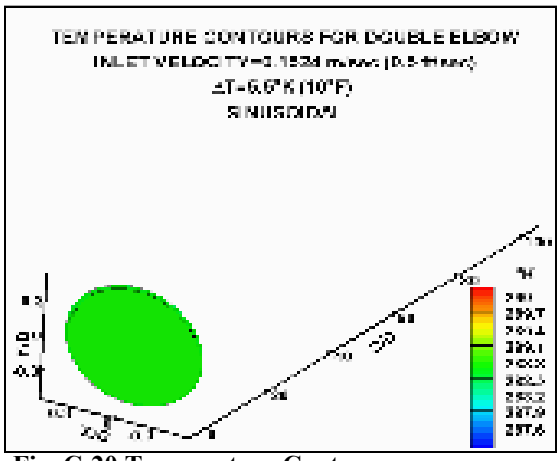

Fig. C-20 Temperature Contours
V_0=0.1524 m/sec, ΔT_{wall}=-5.5°K Sinusoidal

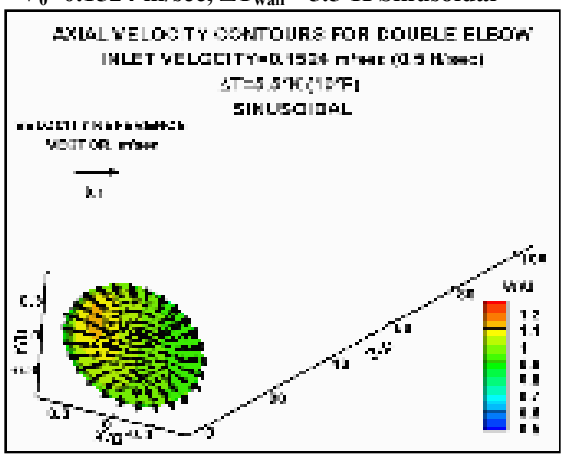

Fig. C-21Axial Velocity Contours
V_0=0.1524 m/sec, ΔT_{wall}=-5.5°K Sinusoidal

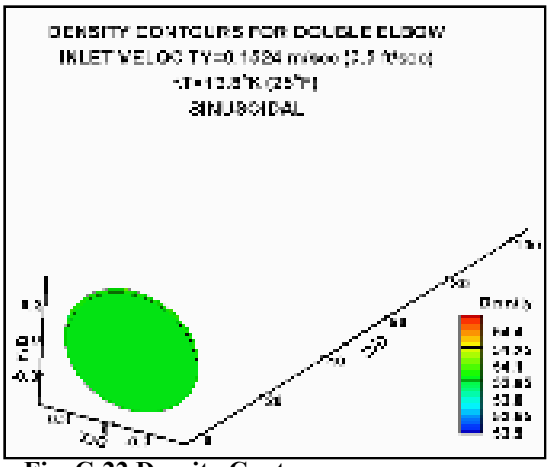

Fig. C-22 Density Contours
V_0=0.1524 m/sec, ΔT_{wall}=-13.8°K Sinusoidal

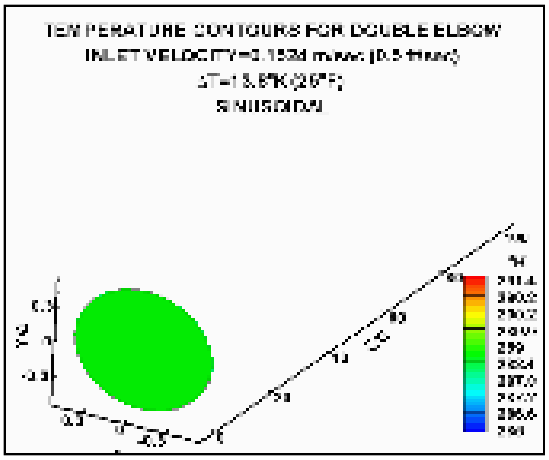

Fig. C-23 Temperature Contours
V_0=0.1524 m/sec, ΔT_{wall}=-13.8°K Sinusoidal

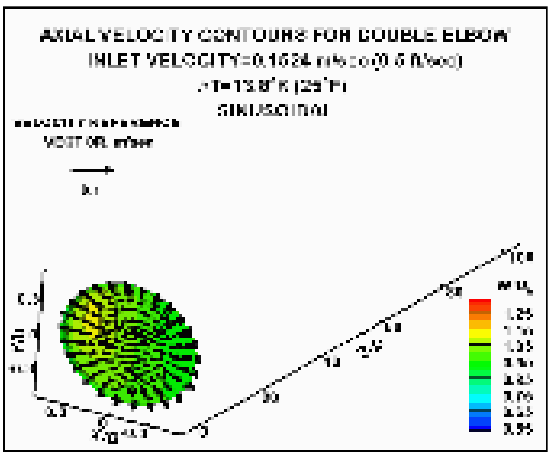

Fig. C-24 Axial Velocity Contours
V_0=0.1524 m/sec, ΔT_{wall}=-13.8°K Sinusoidal

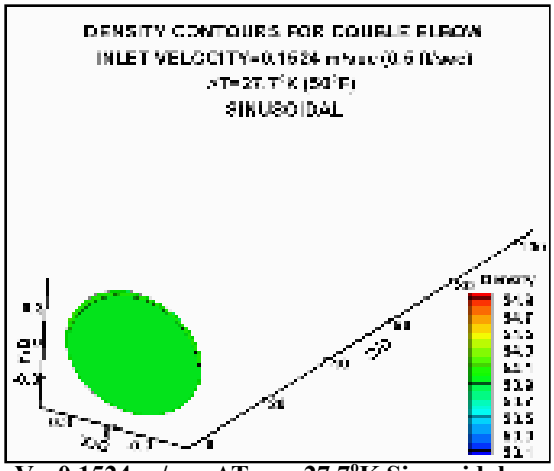

V_0=0.1524 m/sec, ΔT_{wall}=-27.7°K Sinusoidal

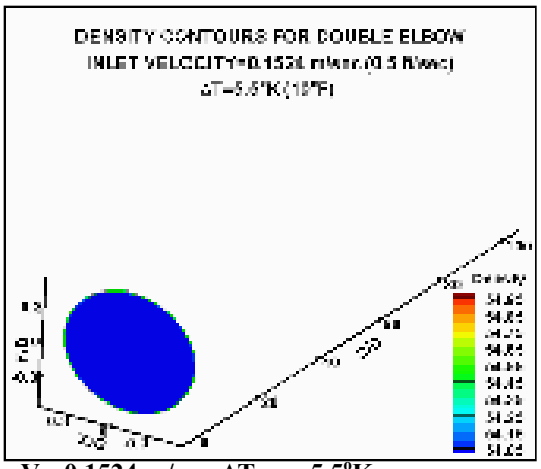

V_0=0.1524 m/sec, ΔT_{wall}=-5.5°K

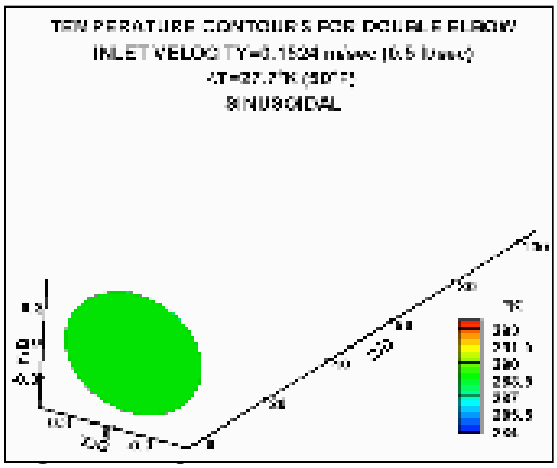

V_0=0.1524 m/sec, ΔT_{wall}=-27.7°K Sinusoidal

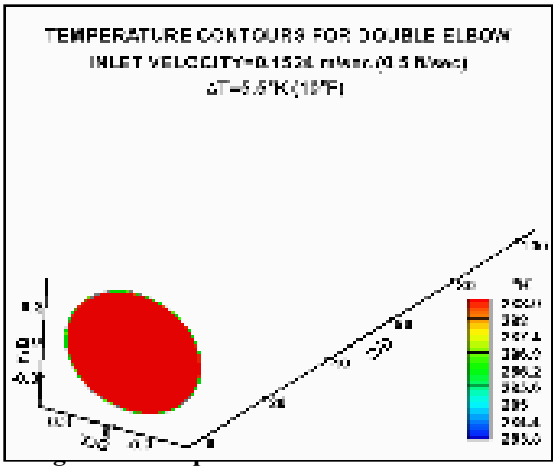

V_0=0.1524 m/sec, ΔT_{wall}=-5.5°K

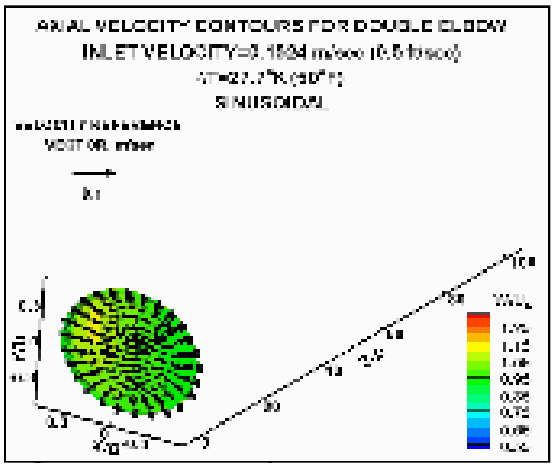

V_0=0.1524 m/sec, ΔT_{wall}=-27.7°K Sinusoidal

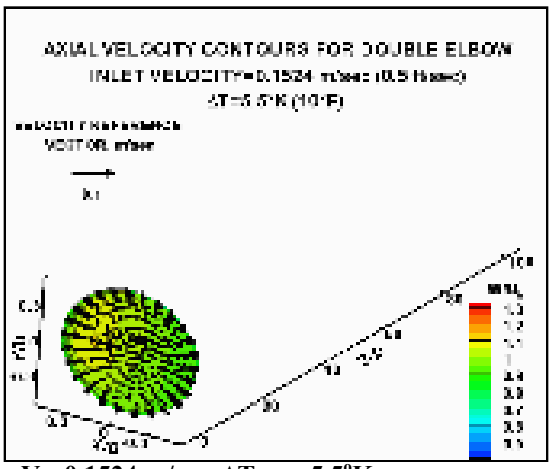

V_0=0.1524 m/sec, ΔT_{wall}=-5.5°K

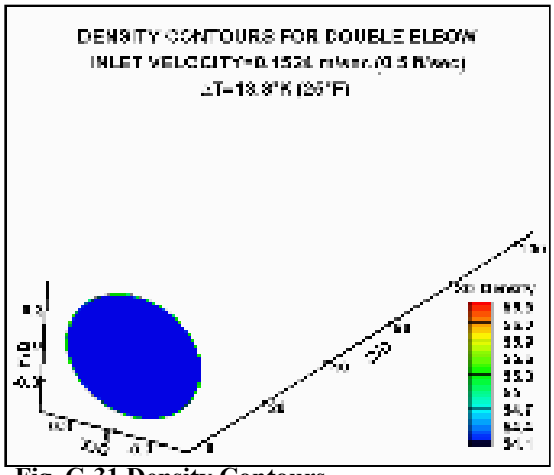

Fig. C-31 Density Contours
V_0=0.1524 m/sec, ΔT_{wall}=-13.8°K

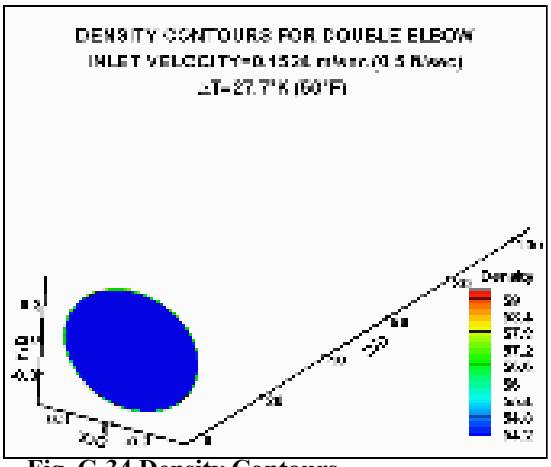

Fig. C-34 Density Contours
V_0=0.1524 m/sec, ΔT_{wall}=-27.7°K

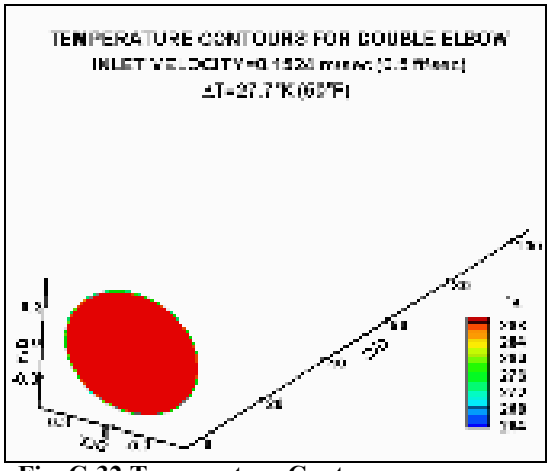

Fig. C-32 Temperature Contours
V_0=0.1524 m/sec, ΔT_{wall}=-13.8°K

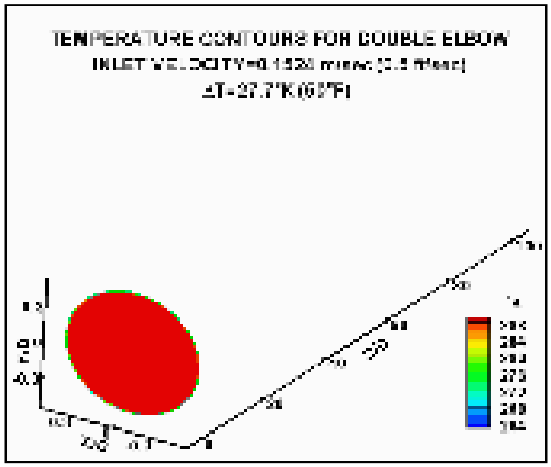

Fig. C-35 Temperature Contours
V_0=0.1524 m/sec, ΔT_{wall}=-27.7°K

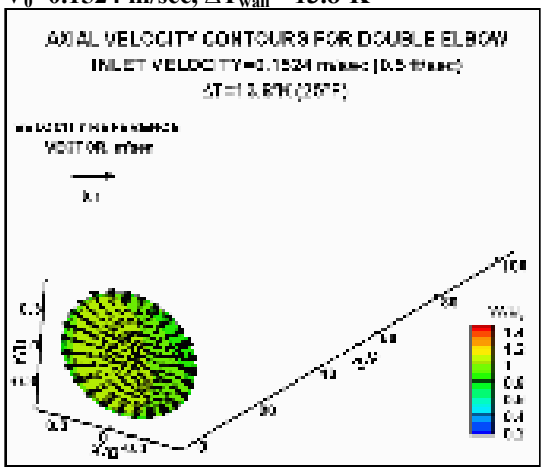

Fig. C-33 Axial Velocity Contours
V_0=0.1524 m/sec, ΔT_{wall}=-13.8°K

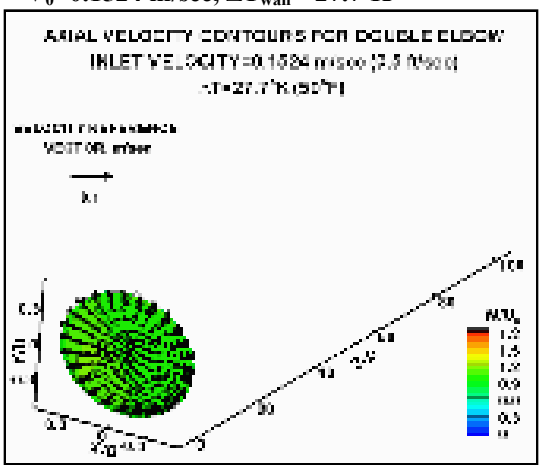

Fig. C-36 Axial Velocity Contours
V_0=0.1524 m/sec, ΔT_{wall}=-27.7°K

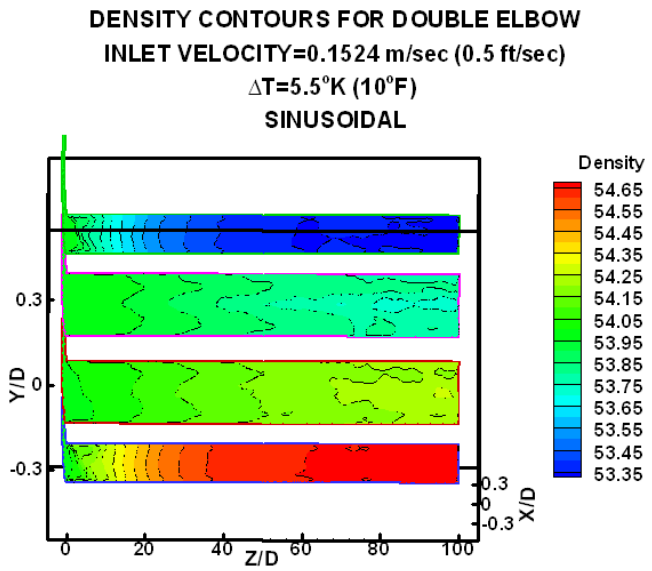

Fig. C-37 Density Slice Contours
V_0=0.1524 m/sec, ΔT_{wall}=5.5°K Sinusoidal

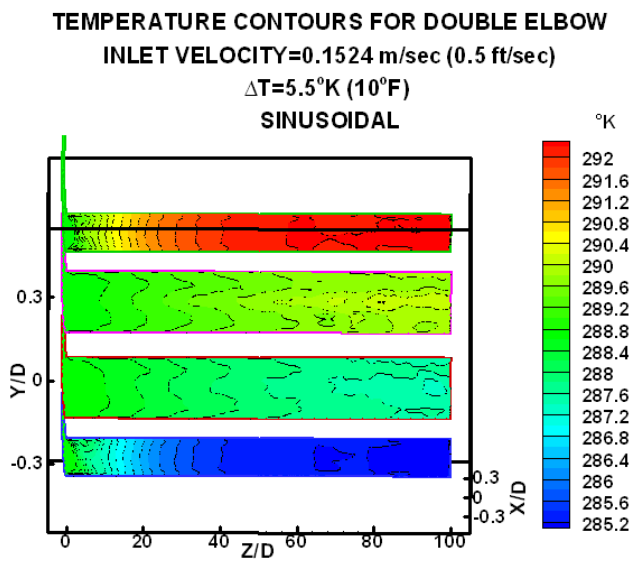

Fig. C-38 Temperature Slice Contours
V_0=0.1524 m/sec, ΔT_{wall}=5.5°K Sinusoidal

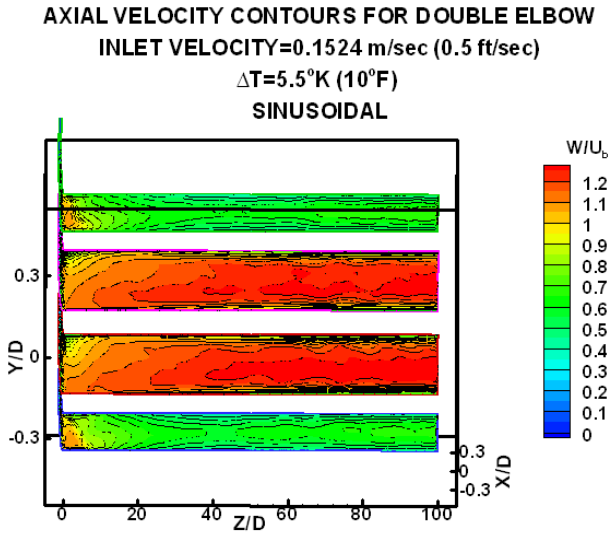

Fig. C-39 Axial Velocity Slice Contours
V_0=0.1524 m/sec, ΔT_{wall}=5.5°K Sinusoidal

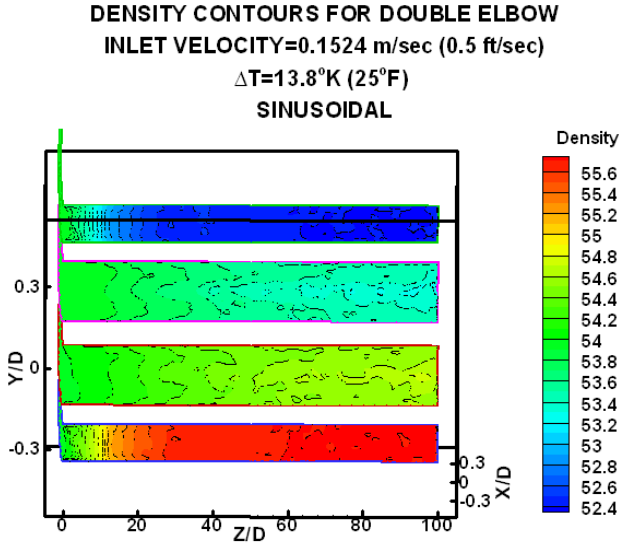

Fig. C-40 Density Slice Contours
V_0=0.1524 m/sec, ΔT_{wall}=13.8°K Sinusoidal

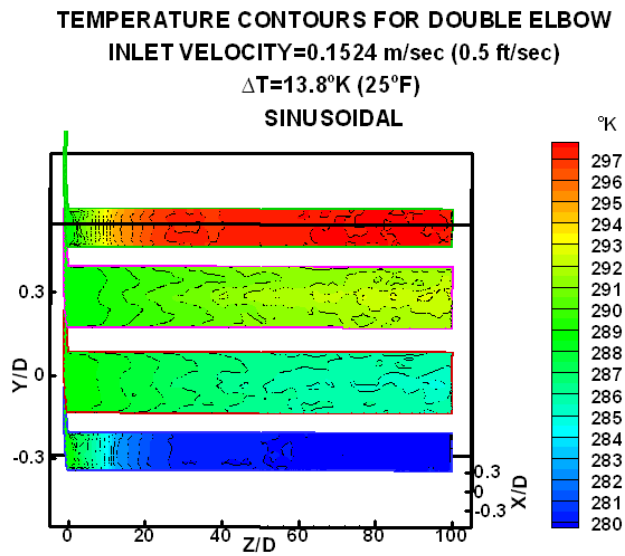

Fig. C-41 Temperature Slice Contours
V_0=0.1524 m/sec, ΔT_{wall}=13.8°K Sinusoidal

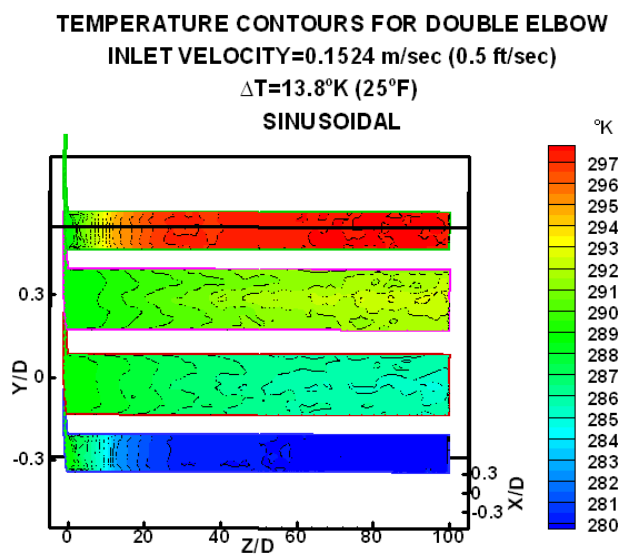

Fig. C-42 Axial Velocity Slice Contours
V_0=0.1524 m/sec, ΔT_{wall}=13.8°K Sinusoidal

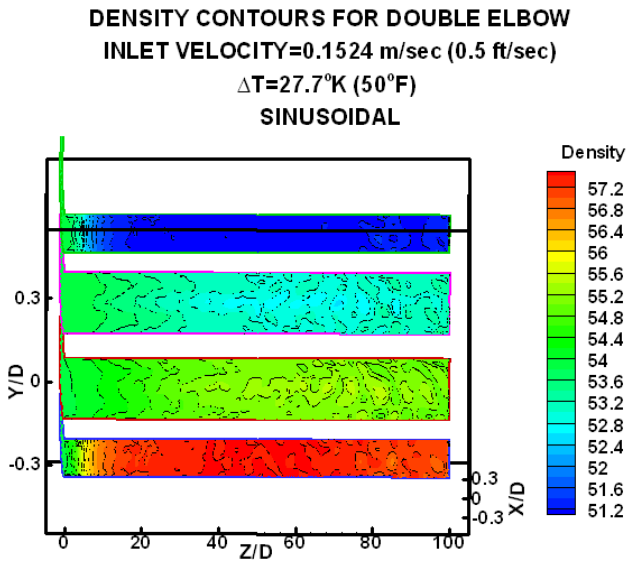

Fig. C-43 Density Slice Contours
V_0=0.1524 m/sec, ΔT_{wall}=27.7°K Sinusoidal

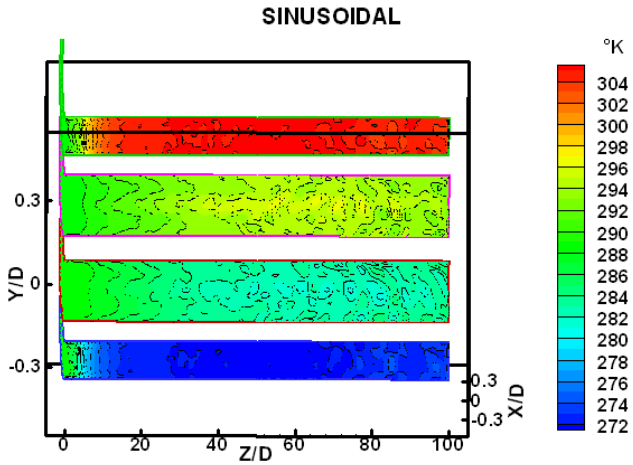

Fig. C-44 Temperature Slice Contours
V_0=0.1524 m/sec, ΔT_{wall}=27.7°K Sinusoidal

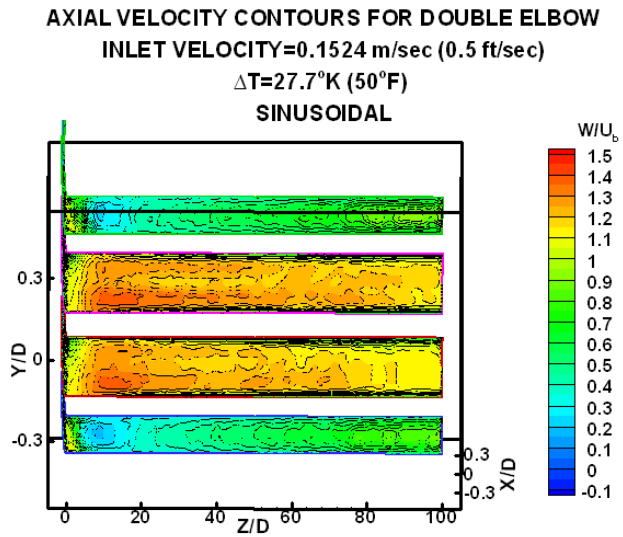

Fig. C-45 Axial Velocity Slice Contours
V_0=0.1524 m/sec, ΔT_{wall}=27.7°K Sinusoidal

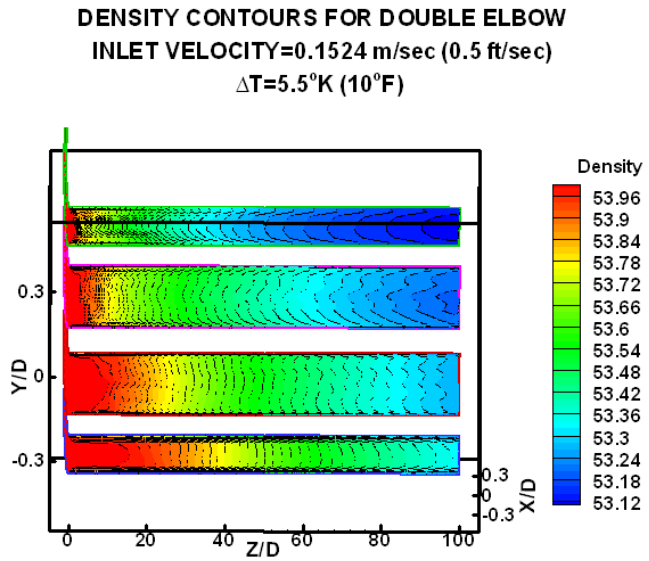

Fig. C-46 Density Slice Contours
V_0=0.1524 m/sec, ΔT_{wall}=5.5°K

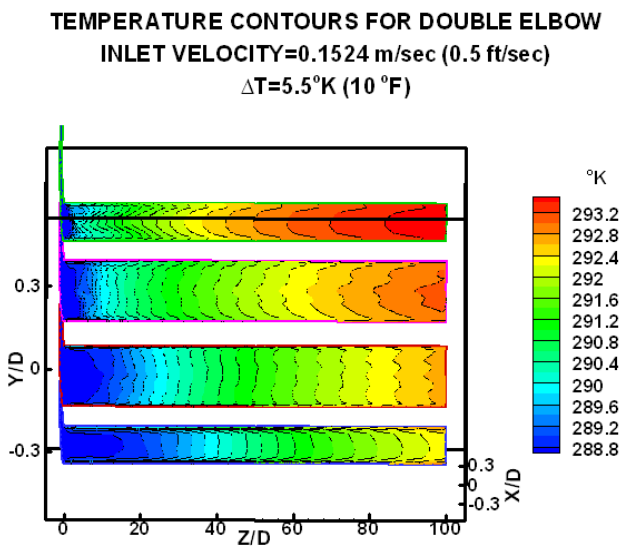

Fig. C-47 Temperature Slice Contours
V_0=0.1524 m/sec, ΔT_{wall}=5.5°K

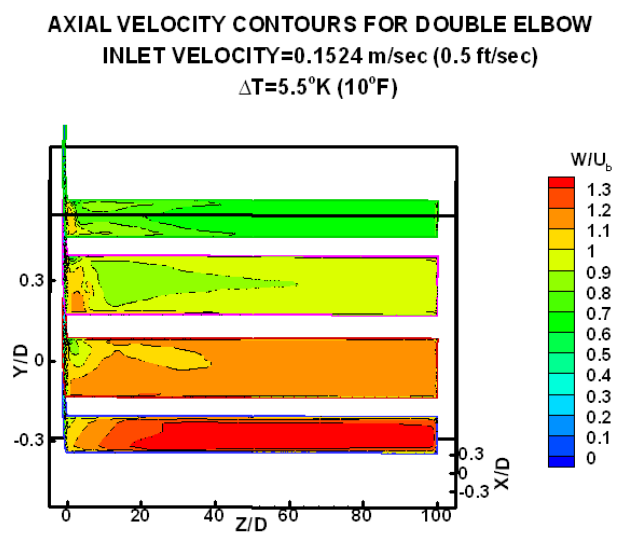

Fig. C-48 Axial Velocity Slice Contours
V_0=0.1524 m/sec, ΔT_{wall}=5.5°K

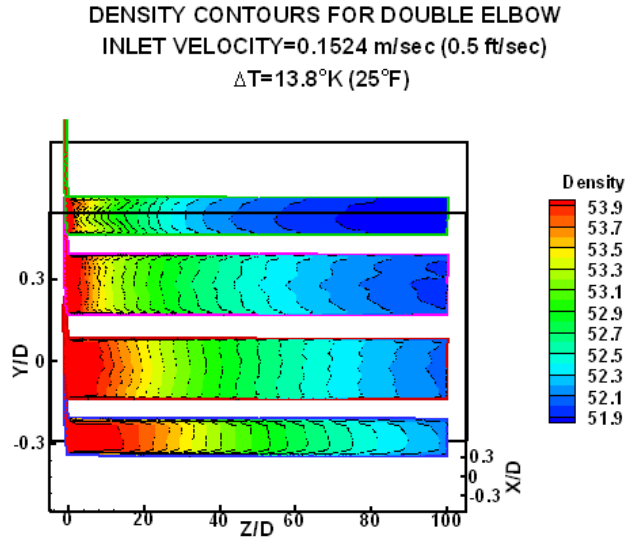

Fig. C-49 Density Slice Contours
V_0=0.1524 m/sec, ΔT_{wall}=13.8°K

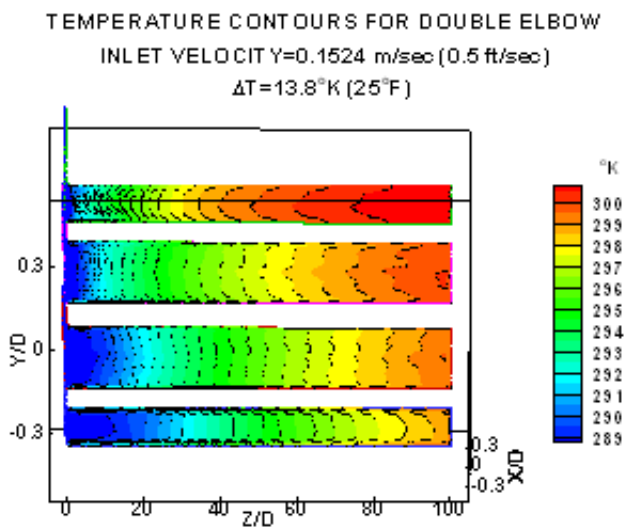

Fig. C-50 Temperature Slice Contours
V_0=0.1524 m/sec, ΔT_{wall}=13.8°K

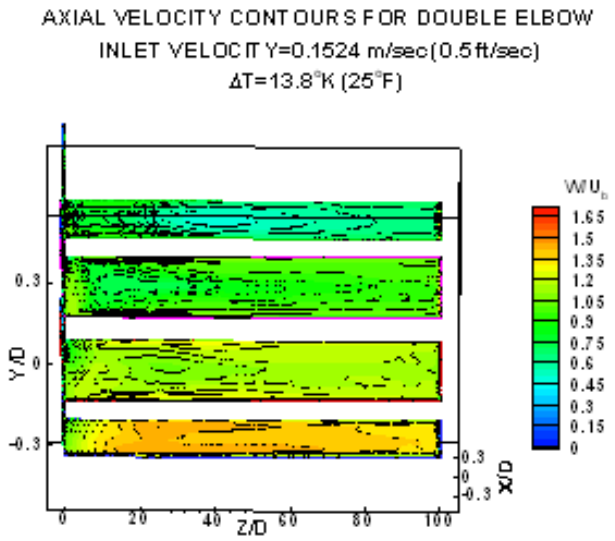

Fig. C-51 Axial Velocity Slice Contours
V_0=0.1524 m/sec, ΔT_{wall}=13.8°K

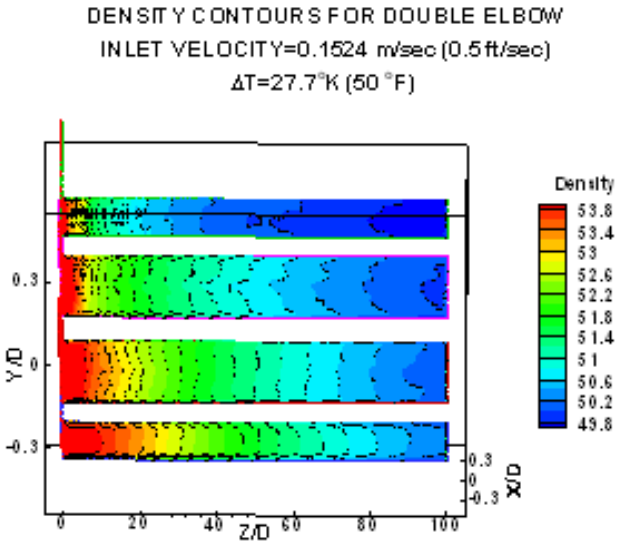

Fig. C-52 Density Slice Contours
V_0=0.1524 m/sec, ΔT_{wall}=27.7°K

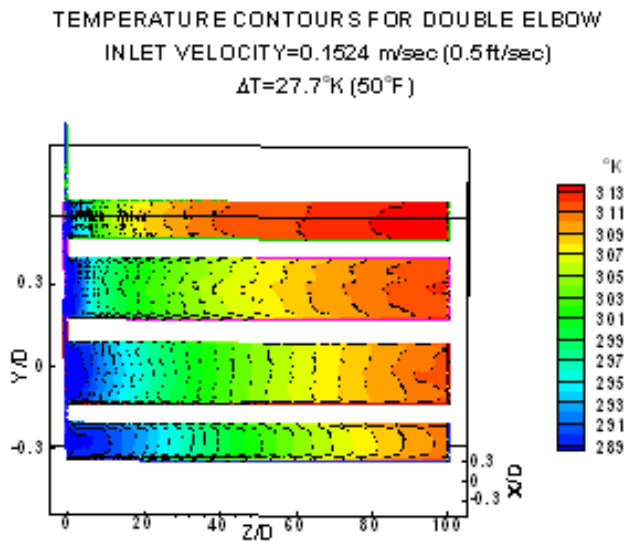

Fig. C-53 Temperature Slice Contours
V_0=0.1524 m/sec, ΔT_{wall}=27.7°K

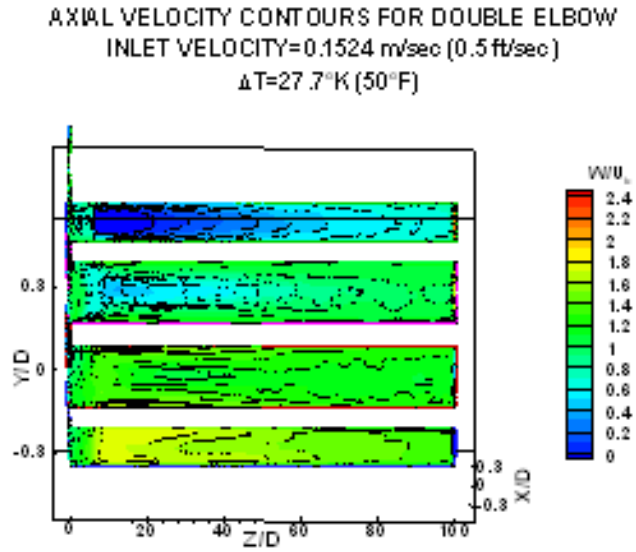

Fig. C-54 Axial Velocity Slice Contours
V_0=0.1524 m/sec, ΔT_{wall}=27.7°K

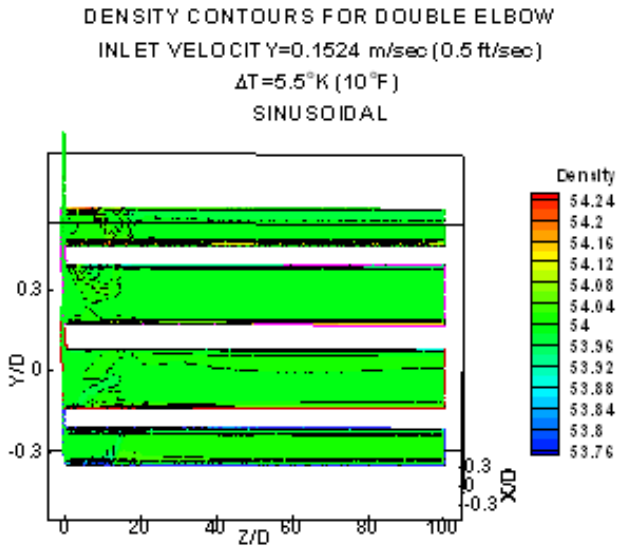

Fig. C-55 Density Slice Contours
V_0=0.1524 m/sec, ΔT_{wall}=-5.5°K Sinusoidal

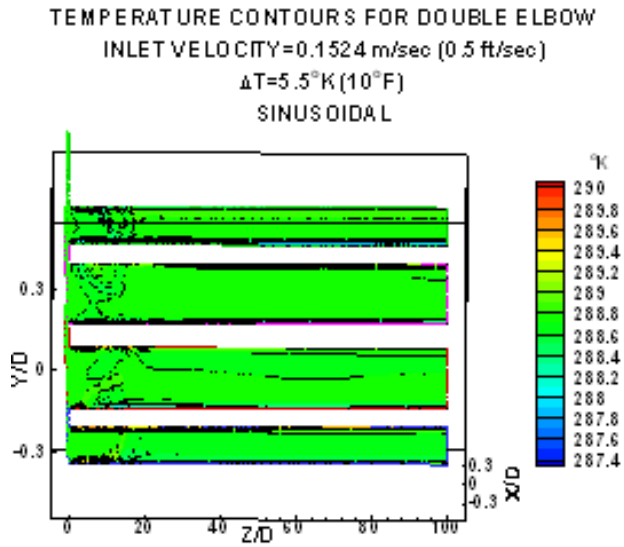

Fig. C-56 Temperature Slice Contours
V_0=0.1524 m/sec, ΔT_{wall}=-5.5°K Sinusoidal

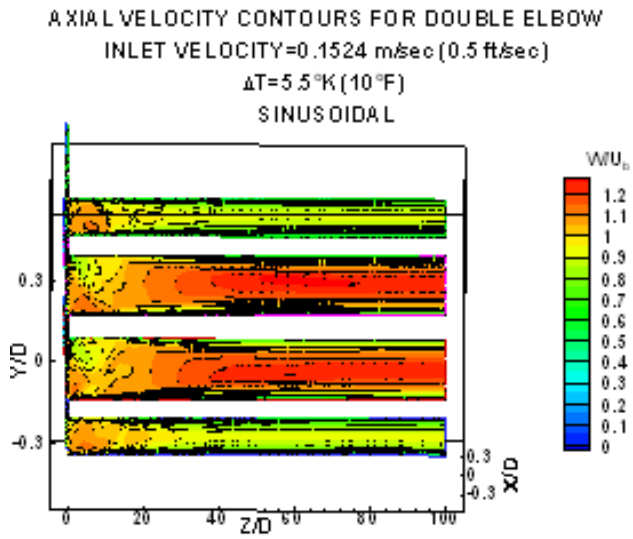

Fig. C-57 Axial Velocity Slice Contours
V_0=0.1524 m/sec, ΔT_{wall}=-5.5°K Sinusoidal

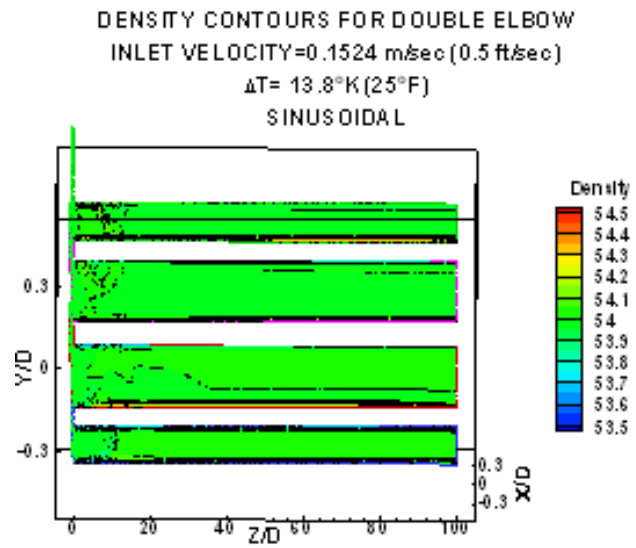

Fig. C-58 Density Slice Contours
V_0=0.1524 m/sec, ΔT_{wall}=-13.8°K Sinusoidal

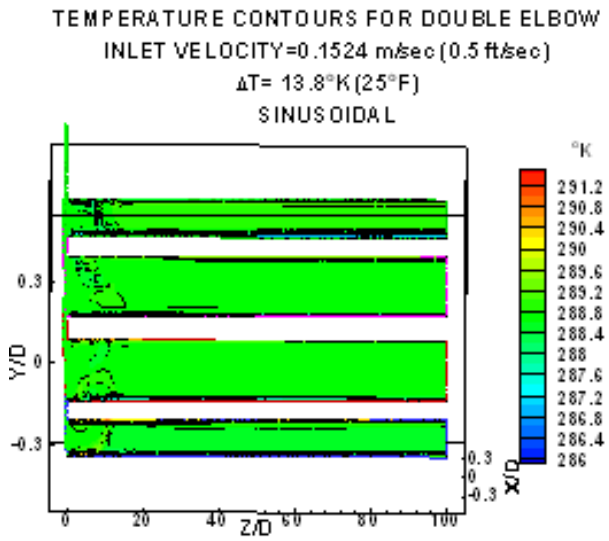

Fig. C-59 Temperature Slice Contours
V_0=0.1524 m/sec, ΔT_{wall}=-13.8°K Sinusoidal

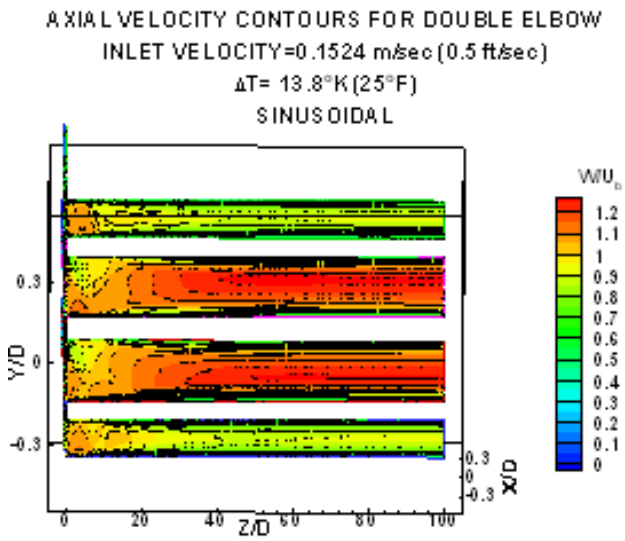

Fig. C-60 Axial Velocity Slice Contours
V_0=0.1524 m/sec, ΔT_{wall}=-13.8°K Sinusoidal

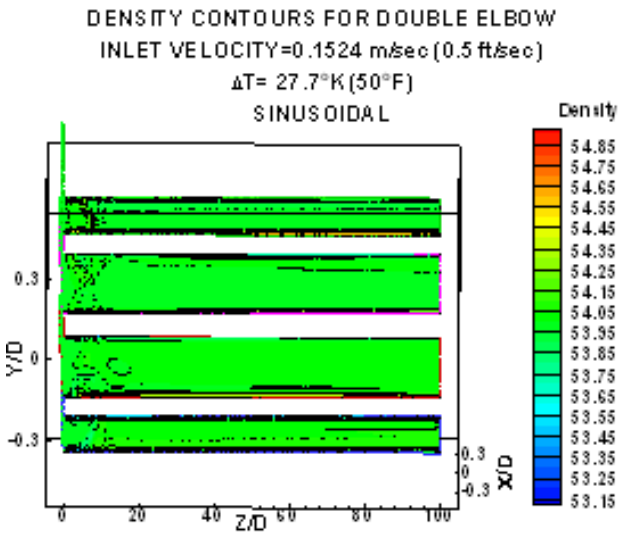

Fig. C-61 Density Slice Contours
V_0=0.1524 m/sec, ΔT_{wall}=-27.7°K Sinusoidal

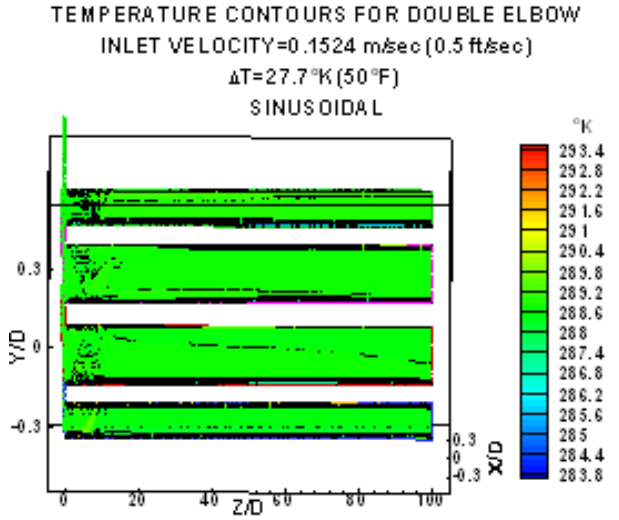

Fig. C-62 Temperature Slice Contours
V_0=0.1524 m/sec, ΔT_{wall}=-27.7°K Sinusoidal

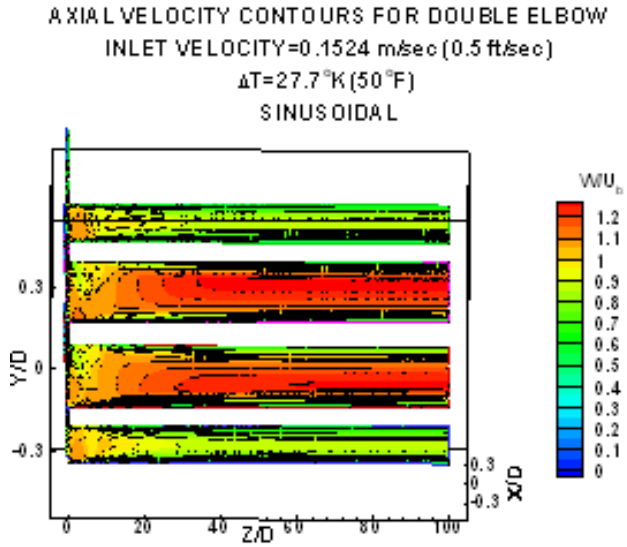

Fig. C-63 Axial Velocity Slice Contours
V_0=0.1524 m/sec, ΔT_{wall}=-27.7°K Sinusoidal

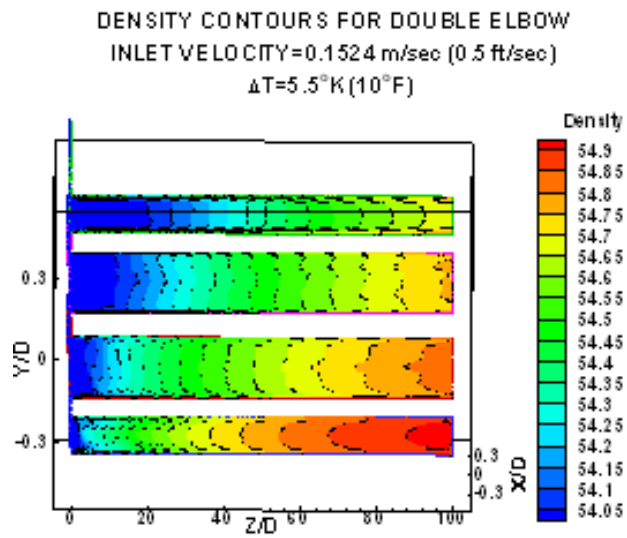

Fig. C-64 Density Slice Contours
V_0=0.1524 m/sec, ΔT_{wall}=-5.5°K

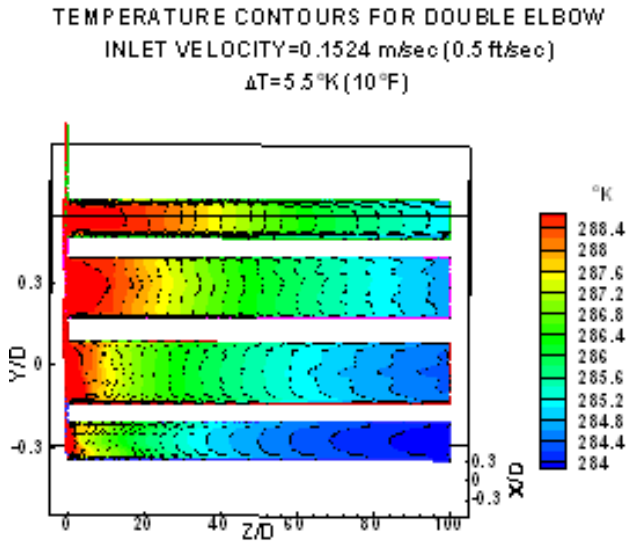

Fig. C-65 Temperature Slice Contours
V_0=0.1524 m/sec, ΔT_{wall}=-5.5°K

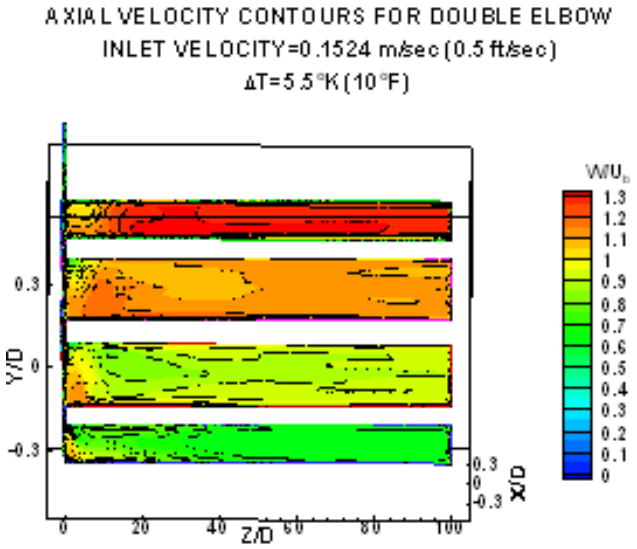

Fig. C-66 Axial Velocity Slice Contours
V_0=0.1524 m/sec, ΔT_{wall}=-5.5°K

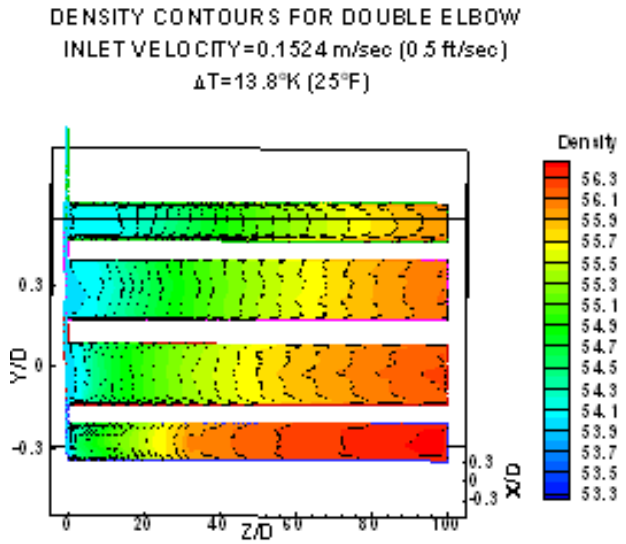

Fig. C-67 Density Slice Contours
V_0=0.1524 m/sec, ΔT_{wall}=-13.8°K

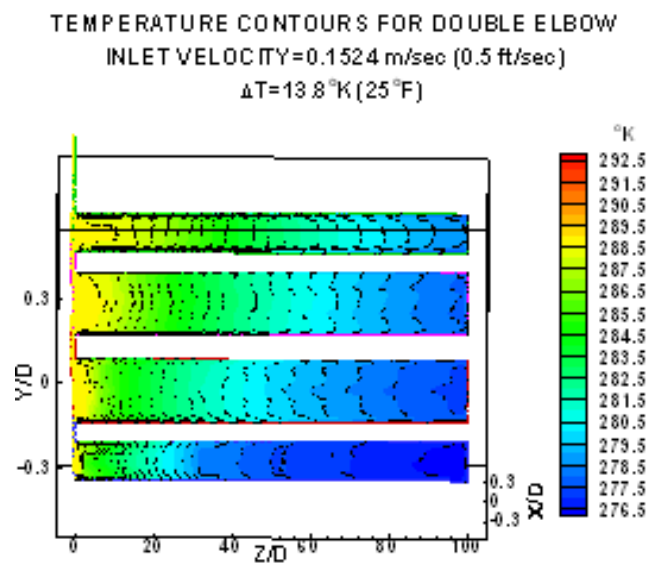

Fig. C-68 Temperature Slice Contours
V_0=0.1524 m/sec, ΔT_{wall}=-13.8°K

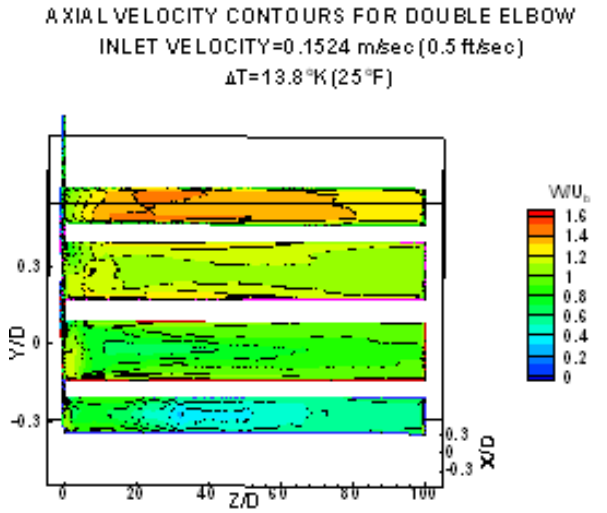

Fig. C-69 Axial Velocity Slice Contours
V_0=0.1524 m/sec, ΔT_{wall}=-13.8°K

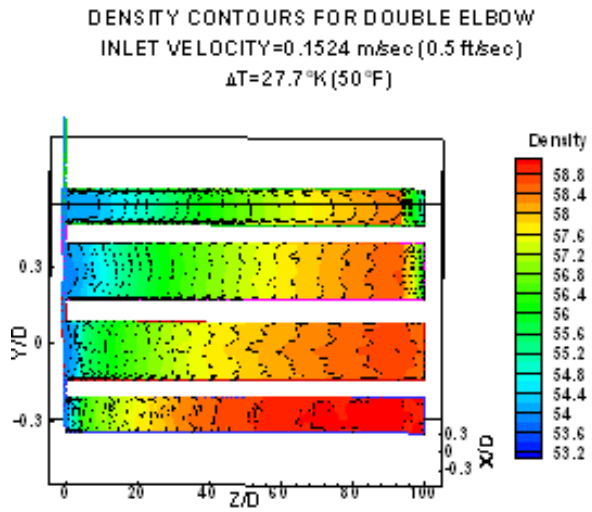

Fig. C-70 Density Slice Contours
V_0=0.1524 m/sec, ΔT_{wall}=-27.7°K

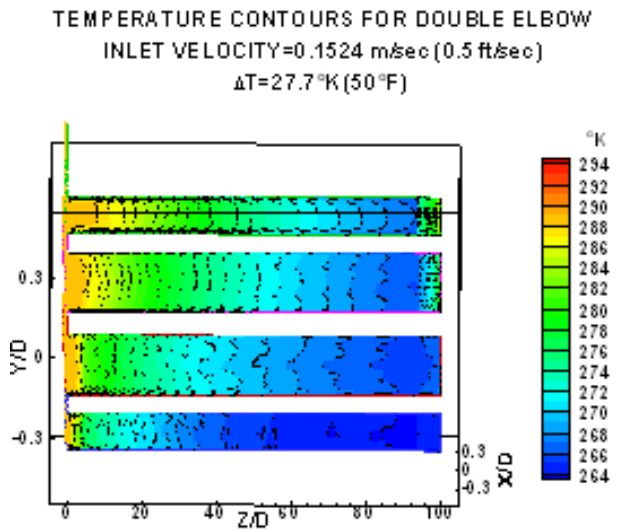

Fig. C-71 Temperature Slice Contours
V_0=0.1524 m/sec, ΔT_{wall}=-27.7°K

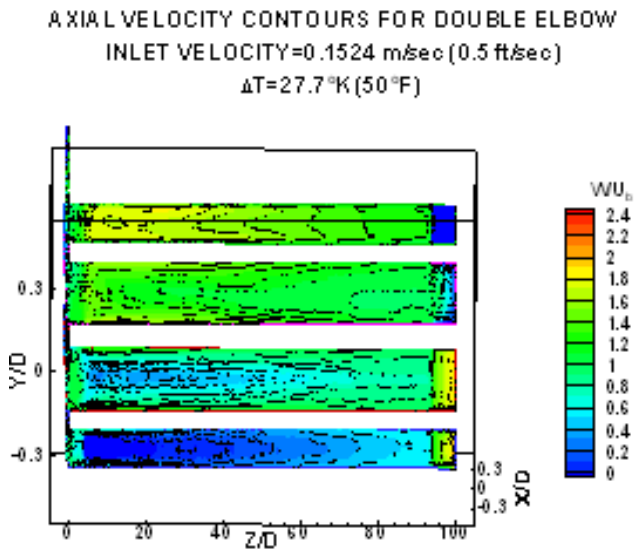

Fig. C-72 Axial Velocity Slice Contours
V_0=0.1524 m/sec, ΔT_{wall}=-27.7°K

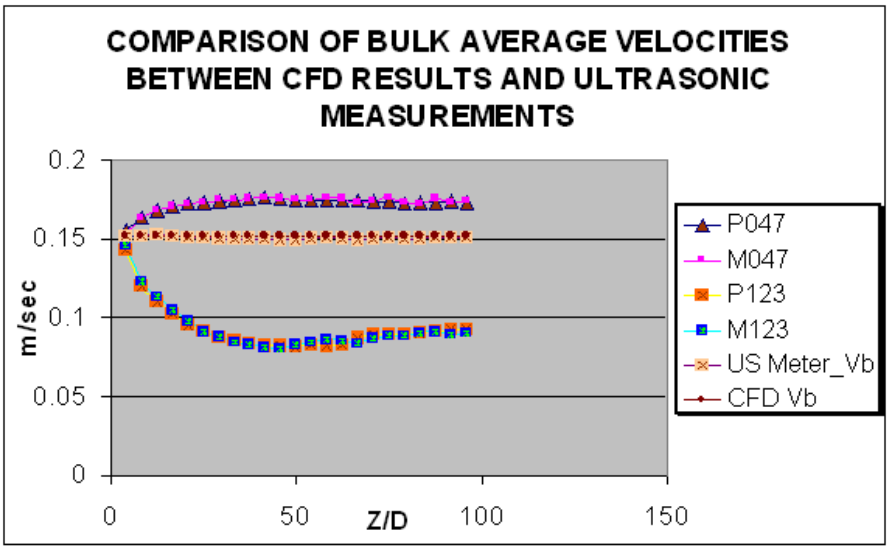

Fig. C-73 Comparison between CFD Vb and Ultrasonic Vb.
V_0=0.1524 m/sec, ΔT_{wall}=5.5°K Sinusoidal

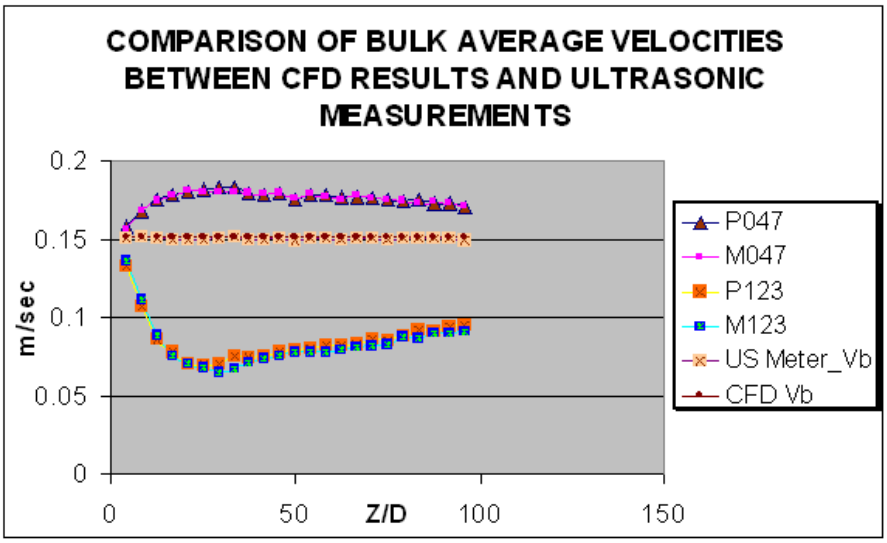

Fig. C-74 Comparison between CFD Vb and Ultrasonic Vb.
V_0=0.1524 m/sec, ΔT_{wall}=13.8°K Sinusoidal

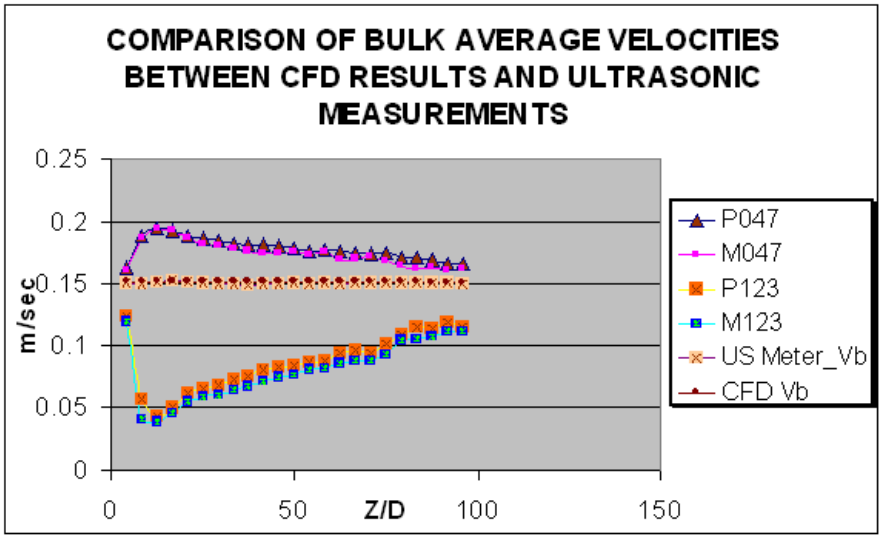

Fig. C-75 Comparison between CFD Vb and Ultrasonic Vb.
V_0=0.1524 m/sec, ΔT_{wall}=27.7°K Sinusoidal

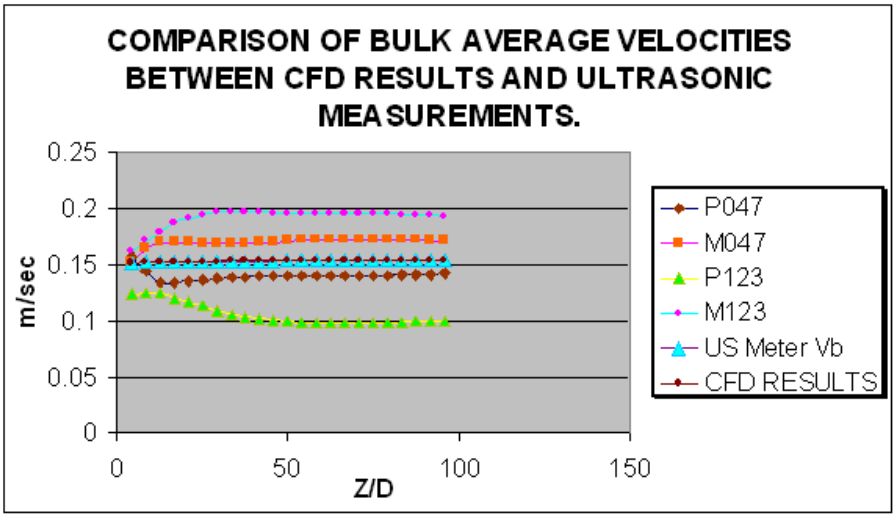

Fig. C-76 Comparison between CFD Vb and Ultrasonic Vb.
V_0=0.1524 m/sec, ΔT_{wall}=5.5°K

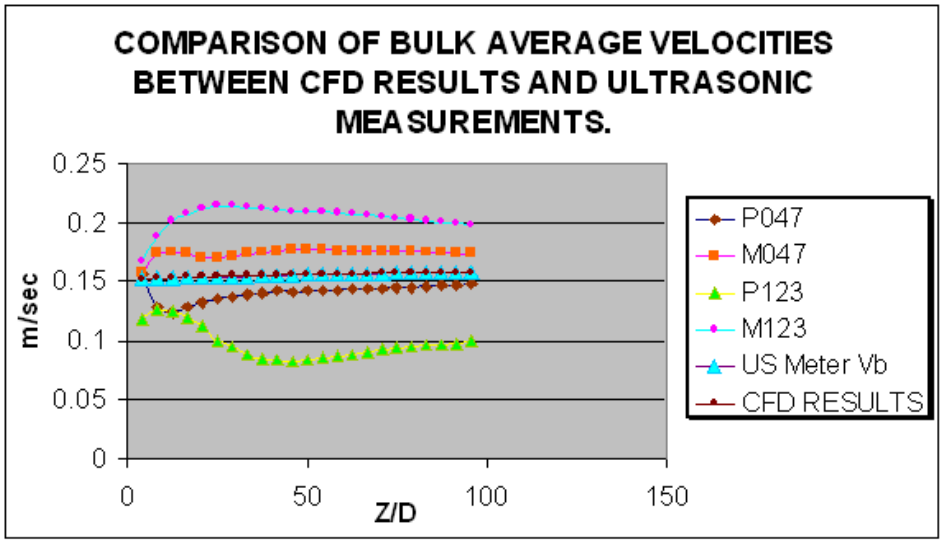

Fig. C-77 Comparison between CFD Vb and Ultrasonic Vb.
V_0=0.1524 m/sec, ΔT_{wall}=13.8°K

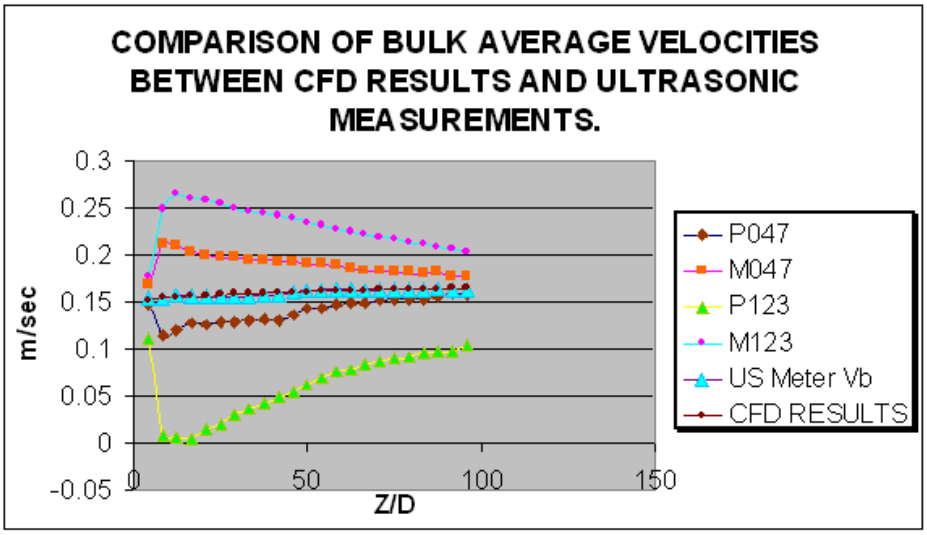

Fig. C-78 Comparison between CFD Vb and Ultrasonic Vb.
V_0=0.1524 m/sec, ΔT_{wall}=27.7°K

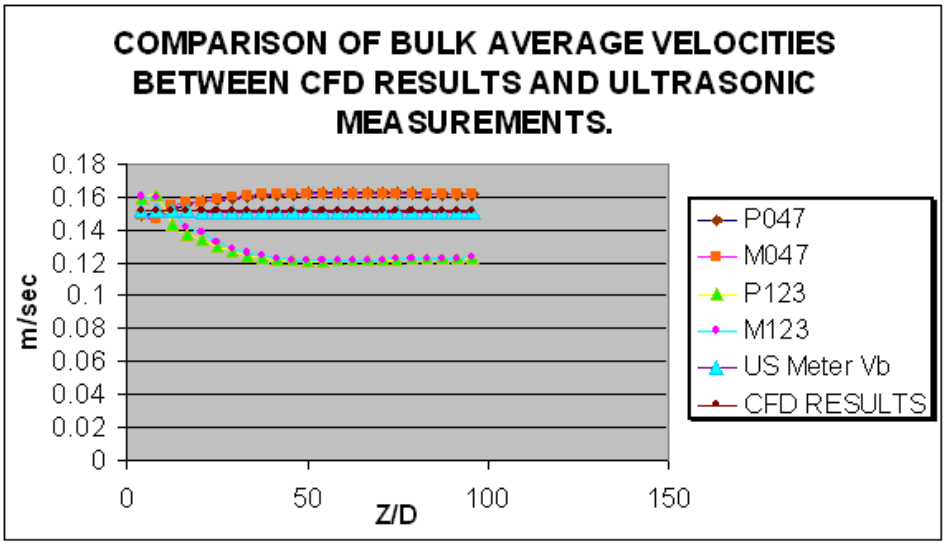

Fig. C-83 Comparison between CFD Vb and Ultrasonic Vb.
V_0=0.1524 m/sec, ΔT_{wall}=-13.8°K

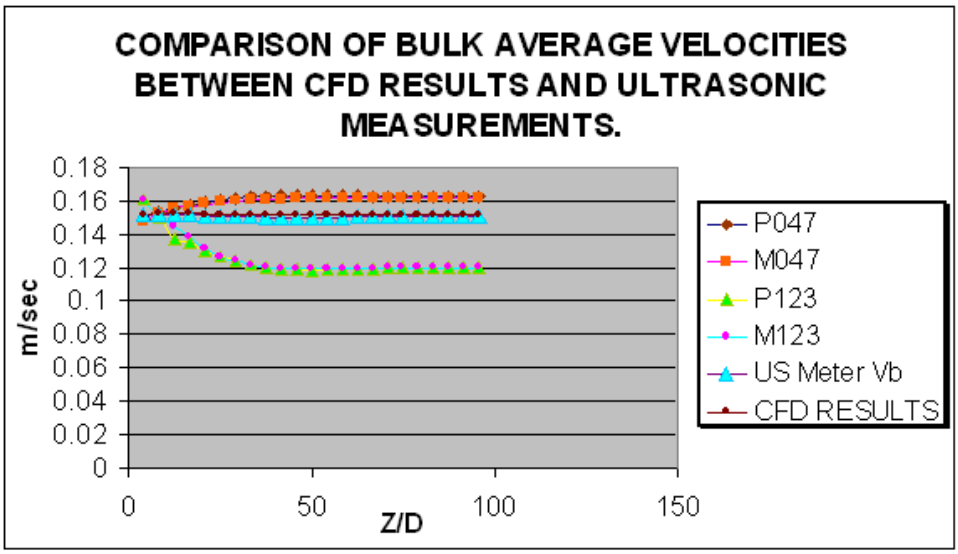

Fig. C-84 Comparison between CFD Vb and Ultrasonic Vb.
V_0=0.1524 m/sec, ΔT_{wall}=-27.7°K

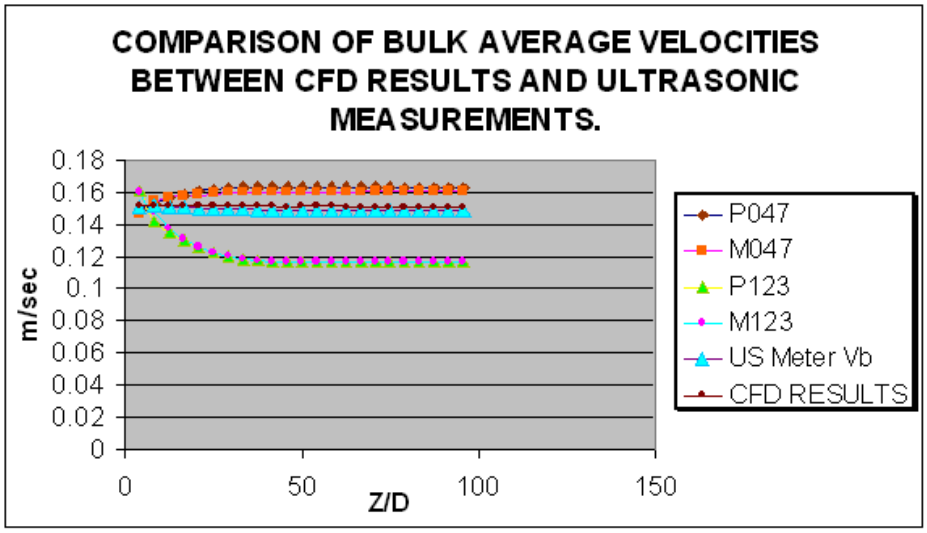

Fig. C-85
V_0=0.304 **idal**

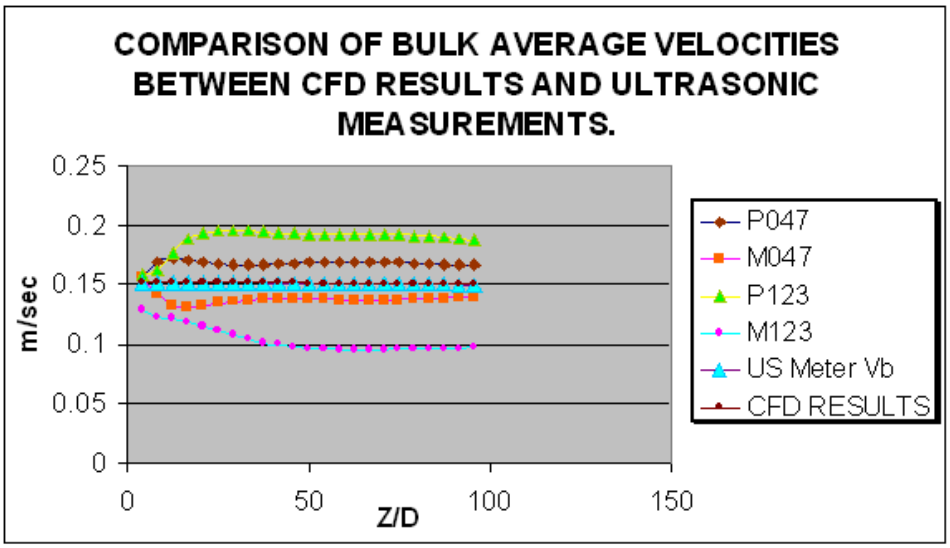

Fig. C-86
V_0=0.304 **al**

Fig. C-87 Axial Velocity Contours
V_0=0.3048 m/sec, ΔT_{wall}=5.5°K Sinusoidal

Fig. C-90 Axial Velocity Contours
V_0=0.3048 m/sec, ΔT_{wall}=13.8°K Sinusoidal

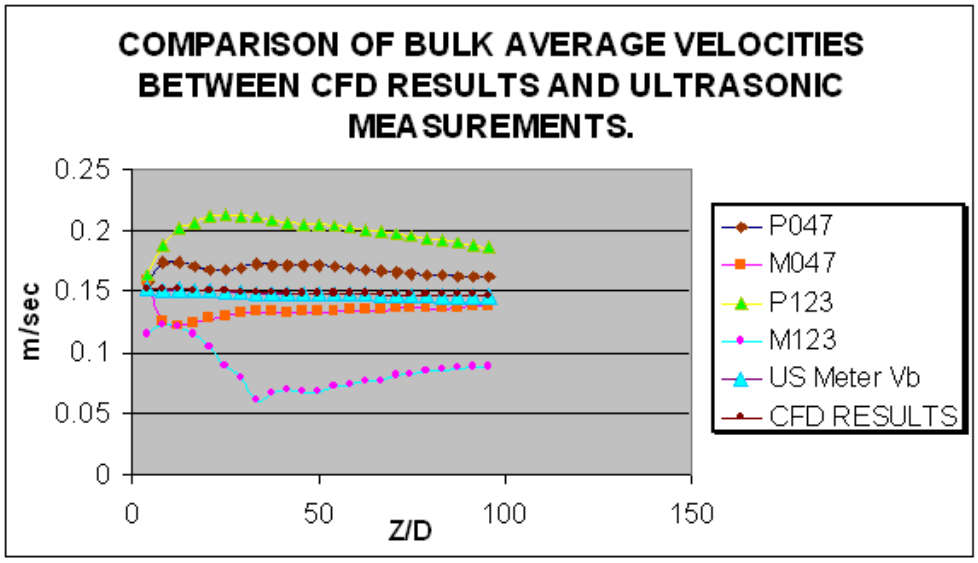

V_0=0.1524 m/sec, ΔT_{wall}=-13.8°K

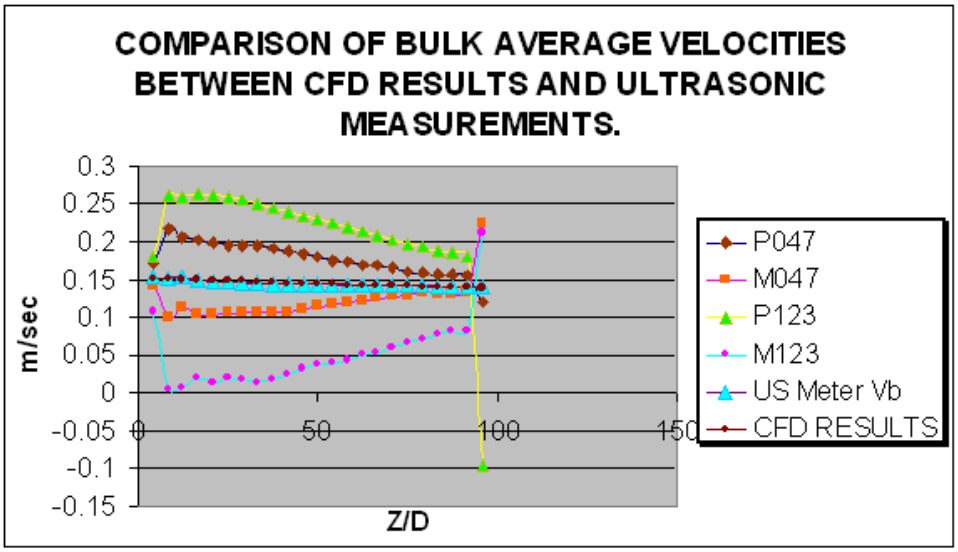

V_0=0.1524 m/sec, ΔT_{wall}=-27.7°K

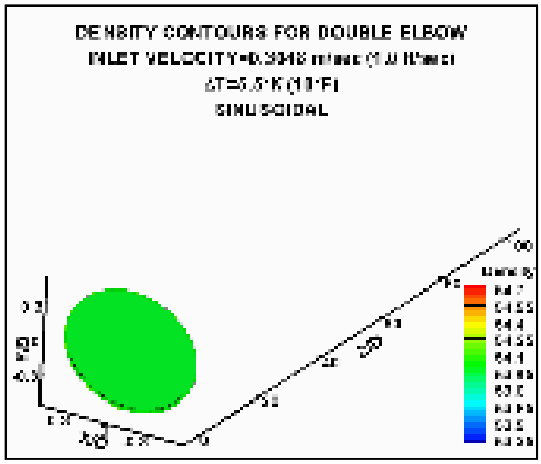

Fig. C-85 Density Contours
V_0=0.3048 m/sec, ΔT_{wall}=5.5°K Sinusoidal

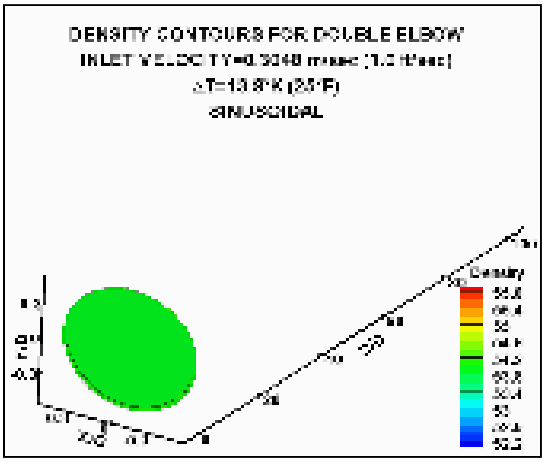

Fig. C-88 Density Contours
V_0=0.3048 m/sec, ΔT_{wall}=13.8°K Sinusoidal

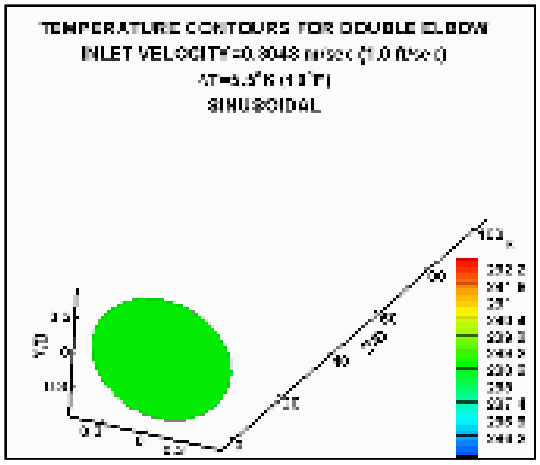

Fig. C-86 Temperature Contours
V_0=0.3048 m/sec, ΔT_{wall}=5.5°K Sinusoidal

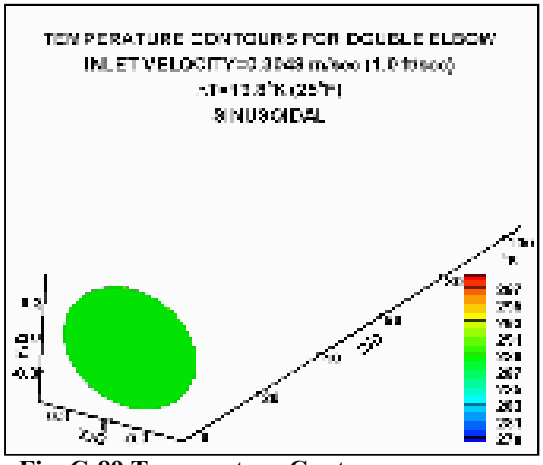

Fig. C-89 Temperature Contours
V_0=0.3048 m/sec, ΔT_{wall}=13.8°K Sinusoidal

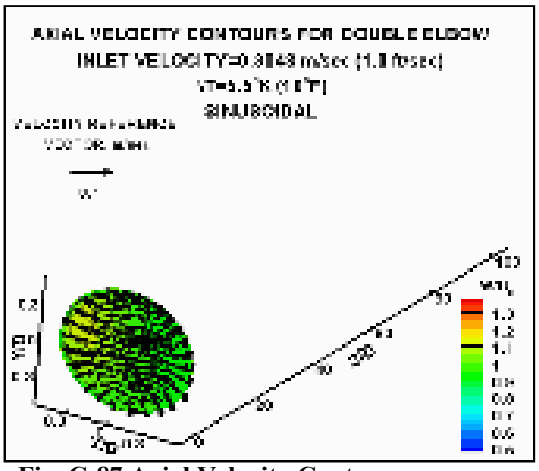

Fig. C-87 Axial Velocity Contours
V_0=0.3048 m/sec, ΔT_{wall}=5.5°K Sinusoidal

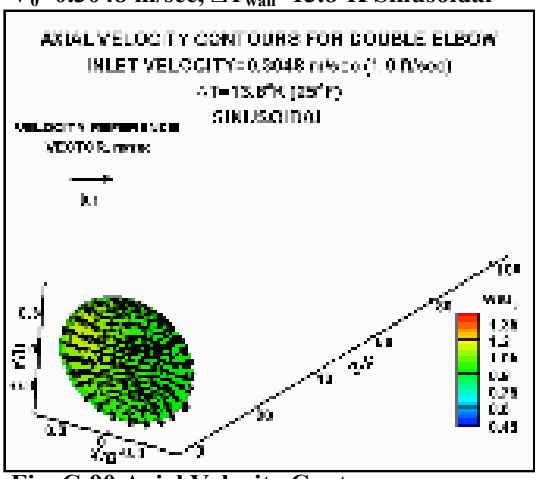

Fig. C-90 Axial Velocity Contours
V_0=0.3048 m/sec, ΔT_{wall}=13.8°K Sinusoidal

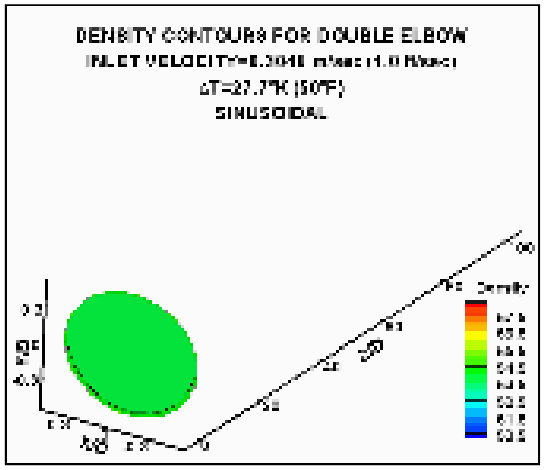

Fig. C-91 Density Contours
V_0=0.3048 m/sec, ΔT_{wall}=27.7°K Sinusoidal

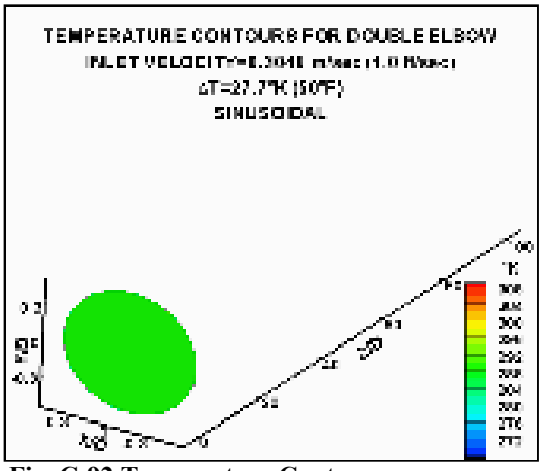

Fig. C-92 Temperature Contours
V_0=0.3048 m/sec, ΔT_{wall}=27.7°K Sinusoidal

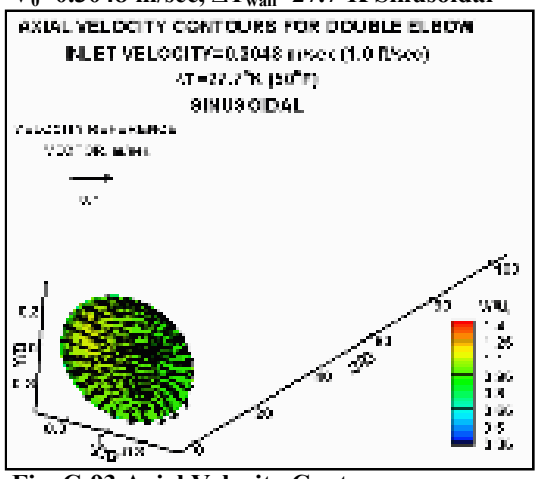

Fig. C-93 Axial Velocity Contours
V_0=0.3048 m/sec, ΔT_{wall}=27.7°K Sinusoidal

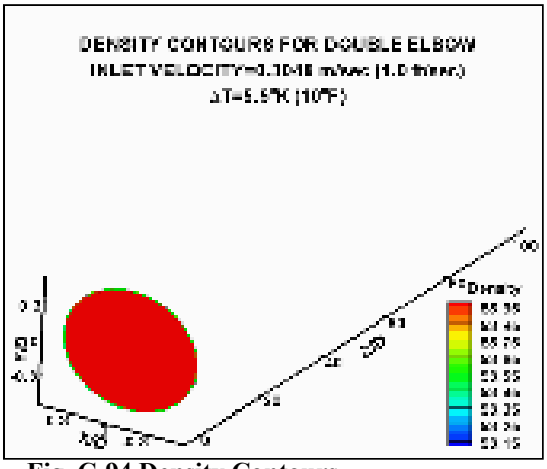

Fig. C-94 Density Contours
V_0=0.3048 m/sec, ΔT_{wall}=5.5°K

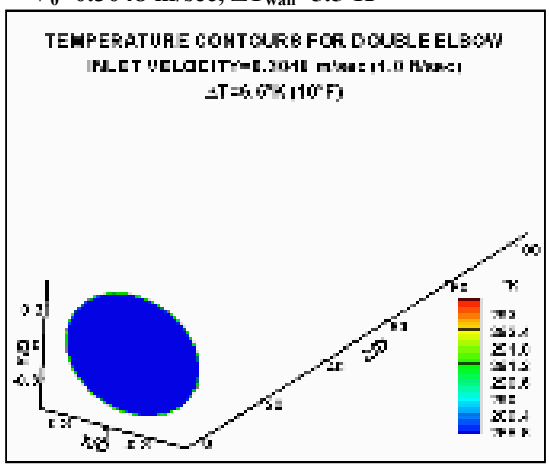

Fig. C-95 Temperature Contours
V_0=0.3048 m/sec, ΔT_{wall}=5.5°K

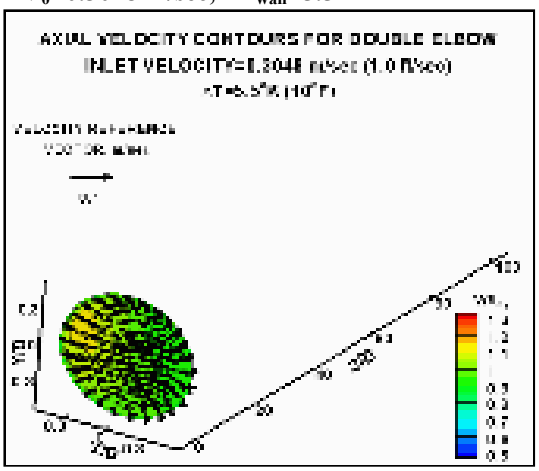

Fig. C-96 Axial Velocity Contours
V_0=0.3048 m/sec, ΔT_{wall}=5.5°K

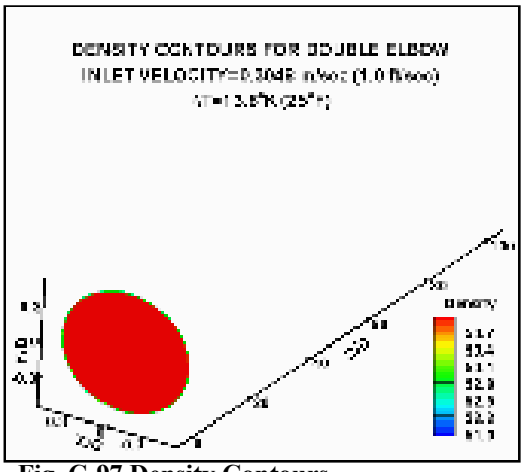

Fig. C-97 Density Contours
V_0=0.3048 m/sec, ΔT_{wall}=13.8°K

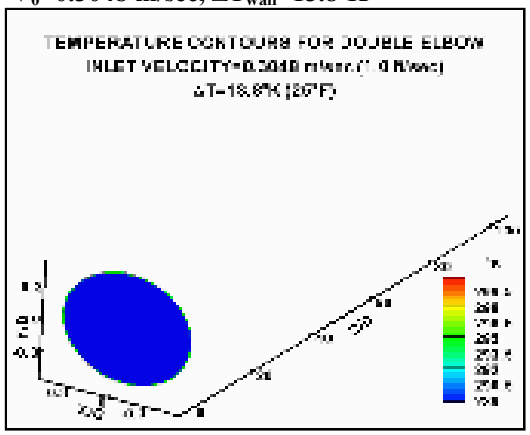

Fig. C-98 Temperature Contours
V_0=0.3048 m/sec, ΔT_{wall}=13.8°K

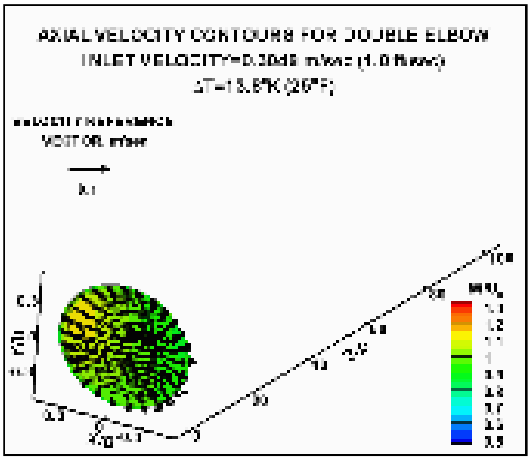

Fig. C-99 Axial Velocity Contours
V_0=0.3048 m/sec, ΔT_{wall}=13.8°K

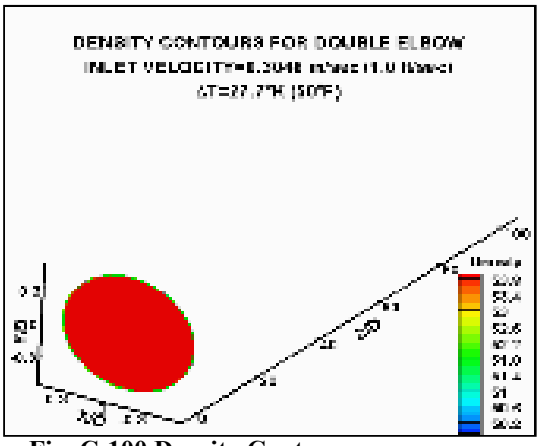

Fig. C-100 Density Contours
V_0=0.3048 m/sec, ΔT_{wall}=27.7°K

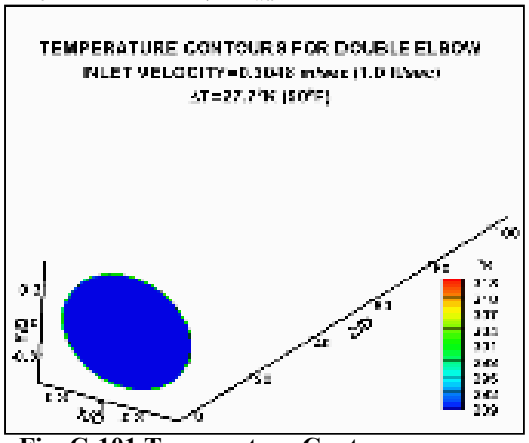

Fig. C-101 Temperature Contours
V_0=0.3048 m/sec, ΔT_{wall}=27.7°K

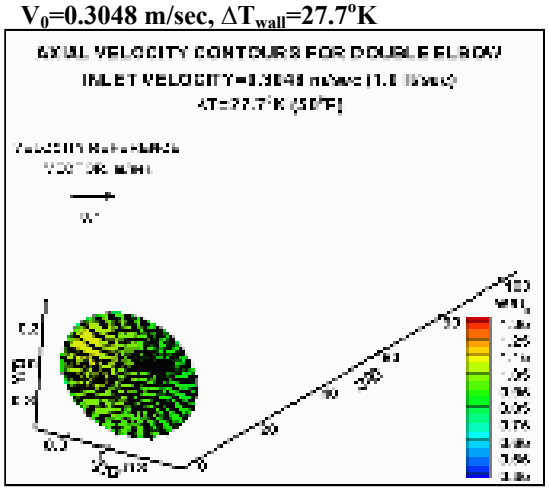

Fig. C-102 Axial Velocity Contours
V_0=0.3048 m/sec, ΔT_{wall}=27.7°K

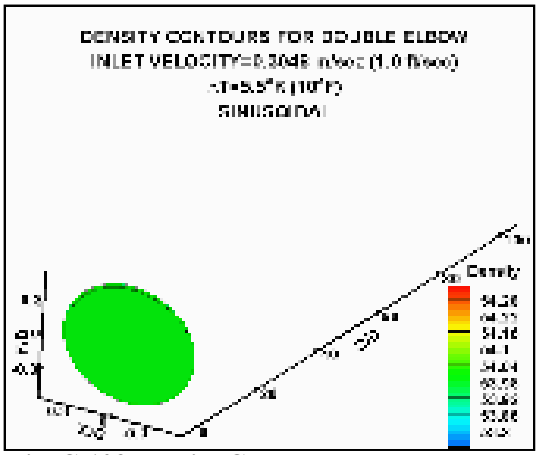

Fig. C-103 Density Contours
V_0=0.3048 m/sec, ΔT_{wall}=-5.5°K Sinusoidal

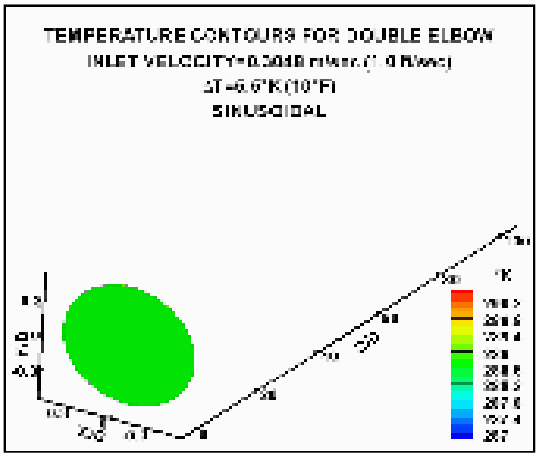

Fig. C-104 Temperature Contours
V_0=0.3048 m/sec, ΔT_{wall}=-5.5°K Sinusoidal

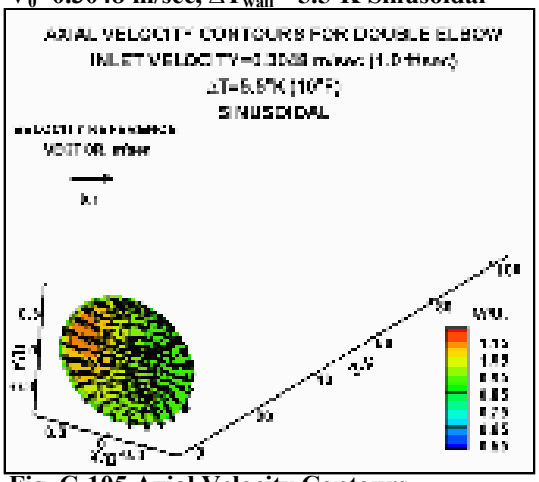

Fig. C-105 Axial Velocity Contours
V_0=0.3048 m/sec, ΔT_{wall}=-5.5°K Sinusoidal

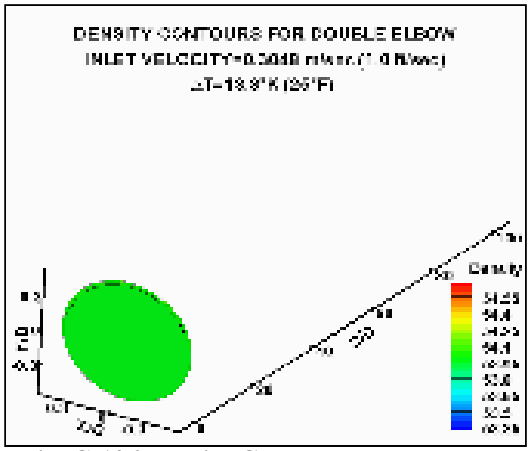

Fig. C-106 Density Contours
V_0=0.3048 m/sec, ΔT_{wall}=-13.8°K Sinusoidal

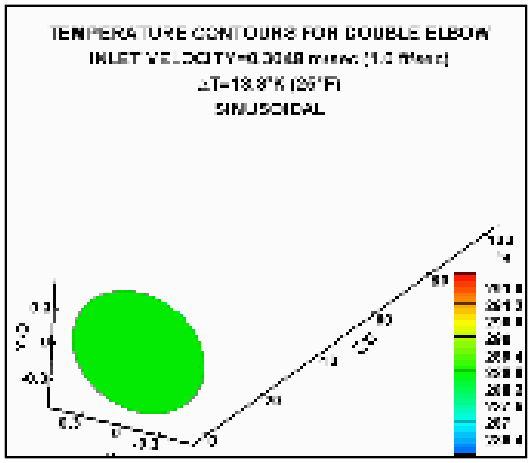

Fig. C-107 Temperature Contours
V_0=0.3048 m/sec, ΔT_{wall}=-13.8°K Sinusoidal

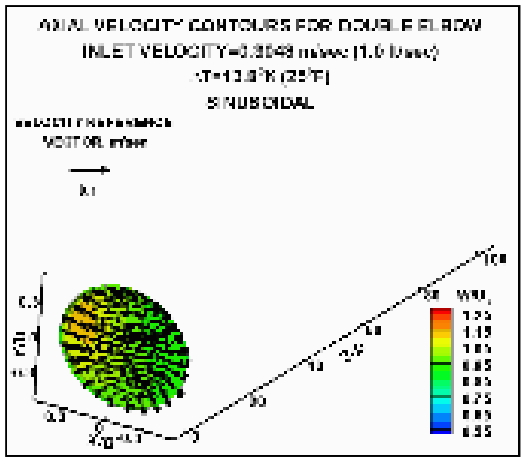

Fig. C-108 Axial Velocity Contours
V_0=0.3048 m/sec, ΔT_{wall}=-13.8°K Sinusoidal

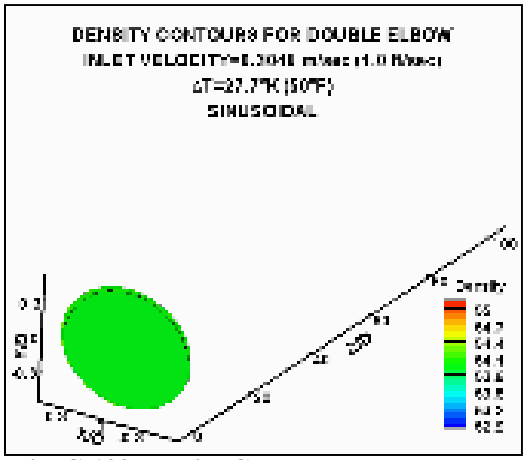

Fig. C-109 Density Contours
V_0=0.3048 m/sec, ΔT_{wall}=-27.7°K Sinusoidal

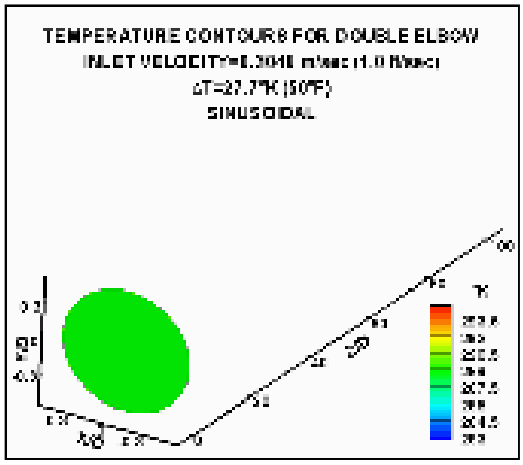

Fig. C-110 Temperature Contours
V_0=0.3048 m/sec, ΔT_{wall}=-27.7°K Sinusoidal

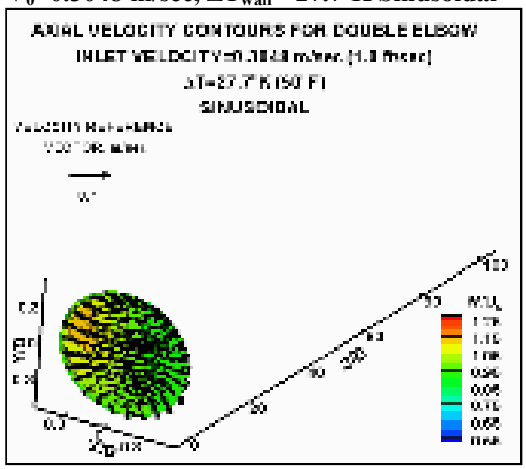

Fig. C-11 Axial Velocity Contours
V_0=0.3048 m/sec, ΔT_{wall}=-27.7°K Sinusoidal

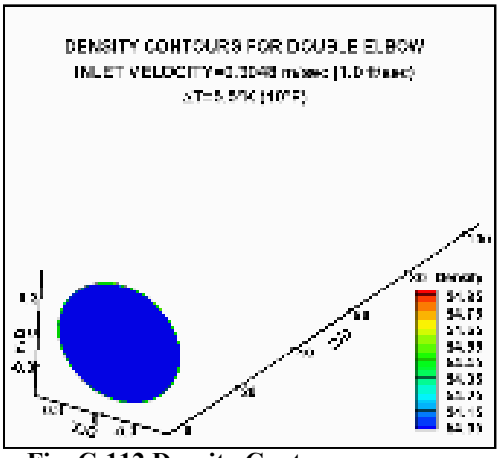

Fig. C-112 Density Contours
V_0=0.3048 m/sec, ΔT_{wall}=-5.5°K

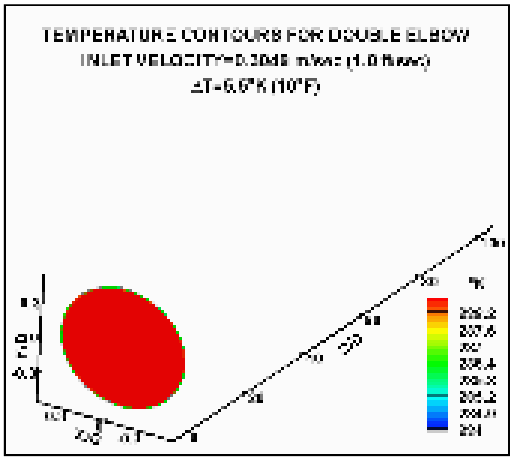

Fig. C-113 Temperature Contours
V_0=0.3048 m/sec, ΔT_{wall}=-5.5°K

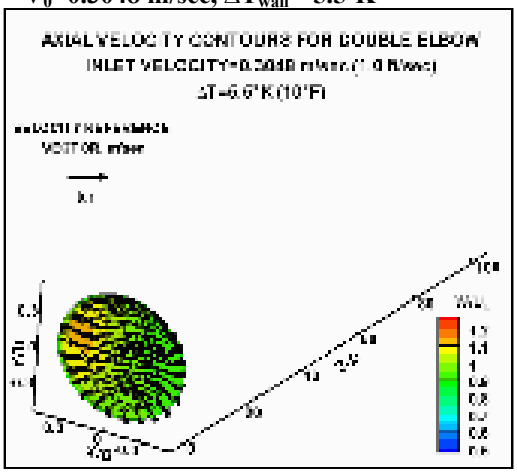

Fig. C-114 Axial Velocity Contours
V_0=0.3048 m/sec, ΔT_{wall}=-5.5°K

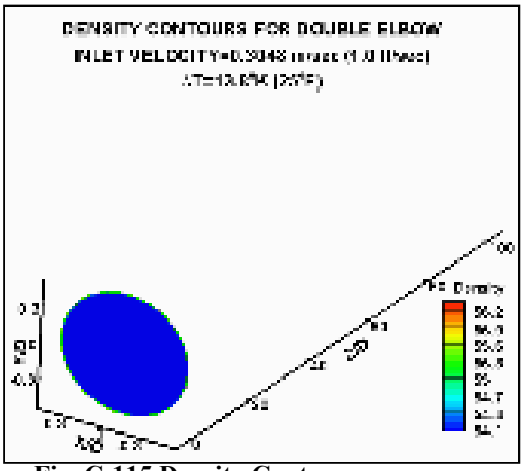

Fig. C-115 Density Contours
V_0=0.3048 m/sec, ΔT_{wall}=-13.8°K

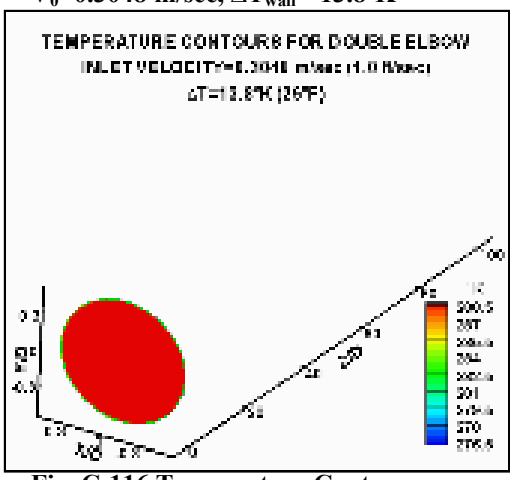

Fig. C-116 Temperature Contours
V_0=0.3048 m/sec, ΔT_{wall}=-13.8°K

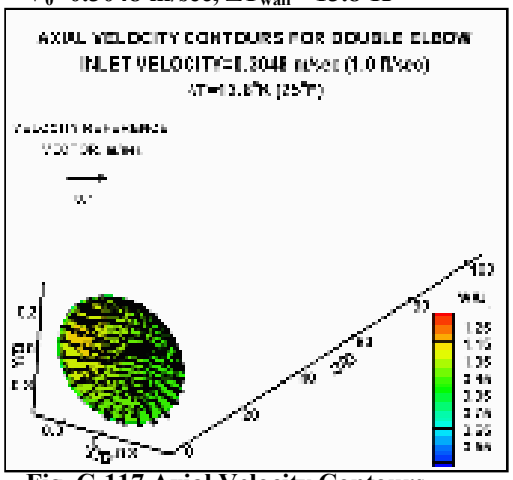

Fig. C-117 Axial Velocity Contours
V_0=0.3048 m/sec, ΔT_{wall}=-13.8°K

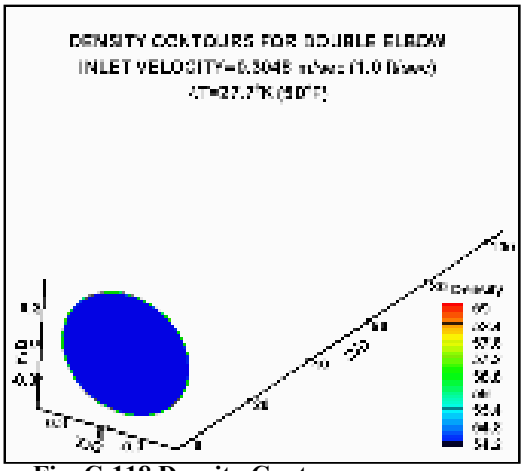

Fig. C-118 Density Contours
V_0=0.3048 m/sec, ΔT_{wall}=-27.7°K

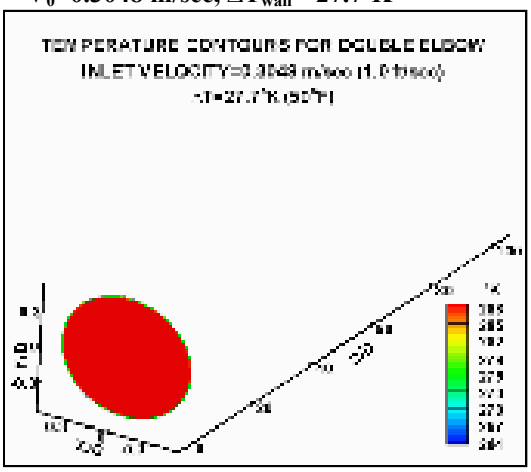

Fig. C-119 Temperature Contours
V_0=0.3048 m/sec, ΔT_{wall}=-27.7°K

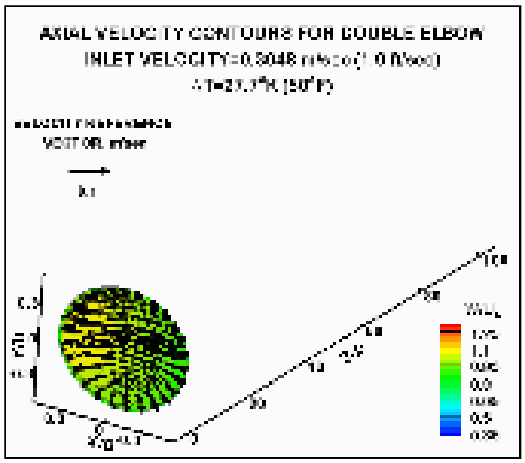

Fig. C-120 Axial Velocity Contours
V_0=0.3048 m/sec, ΔT_{wall}=-27.7°K

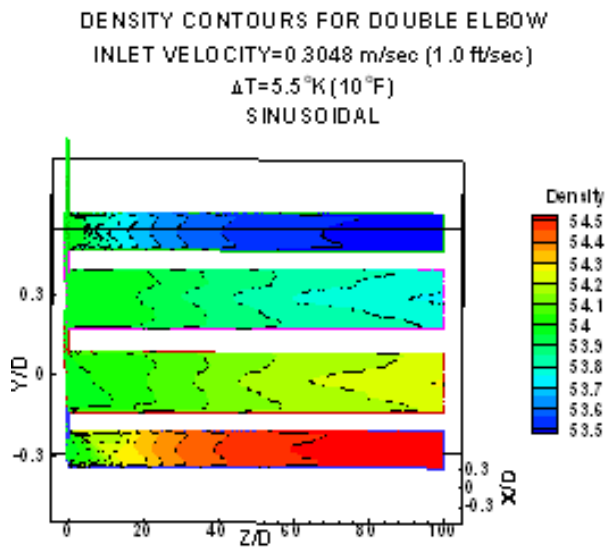

Fig. C-121 Density Slice Contours
V_0=0.3048 m/sec, ΔT_{wall}=5.5°K Sinusoidal

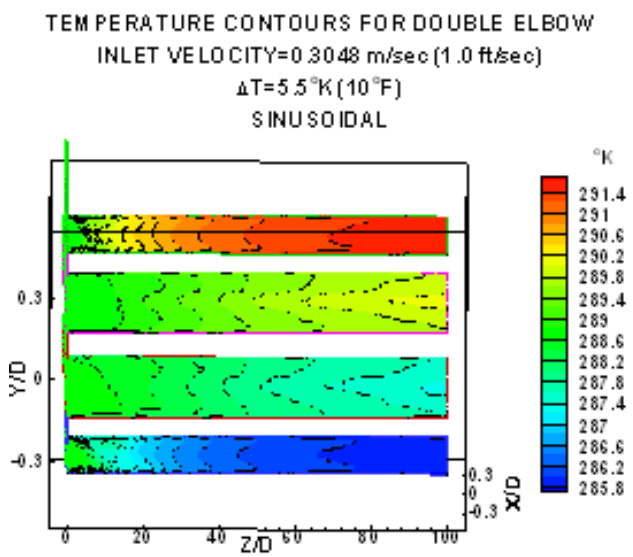

Fig. C-122 Temperature Slice Contours
V_0=0.3048 m/sec, ΔT_{wall}=5.5°K Sinusoidal

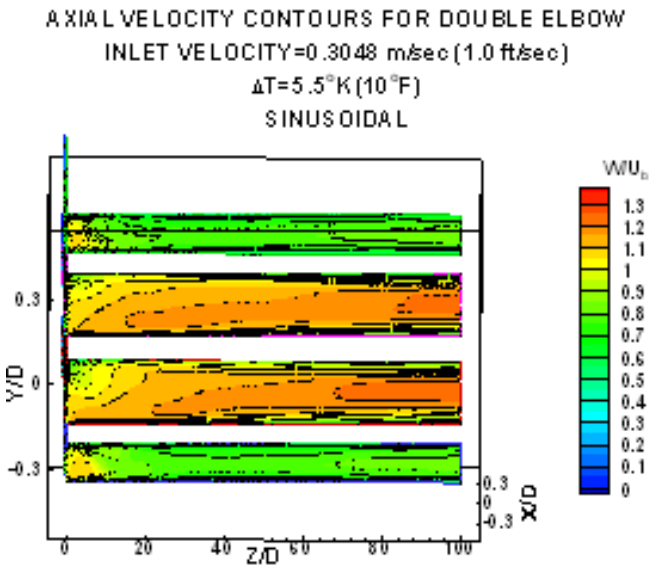

Fig. C-123 Axial Velocity Slice Contours
V_0=0.3048 m/sec, ΔT_{wall}=5.5°K Sinusoidal

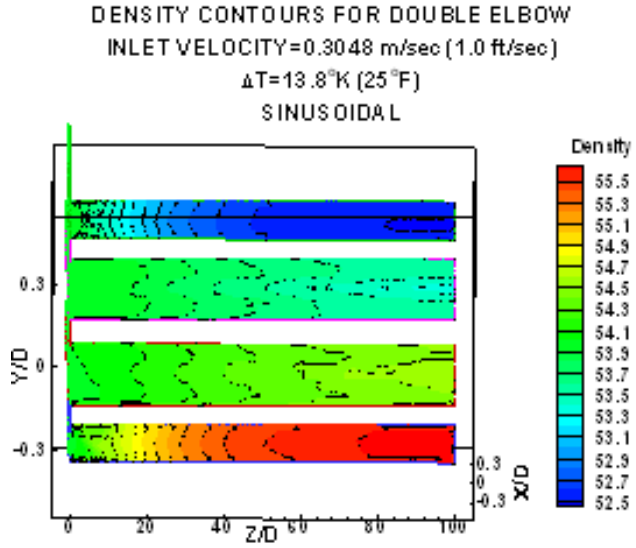

Fig. C-124 Density Slice Contours
V_0=0.3048 m/sec, ΔT_{wall}=13.8°K Sinusoidal

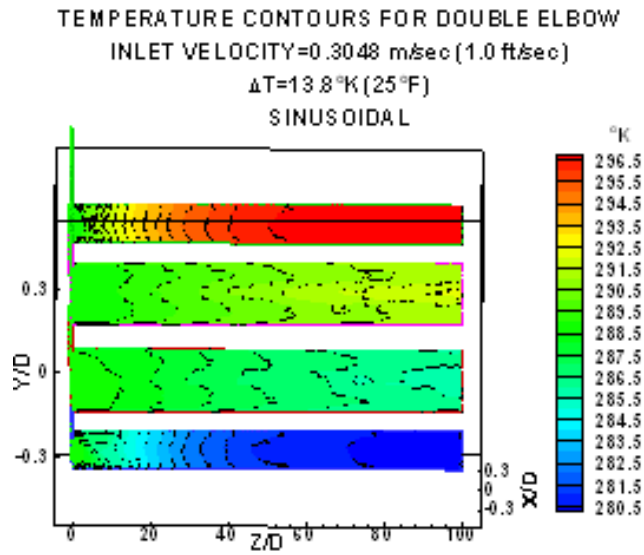

Fig. C-125 Temperature Slice Contours
V_0=0.3048 m/sec, ΔT_{wall}=13.8°K Sinusoidal

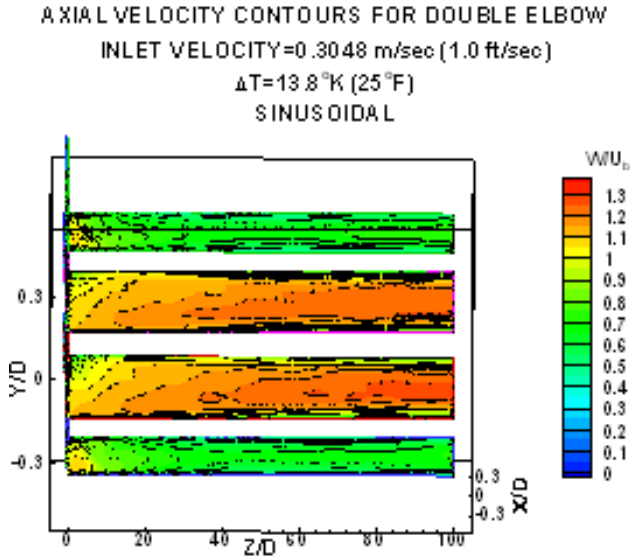

Fig. C-126 Axial Velocity Slice Contours
V_0=0.3048 m/sec, ΔT_{wall}=13.8°K Sinusoidal

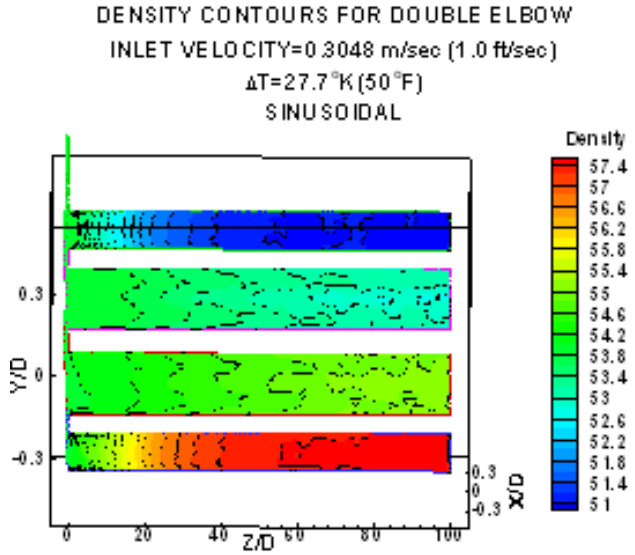

Fig. C-127 Density Slice Contours
V_0=0.3048 m/sec, ΔT_{wall}=27.7°K Sinusoidal

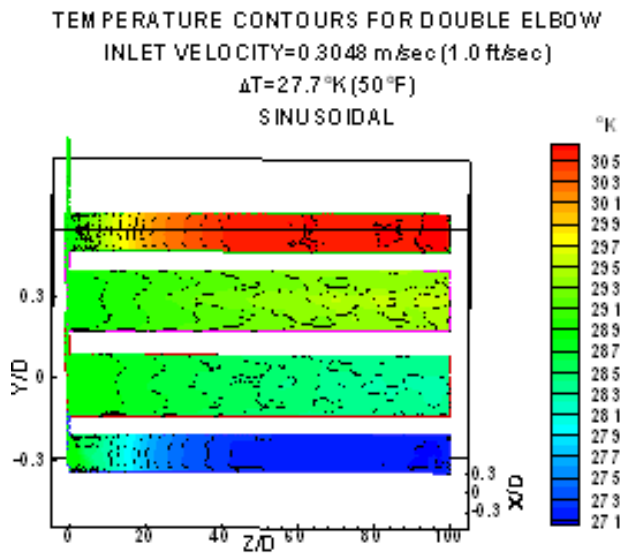

Fig. C-128 Temperature Slice Contours
V_0=0.3048 m/sec, ΔT_{wall}=27.7°K Sinusoidal

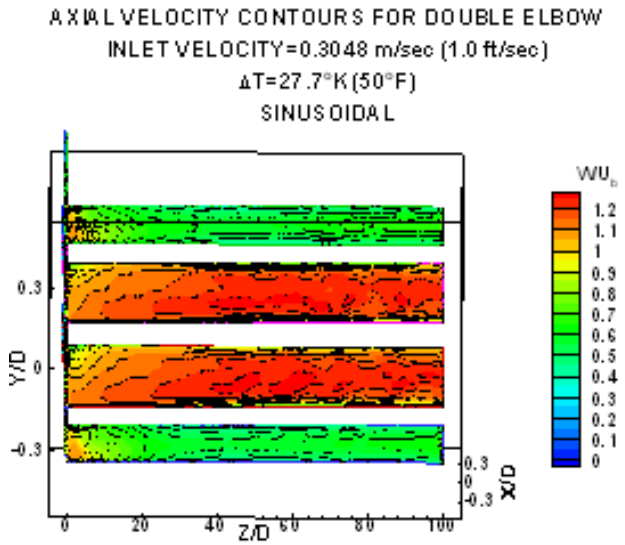

Fig. C-129 Axial Velocity Slice Contours
V_0=0.3048 m/sec, ΔT_{wall}=27.7°K Sinusoidal

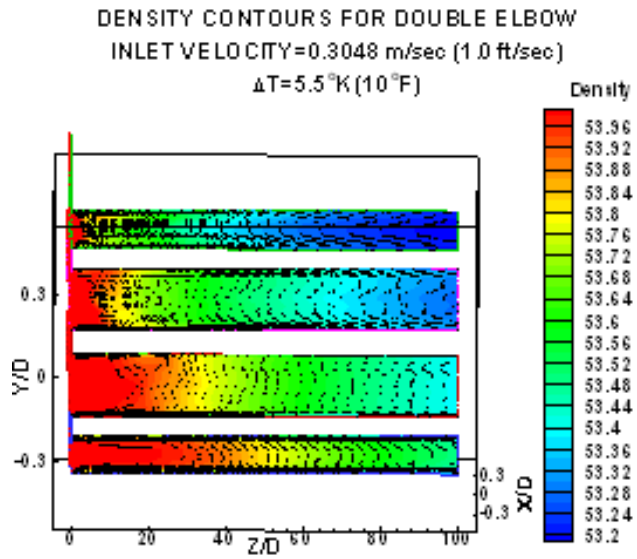

Fig. C-130 Density Slice Contours
V_0=0.3048 m/sec, ΔT_{wall}=5.5°K

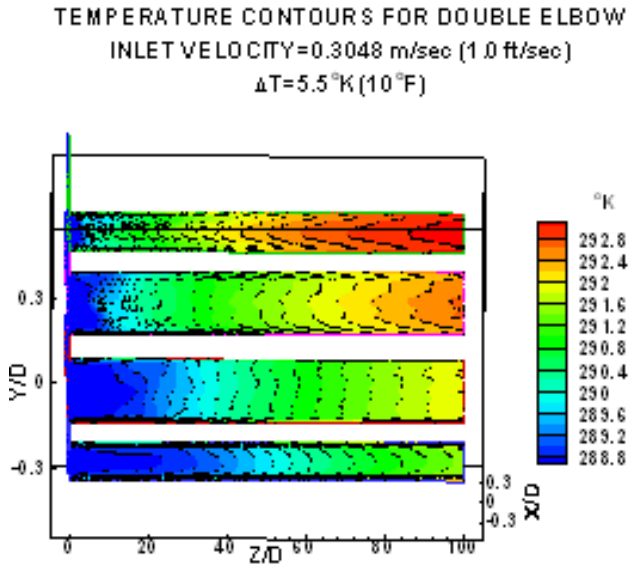

Fig. C-131 Temperature Slice Contours
V_0=0.3048 m/sec, ΔT_{wall}=5.5°K

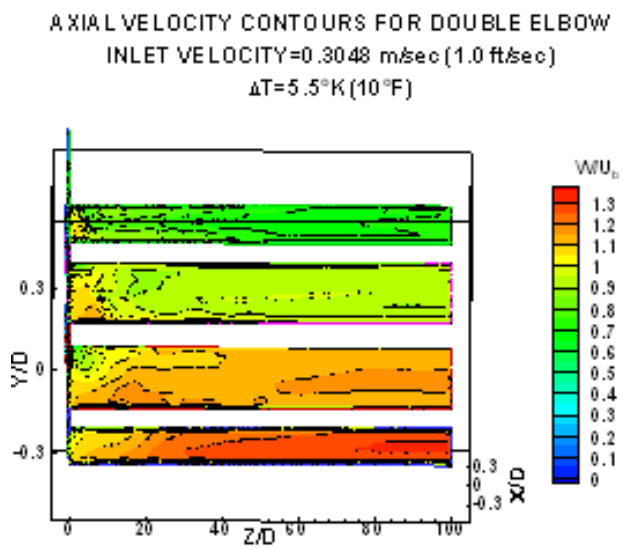

Fig. C-132 Axial Velocity Slice Contours
V_0=0.3048 m/sec, ΔT_{wall}=5.5°K

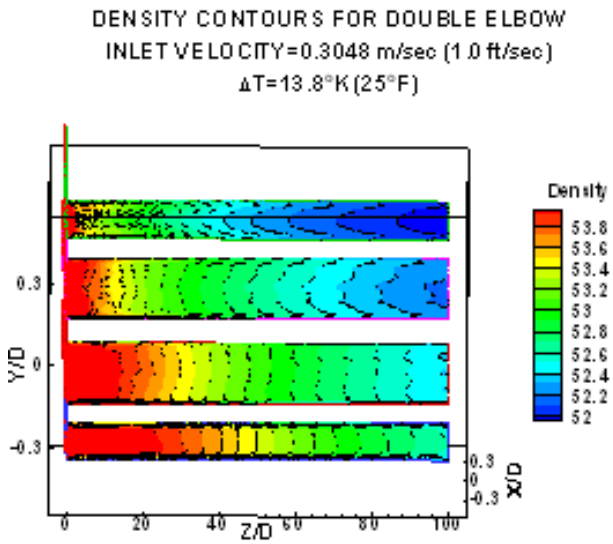

Fig. C-133 Density Slice Contours
V_0=0.3048 m/sec, ΔT_{wall}=13.8°K

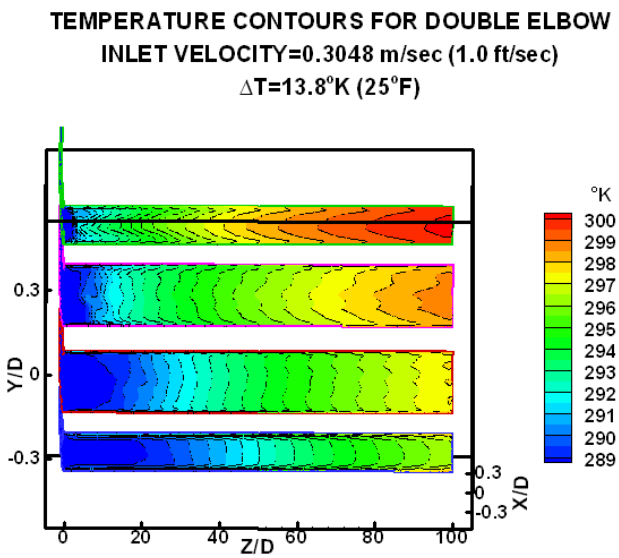

Fig. C-134 Temperature Slice Contours
V_0=0.3048 m/sec, ΔT_{wall}=13.8°K

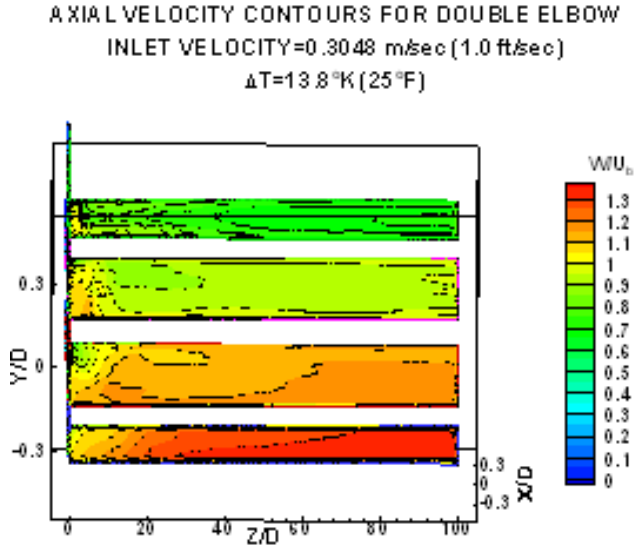

Fig. C-135 Axial Velocity Slice Contours
V_0=0.3048 m/sec, ΔT_{wall}=13.8°K

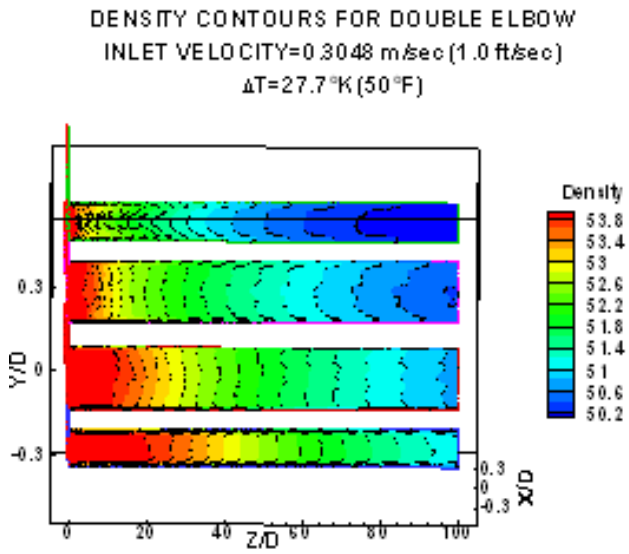

Fig. C-136 Density Slice Contours
V_0=0.3048 m/sec, ΔT_{wall}=27.7°K

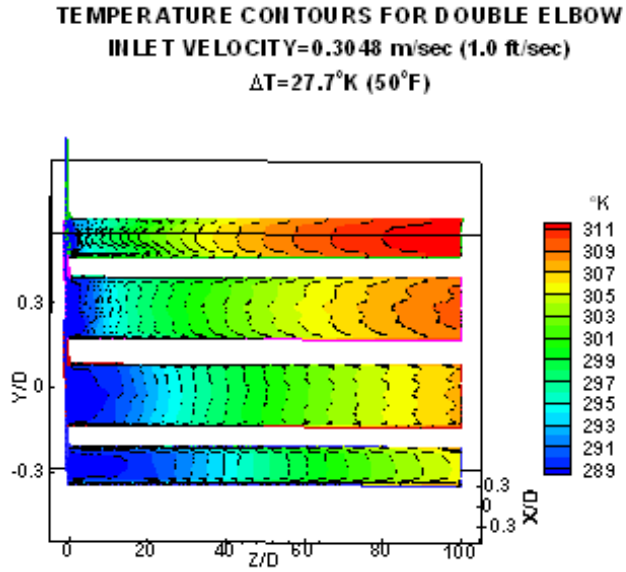

Fig. C-137 Temperature Slice Contours
V_0=0.3048 m/sec, ΔT_{wall}=27.7°K

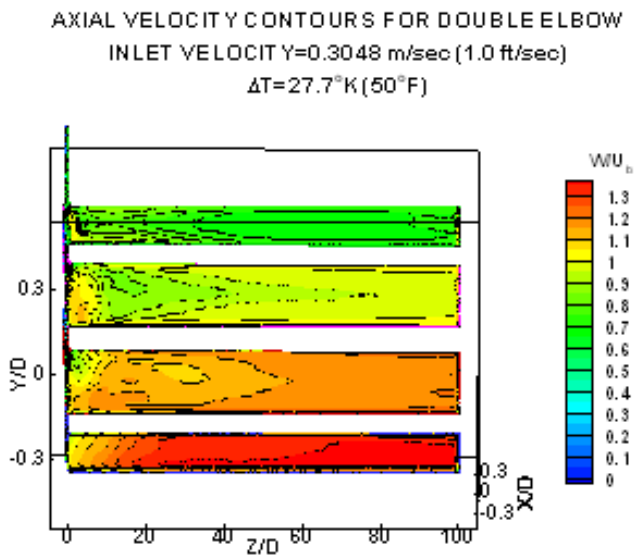

Fig. C-138 Axial Velocity Slice Contours
V_0=0.3048 m/sec, ΔT_{wall}=27.7°K

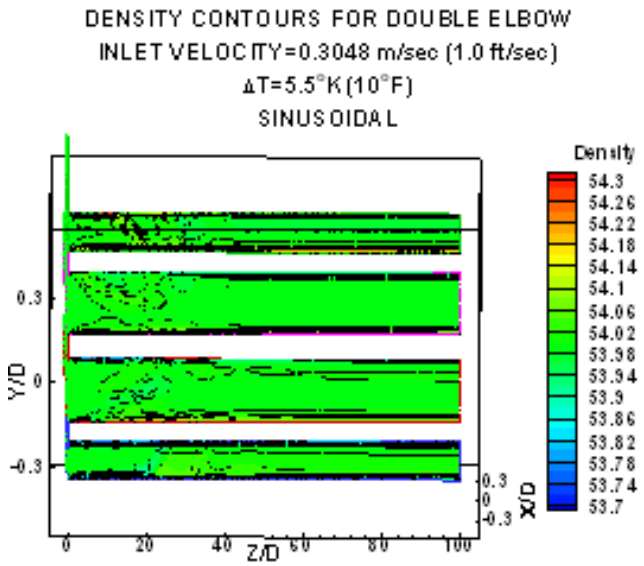

Fig. C-139 Density Slice Contours
V_0=0.3048 m/sec, ΔT_{wall}=-5.5°K Sinusoidal

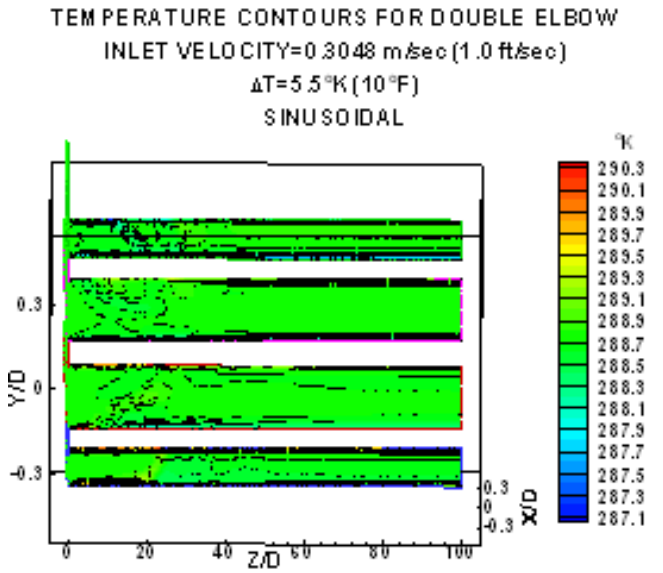

Fig. C-140 Temperature Slice Contours
V_0=0.3048 m/sec, ΔT_{wall}=-5.5°K Sinusoidal

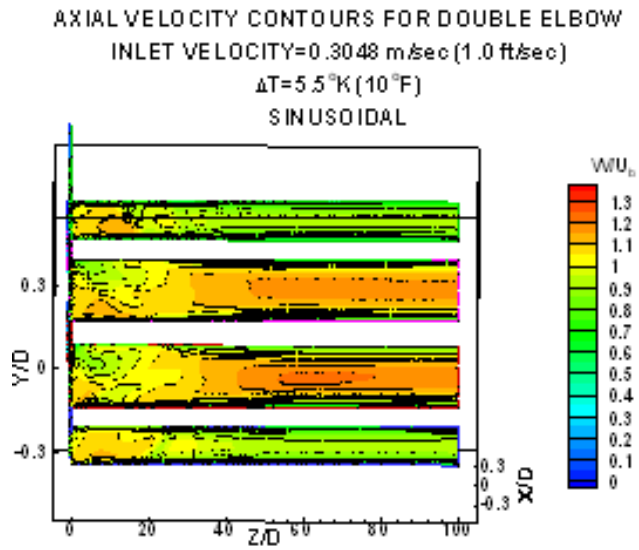

Fig. C-141 Axial Velocity Slice Contours
V_0=0.3048 m/sec, ΔT_{wall}=-5.5°K Sinusoidal

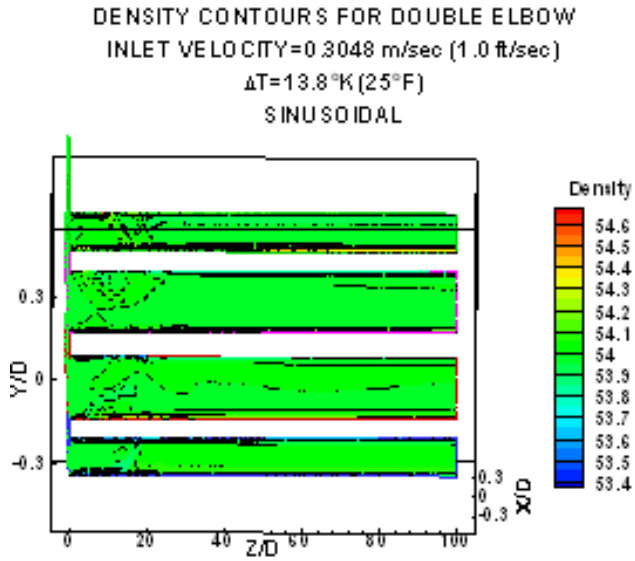

Fig. C-142 Density Slice Contours
V_0=0.3048 m/sec, ΔT_{wall}=-13.8°K Sinusoidal

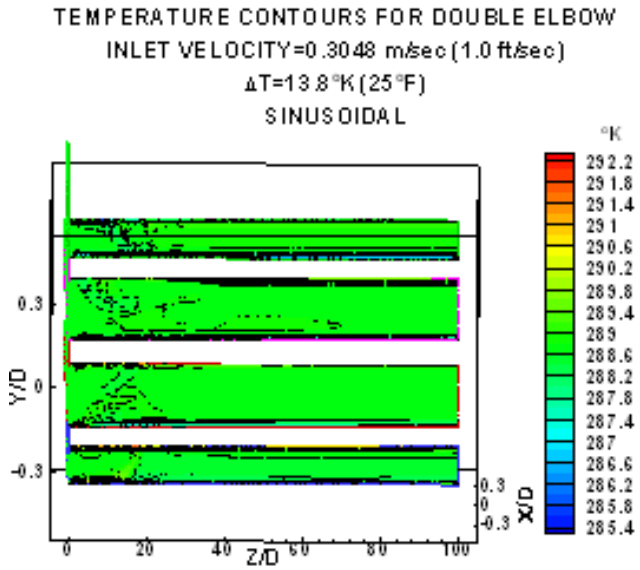

Fig. C-143 Temperature Slice Contours
V_0=0.3048 m/sec, ΔT_{wall}=-13.8°K Sinusoidal

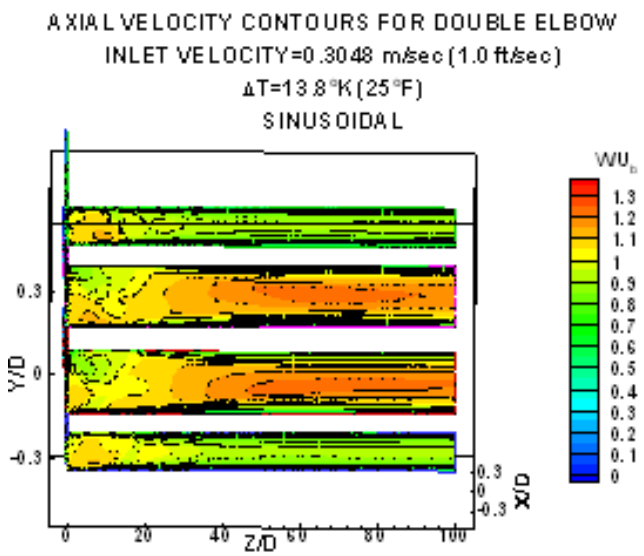

Fig. C-144 Axial Velocity Slice Contours
V_0=0.3048 m/sec, ΔT_{wall}=-13.8°K Sinusoidal

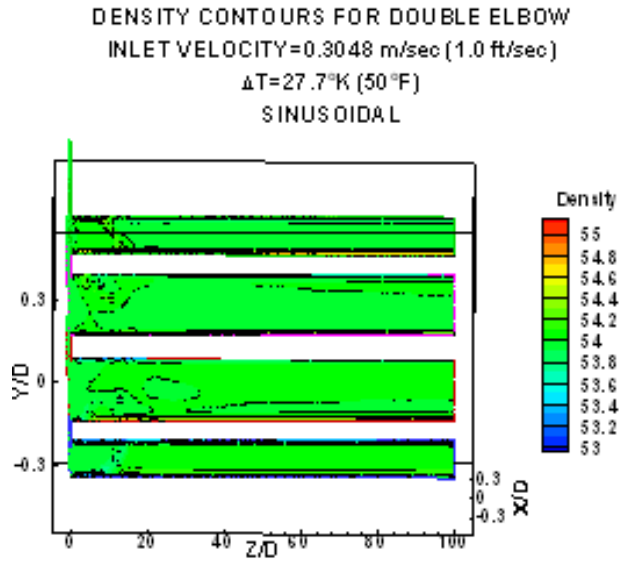

Fig. C-145 Density Slice Contours
V_0=0.3048 m/sec, ΔT_{wall}=-27.7°K Sinusoidal

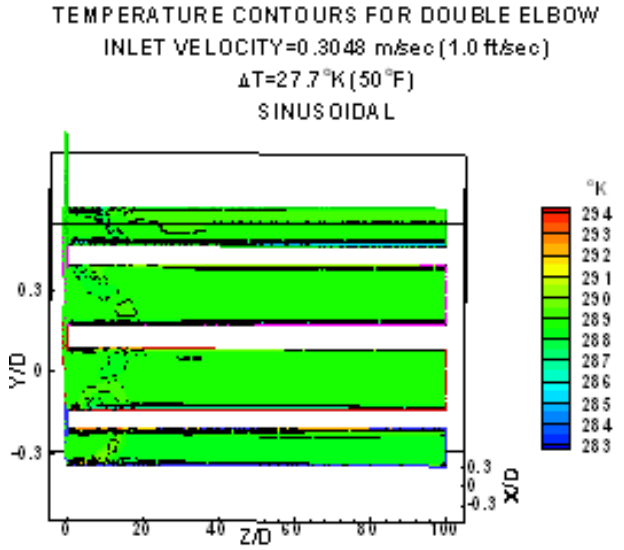

Fig. C-146 Temperature Slice Contours
V_0=0.3048 m/sec, ΔT_{wall}=-27.7°K Sinusoidal

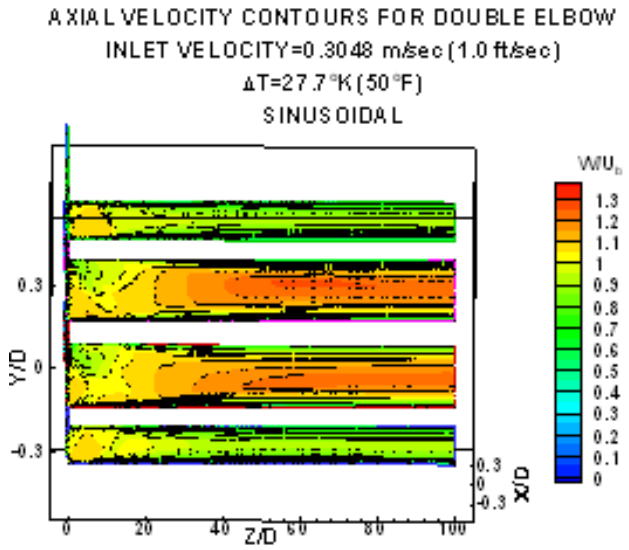

Fig. C-147 Axial Velocity Slice Contours
V_0=0.3048 m/sec, ΔT_{wall}=-27.7°K Sinusoidal

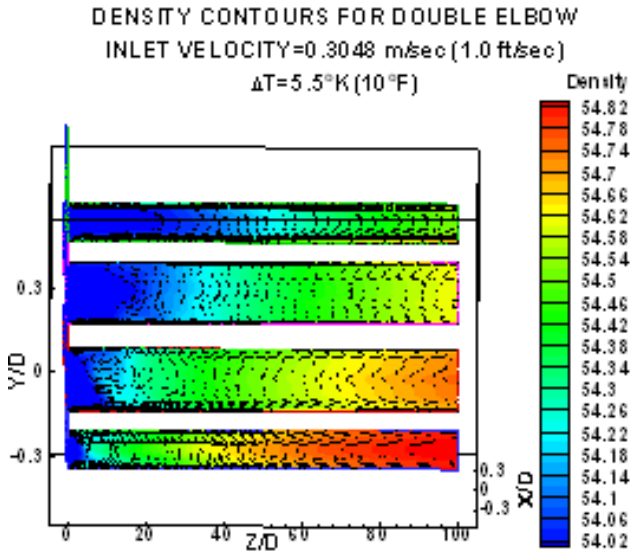

Fig. C-148 Density Slice Contours
V_0=0.3048 m/sec, ΔT_{wall}=-5.5°K

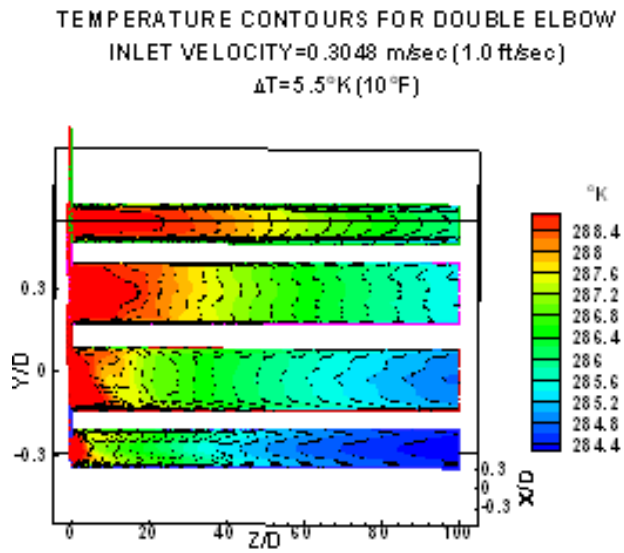

Fig. C-149 Temperature Slice Contours
V_0=0.3048 m/sec, ΔT_{wall}=-5.5°K

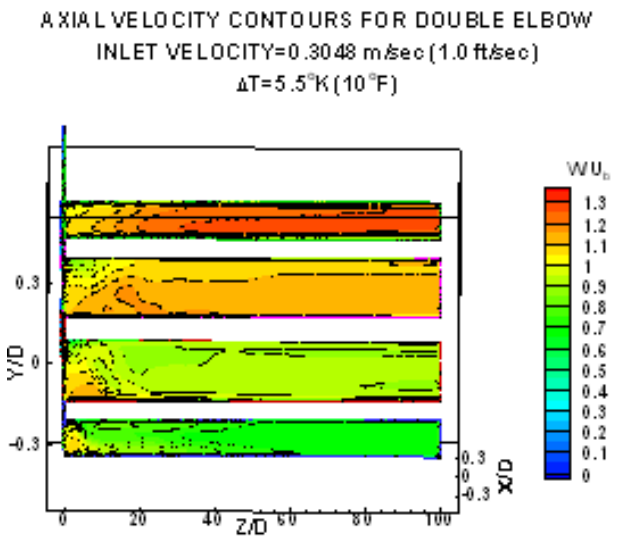

Fig. C-150 Axial Velocity Slice Contours
V_0=0.3048 m/sec, ΔT_{wall}=-5.5°K

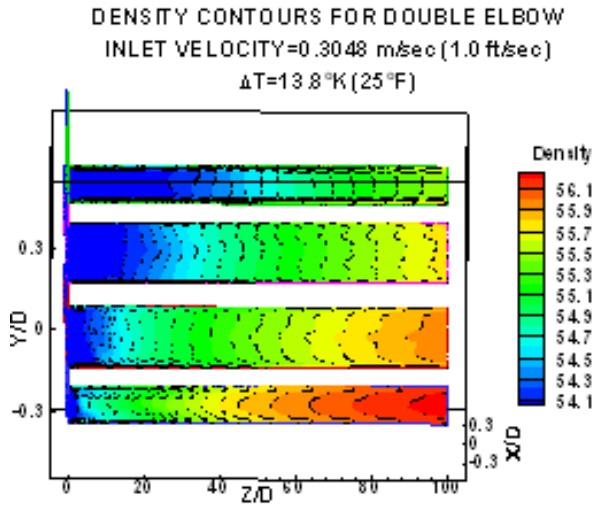

Fig. C-151 Density Slice Contours
V_0=0.3048 m/sec, ΔT_{wall}=-13.8°K

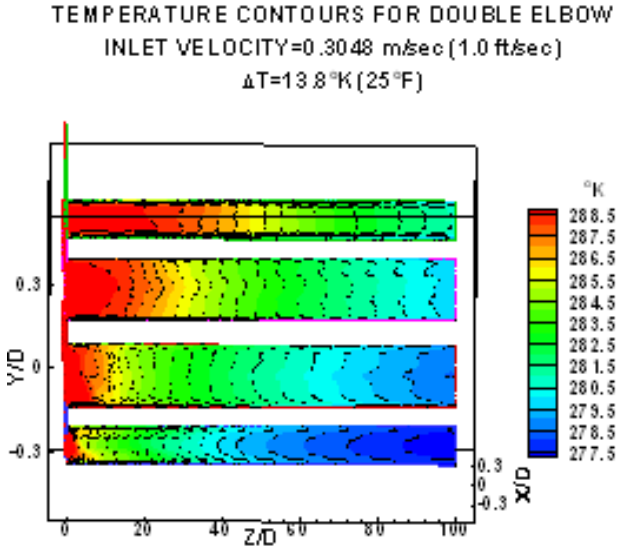

Fig. C-152 Temperature Slice Contours
V_0=0.3048 m/sec, ΔT_{wall}=-13.8°K

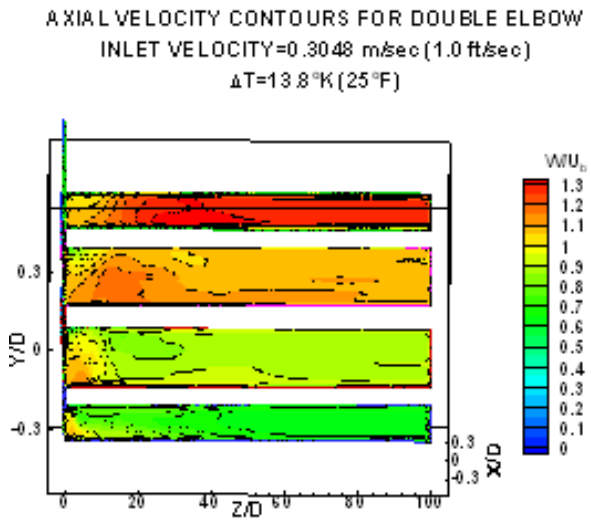

Fig. C-153 Axial Velocity Slice Contours
V_0=0.3048 m/sec, ΔT_{wall}=-13.8°K

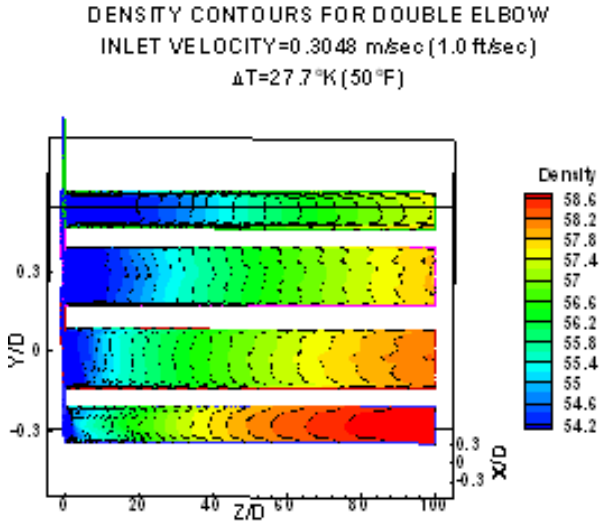

Fig. C-154 Density Slice Contours
V_0=0.3048 m/sec, ΔT_{wall}=-27.7°K

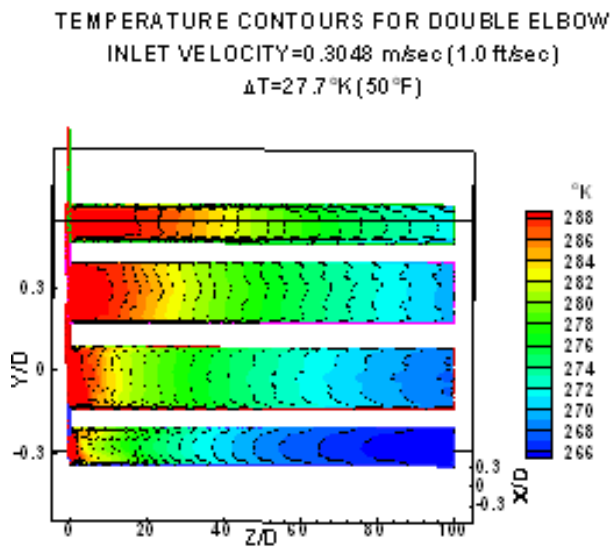

Fig. C-155 Temperature Slice Contours
V_0=0.3048 m/sec, ΔT_{wall}=-27.7°K

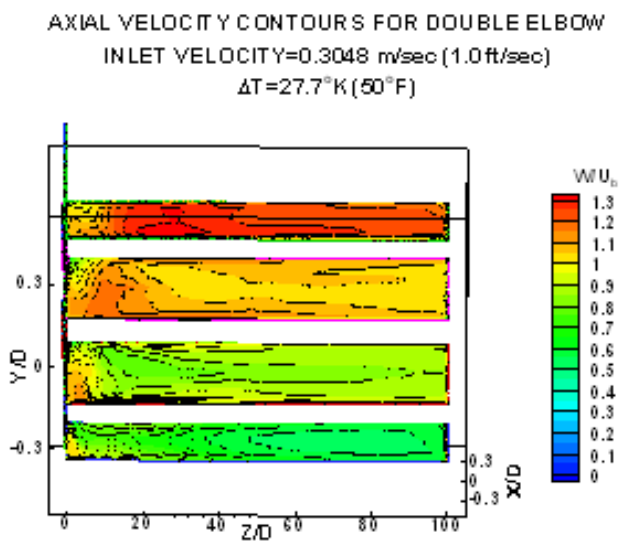

Fig. C-156 Axial Velocity Slice Contours
V_0=0.3048 m/sec, ΔT_{wall}=-27.7°K

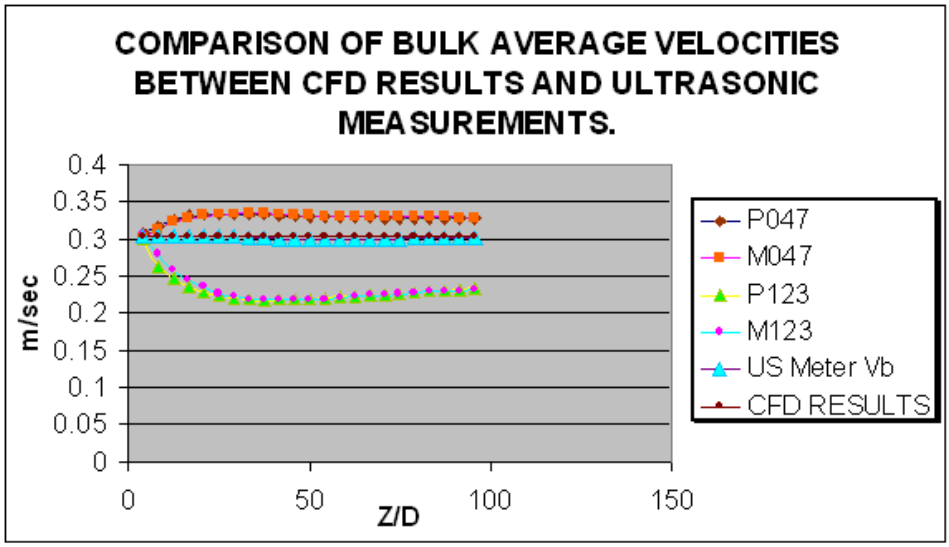

Fig. C-157 Comparison between CFD Vb and Ultrasonic Vb.
V_0=0.3048 m/sec, ΔT_{wall}=5.5°K Sinusoidal

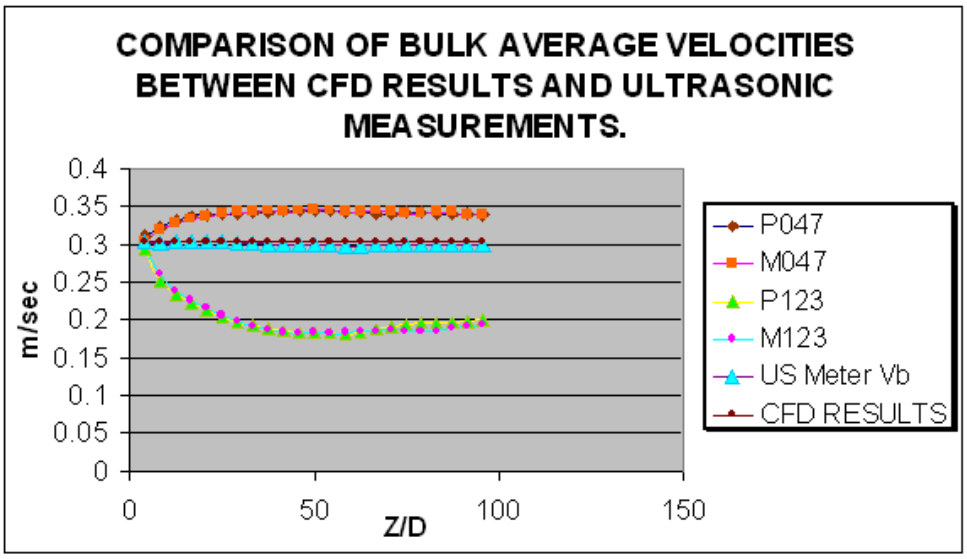

Fig. C-158 Comparison between CFD Vb and Ultrasonic Vb.
V_0=0.3048 m/sec, ΔT_{wall}=13.8°K Sinusoidal

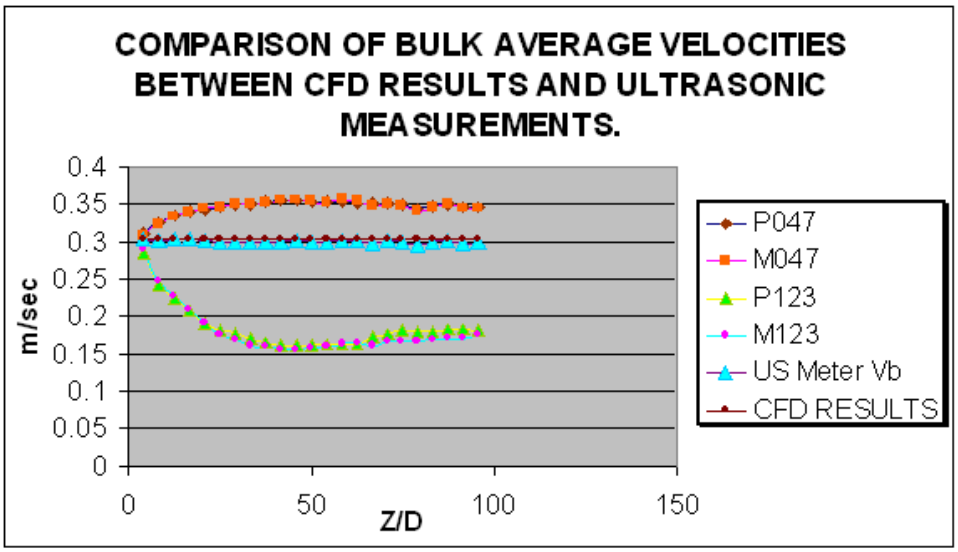

Fig. C-159 Comparison between CFD Vb and Ultrasonic Vb.
V_0=0.3048 m/sec, ΔT_{wall}=27.7°K Sinusoidal

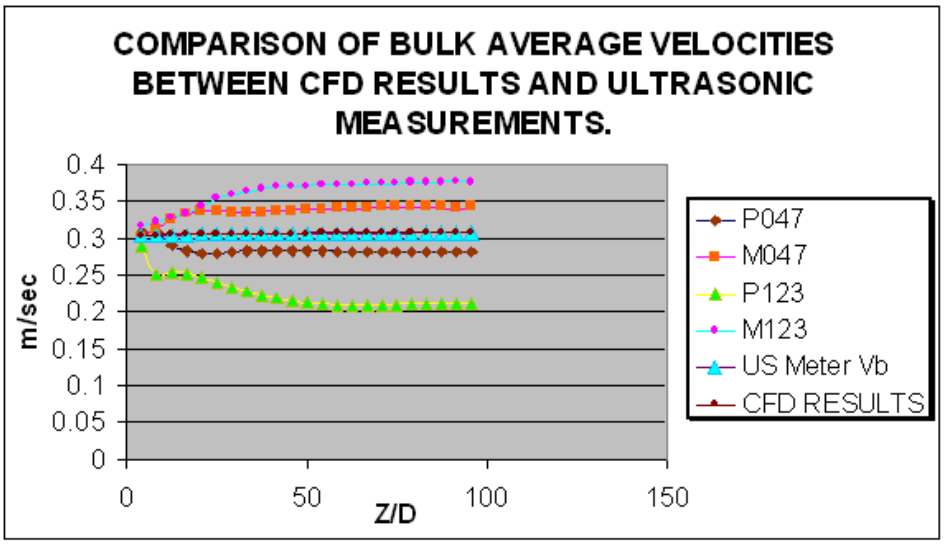

Fig. C-160 Comparison between CFD Vb and Ultrasonic Vb.
V_0=0.3048 m/sec, ΔT_{wall}=5.5°K

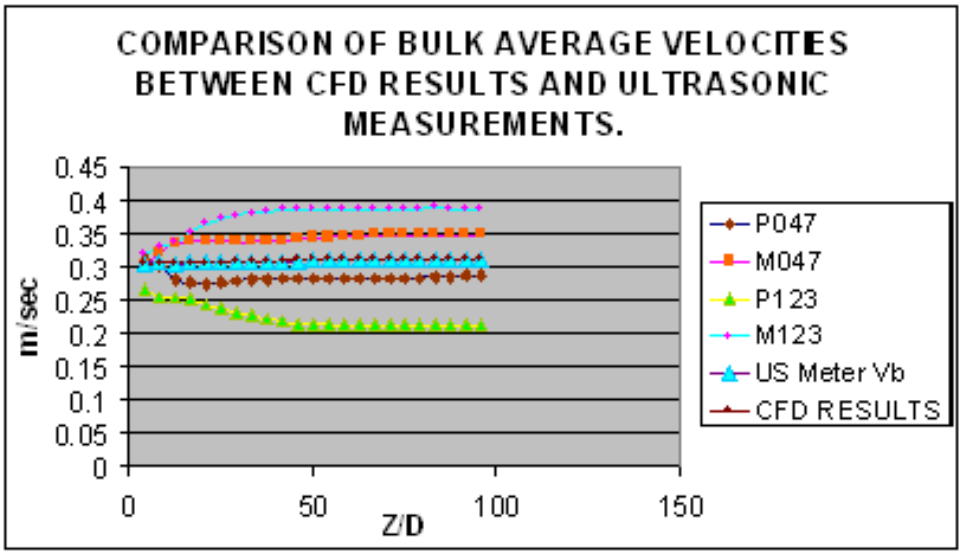

Fig. C-161 Comparison between CFD Vb and Ultrasonic Vb.
V_0=0.3048 m/sec, ΔT_{wall}=13.8°K

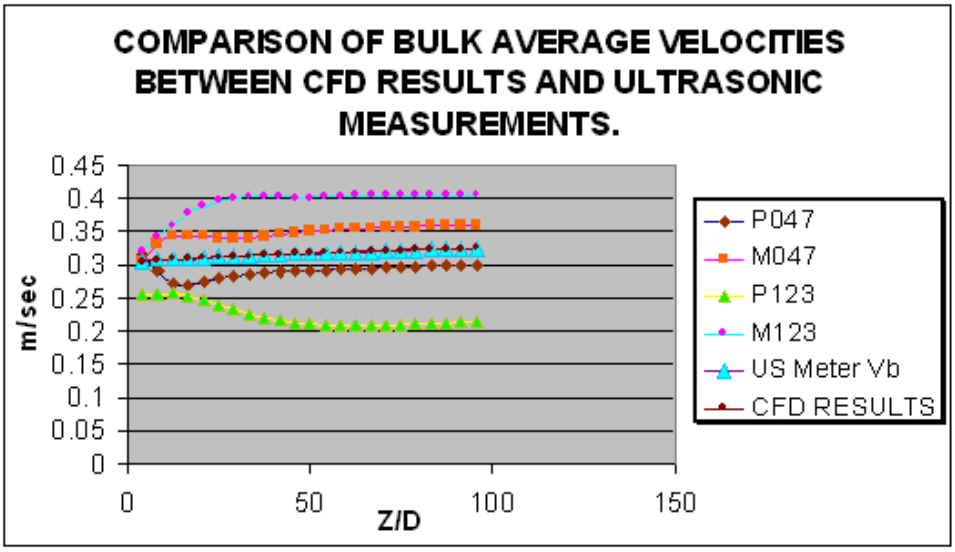

Fig. C-162 Comparison between CFD Vb and Ultrasonic Vb.
V_0=0.3048 m/sec, ΔT_{wall}=27.7°K

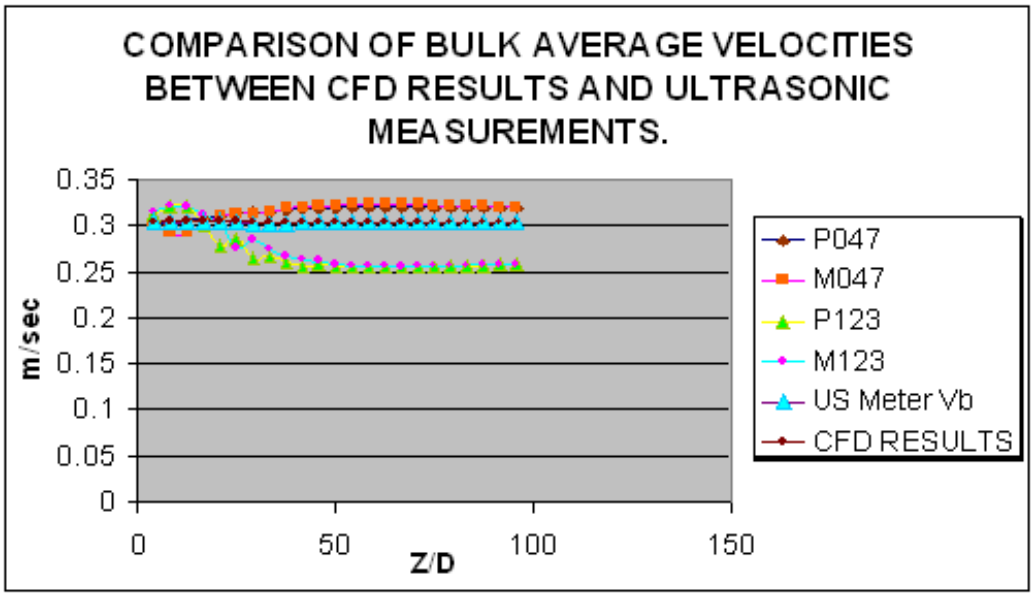

Fig. C-163 Comparison between CFD Vb and Ultrasonic Vb.
V_0=0.3048 m/sec, ΔT_{wall}=-5.5°K Sinusoidal

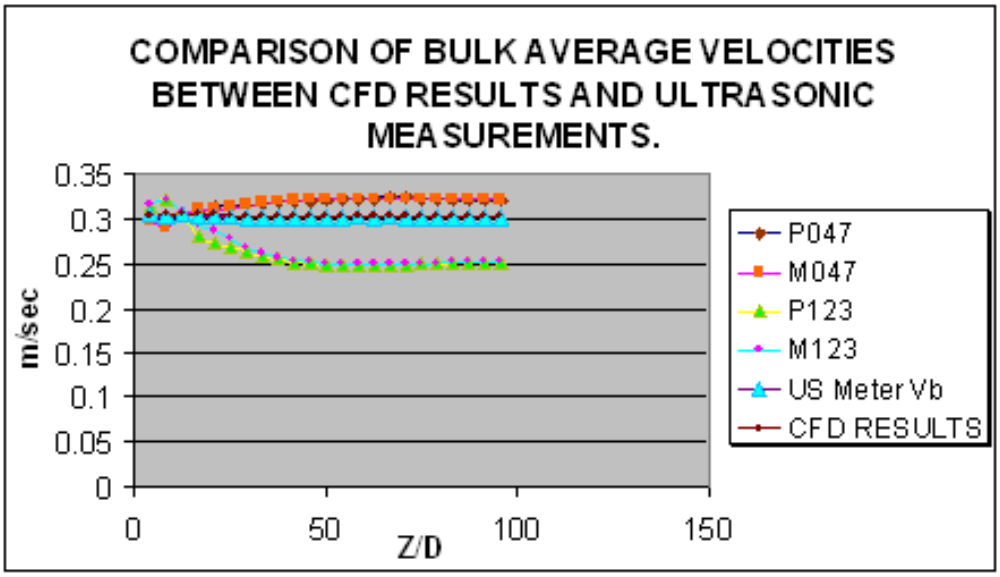

Fig. C-164 Comparison between CFD Vb and Ultrasonic Vb.
V_0=0.3048 m/sec, ΔT_{wall}=-13.8°K Sinusoidal

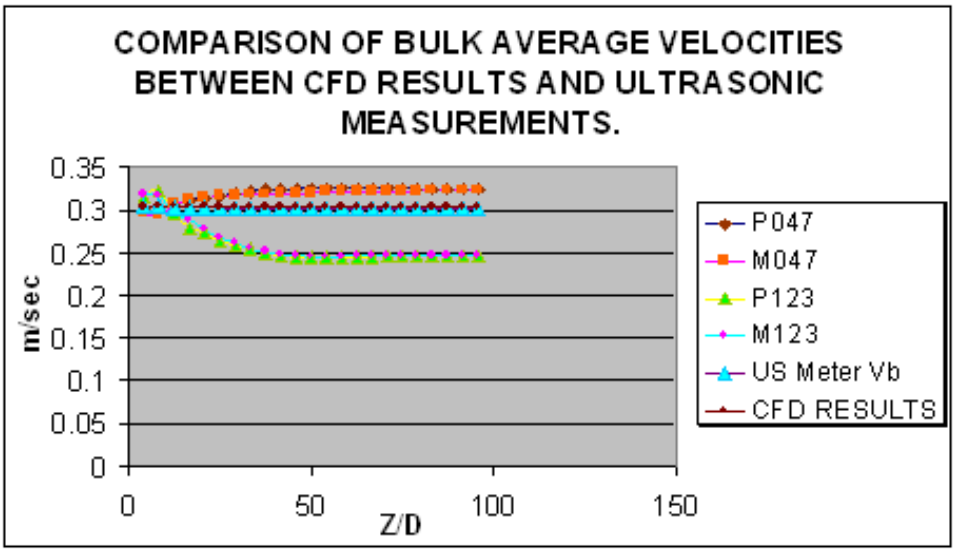

Fig. C-165 Comparison between CFD Vb and Ultrasonic Vb.
V_0=0.3048 m/sec, ΔT_{wall}=-27.7°K Sinusoidal

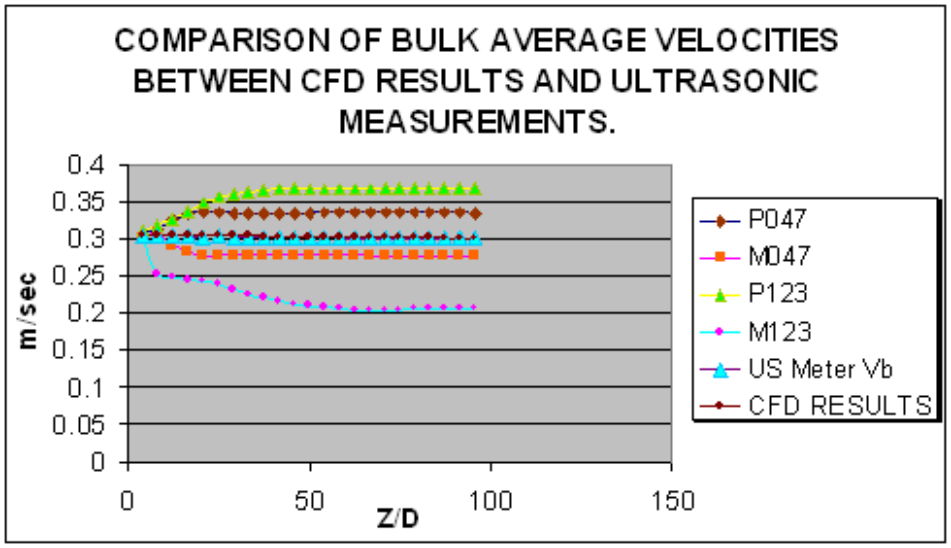

Fig. C-166 Comparison between CFD Vb and Ultrasonic Vb.
V_0=0.3048 m/sec, ΔT_{wall}=-5.5°K

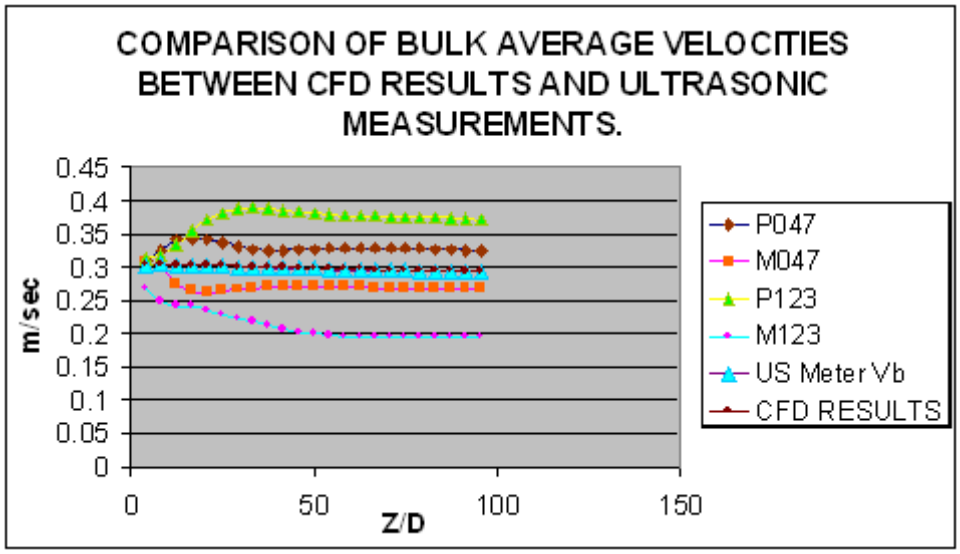

Fig. C-167 Comparison between CFD Vb and Ultrasonic Vb.
V_0=0.3048 m/sec, ΔT_{wall}=-13.8°K

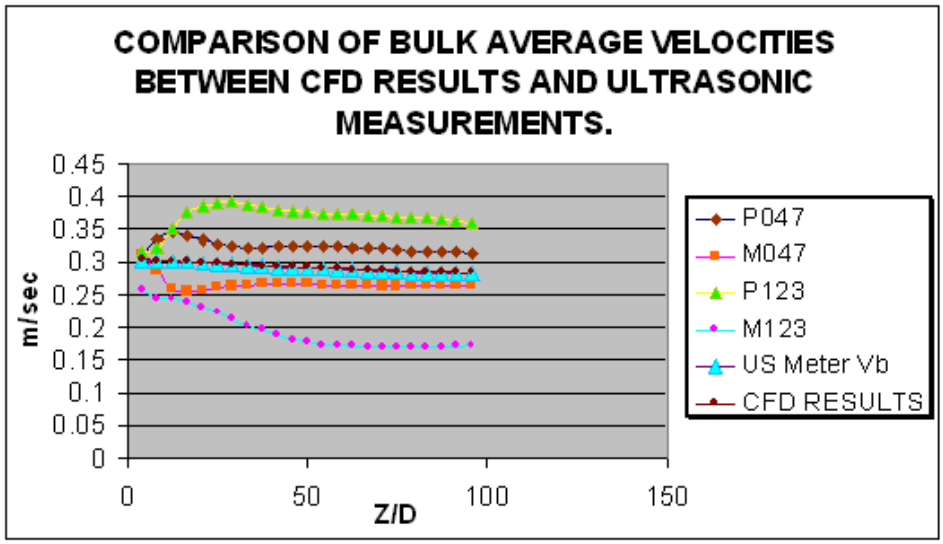

Fig. C-168 Comparison between CFD Vb and Ultrasonic Vb.
V_0=0.3048 m/sec, ΔT_{wall}=-27.7°K

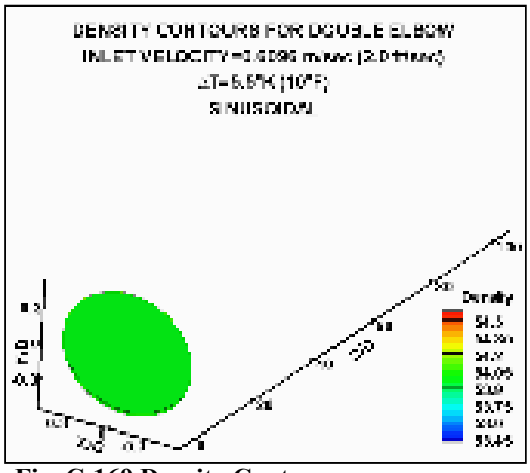

Fig. C-169 Density Contours
V_0=0.6096 m/sec, ΔT_{wall}=5.5°K Sinusoidal

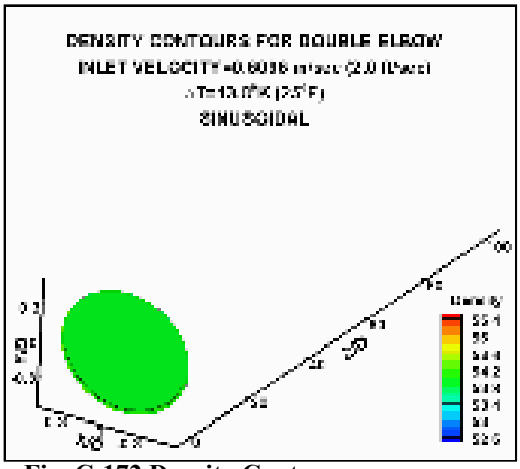

Fig. C-172 Density Contours
V_0=0.6096 m/sec, ΔT_{wall}=13.8°K Sinusoidal

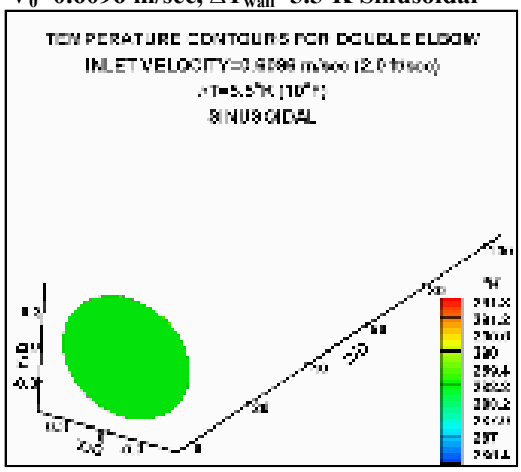

Fig. C-170 Temperature Contours
V_0=0.6096 m/sec, ΔT_{wall}=5.5°K Sinusoidal

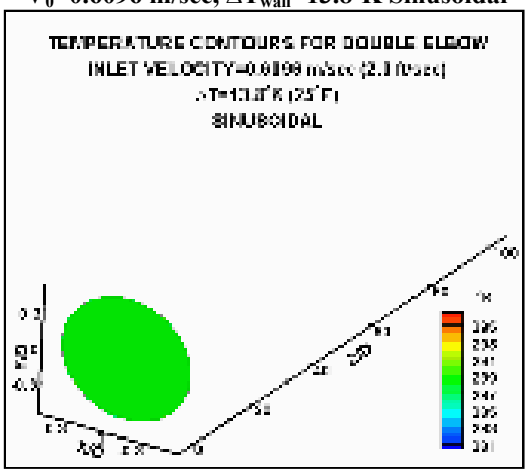

Fig. C-173 Temperature Contours
V_0=0.6096 m/sec, ΔT_{wall}=13.8°K Sinusoidal

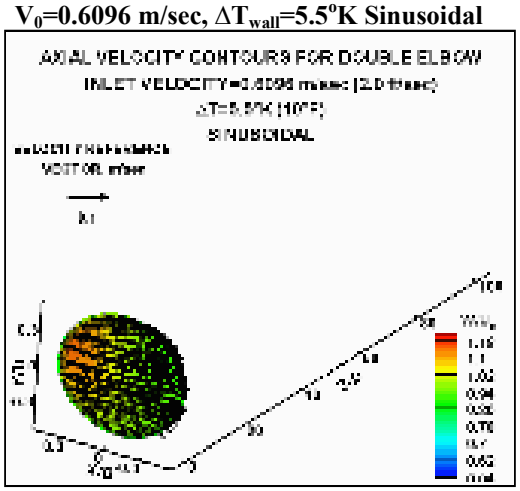

Fig. C-171 Axial Velocity Contours
V_0=0.6096 m/sec, ΔT_{wall}=5.5°K Sinusoidal

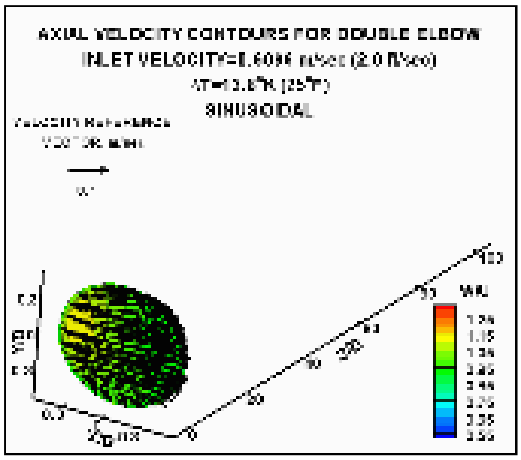

Fig. C-174 Axial Velocity Contours
V_0=0.6096 m/sec, ΔT_{wall}=13.8°K Sinusoidal

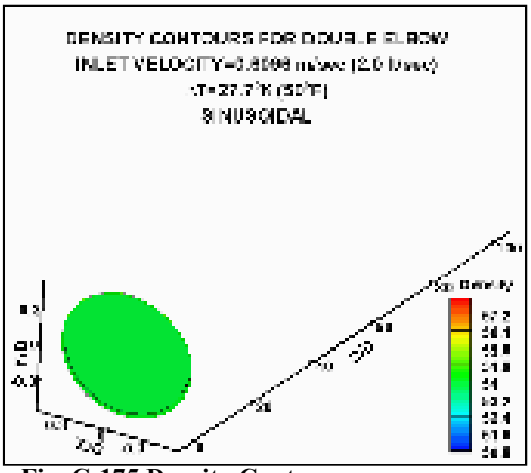

Fig. C-175 Density Contours
V_0=0.6096 m/sec, ΔT_{wall}=27.7°K Sinusoidal

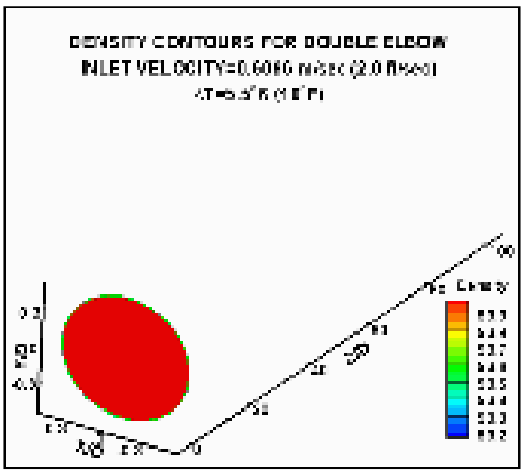

Fig. C-178 Density Contours
V_0=0.6096 m/sec, ΔT_{wall}=5.5°K

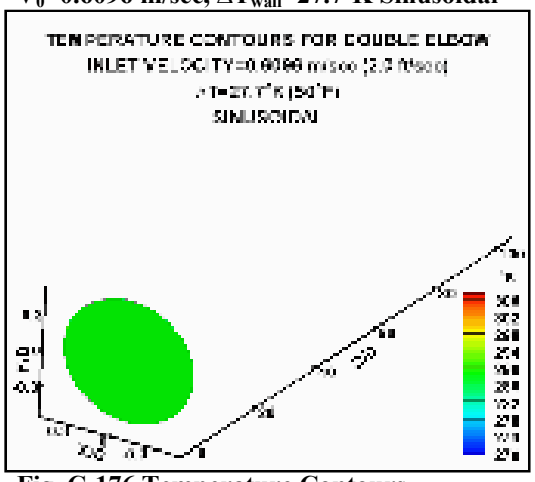

Fig. C-176 Temperature Contours
V_0=0.6096 m/sec, ΔT_{wall}=27.7°K Sinusoidal

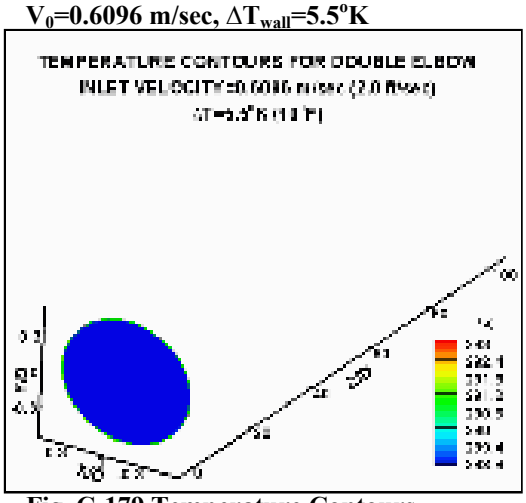

Fig. C-179 Temperature Contours
V_0=0.6096 m/sec, ΔT_{wall}=5.5°K

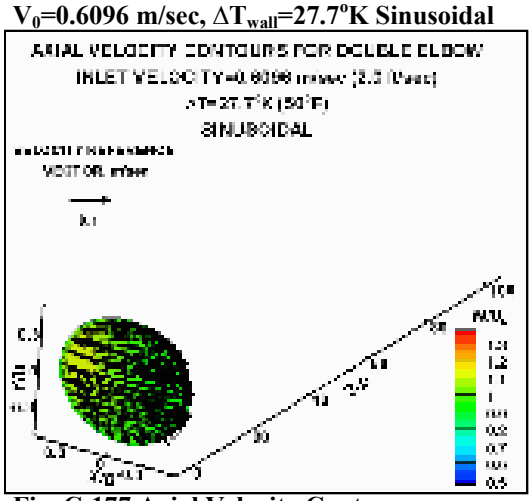

Fig. C-177 Axial Velocity Contours
V_0=0.6096 m/sec, ΔT_{wall}=27.7°K Sinusoidal

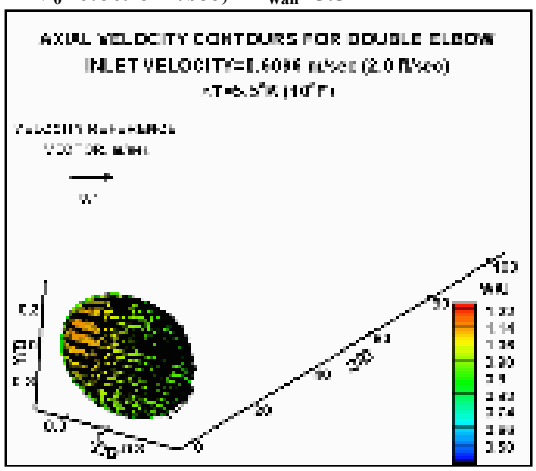

Fig. C-180 Axial Velocity Contours
V_0=0.6096 m/sec, ΔT_{wall}=5.5°K

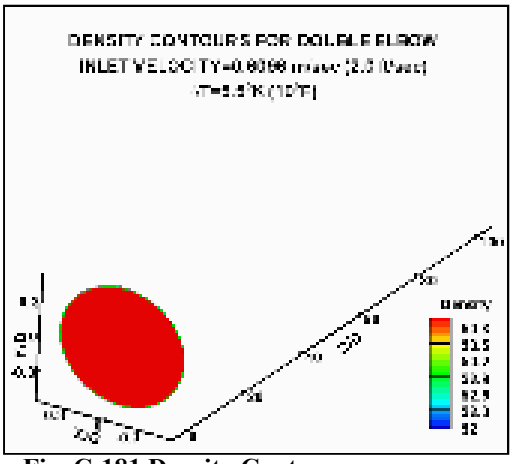

Fig. C-181 Density Contours
V_0=0.6096 m/sec, ΔT_{wall}=13.8°K

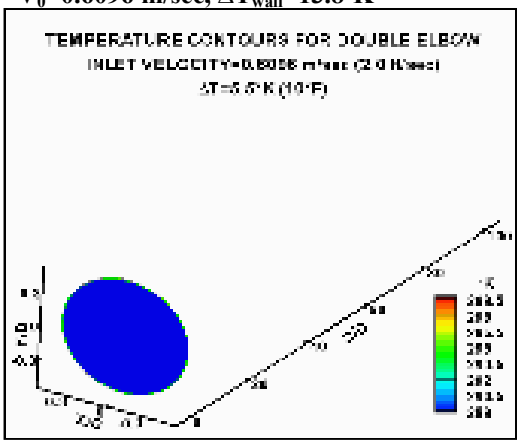

Fig. C-182 Temperature Contours
V_0=0.6096 m/sec, ΔT_{wall}=13.8°K

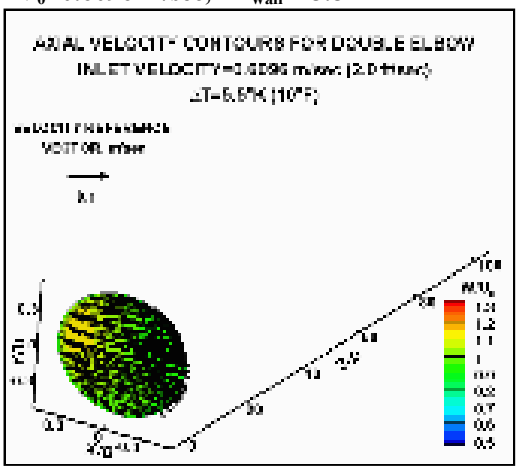

Fig. C-183 Axial Velocity Contours
V_0=0.6096 m/sec, ΔT_{wall}=13.8°K

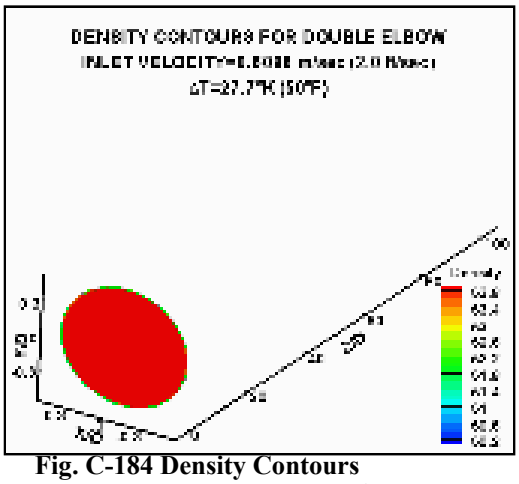

Fig. C-184 Density Contours
V_0=0.6096 m/sec, ΔT_{wall}=27.7°K

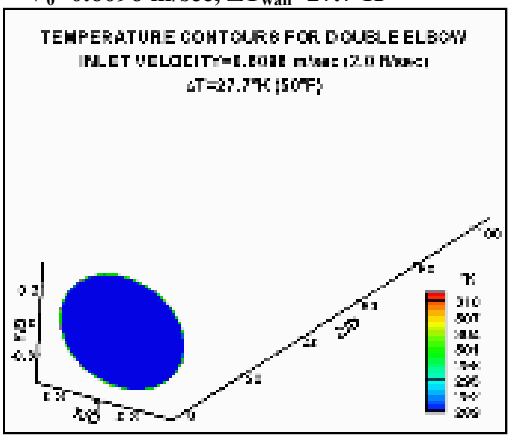

Fig. C-185 Temperature Contours
V_0=0.6096 m/sec, ΔT_{wall}=27.7°K

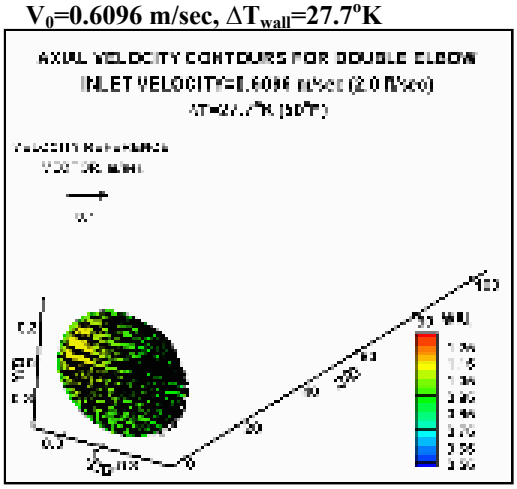

Fig. C-186 Axial Velocity Contours
V_0=0.6096 m/sec, ΔT_{wall}=27.7°K

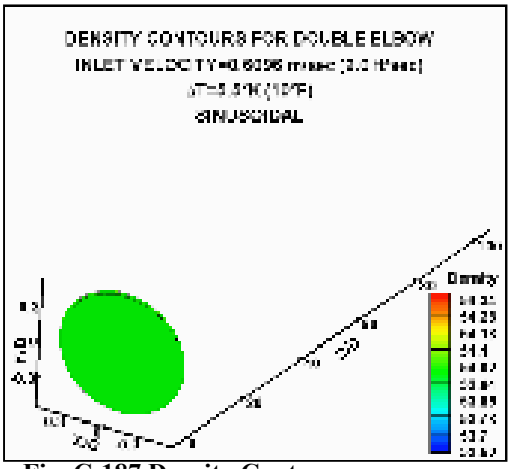

Fig. C-187 Density Contours
V_0=0.6096 m/sec, ΔT_{wall}=-5.5°K Sinusoidal

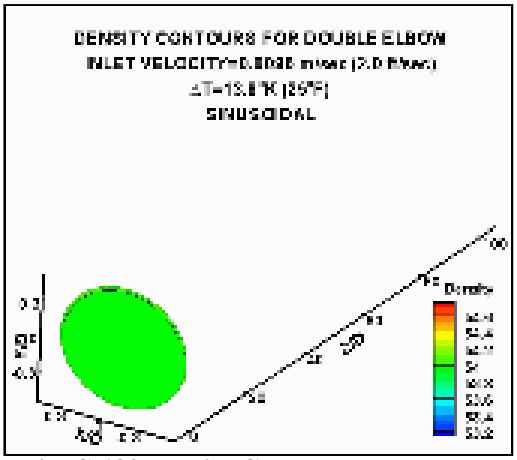

Fig. C-190 Density Contours
V_0=0.6096 m/sec, ΔT_{wall}=-13.8°K Sinusoidal

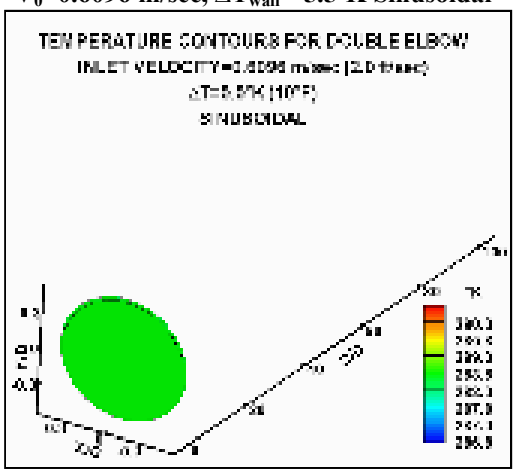

Fig. C-188 Temperature Contours
V_0=0.6096 m/sec, ΔT_{wall}=-5.5°K Sinusoidal

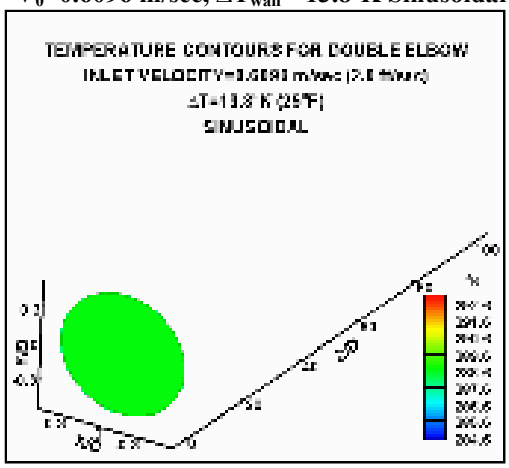

Fig. C-191 Temperature Contours
V_0=0.6096 m/sec, ΔT_{wall}=-13.8°K Sinusoidal

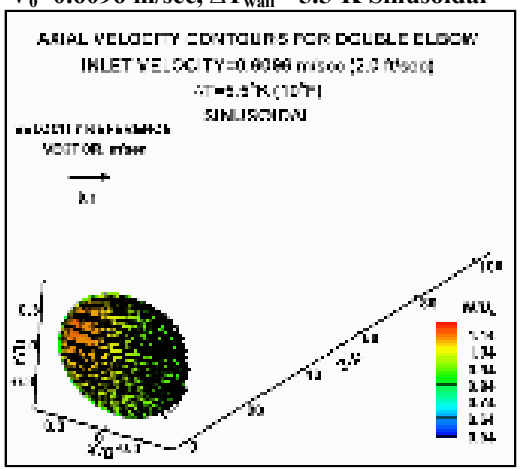

Fig. C-189 Axial Velocity Contours
V_0=0.6096 m/sec, ΔT_{wall}=-5.5°K Sinusoidal

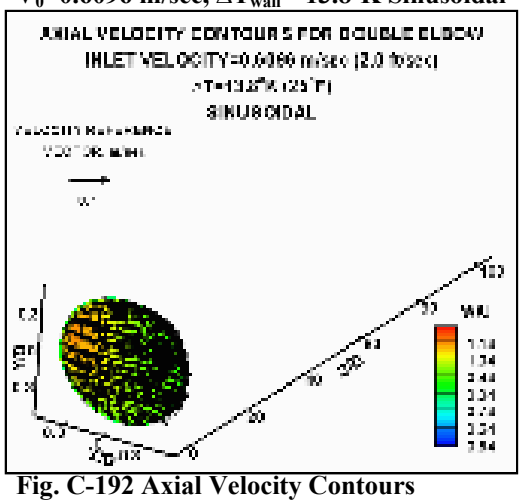

Fig. C-192 Axial Velocity Contours
V_0=0.6096 m/sec, ΔT_{wall}=-13.8°K Sinusoidal

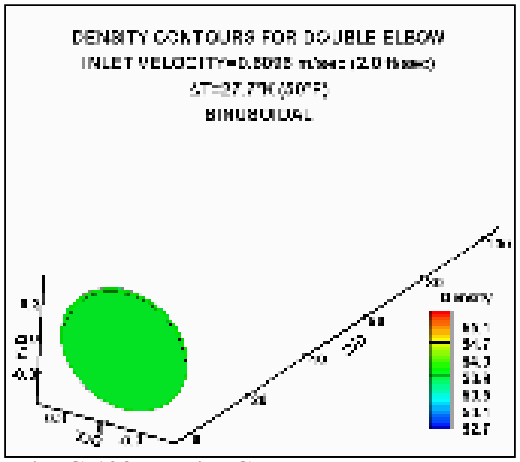

Fig. C-193 Density Contours
V_0=0.6096 m/sec, ΔT_{wall}=-27.7°K Sinusoidal

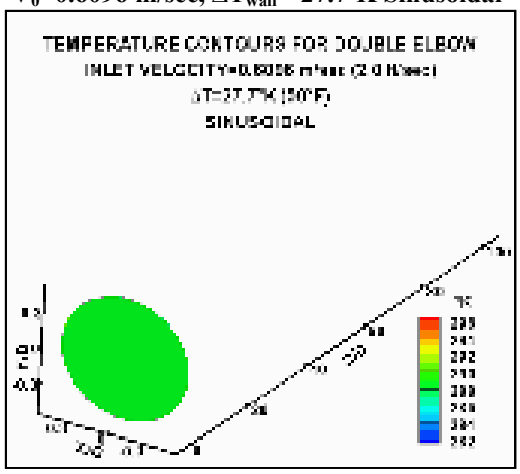

Fig. C-194 Temperature Contours
V_0=0.6096 m/sec, ΔT_{wall}=-27.7°K Sinusoidal

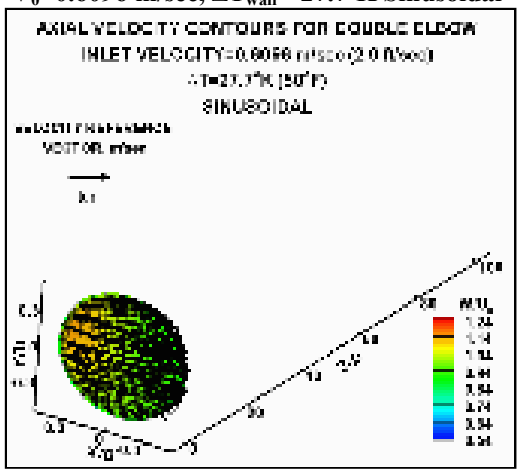

Fig. C-195 Axial Velocity Contours
V_0=0.6096 m/sec, ΔT_{wall}=-27.7°K Sinusoidal

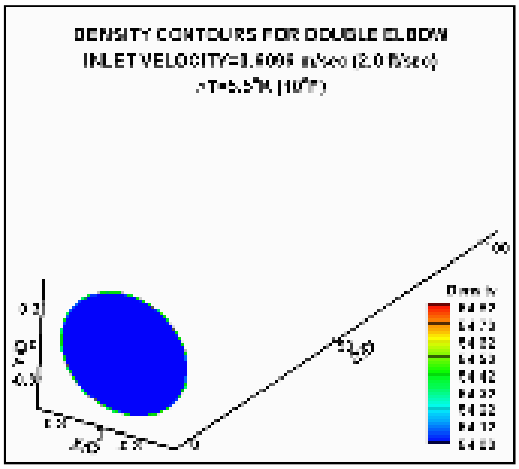

Fig. C-196 Density Contours
V_0=0.6096 m/sec, ΔT_{wall}=-5.5°K

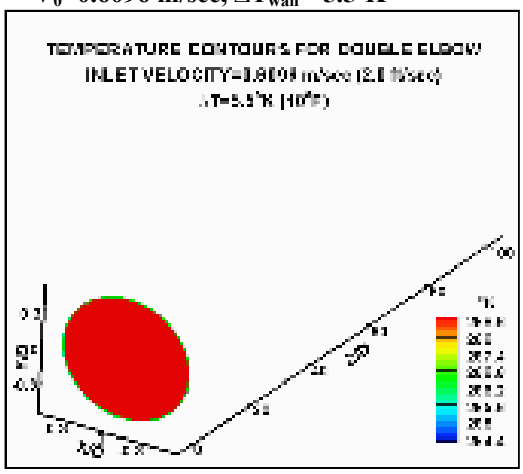

Fig. C-197 Temperature Contours
V_0=0.6096 m/sec, ΔT_{wall}=-5.5°K

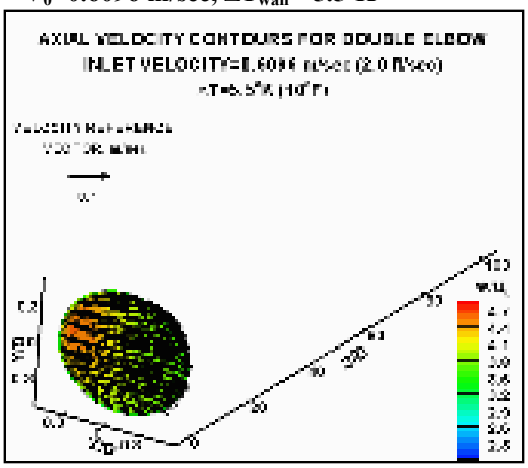

Fig. C-198 Axial Velocity Contours
V_0=0.6096 m/sec, ΔT_{wall}=-5.5°K

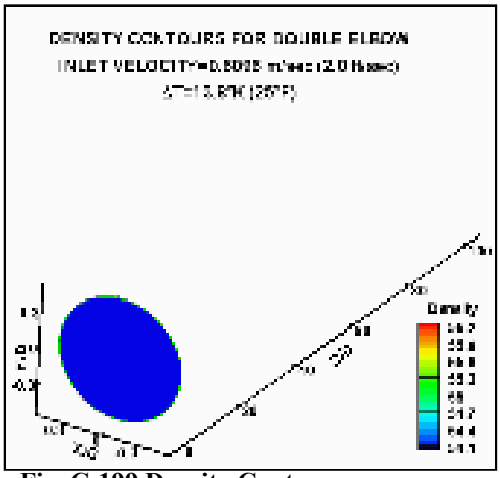

Fig. C-199 Density Contours
V_0=0.6096 m/sec, ΔT_{wall}=-13.8°K

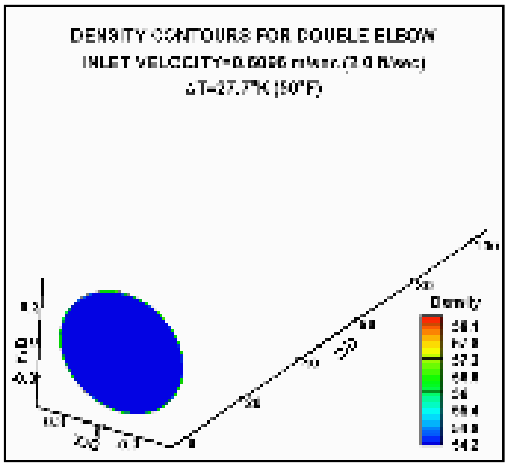

Fig. C-202 Density Contours
V_0=0.6096 m/sec, ΔT_{wall}=-27.7°K

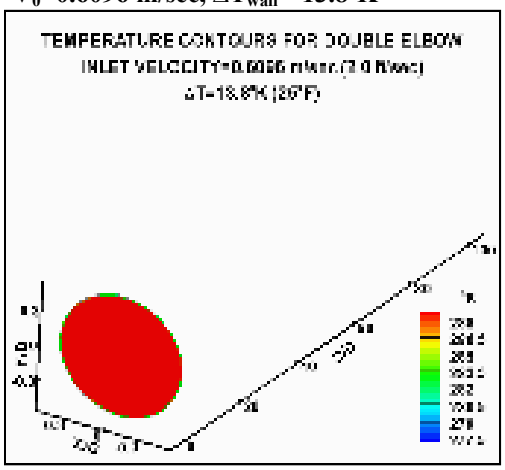

Fig. C-200 Temperature Contours
V_0=0.6096 m/sec, ΔT_{wall}=-13.8°K

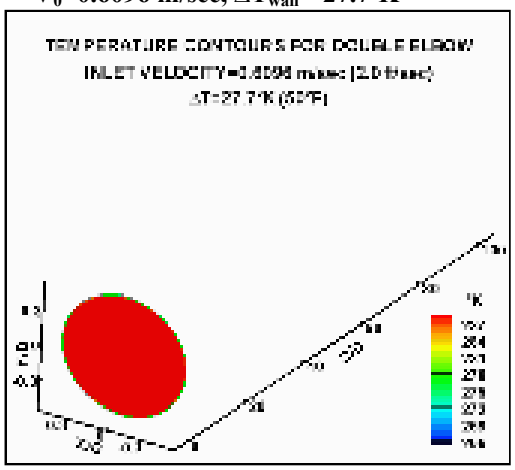

Fig. C-203 Temperature Contours
V_0=0.6096 m/sec, ΔT_{wall}=-27.7°K

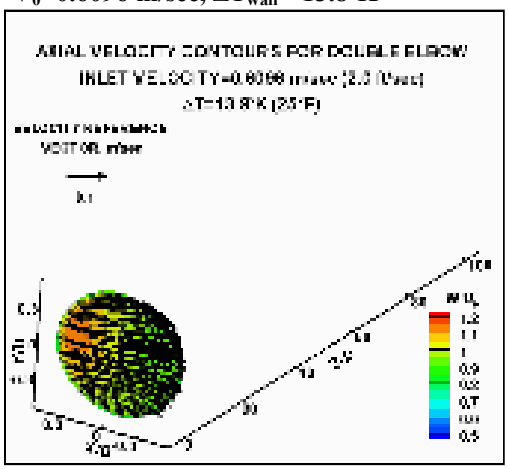

Fig. C-201 Axial Velocity Contours
V_0=0.6096 m/sec, ΔT_{wall}=-13.8°K

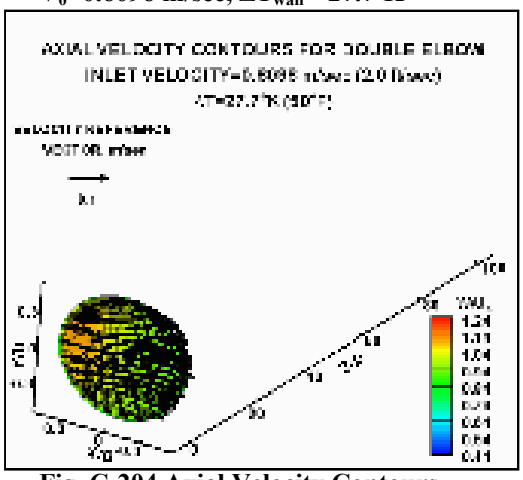

Fig. C-204 Axial Velocity Contours
V_0=0.6096 m/sec, ΔT_{wall}=-27.7°K

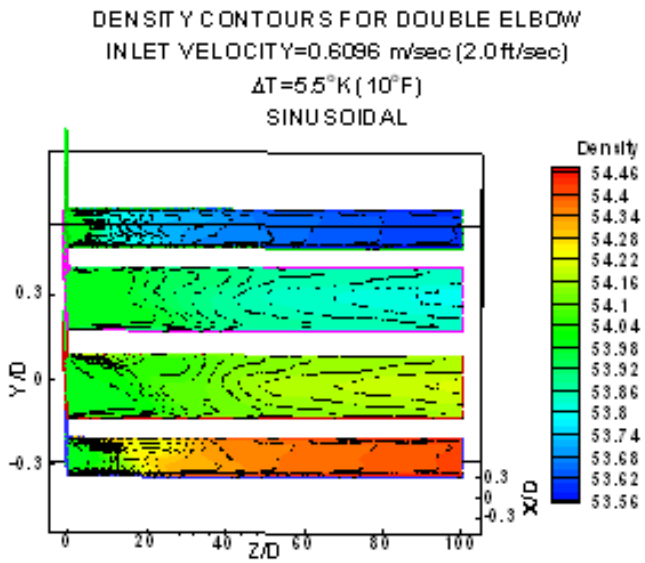

Fig. C-205 Density Slice Contours
V_0=0.6096 m/sec, ΔT_{wall}=5.5°K Sinusoidal

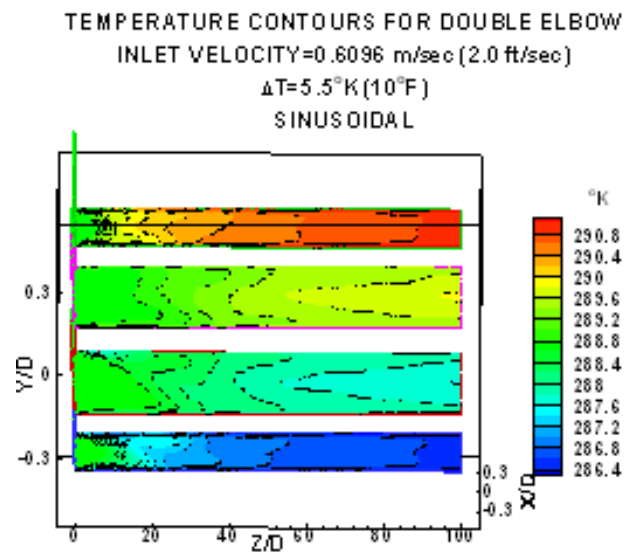

Fig. C-206 Temperature Slice Contours
V_0=0.6096 m/sec, ΔT_{wall}=5.5°K Sinusoidal

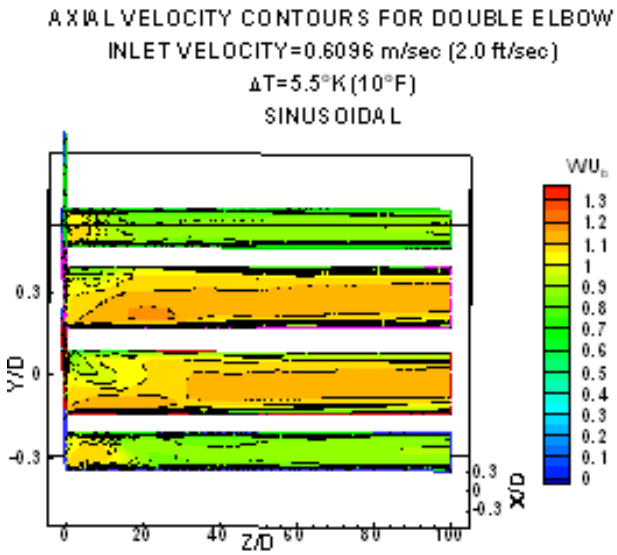

Fig. C-207 Axial Velocity Slice Contours
V_0=0.6096 m/sec, ΔT_{wall}=5.5°K Sinusoidal

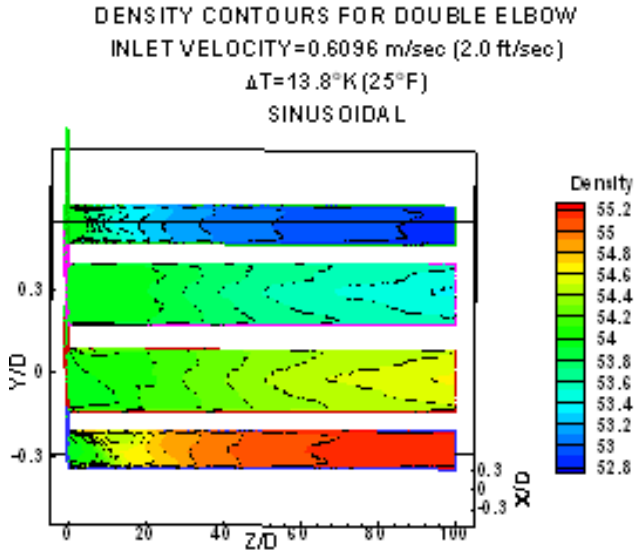

Fig. C-208 Density Slice Contours
V_0=0.6096 m/sec, ΔT_{wall}=13.8°K Sinusoidal

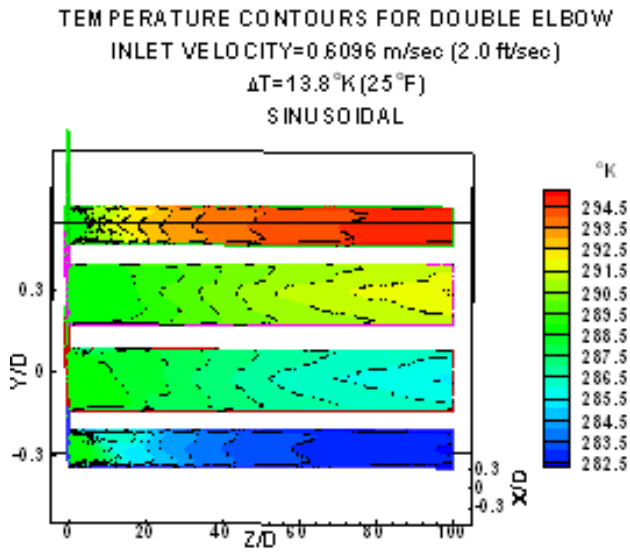

Fig. C-209 Temperature Slice Contours
V_0=0.6096 m/sec, ΔT_{wall}=13.8°K Sinusoidal

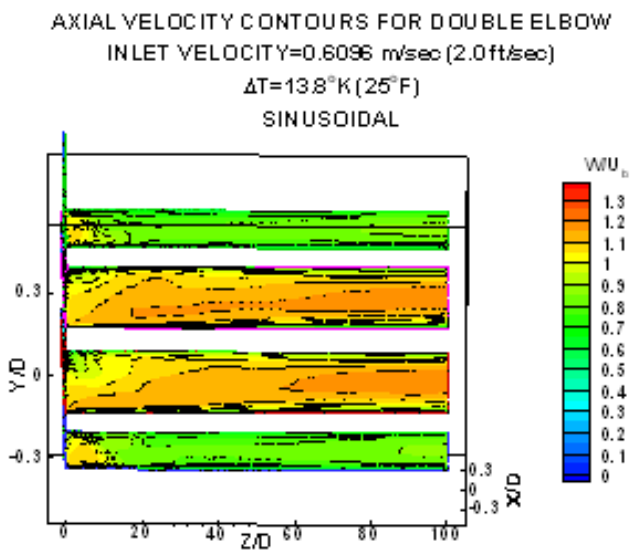

Fig. C-210 Axial Velocity Slice Contours
V_0=0.6096 m/sec, ΔT_{wall}=13.8°K Sinusoidal

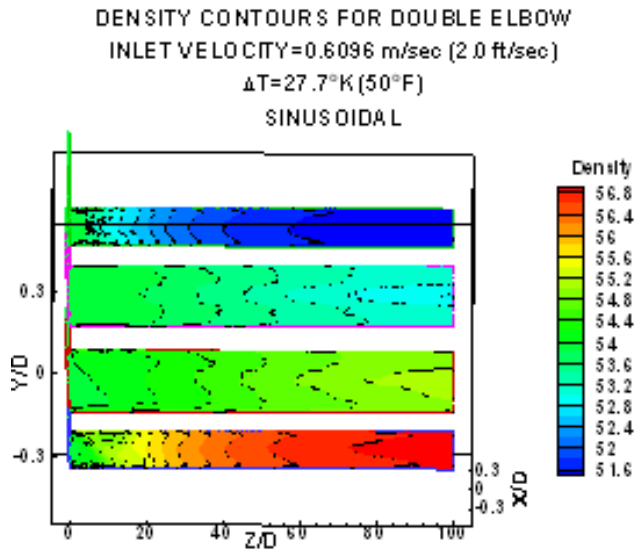

Fig. C-211 Density Slice Contours
V_0=0.6096 m/sec, ΔT_{wall}=27.7°K Sinusoidal

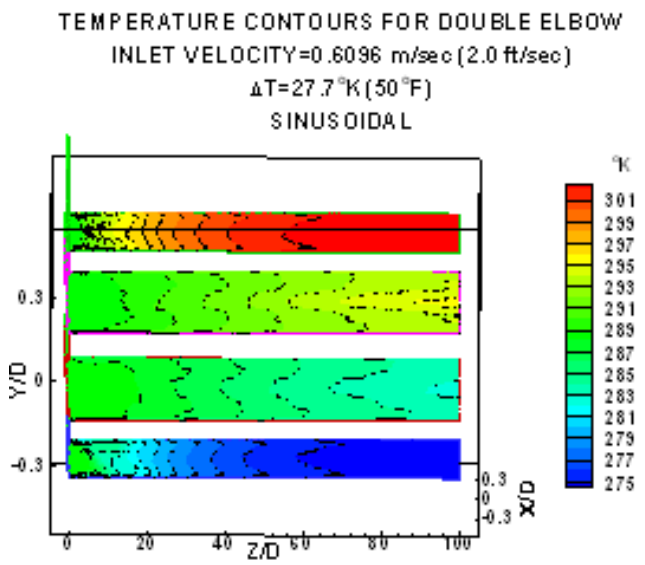

Fig. C-212 Temperature Slice Contours
V_0=0.6096 m/sec, ΔT_{wall}=27.7°K Sinusoidal

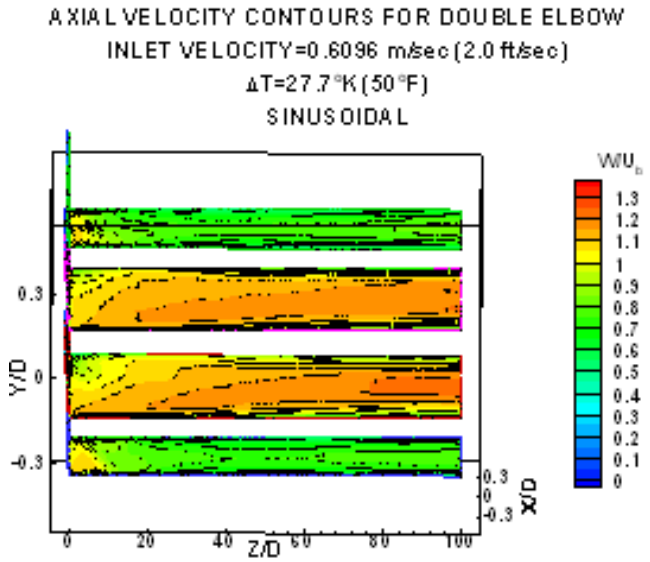

Fig. C-213 Axial Velocity Slice Contours
V_0=0.6096 m/sec, ΔT_{wall}=27.7°K Sinusoidal

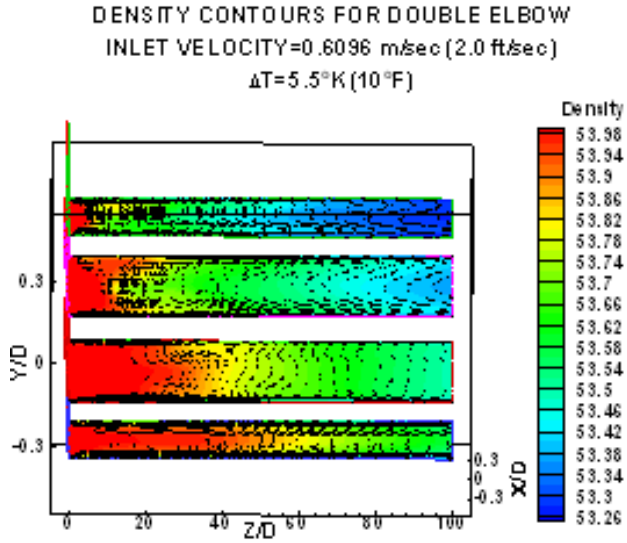

Fig. C-214 Density Slice Contours
V_0=0.6096 m/sec, ΔT_{wall}=5.5°K

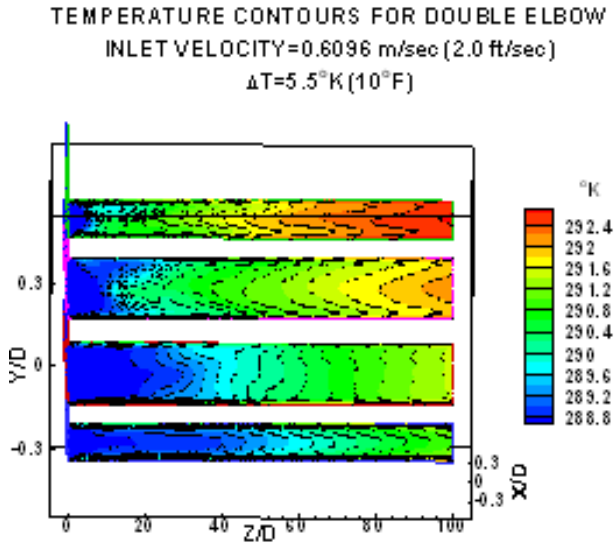

Fig. C-215 Temperature Slice Contours
V_0=0.6096 m/sec, ΔT_{wall}=5.5°K

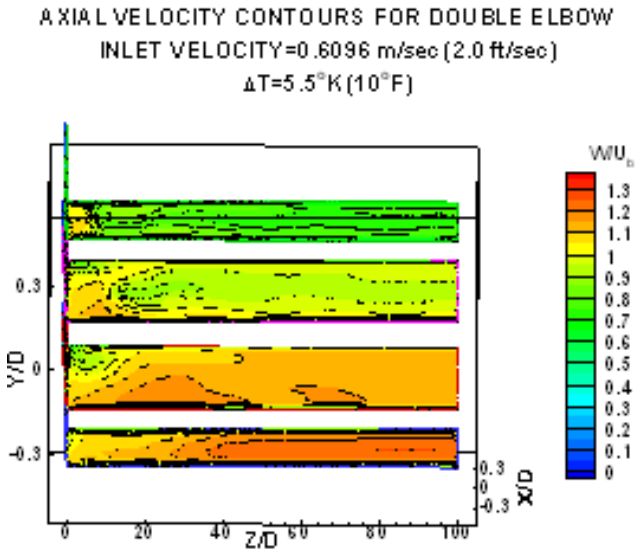

Fig. C-216 Axial Velocity Slice Contours
V_0=0.6096 m/sec, ΔT_{wall}=5.5°K

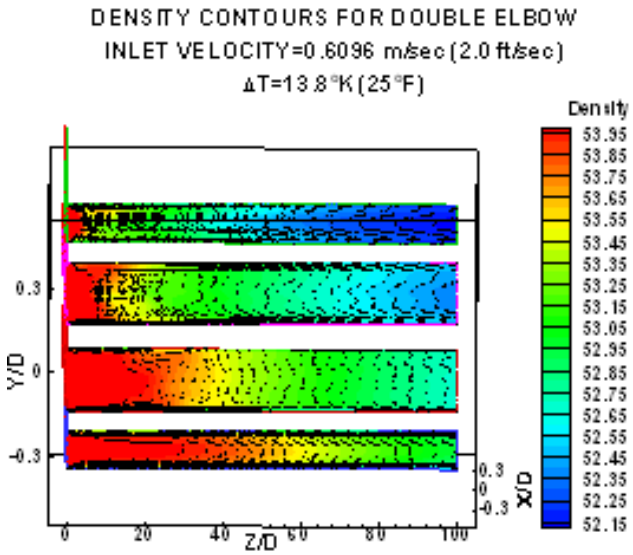

Fig. C-217 Density Slice Contours
V_0=0.6096 m/sec, ΔT_{wall}=13.8°K

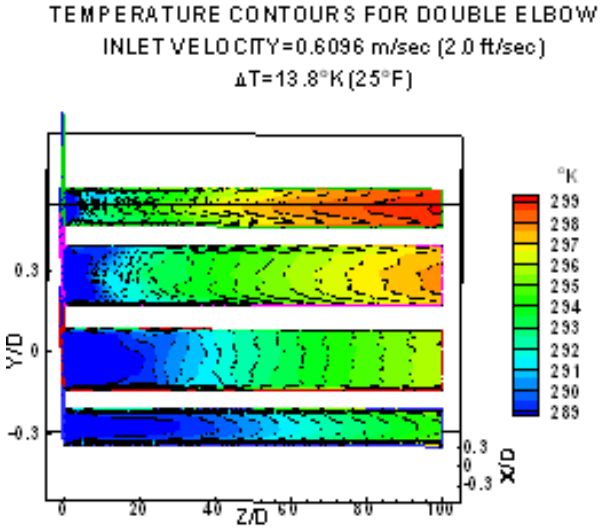

Fig. C-218 Temperature Slice Contours
V_0=0.6096 m/sec, ΔT_{wall}=13.8°K

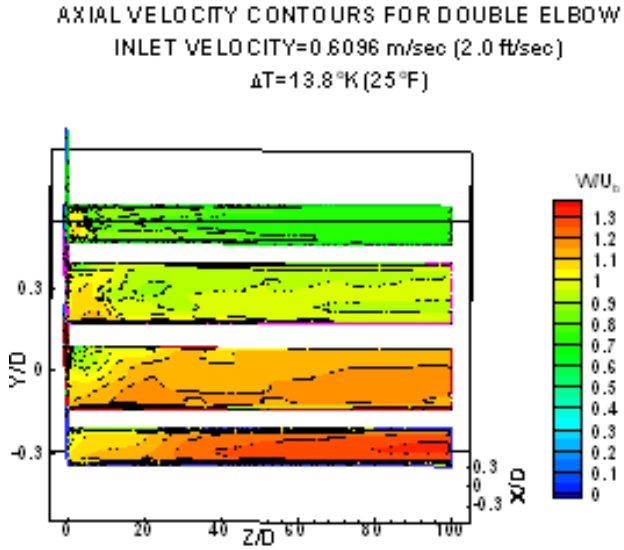

Fig. C-223 Density Slice Contours
V_0=0.6096 m/sec, ΔT_{wall}=-5.5°K Sinusoidal

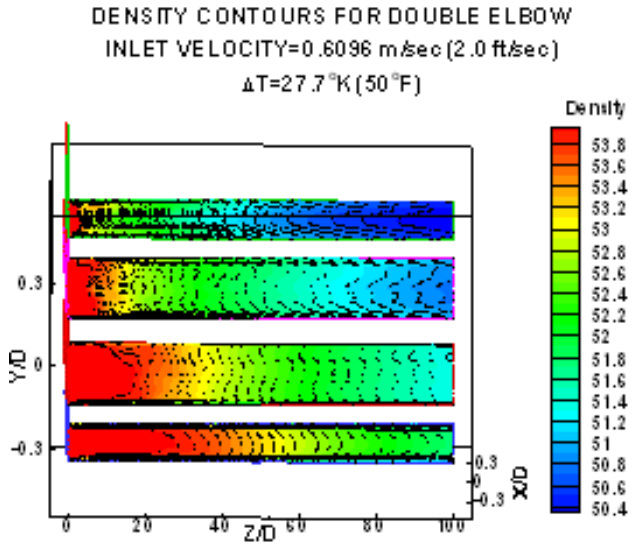

Fig. C-224 Temperature Slice Contours
V_0=0.6096 m/sec, ΔT_{wall}=-5.5°K Sinusoidal

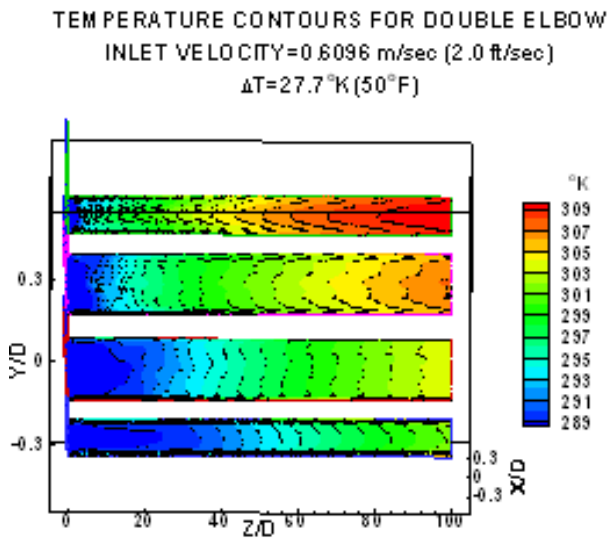

V_0=0.6096 m/sec, ΔT_{wall}=-5.5°K Sinusoidal

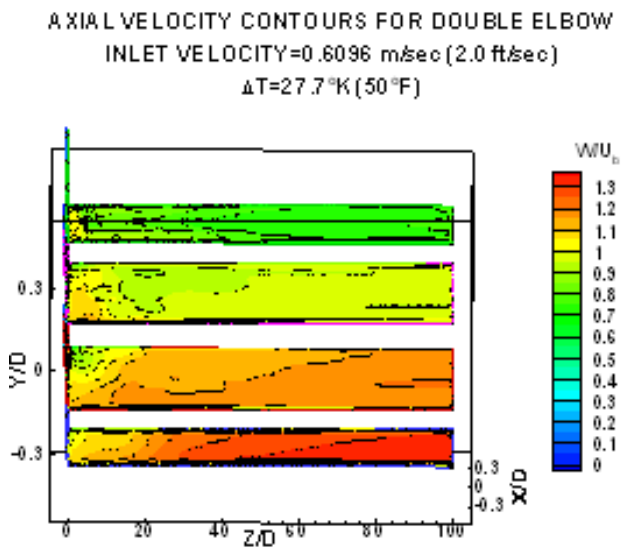

V_0=0.6096 m/sec, ΔT_{wall}=-13.8°K Sinusoidal

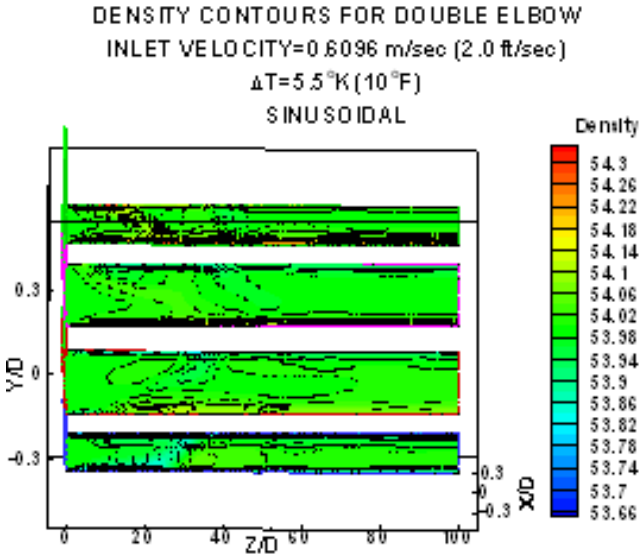

Fig. C-223 Density Slice Contours
V_0=0.6096 m/sec, ΔT_{wall}=-5.5°K Sinusoidal

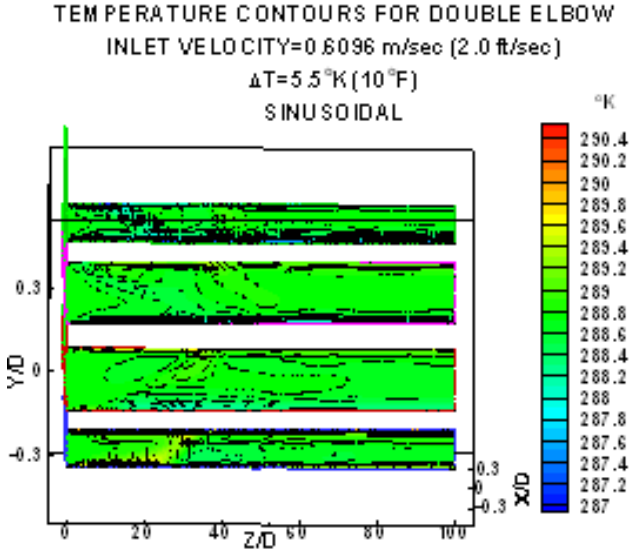

Fig. C-224 Temperature Slice Contours
V_0=0.6096 m/sec, ΔT_{wall}=-5.5°K Sinusoidal

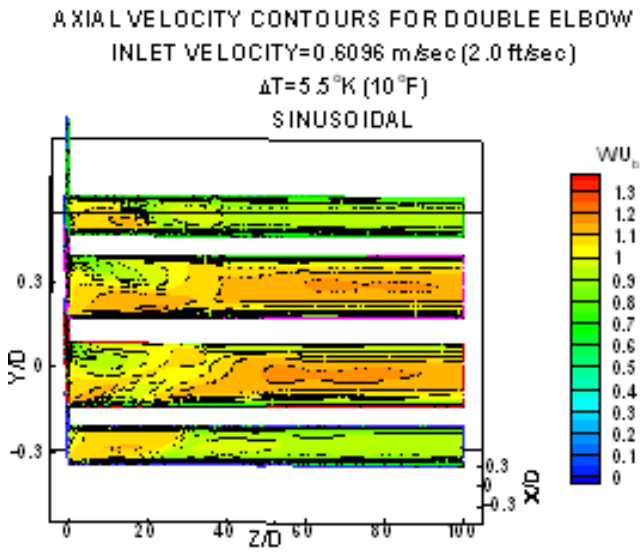

Fig. C-225 Axial Velocity Slice Contours
V_0=0.6096 m/sec, ΔT_{wall}=-5.5°K Sinusoidal

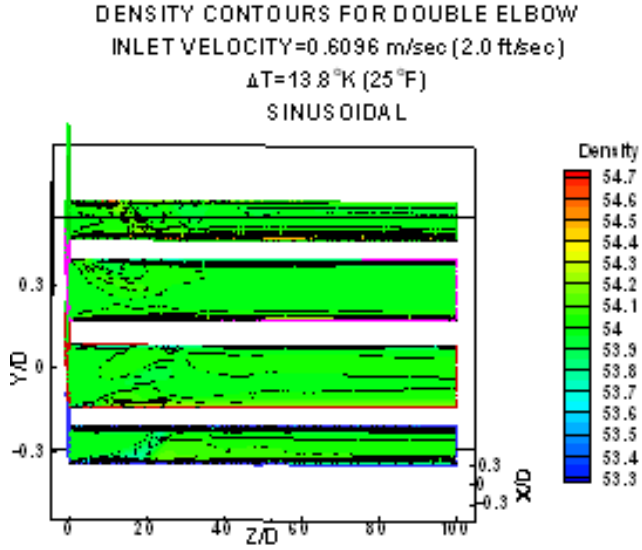

Fig. C-226 Density Slice Contours
V_0=0.6096 m/sec, ΔT_{wall}=-13.8°K Sinusoidal

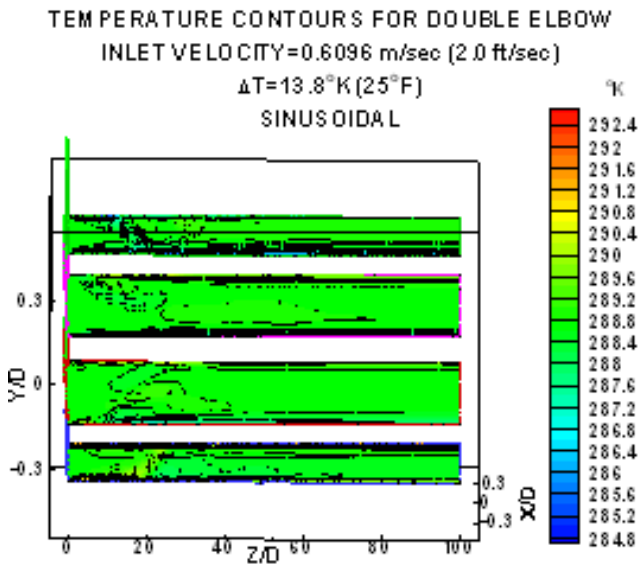

Fig. C-227 Temperature Slice Contours
V_0=0.6096 m/sec, ΔT_{wall}=-13.8°K Sinusoidal

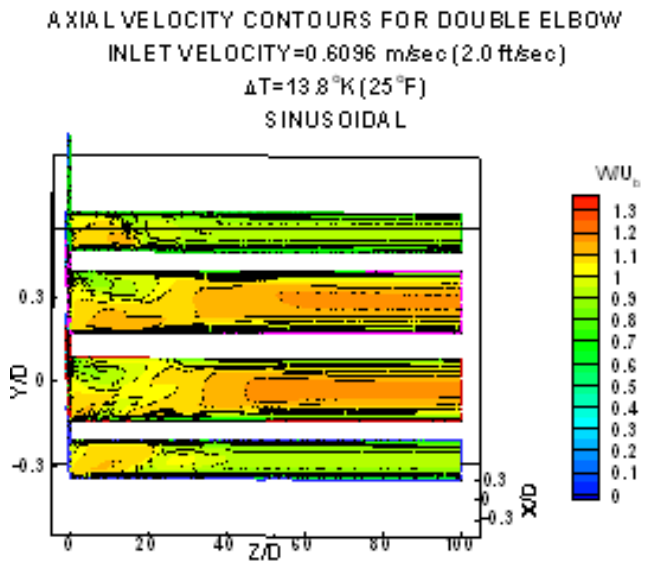

Fig. C-228 Axial Velocity Slice Contours
V_0=0.6096 m/sec, ΔT_{wall}=-13.8°K Sinusoidal

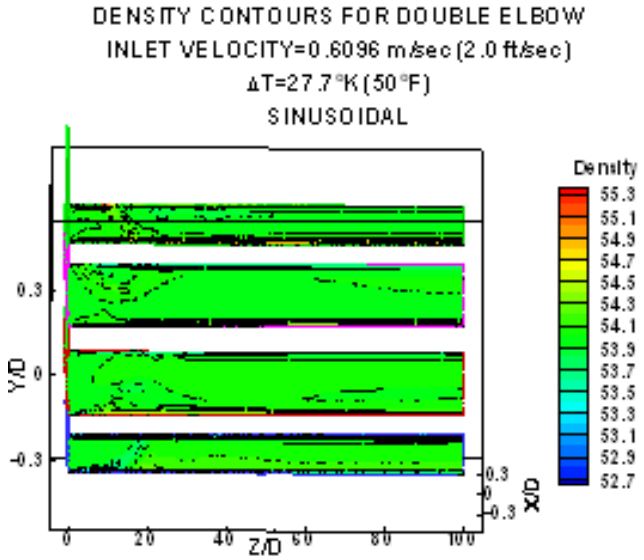

Fig. C-229 Density Slice Contours
V_0=0.6096 m/sec, ΔT_{wall}=-27.7°K Sinusoidal

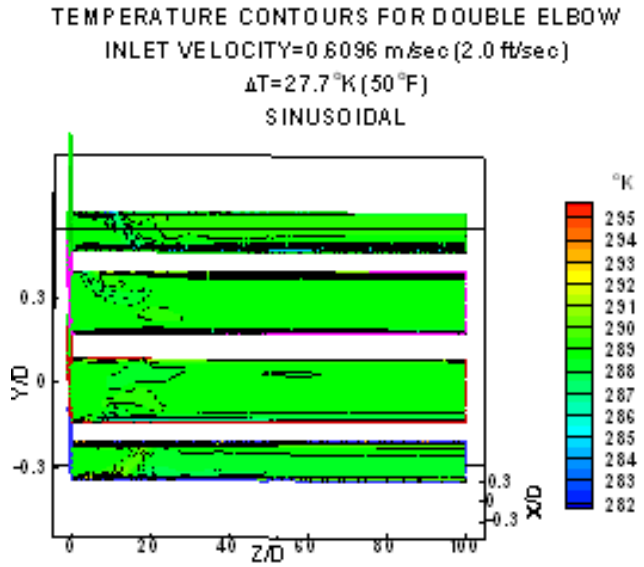

Fig. C-230 Temperature Slice Contours
V_0=0.6096 m/sec, ΔT_{wall}=-27.7°K Sinusoidal

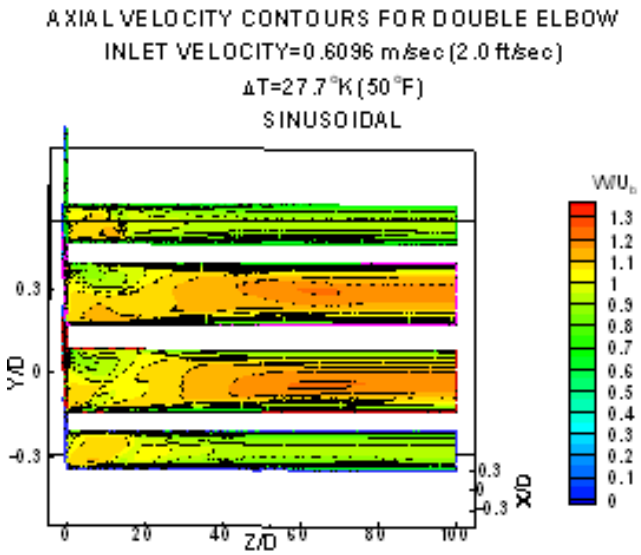

Fig. C-231 Axial Velocity Slice Contours
V_0=0.6096 m/sec, ΔT_{wall}=-27.7°K Sinusoidal

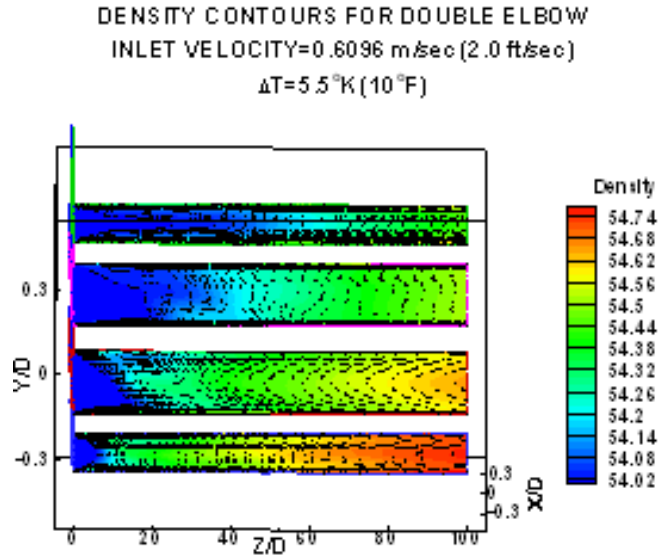

Fig. C-232 Density Slice Contours
V_0=0.6096 m/sec, ΔT_{wall}=-5.5°K

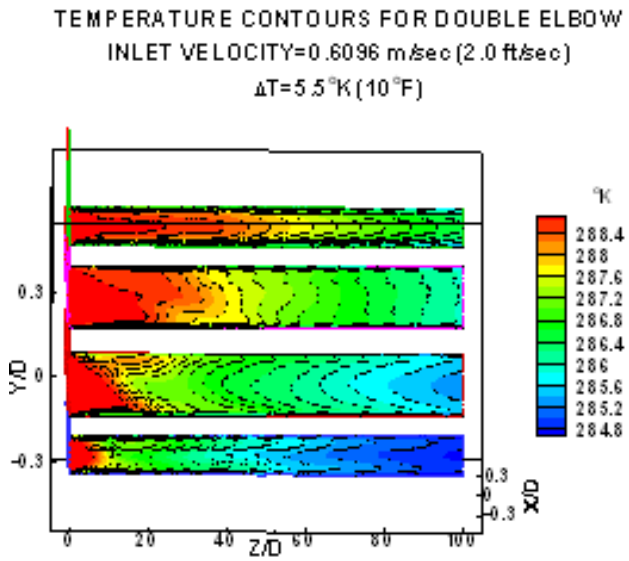

Fig. C-233 Temperature Slice Contours
V_0=0.6096 m/sec, ΔT_{wall}=-5.5°K

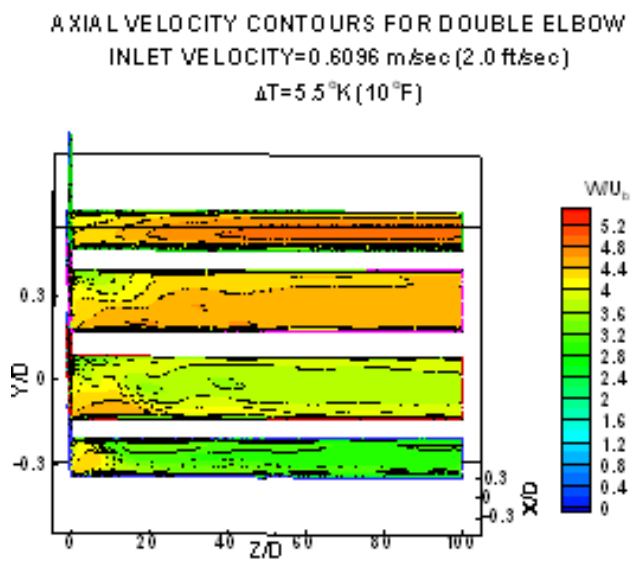

Fig. C-234 Axial Velocity Slice Contours
V_0=0.6096 m/sec, ΔT_{wall}=-5.5°K

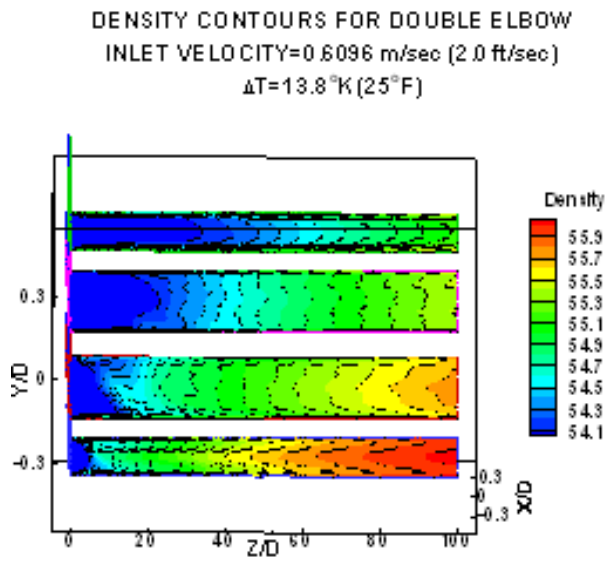

Fig. C-233 Density Slice Contours
V_0=0.6096 m/sec, ΔT_{wall}=-13.8°K

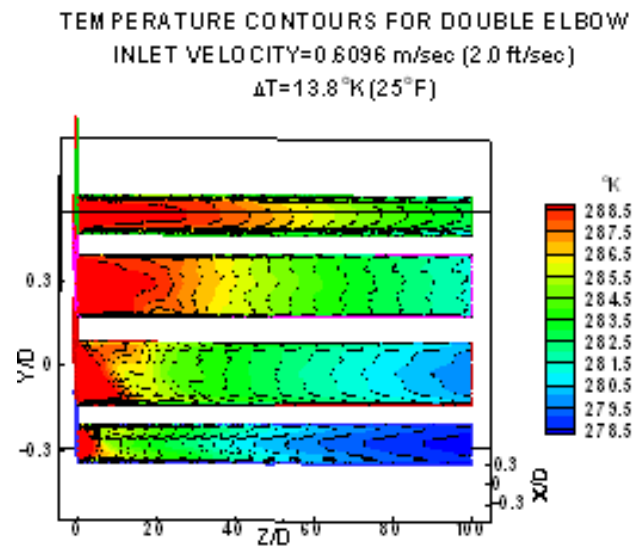

V_0=0.6096 m/sec, ΔT_{wall}=-13.8°K

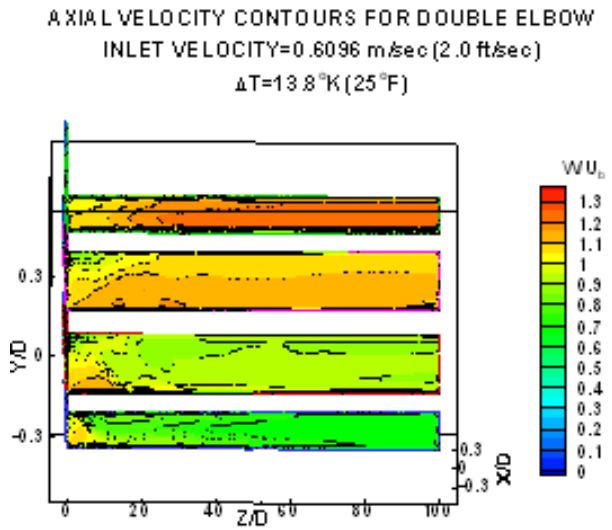

Fig. C-237 Axial Velocity Slice Contours
V_0=0.6096 m/sec, ΔT_{wall}=-13.8°K

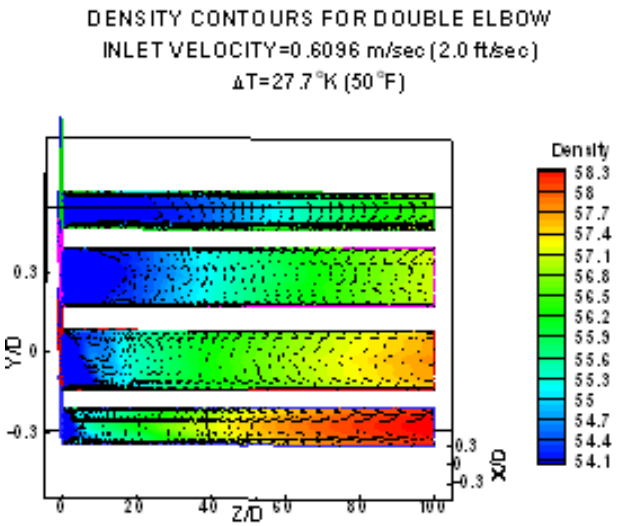

Fig. C-238 Density Slice Contours
V_0=0.6096 m/sec, ΔT_{wall}=-27.7°K

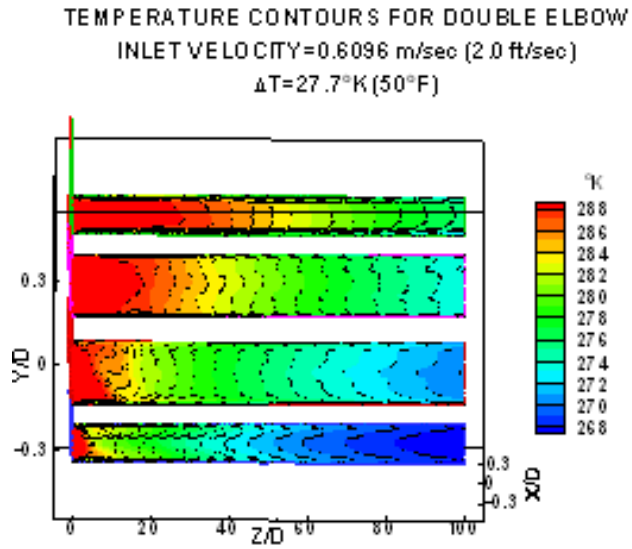

Fig. C-239 Temperature Slice Contours
V_0=0.6096 m/sec, ΔT_{wall}=-27.7°K

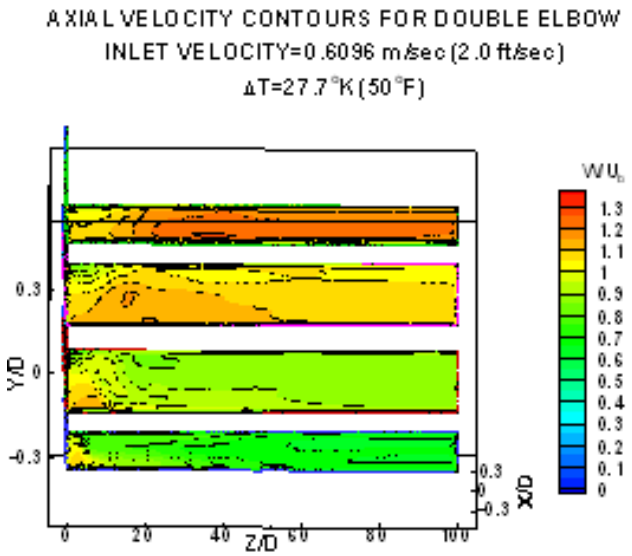

Fig. C-240 Axial Velocity Slice Contours
V_0=0.6096 m/sec, ΔT_{wall}=-27.7°K

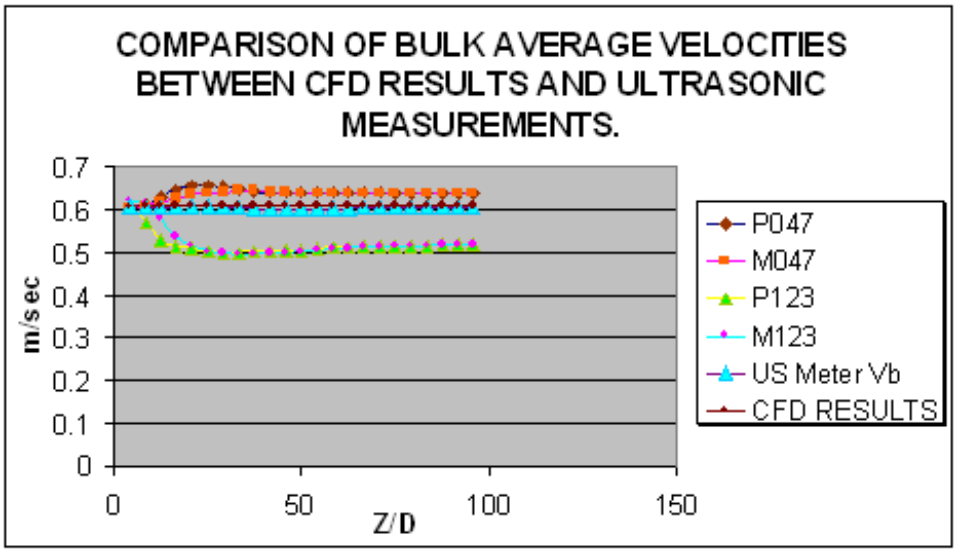

Fig. C-241 Comparison between CFD Vb and Ultrasonic Vb.
V_0=0.6096 m/sec, ΔT_{wall}=5.5°K Sinusoidal

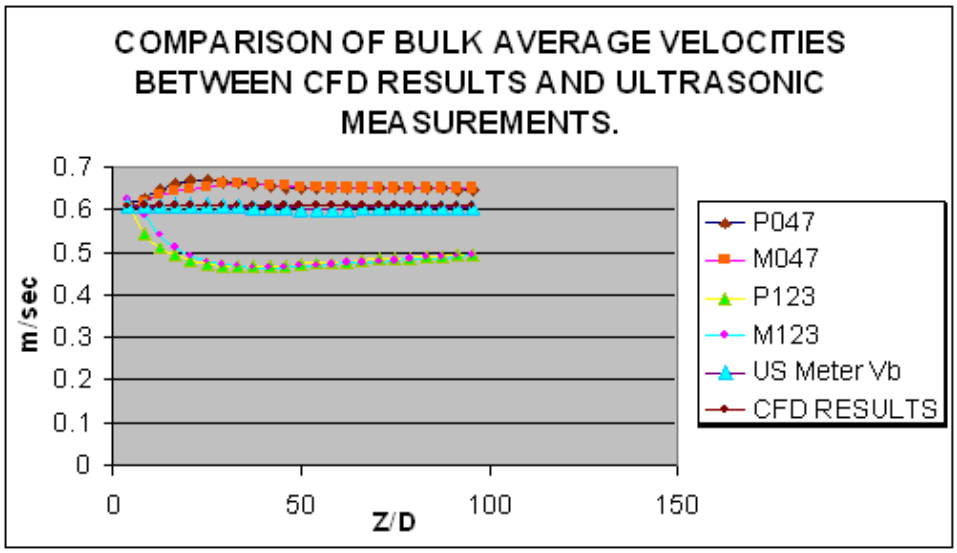

Fig. C-242 Comparison between CFD Vb and Ultrasonic Vb.
V_0=0.6096 m/sec, ΔT_{wall}=13.8°K Sinusoidal

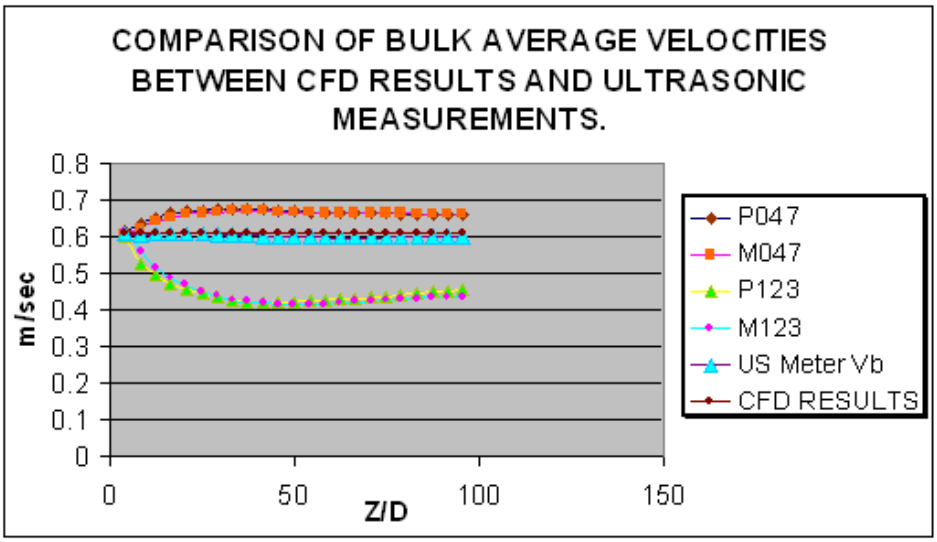

Fig. C-243 Comparison between CFD Vb and Ultrasonic Vb.
V_0=0.6096 m/sec, ΔT_{wall}=27.7°K Sinusoidal

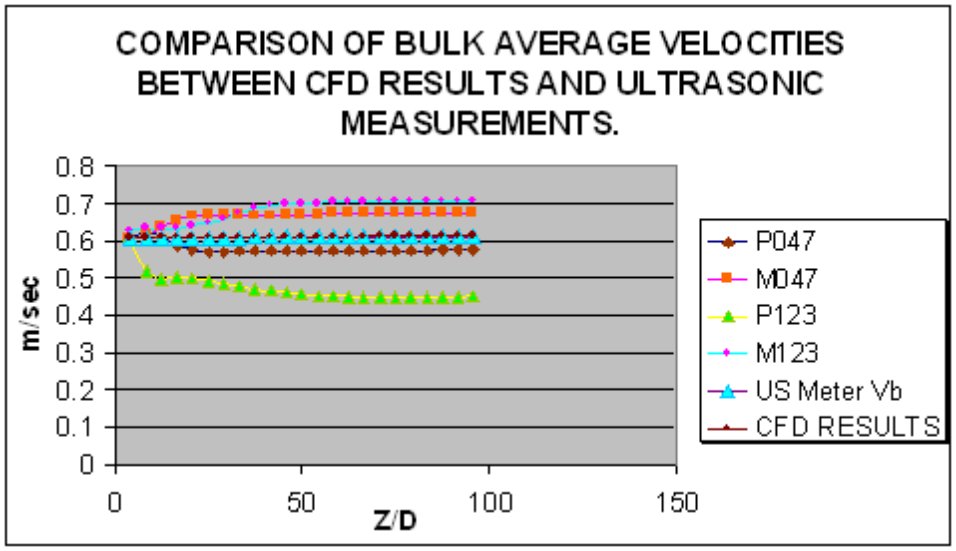

Fig. C-244 Comparison between CFD Vb and Ultrasonic Vb.
V_0=0.6096 m/sec, ΔT_{wall}=5.5°K

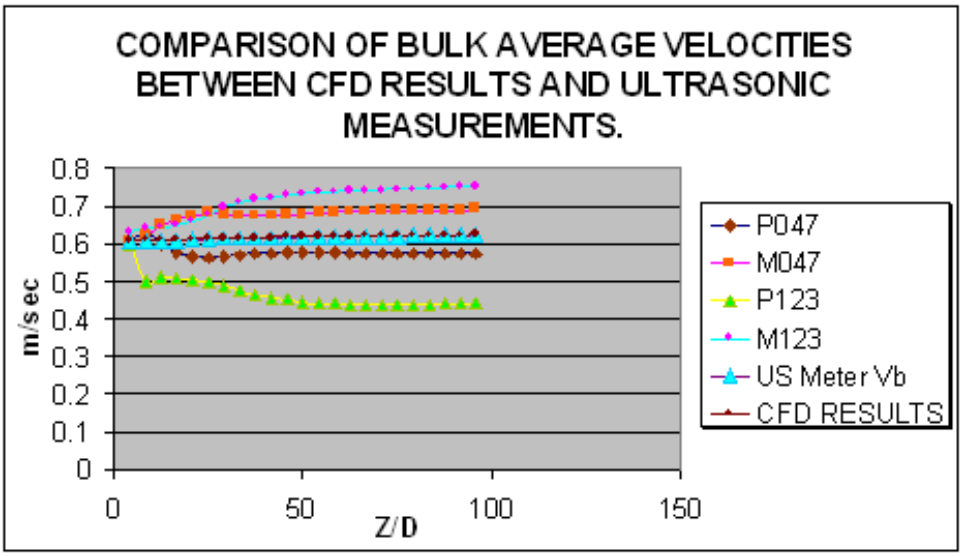

Fig. C-245 Comparison between CFD Vb and Ultrasonic Vb.
V_0=0.6096 m/sec, ΔT_{wall}=13.8°K

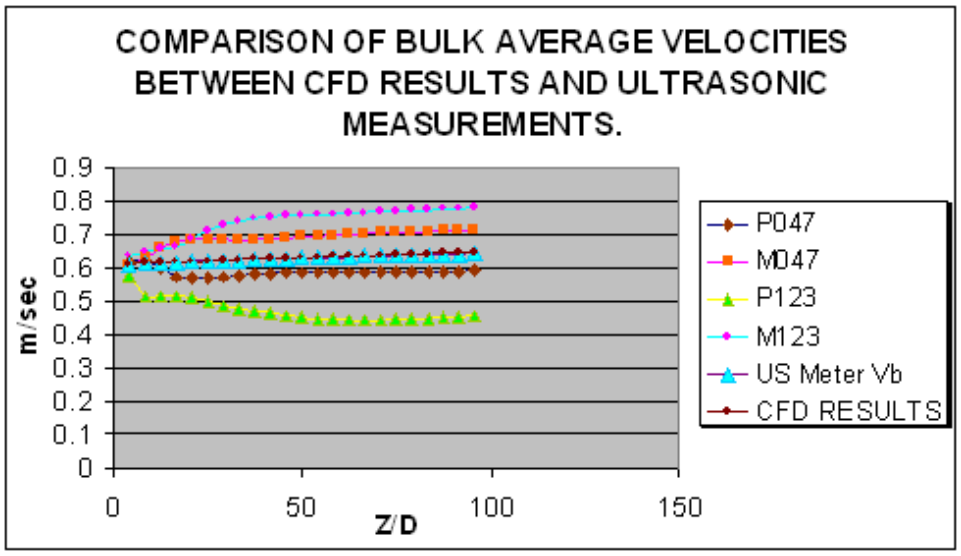

Fig. C-246 Comparison between CFD Vb and Ultrasonic Vb.
V_0=0.6096 m/sec, ΔT_{wall}=27.7°K

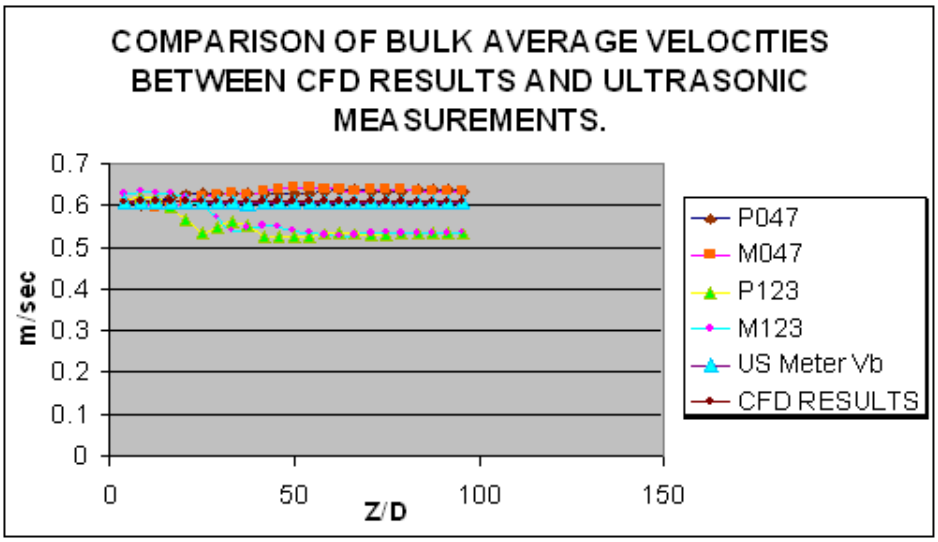

Fig. C-247 Comparison between CFD Vb and Ultrasonic Vb.
V_0=0.6096 m/sec, ΔT_{wall}=-5.5°K Sinusoidal

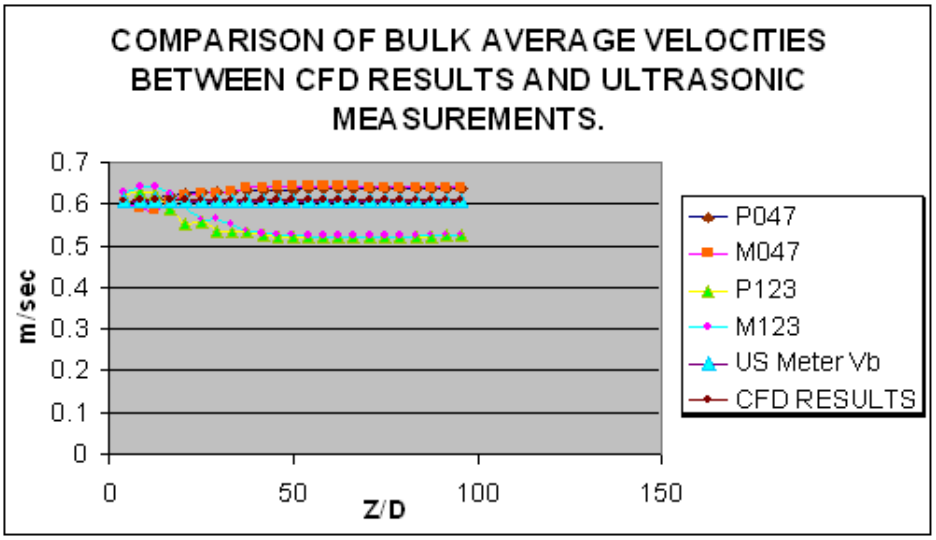

Fig. C-248 Comparison between CFD Vb and Ultrasonic Vb.
V_0=0.6096 m/sec, ΔT_{wall}=-13.8°K Sinusoidal

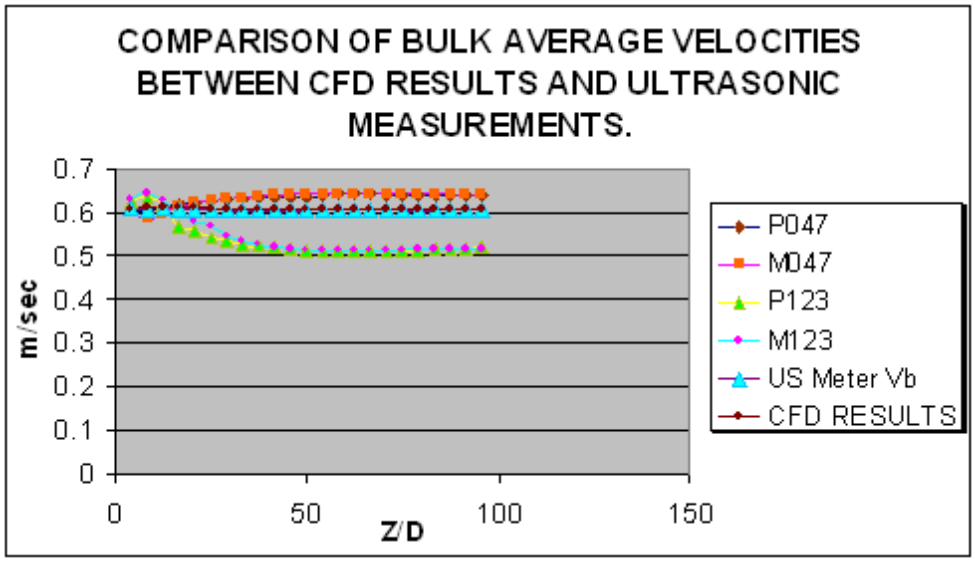

Fig. C-249 Comparison between CFD Vb and Ultrasonic Vb.
V_0=0.6096 m/sec, ΔT_{wall}=-27.7°K Sinusoidal

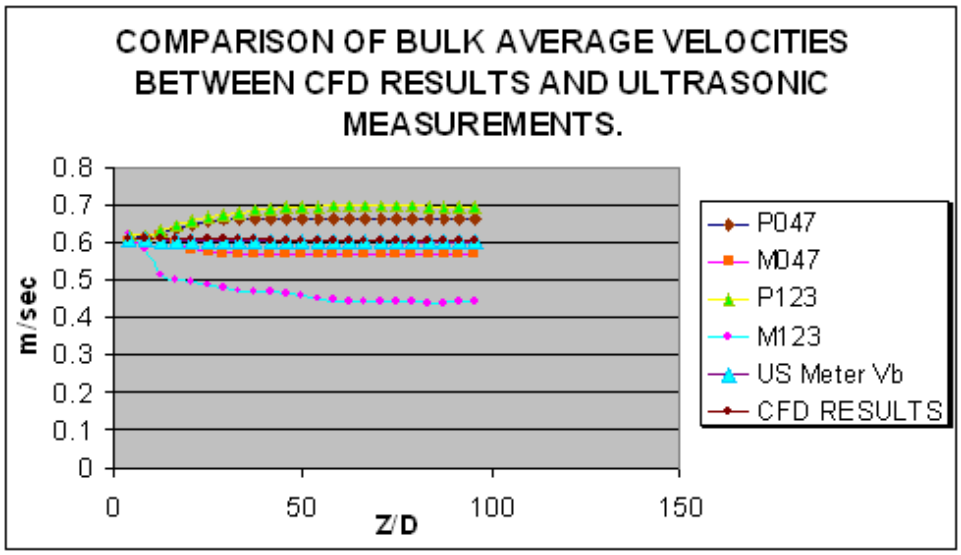

Fig. C-250 Comparison between CFD Vb and Ultrasonic Vb.
V_0=0.6096 m/sec, ΔT_{wall}=-5.5°K

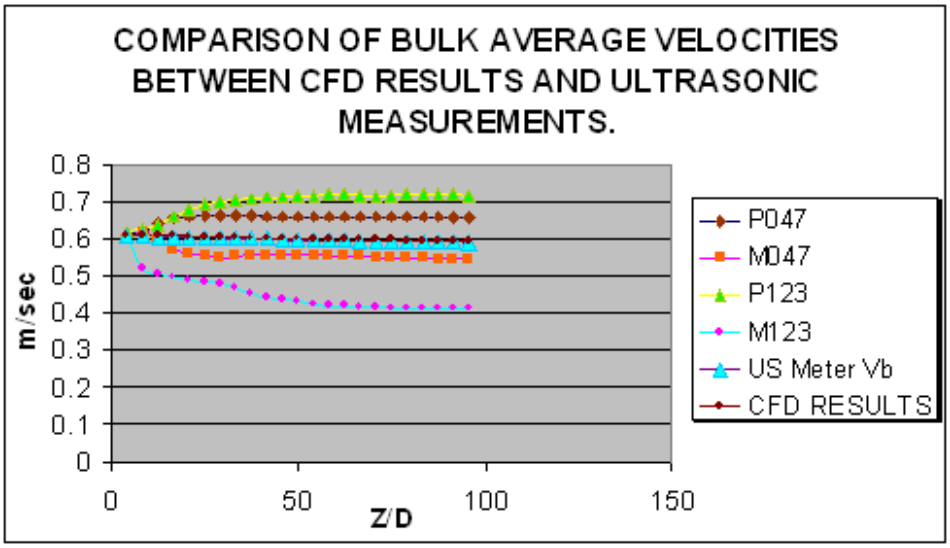

Fig. C-251 Comparison between CFD Vb and Ultrasonic Vb.
V_0=0.6096 m/sec, ΔT_{wall}=-13.8°K

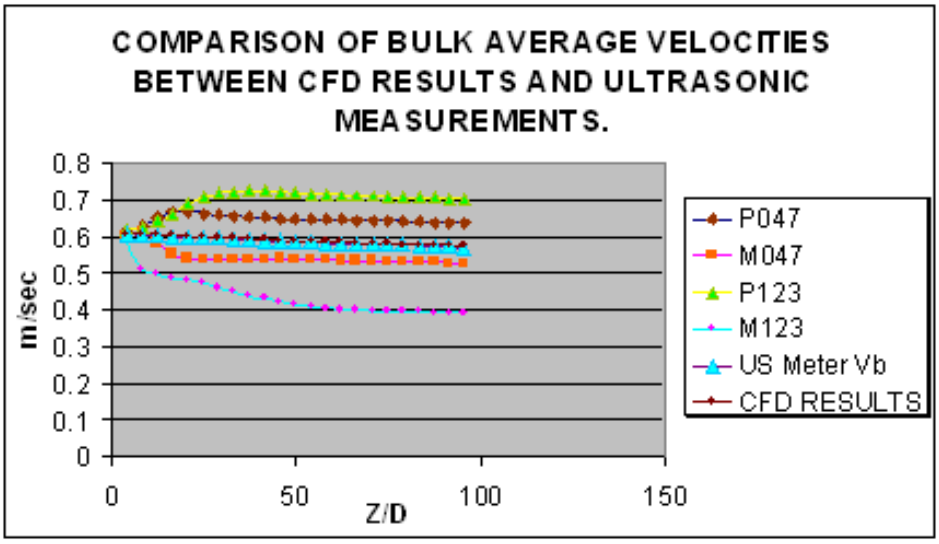

Fig. C-252 Comparison between CFD Vb and Ultrasonic Vb.
V_0=0.6096 m/sec, ΔT_{wall}=-27.7°K

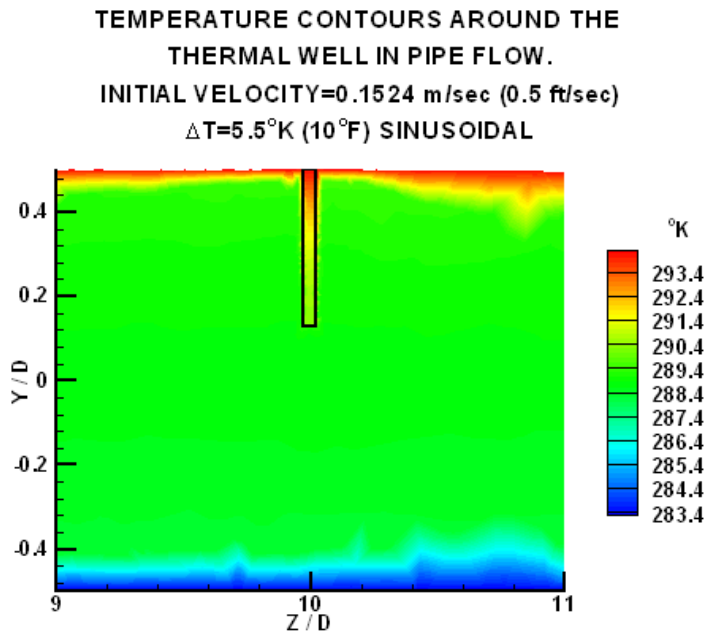

Fig. D-1 Thermal Well Contours
V_0=0.1524 m/sec, ΔT_{wall}=5.5°K Sinusoidal

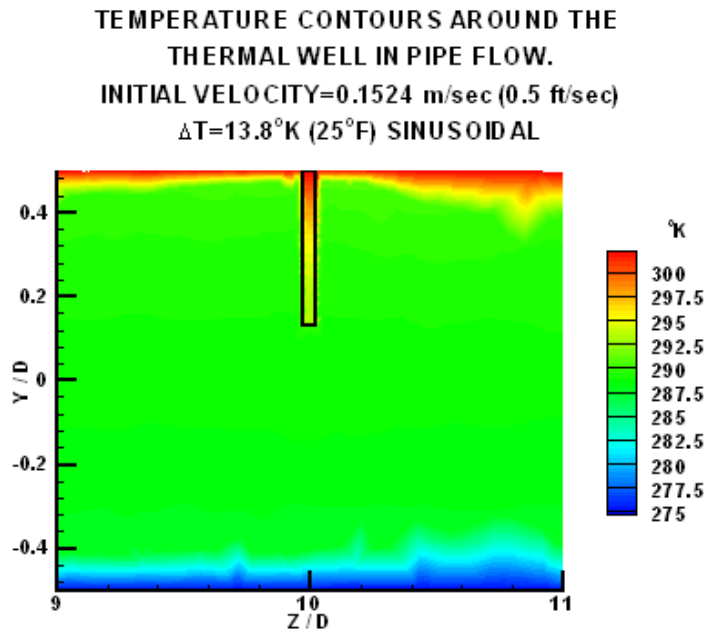

Fig. D-2 Thermal Well Contours
V_0=0.1524 m/sec, ΔT_{wall}=13.8°K Sinusoidal

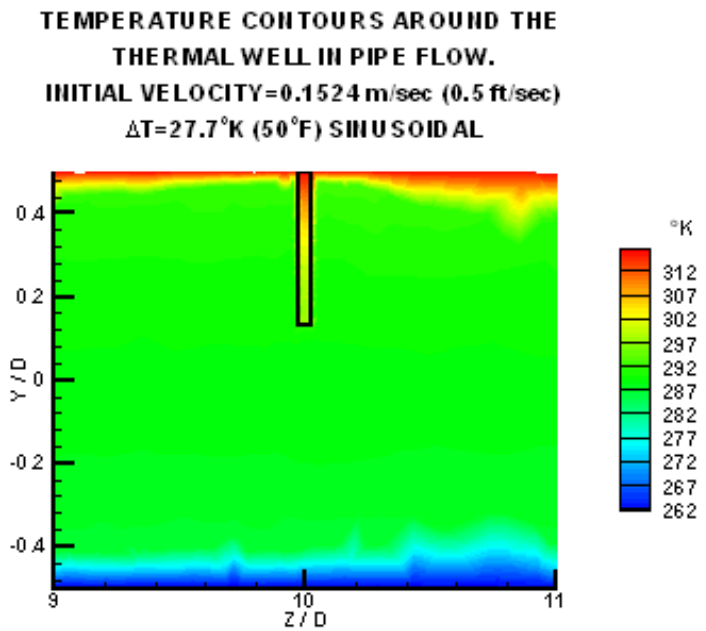

Fig. D-3 Thermal Well Contours
V_0=0.1524 m/sec, ΔT_{wall}=27.7°K Sinusoidal

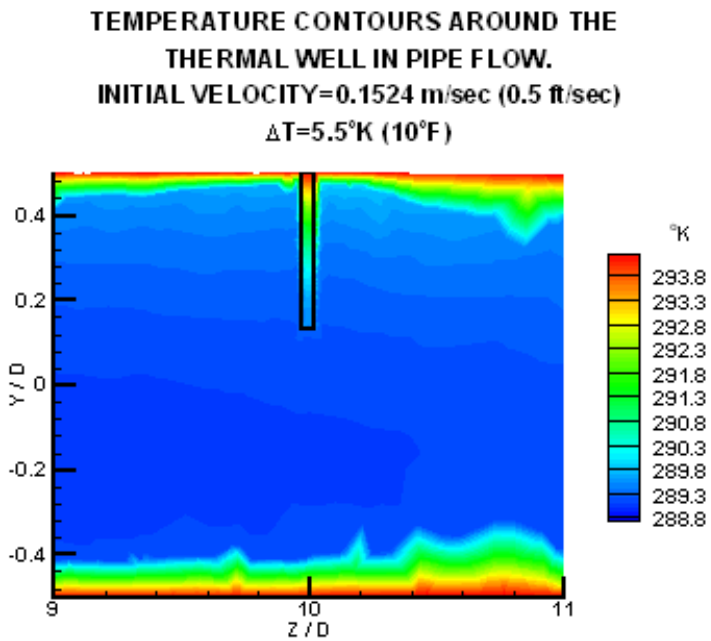

Fig. D-4 Thermal Well Contours
V_0=0.1524 m/sec, ΔT_{wall}=5.5°K

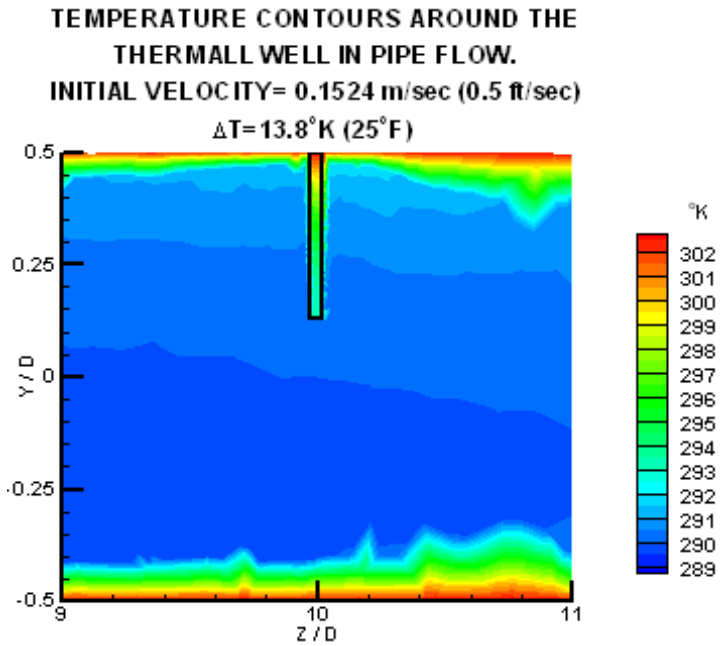

Fig. D-5 Thermal Well Contours
V_0=0.1524 m/sec, ΔT_{wall}=13.8°K

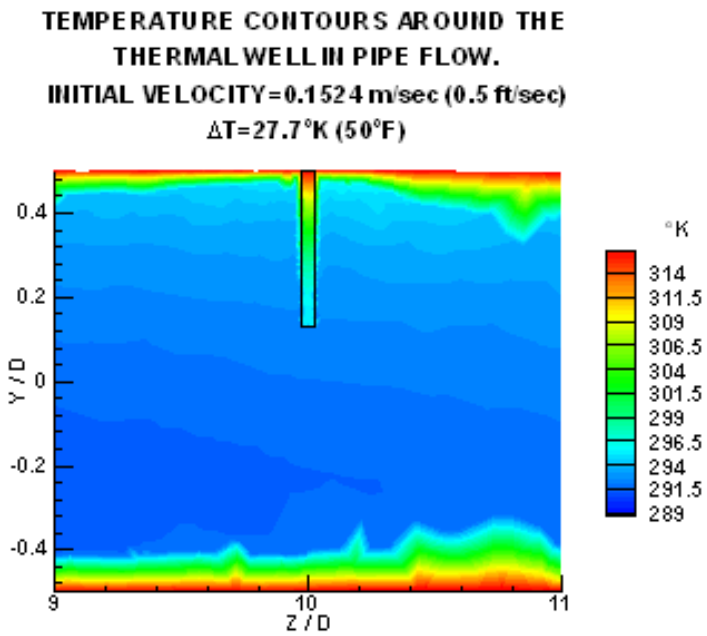

Fig. D-6 Thermal Well Contours
V_0=0.1524 m/sec, ΔT_{wall}=27.7°K

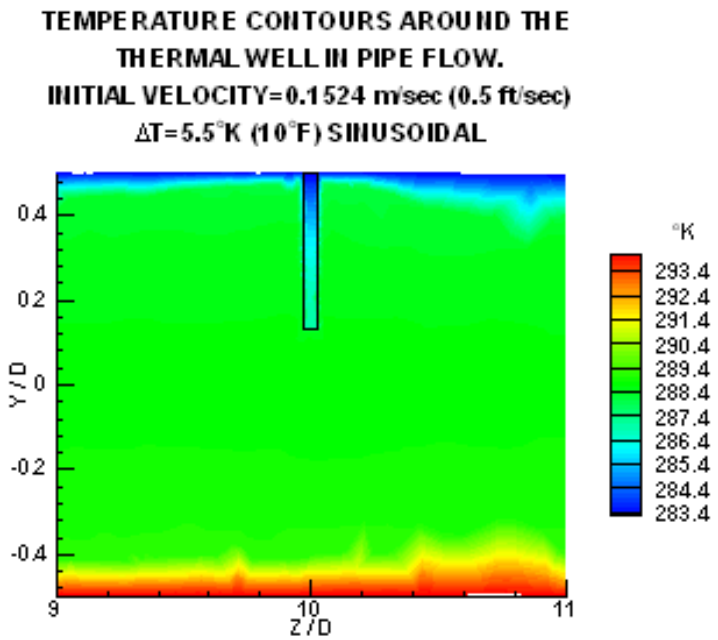

Fig. D-7 Thermal Well Contours
V_0=0.1524 m/sec, ΔT_{wall}=-5.5°K Sinusoidal

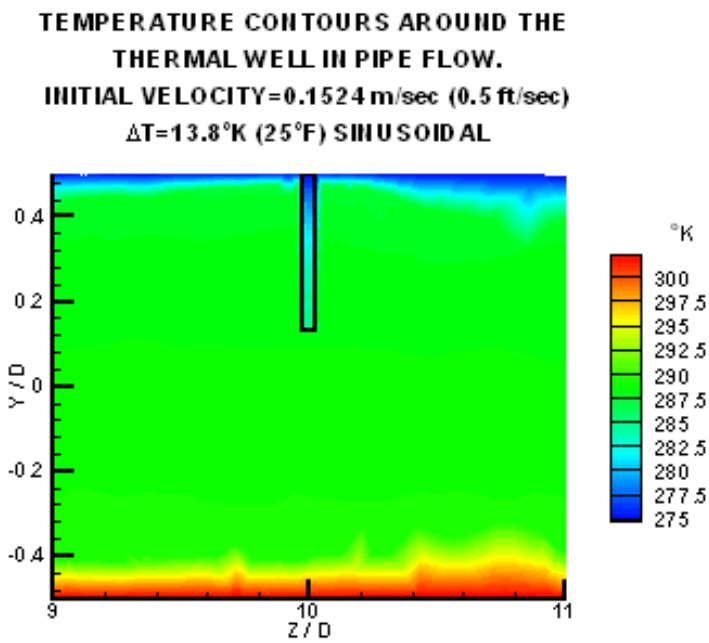

Fig. D-8 Thermal Well Contours
V_0=0.1524 m/sec, ΔT_{wall}=-13.8°K Sinusoidal

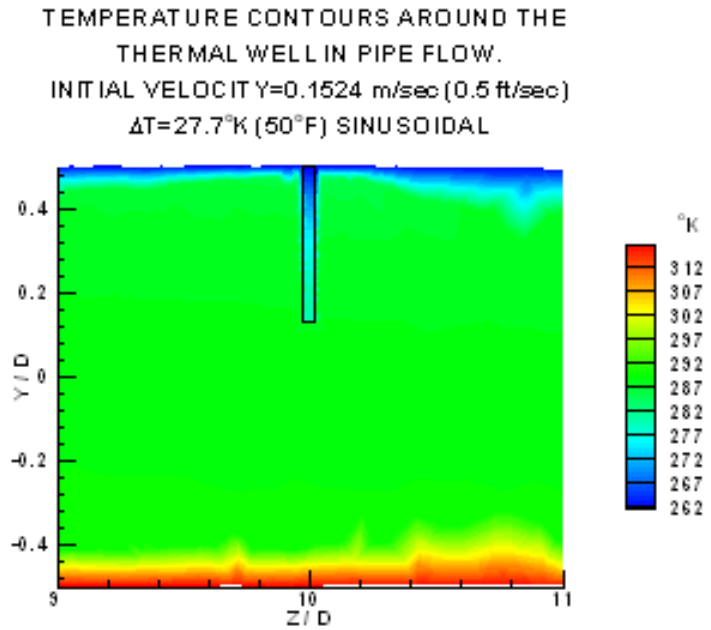

Fig. D-9 Thermal Well Contours
V_0=0.1524 m/sec, ΔT_{wall}=-27.7°K Sinusoidal

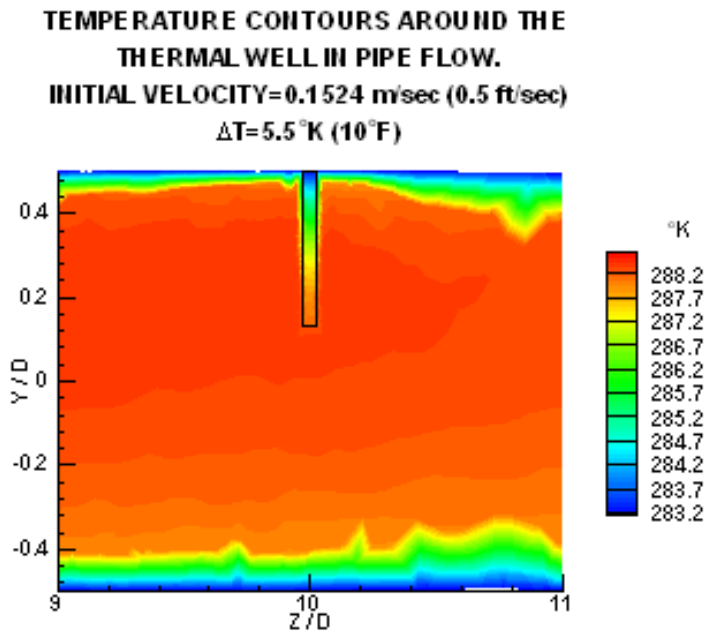

Fig. D-10 Thermal Well Contours
V_0=0.1524 m/sec, ΔT_{wall}=-5.5°K

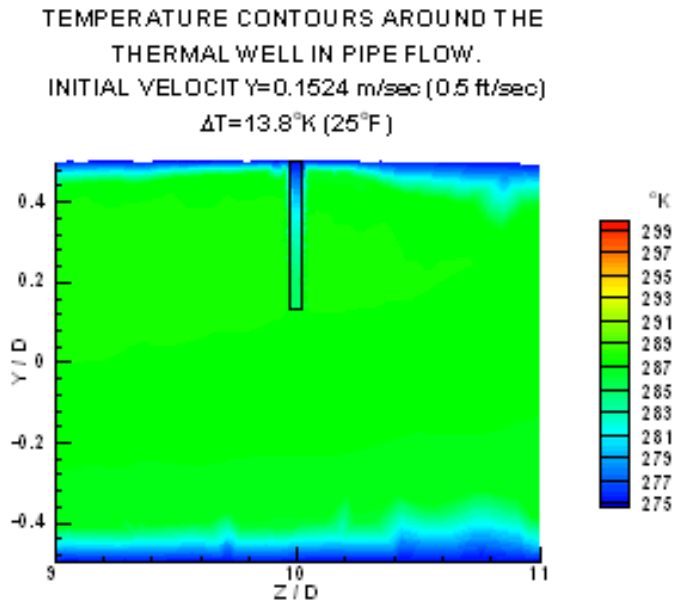

Fig. D-11 Thermal Well Contours
V_0=0.1524 m/sec, ΔT_{wall}=-13.8°K

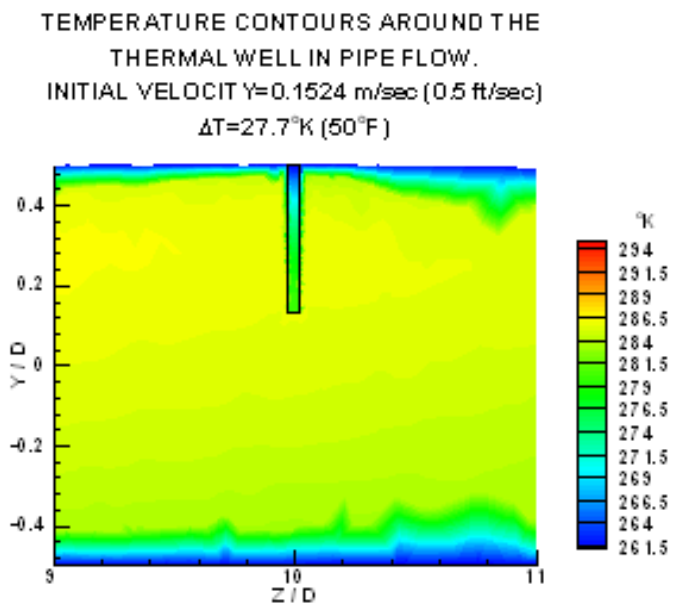

Fig. D-12 Thermal Well Contours
V_0=0.1524 m/sec, ΔT_{wall}=-27.7°K

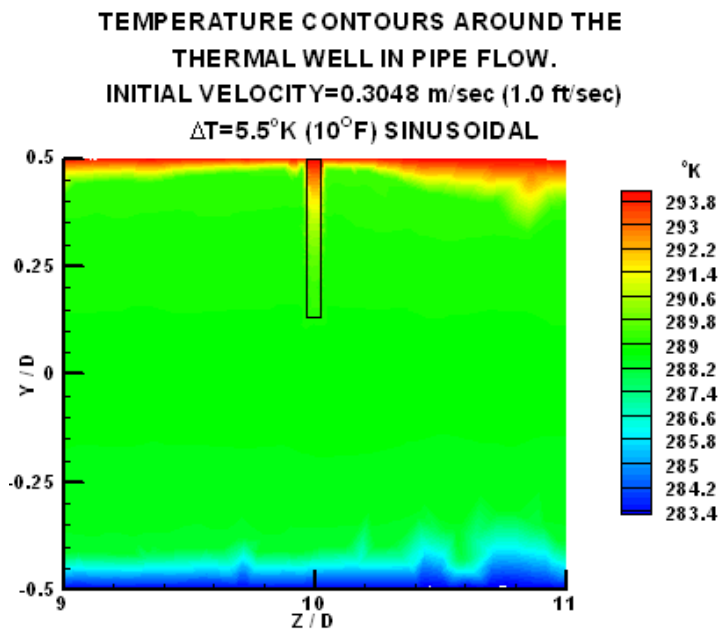

Fig. D-13 Thermal Well Contours
V_0=0.3048 m/sec, ΔT_{wall}=5.5°K Sinusoidal

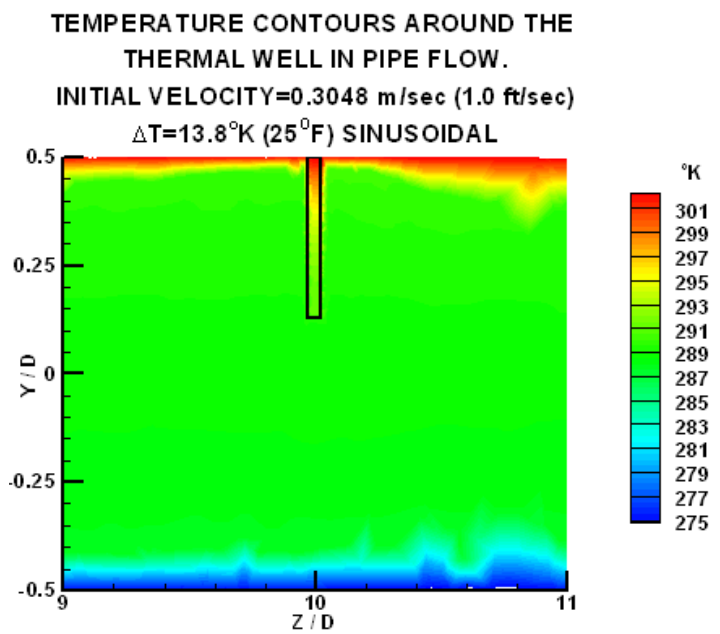

Fig. D-14 Thermal Well Contours
V_0=0.3048 m/sec, ΔT_{wall}=13.8°K Sinusoidal

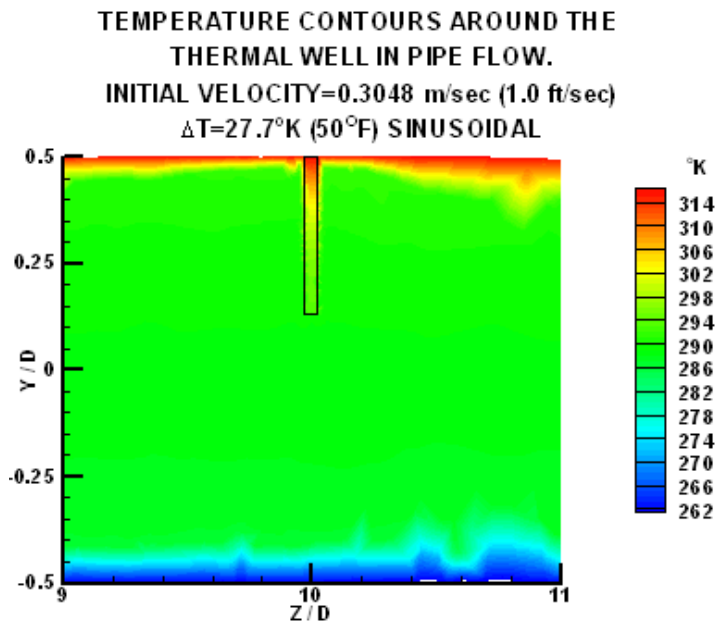

Fig. D-15 Thermal Well Contours
V_0=0.3048 m/sec, ΔT_{wall}=27.7°K Sinusoidal

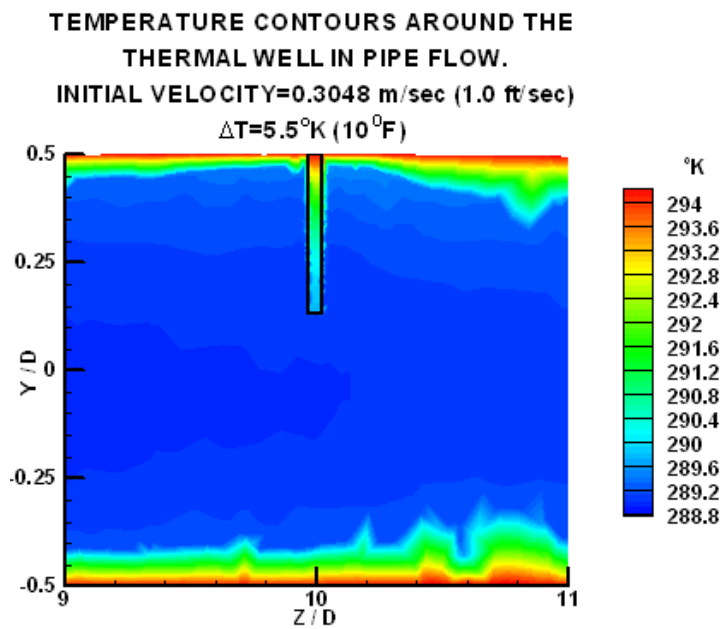

Fig. D-16 Thermal Well Contours
V_0=0.3048 m/sec, ΔT_{wall}=5.5°K

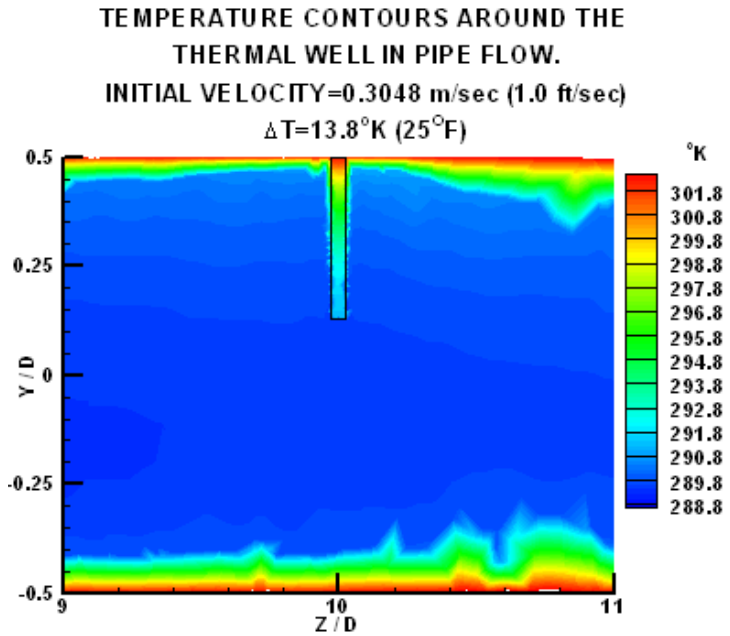

Fig. D-17 Thermal Well Contours
V_0=0.3048 m/sec, ΔT_{wall}=13.8°K

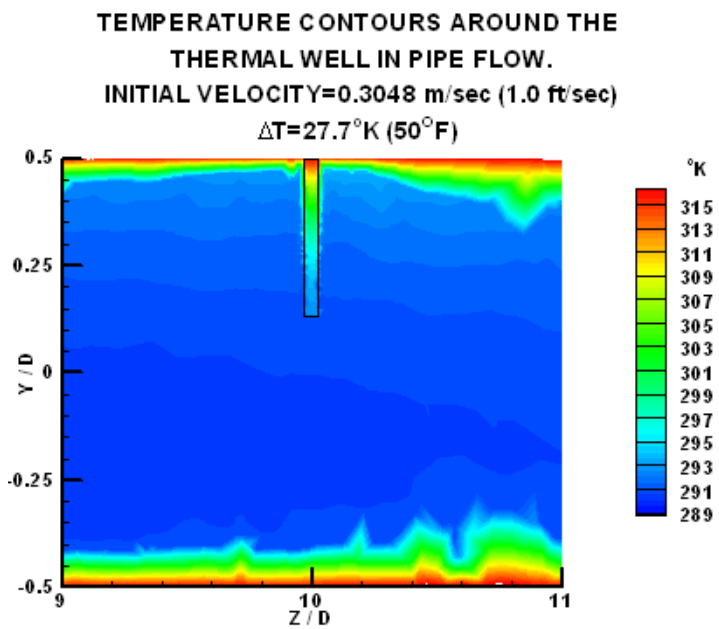

Fig. D-18 Thermal Well Contours
V_0=0.3048 m/sec, ΔT_{wall}=27.7°K

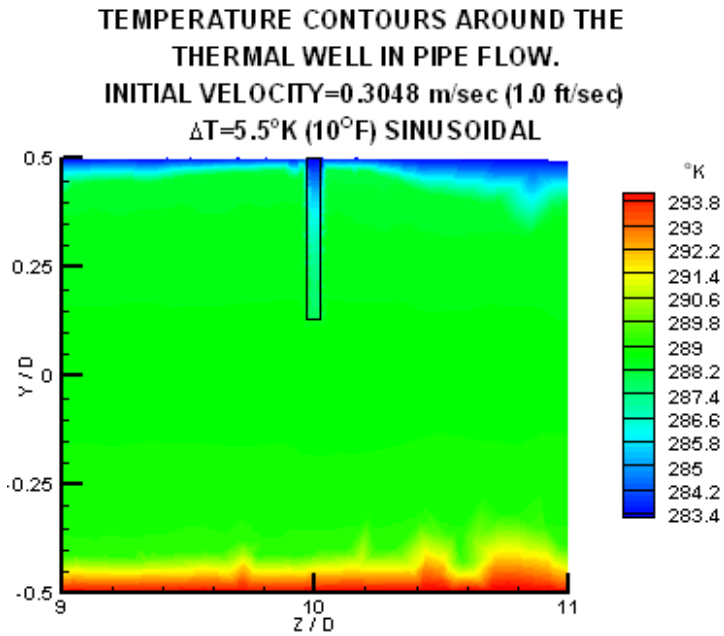

Fig. D-19 Thermal Well Contours
V_0=0.3048 m/sec, ΔT_{wall}=-5.5°K Sinusoidal

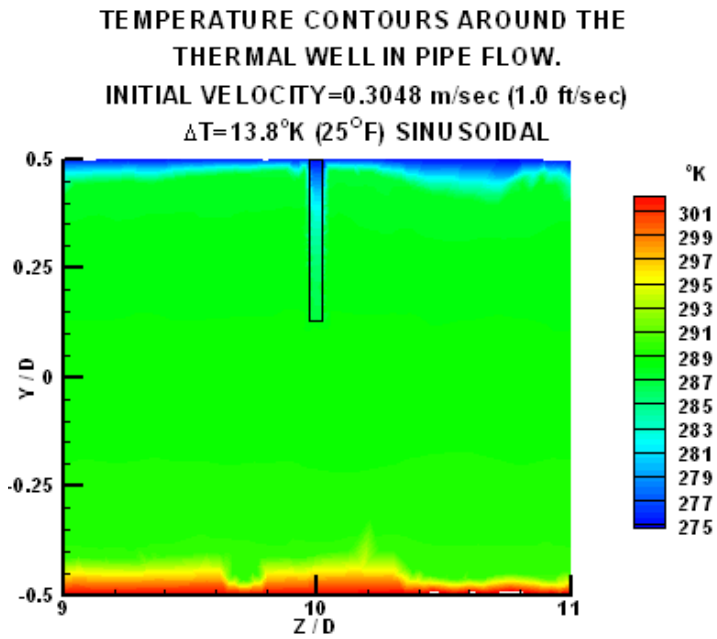

Fig. D-20 Thermal Well Contours
V_0=0.3048 m/sec, ΔT_{wall}=-13.8°K Sinusoidal

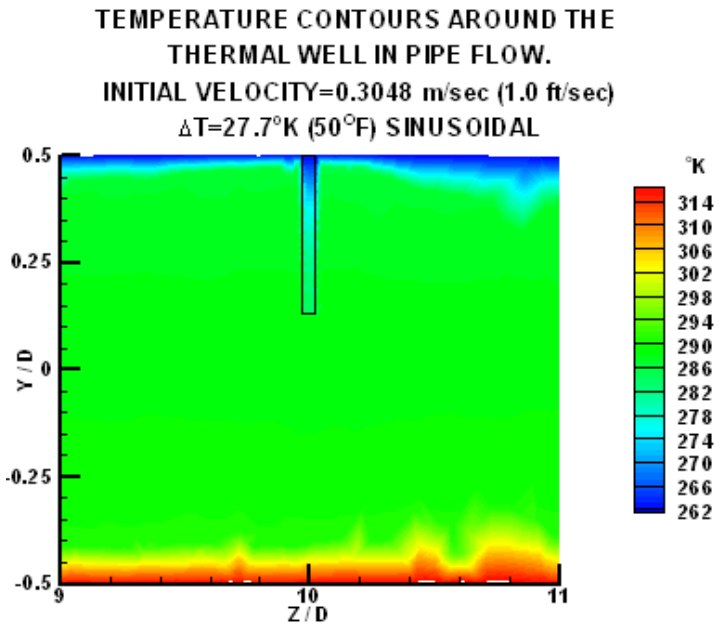

Fig. D-21 Thermal Well Contours
V_0=0.3048 m/sec, ΔT_{wall}=-27.7°K Sinusoidal

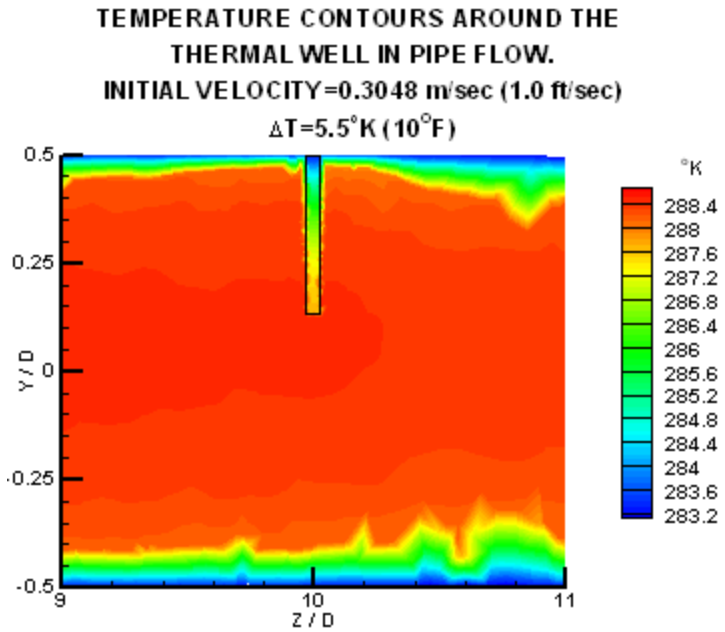

Fig. D-22 Thermal Well Contours
V_0=0.3048 m/sec, ΔT_{wall}=-5.5°K

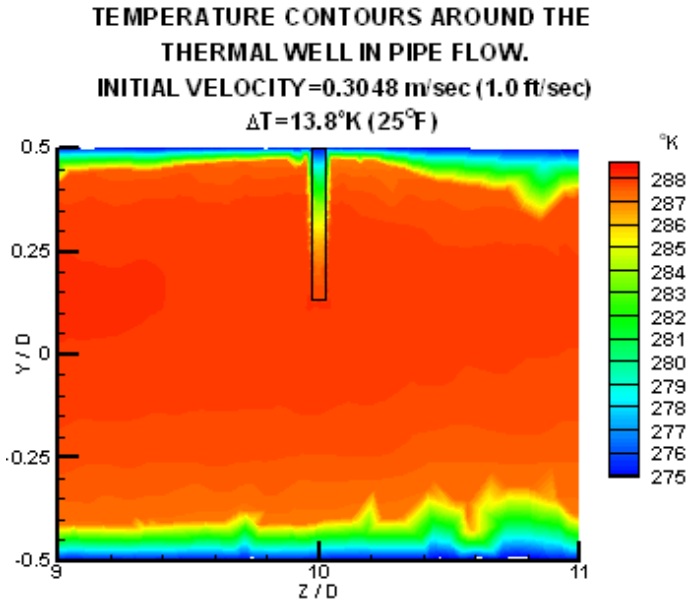

Fig. D-23 Thermal Well Contours
V_0=0.3048 m/sec, ΔT_{wall}=-13.8°K

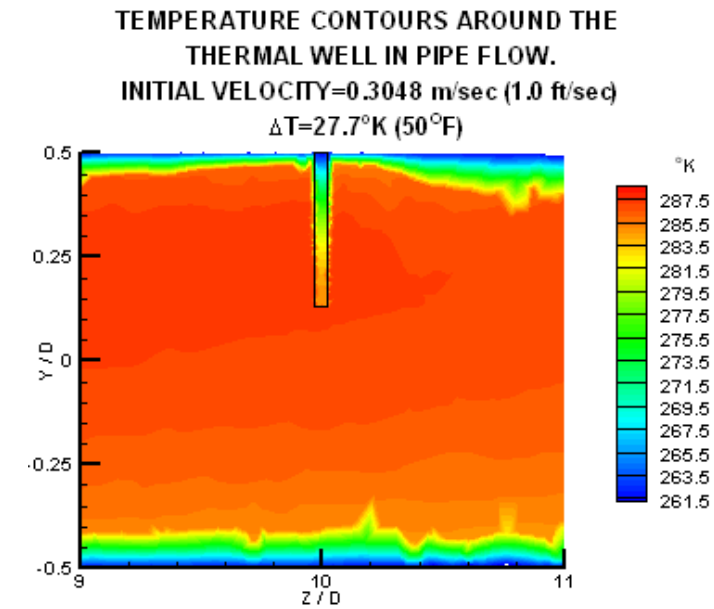

Fig. D-24 Thermal Well Contours
V_0=0.3048 m/sec, ΔT_{wall}=-27.7°K

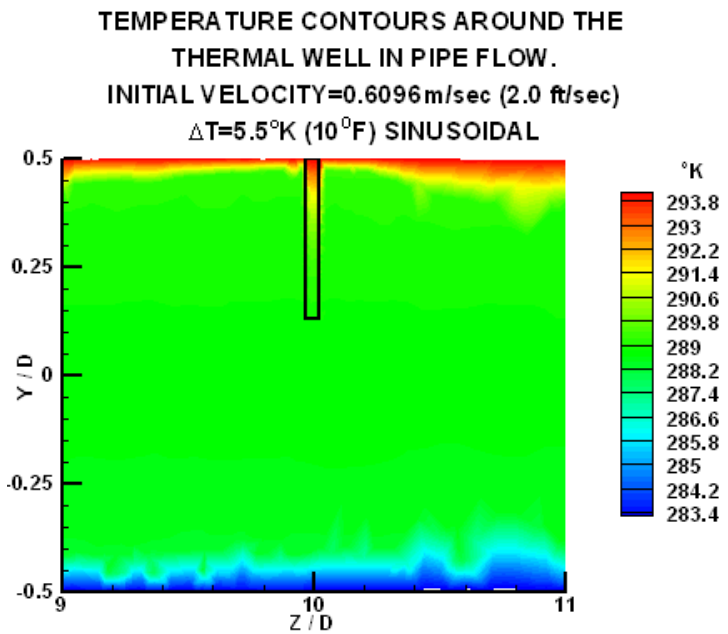

Fig. D-25 Thermal Well Contours
V_0=0.6096 m/sec, ΔT_{wall}=5.5°K Sinusoidal

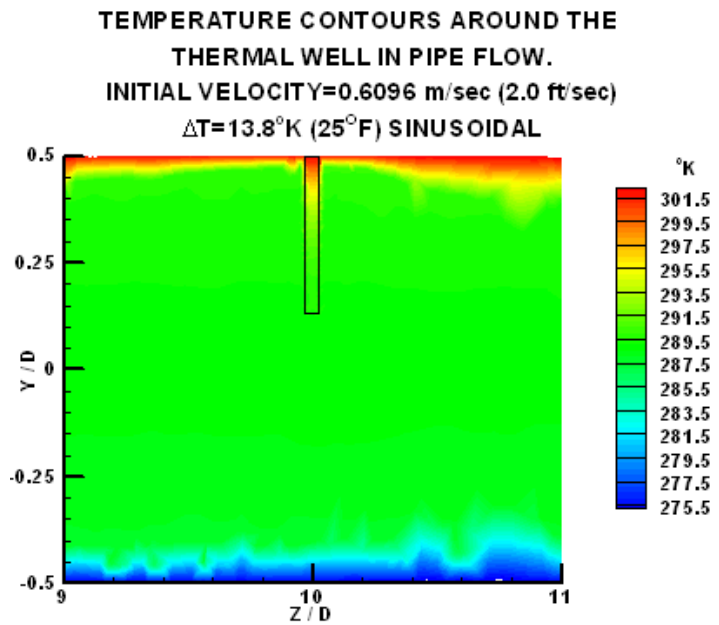

Fig. D-26 Thermal Well Contours
V_0=0.6096 m/sec, ΔT_{wall}=13.8°K Sinusoidal

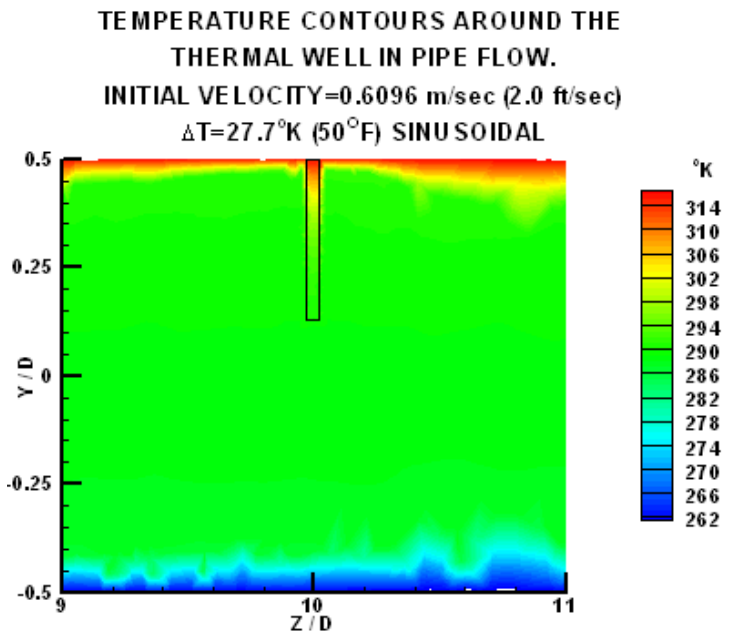

Fig. D-27 Thermal Well Contours
V_0=0.6096 m/sec, ΔT_{wall}=27.7°K Sinusoidal

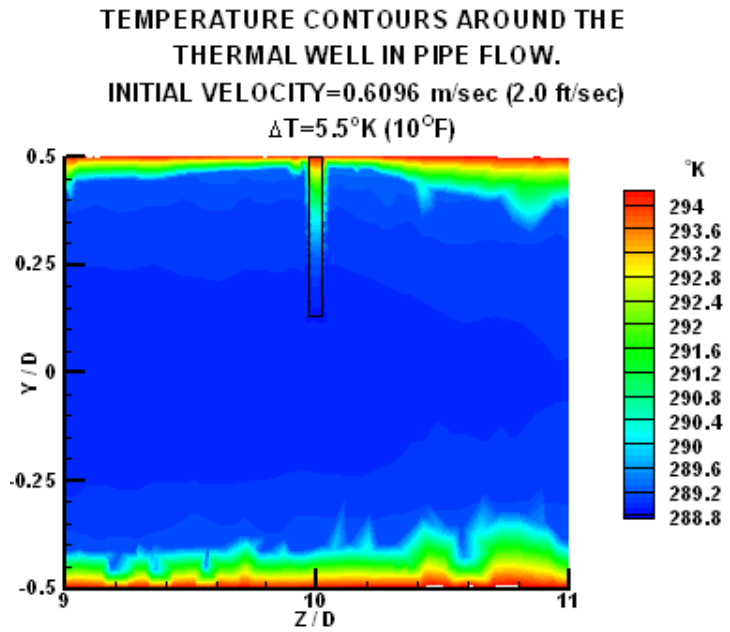

Fig. D-28 Thermal Well Contours
V_0=0.6096 m/sec, ΔT_{wall}=5.5°K

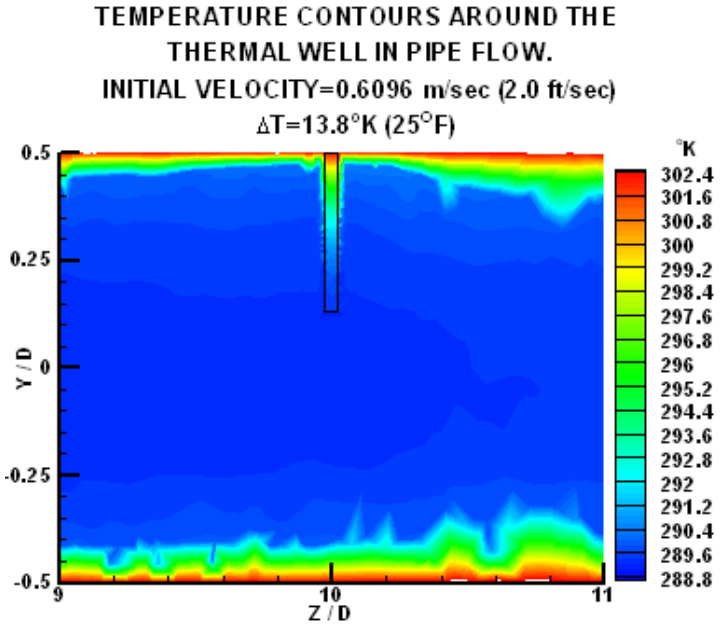

Fig. D-29 Thermal Well Contours
V_0=0.6096 m/sec, ΔT_{wall}=13.8°K

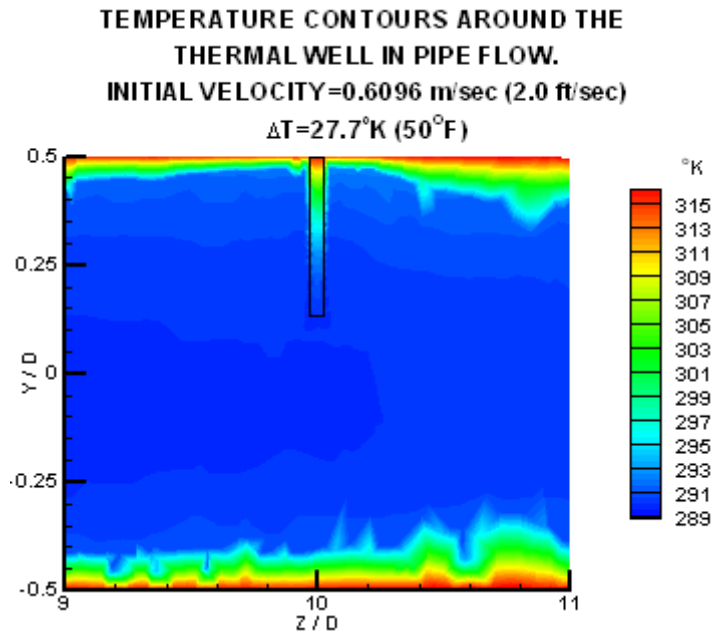

Fig. D-30 Thermal Well Contours
V_0=0.6096 m/sec, ΔT_{wall}=27.7°K

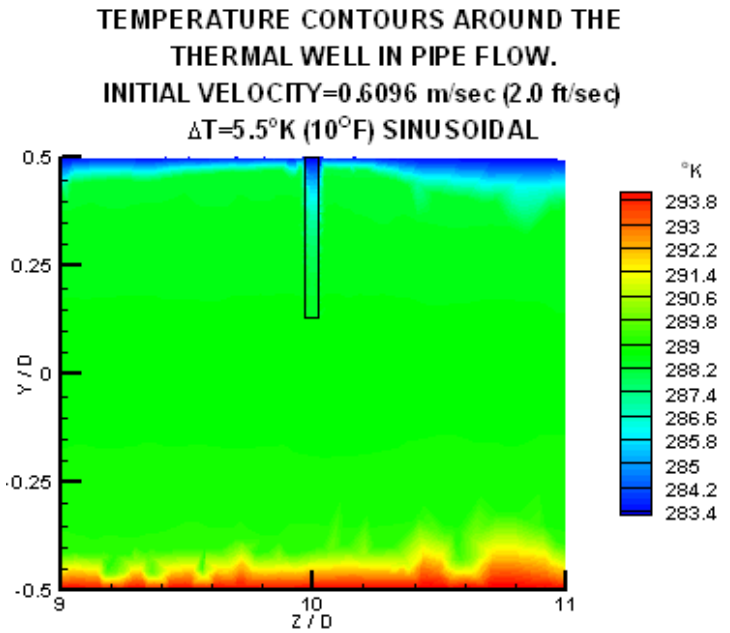

Fig. D-31 Thermal Well Contours
V_0=0.6096 m/sec, ΔT_{wall}=-5.5°K Sinusoidal

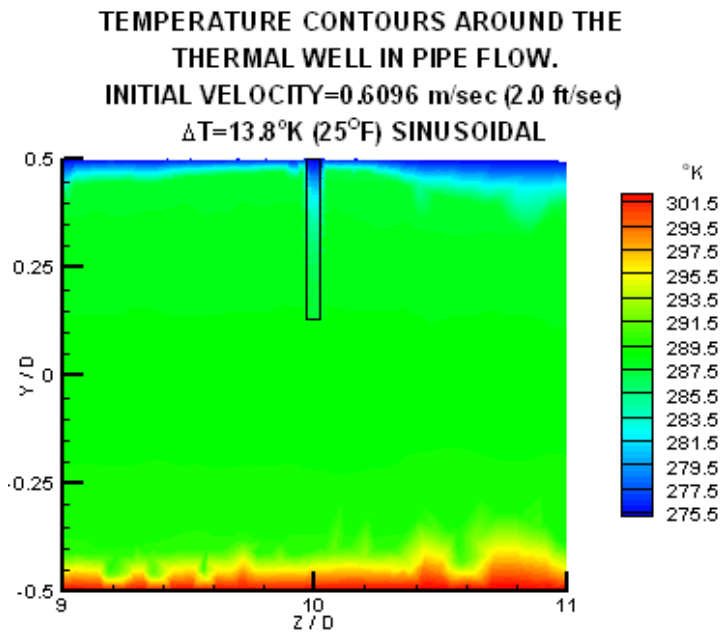

Fig. D-32 Thermal Well Contours
V_0=0.6096 m/sec, ΔT_{wall}=-13.8°K Sinusoidal

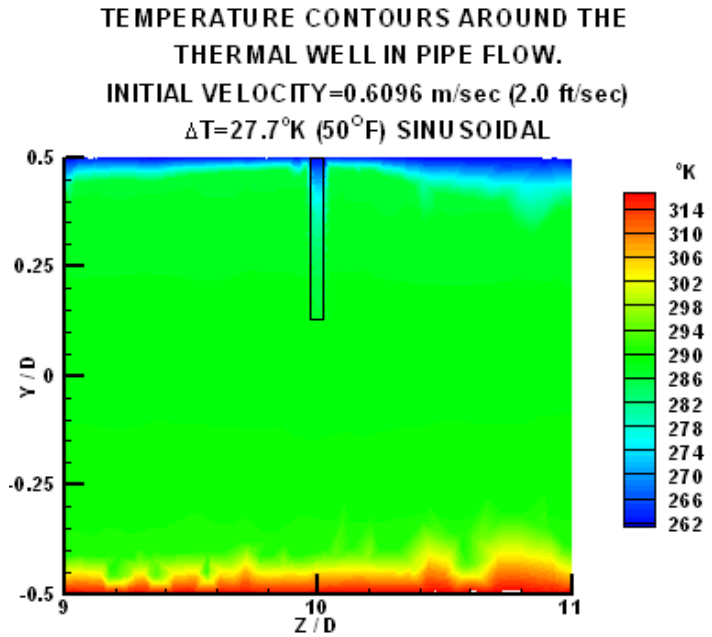

Fig. D-33 Thermal Well Contours
V_0=0.6096 m/sec, ΔT_{wall}=-27.7°K Sinusoidal

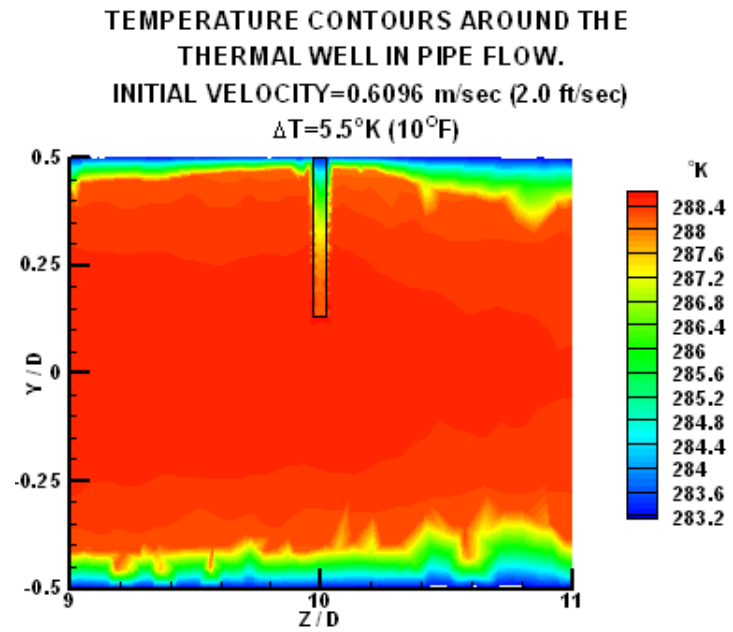

Fig. D-34 Thermal Well Contours
V_0=0.6096 m/sec, ΔT_{wall}=-5.5°K

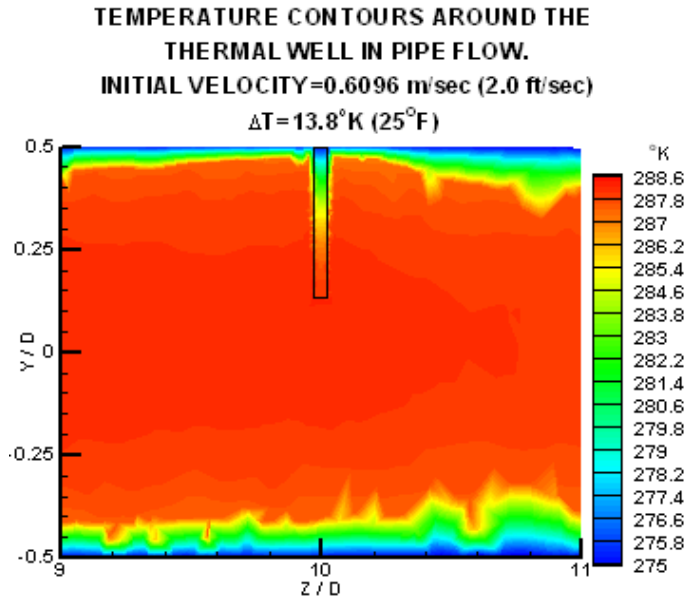

Fig. D-35 Thermal Well Contours
V_0=0.6096 m/sec, ΔT_{wall}=-13.8°K

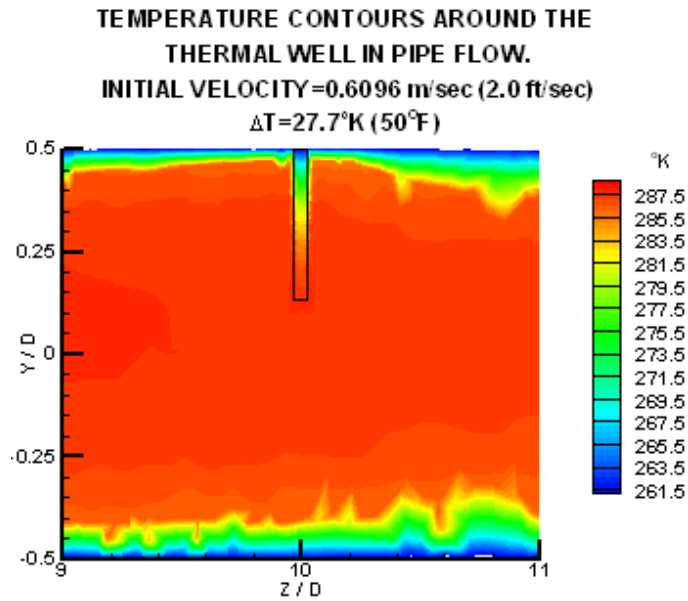

Fig. D-36 Thermal Well Contours
V_0=0.6096 m/sec, ΔT_{wall}=-27.7°K

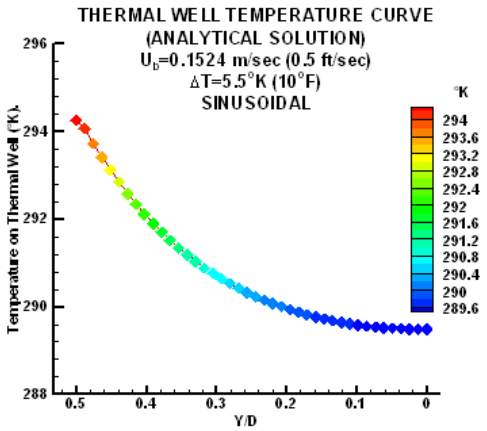

Fig. E-1 Temp Thermal Well (Analytical)
V_0=0.1524 m/sec, ΔT_{wall}=5.5°K Sinusoidal

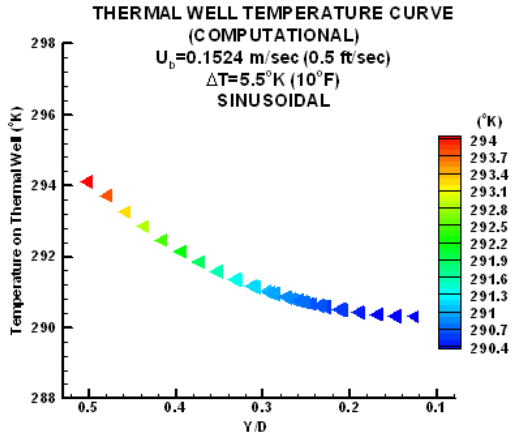

Fig. E-2 Temp Thermal Well (Computational)
V_0=0.1524 m/sec, ΔT_{wall}=5.5°K Sinusoidal

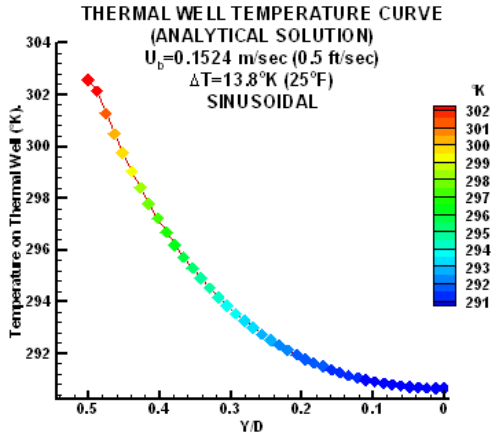

Fig. E-3 Temp Thermal Well (Analytical)
V_0=0.1524 m/sec, ΔT_{wall}=13.8°K Sinusoidal

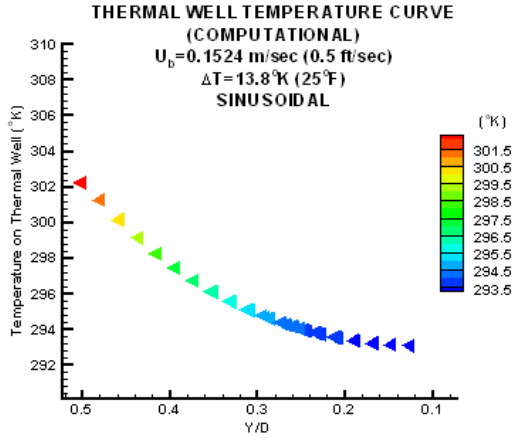

Fig. E-4 Temp Thermal Well (Computational)
V_0=0.1524 m/sec, ΔT_{wall}=13.8°K Sinusoidal

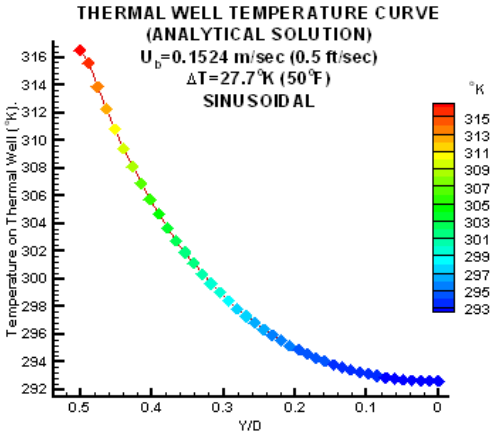

Fig. E-5 Temp Thermal Well (Analytical)
V_0=0.1524 m/sec, ΔT_{wall}=27.7°K Sinusoidal

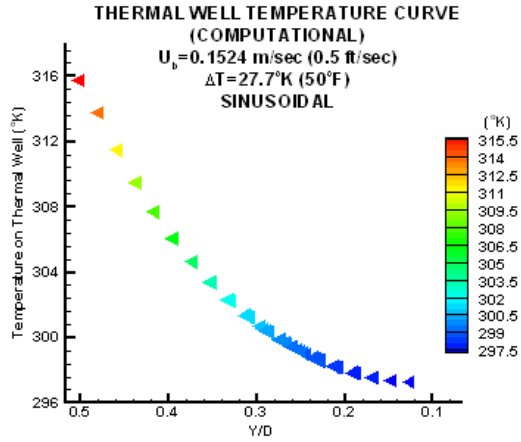

Fig. E-6 Temp Thermal Well (Computational)
V_0=0.1524 m/sec, ΔT_{wall}=27.7°K Sinusoidal

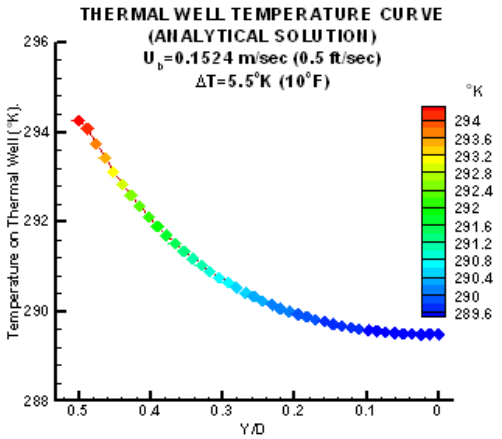

Fig. E-7 Temp Thermal Well (Analytical)
V_0=0.1524 m/sec, ΔT_{wall}=5.5°K

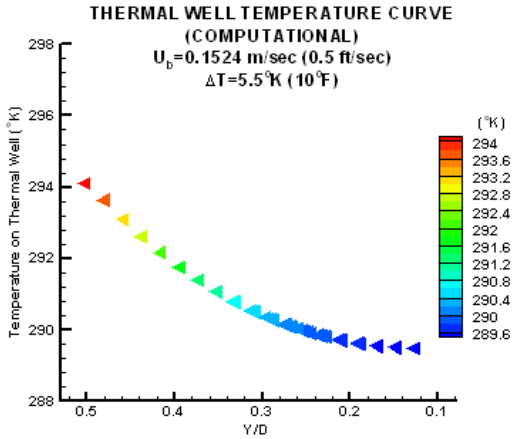

Fig. E-8 Temp Thermal Well (Computational)
V_0=0.1524 m/sec, ΔT_{wall}= 5.5°K

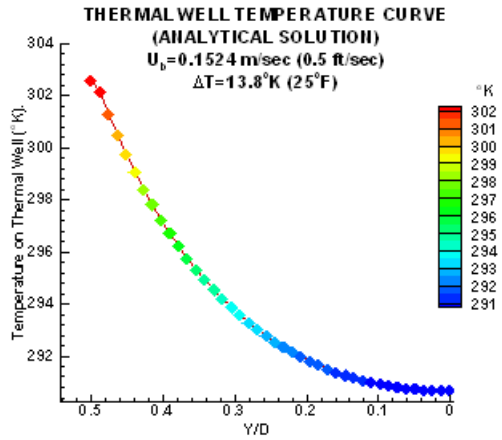

Fig. E-9 Temp Thermal Well (Analytical)
V_0=0.1524 m/sec, ΔT_{wall}=13.8°K

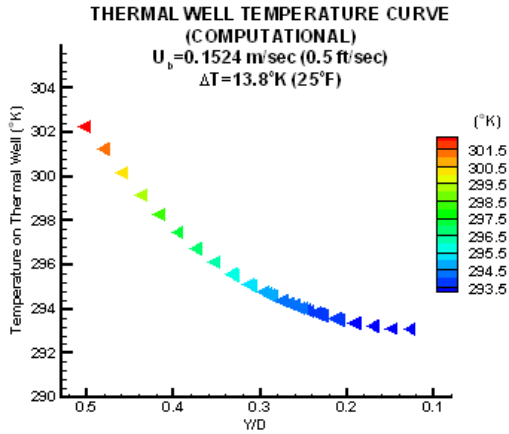

Fig. E-10 Temp Thermal Well (Computational)
V_0=0.1524 m/sec, ΔT_{wall}= 13.8°K

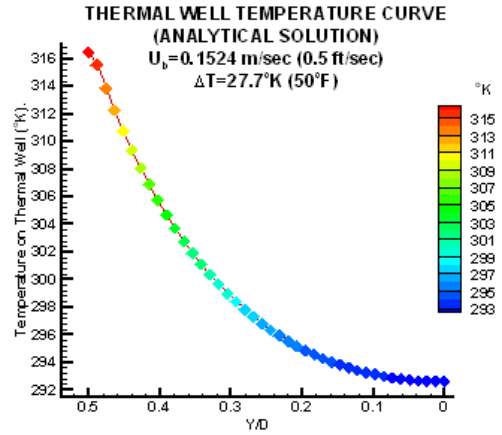

Fig. E-11 Temp Thermal Well (Analytical)
V_0=0.1524 m/sec, ΔT_{wall}=27.7°K

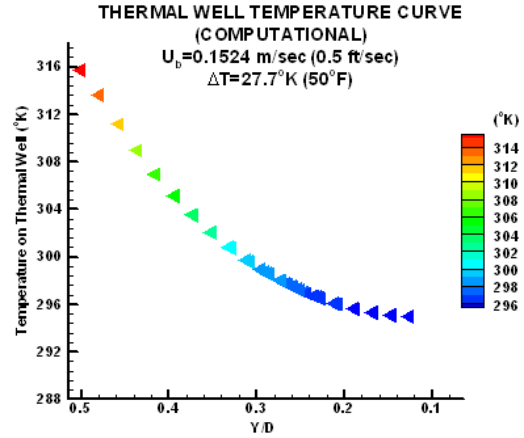

Fig. E-12 Temp Thermal Well (Computational)
V_0=0.1524 m/sec, ΔT_{wall}=27.7°K

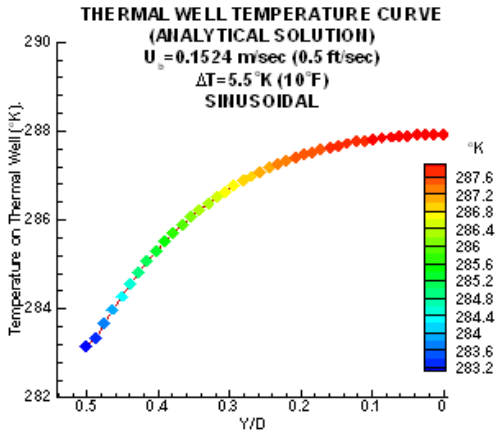

Fig. E-13 Temp Thermal Well (Analytical) V_0=0.1524 m/sec, ΔT_{wall}= -5.5°K Sinusoidal

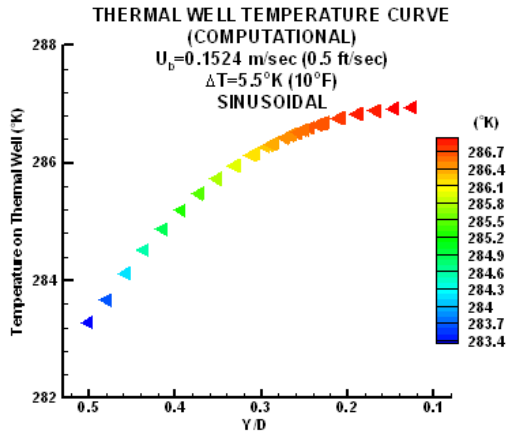

Fig. E-14 Temp Thermal Well (Computational) V_0=0.1524 m/sec, ΔT_{wall}=-5.5°K Sinusoidal

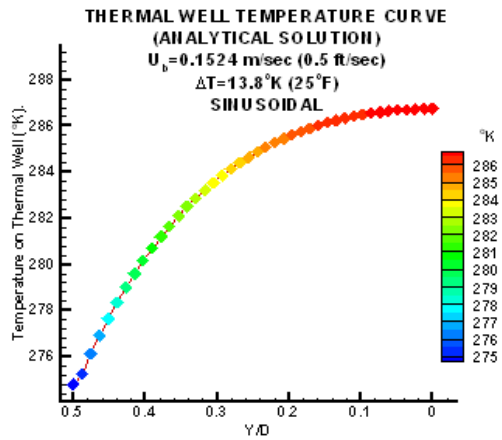

Fig. E-15 Temp Thermal Well (Analytical) V_0=0.1524 m/sec, ΔT_{wall}=-13.8°K Sinusoidal

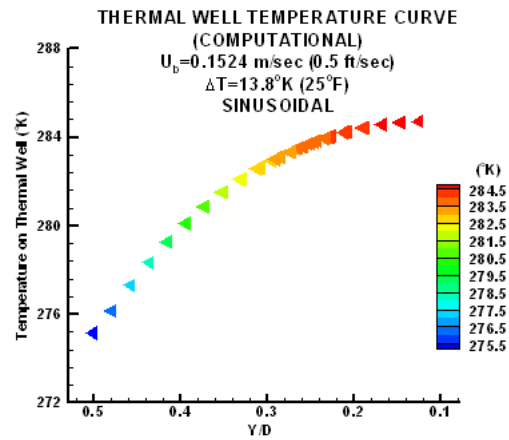

Fig. E-16 Temp Thermal Well (Computational) V_0=0.1524 m/sec, ΔT_{wall}=-13.8°K Sinusoidal

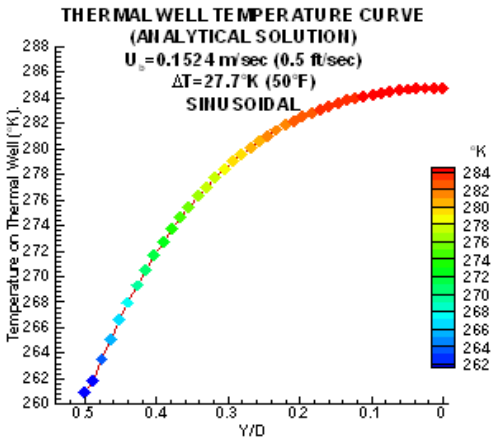

Fig. E-17 Temp Thermal Well (Analytical) V_0=0.1524 m/sec, ΔT_{wall}=-27.7°K Sinusoidal

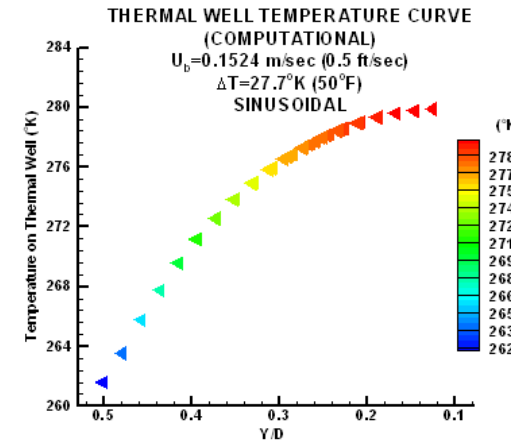

Fig. E-18 Temp Thermal Well (Computational) V_0=0.1524 m/sec, ΔT_{wall}=-27.7°K Sinusoidal

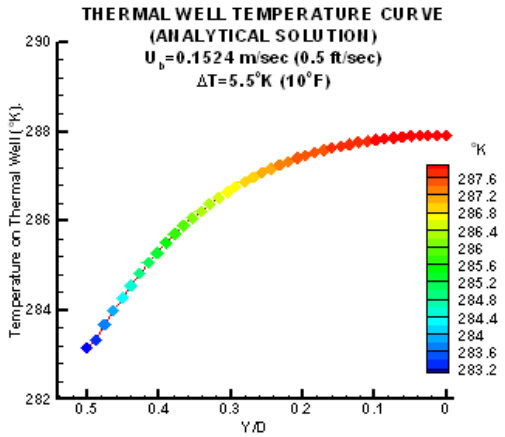

Fig. E-19 Temp Thermal Well (Analytical) V_0=0.1524 m/sec, ΔT_{wall}=-5.5°K

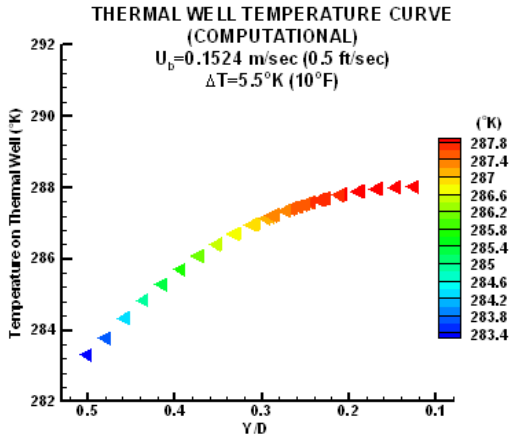

Fig. E-20 Temp Thermal Well (Computational) V_0=0.1524 m/sec, ΔT_{wall}=-5.5°K

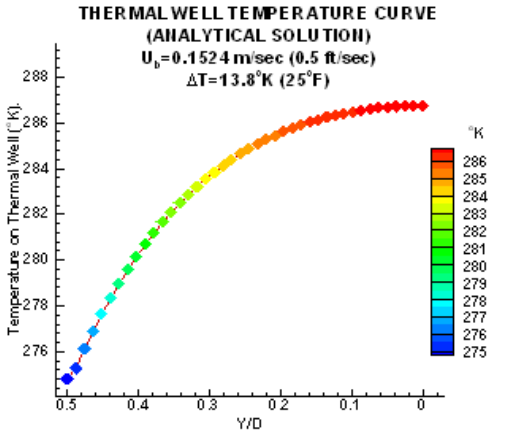

Fig. E-21 Temp Thermal Well (Analytical) V_0=0.1524 m/sec, ΔT_{wall}=-13.8°K

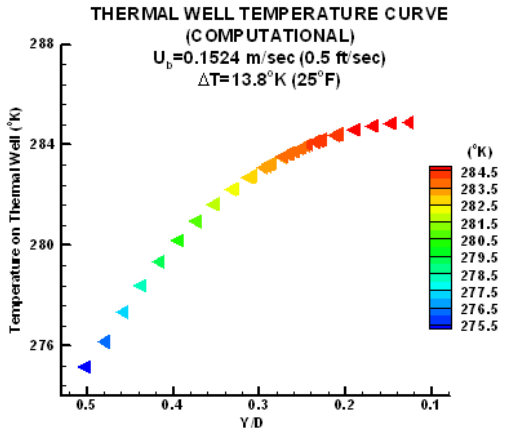

Fig. E-22 Temp Thermal Well (Computational) V_0=0.1524 m/sec, ΔT_{wall}=-13.8°K

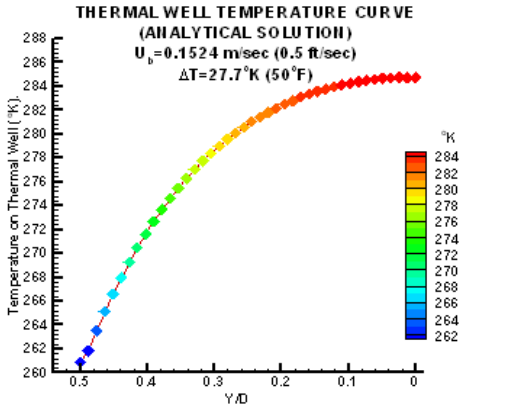

Fig. E-23 Temp Thermal Well (Analytical) V_0=0.1524 m/sec, ΔT_{wall}=-27.7°K

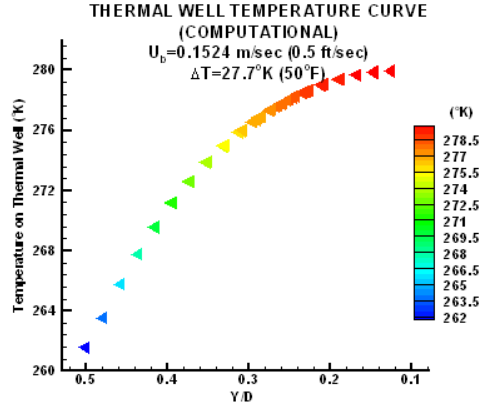

Fig. E-24 Temp Thermal Well (Computational) V_0=0.1524 m/sec, ΔT_{wall}=-27.7°K

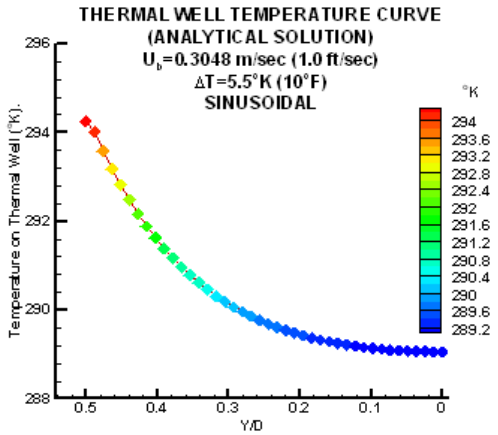

Fig. E-25 Temp Thermal Well (Analytical) V_0=0.3048 m/sec, ΔT_{wall}=5.5°K Sinusoidal

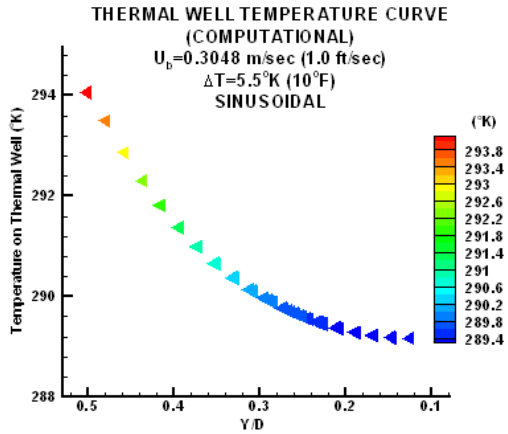

Fig. E-26 Temp Thermal Well (Computational) V_0=0.3048 m/sec, ΔT_{wall}=5.5°K Sinusoidal

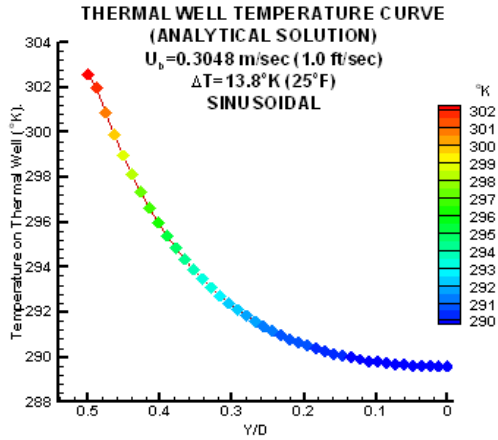

Fig. E-27 Temp Thermal Well (Analytical) V_0=0.3048 m/sec, ΔT_{wall}=13.8°K Sinusoidal

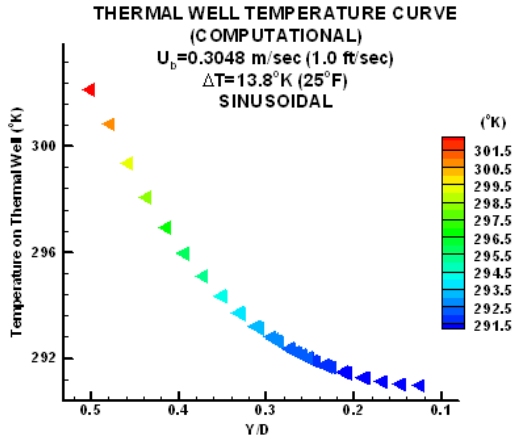

Fig. E-28 Temp Thermal Well (Computational) V_0=0.3048 m/sec, ΔT_{wall}=13.8°K Sinusoidal

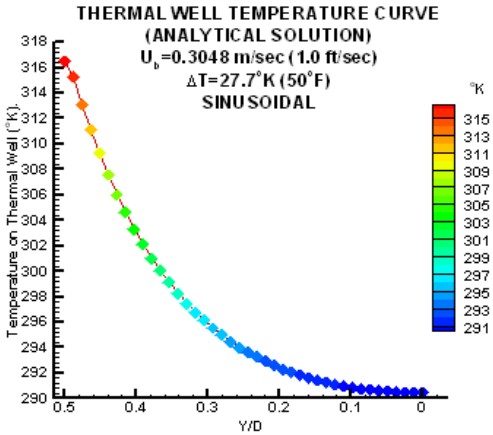

Fig. E-29 Temp Thermal Well (Analytical) V_0=0.3048 m/sec, ΔT_{wall}=27.7°K Sinusoidal

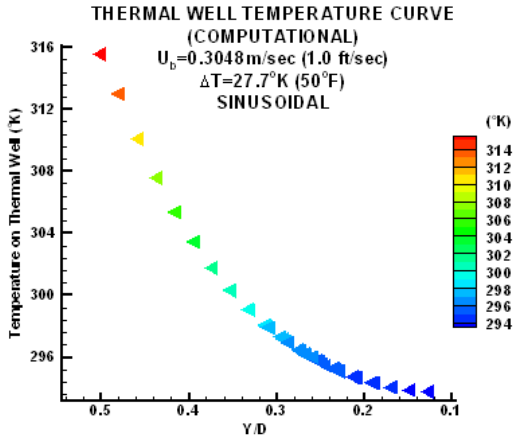

Fig. E-30 Temp Thermal Well (Computational) V_0=0.3048 m/sec, ΔT_{wall}=27.7°K Sinusoidal

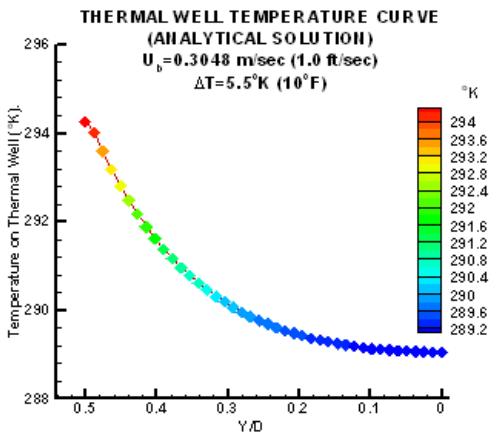

Fig. E-31 Temp Thermal Well (Analytical)
V_0=0.3048 m/sec, ΔT_{wall}=5.5°K

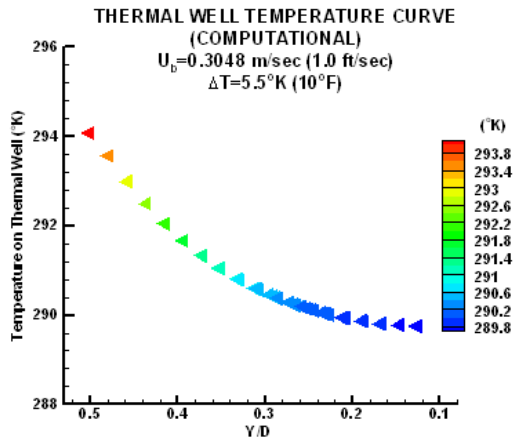

Fig. E-32 Temp Thermal Well (Computational)
V_0=0.3048 m/sec, ΔT_{wall}= 5.5°K

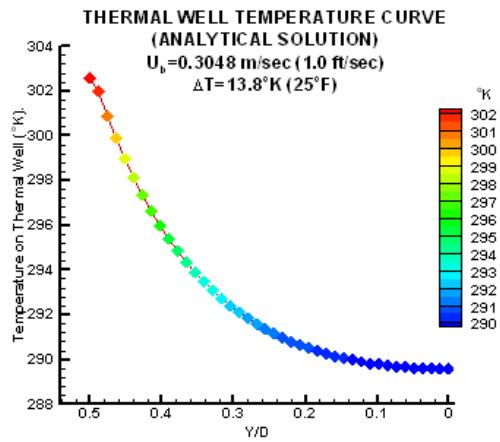

Fig. E-33 Temp Thermal Well (Analytical)
V_0=0.3048 m/sec, ΔT_{wall}=13.8°K

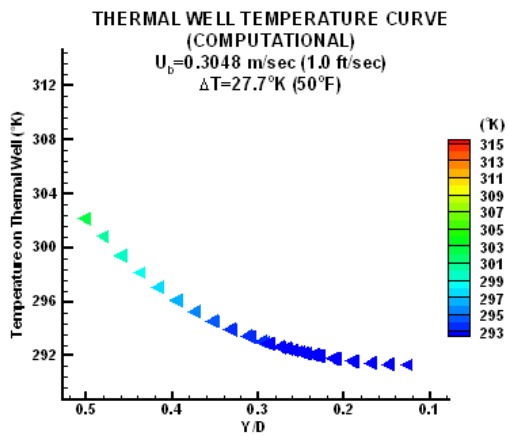

Fig. E-34 Temp Thermal Well (Computational)
V_0=0.3048 m/sec, ΔT_{wall}= 13.8°K

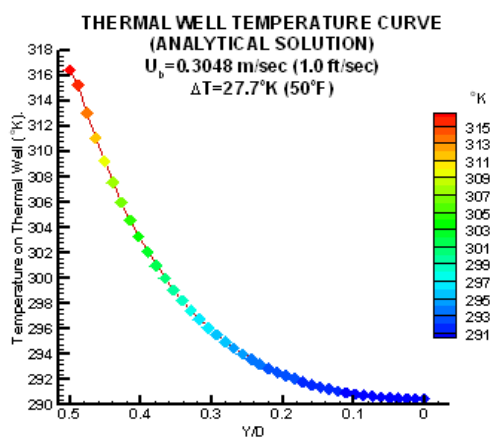

Fig. E-35 Temp Thermal Well (Analytical)
V_0=0.3048 m/sec, ΔT_{wall}=27.7°K

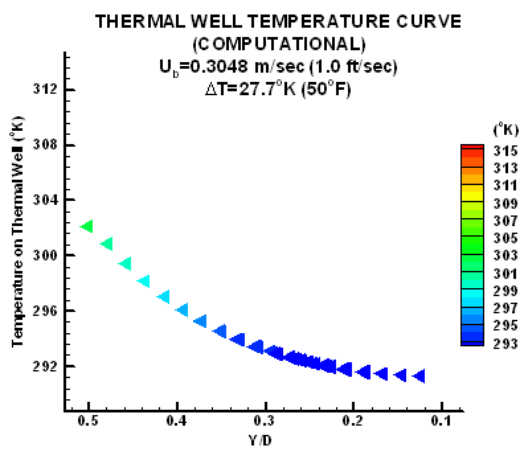

Fig. E-36 Temp Thermal Well (Computational)
V_0=0.3048 m/sec, ΔT_{wall}=27.7°K

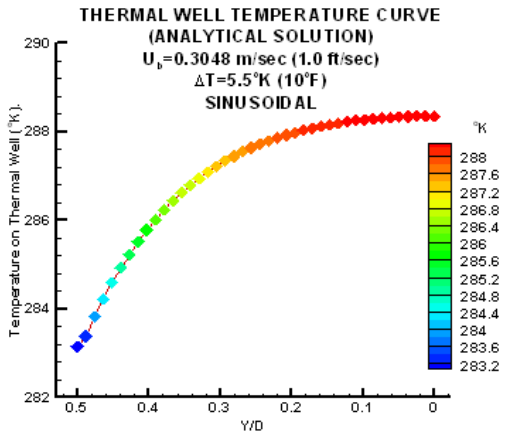

Fig. E-37 Temp Thermal Well (Analytical) V_0=0.3048 m/sec, ΔT_{wall}= -5.5°K Sinusoidal

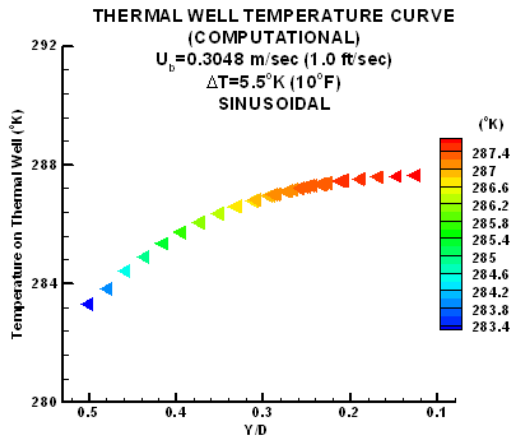

Fig. E-38 Temp Thermal Well (Computational) V_0=0.3048 m/sec, ΔT_{wall}=-5.5°K Sinusoidal

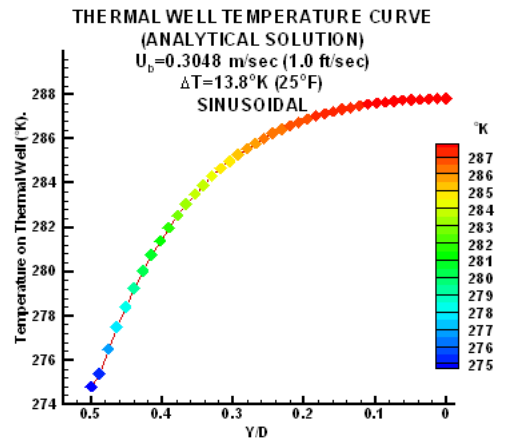

Fig. E-39 Temp Thermal Well (Analytical) V_0=0.3048 m/sec, ΔT_{wall}=-13.8°K Sinusoidal

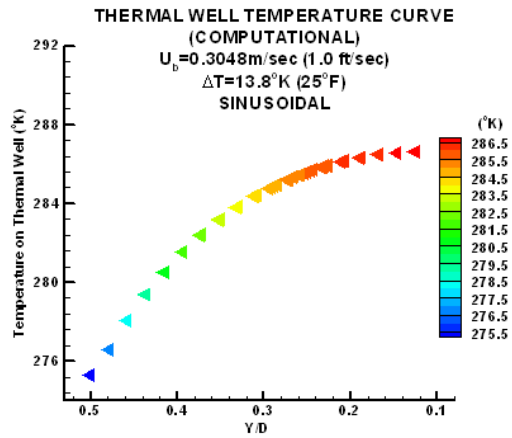

Fig. E-40 Temp Thermal Well (Computational) V_0=0.3048 m/sec, ΔT_{wall}=-13.8°K Sinusoidal

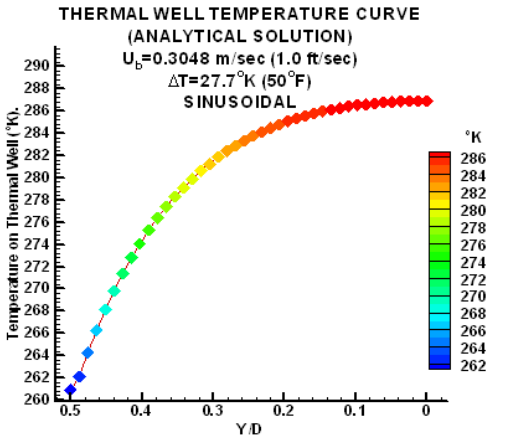

Fig. E-41 Temp Thermal Well (Analytical) V_0=0.3048 m/sec, ΔT_{wall}=-27.7°K Sinusoidal

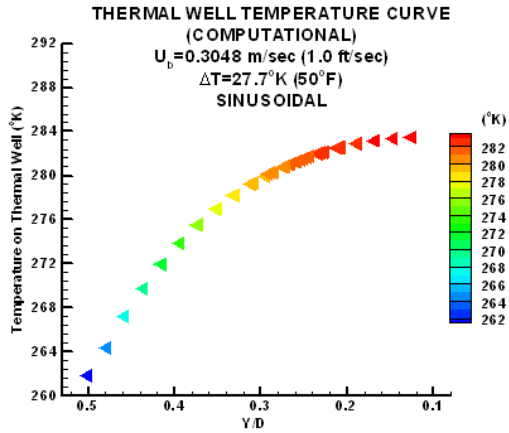

Fig. E-42 Temp Thermal Well (Computational) V_0=0.3048 m/sec, ΔT_{wall}=-27.7°K Sinusoidal

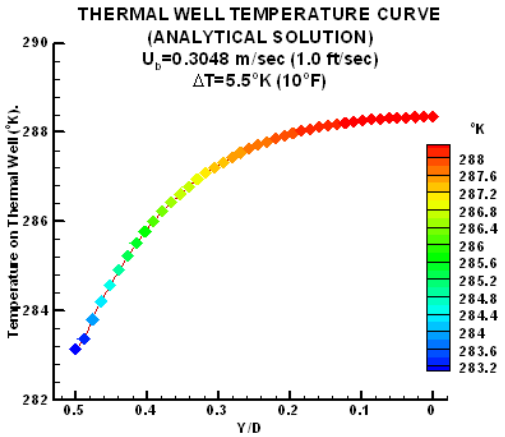

Fig. E-43 Temp Thermal Well (Analytical)
V_0=0.3048 m/sec, ΔT_{wall}=-5.5°K

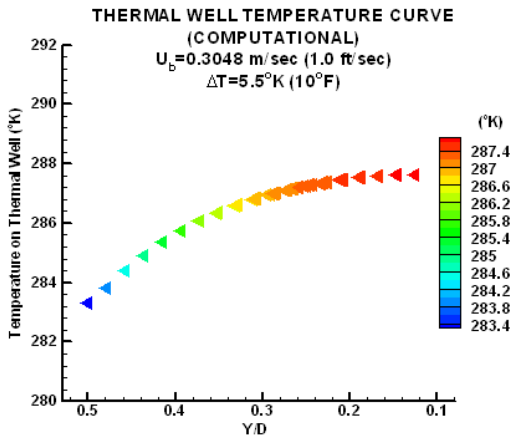

Fig. E-44 Temp Thermal Well (Computational)
V_0=0.3048 m/sec, ΔT_{wall}=-5.5°K

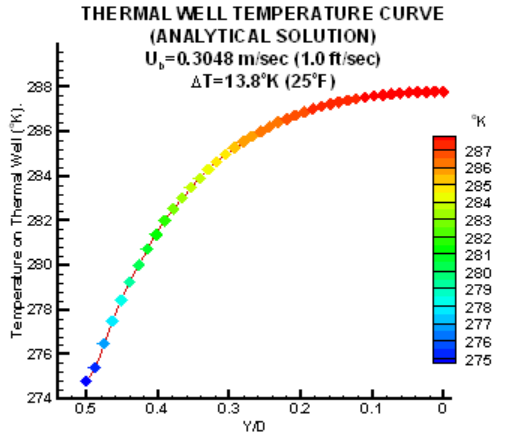

Fig. E-45 Temp Thermal Well (Analytical)
V_0=0.3048 m/sec, ΔT_{wall}=-13.8°K

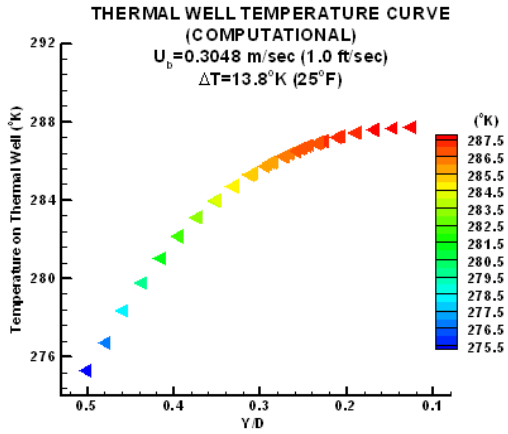

Fig. E-46 Temp Thermal Well (Computational)
V_0=0.3048 m/sec, ΔT_{wall}=-13.8°K

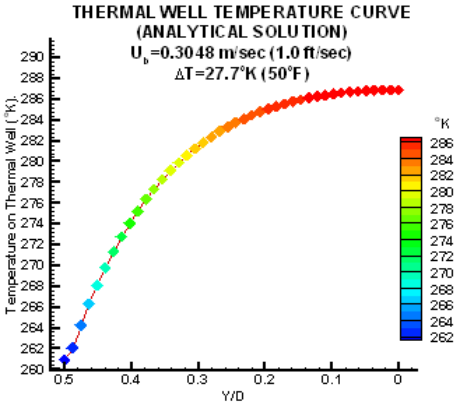

Fig. E-47 Temp Thermal Well (Analytical)
V_0=0.3048 m/sec, ΔT_{wall}=-27.7°K

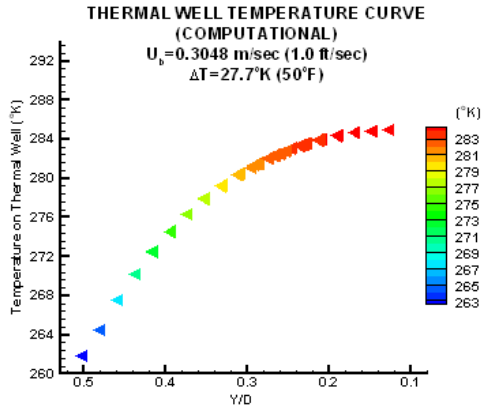

Fig. E-48 Temp Thermal Well (Computational)
V_0=0.3048 m/sec, ΔT_{wall}=-27.7°K

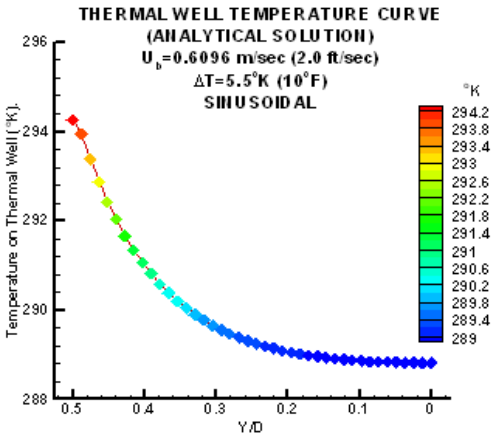

Fig. E-49 Temp Thermal Well (Analytical) V_0=0.6096 m/sec, ΔT_{wall}=5.5°K Sinusoidal

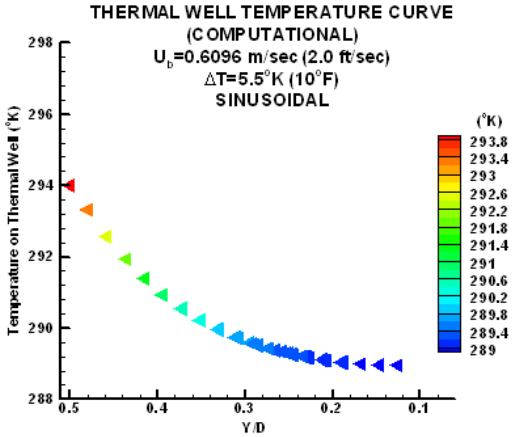

Fig. E-50 Temp Thermal Well (Computational) V_0=0.6096 m/sec, ΔT_{wall}=5.5°K Sinusoidal

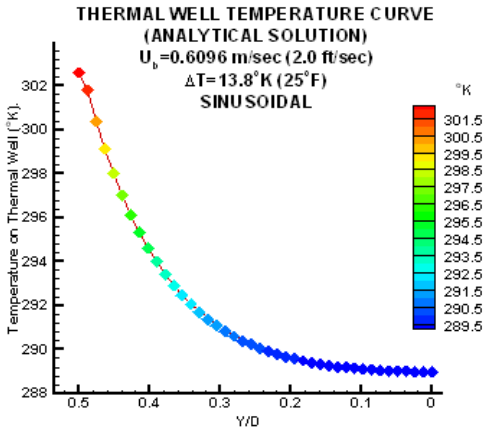

Fig. E-51 Temp Thermal Well (Analytical) V_0=0.6096 m/sec, ΔT_{wall}=13.8°K Sinusoidal

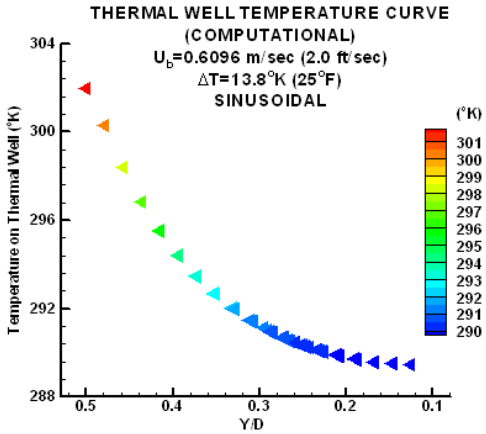

Fig. E-52 Temp Thermal Well (Computational) V_0=0.6096 m/sec, ΔT_{wall}=13.8°K Sinusoidal

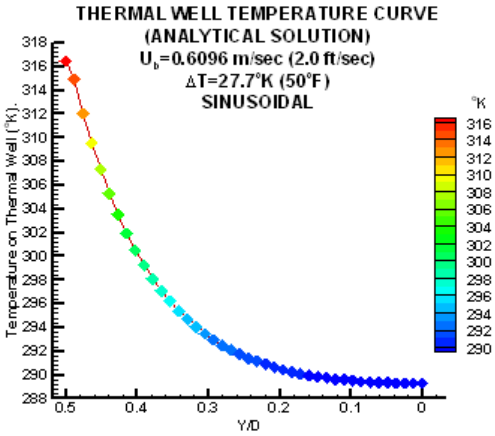

Fig. E-53 Temp Thermal Well (Analytical) V_0=0.6096 m/sec, ΔT_{wall}=27.7°K Sinusoidal

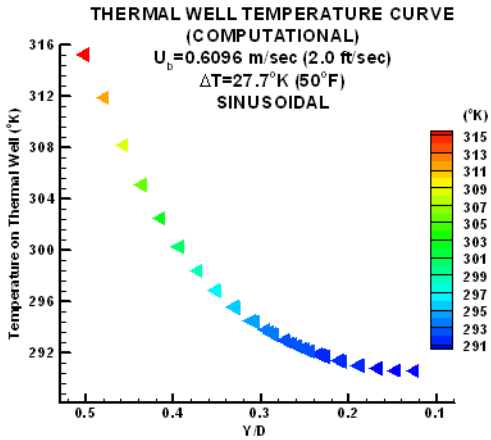

Fig. E-54 Temp Thermal Well (Computational) V_0=0.6096 m/sec, ΔT_{wall}=27.7°K Sinusoidal

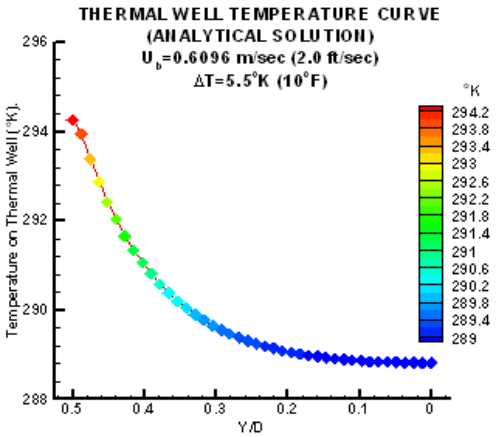

Fig. E-55 Temp Thermal Well (Analytical)
V_0=0.6096 m/sec, ΔT_{wall}=5.5°K

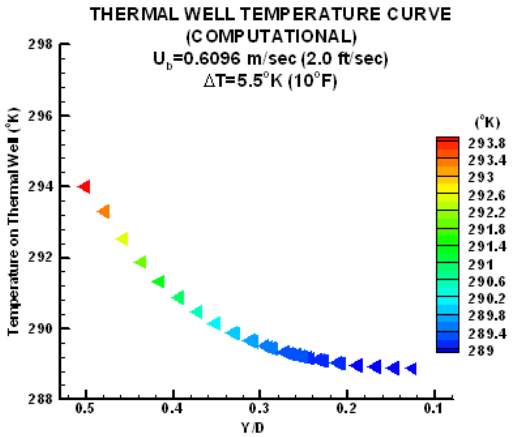

Fig. E-56 Temp Thermal Well (Computational)
V_0=0.6096 m/sec, ΔT_{wall}= 5.5°K

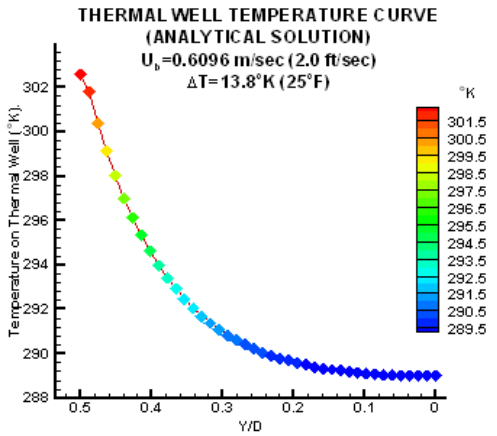

Fig. E-57 Temp Thermal Well (Analytical)
V_0=0.6096 m/sec, ΔT_{wall}=13.8°K

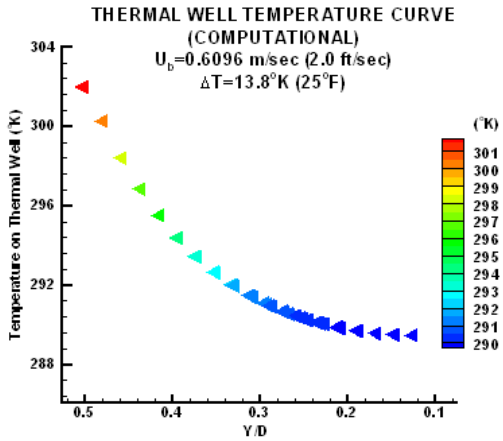

Fig. E-58 Temp Thermal Well (Computational)
V_0=0.6096 m/sec, ΔT_{wall}= 13.8°K

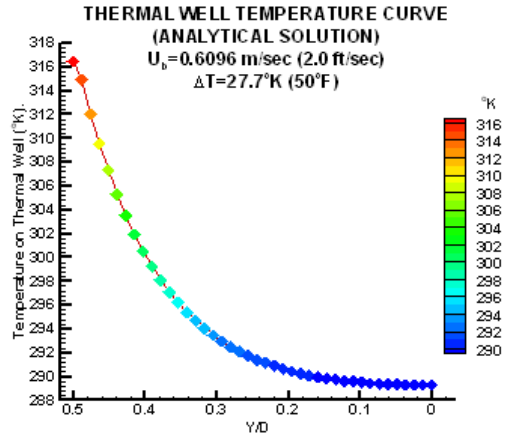

Fig. E-59 Temp Thermal Well (Analytical)
V_0=0.6096 m/sec, ΔT_{wall}=27.7°K

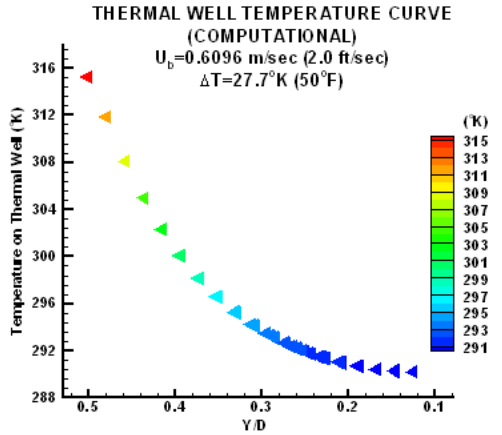

Fig. E-60 Temp Thermal Well (Computational)
V_0=0.6096 m/sec, ΔT_{wall}=27.7°K

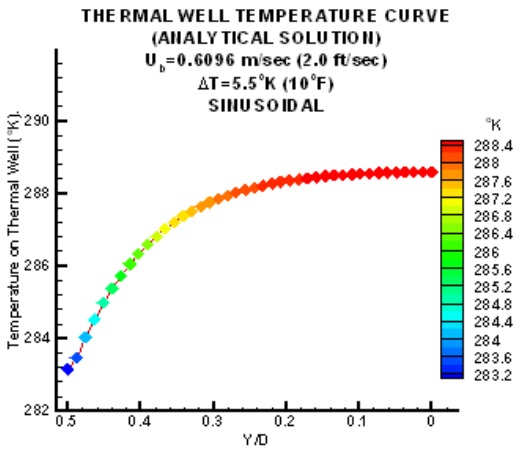

Fig. E-161 Temp Thermal Well (Analytical)
V_0=0.6096 m/sec, ΔT_{wall}= -5.5°K Sinusoidal

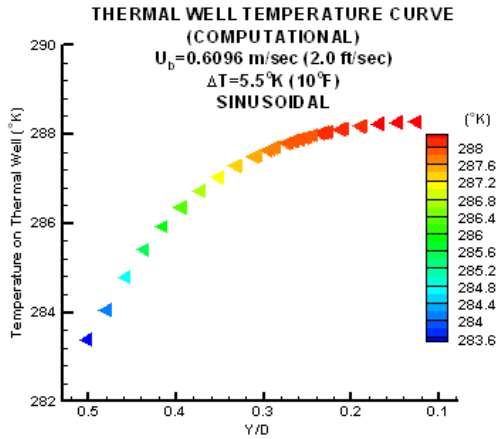

Fig. E-62 Temp Thermal Well (Computational)
V_0=0.6096 m/sec, ΔT_{wall}=-5.5°K Sinusoidal

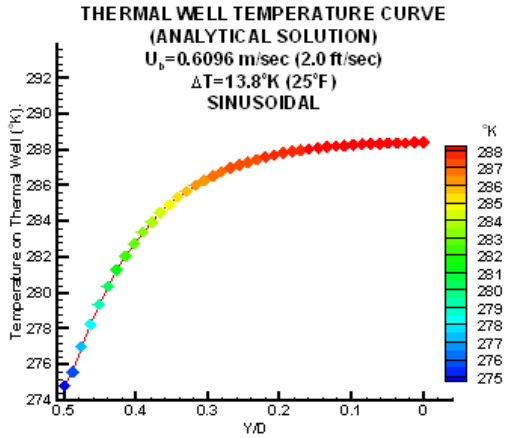

Fig. E-63 Temp Thermal Well (Analytical)
V_0=0.6096 m/sec, ΔT_{wall}=-13.8°K Sinusoidal

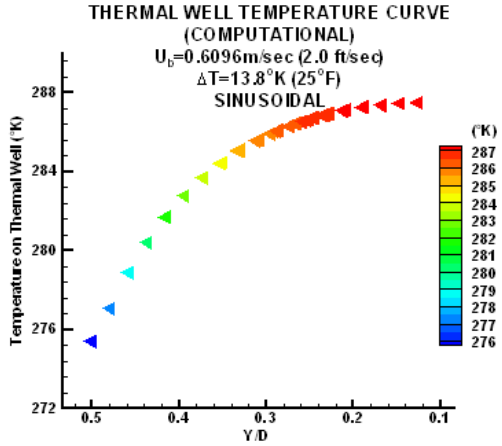

Fig. E-64 Temp Thermal Well (Computational)
V_0=0.6096 m/sec, ΔT_{wall}=-13.8°K Sinusoidal

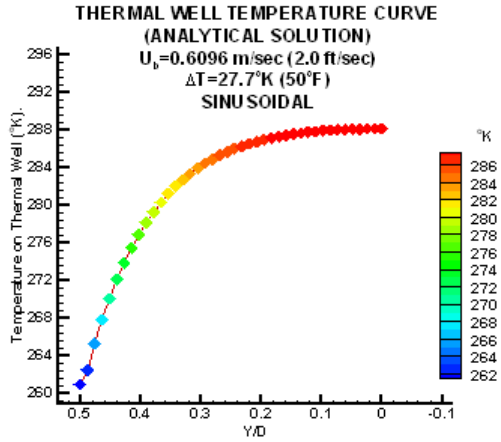

Fig. E-65 Temp Thermal Well (Analytical)
V_0=0.6096 m/sec, ΔT_{wall}=-27.7°K Sinusoidal

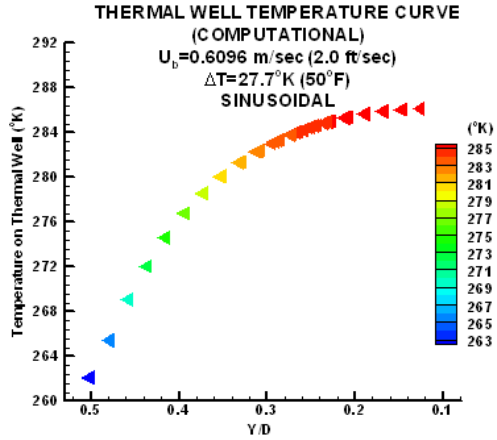

Fig. E-66 Temp Thermal Well (Computational)
V_0=0.6096 m/sec, ΔT_{wall}=-27.7°K Sinusoidal

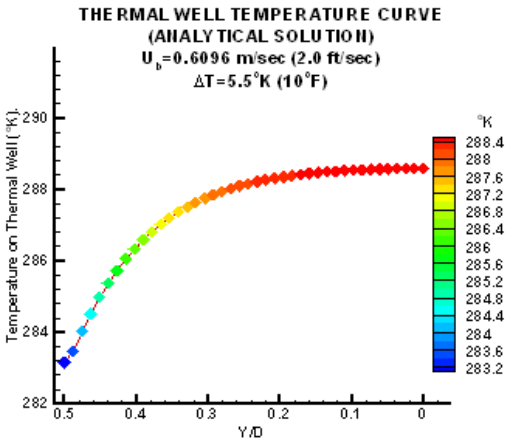

Fig. E-67 Temp Thermal Well (Analytical)
V_0=0.6096 m/sec, ΔT_{wall}=-5.5°K

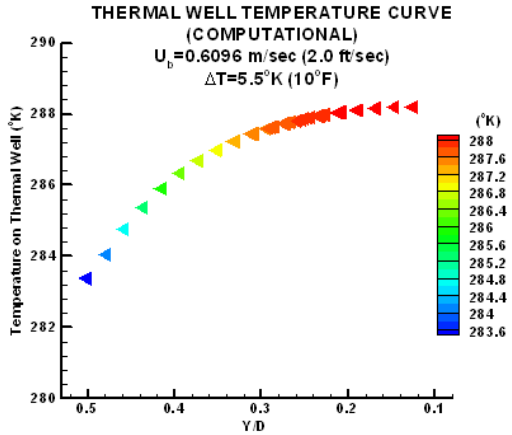

Fig. E-68 Temp Thermal Well (Computational)
V_0=0.6096 m/sec, ΔT_{wall}=-5.5°K

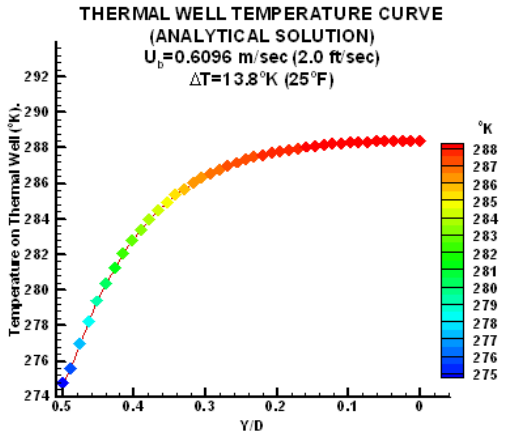

Fig. E-69 Temp Thermal Well (Analytical)
V_0=0.6096 m/sec, ΔT_{wall}=-13.8°K

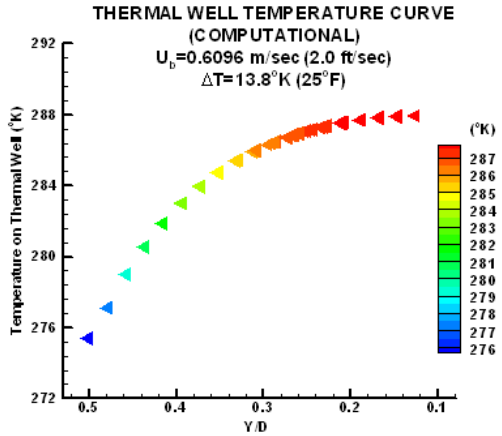

Fig. E-70 Temp Thermal Well (Computational)
V_0=0.6096 m/sec, ΔT_{wall}=-13.8°K

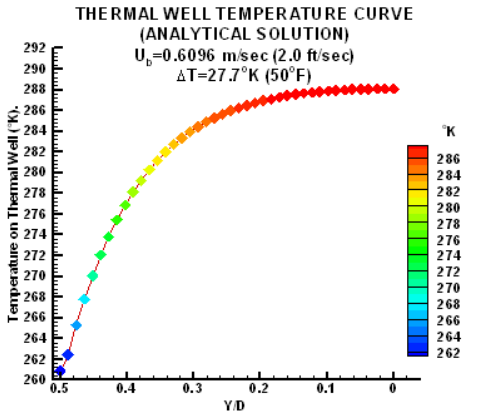

Fig. E-71 Temp Thermal Well (Analytical)
V_0=0.6096 m/sec, ΔT_{wall}=-27.7°K

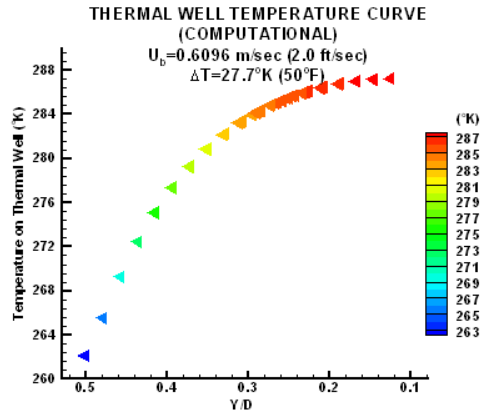

Fig. E-72 Temp Thermal Well (Computational)
V_0=0.6096 m/sec, ΔT_{wall}=-27.7°K

VITA

Pardeep Singh Brar was born on May 11, 1980 in Singapore. He attended Birla Institute of Technology, Ranchi where he earned his B.E. in mechanical engineering in 2002. He continued his studies at Texas A&M University where he earned his M.S. degree in mechanical engineering in 2004. He can be reached at D-1/13, Janakpuri, New Delhi–110058, India or at his e-mail address pardeepbrar@yahoo.com.